RJES

RUSSIAN
JOURNAL *of*
EARTH SCIENCES

Vol. 24
Issue 4

Arctic Water Current in the Bear Island Trough

E. G. Morozov[1,*], **D. I. Frey**[1], **and A. N. Novigatsky**[1]

[1]Shirshov Institute of Oceanology RAS, Moscow, Russia
* **Correspondence to:** Eugene Morozov, egmorozov@mail.ru

Abstract: We analyzed Conductivity-temperature-depth (CTD) and moored Acoustic Doppler Current Profiler (ADCP) measurements in the western Barents Sea carried out onboard the Russian R/V Akademik Mstislav Keldysh (cruise 68) in July–August 2017. A hydrographic section in the Bear Island Trough has been made. Comparison of water properties in the trough and in the sea has been performed. We compared the tidal currents measured on the mooring with those from the TPXO9 model and found that they are quite close.

Keywords: Barents Sea, Norwegian Sea, CTD and ADCP measurements, mooring, tidal ellipses, ocean circulation, tide.

Citation: Morozov, E. G., D. I. Frey, and A. N. Novigatsky (2024), Arctic Water Current in the Bear Island Trough, *Russian Journal of Earth Sciences*, 24, ES4001, EDN: BXWCJO, https://doi.org/10.2205/2024es000925

Research Article

Received: 2 July 2024
Accepted: 29 July 2024
Published: 9 October 2024

Introduction

Interaction between dense and cold Arctic waters and relatively warmer Atlantic waters is an important property of the entire North Atlantic region and a key mechanism of climate formation in Russia and whole Europe. The Barents Sea is an important region of strong interaction between these waters. Together with the Fram Strait it contributes to the water mass exchange between the Arctic and Atlantic oceans [*Giraudeau et al.*, 2016]. The Barents Sea is located in a relatively shallow basin north of Europe (Figure 1).

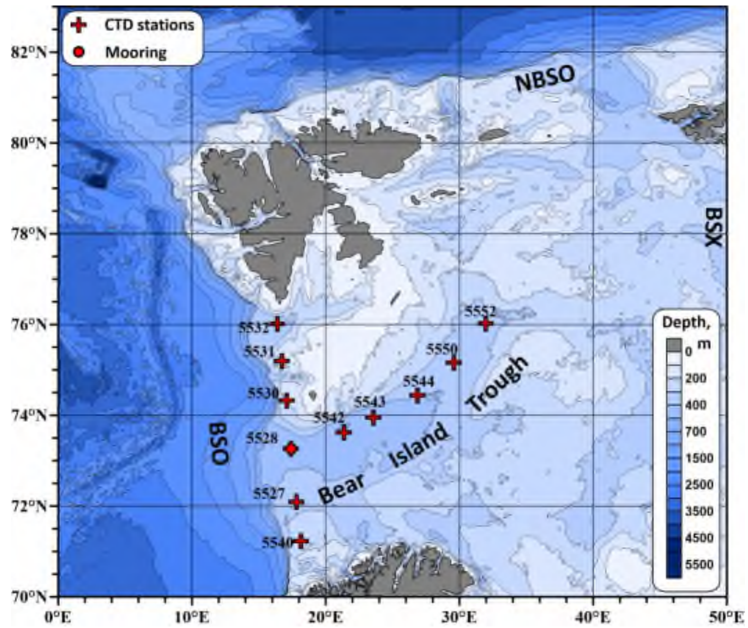

Figure 1. Locations of measurements in the western Barents Sea in July–August 2017. Red crosses show our Conductivity-temperature-depth (CTD) stations; red circle is the site of mooring deployment in the Bear Island Trough. Bathymetry is based on GEBCO 2019 data. Abbreviations: Northern Barents Sea Opening (NBSO); Barents Sea Opening (BSO); Barents Sea Exit (BSX).

The terms for geographical names in the region are the following: the western boundary of the sea is the Barents Sea Opening (BSO) [*Smedsrud et al.*, 2013]; the northern boundary is the Northern Barents Sea Opening (NBSO) [*Lind and Ingvaldsen*, 2012]. The eastern strait between Franz Josef Land and Novaya Zemlya is the Barents Sea Exit (BSX) [*Gammelsrød et al.*, 2009]. Water exchange occurs through all three boundaries [*Årthun et al.*, 2011].

The Bear Island Trough is the deepest channel for the water exchange between the Norwegian and Barents seas. Its depths reach 500 m; the background depths of the upper parts of its walls are 100–200 meters shallower. The length of the trough exceeds 500 km and its width is approximately 100 km. The slow bottom current of the Deep Barents Sea water in the Bear Island Trough is directed to the Norwegian Sea [*Lukashin and Shcherbinin*, 2007].

The flow of cold and dense Barents Sea waters through the Bear Island Trough is one of the partial sources of Iceland-Scotland Overflow Water (ISOW), which is generally formed in the Norwegian Sea. In winter, cold dense water is formed here due to intense heat transfer to the atmosphere. The water mass that is formed when flowing over the sill in the Faroe-Shetland Channel is called Iceland-Scotland Overflow Water (ISOW). This water mass mixes with the warmer and saltier waters of the Northeast Atlantic. As a result, ISOW turns out to be significantly saltier and warmer than the deep water that penetrates into the Atlantic through the Denmark Strait between Greenland and Iceland (Denmark Strait Overflow Water, DSOW).

In the Atlantic Ocean, North Atlantic Deep Water occupies a layer between 1200 and 4000 m. According to [*Koltermann et al.*, 1999], the densest waters are located in the bottom layers of the Arctic Ocean, but they cannot propagate to the Atlantic owing to the shallow thresholds east of Iceland: Iceland-Faroe and Faroe-Shetland submarine ridges with depths of 480 and 840 m, respectively [*Aken and Boer*, 1995; *Dickson and Brown*, 1994; *Koltermann et al.*, 1999; *Lankhorst and Zenk*, 2006]. A deep (650 m) pathway is also located between Greenland and Iceland.

Waters located above the limiting ridges flow to the Atlantic through the Denmark Strait (Denmark Strait Overflow Water, DSOW) [*Jochumsen et al.*, 2012] and Iceland-Scotland thresholds (Iceland-Scotland Overflow Water, ISOW) [*Mauritzen et al.*, 2005; *Olsen et al.*, 2008]. Iceland-Scotland Overflow Water is formed when water from the Norwegian Sea overflows the thresholds east of Iceland. It is generally accepted that North Atlantic Deep Water is formed as a result of mixing between Labrador Sea Water, Iceland-Scotland Overflow Water, Denmark Strait Overflow Water, and Mediterranean Sea Water [*Talley*, 2011]. Oceanographers divide the flow of NADW into three layers: Upper (UNADW), Middle (MNADW), and Lower (LNADW). There is no commonly accepted opinion about the origin of North Atlantic Deep Water components.

The goal of this paper was to analyze the deep flow in the Bear Island Trough based on the data in July–August 2017 and a numerical model. We also compared the measured tides with the existing tidal models based on satellite altimetry.

Data and Methods

On July 23 – August 3, 2017, we occupied two CTD sections across and along the Bear Island Trough in the western Barents Sea. Each section included six stations. We deployed a mooring with an Acoustic Doppler Current Profiler (ADCP) close to the bottom at the point of intersection (station 5528 at 73°15.6′ N, 17°24.6′ E) between these two sections in the deepest part of the Bear Island Trough. The bottom topography along the sections was measured by the Kongsberg EA600 12 kHz single beam echo sounder. The locations of the CTD stations and mooring are shown in Figure 1.

The CTD profiles were measured from the surface to the bottom (3–4 m above the seafloor) using a Sea-Bird SBE 911plus profiler. This CTD system was equipped with two parallel temperature and conductivity sensors; the mean temperature difference between them did not exceed 0.001 °C, while that of salinity was not greater than 0.001 PSU. The raw

CTD data were processed by SBE Data Processing software version 7.23.2 with standard parameters described in [*Sea-Bird Electronics Inc.*, 2014].

We also used the satellite altimetry data and the TPXO9 model [*Egbert and Erofeeva*, 2002] to plot tidal ellipses and analyze tides from the mooring measurements and altimetry.

Results and Discussion

Surface currents in the region of the Bear Island Trough are well studied [*Beszczynska-Möller et al.*, 2012]. Geostrophic currents based on satellite altimetry averaged over 1993–2020 are shown in Figure 2. Atlantic water transported by the North Atlantic Current overflows the Iceland-Scotland Ridge and continues as the Norwegian Atlantic Current. This current maintains a two-branch structure in the Nordic Seas towards the Fram Strait. Both branches follow topography, the eastern branch (the Norwegian Atlantic Slope Current) is a current along the continental slope west of Norway. Part of this flow separates and turns to the north. The western branch of the Norwegian Atlantic Current or Norwegian Atlantic Front Current flows as a topographically guided stream to the Fram Strait. Near Spitsbergen, both branches merge into the West Spitsbergen Current. However, only a part of the West Spitsbergen Current continues into the Arctic Ocean, while a significant amount recirculates in the Fram Strait and returns south to the Nordic Seas [*Schauer et al.*, 2004]. North of Cape Nordkap, the eastern branch (Norwegian Atlantic Slope Current) enters the Barents Sea. Part of the West Spitsbergen Current near Bear Island separates from the main current and turns east. Geostrophic currents based on long term satellite data are shown in Figure 2 and confirm this scheme.

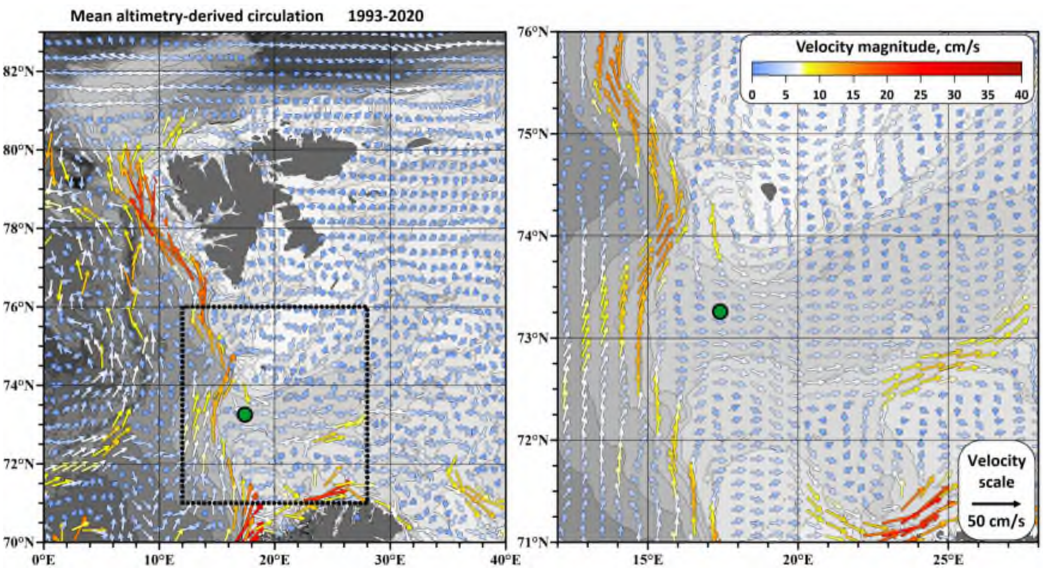

Figure 2. Surface geostrophic currents in the Norwegian Sea based on satellite altimetry averaged over 1993–2020. Part of this map confined by black square is shown in the right panel. The green dot shows location of our mooring in the Bear Island Trough (station 5528).

A similar scheme of currents but based on the altimetry only on the data on July 26, 2017 (the day of our mooring operation) is shown in Figure 3. A distinguishing difference is a stronger southern branch separated from the West Spitsbergen Current west of Bear Island, which turns to the east at 74°N following bottom topography. In addition, the current north of Cape Nordkap is poorly pronounced.

To study the bottom circulation in the region, we applied the Institute of Numerical Mathematics Ocean Model (INMOM) to simulate the circulation in the bottom layer of the Norwegian Sea [*Diansky et al.*, 2002, 2021; *Morozov et al.*, 2019; *Zalesny et al.*, 2012]. This model is based on the system of the so-called primitive ocean hydrodynamic equations in spherical horizontal coordinates. We apply the hydrostatic and Boussinesq approximations and the vertical σ-coordinate system. The results of model simulations are shown in

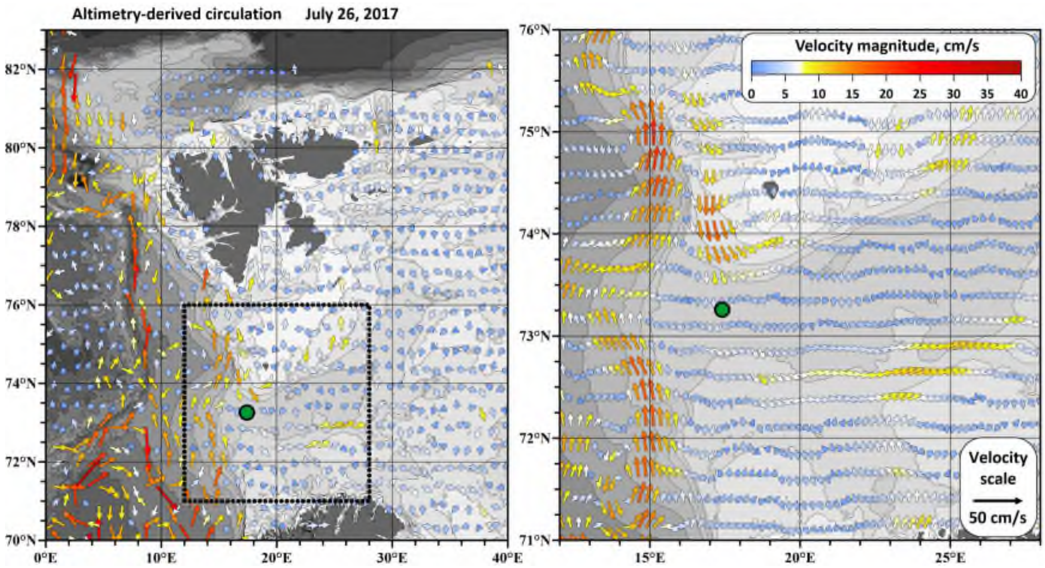

Figure 3. Same as in Figure 2, but on the day of July 26, 2017.

Figure 4, which presents the vectors of currents in the bottom layer in July [*Morozov et al.*, 2019]. Bottom currents are quite weak and generally there are no high-velocity jets in the entire sea except for the bottom stream of the bottom water from the Barents Sea flowing through the Bear Island Trough to the southwest. This bottom stream turns to the north around Spitsbergen. These conclusions are consistent with the conclusions based on the direct measurements in the Bear Island Trough in 2017 [*Frey et al.*, 2017]. The model results for July 2017 are shown in Figure 4.

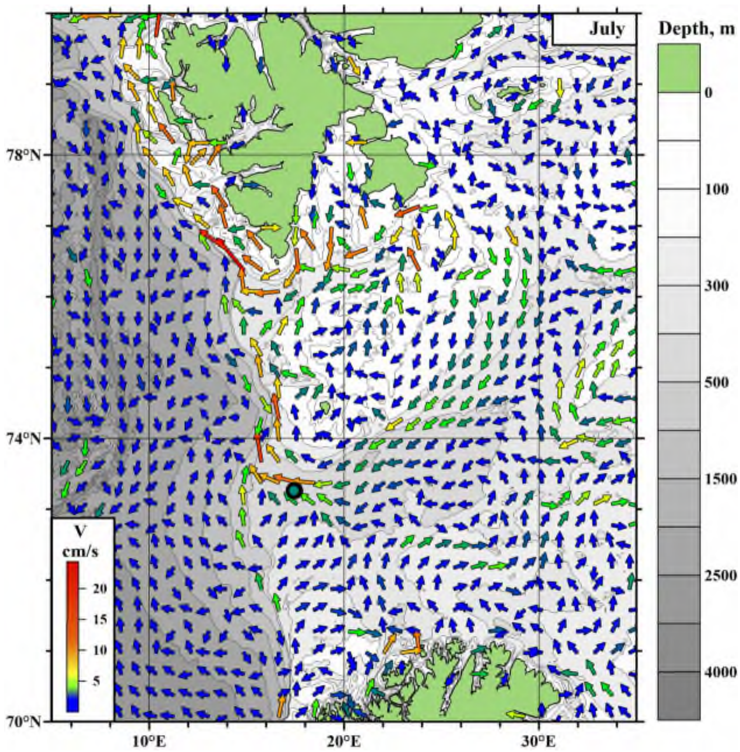

Figure 4. Bottom model currents in the Norwegian Sea based on simulations using the INMOM model for July 2017. The green dot shows the location of our mooring in the Bear Island Trough (station 5528).

This descending flow of cold water in the Bear Island is also illustrated by the water structure over the temperature and salinity sections along the trough. Sections of potential temperature, salinity, and density are shown in Figures 5a, 5b, 5c.

One can see from the figure that a tongue of cold and low saline water descends down the trough. Based on the numerical simulations the velocity of the flow is low. It is of the order of 2–4 cm/s, which gives a time of half a year for a water particle to flow along the trough. In the lower part of the flow the current accelerates, but arrives to the mooring with a lower speed.

The flow in the Bear Island Trough enters the Norwegian Sea at the depths of ~450 m. Thus, the inflowing water appears in the upper part of the water column. The water in the columns up to 850 m deep overflows the Faroe Threshold and becomes part of Iceland-Scotland Overflow Water. Figure 6 shows comparison between the water density in the deep open part of the Norwegian Sea and that in the Bear Island Trough. The water density in the Bear Island Trough is lower than in the open sea because of the excess of freshwater from land, while the water in the open sea is in direct contact with the Arctic Ocean.

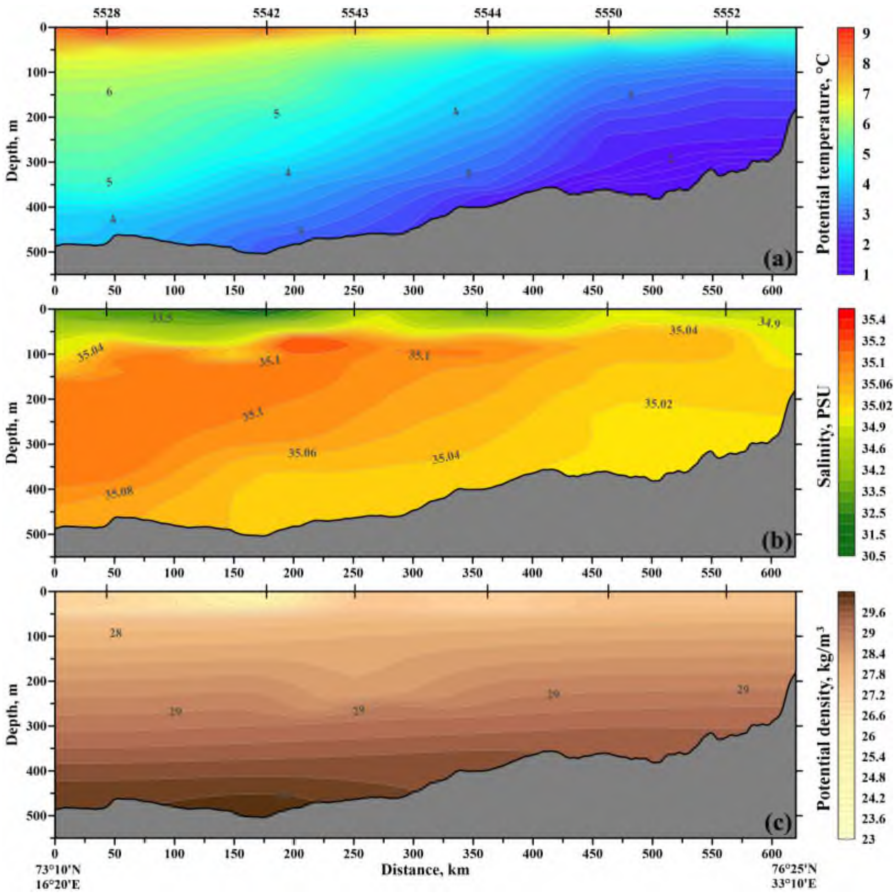

Figure 5. Sections of potential temperature (a), salinity, (b), and sigma-T density (c) along the Bear Island Trough.

No water descent is seen in the density section because the process is density compensated by the process of double diffusion developing over a time period of approximately half a year. Let us estimate whether conditions allow the existence of double diffusion. Double diffusion occurs when cold and low saline water is located above warmer and more saline water. In our case cold, low saline Arctic water descends into the layers of warmer Atlantic water with greater salinity. Thus, the density flux occurs from top to bottom, and the effective density diffusion is positive, which means that the colder water warms [*Kantha and Clayson*, 2000].

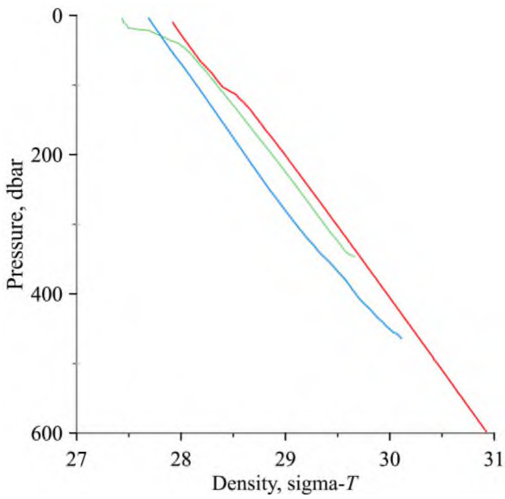

Figure 6. Vertical variation of density at the station in the deep part of the sea at a depth of 3475 m in March 1982 (74.5°N, 4.6°E) (red line) and at stations 5532 (green) and 5550 (blue).

A horizontal flow of colder and less saline water descends in the trough and colder water appears in warmer water of higher salinity. Mechanical mixing occurs, which is accompanied by a faster heat exchange than that with salt and other ions. Warm water of higher salinity in this case ascends. This is a slow process but we estimated the time of the particle motion along the trough as six months, which is enough for this mechanism to be in force.

It was proposed in [*Turner*, 1973] to use the gradient ratio $R_\rho = \alpha T_z/\beta S_z$ to estimate the relative intensity of double diffusion. Here, $\alpha = -\rho^{-1}\partial\rho/\partial T$ is the coefficient of thermal expansion, and $\beta = \rho^{-1}\partial\rho/\partial T$ is the coefficient of salinity compression, ρ is density, and T_z, S_z are vertical gradients of temperature and salinity. The change in density with a change in salinity is approximately 10 times greater than with a change in temperature if they change by one unit. In the ocean, where cold and low saline waters border with warm and salty waters, coefficient R_ρ is close to unity since temperature and salinity have opposite effects on density. Both forms of double diffusion are most intense when coefficient R_ρ is close to unity [*Shi and Wei*, 2007].

Physical parameters are determined from the data of measurements, which makes it possible to study double diffusion structures. Turner angles (Tu) are used to study and classify double diffusion [*Ruddick*, 1983], which are determined by the density coefficient (R_ρ). In our study area in the Bear Island Trough at depths of 300–350 m we have:

$$R_\rho = \frac{\alpha}{\beta}\frac{T_z}{S_z} = 1.9,$$

where, α is the coefficient of thermal expansion, $\alpha = 150 \times 10^{-6}/^\circ$C for temperatures close to 0 °C; β is salinity compression coefficient is $\beta = -7 \times 10^{-4}$ or 0.7 kg/g. The vertical temperature gradient in the study area at depths of 300–350 m is $T_z = 0.008^\circ$C/m, the salinity gradient is $S_z = 0.001$/m. Coefficient $R_\rho = 1.9$ is not very much greater than unity, which gives reason to believe that double diffusion is possible. Double diffusion occurs at positive values of the density ratio R_ρ, that is, in other words, when the vertical gradients of temperature and salinity have the same sign. Density ratio R_ρ is related to the Turner's angle as $R_\rho = \tan Tu$ [*Turner*, 1973]. The most favorable conditions for double diffusion are formed when $R_\rho = 1$ ($Tu = 45^\circ$). In our case $Tu = 60^\circ$ ($\tan 62^\circ = 1.88$).

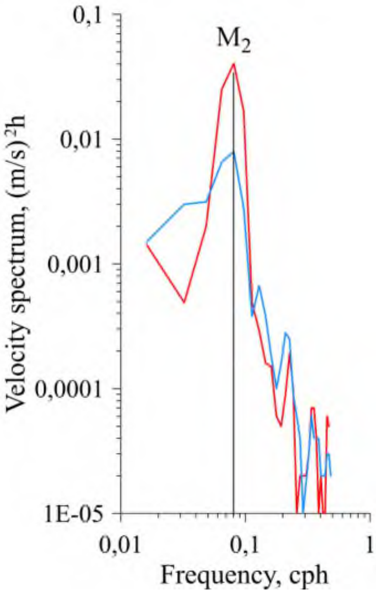

Figure 7. Spectra of velocity fluctuations of the zonal (red) and meridional components (blue) from the mooring.

The mean values of velocity components based on the mooring measurements are $U = -0.04$m/s, $V = 0.06$m/s. The study region is characterized by strong tides, which influence the current in the trough and generate strong tidal internal waves, which in turn facilitate mixing [*Morozov*, 2006; *Morozov and Pisarev*, 2002; *Morozov et al.*, 2017]. The spectrum of velocity fluctuations of the zonal and meridional components reveals peaks at the semidiurnal tidal frequency but we cannot separate the M_2 and S_2 constituents because the time series is very short. The spectra of velocity components are shown in Figure 7.

Let us estimate how strong is the tide using the data of measurements and the TPXO9 tidal model [*Egbert and Erofeeva*, 2002] of the Oregon University. We filtered the velocities of the zonal and meridional components so that all other tidal frequencies except the M_2 and S_2 constituents were filtered out. The time period of the ellipses is from July 25, 18:30 to July 27, 06:50. The tidal ellipses are shown in Figure 8 together with the model ellipses for both the M_2 and S_2 constituents. The measured and model ellipses are quite close, which indicates that the TPXO model is adequate.

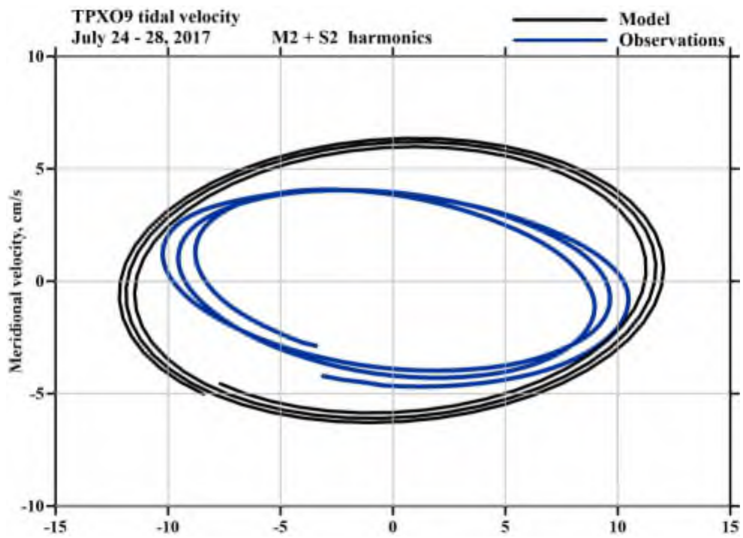

Figure 8. Model (black) and experimental (blue) tidal ellipses. The model ellipses cover a period from July 24 to July 28.

After we subtracted the velocities of the tidal ellipse from the initial data, the mean currents changed from $U = -0.04\,\mathrm{m/s}$, $V = 0.06\,\mathrm{m/s}$, $U = -0.03\,\mathrm{m/s}$, $V = 0.026\,\mathrm{m/s}$. We consider that these values are more reliable than the initial ones that include averaging with tidal velocities. However, the time series is very short but it shows that an opposite mean flow can be present in the trough. Figure 9 illustrates this.

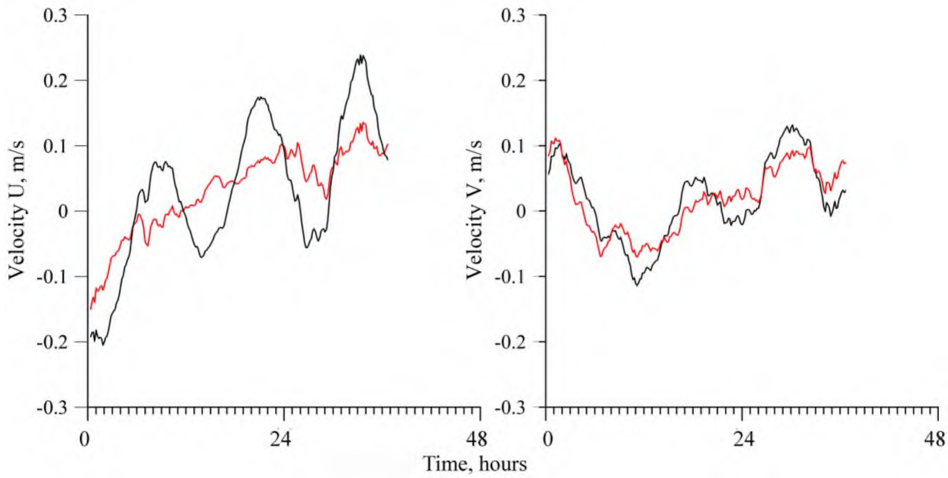

Figure 9. Time series of velocity components (U, left; V, right) before subtracting tidal currents (black) and after subtracting (red).

Figure 10 shows a comparison of the tidal ellipses for four tidal constituents, which indicates that all other constituents are significantly weaker than the M_2 constituent.

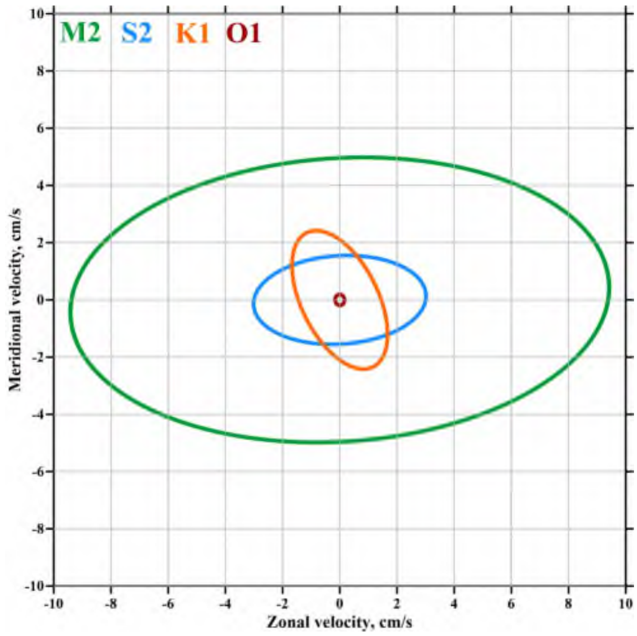

Figure 10. Tidal ellipses for the M_2, S_2, K_1, and O_1 tidal constituents.

Summary and Conclusions

The research deals with oceanographic measurements in the Bear Island Trough, which reveals a flow of Arctic water to the Norwegian Sea. This water becomes part of the Iceland-Scotland Overflow Water. Satellite altimetry was used to map surface geostrophic currents averaged over a long-term period and on the day of measurements. Numerical modeling reveals a bottom current in the trough, which is supported by ADCP measurements on a mooring. Water structure (temperature and salinity sections along the trough) also supports the existence of the bottom flow. Mixing occurs in the trough caused by different processes. Tidal ellipses were calculated from the data of mooring and using the TPXO9 tidal model based on satellite altimetry. The M_2 tide dominates in the region.

Acknowledgments. This work was supported by the State Assignment of the Shirshov Institute of Oceanology (FMWE-2023-0002 analysis of field measurements) and the Russian Science Foundation grant 22-77-10004 (modeling).

References

Aken, H. M. V., and C. J. D. Boer (1995), On the synoptic hydrography of intermediate and deep water masses in the Iceland Basin, *Deep Sea Research Part I: Oceanographic Research Papers*, *42*(2), 165–189, https://doi.org/10.1016/0967-0637(94)00042-Q.

Beszczynska-Möller, A., E. Fahrbach, U. Schauer, and E. Hansen (2012), Variability in Atlantic water temperature and transport at the entrance to the Arctic Ocean, 1997-2010, *ICES Journal of Marine Science*, *69*(5), 852–863, https://doi.org/10.1093/icesjms/fss056.

Diansky, N. A., A. V. Bagno, and V. B. Zalesny (2002), Sigma model of global ocean circulation and its sensitivity to variations in wind stress, *Izvestiya, Atmospheric and Oceanic Physics*, *38*(4), 537–556.

Diansky, N. A., E. G. Morozov, V. V. Fomin, and D. I. Frey (2021), Spread of Pollution from a Bottom Source in the Norwegian Sea, *Izvestiya, Atmospheric and Oceanic Physics*, *57*(2), 197–207, https://doi.org/10.1134/S0001433821020043.

Dickson, R. R., and J. Brown (1994), The production of North Atlantic Deep Water: Sources, rates, and pathways, *Journal of Geophysical Research: Oceans*, *99*(C6), 12,319–12,341, https://doi.org/10.1029/94JC00530.

Egbert, G. D., and S. Y. Erofeeva (2002), Efficient Inverse Modeling of Barotropic Ocean Tides, *Journal of Atmospheric and Oceanic Technology*, *19*(2), 183–204, https://doi.org/10.1175/1520-0426(2002)019<0183:EIMOBO>2.0.CO;2.

Frey, D. I., A. N. Novigatsky, M. D. Kravchishina, and E. G. Morozov (2017), Water structure and currents in the Bear Island Trough in July-August 2017, *Russian Journal of Earth Sciences*, *17*(3), https://doi.org/10.2205/2017ES000602.

Gammelsrød, T., Ø.. Leikvin, V. Lien, et al. (2009), Mass and heat transports in the NE Barents Sea: Observations and models, *Journal of Marine Systems*, *75*(1–2), 56–69, https://doi.org/10.1016/j.jmarsys.2008.07.010.

Giraudeau, J., V. Hulot, V. Hanquiez, et al. (2016), A survey of the summer coccolithophore community in the western Barents Sea, *Journal of Marine Systems*, *158*, 93–105, https://doi.org/10.1016/j.jmarsys.2016.02.012.

Jochumsen, K., D. Quadfasel, H. Valdimarsson, and S. Jónsson (2012), Variability of the Denmark Strait overflow: Moored time series from 1996–2011, *Journal of Geophysical Research: Oceans*, *117*(C12), https://doi.org/10.1029/2012JC008244.

Kantha, L. H., and C. A. Clayson (2000), *Small Scale Processes in Geophysical Fluid Flows, Volume 67 (International Geophysics)*, 750 pp., Academic Press.

Koltermann, K. P., A. V. Sokov, V. P. Tereschenkov, et al. (1999), Decadal changes in the thermohaline circulation of the North Atlantic, *Deep Sea Research Part II: Topical Studies in Oceanography*, *46*(1–2), 109–138, https://doi.org/10.1016/S0967-0645(98)00115-5.

Lankhorst, M., and W. Zenk (2006), Lagrangian Observations of the Middepth and Deep Velocity Fields of the Northeastern Atlantic Ocean, *Journal of Physical Oceanography*, *36*(1), 43–63, https://doi.org/10.1175/JPO2869.1.

Lind, S., and R. B. Ingvaldsen (2012), Variability and impacts of Atlantic Water entering the Barents Sea from the north, *Deep Sea Research Part I: Oceanographic Research Papers*, *62*, 70–88, https://doi.org/10.1016/j.dsr.2011.12.007.

Lukashin, V. N., and A. D. Shcherbinin (2007), The nepheloid layer and horizontal sedimentary matter fluxes in the Norwegian Sea, *Oceanology*, *47*(6), 833–847, https://doi.org/10.1134/S0001437007060082.

Mauritzen, C., J. Price, T. Sanford, and D. Torres (2005), Circulation and mixing in the Faroese Channels, *Deep Sea Research Part I: Oceanographic Research Papers*, *52*(6), 883–913, https://doi.org/10.1016/j.dsr.2004.11.018.

Morozov, E. (2006), Internal Tides. Global Field of Internal Tides and Mixing Caused by Internal Tides, in *Waves in Geophysical Fluids*, pp. 271–332, Springer Vienna, https://doi.org/10.1007/978-3-211-69356-8_6.

Morozov, E. G., and S. V. Pisarev (2002), Internal tides at the Arctic latitudes (numerical experiments), *Oceanology*, *42*(2), 153–161.

Morozov, E. G., I. E. Kozlov, S. A. Shchuka, and D. I. Frey (2017), Internal tide in the Kara Gates Strait, *Oceanology*, *57*(1), 8–18, https://doi.org/10.1134/S0001437017010106.

Morozov, E. G., D. I. Frey, N. A. Diansky, and V. V. Fomin (2019), Bottom circulation in the Norwegian Sea, *Russian Journal of Earth Sciences*, *19*(2), 1–6, https://doi.org/10.2205/2019ES000655.

Olsen, S. M., B. Hansen, D. Quadfasel, and S. Østerhus (2008), Observed and modelled stability of overflow across the Greenland-Scotland ridge, *Nature*, *455*(7212), 519–522, https://doi.org/10.1038/nature07302.

Årthun, M., R. B. Ingvaldsen, L. H. Smedsrud, and C. Schrum (2011), Dense water formation and circulation in the Barents Sea, *Deep Sea Research Part I: Oceanographic Research Papers*, *58*(8), 801–817, https://doi.org/10.1016/j.dsr.2011.06.001.

Ruddick, B. (1983), A practical indicator of the stability of the water column to double-diffusive activity, *Deep Sea Research Part A. Oceanographic Research Papers*, *30*(10), 1105–1107, https://doi.org/10.1016/0198-0149(83)90063-8.

Schauer, U., E. Fahrbach, S. Osterhus, and G. Rohardt (2004), Arctic warming through the Fram Strait: Oceanic heat transport from 3 years of measurements, *Journal of Geophysical Research: Oceans*, *109*(C6), https://doi.org/10.1029/2003JC001823.

Sea-Bird Electronics Inc. (2014), *Seasoft V2: SBE Data Processing*.

Shi, J., and H. Wei (2007), Evidence of double diffusion in the East China Sea, *Journal of Marine Systems*, *67*(3–4), 272–281, https://doi.org/10.1016/j.jmarsys.2006.04.017.

Smedsrud, L. H., I. Esau, R. B. Ingvaldsen, et al. (2013), The role of the Barents Sea in the Arctic climate system, *Reviews of Geophysics*, *51*(3), 415–449, https://doi.org/10.1002/rog.20017.

Talley, L. D. (2011), *Descriptive Physical Oceanography*, Elsevier, https://doi.org/10.1016/C2009-0-24322-4.

Turner, J. S. (1973), *Buoyancy Effects in Fluids*, Cambridge University Press, https://doi.org/10.1017/CBO9780511608827.

Zalesny, V. B., N. A. Diansky, V. V. Fomin, S. N. Moshonkin, and S. G. Demyshev (2012), Numerical model of the circulation of the Black Sea and the Sea of Azov, *Russian Journal of Numerical Analysis and Mathematical Modelling*, *27*(1), https://doi.org/10.1515/rnam-2012-0006.

Surface Transport of Technical Waters from Fukushima NPP to the South Kuril Fishing Zone

M. V. Budyansky[1,2*], T. V. Belonenko[1], M. A. Lebedeva[1,2], and A. A. Udalov[2]

[1]St. Petersburg State University, St. Petersburg, Russia
[2]Il'ichev Pacific Oceanological Institute FEB RAS, Vladivostok, Russia
* **Correspondence to:** Tatyana Belonenko, btvlisab@yandex.ru

Abstract: This study explores the potential for the penetration of technical waters from the Fukushima nuclear power plant (Fukushima NPP) into the fishing areas of Russia. Using a Lagrangian approach, which examines the advection of a large number of passive markers simulating waters released from the Fukushima NPP, the typical transport pathways to the South Kuril Islands are investigated, and an estimate of the time of such transport is provided. Calculations are conducted using satellite-derived and modelled velocity fields for the test year from August 24, 2022, to August 24, 2023. This study focuses on the advection of Lagrangian markers and highlights the potential for the rapid arrival of them from the Fukushima NPP into the southern Kuril region. This article emphasizes the importance of considering the seasonal variability in Kuroshio meandering and the impact of local mesoscale vortex advection related to the propagation of Lagrangian markers from the Fukushima NPP.

Keywords: Fukushima nuclear power plant, Lagrangian markers, South Kuril region, simulation, simulated particles, advection, vortex.

Citation: Budyansky, M. V., T. V. Belonenko, M. A. Lebedeva, and A. A. Udalov (2024), Surface Transport of Technical Waters from Fukushima NPP to the South Kuril Fishing Zone, *Russian Journal of Earth Sciences*, 24, ES4002, EDN: VQKJUM, https://doi.org/10.2205/2024es000934

1. Introduction

The powerful earthquake and subsequent catastrophic tsunami that struck the north-eastern coast of Honshu Island, Japan, on March 11, 2011, caused a technological disaster at the Fukushima NPP, alongside significant human casualties and extensive destruction of coastal settlements. This incident led to widespread radioactive contamination of the atmosphere and Pacific waters east of Japan. Numerous residents in the Sakhalin region, Russia, expressed apprehension regarding the potential transport of radioactive waters to the shores of the southern Kuril Islands and the subsequent radioactive contamination of fish and other seafood products entering the market. These concerns have not completely disappeared even today.

In 2011, a substantial amount of debris, including cars, refrigerators, house fragments, and other waste, was swept from the Japanese coast. These materials coalesced into dense masses that ultimately reached the shores of the USA, following the primary path of the Kuroshio Current and the North Pacific Ocean Current [*NOAA*, 2013]. However, there was a tangible risk concerning potential contamination of waters in the northwestern region of the Pacific Ocean. These areas are rich in fish and squid [*Buslov*, 2013]. The economic importance of the northwestern part of the Pacific Ocean is mainly associated with its substantial bioproductivity, a characteristic significantly influenced by oceanographic conditions.

Currently, a significant amount of water that is used to cool reactors has accumulated at operational stations. Following the incident at the Fukushima NPP in March 2011, seawater remains necessary for cooling the reactor cores. The "contaminated" water, containing radionuclides, has been gathered in tanks and subjected to treatment at the Fukushima NPP site. Despite objections from neighbouring countries, primarily Russia

Research Article

Received: 27 May 2024
Accepted: 29 August 2024
Published: 14 October 2024

and China, the International Atomic Energy Agency (IAEA) gave consent for the discharge of "contaminated" water. In 2021, the Japanese government made the decision to progressively release treated water into the Pacific Ocean, commencing on August 24, 2023, with a planned duration extending over the next three decades.

In Figure 1, the study area is depicted along with a generalized schematic representation of the main currents. The oceanographic conditions in the region are characterized by significant heterogeneity and spatiotemporal variability. From the Pacific side, the Kuril Islands are bathed by the Oyashio Current, an extension of the East Kamchatka Current. The Oyashio Current intensifies in the vicinity of the Bussol Strait due to the inflow of waters from the Sea of Okhotsk. North of the Bussol Strait, the Oyashio Current tends to weaken, but to the south, after the influx of Okhotsk Sea waters occurs, its flow strengthens, and the discharge increases threefold [*Belonenko et al.*, 1997; *Kawai*, 2013]. The main branches of the Oyashio Current, the first and the second, are the most stable. The first follows along the shelf and slope depths toward Hokkaido, while the second moves south or southwest of Iturup. In addition to the cold waters from the Sea of Okhotsk flowing through the Ekaterina and Friz straits, the warm Soya Current also enters the southern Kuril region of the Pacific Ocean. Complex vortex formations in this region are generated and intensified by the opposing movement of the northeast branch of the Kuroshio. Its main current wedges between the first and second branches of the Oyashio [*Itoh and Yasuda*, 2010].

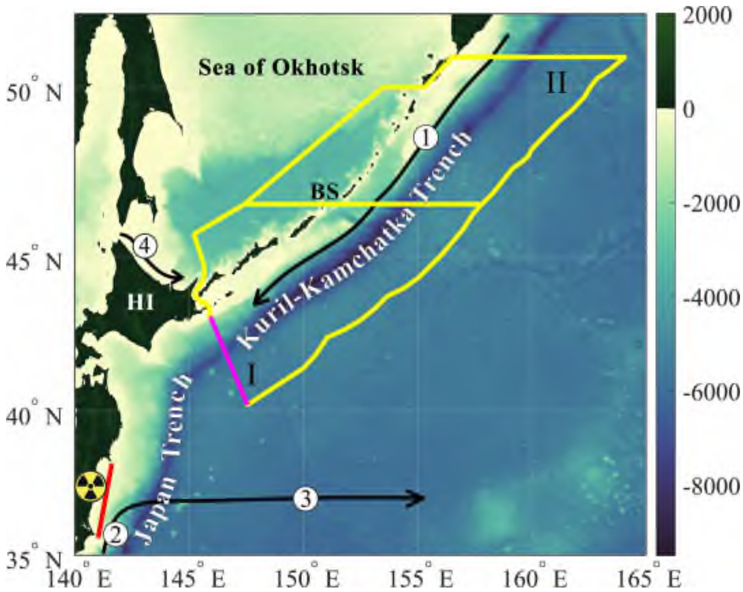

Figure 1. The study area. The location of the Fukushima NPP (coordinates 37°25'12.0" N, 141°2'58.0" E) is indicated by the radiation hazard symbol ☢. The yellow line represents the boundaries of the South Kuril Fishing Zone (SKFZ) – I and North Kuril Fishing Zone (NKFZ) – II. The pink segment denotes the southwest border of the SKFZ. The red segment (35.6°N, 141°E–38.3°N, 141.6°E) is located near the Fukushima NPP (trajectories of simulated particles start here). The bottom topography is shown in colour shading. The boundaries of the SKFZ and NKFZ were determined according to the government documents of the Russian Federation. 1 – the Oyashio Current, an extension of the East Kamchatka Current, 2 – the Kuroshio Current, 3 – the Kuroshio Extension, and 4 – Soya Current; HI – Hokkaido Island and BS – Bussol Strait.

The area under investigation is commonly referred to as the Kuroshio-Oyashio confluence zone or a subarctic frontal area [*Belonenko et al.*, 1997; *Kawai*, 2013]. Here, the Kuroshio Extension lengthens the Kuroshio Current, which changes its course to the east at approximately 35°. This results in a strong, meandering jet forming a boundary between warm subtropical and cold subarctic waters. This region undergoes an exceptionally robust exchange of heat between the atmosphere and the ocean, exhibiting the highest level of eddy kinetic energy. The Kuroshio-Oyashio confluence zone is rich in diverse mesoscale eddies that play a crucial role in facilitating the transfer of heat, salt, nutrients, carbon, pollutants, and other tracers across the ocean.

At the southern Kuril Islands, powerful anticyclonic eddies form as a result of the detachment of warm tongues and meanders of the Kuroshio. These eddies are long-lived, with lifespans ranging from 2 to 3 months to several years [*Travkin et al.*, 2022; *Udalov et al.*, 2023]. Interestingly, upon entering the southern Kuril region, mesoscale eddies continue to move northeastward along the Kuril Trench. They pass over deep-sea trenches not close to the coast, and most often, they disintegrate near the islands of Urup and Iturup [*Udalov et al.*, 2023]. The described dynamics and variability of oceanographic conditions in the waters near the Kuril Islands are reflected in the abundance and composition of the biota in this region. Extending from the Kamchatka Peninsula to Hokkaido Island, this area plays a crucial role in Russia's fishing industry, serving as a hub for the industrial exploitation of aquatic resources [*Buslov*, 2013; *Shuntov*, 2022].

The basis of the fishery in the region is fish. On average, over this period, it amounted to almost 80%. In addition to fish, there was a significant harvest of molluscs. These organisms are harvested using vessels of various types [*Buslov*, 2013]. This region is a crucial Russian area for the fishing of fish and squid, holding immense significance for ensuring Russia's food security. How the discharge of polluted waters from the Fukushima NPP will affect fish and squid is a matter of research for future years.

The issues of radioactive contamination are actively studied from the perspective of continuous dosimetry and numerical modelling of radioactive contamination involving various radionuclides [*Budyansky et al.*, 2015; *Prants*, 2014; *Prants et al.*, 2017a]. However, this particular work is dedicated to assessing the time and pathways of the potential spread of contamination into fishing areas, in which we assess the time and pathways of the potential spread of contamination into fishing areas [*Maderich et al.*, 2024]. *Smith et al.* [2023] declare that fears of radiation are likely to damage the livelihoods of fishing communities lying in the path of Fukushima NPP waters, which is still recovering from fishing bans and reputational damage caused by the 2011 accident. Although radiation protection science unequivocally asserts today that the planned release of Fukushima wastewater poses no substantial threat to Pacific Ocean organisms or consumers of seafood impacted by Fukushima PP discharge governments and researchers worldwide are expected to closely monitor radioactivity in the Pacific Ocean during the release [*IAEA*, 2018, 2023].

We focus only on the advection of marker tracers from the Fukushima NPP into the areas of Russian coastal waters in this paper. We do not provide a quantitative assessment concentration assessment of the more than 62 radionuclides discharged into the water, which the Advanced Liquid Processing System cannot remove [*TEPCO*, 2023]. We study here only the pathways and mechanisms of Lagrangian marker advection which can reach the southern Kuril region from the Fukushima NPP. In this study, we call the Lagrangian markers which advection start from the Fukushima NPP the simulated particles. This analysis is extremely important because the release of "contaminated" radioactive water from Fukushima NPP is planned to take place in the future over an extended period. It is worth noting that ocean circulation and advection of water in this small area have never been studied in detail before.

We examine one year from August 24, 2022, to August 24, 2023. In other words, we are analysing the scenario of what would have happened with the spread of radioactive waters in the region if the release of "contaminated" water had occurred on August 24, 2022. We also consider the dependence of marker numbers on seasons and reveal the months when the number of these markers in the South Kuril region is the largest. The study area is in the South Kuril Fishing Zone (SKFZ) where commercial fishing of fish and squid is conducted (Figure 1).

2. Methods

Lagrangian modelling is employed to study the transport properties of fluid elements [*Budyansky et al.*, 2015; *Prants*, 2014; *Prants et al.*, 2017a,b,c]. Lagrangian modelling enables the study of the paths and durations of dispersion of water parcels with a high degree of accuracy. For this purpose, we use a marker tracking method. This method involves calculating a large number of trajectories for passive tracers simulating contamination in the SKFZ. The simulation of water circulation in oceanic basins is effectively performed using Lagrangian methods, which provide a detailed account of transport and mixing within a specific area by calculating the trajectories of numerous artificial passive particles. In turbulent or chaotic flows, visualizing trajectories of particles advected by satellite-derived or numerical-model velocity fields results in a complex web of intertwined paths that can be challenging to interpret [*Prants et al.*, 2017c].

To utilize the Lagrangian approach, a dense mesh of artificial particles is numerically advected backward and forward in time from a fixed date.

By analysing the simulation results in reverse time, researchers can determine the origins of fluid particles passing through specific points. This approach is particularly valuable for studying circulation in basins with only a few incoming water masses, such as the study area. The trajectories of Lagrangian particles are computed by solving the advection equations

$$\frac{\mathrm{d}\lambda}{\mathrm{d}t} = u(\lambda,\varphi,t), \quad \frac{\mathrm{d}\varphi}{\mathrm{d}t} = v(\lambda,\varphi,t), \tag{1}$$

where u and v are the angular zonal and meridional components of the AVISO or GLORYS12V1 (NEMO) velocity field, respectively, and φ and λ are the latitude and longitude, respectively.

Angular velocities are employed due to their simplicity in equations when dealing with the Earth's spherical geometry. To ensure precise numerical results, bicubic spatial interpolation and temporal smoothing using third-order Lagrangian polynomials are applied. The Lagrangian trajectories are calculated by integrating equations (1) utilizing the fourth-order Runge-Kutta scheme with a fixed time step of 0.001 days. This meticulous numerical approach ensures accurate simulations and reliable results.

In the present study, stationary points in the velocity field on a given date are marked on geographical maps with triangles and crosses. Elliptic stationary points, shown as triangles and located at the centers of vortices, are points around which the movement is stable and circular. Hyperbolic stationary points, shown as crosses, are situated between the vortices and are unstable, with two directions along which the waters converge to such a point, and two others along which they diverge [*Budyansky et al.*, 2015; *Prants*, 2014; *Prants et al.*, 2017a,b,c].

3. Data

To construct Eulerian flow maps, we utilize two sources of information: geostrophic velocities based on AVISO satellite altimetry data with a spatial resolution of 1/4° and current velocities on the 0.5 m depth level obtained from the global high-resolution ocean reanalysis GLORYS12V1 (Global Ocean Physics Reanalysis) with a spatial resolution of 1/12°, created using NEMO (Nucleus for European Modelling of the Ocean). Both products are available on the Copernicus Marine Environment Monitoring Service portal (CMEMS) (https://data.marine.copernicus.eu/product/GLOBAL_ANALYSISFORECAST_PHY_001_024/description). The study covers one period from August 24, 2022, to August 24, 2023. The Lagrangian modelling algorithms are configured for calculations based on data from one year ago. Essentially, we use a two-year dataset from AVISO and GLORYS12V1 (NEMO) spanning from August 24, 2021, to August 24, 2023.

a. Geostrophic currents from the merged altimeter data

The geostrophic velocities from AVISO are the result of merged measurements from all altimetric missions – Jason-3, Sentinel-3A, HY-2A, Saral/AltiKa, CryoSat-2, Jason-2, Jason-1, T/P, ENVISAT, GFO, and ERS1/2 – covering the period from 1993 to the present. The data were merged via the optimal interpolation method [*CMEMS*, 2020]. The spatial averaging of the data was performed at a resolution of 1/4° latitude and longitude, with a temporal resolution of 1 day.

The idea of using the AVISO velocity field for the advection of passive markers simulating radioactive contamination is not new and has been used by the authors before. It is a region of strongly seasonal water mass formation for mode waters of varying flavors and evolution [*Dong et al.*, 2017; *Kawakami et al.*, 2015; *Oka and Qiu*, 2011; *Oka et al.*, 2011; *Qiu et al.*, 2006; *Suga and Hanawa*, 1995; *Zhang et al.*, 2021]. The 2012 research expedition conducted by the V. I. Il'ichev Pacific Oceanological Institute of the Far Eastern Branch of the Russian Academy of Sciences revealed that, despite the subduction of radioactive contamination to depths of 100–500 meters within anticyclones, concentrations of simulated particles, as determined by AVISO, exhibited a strong correlation with field dosimetry data [*Budyansky et al.*, 2015].

b. Currents from the GLORYS12V1 (NEMO) reanalysis

The GLORYS12V1 (NEMO) product is based on a global real-time forecasting system. The model relies on the NEMO model with forcing from the ECMWF ERA-Interim dataset. The GLORYS12V1 (NEMO) product assimilates in situ and satellite data from missions such as Topex/Poseidon, Jason-1, 2, MODIS Terra/Aqua, and AVHRR NOAA, as well as from drifting buoys such as Argo and drifters, other natural observations, and oceanographic surveys. Observations are assimilated into the NEMO model using a low-order Kalman filter. GLORYS12V1 (NEMO) accurately captures intricate surface dynamics at a small scale and shows robust agreement with independent data not included in the assimilation process. GLORYS12V1 (NEMO) offers a dependable representation of the physical ocean state, making it valuable for studying many ocean exploration tasks and enabling applications such as seasonal forecasts. Moreover, its high-quality data make it a valuable resource for regional purposes and provide essential physical parameters for areas such as marine biogeochemistry [*Lellouche et al.*, 2021]. We used geostrophic velocities on a 0.5 m depth level. The spatial average of the data was taken at 1/12° latitude and longitude, with a temporal resolution of 1 day.

4. Results

4.1. Ocean Circulation in the Research Area Using AVISO and GLORYS12V1 (NEMO) Data

The research area to the east of Japan is bounded to the south and north by the meandering currents of the strong warm Kuroshio current and the cold Oyashio current. These currents coincide with their respective hydrological fronts. The segment of the Kuroshio system from the island of Honshu to the Imperial Mountains is called the Kuroshio Extension. At approximately 42°–43°N latitude, the Oyashio current turns eastwards (this is known as the Second Branch of the Oyashio). The region where the Kuroshio and Oyashio interact is one of the most dynamically active areas in the world ocean and exhibits variability in oceanographic fields over a wide range of spatial and temporal scales [*Belonenko et al.*, 2009]. Observations indicate that at certain intervals, the Kuroshio and Oyashio currents split into individual branches, indicating the bifurcation of the currents.

The strength (transport) of the Kuroshio varies along its path and seasonally, with a speed reaching 2.5 m/s [*Qu et al.*, 2001]. The velocities in the Oyashio Current are significantly lower than those in the other regions, and in February, they reach 0.5–1.0 m/s. However, in summer, the Oyashio current significantly weakens, with speeds not exceeding 0.25–0.35 m/s [*Belonenko et al.*, 1997]. This process facilitates the penetration of water from the south, mixing water of different origins, and detachment of filaments from eddies, ultimately leading to the entry of potentially "contaminated" waters into the North Pacific Ocean. Figure 2 shows the mean currents averaged for September 2022 and April 2023. The calculations were performed using altimetry data and GLORYS12V1 (NEMO) data.

The meandering Kuroshio current, characterized by high velocities, is highlighted in dark colour. The transport of the Kuroshio near the coast of Japan reaches 65 Sv (1 Sv = 10^6 m^3/s), but this transport exhibits pronounced seasonal variability [*Sekine and Kutsuwada*, 1994]. Figure 2 clearly shows that the spatial position of the Kuroshio current changes. In April, the current forms a meander close to Hokkaido Island, adjacent to the part of the coast where the Fukushima NPP is located. In September, this meander shifts eastwards by approximately 200 km, creating a loop that eventually detaches from the main current, forming the so-called Kuroshio Ring [*Tomosada*, 1986]. The seasonal variability in the Kuroshio current can impact the transport of potentially "contaminated" waters toward the Kuril shores and the Russian fish and squid harvesting area. Figure 2 displays the northern branch of the Kuroshio Extension, recognized as the North Pacific Current. This current originated from the interaction between the Kuroshio current, which shifts northward along the coast of Japan, and the Oyashio current, a cold subarctic current that flows southward and circulates counterclockwise along the western region of the northern Pacific Ocean [*Venti and Billups*, 2013]. The speed of the North Pacific Current decreases from west to east, ranging from approximately 0.5 to 0.1 m/s, with transport of 15–35 Sv.

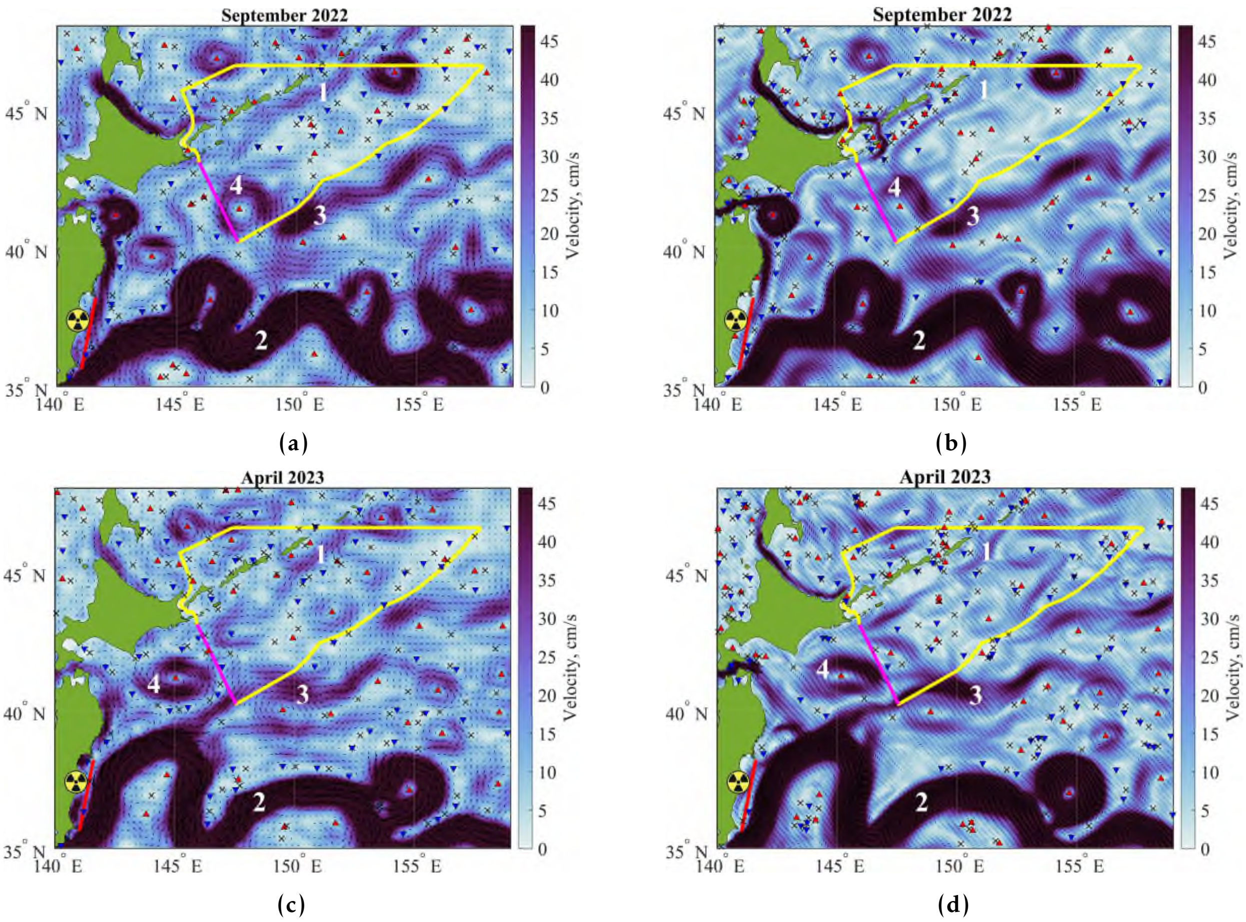

Figure 2. Geostrophic currents, derived from AVISO (left) and GLORYS12V1 (NEMO) (right) averaged for September 2022 and April 2023. Currents: 1 – Oyashio, 2 – Kuroshio, 3 – North Pacific Current, and 4 – quasistationary anticyclone. Arrows indicate current vectors, and the colour scale corresponds to the magnitude of the change in speed. The yellow line indicates the location of the SKFZ area; the pink line shows the boundary of the SKFZ closest to the Fukushima NPP. The red triangles ▲ correspond to anticyclone centres, and the blue triangles ▼ indicate cyclones. The black crosses represent the hyperbolic points.

To the east of Hokkaido in the region of 40°N, 150°E, there is a quasistationary anticyclone, and a cyclone is situated slightly to the north. Notably, in this part of the water body, north of the main Kuroshio current, there are several mesoscale eddies – cyclones and anticyclones – the centers of which are indicated in Figure 2 by blue and red triangles, respectively. The generation of these eddies is mainly attributed to the meandering of the Kuroshio current and its barotropic and baroclinic instability [*Udalov et al.*, 2023]. This process is accompanied by the formation of an ordered system of anticyclones that propagate along the steep side of the Kuril Trench to the northeast, acquiring the characteristics of trench waves [*Gnevyshev et al.*, 2023; *Travkin et al.*, 2022]. Both cyclones and anticyclones, through rotation, while simultaneously moving northwards, can participate in the transport of potentially "contaminated" waters toward the shores of the Kuril Islands.

It is worth noting that calculations conducted with different datasets yield similar results so it is the validation of the model and of course it is related to the higher resolution of the model output, although it is fair to acknowledge that the number of eddies, as indicated by the blue and red triangles in Figure 2, differs between the AVISO and GLORYS12V1 (NEMO) data. This difference may be associated with the higher resolution of the velocity field in the GLORYS12V1 (NEMO) data.

4.2. Distribution of potentially "contaminated" waters in the study area

Every day from August 24, 2022, to August 24, 2023, a rectangular area with coordinates 40°–48.5°N, 145°–159°E was seeded with particles on a uniform grid of 700×700 nodes, totaling 49×10^4 markers. Then, for each particle, advection equations (1) were solved backward over 365 days, and trajectories were calculated. Figure 3 depicts the outcomes of Lagrangian modeling, illustrating the spatial distribution of Lagrangian particles and the recording of simulated particles in the study area. The experiment was conducted concurrently using AVISO and GLORYS12V1 (NEMO) data. The experiment unfolds as follows.

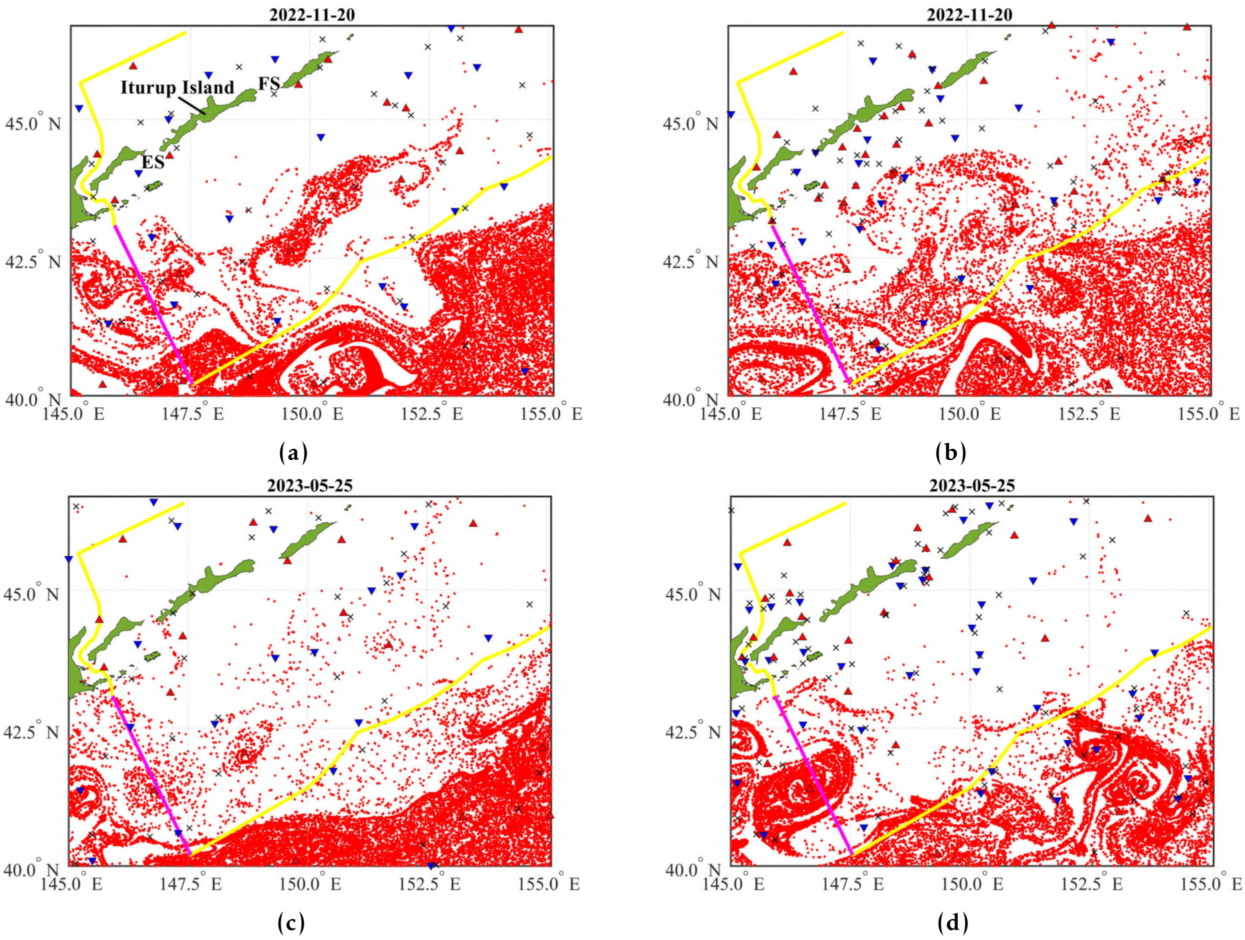

Figure 3. Spatial distribution of "contaminated" markers (shown as red dots) based on the altimetric AVISO (left) and GLORYS12V1 (NEMO) (right) data for specific dates: November 20, 2022, and May 25, 2023. Triangles and crosses represent the same features as in Figure 2. Green is the land; ES is the Ekaterina strait, and FS is the Friz strait.

The markers whose trajectories in the past intersected the segment 35.6°N, 141°E–38.2°N, 141.6°E (shown as a red line located close to the Fukushima NPP in Figure 1) were colored red and detected in Figure 3. These markers correspond to potentially simulated particles from the Fukushima NPP. Although, as claimed by many experts, the main portion of this water is indeed picked up by the Kuroshio Current and carried eastwards into the Pacific Ocean away from the shores of Japan, the potentially "contaminated" waters can be detected near the Kuril Islands. Figure 3 shows that the simulated particles reach the boundaries of the SKFZ and are carried northward. They also enter the Sea of Okhotsk through the Kuril Strait. Simulated particles emanating from the Fukushima NPP source outline circulation structures including eddies. Figure 3 shows that the primary concentration of the markers was outside the SKFZ. Indeed, the main portion of simulated particles from the Fukushima NPP, along with the Kuroshio, disperse eastwards. However, a substantial portion of them goes in a northern direction, crossing the boundaries of the SKFZ.

In Figure 3, we do not expect a 100% match in the distribution of markers, as the AVISO and GLORYS12V1 (NEMO) fields differ in spatial resolution and coastline shape. This causes markers in the AVISO field to "stick" near the shore, increasing their advection time in the study area. In the GLORYS12V1 field, a greater number of smaller-scale vortices are resolved, leading to the formation of compact "patches" of markers.

4.3. Temporal variability of simulated particle distribution from the Fukushima NPP

Then, we study temporal variability in the number of simulated particles the within the SKFZ based on AVISO and GLORYS12V1 (NEMO) data (Figure 4). All the markers that intersect the red segment in Figure 1 (the discharge boundary from the Fukushima NPP) are coloured red and are plotted of the map (see examples in Figure 3).

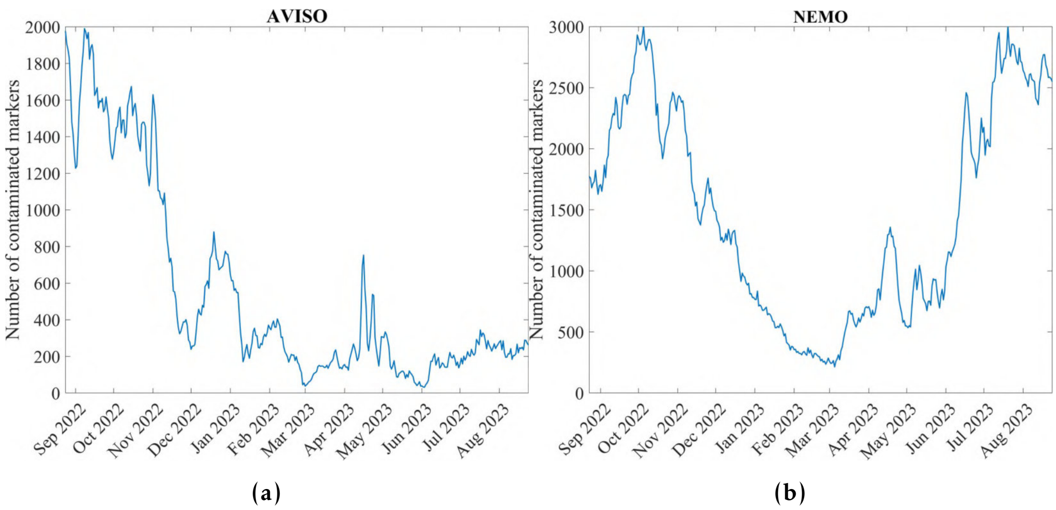

Figure 4. Temporal variability in the number of "contaminated" markers inside the SKFZ. The counts for AVISO and GLORYS12V1 (NEMO) data were collected daily from August 24, 2022, to August 24, 2023. The trajectory of each marker was calculated backward in time for a duration of 1 year.

Notably, the temporal variability plots calculated using the Lagrangian modeling but based on different datasets exhibited differences. The main distinction lies in the presence of peaks in the GLORYS12V1 (NEMO) data during the summer period, while these peaks are absent in the AVISO data.

This discrepancy may be attributed to the highly fragmented coastline in the AVISO data, which trapped some markers near the shore or this could be related to the different number of vortices in the GLORYS12V1 (NEMO) and AVISO data. The observed difference in the total number of simulated particles between the GLORYS12V1 (NEMO) and AVISO data may be attributed to the coastline resolution issue mentioned earlier. It is important to note, however, that both graphs show elevated values of simulated particles in September–

October, with a decrease during the winter period. Notably, the autumn season corresponds to the peak fishing period for most pelagic fish and squid in the SKFZ.

4.4. Estimation of the time required for simulated particles to reach the SKFZ boundary

Graphs illustrate the distribution of the number of simulated particles over time as they arrived at the southwest border of the SKFZ are shown in Figure 5. These graphs were generated using real-time marker advection data. Every day, from August 24, 2022, to June 6, 2023, 50,000 markers were launched on the red segment (Figure 1) near the eastern coast of Honshu. The choice of this segment is associated with the specific shape of the coastline according to AVISO data.

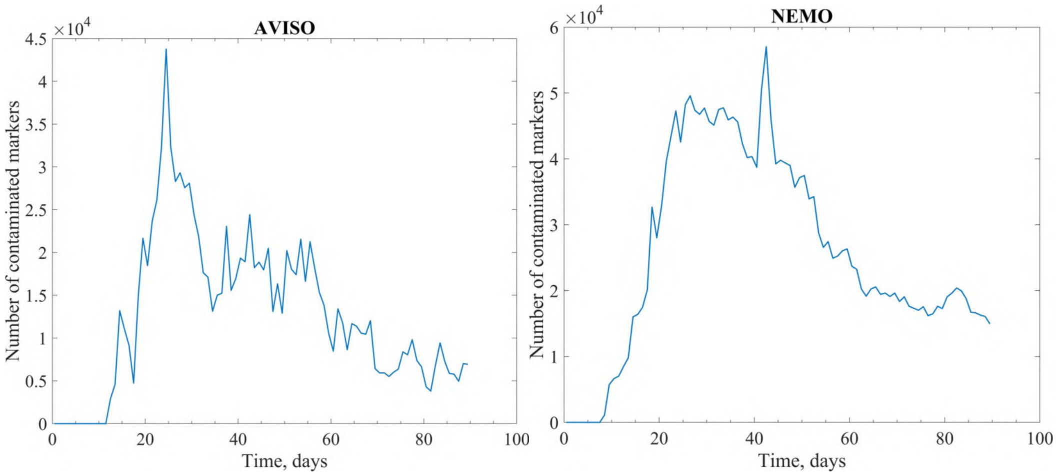

(a) **(b)**

Figure 5. Distribution of the number of "contaminated" markers over time upon reaching the southern boundary of the SKFZ based on AVISO data (top) and GLORYS12V1 (NEMO) data (bottom). The abscissa axis represents days since the potentially "contaminated" waters discharge, and the ordinate axis represents the number of "contaminated" markers inside the SKFZ. Only markers that crossed the southern boundary of the SKFZ (pink segment in Figure 1) were considered.

Subsequently, each trajectory was calculated in real-time for 90 days after the launch date. In the graph calculated using the AVISO dataset, there is a prominent peak at 13 days. A similar peak is observed at 20 days in the GLORYS12V1 (NEMO) data, and the first simulated particles cross the SKFZ boundary just 8 days after the initial launch.

The first markers in GLORYS12V1 are advected to the selected segment somewhat faster than in AVISO because the coastline shape in AVISO is coarser, which may lead to delays in marker movement near the shore. The shift of the peak of "fast" markers towards higher travel times in GLORYS12V1 is related to the higher resolution of the velocity field in GLORYS12V1 compared to AVISO. This higher resolution in GLORYS12V1 reveals more vortex structures, which act as transport barriers to the unidirectional advection of markers from the release zone to the selected segment. Differences in the methodology of obtaining AVISO and GLORYS12V1 (NEMO) data, as well as in spatial resolution and temporal discretization, can lead to discrepancies in the results. It is important to note that both data sets indicate a potential hazard associated with the spread of contaminated waters. In this context, quantitative estimates are less significant than qualitative conclusions.

It is important to note that according to the GLORYS12V1 (NEMO) reanalysis data, simulated particles can reach SKFZ in just 8 days. The maximum values of simulated particles are 4.3×10^4 at 21 days according to AVISO data and 5.7×10^4 at 40 days according to GLORYS12V1 (NEMO) data. By 60 days after the discharge date, the number of simulated particles reaching SKFZ had decreased by 2–3 times but remained considerable.

4.5. Direct experiment involving the advection of the "contaminated" patch from the Fukushima NPP

The time required for the simulated particles to reach the boundaries of the South Kuril Fishing Zone (SKFZ) depends on the current circulation. This includes factors such as the shape and size of the Kuroshio meander (see Figure 2) and the local composition of mesoscale eddies with different polarities. Figure 6 identifies instances where the marker spot reached the boundaries of the SKFZ most rapidly. In the present study, the starting date was May 25, 2023.

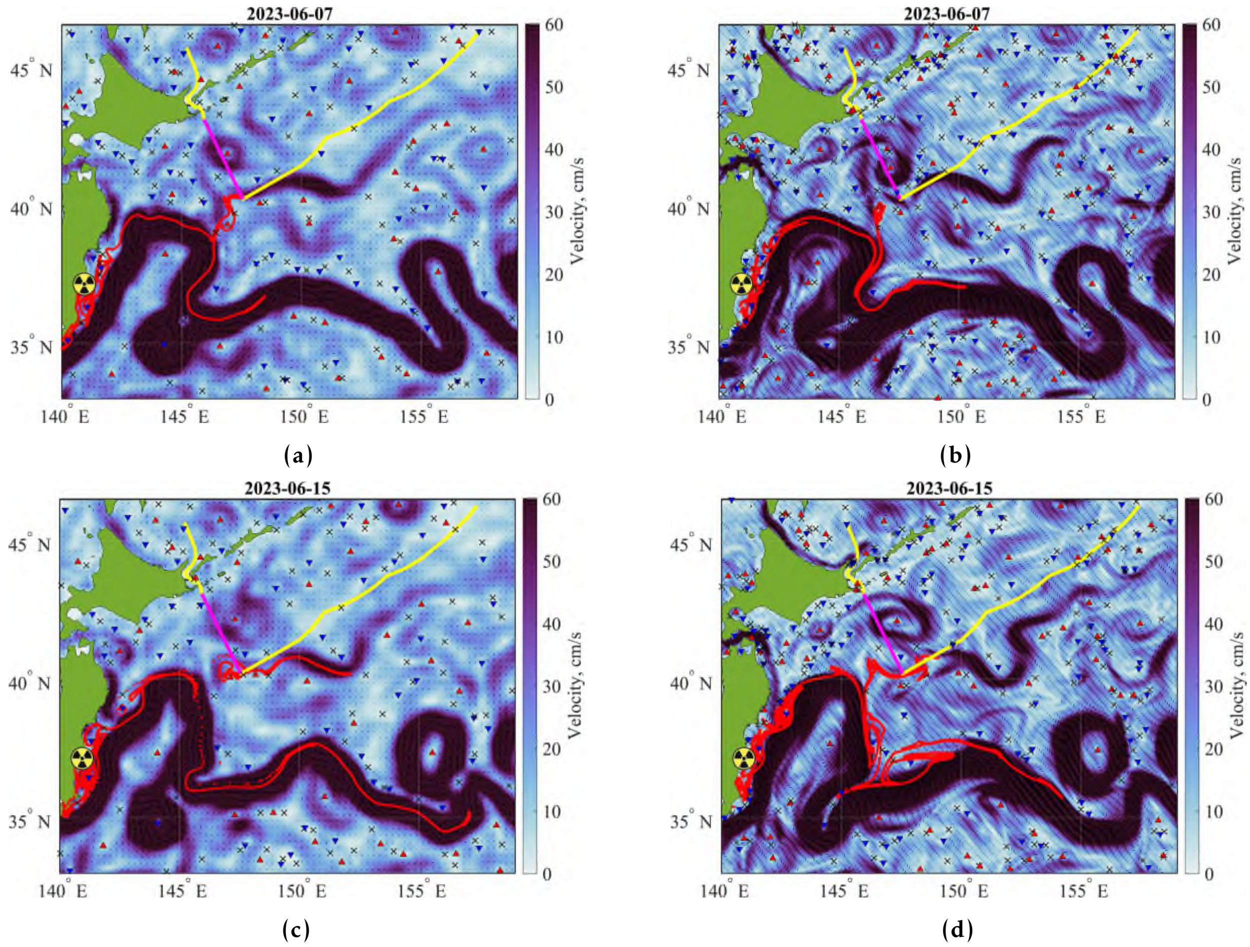

Figure 6. Velocity field based on AVISO data (left) and GLORYS12V1 (NEMO) data (right) showing the evolution of the patch of the "contaminated" markers from the Japanese coast near the Fukushima NPP (the segment, as well as the patch, are shown in red; see also Figure 1). The launch date of the markers is May 25, 2023. The "contaminated" markers reached the southwestern boundary of the SKFZ (indicated in pink) 13 days after launch.

It is important to note that the experiment tracking the fast advection of the patch from the Fukushima coast to the SKFZ was conducted similarly for both AVISO and GLORYS12V1 (NEMO). A total of 50,000 markers were released along the red segment (Figure 1) near the eastern coast of Honshu, after which the evolution of this patch was tracked. In Figure 6, images of the patch evolution 13 and 20 days after the launch date are shown. The rapid transport of markers is associated with the entrainment of the patch by the Kuroshio meander, which, during this period, was pressed against the eastern coast of Japan. The subsequent mechanism of advection of simulated particles into the SKFZ is linked to the detachment of a portion of the patch by the local system of mesoscale vortices that formed on the northern periphery of the Kuroshio meander. It is important to note that a similar mechanism of fast transport is observed in both the AVISO and GLORYS12V1 (NEMO) datasets.

Note the formation of characteristic U-shaped folds in the pollution patch as it passes near hyperbolic points (Figure 6) formed between the vortices and on the periphery of the Kuroshio meander. Such deformation leads to a rapid increase in the perimeter of the patch and additional expansion of the "polluted" area [*Prants et al.*, 2017c].

4.6. Dependence of the "contamination" in the South Kuril Fishing Zone on the date of potentially "contaminated" water discharge

The more important statement for this study is that as seen in previous analyses the particles following the north wall of the Kuroshio Extension eastward but tend to spread northward at the hyperbolic point mentioned. Figure 7 shows the distribution of the number of simulated particles reaching the South Kuril Fishing Zone (SKFZ) based on the date of their release. Importantly, we are examining a hypothetical scenario in which simulated particles are released from August 24, 2022, to August 24, 2023. Each day, 50,000 markers were released along the red segment (see Figure 1). The obtained estimates vary between the different datasets of AVISO and GLORYS12V1 (NEMO).

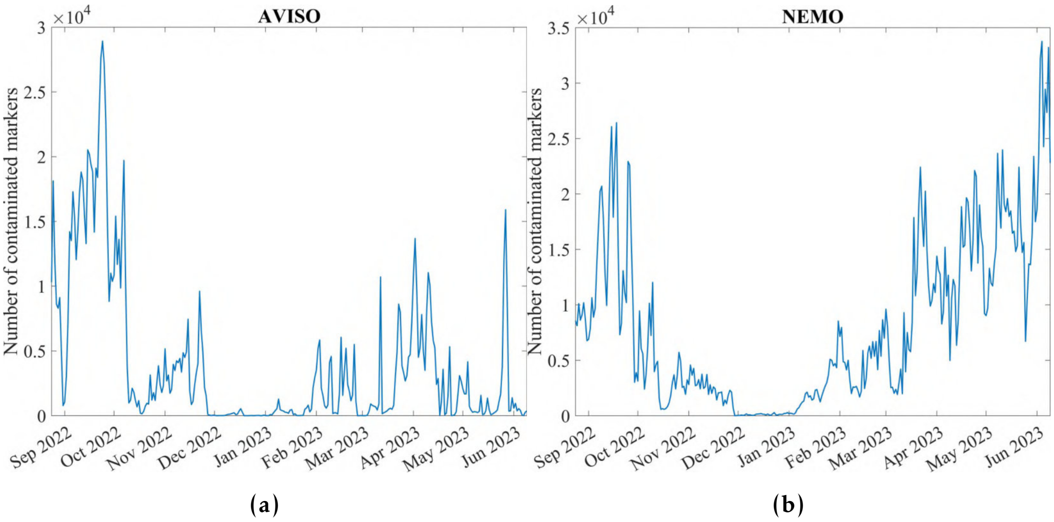

Figure 7. Distribution of the number of "contaminated" markers reaching the southwest border of the SKFZ based on the dates of their release from the Japanese coast (red segment in Figure 1). The AVISO data (top) and GLORYS12V1 (NEMO) data (bottom) are used.

If discharge occurs in December-January, only a negligible number of simulated particles enter the South Kuril fishing zone (SKFZ). The opposite situation is observed in other months when the number of markers is measured in tens of thousands. It is noteworthy that the obtained estimates vary for different datasets: a maximum of 2.75×10^4 is reached in October 2022 according to AVISO data, and 3.75×10^4 is reached in June 2023 according to GLORYS12V1 (NEMO) data. This implies that the discharge of simulated particles in these months leads to significant contamination of the SKFZ, and the period from December to January is the most favourable period for discharge.

It is important to note that we analysed only a single year of data so the results are presented as an example of the variability one might expect.

4.7. Density of tracer tracks of the potentially "contaminated" markers

In Figure 8, sets of maps depicting the density of trajectories of tracers (dasymetric maps) are presented for simulated particles launched near the eastern coast of Japan during September, November 2022, and April 2023. To construct these maps, we divide the study area (35–44°N, 140°–150°E) into a uniform grid of 400×400 rectangular cells. For each cell, the daily count of tracks left by the trajectories of simulated particles was then calculated.

The mechanisms of their transport to the boundary of the SKFZ and, consequently, the estimates of density and spatial distribution of traces depend on the existing hydrological regime in the region. In some periods, the regime is influenced primarily by the developing

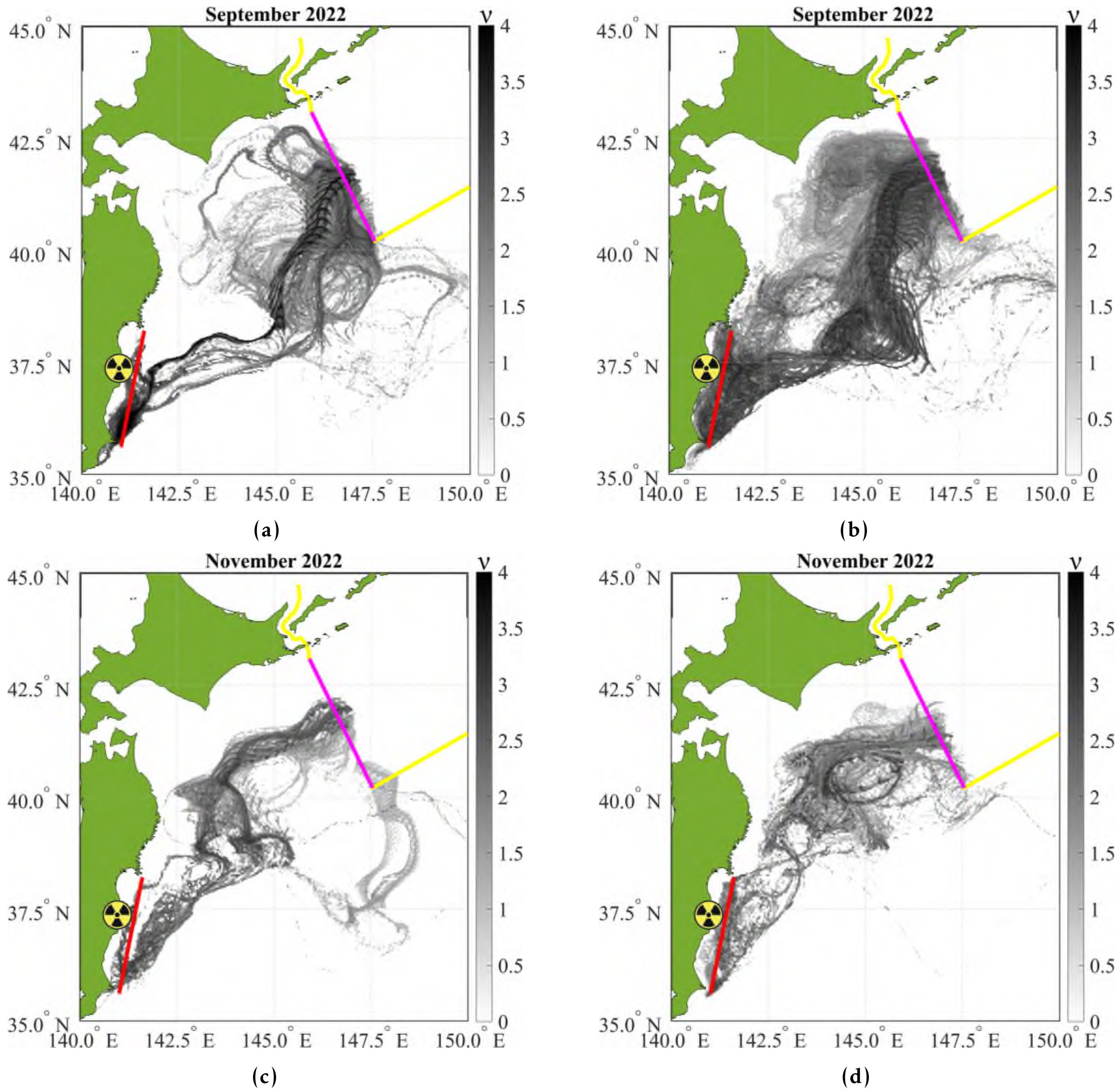

Figure 8. Density (dasymetric) maps of "contaminated" markers trajectories released from the Fukushima NPP in September, November 2022, and April 2023, reaching the southwest segment of the SKFZ. The calculation is based on AVISO data (left) and GLORYS12V1 (NEMO) data (right). The scale presents $\nu = log\varphi$, where φ is the density of daily tracks of the trajectories.

first meander of the Kuroshio Current, while in others, mesoscale vortex advection takes precedence.

It is important to note that the shapes of the patches for the same months are very similar on the maps calculated based on the AVISO velocity field and the GLORYS12V1 (NEMO) reanalysis. However, according to the modeling results based on GLORYS12V1 (NEMO), the density of the traces is greater than that from the AVISO data. This difference could be attributed to a greater number of markers trapped near the coast when computing trajectories based on AVISO data. The coastline mask of Honshu Island is more jagged in AVISO than in GLORYS12V1 (NEMO).

4.8. Distribution of the number of simulated particles by the date of arrival at the boundary of the SKFZ

The distribution of the markers by the date that they reached the southwest boundary of the SKFZ is shown in Figure 9. The presence of peaks in certain months indicates that more careful dosimetry should be conducted during these months when organizing fishing activities.

According to AVISO, the highest penetration of simulated particles occurs in November 2022, when the penetration reaches 15×10^4 however, in other months, this number does not exceed 3×10^4. According to the GLORYS12V1 (NEMO) data, several peaks of $3–5 \times 10^4$ were identified for different months, with the maximum values also occurring in November 2022. This indicates that the highest number of simulated particles reached the boundary of the SKFZ in November. The lowest number of markers reached the SKFZ boundary during the period from February to April.

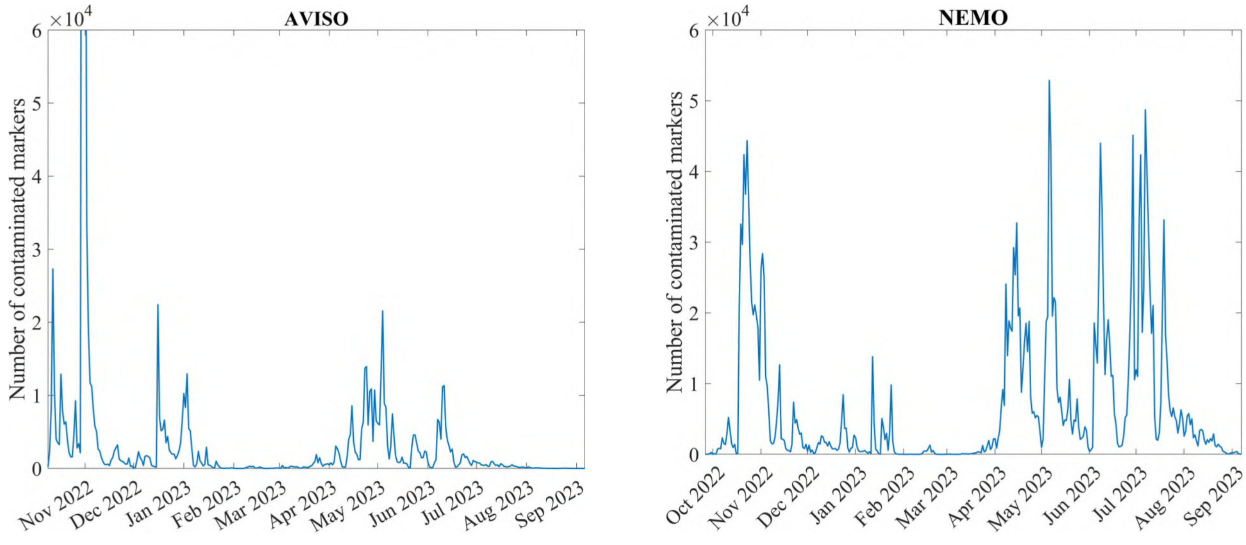

(a) **(b)**

Figure 9. Distribution of the number of "contaminated" markers by the date of arrival at the southwest border of the SKFZ since August 24, 2022.

5. Discussion and Conclusions

A series of studies analysing the spread of radioactive contamination in the ocean emerged [see reviews in works by *Budyansky et al.*, 2015; *Prants*, 2014; *Prants et al.*, 2017a,b,c] These studies utilized in situ measurements of radionuclide concentrations and altimetric velocity fields constructed from satellite measurements. Lagrangian modeling methods were employed to simulate the dispersion of potentially simulated particles. Research has shown that the primary mechanisms contributing to the spread of contamination in the Pacific Ocean include existing ocean current systems and vortex advection.

Using the Lagrangian approach, we focus on the advection of simulated particles from the Fukushima NPP called here simulated particles and solve the problems of identifying their transport corridors. We also study the seasonal variability of this advection. A similar approach was previously used by the authors in modeling the transfer of caesium 137 and 134 after the Fukushima NPP accident in the period from 2011 to 2021 based on the AVISO velocity field [*Budyansky et al.*, 2015, 2022].

Thus, the purpose of this work is to identify the possible transport corridors and mechanisms of advection from sites where potentially "contaminated" waters are discharged from the Fukushima NPP. This study is based on two types of data: 1) current velocity fields calculated from satellite altimetry data provided by AVISO and 2) velocities extracted from the global high-resolution reanalysis, GLORYS12V1 (NEMO). The calculation of the advection of markers in the GLORYS12V1 (NEMO) field for this area is new. We employ some original approaches like dasymetric maps developed within the framework of Lagrangian modeling to study the advection of potentially "contaminated" waters in areas that are adjacent to the Kuril Ridge. Note, that this is a region of traditional Russian fisheries for fish and squid.

The chosen analysis period spans one year before the actual discharge of potentially "contaminated" waters, i.e., from August 24, 2022, to August 24, 2023. Note that a comparison of the charts for AVISO and GLORYS12V1 (NEMO) reveals a good correspondence in terms of the times and paths of arrival, and most importantly, that the transfer mechanisms coincide i.e. picking up by the Kuroshio meander and advection by a local vortex system.

The main conclusion drawn from this study is that the potentially "contaminated" waters can arrive in the areas of commercial fisheries for fish and squid in the SKFZ. The primary mechanisms through which these simulated particles reach fishing areas are the meandering of the Kuroshio current and vortex advection. During the spring months, the first Kuroshio meander closely approaches the coasts of Japan, while the existing system of cyclones and anticyclones to the north carries simulated particles into the fishing areas. These markers gradually accumulate and disperse across the region.

We found that there is a regime in which simulated particles from the Fukushima NPP can cross the southwestern boundary of the subarctic frontal zone (SKFZ) within 8–13 days. This situation corresponds to the time when the first meander of the Kuroshio Current approaches the eastern coast of Hokkaido. We conducted a direct experiment on the transport of marker patches from the release of Fukushima NPP water and analysed their trajectories. The marker patch elongates into a strip along the northern flank of the meandering Kuroshio current. However, some markers break away from the initial patch and are then picked up by the system of mesoscale vortices, which push these markers into the SKFZ.

This study demonstrates one of the possible mechanisms for the entry of simulated particles into the SKFZ. We analysed the dependence of the number of simulated particles in the SKFZ on the date of potentially "contaminated" waters release. It is revealed that the most unfavourable months for release for the SKFZ are the summer and autumn months. A strong seasonal dependence of the advection of a large number of simulated particles into the fishing zone is demonstrated, depending on the discharge month. Thus, during the period from 2022 to 2023, when discharged in certain months, the quantity of markers exceeds several times the amount discharged in winter – a difference of several orders of magnitude specifically for the considered year. Conversely, the lowest risk of potential "contamination" is observed in December and January. The more important statement for this study is that as seen in previous analyses the particles following the north wall of the Kuroshio Extension eastward but tend to spread northward at the hyperbolic point mentioned.

The dasymetric maps we constructed depict the so-called "transport corridors" through which potentially "contaminated" waters enter the SKFZ. In different months, these "transport corridors" have varying widths and densities, depending on the quantity of simulated particles.

We also analysed the number of simulated particles in the SKFZ based on the dates of their arrival at the southwestern border of the Kuril-Kamchatka Trench. The highest number of simulated particles reached the border in November 2022. This implies that more careful dosimetry should be conducted in November during the organization of fishing activities in the SKFZ.

Although recent releases from Fukushima NPP are projected to have minimal impacts on seafood consumers and the marine ecosystem, as indicated by various studies and reports [*IAEA*, 2018, 2023; *Maderich et al.*, 2024; *Smith et al.*, 2023; *TEPCO*, 2023, and references herein], our research underscores the critical importance of continuous monitoring in the region including the SKFZ. This imperative arises from several key factors that warrant sustained attention and surveillance. Firstly, the dynamic nature of ocean currents can disperse contaminants over vast distances so it necessitates ongoing monitoring to track the trajectory and dispersion patterns of released substances. Secondly, the complexity of interactions within marine ecosystems requires constant vigilance to detect any subtle changes or unexpected consequences that may arise from the Fukushima NPP releases. This includes monitoring the health and behaviour of marine organisms, as well as assessing any alterations in biodiversity and ecosystem dynamics. Furthermore, the evolving nature of environmental conditions, influenced by factors such as climate change and other anthropogenic stressors, underscores the need for continuous monitoring to adapt and refine our understanding of the potential impacts of Fukushima NPP releases in a changing environment.

AVISO and GLORYS12V1 (NEMO) are two distinct sources of information that are not required to duplicate each other. AVISO provides data based on satellite measurements, whereas the GLORYS12V1 reanalysis utilizes the NEMO hydrodynamic model, which is based on the equations of motion. Differences in the methodology of obtaining data from AVISO and GLORYS12V1 (NEMO), as well as in spatial resolution and temporal discreteness, can lead to discrepancies in the results. It is important to note that both data sets indicate a potential hazard related to the spread of "contaminated" waters. In this context, qualitative conclusions are more significant than quantitative assessments. The main conclusion is that regardless of the type of data chosen, the potential hazard of spreading "contaminated" waters must be taken into account.

It is apparent that Japan has chosen the most cost-efficient way to deal with the contaminated water; however, great opposition and concerns have been aroused internationally due to the harmful ecotoxicological features of radioactive materials [*Bezhenar et al.*, 2021; *Lu et al.*, 2021]. Moreover, several scientists believe that it is necessary to organize not only dosimetric but also spectrometric monitoring during fishing activities in months with higher contamination levels in the Kuril zone [*Paraskiv et al.*, 2022]. Unlike many studies that analyze the concentrations of radioactive isotopes and their toxicological harm to biota using various methods [*Bezhenar et al.*, 2021; *Lu et al.*, 2021; *Men*, 2021], our research focuses on studying the pathways of potentially contaminated water and the time it takes for these waters to reach the area of traditional Russian fishing. We demonstrate the possibility of their entry into the coastal waters of the Kuril region and show that there is a possibility of minimizing damage, which is determined by choosing the optimal dates for discharging contaminated technical waters from the Fukushima NPP.

In conclusion, although preliminary evaluations may imply negligible immediate risks, the complex and interrelated dynamics within marine systems necessitate continuous monitoring to ensure a thorough comprehension of the persistent implications arising from the discharge of water from Fukushima NPP. This sustained vigilance is imperative for the preservation of marine ecosystems and the cultivation of trust among seafood consumers in the respective region. Enhancing the understanding of marker advection processes will serve to optimize the ongoing monitoring efforts.

Acknowledgements. The research was carried out with the support of St. Petersburg University, grant No. 116442164. The work of M.B. and A.U. on the Lagrangian analysis of passive marker advection is supported by the Russian Science Foundation (RSF) (grant No. 23-17-00068) with the help of a high-performance computing cluster at the Pacific Oceanological Institute (State Task No. 124022100072-5).

References

Belonenko, T. V., D. K. Staritsyn, V. R. Foux, et al. (1997), *The Origins of Oyasio*, 248 pp., St. Petersburg State University, St. Petersburg (in Russian).

Belonenko, T. V., V. V. Koldunov, D. K. Staritzyn, et al. (2009), *Sea-sureface level variability in the North-western Pacific*, 309 pp., SMIO Press, Saint-Petersburg (in Russian).

Bezhenar, R., H. Takata, G. de With, and V. Maderich (2021), Planned release of contaminated water from the Fukushima storage tanks into the ocean: Simulation scenarios of radiological impact for aquatic biota and human from seafood consumption, *Marine Pollution Bulletin*, *173*, 112,969, https://doi.org/10.1016/j.marpolbul.2021.112969.

Budyansky, M. V., V. A. Goryachev, D. D. Kaplunenko, et al. (2015), Role of mesoscale eddies in transport of Fukushima-derived cesium isotopes in the ocean, *Deep Sea Research Part I: Oceanographic Research Papers*, *96*, 15–27, https://doi.org/10.1016/j.dsr.2014.09.007.

Budyansky, M. V., P. A. Fayman, M. Y. Uleysky, and S. V. Prants (2022), The impact of circulation features on the dispersion of radionuclides after the nuclear submarine accident in Chazhma Bay (Japan Sea) in 1985: A retrospective Lagrangian simulation, *Marine Pollution Bulletin*, *177*, 113,483, https://doi.org/10.1016/j.marpolbul.2022.113483.

Buslov, A. V. (Ed.) (2013), *Fishing Resources Harvesting in the Waters of the Kuril Ridge: Modern Structure, Dynamics and Key Elements*, 264 pp., SakhNIRO, Yuzhno-Sakhalinsk (in Russian).

CMEMS (2020), *Product user manual for sea level SLA products. CMEMS-SL-PUM-008-032-062*.

Dong, D., P. Brandt, P. Chang, et al. (2017), Mesoscale Eddies in the Northwestern Pacific Ocean: Three-Dimensional Eddy Structures and Heat/Salt Transports, *Journal of Geophysical Research: Oceans*, *122*(12), 9795–9813, https://doi.org/10.1002/2017JC013303.

Gnevyshev, V. G., V. S. Travkin, and T. V. Belonenko (2023), Topographic Factor and Limit Transitions in the Equations for Subinertial Waves, *Fundamental and Applied Hydrophysics*, *16*(1), 8–23, https://doi.org/10.48612/fpg/92rg-6t7h-m4a2.

IAEA (2018), Regulatory control of radioactive discharges to the environment, *Tech. rep.*, International Atomic Energy Agency.

IAEA (2023), IAEA Comprehensive Report on the Safety Review of the ALPS-Treated Water at the Fukushima Nuclear Power Station, *Tech. rep.*, International Atomic Energy Agency.

Itoh, S., and I. Yasuda (2010), Water Mass Structure of Warm and Cold Anticyclonic Eddies in the Western Boundary Region of the Subarctic North Pacific, *Journal of Physical Oceanography*, *40*(12), 2624–2642, https://doi.org/10.1175/2010JPO4475.1.

Kawai, H. (2013), Hydrography of the Kuroshio Extension, in *Kuroshio: Physical Aspects of the Japan Current*, pp. 235–352, University of Washington Press.

Kawakami, Y., S. Sugimoto, and T. Suga (2015), Inter-annual zonal shift of the formation region of the lighter variety of the North Pacific Central Mode Water, *Journal of Oceanography*, *72*(2), 225–234, https://doi.org/10.1007/s10872-015-0325-1.

Lellouche, J.-M., E. Greiner, R. Bourdallé-Badie, et al. (2021), The Copernicus Global 1/12° Oceanic and Sea Ice GLORYS12 Reanalysis, *Frontiers in Earth Science*, *9*, https://doi.org/10.3389/feart.2021.698876.

Lu, Y., J. Yuan, D. Du, B. Sun, and X. Yi (2021), Monitoring long-term ecological impacts from release of Fukushima radiation water into ocean, *Geography and Sustainability*, *2*(2), 95–98, https://doi.org/10.1016/j.geosus.2021.04.002.

Maderich, V., D. Tsumune, R. Bezhenar, and G. de With (2024), A critical review and update of modelling of treated water discharging from Fukushima Daiichi NPP, *Marine Pollution Bulletin*, *198*, 115,901, https://doi.org/10.1016/j.marpolbul.2023.115901.

Men, W. (2021), Discharge of contaminated water from the Fukushima Daiichi Nuclear Power Plant Accident into the Northwest Pacific: What is known and what needs to be known, *Marine Pollution Bulletin*, *173*, 112,984, https://doi.org/10.1016/j.marpolbul.2021.112984.

NOAA (2013), Severe Marine Debris Event Report: Japan Tsunami Marine Debris. Overview and Update to Congress, *Tech. rep.*, U.S. Department of Commerce.

Oka, E., and B. Qiu (2011), Progress of North Pacific mode water research in the past decade, *Journal of Oceanography*, *68*(1), 5–20, https://doi.org/10.1007/s10872-011-0032-5.

Oka, E., S. Kouketsu, K. Toyama, et al. (2011), Formation and Subduction of Central Mode Water Based on Profiling Float Data, 2003-08, *Journal of Physical Oceanography*, *41*(1), 113–129, https://doi.org/10.1175/2010JPO4419.1.

Paraskiv, A. A., N. N. Tereshchenko, V. Y. Proskurnin, et al. (2022), Accumulation Ability of Hydrobionts and Suspended Matter in Relation to Plutonium Radioisotopes in Coastal Waters (Sevastopol Bay, the Black Sea), *Vestnik Tomskogo gosudarstvennogo universiteta. Biologiya*, (60), 78–101, https://doi.org/10.17223/19988591/60/5.

Prants, S. V. (2014), Chaotic Lagrangian transport and mixing in the ocean, *The European Physical Journal Special Topics*, *223*(13), 2723–2743, https://doi.org/10.1140/epjst/e2014-02288-5.

Prants, S. V., M. V. Budyansky, and M. Y. Uleysky (2017a), Lagrangian simulation and tracking of the mesoscale eddies contaminated by Fukushima-derived radionuclides, *Ocean Science*, *13*(3), 453–463, https://doi.org/10.5194/os-13-453-2017.

Prants, S. V., M. V. Budyansky, and M. Y. Uleysky (2017b), Statistical analysis of Lagrangian transport of subtropical waters in the Japan Sea based on AVISO altimetry data, *Nonlinear Processes in Geophysics*, *24*(1), 89–99, https://doi.org/10.5194/npg-24-89-2017.

Prants, S. V., M. Y. Uleysky, and M. V. Budyansky (2017c), *Lagrangian Oceanography: Large-scale Transport and Mixing in the Ocean*, Springer International Publishing, https://doi.org/10.1007/978-3-319-53022-2.

Qiu, B., P. Hacker, S. Chen, et al. (2006), Observations of the Subtropical Mode Water Evolution from the Kuroshio Extension System Study, *Journal of Physical Oceanography*, *36*(3), 457–473, https://doi.org/10.1175/JPO2849.1.

Qu, T., H. Mitsudera, and B. Qiu (2001), A Climatological View of the Kuroshio/Oyashio System East of Japan, *Journal of Physical Oceanography*, *31*(9), 2575–2589, https://doi.org/10.1175/1520-0485(2001)031<2575:ACVOTK>2.0.CO;2.

Sekine, Y., and K. Kutsuwada (1994), Seasonal Variation in Volume Transport of the Kuroshio South of Japan, *Journal of Physical Oceanography*, *24*(2), 261–272, https://doi.org/10.1175/1520-0485(1994)024<0261:SVIVTO>2.0.CO;2.

Shuntov, V. P. (2022), *Biology of the Far Eastern Seas of Russia, Volume 3*, 445 pp., TINRO Center, Vladivostok (in Russian).

Smith, J., N. Marks, and T. Irwin (2023), The risks of radioactive wastewater release, *Science*, *382*(6666), 31–33, https://doi.org/10.1126/science.adi5446.

Suga, T., and K. Hanawa (1995), The Subtropical Mode Water Circulation in the North Pacific, *Journal of Physical Oceanography*, *25*(5), 958–970, https://doi.org/10.1175/1520-0485(1995)025<0958:TSMWCI>2.0.CO;2.

TEPCO (2023), Partial Revision of the Application for approval to amend the Implementation Plan for Fukushima Daiichi Nuclear Power Station as Specified Nuclear Facility, *Tech. rep.*, Tokyo Electric Power Company Holdings.

Tomosada, A. (1986), Generation and decay of Kuroshio warm-core rings, *Deep Sea Research Part A. Oceanographic Research Papers*, *33*(11–12), 1475–1486, https://doi.org/10.1016/0198-0149(86)90063-4.

Travkin, V. S., T. V. Belonenko, and A. V. Kochnev (2022), Topographic waves in the Kuril region, *Sovremennye problemy distantsionnogo zondirovaniya Zemli iz kosmosa*, *19*(5), 222–234, https://doi.org/10.21046/2070-7401-2022-19-5-222-234 (in Russian).

Udalov, A., M. Budyansky, and S. Prants (2023), A census and properties of mesoscale Kuril eddies in the altimetry era, *Deep Sea Research Part I: Oceanographic Research Papers*, *200*, 104,129, https://doi.org/10.1016/j.dsr.2023.104129.

Venti, N. L., and K. Billups (2013), Surface water hydrography of the Kuroshio Extension during the Pliocene-Pleistocene climate transition, *Marine Micropaleontology*, *101*, 106–114, https://doi.org/10.1016/j.marmicro.2013.02.004.

Zhang, Z., H. Nakamura, and X.-H. Zhu (2021), Seasonal velocity variations over the entire Kuroshio path part II: dynamical interpretation for the current speed variation, *Journal of Oceanography*, *77*(5), 745–761, https://doi.org/10.1007/s10872-021-00603-8.

Russian Journal of Earth Sciences

May 11–12 Extreme Space Weather Events Brief and Dose Rate Model Response

V. A. Burov[1], **K. I. Kholodkov**[1,2*], **and I. M. Aleshin**[1,2,3],

[1]Fedorov Institute of Applied Geophysics, Moscow, Russia
[2]Schmidt Institute of Physics of the Earth of the Russian Academy of Sciences, Moscow, Russia
[3]Geophysical Center of the Russian Academy of Sciences, Moscow, Russia
* **Correspondence to:** Kirill Kholodkov, keir@ifz.ru

Abstract: In this brief paper, we analyze space weather events that occurred on May 11 and 12, 2024, from the perspective of an operational space weather center that provides advisories for civil aviation. One of the key metrics monitored by the center is the radiation dose rate at operational flight altitudes. A model implemented by the center provides the dose rate in real time. The model showed that dangerous levels were momentarily exceeded just above the usual 30,000 feet level during the events. This paper highlights differences in models used by various space weather centers, emphasizing the need for harmonization.

Keywords: space weather, solar proton event, radiation dose rate, civil aviation, ICAO.

Citation: Burov, V. A., K. I. Kholodkov, and I. M. Aleshin (2024), May 11–12 Extreme Space Weather Events Brief and Dose Rate Model Response, *Russian Journal of Earth Sciences*, 24, ES4003, EDN: PBJAET, https://doi.org/10.2205/2024es000929

Introduction

Space weather is a set of phenomena in interplanetary space that occurs as a result of changes in the Sun. Over the past decade, there has been a steady increase in society's awareness of the fact that space weather represents a substantial threat to the technological infrastructure [*Fiori et al.*, 2022; *Green and Baker*, 2015; *Hapgood*, 2011; *Kauristie et al.*, 2021; *Schrijver et al.*, 2015]. In some publications [*Burns et al.*, 2007], the impact of space weather phenomena has been explored, with a particular emphasis on the response of the ionosphere in relation to coronal mass ejections (CMEs) as the primary hazard. Recently, several scholars have directed their attention specifically towards the impact [*Yasyukevich et al.*, 2018] on positioning accuracy during periods of ionospheric disturbances. Other studies have shown the effects of powerful X-ray flares on the ionosphere.

Today, aviation relies heavily on technologies that are vulnerable to space weather disturbances. Prominent examples of these technologies are global navigation satellite systems (GNSS) and over-the-horizon high-frequency (HF) radio communications. X-ray flares can cause serious problems for precision positioning and GNSS (Global Navigation Satellite System) navigation services. Solar flares have been shown to affect navigation services for up to several hours, leading to critical situations in various navigation applications [*Burns et al.*, 2007; *Kauristie et al.*, 2021]. These energetic protons have the potential to reach Earth and pose a threat to aircraft operating in polar regions by degrading HF-communication capabilities.

However, it's not only technology that suffers from space weather disturbances. Aircraft flying at typical commercial and corporate airline altitudes are constantly exposed to high-energy charged particles and secondary neutrons of cosmic origin. These types of particles, known as galactic cosmic rays (GCR) that originate outside our solar system, and solar energetic particles (SEPs) can affect aircraft microelectronics systems and the health of airline crew members and passengers [*Barannikov et al.*, 1987; *Beck et al.*, 2008]. Flights on high-latitude or intercontinental routes may exceed the maximum public and fetal exposure limits during a single solar energetic particle event and through multiple

Research Article

Received: 8 May 2024
Accepted: 15 August 2024
Published: 14 October 2024

(~ 5–10) high-latitude round-trip flights due to GCR exposure. It is important to note that while some countries monitor airline crew radiation exposure, many do not, leaving airline crews as the only occupational group exposed to unquantified and undocumented radiation levels over their careers.

The discussion about the significant impact of space weather on aviation has increased since the beginning of the 21st century. Following the IATA's letter to ICAO in November 2011 requesting a discussion on space weather's impact on aviation, ICAO has been evaluating the use of space weather data in civil aviation. The discussion found its way into the amendment to Annex 3 of Meteorological Service for International Air Navigation. The document regulates the form and way the information on the space weather phenomena reaches the civil aviation stakeholders. The informational message is called the advisory and comes in moderate and severe form. The thresholds for moderate and severe advisories are fixed in the same document. ICAO also initiated a process to establish space weather centers in 2017. Twenty-two countries expressed interest in becoming space weather information providers. Finally, three groups were selected: the US, PECASUS (consisting of Finland, the UK, Germany, Poland, Austria, Italy, the Netherlands, Belgium, and Cyprus), and ACFJ (comprising Australia, Canada, France, and Japan), which have been designated as global centers by ICAO. As of 2022, CRC (China-Russia Consortium) joined as another global center.

China-Russia Consortium [*Kholodkov et al.*, 2021] consists of three organisations: Fedorov Institute of Applied Geophysics (IAG) of Roshydromet, Aviation Meteorological Center (AMC) of Civil Aviation Administration of China and National Center for Space Weather of China Meteorological Administration. Currently, IAG and AMC both act as full-featured space weather centers in round-robin, backing up each other. Besides the duty, CRC organisations also perform research and analysis tasks to improve methods, instruments and regulations. IAG has performed an analysis of recent extreme space weather events in terms of potential industry response. The event is special in a way that it highlighted the differences in methods used to compute the effect of the particular space weather phenomena.

May 11–12 Extreme Space Weather Events

The extreme space weather events observed on May 11–12 were caused by the passage of active region 3664. Hereby we will use the NOAA active region classification. This was the most intense group in this cycle of solar activity, with an area reaching 2400 millionths of the Sun's visible hemisphere, 20 times the size of the Earth. The magnetic configuration was complex, with a beta-gamma-delta pattern, and there were about 50 multipolar spots, large electric currents. In addition, the maximum activity occurred during its passage across the solar disk, where the position of the group was optimal for impacting the Earth's magnetosphere. During this time, there were 6 X-ray class flares, some accompanied by solar particle events, which caused significant difficulties in radio communication and navigation. These events were further amplified by the strongest magnetic storm in the past 21 years. This complex of phenomena resulted in the extreme space weather conditions. Disturbances that are classified as extreme manifestations of solar activity, similar to the “Halloween” storms that occurred in October-November 2003, have been observed.

On May 9, two X-class solar flares were observed within this group. The first flare, X2.2, occurred at 09:13 UT, and the second, X1.1, occurred at 09:17:44 UT. During May 8 and 9, four CME events were recorded, all of which were classified as geoeffective. It is important to note that only those CME events that are directed towards Earth can have a geoeffect, and these events constitute a minority. Three of the CMEs were expected to arrive at Earth on May 10 at around 10:00 UT ±10 hours.

On May 10, three more flares occurred (see Figure 1), with the first being X3.9 at 16:40 UT and the others being X5.8 and X1.5 at 18:01:23 UT and 19:43:33 UT respectively. The proton flux from these flares was recorded at a peak flux value of 207 PFUs (Particle Flux Units, particles $\times\,s^{-1} \times sr^{-1}$) at 17:40 UT. This event was classified as a solar proton event.The event began at 01:40 UT following the X5 flare and the X3 flash. Both of these events were linked to the coronal mass ejection (CME).

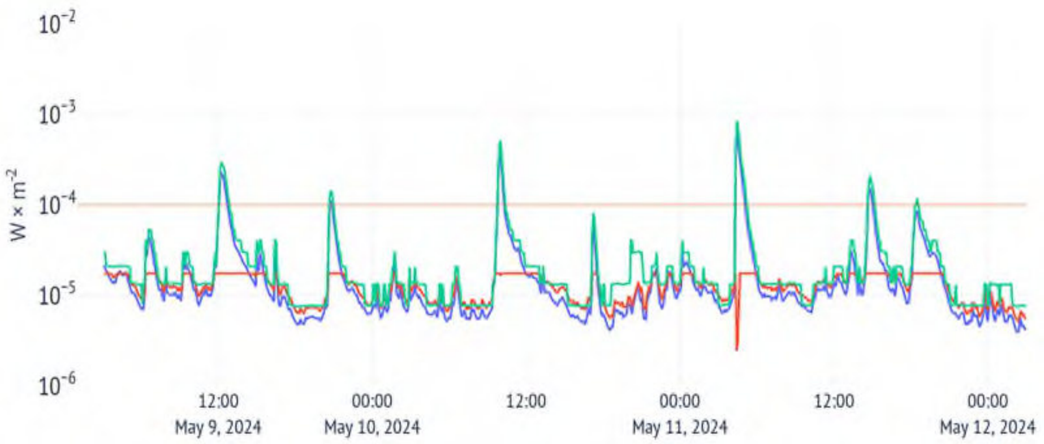

Figure 1. X-Ray flux (in watts × m^{-2}) at GEO from the GOES-16 spacecraft (blue) and GOMS-5 (Elektro-L N4) mission (red – precise measurements, green – coarse measurements). Orange line is the X1 threshold.

On May 10, the speed of the solar wind near Earth doubled to approximately 700 km/s after the arrival of the CME. On May 11, it reached a maximum value of 993 km/s. The peak total intensity of the interplanetary magnetic field (IMF) was 56 nT, and the range of the north-south component (Bz) was between +22 and −50 nT. During this period, Bz was predominantly oriented southward.

Proton fluxes observed during this time were relatively low (level S2) as seen on Figure 2. However, an important aspect of this event is worth noting: a geomagnetic storm occurred (see K-indices on Figure 3). The extent to which proton fluxes from solar flares penetrate and generate secondary particles that create cosmic radiation is dependent not only on the initial proton flux density, but also on the disruption of the magnetic field. Large geomagnetic storms can cause increased penetration and higher dose rates in the atmosphere compared to when there are no disturbances. Our dose calculation model takes this factor into account, as well as variations in the spectrum of primary radiation fluxes.

According to our model, if CRC was operating (on-duty) at the time, we would have issued a moderate type advisory on May 11 between 03 and 08 UTC. Figure 4 shows the examples of dose rate maps with contours of radiation dose rate in mSv/hour for an altitude of 12.2 km (40,000 ft).

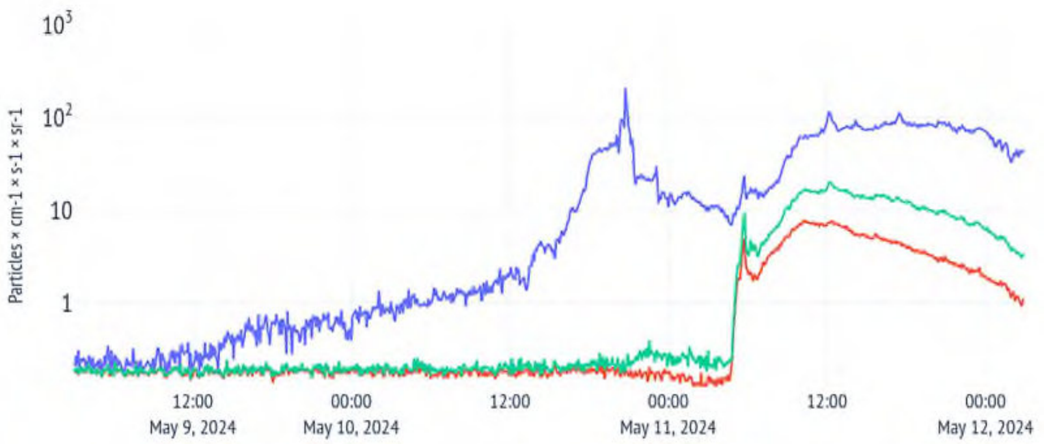

Figure 2. Proton flux (in PFU) at GEO of GOES-series spacecraft. Protons with energies ≥ 10 MeV in blue, ≥ 100 MeV in red, ≥ 50 MeV in green.

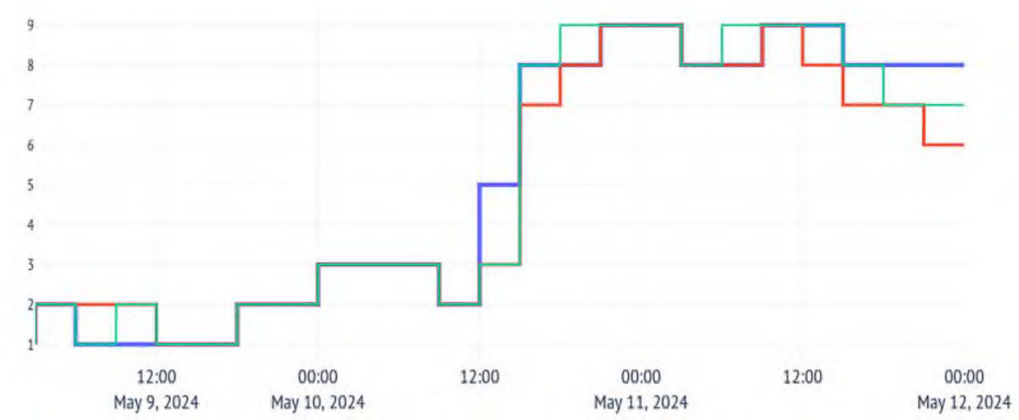

Figure 3. Planetary K-indexes from GFZ German Research Centre for Geosciences (blue), Institute of Applied Geophysics (red), and Space Weather Prediction Center (green).

The on-duty center (ACFJ) issued advisories on communication and positioning degradation but no radiation dose rate advisory. Every space weather center operates their own radiation dose rate model. According to the model that was used by the on-duty ACFJ during the period this event did not require the advisory to be issued. We believe that the differences in our estimates of the solar flare dose rate are due to different methods of calculating solar proton spectra. We calculate the spectrum based on flux measurements from spacecraft, which include a flux with energies between 100 and 500 MeV. In contrast, the calculations based on neutron monitors [e.g., *Lantos et al.*, 2003; *Latocha et al.*, 2009] largely ignores particles of these energies, focusing instead on particles with higher energies. Additionally, we assume that more solar protons reach the atmosphere during strong magnetic storms.

(a) Panel 1

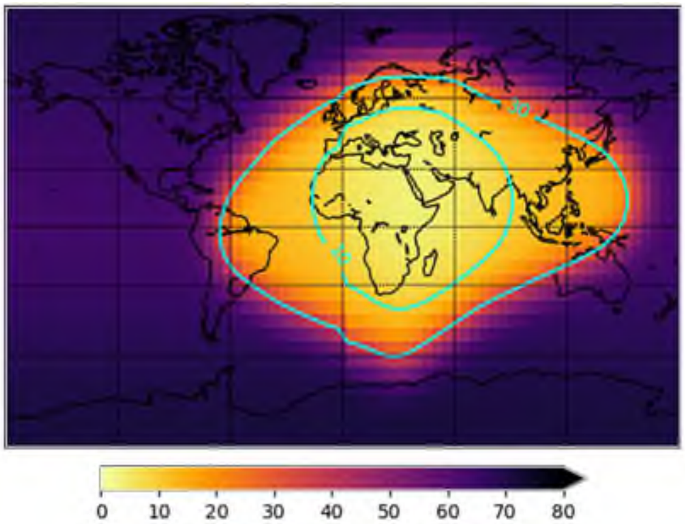

(b) Panel 2

Figure 4. Panel 1 and 2: Radiation dose rate maps (in μSv/hour) for altitude of 12.2 km (40,000 ft) during the onset of the event (02:08:22 UTC and 02:18:23 UTC).

Results

The results that different highlight the importance of model harmonisation that is currently work in progress by Space Weather Center Coordination Group. We expect the fruitful outcome that would increase the confidence among models used by the centers and ultimately increase safety for aviation. Along with harmonisation, the regular scientific-grade onboard dosimetry data will come handy for verification and tuning of the models. As SPEs cannot be forecasted the required equipment shall be installed onboard a small portion of operation civil aviation fleet in order to acquire dosimetry data in case future SPEs happen.

Acknowledgements. Data shown is provided by IAG, NOAA, GFZ, as aggregated at the CRC operations facility at Fedorov Institute of Applied Geophysics. This work is supported by State Assignments of Schmidt Institute of Physics of the Earth of the Russian Academy of Sciences and Geophysical Center of the Russian Academy of Sciences.

References

Barannikov, Y. I., O. A. Barsukov, and P. F. Gavrilov (1987), Calculation of ionizing radiation levels along trajectories of high-altitude flights, *JPRS Report Science Technology USSR Space*, *21*(2), 102–109.

Beck, P., D. T. Bartlett, P. Bilski, et al. (2008), Validation of modelling the radiation exposure due to solar particle events at aircraft altitudes, *Radiation Protection Dosimetry*, *131*(1), 51–58, https://doi.org/10.1093/rpd/ncn238.

Burns, A. G., S. C. Solomon, W. Wang, and T. L. Killeen (2007), The ionospheric and thermospheric response to CMEs: Challenges and successes, *Journal of Atmospheric and Solar-Terrestrial Physics*, *69*(1–2), 77–85, https://doi.org/10.1016/j.jastp.2006.06.010.

Fiori, R., V. V. Kumar, D. H. Boteler, and M. B. Terkildsen (2022), Occurrence rate and duration of space weather impacts on high-frequency radio communication used by aviation, *Journal of Space Weather and Space Climate*, *12*, 21, https://doi.org/10.1051/swsc/2022017.

Green, L., and D. Baker (2015), Coronal mass ejections: a driver of severe space weather, *Weather*, *70*(1), 31–35, https://doi.org/10.1002/wea.2437.

Hapgood, M. A. (2011), Towards a scientific understanding of the risk from extreme space weather, *Advances in Space Research*, *47*(12), 2059–2072, https://doi.org/10.1016/j.asr.2010.02.007.

Kauristie, K., J. Andries, P. Beck, et al. (2021), Space Weather Services for Civil Aviation-Challenges and Solutions, *Remote Sensing*, *13*(18), 3685, https://doi.org/10.3390/rs13183685.

Kholodkov, K., I. Aleshin, A. Arakelov, V. Burov, A. Vasiliev, and S. Ivanov (2021), Sino-Russian Space Weather Effort for Global Air Navigation Safety, *Russian Journal of Earth Sciences*, *21*(4), https://doi.org/10.2205/2021ES000774.

Lantos, P., N. Fuller, and J.-F. Bottollier-Depois (2003), Methods for Estimating of Radiation Doses Received by Commercial Aircrew, *Aviation*, *Space and Environmental Medicine*, *74*(7), 746–752.

Latocha, M., P. Beck, and S. Rolle (2009), AVIDOS-a software package for European accredited aviation dosimetry, *Radiation Protection Dosimetry*, *136*(4), 286–290, https://doi.org/10.1093/rpd/ncp126.

Schrijver, C. J., K. Kauristie, A. D. Aylward, et al. (2015), Understanding space weather to shield society: A global road map for 2015-2025 commissioned by COSPAR and ILWS, *Advances in Space Research*, *55*(12), 2745–2807, https://doi.org/10.1016/j.asr.2015.03.023.

Yasyukevich, Y., E. Astafyeva, A. Padokhin, et al. (2018), The 6 September 2017 X-Class Solar Flares and Their Impacts on the Ionosphere, GNSS, and HF Radio Wave Propagation, *Space Weather*, *16*(8), 1013–1027, https://doi.org/10.1029/2018SW001932.

Solving Inverse Magnetometry Problems Using Fuzzy Logic

S. M. Agayan[1], **Sh. R. Bogoutdinov**[*,1,2], **and I. Y. Firsov**[1]

[1]Geophysical Center RAS, Moscow, Russia
[2]Schmidt Institute of Physics of the Earth RAS, Moscow, Russia
* **Correspondence to:** Shamil Bogoutdinov, shm@gcras.ru.

Abstract: Integration interpretation of geophysical anomalies is a procedure for extracting geological and geophysical information about the object under study from observed physical fields. Interpretations are closely related to solutions of systems of linear algebraic equations (SLAE), therefore the possibility of the most complete and constructive description of all solutions of SLAE is of particular importance. It will allow you to take into account all additional information about the object and obtain the highest quality interpretation. The paper presents the authors' results on the constructive description of SLAE solutions and its application to the construction of gravimetric interpretations.

Keywords: system of linear algebraic equations; inverse magnetometry problem; constructive description of solutions; projection method.

Citation: Agayan, S. M., Sh. R. Bogoutdinov, and I. Y. Firsov (2024), Solving Inverse Magnetometry Problems Using Fuzzy Logic, *Russian Journal of Earth Sciences*, 24, ES4004, EDN: ZMRLJG, https://doi.org/10.2205/2024es000932

Introduction

Interpretation of geophysical anomalies is a process of extraction of information from observed physical field data, which contain a large amount of geological information in a hidden form. The main objective of data interpretation is to extract this information in order to solve a specific geological problem. Interpretation is not a strictly structured process, and to perform the task, the interpreter must be a skilled individual, and possess all the tools to extract the geological information from the geophysical fields. However, based on geophysical data alone, it is only possible to formally describe the distribution of physical properties, and there may be infinite amounts of examples of such distributions. Therefore, to perform a meaningful interpretation, all available a priori geological and geophysical information on the object under study is required. Interpretation is also mainly carried out within the framework of certain models, which is a set of simplifications and assumptions for this particular problem.

One of the principal methods for solving inverse problems of geophysics is the regularization method. The classic theory of regularization of systems of linear algebraic equations (SLAEs) was created in the works of Tikhonov, Ivanov, and Lavrentiev, as well as in multiple works of their follower in the 1960s–1980s [*Tikhonov and Arsenin*, 1979; *Turchin and Turovtseva*, 1973; *Zelenyi et al.*, 2018].

One of the objectives of the interpretation process is to determine the parameters of objects that create the studied anomaly field. Such problems are called "inverse problems", which refer to under determined problems of mathematical physics.

Existing methods for solving the inverse problems, such as the regularization technique, mostly search for a quasi-resolution, which may not be a solution to the source problem, but only an approximation to it.

In this study we consider an approach that allows us to describe a set of solutions that satisfy the problem and to search among these equivalent solutions for a model that best satisfies the available a priori information about the distribution of model properties.

A constructive description of the variety of solutions $\Phi(A,b)$ of a linear system $Ax=b$ in the finite-dimensional Euclidean space E allows us to consider a priori information about the properties of the desired solution x^f by searching for it on the variety $\Phi(A,b)$.

Research Article

Received: 17 November 2023
Accepted: 27 August 2024
Published: 15 October 2024

Technically, it looks like this: the expert point of view on the desired solution x^f is formalized by a non-negative functional F on $\Phi(A,b)$, and the solution x^f minimizes it. If there are several points of view on x^f and a system of functionals $\mathcal{F} = (F_1, \ldots, F_k)$ is responsible for them, then the search for x^f is reduced to a multi-criteria choice $B(\Phi(A,b),\mathcal{F})$ relative to $\mathcal{F}$ on $\Phi(A,b)$.

The above is graphically conveyed by the diagram

$$Ax = b \to \Phi(A,b) \to \mathcal{F} \to B(\Phi(A,b),\mathcal{F}) \to x^f. \tag{1}$$

The first transition in (1) relates entirely to linear algebra and in this paper will be performed using the Gramm-Schmidt orthogonalization.

The second transition in (1) formalizes the a priori information about the sought solution x^f into a system of functionals $\mathcal{F}$ on the manifold $\Phi(A,b)$ and therefore requires a wide range of methods (fuzzy mathematics, machine learning, etc.).

We construct a formalization of three expert statements E_μ, E_S and their conjunctions $E_{\mu S} = E_\mu \wedge E_S$. Let us give their formulations:

- Statement E_μ: "the sought solution x^f is similar to the known vector μ".
- Statement E_S: let the coordinates in E be indexed by a known set I, so that any x of E can be considered as a function on I: $x : i \to x_i, i \in I$. Let us denote by S the partition $I = I_1 \vee \cdots \vee I_k$ and consider a vector x to be S-homogeneous if it is constant on every I_k.
  E_S: "the desired solution x^f is S-homogeneous".
- Statement $E_{\mu S}$: "the sought solution x^f is similar to the vector μ and is homogeneous with respect to the partition S".

The third transition in (1) is a broad optimization of functionals from $\mathcal{F}$ on the manifold $\Phi(A,b)$, involving both classical continuous methods (gradient, penalty functions, etc.) and discrete ones (choice theory, neural networks, etc.).

In the present paper the optimization on $\Phi(A,b)$ is performed by analytical methods: the gradients of the functionals associated with statements E_μ, E_S, $E_{\mu S}$ will be explicitly found, and with their help the variants of the true solution x^f.

Examples illustrating theoretical constructions are mainly related to gravimetry and are of both artificial and natural origin.

Projection method

The initial space E is assumed to be n-dimensional Euclidean space with respect to the scalar product $(,)$.

In a linear system

$$Ax = b \equiv (a_i, x) = b_i;\ i = 1, \ldots, m,\ x \in E, \tag{2}$$

A simultaneously means both the set of vectors a_i from E and the matrix $m \times n$ with vectors a_i as rows, $b = (b_i|_{i=1}^m)$.

The projection method, as applied to the system (2), consists in efficiently constructing the manifold of its solutions $\Phi(A,b)$. This problem was solved by the authors in [*Agayan et al.*, 2020] based on the systematic use of the orthoprojector $H(a)$ perpendicular to $a \in E$: $H(a) = 1 - \frac{aa^\top}{a^\top a}$ if $A \neq 0$, and $H(0) = 1$.

In the present paper, the Gramm-Schmidt orthogonalization will have a major role in the presentation of the projection method.

Homogeneous systems

For the homogeneous system $Ax = 0$ the solution space $\Phi(A,0)$ coincides exactly with the orthogonal addition in E to the subspace $L(A)$ generated by A: $\Phi(A,0) = L(A)^{\perp}$. Therefore to solve the system $Ax = b$ we have to construct an orthoprojector

$$H = H(A) : E \to L(A)^{\perp}.$$

Let us do this using the Gramm-Schmidt orthogonalization process: if $G = \{g_i|_{i=1}^{N}$, $N = \operatorname{rang} A\}$ its result for the set A: $G = \mathrm{GSh}(A)$, then

$$H(A)(x) = x - \sum_{i=1}^{N} \frac{(x, g_i)}{(g_i, g_i)} g_i \ \forall x \in E. \tag{3}$$

Inhomogeneous systems

The solution of the inhomogeneous system $Ax = b$ is the sum of the partial x^* and the homogeneous one, so $\Phi(A,b) = x^* + \Phi(A,0)$. In the search for the solution x^* we will use the equivalence given below and the realization of its right-hand side using GSh orthogonalization:

$$x \in \Phi(A,b) \equiv \begin{array}{l} x \text{ vector in } E, \text{ whose image } Ax \text{ is the} \\ \text{projection } b \text{ on the image } \operatorname{Im} A \text{ in } \mathbb{R}^m \end{array}.$$

The system $P = \{Ae_j|_{j=1}^{n}\}$ generates an image in $\operatorname{Im} A$ in $\mathbb{R}^m$. Let us apply the orthogonalization of GSh to P and obtain an orthogonal system $G = \mathrm{GSh}(P)$: $G = \{g_i|_{i=1}^{N}$, $N = \operatorname{rang} P\}$.

We need prototypes of y_i vectors g_i under mapping A: $Ay_i = g_i$. If we know vectors y_i, then

$$b = \sum_{i=1}^{N} \frac{(b, g_i)}{(g_i, g_i)} g_i = \sum_{i=1}^{N} \frac{(b, g_i)}{(g_i, g_i)} Ay_i = A\left(\sum_{i=1}^{N} \frac{(b, g_i)}{(g_i, g_i)} y_i\right).$$

Thus, the vector

$$x^* = \sum_{i=1}^{N} \frac{(b, g_i)}{(g_i, g_i)} y_i \tag{4}$$

will give us a partial solution to the system $Ax = b$.

We construct vectors g_i and y_i iteratively. We start with g_i: if $g_1, \ldots, g_{i-1}$, $i \geq 2$ are known, then according to GSh:

$$g_i = Ae_i - \sum_{k=1}^{i-1} \frac{(Ae_i, g_k)}{(g_k, g_k)} g_k. \tag{5}$$

Starting with $g_1 = Ae_1$.

If the vectors $y_1, \ldots, y_{i-1}$, $i \geq 2$ are known, then taking into account (5)

$$g_i = Ae_i - \sum_{k=1}^{i-1} \frac{(Ae_i, g_k)}{(g_k, g_k)} Ay_k = A\left(e_i - \sum_{k=1}^{i-1} \frac{(Ae_i, g_k)}{(g_k, g_k)} y_k\right).$$

Thus,

$$y_i = e_i - \sum_{k=1}^{i-1} \frac{(Ae_i, g_k)}{(g_k, g_k)} y_k. \tag{6}$$

Starting with $y_1 = e_1$.

To summarize: the effective parametrization of the variety of the solution $\Phi(A,b)$ of the linear system $Ax = b$ with the help of the GSh orthogonalization is the correspondence

$$x = x^* + Hs,\ s \in E, \tag{7}$$

where H and x^* are given by the formulas (3) and (4).

Example 1. *A system of linear equations is given $Ax = b$:*

$$A = \begin{pmatrix} 2 & -1 & 1 & 2 & 3 \\ 6 & -3 & 2 & 4 & 5 \\ 6 & -3 & 4 & 8 & 13 \\ 4 & -2 & 3 & 4 & 2 \end{pmatrix}; \quad b = \begin{pmatrix} 2 \\ 3 \\ 9 \\ 1 \end{pmatrix}. \tag{8}$$

After implementation Gramm-Schmidt orthogonalisations for the system $P = \{Ae_j|_{j=1}^n\}$, we obtain an orthogonal system $G = GSh(P)$: $G = \{g_i|_{i=1}^N, N = \operatorname{rang} P = 3\}$ (5)

$$\begin{array}{lcl} g_1^\top & = & (\ 2.000,\ \ 6.000,\ \ 6.000,\ \ 4.000); \\ g_2^\top & = & (-0.087,\ -1.261,\ 0.740,\ \ 0.826); \\ g_3^\top & = & (\ 0.123,\ -0.215,\ 0.954,\ -1.169). \end{array}$$

and the corresponding system Y: $Y = \{y_i|_{i=1}^N, N = \operatorname{rang} P = 3\}$ (6)

$$\begin{array}{lcl} y_1^\top & = & (\ 1.000,\ 0.000,\ \ 0.000,\ 0.000,\ 0.000); \\ y_2^\top & = & (-0.543,\ 0.000,\ \ 1.000,\ 0.000,\ 0.000); \\ y_3^\top & = & (-0.231,\ 0.000,\ -1.415,\ 1.000,\ 0.000). \end{array}$$

By substituting the calculated g_i, y_i, $i = 1,2,3$ into (4), we obtain a partial solution to our system

$$x^* = (-0.5,\ \ 0.0,\ \ -3.0,\ \ 3.0,\ \ 0.0).$$

The discrepancy in the solution obtained is $||Ax - b|| = 8.189e^{-15}$.

Statement E_μ

The variety $\Phi(A,b)$ serves as the domain of determining an arbitrary statement about the true solution x^f. We will begin with the most basic of these, namely, the statement E_μ about the similarity of x^f to the known vector μ of E. Two interpretations will be given and analyzed.

First Interpretation

In this case, the similarity of x^f and μ is understood metrically as proximity in E: "x^f is the closest point to μ on the variety of solutions $\Phi(A,b)$".

If $x^* + Hs$ parameterizes $\Phi(A,b)$ (7), then the solution $\tilde{x}^f = x^* + HS^f$, which is a variant of the true solution x^f based on this interpretation of statement E_μ, is reduced to unconditional minimization by s on E the first version of the F_μ function:

$$F_\mu(s) = \left\| x^* + Hs - \mu \right\|^2; \quad \operatorname{grad} F_\mu(s) = H^\top Hs - H^\top(\mu - x^*), \tag{9}$$

which leads to a linear system of equations on the sought parameter s^f:

$$H^\top Hs^f = H^\top(\mu - x^*), \tag{10}$$

which can be solved by the projection method.

Example 2. *For the system* (8) *we will look for a solution close to the known vector* μ. *As* μ *a zero vector is taken, so in this case the problem is reduced to finding the minimum by norm solution* x^f.

To solve the problem, just construct the projector H [Agayan et al., 2020] *and, assuming* $A = H^\top H$, $b = -H^\top x^*$, *find* s^f (10). *Using the* (3)–(10) *approach described above, we get* s^f *and* x^f:

$$\begin{array}{lcl} s^f & = & (48.500, \ -24.000, \ 0.000, \ 0.000, \ 0.000); \\ x^f & = & (-0.108, \ 0.054, \ -0.084, \ 0.084, \ 0.729). \end{array}$$

The uncertainty of the resulting solution $\left\|Ax^f - b\right\| = 6.286e^{-14}$. *The norm of* $\left\|x^f\right\| =$ 0.74849, *while the norm of* x^* *from the example* 1 *is* 4.27200.

Second Interpretation

This version of the similarity of x^f and μ is more invariant with respect to μ and in a sense semicorrelated: "x^f is the closest point on $\Phi(A,b)$ to the line $L(\mu)$ generated by vector μ".

In this case, the search for $\tilde{x}^f = x^* + Hs$ (a variant of x^f based on statement E_μ) is reduced to absolute minimization by s and t on the product $E \times \mathbb{R}$ of the second version of the F_μ functional:

$$F_\mu(s) = \left\|x^* + Hs - \mu t\right\|^2.$$

The desired pair of parameters (s^f, t^f) is obtained as a solution to a linear system

$$\begin{pmatrix} H^\top \mu & -H^\top \mu \\ -\mu^\top H & ||\mu||^2 \end{pmatrix} \begin{pmatrix} s^f \\ t^f \end{pmatrix} = \begin{pmatrix} -H^\top x^* \\ (x^*, \mu) \end{pmatrix}$$

and $x^f = x^* + Hs^f$.

Example 3. *This example is related with the inverse problem of gravimetry on a two-dimensional model with a given density grid* ρ (*Figure 1*).

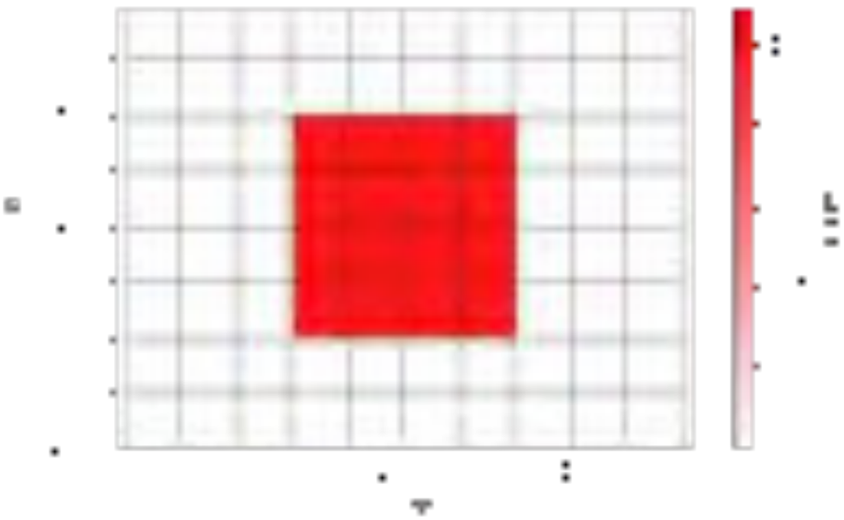

Figure 1. Density grid.

In this case x_j *– the unknown density in jth rectangular cell with vertices* σ_ν^j, $\nu = 1,2,3,4$; b_i *– the value of the observed field at point* s_i *on the surface;* a_{ij} *– the conversion factor for the density j-th cell in the attraction at ith observation point. We have:*

$$b_i = \sum_j a_{ij} x_j,$$
$$a_{ij} = Re(G(s_i, \sigma^j)).$$

The complex gravitational potential $G(s,\sigma)$ *is calculated using the formula* [Bulychev et al., 2010]:

$$G(s,\sigma) = G\delta \sum_{\nu=1}^{N} (\alpha_\nu s + \beta_\nu - \overline{s}) \ln \frac{\sigma_{\nu+1} - s}{\sigma_\nu - s},$$
$$\alpha_\nu(\sigma) = \frac{\overline{\sigma}_{\nu+1} - \overline{\sigma}_\nu}{\sigma_{\nu+1} - \sigma_\nu},$$
$$\beta_\nu(\sigma) = \overline{\sigma}_\nu - \alpha_\nu \sigma_\nu,$$

where G is the universal gravitational constant, δ *is the density of the cell (in this case taken as unit),* σ_ν *is the complex coordinate of the* $\nu - th$ *vertex of the quadrangle,* $\overline{s}$ *and* $\overline{\sigma}$ *are complex conjugate quantities.*

Figure 2 shows a given density distribution ρ *and a priori information* μ*, which is equal to a slightly noisy half of the original model density.*

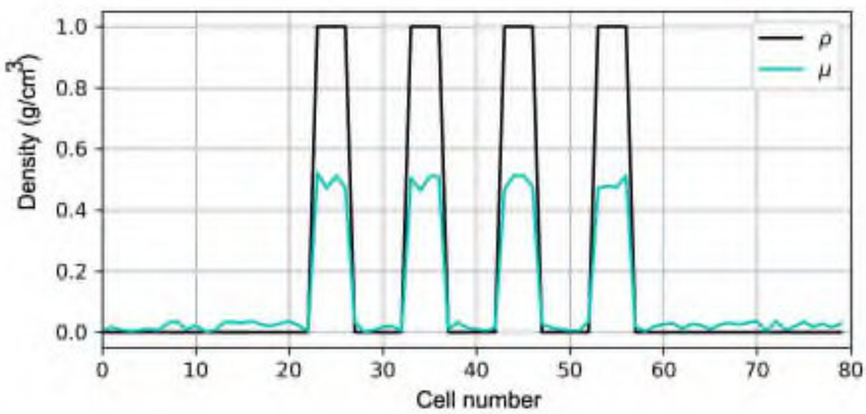

Figure 2. Source model density and a priori information.

Figure 3 shows the density distributions x^f *and* x^T *found, respectively, using the projection method* (10) *and the Tikhonov regularisation method* [Tikhonov and Arsenin, 1979] *with* $\alpha = 0.1$. *It can be seen that while the Tikhonov regularisation method adds uninformative background values to the a priori model, the method under study uses a priori information in order to find a similar solution on the variety of solutions. This way, the main information is concentrated where the interpreter wants it to be.*

1. *Solution evaluation by projection method (scheme* (10)*):*

$$\left\| x^f - \rho \right\| = 0.4382, \qquad \left\| Ax^f - b \right\| = 5.305e^{-7}.$$

2. *Evaluation of the solution by the Tikhonov regularization method* ($\alpha = 0.001$)*:*

$$\left\| x^T - \rho \right\| = 1.7667, \qquad \left\| Ax^T - b \right\| = 1.062e^{-2}.$$

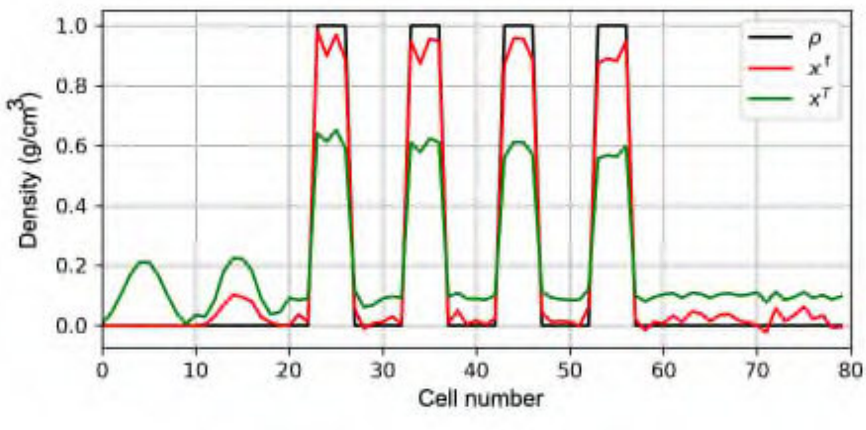

Figure 3. Comparison of solutions with the initial model.

Statement E_S

Let the coordinates in the space $E = \mathbb{R}^N(x)$ be indexed by the set I $(N = |I|)$, so that any vector $x \in E$ can be considered a function on I: $x:\ i \to x_i, i \in I$.

Let us denote by S the disjunctive partition $I = I_1 \vee \cdots \vee I_K$, $S = \{I_k|_{k=1}^K\}$ and consider the vector x S-homogeneous if it is constant on each block $I_k, k = 1,\ldots,K$. Let us formulate a statement E_S:

E_S: "the true solution x^f of the system $Ax = b$ S-homogeneous".

The attention to E_S is not accidental, since homogeneity –a fundamental property of nature (we can just look at geology).

Formalization E_S

Any vector $x \in E$ is naturally associated with a S-homogeneous vector, which we call S-averaging x and denote by $M_S x$:

$$(M_S x)_i = \frac{\sum_{j \in I_k} x_j}{|I_k|}, \text{ if } i \in I_k. \tag{11}$$

The correspondence $x \to M_S x$ – projector in E, the quadratic deviation $F_S(x)$ from which quantitatively characterizes the S-homogeneity of x and thus formalizes the statement E_S

$$F_S(x) = ||x - M_S x||^2. \tag{12}$$

Let us represent $F_S(x)$ through intra-block homogeneity uncertainties. To do this, denote by pr^k: $E \to \mathbb{R}^{|I_K|}$ the mapping of constraint x to block I_k: $x \to x^k = x|_{I_k}$, and by $F_k(x) = \left\|x^k - \overline{x^k}\right\|^2$ the deviation x^k from its mean $\overline{x^k}$.

This deviation can be understood as an inverse quantitative characteristic of the homogeneity of the vector $x^k \in \mathbb{R}^{|I_k|}$ with respect to the trivial partition of the block I_k consisting only of itself. Therefore

$$\left\|x^k - \overline{x^k}\right\|^2 = F_{I_k}(x^k) \text{ and } F_k(x) = F_{I_k}(\mathrm{pr}^k x). \tag{13}$$

From the very definition (12) of the function $F_S(x)$ follows the equality

$$F_S(x) = \sum_{k=1}^K F_k(x). \tag{14}$$

For any i of block I, the equality $|x_i - M_S x|^2 = |x_i - \overline{x^k}|^2$ is true.

Gradient E_S

The calculation of the gradient $\operatorname{grad} F_k(x)$ is much related to the calculation of the gradient $\operatorname{grad} F_{I_k}(x^k)$. Without loss of generality, we do this below for the function $F_I(x)$ in E. The gradients $\operatorname{grad} F_{I_k}(x^k)$ must then be assembled together using the projectors $\operatorname{pr}^k x$ to obtain $\operatorname{grad} F_S(x)$ (14). Let us do this first for the so-called S partition consistent with I, and then reduce the general case of S to a consistent one.

Each block I_k of partition S has within it an ordering $I_k = \{i_1^k < \cdots < i_{|I_k|}^k\}$, induced by the outer ordering on I: $I = \{i_1 < \cdots < i_N\}$.

Thus, any index i has two coordinates $i = i_j^k$ associated with the partition S besides its main number m in I: $i = i_m$, $m = m(i)$:

$k = k(i,S)$ – the number of the block I_k of partition S, which includes index i;
$j = j(i,S)$ – internal index number i directly in block I_k.

Call a partition S consistent with I if

$$m(i) = \sum_{k<k(i,S)} |I_k| + j(k,S),\ \forall i \in I. \tag{15}$$

Informally, this means that S is a partition of I into consecutive segments $I_1 = \{i_1,\ldots,i_{|I_1|}\}$, $I_2 = \{i_{|I_1|+1},\ldots,i_{|I_1|+|I_2|}\}$ and so on.

Let us find $\operatorname{grad} F_S(x)$ for such S and start, as mentioned above, by calculating the gradients $\operatorname{grad} F_{I_k}(x^k)$ for all $k = 1,\ldots,K$ on the example $\operatorname{grad} F_I(x)$.

So, $x = (x_1,\ldots,x_N)$, $N = |I|$

$$F_I(x) = \sum_{i=1}^{N}\left(x_i - \frac{\sum_{j=1}^{N} x_j}{N}\right)^2 = \sum_{i=1}^{N} \frac{\left((N-1)x_i - \sum_{j\neq i} x_j\right)^2}{N^2}.$$

By selecting the coordinate x_1, calculate the derivative $\frac{\partial F_I}{\partial x_1}$

$$F_I(x) = \frac{\left((N-1)x_1 - x_2 - \cdots - x_N\right)^2}{N^2} + \frac{\left(-x_1 + (N-1)x_2 - \cdots - x_N\right)^2}{N^2} + \\ + \cdots + \frac{\left(-x_1 - x_2 - \cdots + (N-1)x_N\right)^2}{N^2}$$

Taking the derivative, we get

$$\frac{\partial F_I(x)}{\partial x_1} = \frac{(N-1)}{N^2}\left((N-1)x_1 - x_2 - \cdots - x_N\right) - \frac{1}{N^2}\left(-x_1 + (N-1)x_2 - \cdots - x_N\right) - \\ - \cdots - \frac{1}{N^2}\left(-x_1 - x_2 - \cdots + (N-1)x_N\right)$$

After transformations we get the following equality

$$\frac{\partial F_I(x)}{\partial x_1} = x_1 - \frac{1}{N}\sum_{i=1}^{N} x_i.$$

Similarly for x_k, $k > 1$

$$\frac{\partial F_I(x)}{\partial x_k} = x_k - \frac{1}{N}\sum_{i=1}^{N} x_i.$$

So that

$$\operatorname{grad} F_I(x) = x - \frac{\operatorname{tr} x}{N}\vec{1} = \left(1_N - \frac{1}{N}E_N\right)(x),$$

where $\vec{1}$ is a vector with unit coordinates from E, 1_N (E_N) — identity matrix (constant matrix with unit elements) of order N.

Recalling that $N = |I|$, let

$$G_I = 1_{|I|} - \frac{1}{|I|} E_{|I|},$$

and conclude: for $k = 1, \dots, K$

$$\operatorname{grad} F_{I_k}(x^k) = G_{I_k}(x^k),$$

where

$$G_{I_k} = 1_{|I_k|} - \frac{1}{|I_k|} E_{|I_k|}.$$

Due to the consistency of the partition S with I, the union of the gradients $\operatorname{grad} F_{I_k}(x^k)$ is given by the product of the block matrix $G_S = \{G_{I_k}|_{k=1}^K\}$ and vector x in the representation $x = (x^k|_{k=1}^K)$:

$$\operatorname{grad} F_S(x) = G_S(x) = \begin{Vmatrix} G_{I_1} & & 0 \\ & \ddots & \\ 0 & & G_{I_K} \end{Vmatrix} \cdot \begin{Vmatrix} x^1 \\ \vdots \\ x^K \end{Vmatrix}.$$

If the partition S is not consistent with I in coordinates x, then, keeping the same notation S, the transition in space E from coordinates x to new coordinates y:

$$x_i = y_{\sum_{k<k(i,S)} |I_k|} + j(i,S),$$

we obtain the consistency of the partition S with the set of indices I in coordinates y (15).

Using the invariance of S-homogeneity from coordinates, let us calculate the S-homogeneity of any vector x of E in its y-coordinates

$$F_S(x) = F_S(y(x)).$$

Hence, taking into account the rule of differentiation of the superposition we have the gradient in the general case

$$\operatorname{grad} F_S(x) = S^\top G_S S x.$$

The last step in formalizing the statement E_S – the superposition of the functional $F_S(x)$ with the parameterization $x = x^* + Hs$, which we denote by $F_S(s)$ and give its gradient

$$\operatorname{grad} F_S(s) = H^\top S^\top G_S S(x^* + Hs). \tag{16}$$

To summarize: the search for the true solution $x^f = x^* + Hs : a$ based on S-homogeneity reduces to the solution of the linear system

$$H^\top S^\top G_S S H s^f = -H^\top S^\top G_S S x^*. \tag{17}$$

In its pure form, statement E_S tells only about the S-homogeneity of the true solution x^f, which is highly ambiguous and therefore ineffective.

To reduce the ambiguity of statement E_S, we need to connect it to some other statement about x^f. We do this below by connecting the statement E_S with the statement E_μ in the first treatment.

Statement $E_{\mu S}$

The conjunction $E_{\mu S}$ = {desired solution x^f of the system $Ax = b$ is similar to the vector μ and S-homogeneous} will be realized by the α-linear connection $F_\alpha(s)$ of functionals $F_S(s)$ (16) and $F_\mu(s)$ (9); $\alpha \in [0,1]$:

$$F_\alpha(s) = F_{\mu S}^\alpha(s) = \alpha F_S(s) + (1-\alpha) F_\mu(s) \tag{18}$$

Then

$$\operatorname{grad} F_\alpha(s) = \alpha H^\top S^\top G_S S(x^* + Hs) + (1-\alpha)(H^\top Hs - H^\top(\mu - x^*))$$

and therefore finding the true solution $x^f = x^* + Hs^f$ based on the statement $E_{\mu S}$ is reduced to solving a linear system

$$(\alpha(SH)^\top G_S SH + (1-\alpha)H^\top H)s^f = -\alpha(SH)^\top G_S Sx^* + (1-\alpha)H^\top(\mu - x^*). \tag{19}$$

The last part of this article is devoted to examples of inference (19) based on judgement $E_{\mu S}$.

Synthetic point example of finding a solution using the $F_{s\mu}$ functional

Let us consider the obtained results of solving the inverse problem from the point of view of closeness to the true density distribution.

Let us construct a two-dimensional synthetic model with 32 × 32 points horizontally and vertically. The distance between the points is 129 m horizontally and 32 m vertically. As points we take spheres with radius $R = 10$ m approximated by points. The observed effect is calculated by the formula (20).

$$V_z = G\frac{4}{3}\pi R^3 \sigma \frac{\zeta - z}{((\xi - x)^2 + (\gamma - y)^2 + (\zeta - z)^2)^{3/2}}, \tag{20}$$

where x, y, z are coordinates of the observation point, ξ, γ, ζ are coordinates of the center of the sphere, G is the gravitational constant, R is the sphere radius, σ is the sphere density.

The system $Ax = b$ describes the gravitational effect of the density environment. The system of linear equations can be written as follows:

$$\begin{aligned} &a_{11}x_1 + a_{12}x_2 + \cdots + a_{11}x_n = b_1 \\ &a_{21}x_1 + a_{22}x_2 + \cdots + a_{21}x_n = b_2 \\ &\ldots \\ &a_{m1}x_1 + a_{m2}x_2 + \cdots + a_{m1}x_n = b_m, \end{aligned} \tag{21}$$

where x_i are the unknown densities, a_{ji} is the effect of the i-th sphere with unit radius at observation point j, b_j is the value of the observed field at point j.

The structure of the model is the disjunctive union into 2 × 2 blocks (Figure 4). The densities of points on the grid vary from 1 to 4, but they are the same in blocks 2 × 2 (Figure 5a).

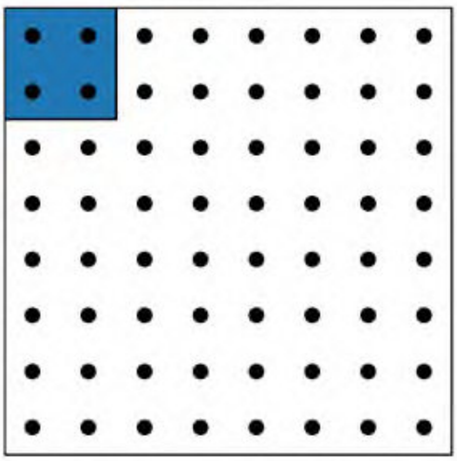

Figure 4. Explanation of combining grid points into block structures.

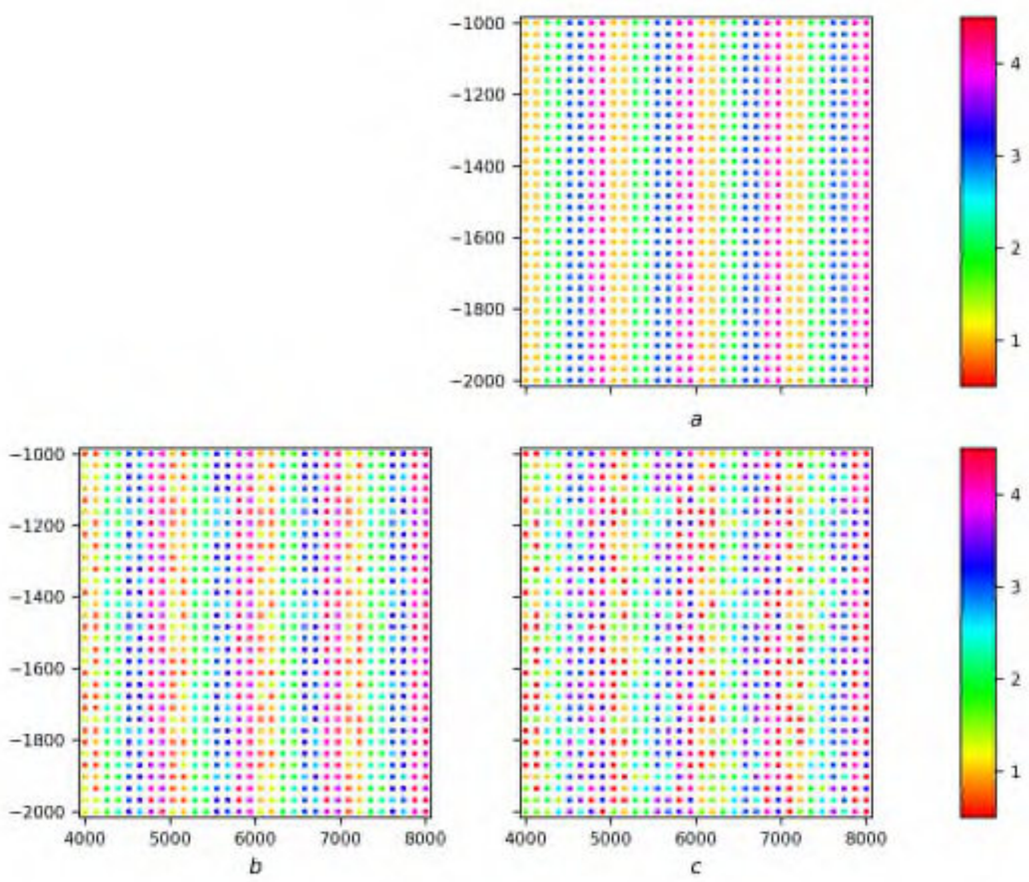

Figure 5. a – initial density distribution (ρ);
b – μ_1=ρ+random noise 10%; c – μ_2=ρ+random noise 20%.

The number of observation points is 51 in the range from 0 to 12,000 m. Figure 6 shows the response on the surface of the initial density distribution (Figure 5a).

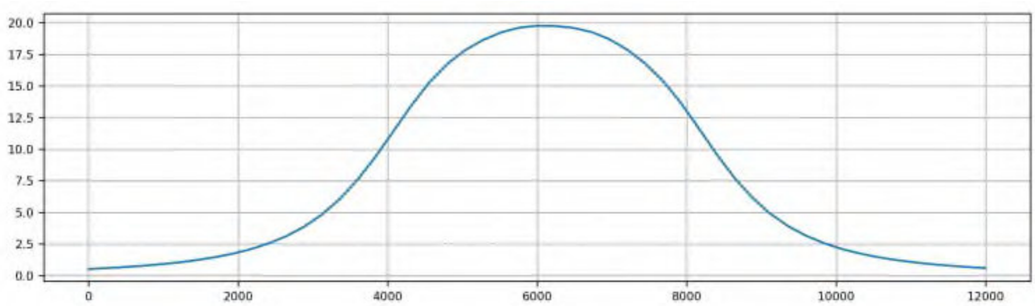

Figure 6. Response on the surface from the original density distribution.

To test the performance of the $F_{s\mu}$ functional, we introduce two vectors μ_1 (Figure 5b) and μ_2 (Figure 5c), which are equal to the original point density (Figure 5a) with the addition of random noise of maximum amplitude 10 and 20 percent, respectively, of the scatter of the original density, and consider its results on the 2×2 block system at α = 0.0, 0.1, 0.5, 0.99.

Figure 7 shows the results of finding solutions for the a priori density distribution μ_1 (Figure 5b). The Table 1 summarizes the quality criteria for the obtained solutions.

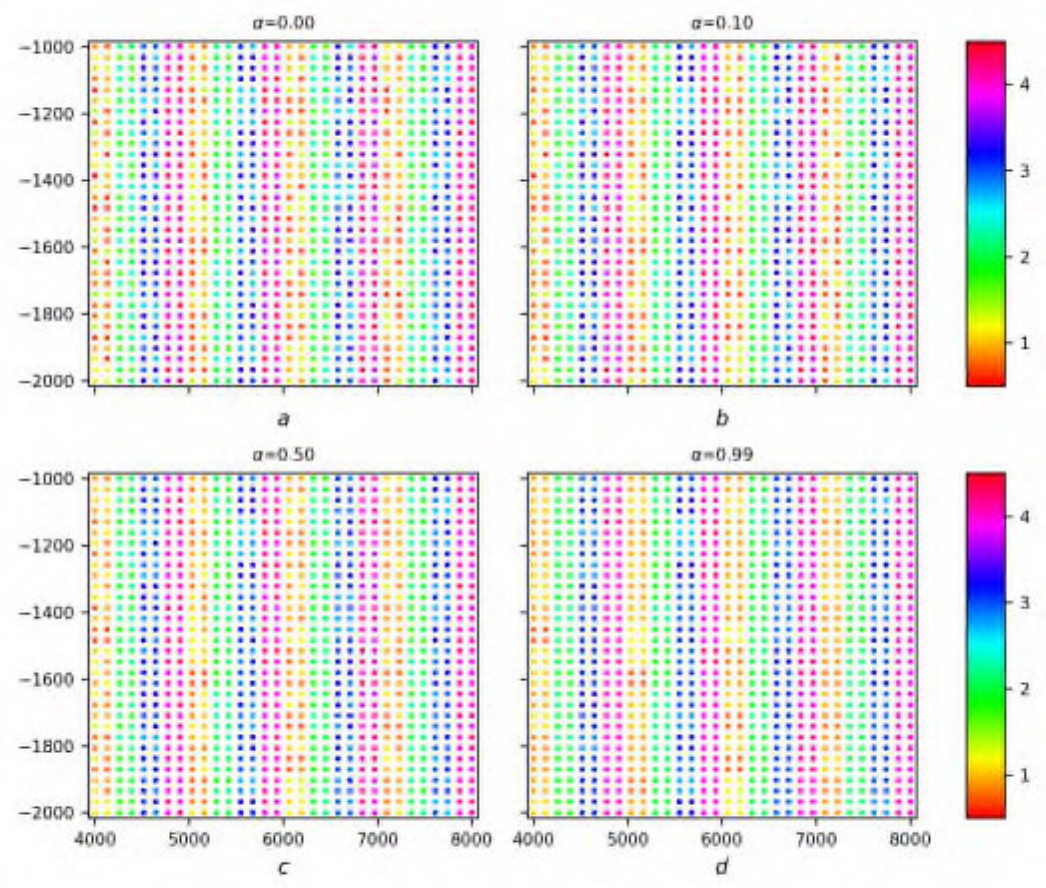

Figure 7. Finding a solution using the $F_{s\mu_1}$ functional on blocks 2×2:
a – $\alpha = 0.0$, b – $\alpha = 0.1$, c – $\alpha = 0.5$, d – $\alpha = 0.99$.

Table 1. Quality criteria of obtained solutions for a priori distribution of densities μ_1

	Homogeneity	Closeness to ρ	Final criterion
$\alpha = 0.00$	—	7.69714	7.69714
$\alpha = 0.10$	6.18796	7.07885	6.98976
$\alpha = 0.50$	3.44360	4.85407	4.14883
$\alpha = 0.99$	0.07234	3.38303	0.10545

The Figure 8 shows the results of finding solutions for the a priori density distribution μ_2 (Figure 5c). The Table 2 summarizes the quality criteria for the obtained solutions.

Analysis of the Table 1 and Table 2 shows that as the parameter α increases, the homogeneity criterion and the criterion of closeness to ρ decreases. The final quality criterion at $\alpha = 0.99$ is much better, since the method, gives more weight to information about the uniform distribution of densities within blocks than to information about the distribution itself. Thus, due to the fact that the ideal initial structure of blocks (and derivatives of it) is used, we see that the method gives a better approximation to the initial model of density distribution, with a larger α.

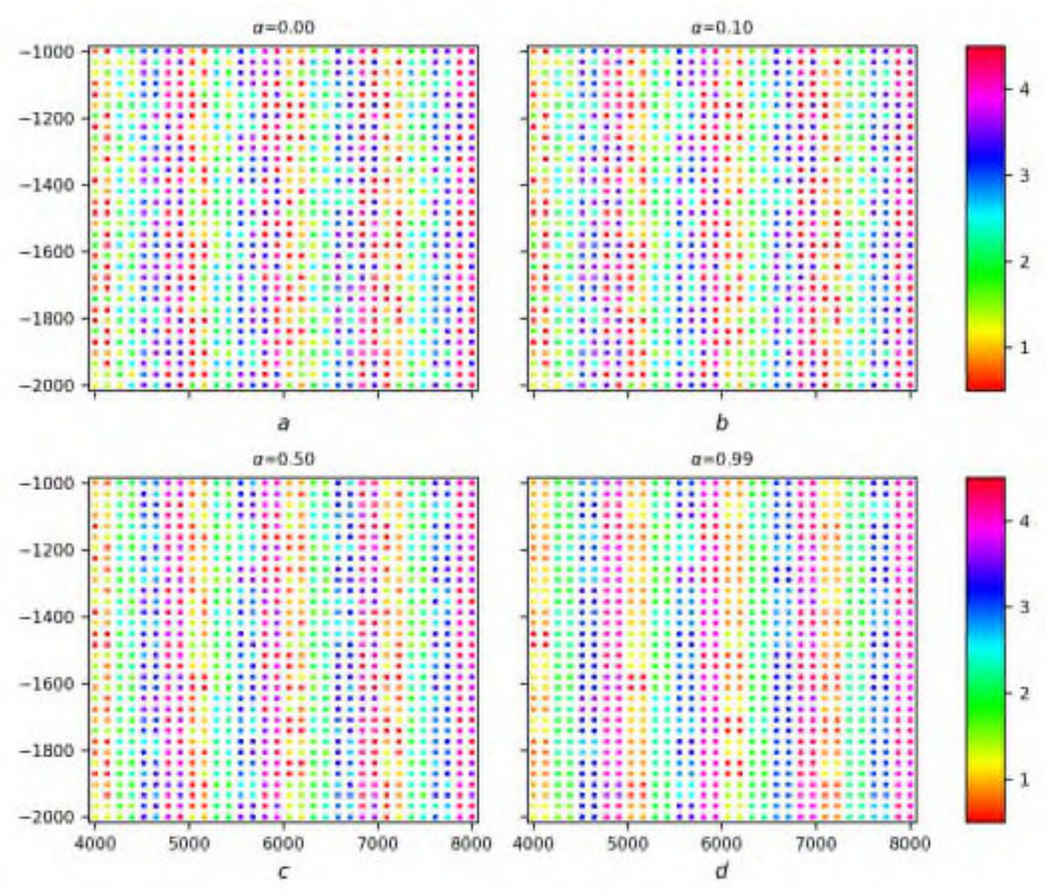

Figure 8. Finding a solution using the $F_{s\mu_2}$ functional on blocks 2×2: a – $\alpha = 0.0$, b – $\alpha = 0.1$, c – $\alpha = 0.5$, d – $\alpha = 0.99$.

Table 2. Quality criteria of obtained solutions for a priori distribution of densities μ_2

	Homogeneity	Closeness to ρ	Final criterion
$\alpha = 0.00$	—	15.39493	15.39493
$\alpha = 0.10$	12.37600	14.15752	13.97937
$\alpha = 0.50$	6.88721	9.70820	8.29771
$\alpha = 0.99$	0.14477	6.76424	0.21096

Example of finding a solution on the geological and geophysical model of the Norilsk Nickel deposit

Geological and geological-geophysical model of the deposit

The section of the liquation deposit of the Norilsk ore zone, known as of 2017 [*Kulikov*, 2017], was taken as the basis of the numerical model. The geological section of the Norilsk area in the first approximation is a subhorizontal-layered environment, represented (from bottom to top) by carbonate-terrigenous sediments of the Paleozoic, carbonized terrigenous sediments of the Tungussian series, stratified strata of basalts and tuffs of the main composition of the Permian – Lower Triassic (Figure 9) [*Kulikov*, 2017].

In spite of the fact that ore-bearing intrusions of Norilsk type are characterized by increased values of density, it is extremely difficult to identify in the observed gravity (dg) field anomalous effects from these objects. The reasons are: a relatively weak level of

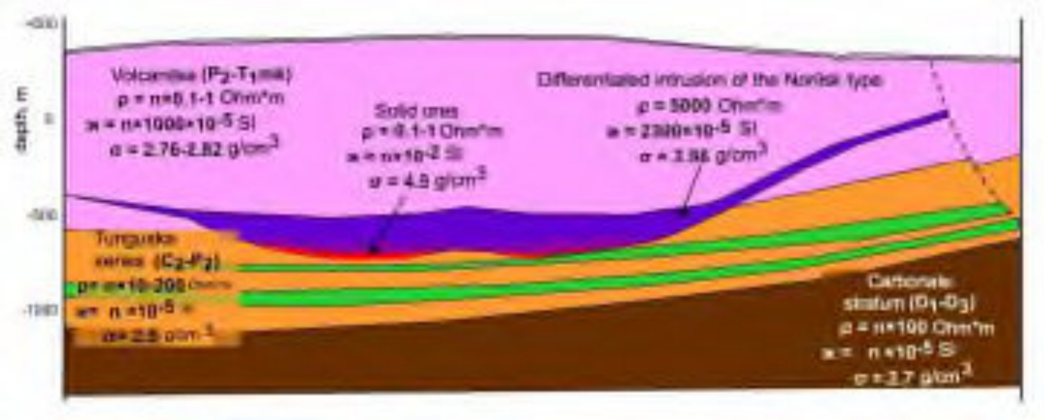

Figure 9. Generalized petrophysical model of the section that is typical for the Norilsk ore zone [*Kulikov*, 2017].

Table 3. Petrophysical characteristics of the Norilsk ore zone section [*Kulikov*, 2017]

Horizons		Density, g/cm^3
Quaternary (Q)		2.22
Mokulaevskaya Formation (T_1mk)	Vulcanites (Basalts)	2.72–2.82
Moronga Formation (T_1mr)		
Nadezhdinskaya Formation (T_1nd)		
Khakancha Formation (T_1hk + gd)		
Syverminskaya Formation (T_1sv)		
Ivakinsky Formation (P_1iv)		
Tunguska series ($C_2 - P_2$)		2.5
United ($D_2 - D_3$)	Carbonate Strata	2.78
Manturovskaya Formation (D_2mt)		2.76
Razvedochninskaya Formation (D_1rz)		2.67
Kureya Formation (D_1kr)		2.73
Zubovskaya Formation (D_1zb)		2.76
Intrusions of the Norilsk type		2.9–3.1
Ore-Free Intrusions		2.95-3
Solid Ores		4.5
Disseminated Ores		4

the useful signal; the presence of intense anomalies-interference due to physical inhomogeneities of the surrounding environment; specific distortions of anomalies associated with the mountainous terrain, etc [*Kulikov*, 2017].

Under favorable conditions, differentiated ore-bearing intrusions, at depths of up to 1200–1500 m, can be detected by means of gravity prospecting. Ore knots, which are a set of spatially convergent ore-bearing intrusions, can be detected by gravity survey at depths of up to 3000 m [*Kulikov*, 2017].

Based on the above data on the form of occurrence of layers, intrusions and their properties, a two-dimensional geological and geophysical model of the section typical for

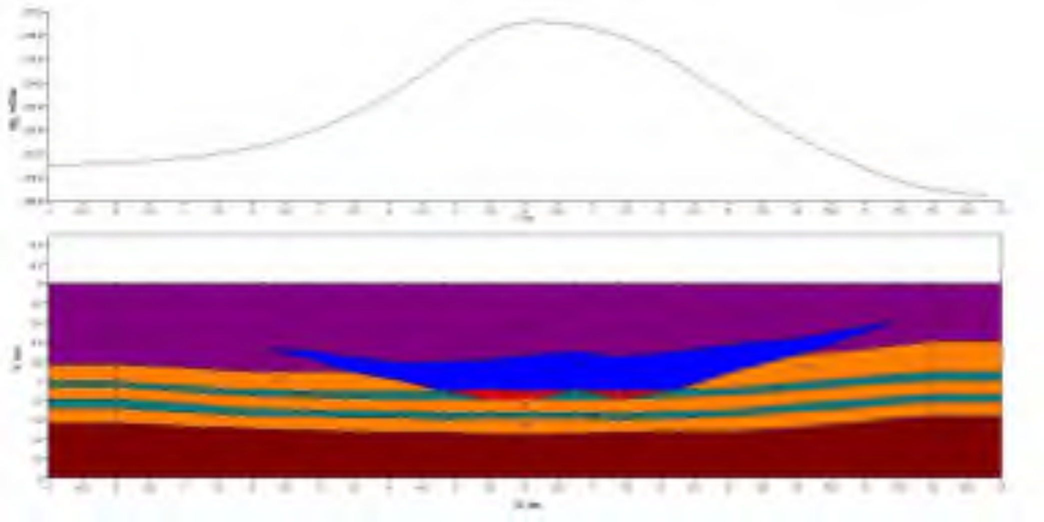

Figure 10. Geological and geophysical model created on the basis of data on the Norilsk ore zone.

the Norilsk ore zone was created. This model is shown in Figure 10, distance in km, density in g/cm^3.

Results of the search for solutions

To solve the direct gravity problem for the two-dimensional model, we used the complex variable function theory for a polygon with constant density [*Bulychev et al.*, 2010].

The system $Ax = b$ describes the gravitational effect of the dense environment. The system of linear equations can be written as follows, by analogy with the system (21):

$$[a_{ji}][x_i] = [b_j] \tag{22}$$

where x_i are the unknown densities, a_{ji} is the effect of $i-o$ block at observation point j, b_j is the value of the observed field at point j.

In order to apply the projection method, the two-dimensional model of the section (Figure 10) was split into blocks (Figure 11). The resulting model is called the "initial" model, and we assume that we know only the observed field from this model. During the study, we assume that only the useful signal is selected in the observed field and that there is no noise component in it. Also, to take advantage of the ability to account for the F_s functional, let us represent our existing model as a density grid, 50 by 60 cells horizontally and vertically, with dimensions of 240 m horizontally and 40 m vertically, assigning cells to the density of the original model and relating each cell to the block model of the Figure 11. The resulting model is shown in Figure 12.

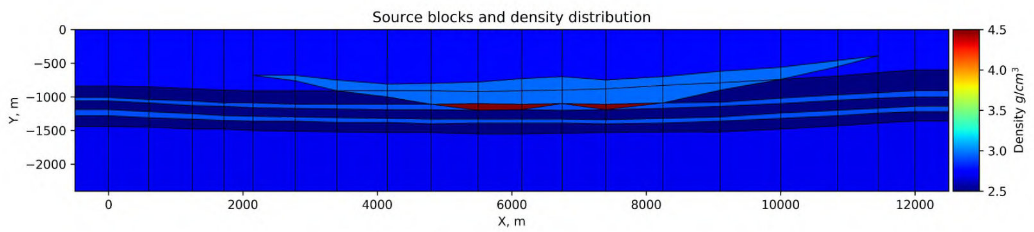

Figure 11. Initial geological and geophysical model split into blocks.

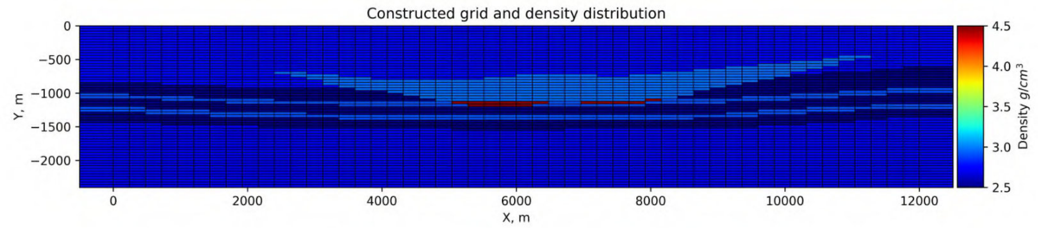

Figure 12. Initial geological and geophysical model represented in the form of a grid.

The method was tested on a geological geophysical example, taking into account a priori information about the density distribution and block structures consisted of cells.

First, we show the dependence of the result on α. The block structures for each example are constant, a noisy initial model of 0.3 g/cm^3 has been used as the density distribution, α is taken equal to 0.0, 0.1, 0.3, 0.5, 0.9, 1.0. The standard deviation of the obtained solution from the original density distribution is shown in the Table 4. We see that when α equals 1.0, when only the formalization of E_S is included in the solution, the deviation is the largest, and the best value of α is chosen by the interpreter when he tries to find a compromise between the two statements $E_\mu \wedge E_S$.

Table 4. The standard deviation of the resulting solution from the original density distribution for different α

α	$\|\|x - x^f\|\|$
0.0	7.46037
0.1	6.75904
0.3	5.37339
0.5	4.03042
0.9	1.88739
1.0	3102.58

We show the results of inverse problem solutions for different α under different initial conditions. The block structures for each example are constant, a noisy initial model was used as the density distribution, at 0.1, 0.3 and 0.5 g/cm^3, α is taken equal to 0.1, 0.5, 0.9, 0.9(9). The results of the search for solutions are shown in the figures below. It can be seen that the gravitational field from the resulting models when solving the inverse problem coincides with the original observable field. It is also seen that the resulting model visually approximates the original model as α increases. However, it is worth noting that at α equal to 0.9(9) we see a picture of highly inhomogeneous medium, since almost no a priori information about the initial density distribution is taken into account.

Appendix A presents the plots (Figures A1–A21) of the observed field for the original model, the model after partitioning into cells, noisy a priori information, and the result of the solution search are also presented.

Conclusion

The projection method with respect to the system $Ax = b$ consists in efficiently constructing the variety of its solutions $\Phi(A, b)$. In the present paper this is done using the Gramm-Schmidt orthogonalization.

Knowledge of $\Phi(A, b)$ allows us to take into account a priori expert information about the properties of the solution x^f and restrict its search to $\Phi(A, b)$. In this paper, this is done for three expert statements: E_μ, E_S and their conjunction $E_{\mu S} = E_\mu \wedge E_S$.

The judgement E_μ about the similarity of the solution x^f with the known vector μ is implemented on $\Phi(A, b)$ in two ways. It is shown by examples that each of them works better than the traditional way of accounting for μ based on Tikhonov regularization.

The E_S judgement of S-homogeneity of x^f by itself is of little use due to great ambiguity, but its coupling to $E_{\mu S}$ with the scheme E_μ gives good results: if the initial solution x^f is indeed S-uniform, then the result $x_{\mu S}$ of its search by the scheme $E_{\mu S}$ turns out to be closer to x^f than the result x_μ of the search by the scheme E_μ: $\left\|x_{\mu S} - x^f\right\| < \left\|x_\mu - x^f\right\|$ (based on the results for finding a solution for the ore problem based on the geological geophysical model of the Norilsk Nickel deposit).

In reality, information x^f is fuzzy: the expert knows more about some things and less about others. Therefore, the authors see a natural extension of research in constructing fuzzy variants of schemes, E_μ, E_S, $E_{\mu S}$.

Acknowledgments. This work was funded by the Russian Science Foundation (project No. 24-17-00346).

Appendix A

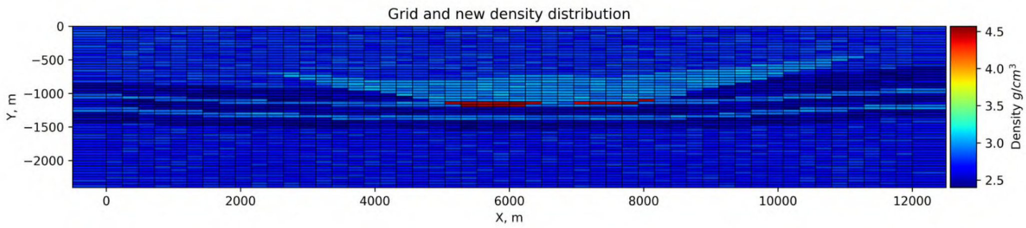

Figure A1. Noisy a priori model at 0.1 g/cm^3.

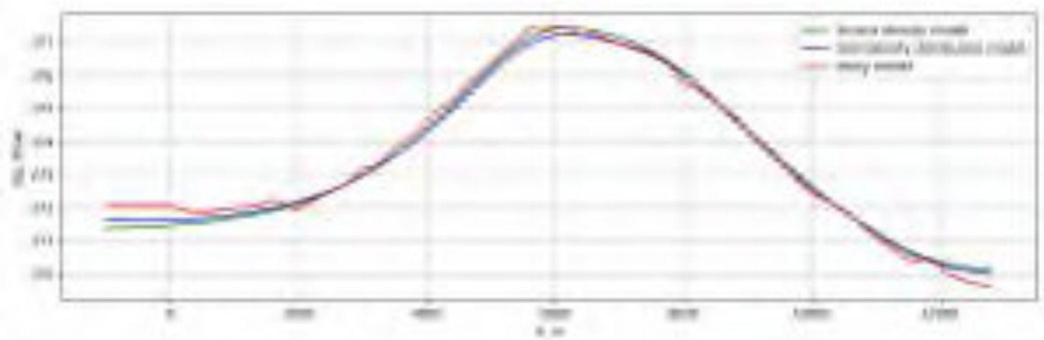

Figure A2. Comparison of observed field plots from the original cell-split model and the a priori model at 0.1 g/cm^3 noisiness.

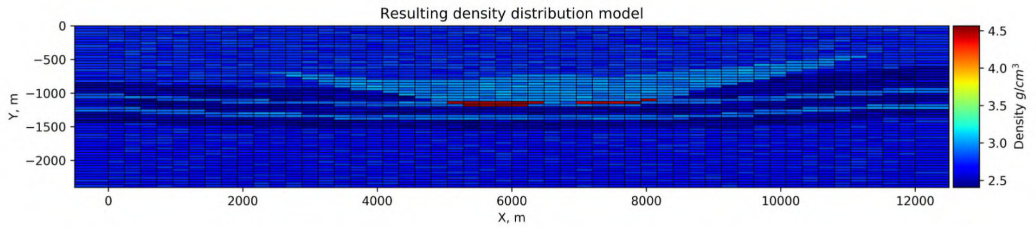

Figure A3. The result of searching for a solution using an a priori model with a noise of 0.1 g/cm^3 and α equal to 0.1.

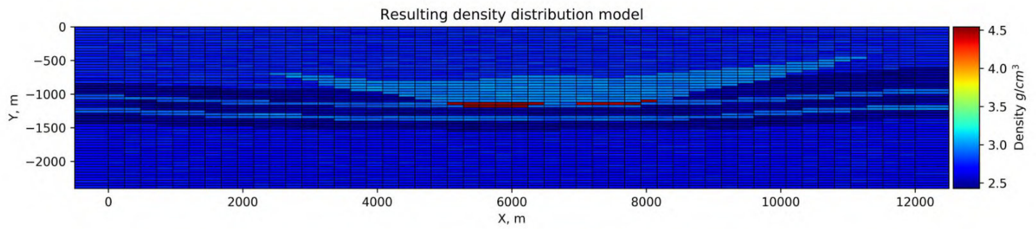

Figure A4. The result of searching for a solution using an a priori model with a noise of 0.1 g/cm^3 and α equal to 0.5.

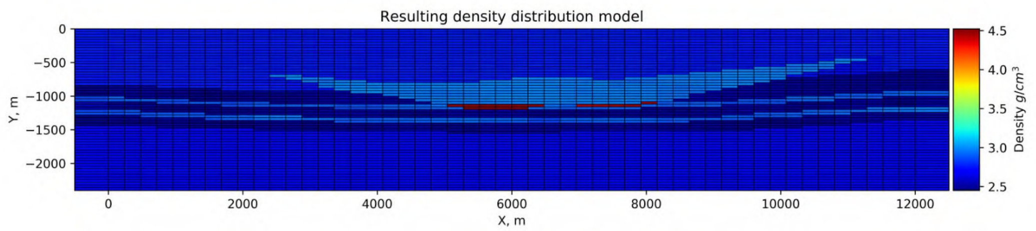

Figure A5. The result of searching for a solution using an a priori model with a noise of 0.1 g/cm^3 and α equal to 0.9.

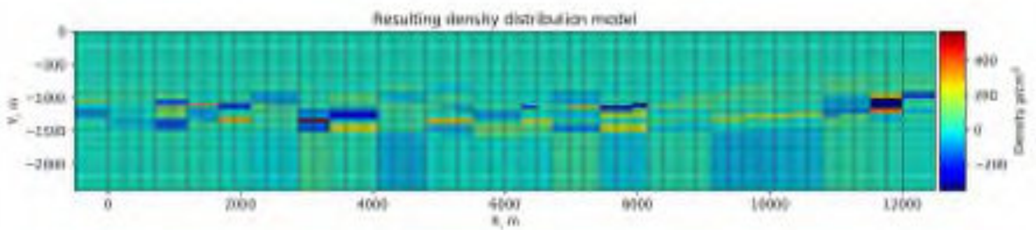

Figure A6. The result of searching for a solution using an a priori model with a noise of 0.1 g/cm^3 and α equal to 0.9(9).

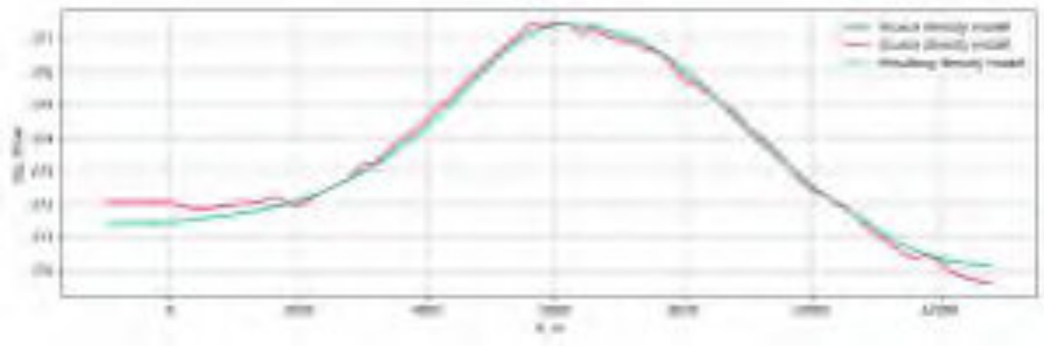

Figure A7. Comparison of observed field plots from the source model, the a priori model at 0.1 g/cm^3 noisiness and the resulting models.

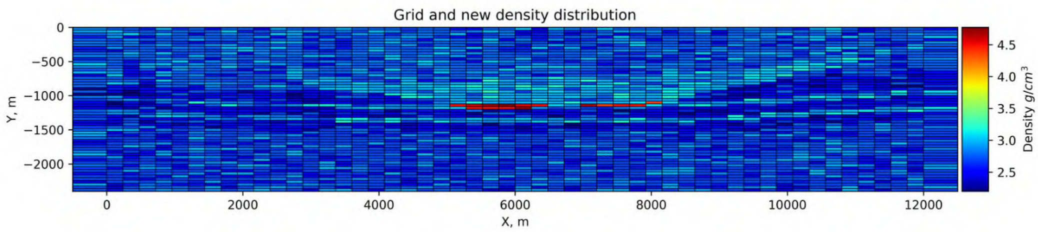

Figure A8. Noisy a priori model at 0.3 g/cm^3.

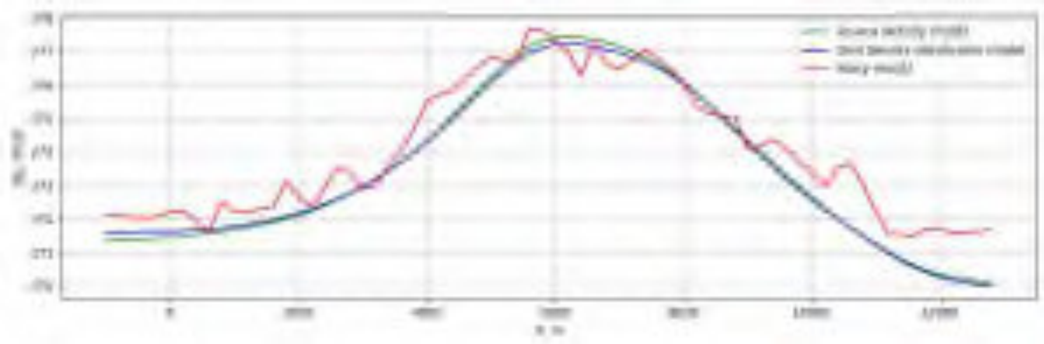

Figure A9. Comparison of observed field plots from the original cell-split model and the a priori model at 0.3 g/cm^3 noisiness.

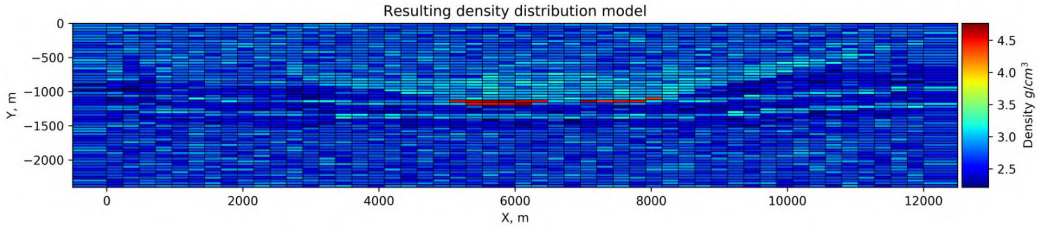

Figure A10. The result of searching for a solution using an a priori model with a noise of 0.3 g/cm^3 and α equal to 0.1.

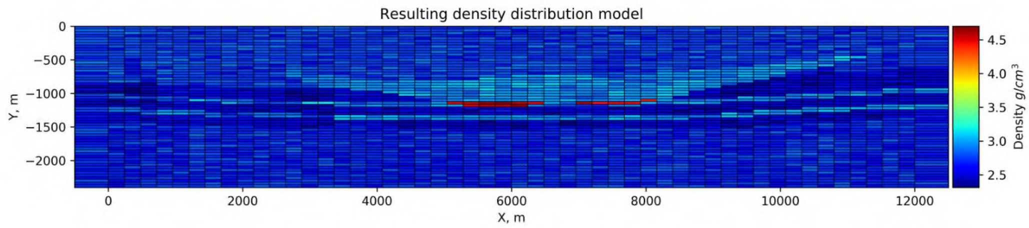

Figure A11. The result of searching for a solution using an a priori model with a noise of 0.3 g/cm^3 and α equal to 0.5.

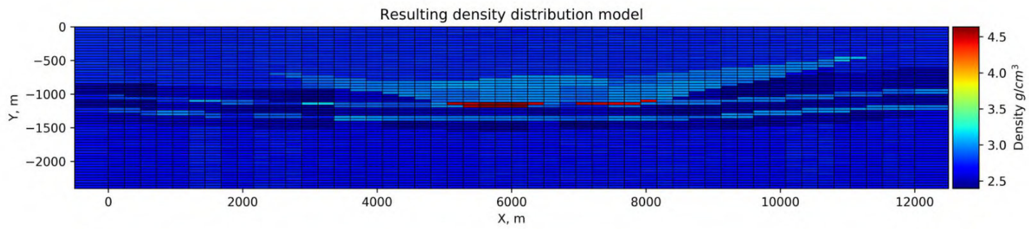

Figure A12. The result of searching for a solution using an a priori model with a noise of 0.3 g/cm^3 and α equal to 0.9.

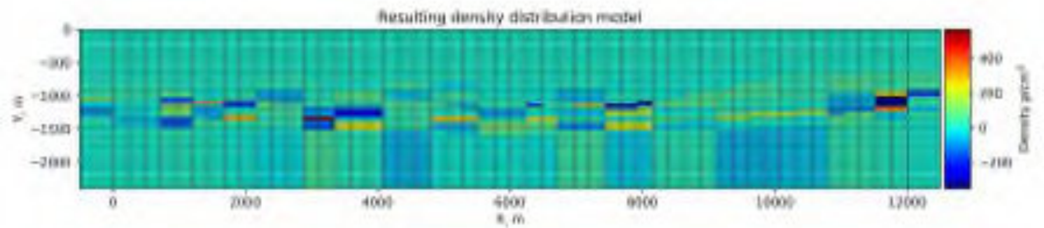

Figure A13. The result of searching for a solution using an a priori model with a noise of 0.3 g/cm^3 and α equal to 0.9(9).

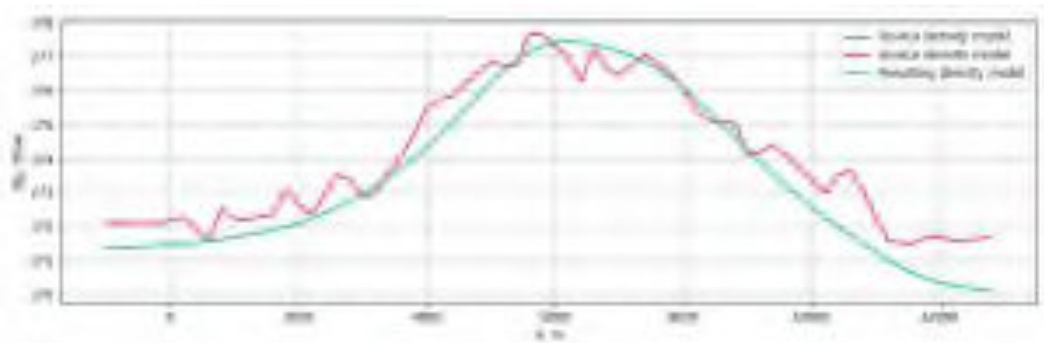

Figure A14. Comparison of observed field plots from the source model, the a priori model at 0.3 g/cm^3 noisiness and the resulting models.

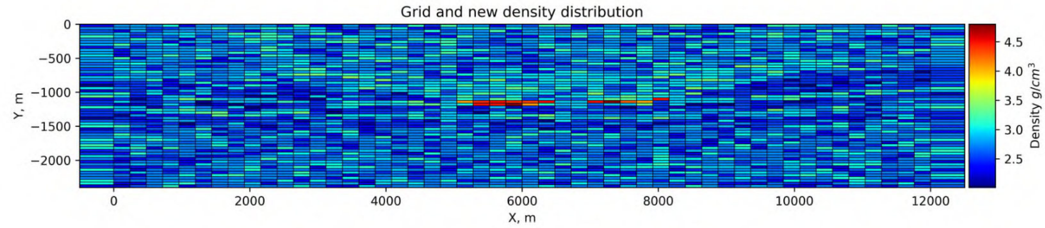

Figure A15. Noisy a priori model at 0.5 g/cm^3.

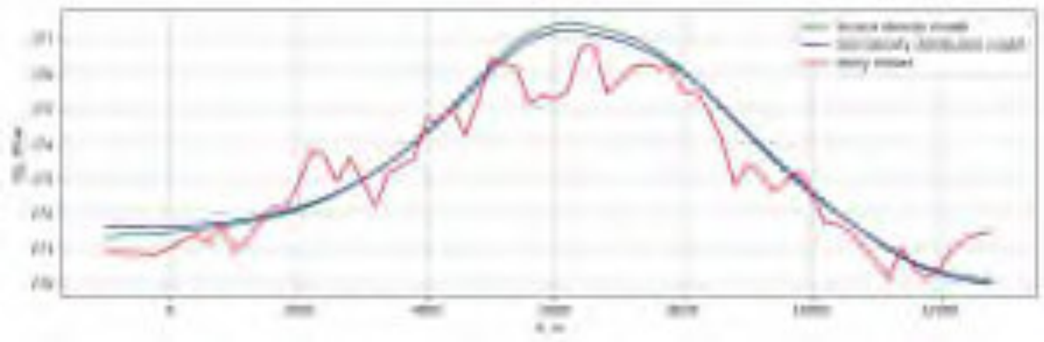

Figure A16. Comparison of observed field plots from the original cell-split model and the a priori model at 0.5 g/cm^3 noisiness.

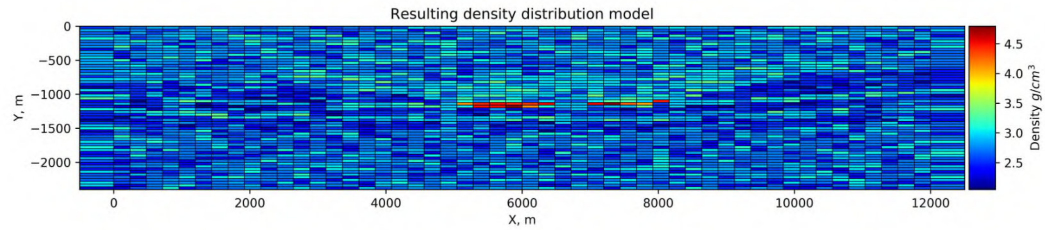

Figure A17. The result of searching for a solution using an a priori model with a noise of 0.5 g/cm^3 and α equal to 0.1.

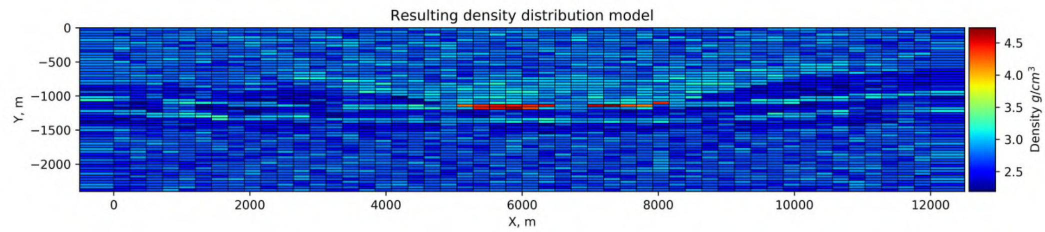

Figure A18. The result of searching for a solution using an a priori model with a noise of 0.5 g/cm^3 and α equal to 0.5.

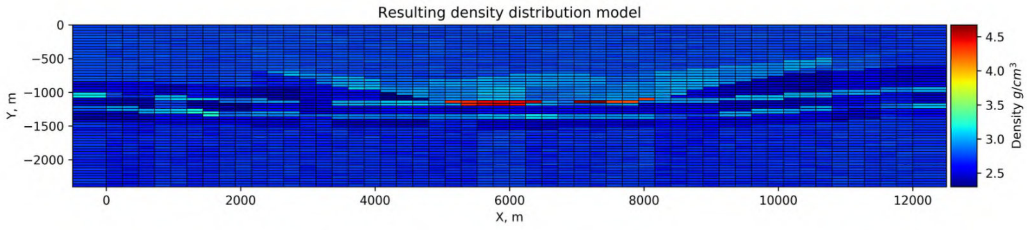

Figure A19. The result of searching for a solution using an a priori model with a noise of 0.5 g/cm^3 and α equal to 0.9.

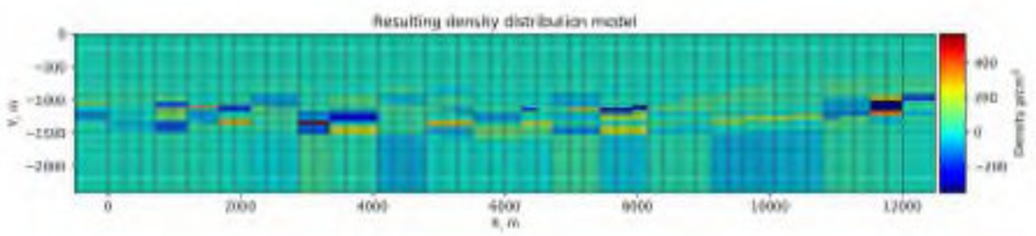

Figure A20. The result of searching for a solution using an a priori model with a noise of 0.5 g/cm^3 and α equal to 0.9(9).

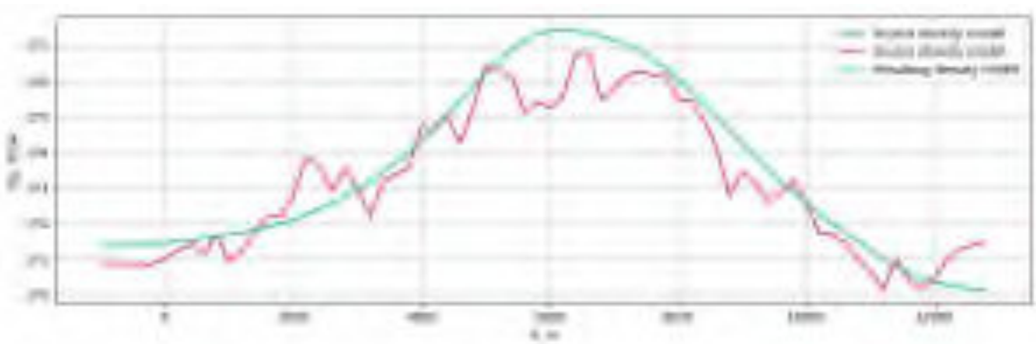

Figure A21. Comparison of observed field plots from the source model, the a priori model at 0.5 g/cm^3 noisiness and the resulting models.

References

Agayan, S. M., S. R. Bogoutdinov, A. A. Bulychev, A. A. Soloviev, and I. A. Firsov (2020), A Projection Method for Solving Systems of Linear Equations: Gravimetry Applications, *Doklady Earth Sciences*, *493*(1), 530–534, https://doi.org/10.1134/s1028334x20070053.

Bulychev, A. A., I. V. Lygin, and V. R. Melikhov (2010), *Numerical methods for solving direct problems of gravity and magnetic exploration (lecture notes)*, 164 pp., Geological Faculty of Moscow State University M. V. Lomonosov, Moscow (in Russian).

Kulikov, V. A. (2017), *Geophysics of solid field minerals*, 208 pp., PolyPRESS LLC, Moscow (in Russian).

Tikhonov, A. N., and V. Y. Arsenin (1979), *Methods for solving incorrect problems*, 283 pp., Nauka, Moscow (in Russian).

Turchin, V. F., and L. S. Turovtseva (1973), A method of statistical regularization with a posteriori estimation of the error in the original data, *Doklady Akademii Nauk SSSR*, *212*(3), 561–564 (in Russian).

Zelenyi, M., M. Poliakova, A. Nozik, and A. Khudyakov (2018), Application of Turchin's method of statistical regularization, *EPJ Web of Conferences*, *177*, 07,005, https://doi.org/10.1051/epjconf/201817707005.

RUSSIAN JOURNAL of EARTH SCIENCES

The Gulf Stream Structure and Meandering Based on the CTD and SADCP Measurements in 1989–1990 and 2014–2015

T. A. Demidova[1,*], **E. G. Morozov**[1], **and B. N. Filyushkin**[1]

[1]Shirshov Institute of Oceanology RAS, Moscow, Russia
* **Correspondence to:** Eugene Morozov, egmorozov@mail.ru

Abstract: An review of field studies in the Gulf Stream region carried out by the authors in two periods with a break of 25 years is presented to summarize the results. The studies in the early period included hydrographic surveys in the area of a southern meander of the Gulf Stream (1989) and in the area of dividing of a single jet of the current into separate branches: in the Gulf Stream delta (1990). The second, recent, stage includes on-route surveys with SADCP profiler in 2014–2015 while crossing the meandering Gulf Stream at mid-latitudes to study its detailed high-resolution velocity field structure.

Keywords: Gulf Stream, meanders, rings, cores, CTD-survey, Gulf Stream delta, transport, SADCP, vertical and horizontal velocity shears.

Citation: Demidova, T. A., E. G. Morozov, and B. N. Filyushkin (2024), The Gulf Stream Structure and Meandering Based on the CTD and SADCP Measurements in 1989–1990 and 2014–2015, *Russian Journal of Earth Sciences*, 24, ES4005, EDN: FQIEYJ, https://doi.org/10.2205/2024es000920

1. Introduction

Despite the high degree of study of the Gulf Stream [*Baranov*, 1988; *Fuglister*, 1951; *Guo et al.*, 2023; *Muglia et al.*, 2022; *Richardson*, 2001; *Rossby et al.*, 2014; *Seidov et al.*, 2019], the results of experimental expeditionary work in the region are still in high demand due to its high synoptic and mesoscale variability. There are still many unresolved questions about the physics and mechanisms of formation of the Gulf Stream mesoscale eddies (without discussing processes on the scale of planetary interaction), instability in its frontal zones, vertical and horizontal mixing, etc. To address these issues, there is an increasing need to sharply increase the resolution of ocean models, requiring appropriate parameterization of them based on high-resolution in situ data. Validation of satellite data also requires a variety of field data.

Most of the huge accumulated volume of field measurements, and in particular, in the Gulf Stream region, is stored in World Databases. However, it is likely that a comparable amount remains in the internal collections of research organizations unknown to the scientific community. The Shirshov Institute of Oceanology, Russian Academy of Sciences, with its almost 80-year history of expeditionary activities is no exception.

Field studies of the Gulf Stream have been performed by authors in several cruises in two periods with a break of 25 years. The early period covers hydrographic surveys in 1989 and 1990. The works were parts of broader international projects devoted to the ocean-atmosphere interaction (Atlantex 90 Program [*Gulev et al.*, 1992]), to the circulation of the world ocean WOCE [*Ivanov and Morozov*, 1991]. The second, recent, stage included on-route surveys with SADCP profiler in 2014–2015 during crossing the Gulf Stream.

The goal of this paper is to present information and review of the results of the field studies of the Shirshov Institute of Oceanology in the Gulf Stream region.

2. Early studies of the Gulf Stream: 1989 and 1990

The most important role in the processes of heat and mass transport in the North Atlantic belongs to the eddies that form in the Gulf Stream system. These include cold and warm rings, as well as eddies of the cyclonic and anticyclic type that are formed in the

RESEARCH ARTICLE

Received: 21 May 2024
Accepted: 12 July 2024
Published: 18 October 2024

frontal zone of the Gulf Stream [*Auer*, 1987; *Baranov*, 1988; *Ginzburg and Fedorov*, 1984; *Muglia et al.*, 2022]. Despite many specialized studies in the Gulf Stream region, the physical mechanisms of the interaction of eddies with each other and with the current itself are not completely understood. To a greatest extent, this is due to the rapid variability of processes and, in addition, it is not always possible to provide multidisciplinary measurements that combine satellite observations with hydrographic surveys and current measurements.

Such comprehensive studies were organized in two cruises of the Shirshov Institute of Oceanology, Russian Academy of Sciences in 1989 and 1990 in the northeastern Gulf Stream system to study its meanders and eddy formation as well as structure and locations of the Stream branches.

2.1. Measurements in 1989: CTD surveys in a Gulf Stream meander

Information about the experiment. In September–October 1989, during cruise 2 of the R/V "Akademik Ioffe", hydrographic studies were carried out on the southern periphery of the Gulf Stream in the area of its strong meandering at the site with coordinates 36.0°–39.5°N and 60.0°–62.1°W. In the modern understanding [*Seidov et al.*, 2019], the test site belongs to the Gulf Stream extension.

Two CTD surveys of the area were performed with an interval of 10 days. The first survey was from September 20 to 22, 1989 and the second one from October 2 to 5. On each survey, 18 CTD casts were made with a Neil Brown Mark III CTD probe. The surveys covered an area of 200 × 90 miles. The measurement accuracy was 0.005 °C for temperature and 0.001 S/m for electrical conductivity. The goal was to trace the evolution of the Gulf Stream and the meander on a monthly scale, which was first detected on the satellite sea image. The main objective was to experimentally determine their thermohaline structure at successive time intervals.

Analysis of hydrographic surveys at the sites was performed in conjunction with the results of current velocity measurements and three-hour standard weather data. Vertical profiling of current velocities up to a depth of 700 m was performed on the route of the ship with an onboard acoustic Doppler profiler of the RD-VM075 type (76.8 MHz) with CTD-casts. Velocity measurement accuracy according to the manufacturer was 0.5 cm/s + 0.2% of the measured value. However, due to high measurement error of the absolute speed velocity results in a qualitative picture only.

NOAA satellite materials, an image of the sea surface, corresponding to the beginning of the first hydrological survey, and a map of the results of the analysis of sea surface temperature at time of the surveys [*NOAA*, 1989] were used to interpret the measurement results.

Main results: temperature structure of meander and its development [after *Dykhno et al.*, 1992]. Two CTD-surveys covered a region with a cyclonic meander of the Gulf Stream previously detected on the satellite image. The first survey covered the central part of the meander in the southern part of the Gulf Stream jet. The second survey showed the changes that occurred in 10 days. Temperature distribution maps based on the CTD data at the two stages at a depth of 400 m are shown in Figure 1a,b. The density section corresponding to Figure 1a is shown in Figure 2.

It was shown based on the temperature and density distributions at different depths during the first survey that there was an inflow of cold water from the northwest. On the surface, the inflow only touches the northwestern part of the site. At a depth of 400 m (Figure 1a), the inflow occupies a significant part of the survey area, that is, cold water penetrates under warm water like a wedge. It was the deepest part of the meander, which spread to the southwest. The intrusion of cold waters under warm waters is also confirmed by the density meridional section along 62°7'W (Figure 2).

After 10 days (the time between surveys) the pattern of distribution changed. The second survey (Figure 1b) recorded a number of changes in the temperature and density structure and showed that the core of the Gulf Stream had moved north. This led to

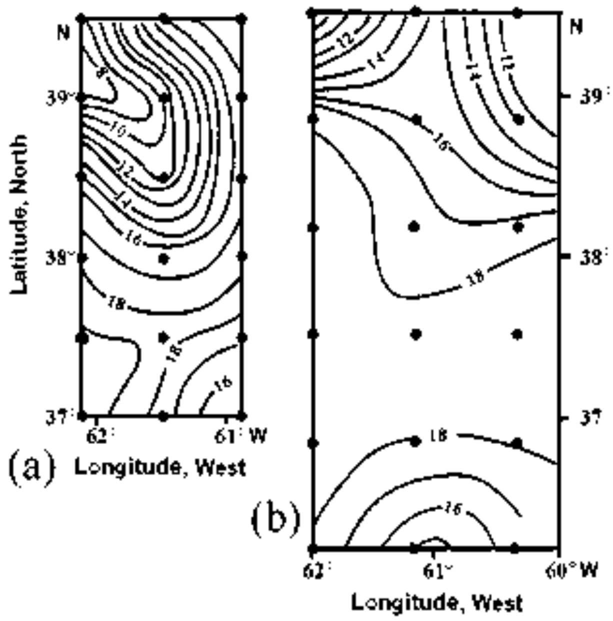

Figure 1. Maps of temperature at 400 m based on the data of the two CTD-surveys in the Gulf Stream region. (a) Survey 1 on September 20–22, and (b) Survey 2 on October 2–5, 1989. Black dots indicate CTD stations, curved solid lines show isotherms.

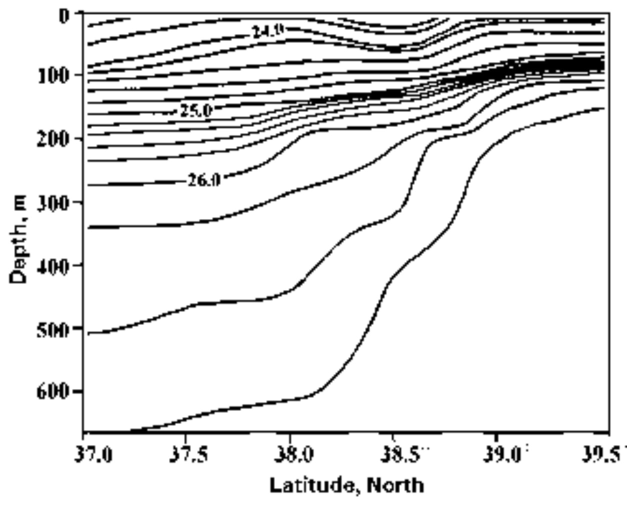

Figure 2. Section of density along 62°7′ W based on the data of the first survey on September 20–22, 1989. Solid lines show isolines of density σ_T.

an increase in the distance between the Gulf Stream core and the meander. Hence, the considered meandering of the Gulf Stream in the southern direction failed to transform into a new cold ring. Thus, it became clear from the thermohaline data that the inflow was determined by the flow of cold water of the meander, and that the meander was spreading to the southwest.

This inflow was also detected on the current velocity sections along the same meridian 62°7′W (not shown here). The velocity structure corresponds to the development of the meander in the southern direction and the resulting inflow of warm waters in the northern direction (since the meander carried cold water). In particular, a maximum speed of 70 cm/s was gained at the southern border of the inflow of cold water at 38°30′N. The joint analysis confirmed that the results reflected the development of a cyclonic meander.

2.2. Measurements in 1990: Survey in the Gulf Stream Delta

Information about the experiment. East of 50°W and south of the Great Banks, the Gulf Stream, being generally a unified flow, breaks up into several multidirectional branches. This is the region of the Gulf Stream delta.

The first branch, the North Atlantic Current, flows northward along the eastern side of the Grand Banks as a western boundary current reaching 50°N, where it meets the Labrador Current, turns more eastward, and crosses the Mid-Atlantic Ridge. The second branch of the Gulf Stream flows south-eastward from the region of the Grand Banks, crosses the Mid-Atlantic Ridge, and then flows eastward near 34°N as the Azores Current [*Richardson*, 2001].

In April–June 1990, we conducted CTD-surveys in the area of the Gulf Stream delta within the WOCE program. The experiment took place south of the Newfoundland Bank in the zone of interaction between the subtropical anticyclonic and subpolar cyclonic gyres limited by coordinates 52°N, 38°N, 50°W, 36°W. In a test site of 300 × 300 miles the measurements were done with a 30 miles interval between stations and also several transects with CTD-casts were made to cross individual jets. CTD-casts were carried out up to 2000 m deep at stations located along a contour covering the Gulf Stream delta, the upper parts of the North Atlantic Current and its branches with individual sections inside the contour. The survey was repeated in April, May, and June and included two eddy-resolving hydrographic surveys in the southwestern corner of the Gulf Stream test area. In addition, current measurements were taken at moorings along 36°W transect.

The main goal of the research was to expand our knowledge about the variability of processes in the Gulf Stream delta.

Main results [after *Ivanov and Morozov*, 1991]. The main results included determination of the location and evolution of the branches, their meanders, and quasi-stationary rings, as well as assessing the transport of the main flow and individual branches. In a generalizing work by [*Baranov*, 1988], the characteristic types of circulation in the Gulf Stream were distinguished and the transports of the main jets were given.

Table 1 shows the transports of various Gulf Stream jets based on the measurements in 1990 and according to [*Baranov*, 1988]. During the three stages of work from April to June 1990, the total transport of the Gulf Stream did not change strongly and remained within a range of 62–63 Sv, while the transports of each of the jets changed.

An example of the position of branches and detected two quasi-stationary rings are presented in Figure 3 that shows a scheme of individual branches split off from the single flow of the Gulf Stream, which is outlined at the left edge of the southwestern corner of the area. This survey was made in May 1990, during the second stage of measurements. The eddy-resolving survey area is distinguished by the condensation of station points in the lower left corner of Figure 3.

It was shown earlier in [*Clarke et al.*, 1980] based on the geostrophic calculations and instrumental measurements of currents that the barotropic component of the Gulf Stream transport is close to 40%. According to our current measurements on moorings, the barotropic component represents 60% of the transport.

Baranov [*Baranov*, 1988] proposed that two causes lead to branching of the Gulf Stream in the delta region. The first mechanism takes place when the Gulf Stream approaches the underwater ridge southwest of the Newfoundland Bank forming a cyclonic meander. Here, the current splits; the central and northern branches flow around the continental slope and continue to the northeast as the northern branch of the North Atlantic Current. The southern branch turns to the south and forms the southern branch of the Gulf Stream.

The other form of overflowing the ridge takes place regardless the flow consists of one or two branches. The northern part (Slope water of the upper layer) overflows the ridge and continues as the northern branch of the North Atlantic Current. The southern branch turns around the ridge reaching the bottom and forms a cyclonic meander in the final stage of its development. A cyclonic ring is formed in the center of the meander.

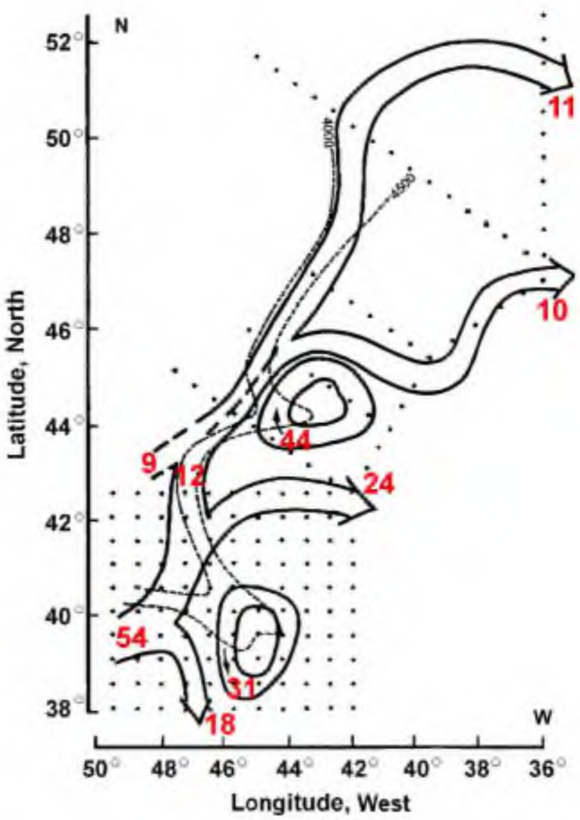

Figure 3. Scheme of the Gulf Stream branches based on the data in 1990. The dots indicate stations, dashed lines show isobaths of 4000 and 4500 m. Red numerals show transport of water in Sverdrups on May 28–June 13, 1990. Two quasi-stationary rings are also shown on the map.

Table 1. Transport in Sverdrups (Sv.) of the Gulf Stream branches as measured in 1990 [*Ivanov and Morozov*, 1991] and mean transports from [*Baranov*, 1988]

Currents, jets	1990	Mean transports from [*Auer*, 1987]
Slope Current 1	9	10–12
Gulf Stream	54	46.8
Southern Branch of Gulf Stream	18	21
North Atlantic Current	45	35.6
Northern branch	11	10–15
Central branch	10	10–15
Southern branch	24	15.6

3. SADCP studies of the Gulf Stream velocity in 2014 and 2015

The second part of our review includes our recent research with an onboard SADCP profiler in the middle of the Gulf Stream. In 2014, the Gulf Stream was crossed at about 39°N, 50°W by the ship heading 170° and in 2015 this occurred at 39.5°N, 61.0°W when the vessel was heading 150°. All data were analyzed together with available satellite materials.

In 2014 and 2015, detailed high-resolution velocity field structure of the meandering Gulf Stream and its fontal zones was studied with the shipborne RDI-Teledyne current profiler "Ocean Surveyor 75" (TRDI, 76.8 kHz) (SADCP). Two sections up to 700 m deep were carried out on the routes of the R/V "Akademik Sergey Vavilov" from St. John's (2014) and Halifax (2015) heading approximately southeast. Standard package was applied for data processing. The vertical space resolution was 8 m (a vertical bin) and the uppermost velocity measurement depth was 16 m. The results of velocity measurements with 15-min averaging of initial data over time are considered. Since the ship's speed was 9 to 13 knots, this provides horizontal space resolution of about 4–6 km.

3.1. Measurements in 2014: a cold ring

Information about the experiment. The crossing of the Gulf Stream was from September 30 to October 1, 2014 in the range of latitudes between 33° and 40°N. The ship's speed was 12–13 knots. When approaching the northern edge of the Gulf Stream, the ship appeared in a counter current, which slowed down the ship by two knots. This could most likely be caused by a strong northward current on a segment of the Gulf Stream sharply deviating to the north as is shown in [*Dzhiganshin and Polonsky*, 2009, Figure 1] on a typical snapshot of the Gulf Stream jet (~ 38° to 41°N, 51°W).

Main results. The meandering Gulf Stream on October 1, 2014 is shown on the map of the absolute dynamic topography in Figure 4.

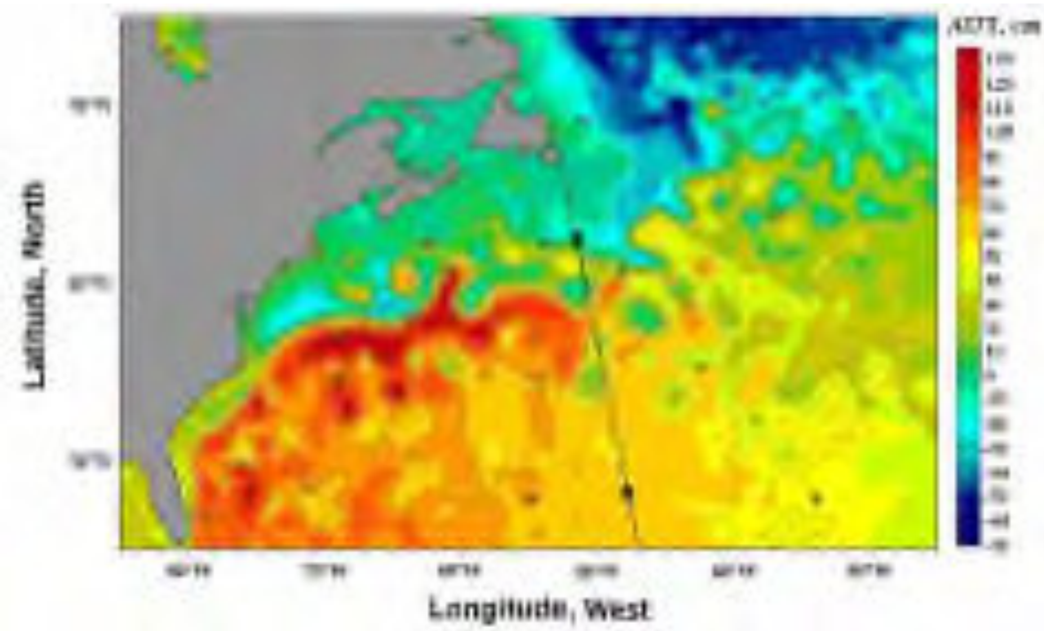

Figure 4. Absolute dynamic topography (ADT) of the Gulf Stream area on October 1, 2014 based on the satellite altimetry data. The ship's route is shown with a black line. Black circles on the line limit the position of the velocity section in Figure 5. Satellite altimetry gridded product [*Pujol et al.*, 2016] available from Copernicus Marine Environment Monitoring Service (CMEMS, http://marine.copernicus.eu/).

A section of the meridional velocity component along the route is shown in Figure 5. The section crosses two positive velocity flows (Figure 5) in the latitude ranges on the surface 38.5°–40.0°N, 34.0°–36.6°N. According to the measurement data, they both extended from the surface to a measurement depth of 700 m. Within the depths of the section, the vertical geometric structure of both jets remains almost unchanged. The velocity shows gradual decrease with the depth. The preferential directions of transport in both cases are to the NNE (north-northeast) almost opposite to the motion of the vessel heading ~ 170° in a very unfavorable direction for the ship motion upstream.

The Northern flow (Figure 5) is about 130 km wide and corresponds to the main Gulf Stream jet with its core centered at latitude of 39°N with the maximum velocity magnitude 148 cm/s at the minimum accessible depth 16 m. The meridional components reached 135 cm/s in the core and, in general, significantly exceeded the latitudinal ones. An isotach

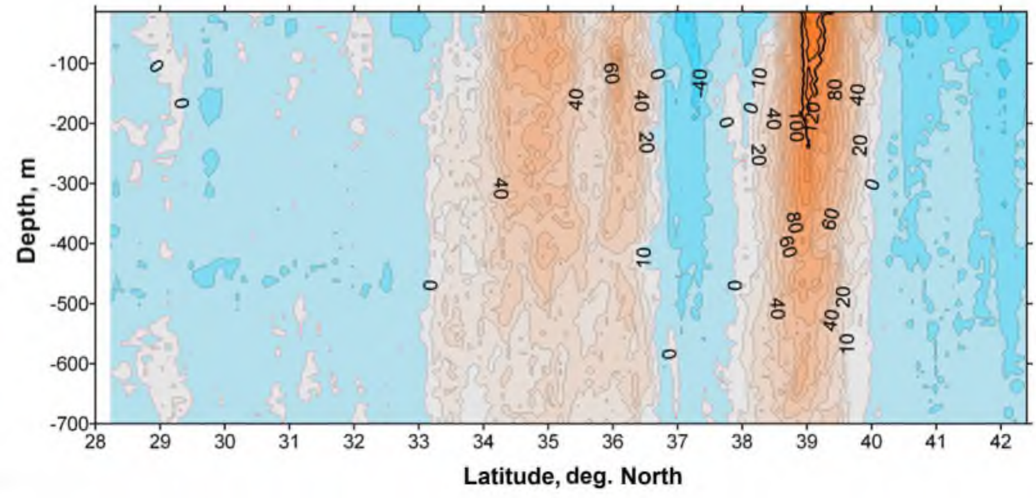

Figure 5. Section of meridional velocity across the Gulf Stream in the period September 30–October 1, 2014. Beige color shows positive downstream velocity, light blue shows countercurrent (negative velocity). North is on the right.

of 120 cm/s outlines the core in the depth range from the surface to ~ 150 m. Velocities above the core on the surface reached 150 cm/s.

The flow with positive velocities south of the main jet was 228 km wide on the surface (34.0°–36.5°N) and included two narrow cores of high speed exceeding 40–60 cm/s, extending to a depth of 300–400 m. On the dynamic topography map Figure 4, the latter correspond to two small isometric depressions of topography (green color relative to the surrounding ocean surface) within a less deepened meridionally elongated depression (lighter green color against orange background). Similar structures at 35°–36°N, which are quasi-stationary cold rings, are characteristic of the zone south of the southern front of the Stream and are also reflected as typical in the snapshot on generalized schematic maps [*Seidov et al.*, 2019, Figure 2]. The larger apparent width of the ring relative to the width of the main jet in Figure 5 is associated in our case with its elongated shape in a direction close to the direction of the section itself, although, in general, rings with a diameter larger than those of the Gulf Stream are widespread.

Thus, the southern flow with positive velocities on the section in Figure 5 is an evolving transformed cyclonic eddy of elongated form carrying relatively cold water. It penetrates at least to a depth of 700 m and has two small cores of about 300 m deep. Typical parameters of a young cold ring known from publications are as follows: ring diameters are about 200 km, rotation speeds are up to 2 m/s, translation motion speed is 2–3 cm/s, lifetime is 2–3 years. Temperature differences on the surface are 2–3°C.

As to Figure 5, the found cold ring is separated from the main jet of the Gulf Stream by a countercurrent of negative velocity with a width of over 130 km on the surface. Considering, as above, that the translation ring speed is 2–3 cm/s, one can say that the ring separation from the jet occurred much earlier than two months ago.

Countercurrents with relatively cold water to the north and relatively warm water to the south were recorded around the Gulf |Stream. Their speeds were up to 40 cm/s both north and south of the jet. South of the revealed ring structure there was warmer water with speeds up to 20 cm/s and rare patches to 30 cm/s.

3.2. Measurements in 2015: three cores, frontal high gradient zones

Information about the experiment. On September 14, 2015, we crossed the Gulf Stream almost normal to the current. The same OS-75 shipborne profiler as in 2014 was used for velocity measurements and the same parameters were set.

Main results. The sea surface temperature map based on satellite measurements on September 9, 2015 (a few days before crossing) is shown in Figure 6.

The NOAA 1/4° Daily Optimum Interpolation Sea Surface Temperature (OISST) is a long-term Climate Data Record that incorporates observations from different platforms (satellites, ships, buoys, and Argo floats) into a regular global grid. The dataset is interpolated to fill gaps on the grid and from a spatially complete map of sea surface temperature. Satellite and ship observations are referenced to buoys to compensate for platform differences and sensor biases. [*Huang et al.*, 2021].

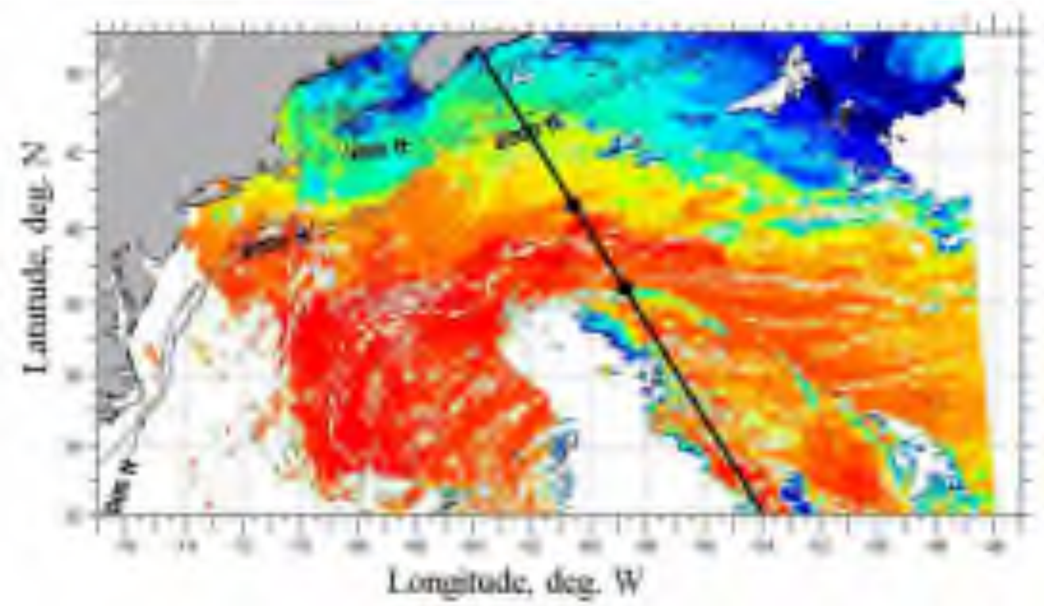

Figure 6. Sea surface temperature map of the Gulf Stream region on September 9, 2015. The route of the ship is shown with a black line. Black circles on the line limit the position of the velocity section in Figure 9 on September 14. Sea surface temperature gridded product [*Huang et al.*, 2021] available from Copernicus Marine Environment Monitoring Service (CMEMS, http://marine.copernicus.eu/).

Figure 7 shows a map of absolute dynamic topography based on the satellite altimetry data on September 14, 2015. The map clearly reveals the state of the currents and meanders.

3.2.1. Estimation of the main direction of the Stream

Estimation of the main direction of the Gulf Stream transport was made using the polar diagram (Figure 8) based on the measurement data. One can see that the direction of most of high-speed values falls in the sector from 50 to 75°. The mean direction of transport of the Gulf Stream during its intersection was about 60°. Velocities along 60° will be further considered as longitudinal velocities directed downstream.

It is interesting to note that a certain confinement of the directions of the entire ensemble of medium-high velocities of 0.5–1.0 m/s to (blue dots) in two sectors 55°–60° and 65°–70° is seen. This fact may reflect the splitting of the flow with such velocities. This picture becomes clearer when separately considering the velocity directions in the Gulf Stream cores found in the section in Figure 9, the lower one ("main") (turquoise squares) and two near-surface cores, the northern one (purple circles) and southern one (orange triangles). The water in these cores propagates along mean directions of 65° (lower one), 60° (northern one), and 70° (southern one).

3.2.2. Section of the longitudinal component

A section of the longitudinal component of the current (direction of 60°) is shown in Figure 9a. Red color shows the regions with velocities directed along the main direction of the Stream; blue color corresponds to countercurrents (negative values on the

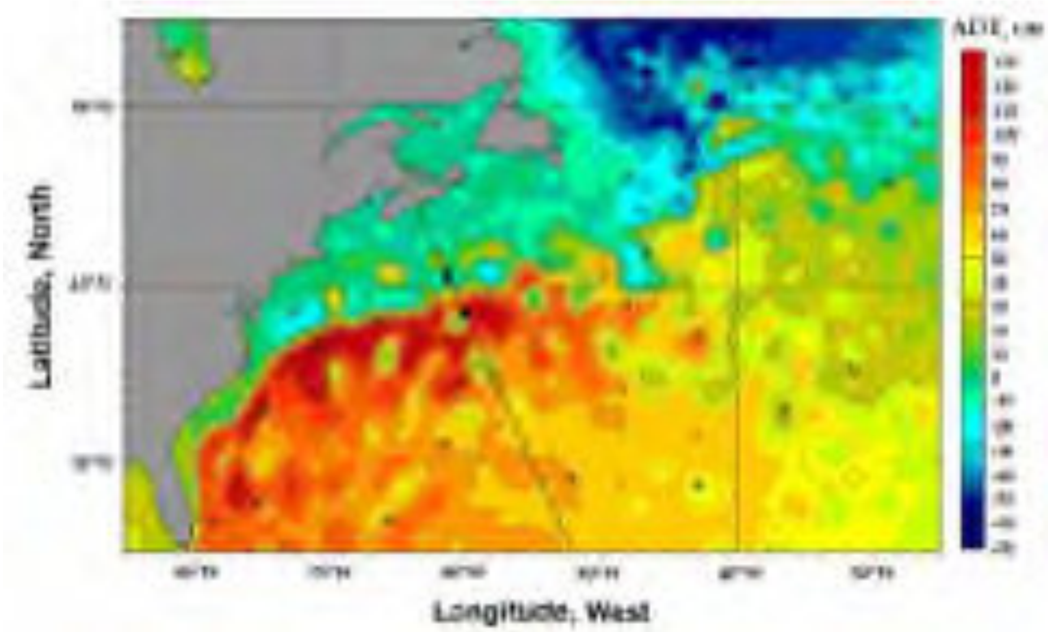

Figure 7. Absolute dynamic topography (ADT) of the Gulf Stream area on September 14, 2015. The ship route is shown with a black line. Black circles on the line mark the position of the velocity section in Figure 9. Same data source as in Figure 4.

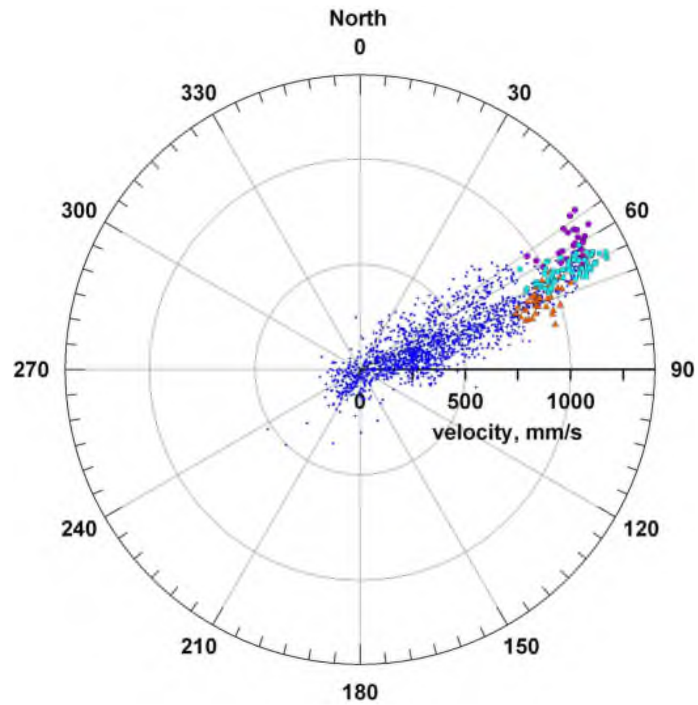

Figure 8. Polar diagram of the direction of currents measured by SADCP during the crossing of the Gulf Stream region on September 14, 2015. Blue dots refer to the entire stream, purple circles to the upper northern core, orange triangles to the upper southern core, and turquoise squares to the lower core (in Figure 9).

velocity scale). The geometric structure of the Gulf Stream (positive velocities) had a trapezoidal shape, narrowing from top to bottom. On the surface, the flow was fixed in the latitude interval 40.15°–38.75°N and had a width of 160–180 km across the flow; at a depth of 730 m its width decreased to 80 km (39.35°–39.20°N).

The maximum velocity on the surface did not exceed 140 cm/s, velocity of 143 cm/s was found at a depth of 190 m in the low core. At the maximum measurement depth of 730 m, the velocity was still about 30 cm/s and higher (Figure 9). The lower boundary of the Gulf Stream flow has not been determined due to the limitation of the depth of the signal.

The negative velocities of the background countercurrent in the presented cross-section gradually increased from the boundaries of the Gulf Stream in both directions, reaching −50 cm/s and higher at the southern and northern boundaries of the section. Such intense countercurrents probably reflect the high speeds of the peripheral edges of small rings. One can see on the map in Figure 7 that the ends of the profile from the south and north sides touch similar structures.

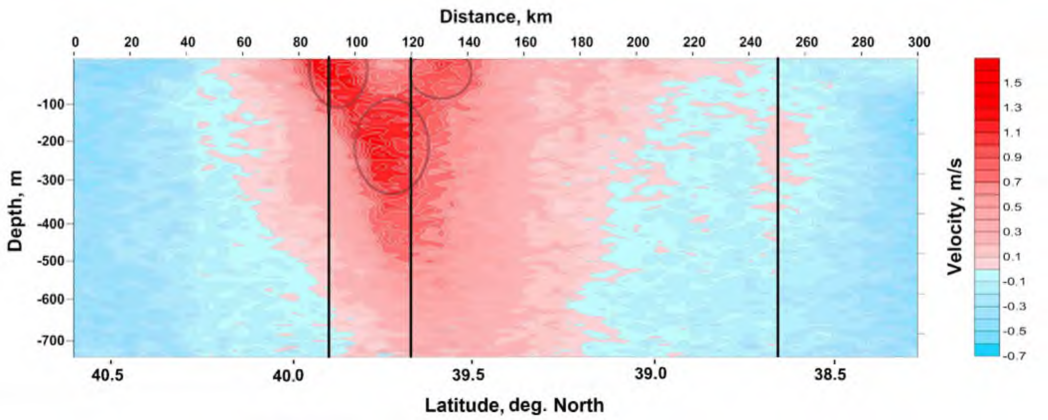

Figure 9. Cross-section of longitudinal (east-northeastern) component of velocity of the Gulfstream in 60° direction on September 14, 2015. Positive values (rose) indicate downstream flow. The vertical lines indicate position of the profiles in Figure 11. Three cores of warm flow are outlined by ovals.

Three cores of the Gulf Stream. The intense core of the warm current with velocities of the order of 1 m/s and more are well expressed in this area. It is clearly seen that it is divided into three separate smaller cores. A two-jet structure of currents is observed on the surface, which merges into one jet deeper than 100 m. This lower core with velocities of 120–140 cm/s, which occupies the central part of the Stream to a depth 100–400 m or even deeper, is characterized by a somewhat greater intensity and greater vertical thickness than the surface jets.

This core on its northern side borders a narrow transitional region in which high gradients of the velocity field are expected both in depth and horizontally, causing the likely development of both vertical and horizontal current shears. The presence of a strong velocity shear in this transition zone may ensure continuous contact of the external cold countercurrent (from the Labrador) with the main jet of the warm current. This is even better seen in Figures 10 and 11a in this area and we will discuss this later considering velocity variations on the horizontal and vertical profiles.

As follows from above when considering the polar diagram in Figure 8, the splitting of the lower main core towards the surface is accompanied by a notable change in the direction of the velocity of the upper jets. While the mean flow direction in the lower core is 65°, in the northern and southern near-surface cores it is 60° and 70°.

Isometric fragment. In the interval 38.6°–38.7°N at depths from 150 to 300 m, a quasi-isometric zone of low positive velocities (0.1–0.2 m/s) with a width of about 20 km is observed. Perhaps this is a previously separated small fragment of the main stream. This is presumably due to instability and meandering of the current.

Transport. The transport of the Gulf Stream within the measured boundaries was about 40 Sv (directed at 60°). This is lower than the known estimates of the Gulf Stream mean transports [*Baranov*, 1988, Table 1; *Dzhiganshin and Polonsky*, 2009; *Ivanov and Morozov*, 1991; *Rossby et al.*, 2014] since our measurements only penetrated down to 730 m, while the literature estimates of the Gulf Stream transport are usually given for the entire jet. An additional complication when comparing transports from different authors is the difference or lack of information about the time averaging of the data.

3.2.3. Horizontal profiles

Figure 10a,b and c show horizontal profiles of typical variations of longitudinal velocity (velocity normal to the cross section) at the depths of 16 m (a), 48 m (b), and 112 m (c). As to Figure 9, these depths of measurements are located within the upper cores (Figures 10a and 10b) and in the transition from the upper cores to the lower core (Figure 10c), where one at 112 m touches slightly the upper uppermost parts of the lower core. In a layer at depths from 16 m to 48 m, there are pronounced velocity maxima of 1.3–1.4 m/s in the left jet and 1.1–1.2 m/s in the right one (Figure 10a,b). The maximum velocity at a depth of 112 m (on the upper periphery of the lower core) is 1.3 m/s.

These three profiles detail the splitting structure of the two Stream's cores on the surface with their subsequent merging at a depth below 100 m (into the third core), which was reflected in a general form in the section in Figure 9. It is seen that below 50 m, this splitting into two jets quickly smoothed out, so that at depths below 100 m, the horizontal variations of velocity have a single maximum (Figure 10c). One can say that the core of the warm Stream has a Y-shaped cross-section.

Many reasons may cause such a 100 m deep slowdown in speed around 39.75°N. For instance, there are not uncommon complications of the Gulf Stream jet by sub-mesoscale currents occurring on lateral scales of 100 m–10 km and associated with density structures, filaments, eddies, topographic wakes, etc. [*Gula et al.*, 2014]. We also do not exclude an influence of the regional local topography on the ship route proposed in [*Frey et al.*, 2023]. However, we cannot expect a notable influence of the most significant topographic features: Cape Hatteras (at ~1400 km) and Newfoundland Bank (at ~1000 km), located too far from the core location.

3.2.4. Peripheral high-gradient zones

One can see in Figure 9 that all three cores of the Gulf Stream are bordered by transition regions. The narrowest of them, in which the most rapid decrease in velocity occurs, is the northern flank of lower core (on the northern side of the Gulf Stream). Within its limits one could expect high horizontal gradients of the velocities. The presence of significant vertical gradients of velocity could be expected in transition zones along the vertical from the three main cores to the areas of lower intensity flow: in the zone between the upper northern core and the lower one. We will see this below considering vertical profiles.

Examples of horizontal cross-flow profiles (Figure 10) and vertical profiles (Figure 11) confirmed these findings and facilitated the visualization and localization of high-gradient areas.

Horizontal shear of longitudinal velocity. One can see in Figure 10 that stable and high horizontal velocity gradients correspond to the northern peripheral sections of the flow at all three depths. To illustrate the existence of such zones in the Gulf Stream section we will show such an individual interval on the profiles.

In the considered depth range of horizontal profiles from 16 to 112 m, the strongest horizontal velocity change was found on the northern (left) periphery of the upper northern core at a depth of 48 m (Figure 10b). This is an area of steadily decreasing speed to the north between coordinates 39.95°N to 40.30°N with a length of ~ 40 km. It includes small local areas of even sharper variability. In Figure 10b they are limited by vertical black lines.

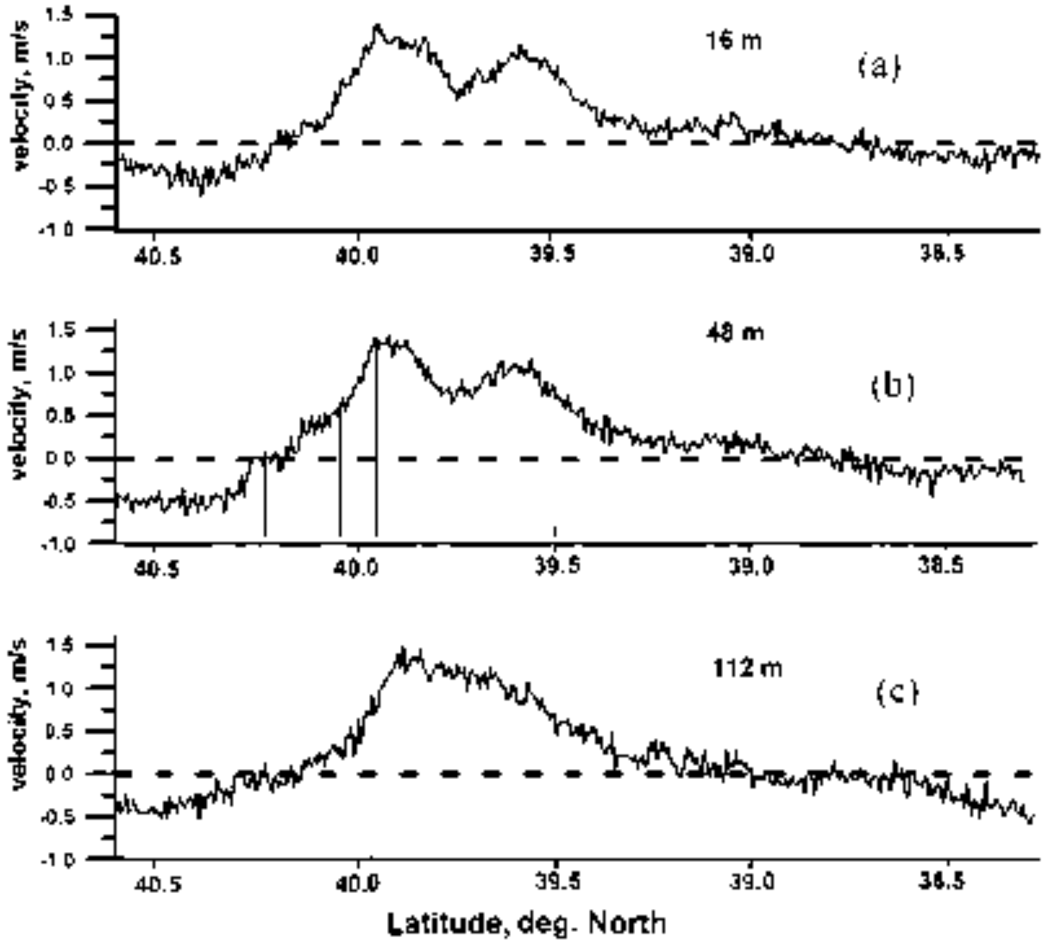

Figure 10. Characteristic variations in the longitudinal velocity (60°, east-northeast) of the Gulf Stream along the ship's route versus latitude at different depths in 2015. At depths of 16 m and 48 m, two current jets are seen, which merge deeper. Black vertical lines mark the intervals for assessing horizontal gradients.

Within the main 40 km section, the velocity changes by 1.6 m/s (from +1.2 m/s to −0.4 m/s). Change in velocity within the local 6-km section between 40.25°N and 40.30°N is 0.4 m/s and within the 12-km section in the range of 39.95°–40.05°N the velocity changes by 0.8 m/s.

From these data, the background mean velocity gradient $\mathrm{d}u/\mathrm{d}r$ (or the horizontal shear of velocity) at 40 km distance is approximately 0.4×10^{-4}/s where u is the longitudinal component of velocity, r is distance. Velocity gradient over smaller interval is ~0.7×10^{-4}/s for each of them. Slightly smaller horizontal shears are likely in the corresponding sections of the other two profiles, at depths of 16 and 112 m.

Such values correspond by the order of magnitude to the published mean horizontal shear of strong currents [*Frey et al.*, 2021]. With that, being of the same order as in the Malvinas Current [*Frey et al.*, 2021], they are several times higher than the horizontal shears at the onshore margins of the latter, which, to our opinion, may be explained by significantly sharper frontal zones of the Gulf Stream.

The given examples of numerical estimates indicate the reality of the occurrence of significant transverse horizontal shears of the longitudinal velocity on the left periphery of the Stream. The presence of strong horizontal shears leads to strong instability in the transition zone and also it indicates the high level of relative vorticity. The latter influences potential vorticity and its conservation that may control, in its turn, important patterns of circulation in the region.

3.2.5. Vertical profiles

Figure 11 shows typical vertical velocity profiles. The profile shown in Figure 11a, crosses the upper northern core and the left periphery of the lower core and has a section with a large vertical gradient of the horizontal velocity at depths from 120 m to 260 m. Over this 140 m interval, the velocity changes from 1.1 m/s to 0.3 m/s; this corresponds to a mean vertical gradient of 5.7×10^{-3}/s. The presence of strong vertical shear of longitudinal velocity means that the flow at the northern periphery of the lower high-speed core of the warm current may be locally unstable. At the same time, the presence of a strong vertical shear in this transition zone, together with the horizontal ones, may ensure continuous contact of the external cold countercurrent (from the Labrador) with the main jet of the warm current.

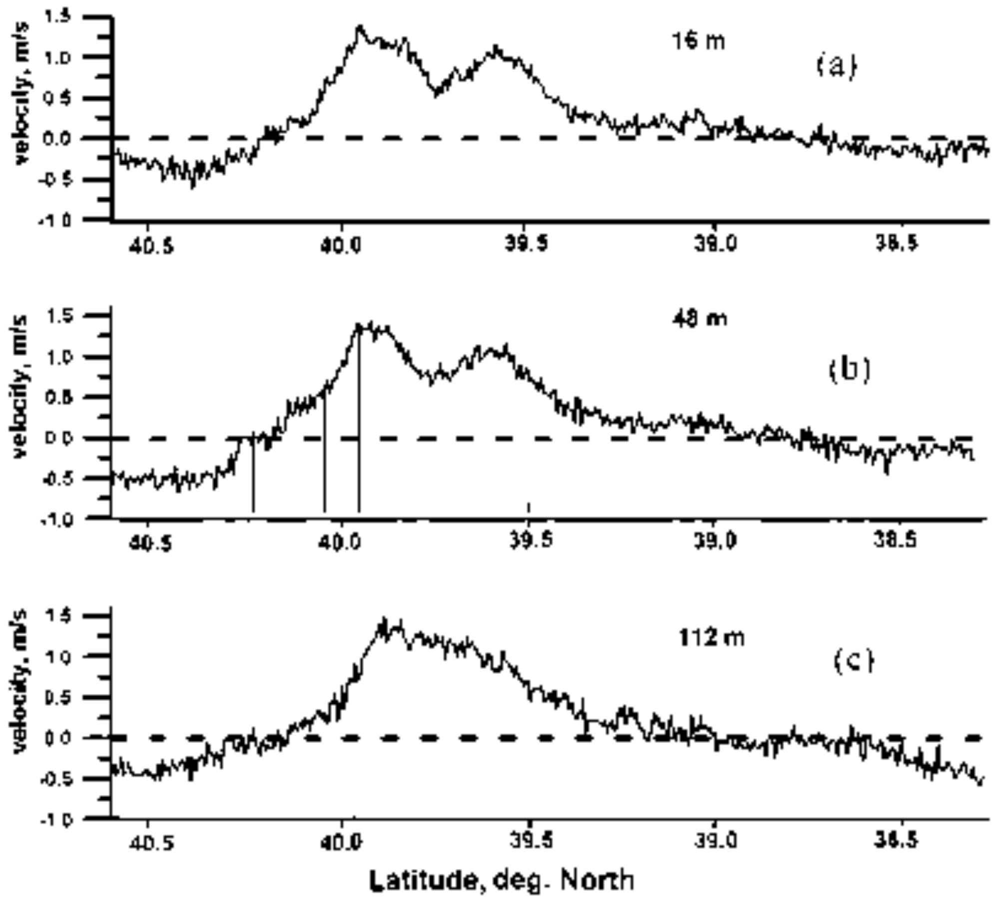

Figure 11. Vertical profiles of longitudinal velocity at three points of the section in 2015. Locations of profiles are shown in Figure 9: (a) 39.87°N; (b) 39.66°N; (c) 38.65°N. Gray bars mark the intervals for assessing vertical gradients.

Figure 11b shows velocity profile passing the north edge of the southern surface core and crossing southern part of the lower core. This profile is different from the peripheral profile in Figure 11a. The difference is that the vertical velocity gradients in the same interval are notably smaller, and the mean profile is convex. However, some high vertical shears (with the opposite sign) were found within smaller intervals, for example between 60 and 110 m, where velocity changes from 0.7 to 1 m/s that gives a mean vertical gradient of 6×10^{-3}/s. Even higher shears can be expected on profiles between two surface cores, in intervals where they intersect a transition zone at about 100 m deep, from low surface velocities to intense ones in the lower core. Strong local instability could be expected inside the area that is important for better understanding the splitting mechanism of the core of the Gulf Stream.

Figure 11c shows the velocity profile at a mark of 250 km crossing a small warm jet at depths from 150 m to 300 m, mentioned above. It can be assumed that this isolated formation is a result of local shear instability on the right periphery of the main current core, presumably due to instability and meandering of the current.

4. Summary

Information and a review of experimental researches in four cruises in the eastern part of the Gulf Stream are presented.

In 1989, based on the eddy-resolving survey including vertical CTD and current velocity profiling the motion of a meander, previously detected on the satellite image, was traced on a monthly scale. The meander was spreading across the test area to the southwest and carried cold water. During the same time, the Stream's core shifted to the north.

In 1990, detailed CTD-surveys in April–June in the region of the Gulf Stream delta traced changes in the Gulf Stream branching and eddy formation. During three months, the total transport of the Gulf Stream did not change strongly and remained within a range of 62–63 Sv, while the transports of each of the jets changed.

In 2014, a detail velocity structure of a transformed cyclonic eddy of elongated form carrying relatively cold water was identified in the velocity section. It penetrated at least to a depth of 700 m and had a complex internal structure with two cores of about 300 m deep.

In 2015, a detailed structure of the longitudinal velocity field revealed a strong core splitting into two to the surface. High velocity gradients leading to strong velocity shears are obvious in the northern vicinities of transition zone of the cores. These may ensure continuous contact of the external cold countercurrent (from the Labrador) with the main jet of the warm current.

Acknowledgments. This work was supported by the State Assignment of the Shirshov Institute of Oceanology (FMWE-2024-0017, ship measurements) and the Russian Science Foundation grant 21-77-20004 (analysis of measurement data).

References

Auer, S. J. (1987), Five-year climatological survey of the Gulf Stream system and its associated rings, *Journal of Geophysical Research: Oceans*, *92*(C11), 11,709–11,726, https://doi.org/10.1029/JC092iC11p11709.

Baranov, E. I. (1988), *Structure and Dynamics of the Gulf Stream Waters*, 251 pp., Gidrometeoizdat, Moscow (in Russian).

Clarke, R. A., H. W. Hill, R. F. Reiniger, and B. A. Warren (1980), Current System South and East of the Grand Banks of Newfoundland, *Journal of Physical Oceanography*, *10*(1), 25–65, https://doi.org/10.1175/1520-0485(1980)010<0025:CSSAEO>2.0.CO;2.

Dykhno, L. A., E. G. Morozov, and B. N. Filyushkin (1992), Formation of eddy structures on the southern periphery of the Gulf Stream, *Oceanology*, *32*(4), 431–434.

Dzhiganshin, G. F., and A. B. Polonsky (2009), Low-frequency variations of the Gulf-Stream transport: description and mechanisms, *Physical Oceanography*, *19*(3), 151–169, https://doi.org/10.1007/s11110-009-9047-5.

Frey, D. I., A. R. Piola, V. A. Krechik, et al. (2021), Direct Measurements of the Malvinas Current Velocity Structure, *Journal of Geophysical Research: Oceans*, *126*(4), https://doi.org/10.1029/2020JC016727.

Frey, D. I., A. R. Piola, and E. G. Morozov (2023), Convergence of the Malvinas Current branches near 44°S, *Deep Sea Research Part I: Oceanographic Research Papers*, *196*, 104,023, https://doi.org/10.1016/j.dsr.2023.104023.

Fuglister, F. C. (1951), Multiple Currents in the Gulf Stream System, *Tellus A: Dynamic Meteorology and Oceanography*, *3*(4), 230–233, https://doi.org/10.3402/tellusa.v3i4.8661.

Ginzburg, A. I., and K. N. Fedorov (1984), *Mushroom shape currents in the ocean (based on the analysis of satellite images. Exploration of the Earth from space*, 227 pp., Foreign Literature Publishing House (in Russian).

Gula, J., M. J. Molemaker, and J. C. McWilliams (2014), Submesoscale Cold Filaments in the Gulf Stream, *Journal of Physical Oceanography*, *44*(10), 2617–2643, https://doi.org/10.1175/JPO-D-14-0029.1.

Gulev, S. K., Y. A. Ivanov, A. V. Kolinko, et al. (1992), Experiment: Atlantex-90, *Meteorology and Hydrology*, (5), 51–61 (in Russian).

Guo, Y., S. Bishop, F. Bryan, and S. Bachman (2023), Mesoscale Variability Linked to Interannual Displacement of Gulf Stream, *Geophysical Research Letters*, *50*(7), https://doi.org/10.1029/2022GL102549.

Huang, B., C. Liu, V. Banzon, et al. (2021), Improvements of the Daily Optimum Interpolation Sea Surface Temperature (DOISST) Version 2.1, *Journal of Climate*, *34*(8), 2923–2939, https://doi.org/10.1175/JCLI-D-20-0166.1.

Ivanov, Y. A., and E. G. Morozov (1991), Water transport in the Gulfstream delta, *Doklady AN SSSR*, *319*(2), 487–490 (in Russian).

Muglia, M., H. Seim, J. Bane, and P. Taylor (2022), An Observation-Based Study of Gulf Stream Meander Kinematics Offshore of Cape Hatteras, *Frontiers in Marine Science*, *9*, https://doi.org/10.3389/fmars.2022.867439.

NOAA (1989), *Oceanographic Monthly Summary. Voluem 9. Number 9*, US Department commerce, Washington.

Pujol, M.-I., Y. Faugère, G. Taburet, et al. (2016), DUACS DT2014: the new multi-mission altimeter data set reprocessed over 20 years, *Ocean Science*, *12*(5), 1067–1090, https://doi.org/10.5194/os-12-1067-2016.

Richardson, P. L. (2001), Florida Current, Gulf Stream, and Labrador Current, in *Encyclopedia of Ocean Sciences*, pp. 554–563, Elsevier, https://doi.org/10.1016/B978-012374473-9.00357-X.

Rossby, T., C. N. Flagg, K. Donohue, A. Sanchez-Franks, and J. Lillibridge (2014), On the long-term stability of Gulf Stream transport based on 20 years of direct measurements, *Geophysical Research Letters*, *41*(1), 114–120, https://doi.org/10.1002/2013GL058636.

Seidov, D., A. Mishonov, J. Reagan, and R. Parsons (2019), Eddy-Resolving In Situ Ocean Climatologies of Temperature and Salinity in the Northwest Atlantic Ocean, *Journal of Geophysical Research: Oceans*, *124*(1), 41–58, https://doi.org/10.1029/2018JC014548.

Satellite-Detected Anomalous Changes in Parameters of Various Geophysical Fields During Earthquakes of $6 \le M \le 7.8$ in Türkiye in February 2023

V. G. Bondur[1,*], **M. N. Tsidilina**[1], **E. V. Gaponova**[1], **O. S. Voronova**[1], **M. V. Gaponova**[1], **N. V. Feoktistova**[1], **and A. L. Zima**[1]

[1]Institute for Scientific Research of Aerospace Monitoring "AEROCOSMOS", Moscow, Russia
* **Correspondence to:** Valery G. Bondur, office@aerocosmos.info

Abstract: Research was conducted using satellite data to study variations in parameters of various geophysical fields manifested in the lithosphere, atmosphere, and ionosphere during the preparation and occurrence of destructive earthquakes of $6 \le M \le 7.8$ in Türkiye in February 2023. Precursor manifestations of these seismic events were satellite-detected in the form of anomalies in parameters of various geophysical fields, including: lineament systems, surface skin temperature and surface air temperature, relative humidity, latent heat flux, integrated flux of outgoing longwave radiation, altitude changes in ionospheric electron density, total electron content of the ionosphere, as well as aerosol optical depth. It was found that the anomalies of all studied geophysical fields detected using satellite data manifested most intensively during the period 3–13 days before the onset of seismic events.

Keywords: Satellite data, anomalies of geophysical fields, earthquake precursors, geodynamics, lineaments, thermal fields, ionosphere, aerosol.

Citation: Bondur, V. G., M. N. Tsidilina, E. V. Gaponova, O. S. Voronova, M. V. Gaponova, N. V. Feoktistova, and A. L. Zima (2024), Satellite-Detected Anomalous Changes in Parameters of Various Geophysical Fields During Earthquakes of $6 \le M \le 7.8$ in Türkiye in February 2023, *Russian Journal of Earth Sciences*, 24, ES4006, EDN: BRWHCY, https://doi.org/10.2205/2024es000930

Research Article

Received: 21 May 2024
Accepted: 30 August 2024
Published: 29 October 2024

1. Introduction

Earthquakes are among the most destructive and least predictable natural disasters. Vast territories, often densely populated, are under the threat of earthquakes. Some of these natural disasters were devastating earthquakes that occurred in Türkiye and neighboring countries in February 2023.

Over the past 23 years (from 2000 to 2023), more than 7000 earthquakes of $5 \le M \le 7.8$ have occurred in Türkiye, including 240 seismic events of $5 \le M \le 6$ and around 20 events of $M \ge 6$ [*Federal Research Center Geophysical Survey of the RAS*, 2023; *United States Geological Survey*, 2023]. The destructive seismic events that occurred in February 2023 in southeastern Türkiye and Syria, including the catastrophic M7.8 earthquake on 6 February 2023, once again vividly demonstrated how massive and devastating their effects can be [*Akhoondzadeh and Marchetti*, 2023; *Bondur et al.*, 2023; *Dal Zilio and Ampuero*, 2023; *Ruzhich et al.*, 2023]. According to the Turkish government, these earthquakes resulted in the death of over 50 thousand people, injuries to over 107 thousand people, and economic losses exceeding 103 billion US dollars. In order to forecast such dangerous natural disasters as earthquakes, it is important to register their precursors [*Sobolev and Ponomarev*, 2003]. The search for earthquake precursors is a quite challenging task [*Keilis-Borok et al.*, 2009; *Mogi*, 1985; *Molchan and Keilis-Borok*, 2008; *Sobolev and Ponomarev*, 2003].

Methods and tools of satellite monitoring play a crucial role in addressing this task [*Akhoondzadeh and Marchetti*, 2023; *Bondur and Smirnov*, 2005; *Bondur et al.*, 2022, 2023; *Mikhailov et al.*, 2023a,b; *Xu et al.*, 2022; *Zhang et al.*, 2021]. The current level of their development and the data products obtained through satellite monitoring allow for the study of anomalous variations in parameters of various geophysical fields during the preparation and occurrence of significant seismic events [*Bondur et al.*, 2022]. Satellite data can be used to register changes in lineament systems, which help to identify structural deformations in epicentral zones and the kinematics of active faults before earthquakes [*Bondur et al.*, 2022]. Anomalies occurring at different heights before an earthquake can also be detected by studying thermal fields from the Earth's surface to the upper cloud boundary [*Bondur et al.*, 2022; *Pulinets et al.*, 2006; *Tronin*, 2000; *Xiong et al.*, 2010]. Anomalies in various ionospheric parameters during the preparation and occurrence of seismic events can be recorded by satellite navigation systems [*Bondur and Smirnov*, 2005; *Bondur et al.*, 2022; *Pulinets and Ouzounov*, 2011; *Smirnov and Smirnova*, 2008]. To register anomalous geodynamics before earthquakes, it is promising to use satellite radio interferometry methods [*Bondur et al.*, 2023; *Mikhailov et al.*, 2023a,b; *Xu et al.*, 2022; *Zhang et al.*, 2021] which were used, among others, to analyze the studied earthquake in Türkiye [*Bondur et al.*, 2023; *Mikhailov et al.*, 2023a,b], as well as modeling methods [*Bondur et al.*, 2016; *Soloviev and Gorshkov*, 2017]. Interesting approaches to determining potential locations of strong earthquakes include use of pattern recognition methods presented in a study [*Gvishiani et al.*, 2020].

For a better understanding of the processes related to the preparation and occurrence of strong earthquakes, it is promising to conduct a joint analysis of parameters of various geophysical fields recorded using satellites during the monitoring of seismically hazardous areas [*Bondur et al.*, 2022; *Jiao et al.*, 2018; *Pulinets and Ouzounov*, 2011].

In this study, a joint analysis of anomalous variations in geophysical fields manifested in the lithosphere, atmosphere, and ionosphere during preparation and occurrence of destructive Türkiye earthquakes in February 2023 was carried out.

2. Research methodology

In order to identify changes in significant parameters of various geophysical fields during the preparation and occurrence of destructive earthquakes in Türkiye in February 2023, an analysis was conducted for changes in lineament systems, parameters of thermal fields and relative humidity, aerosol optical depth (AOD), as well as altitude distribution in ionospheric electron density (N_e) and ionospheric total electron content (TEC).

The assessment of the location of lineament systems was carried out through automated analysis of satellite image fragments of 100×100 km obtained from the Terra satellite (MODIS instrument) with a spatial resolution of 250 meters. Based on the results of this analysis, statistical characteristics of local lineaments (stripes) and rose diagrams of regional lineaments were constructed. For each stripe, the orientation was determined for eight directions: 0°, 22.5°, 45°, 67.5°, 90°, 112.5°, 135°, 157.5° (angle was measured from right to left horizontally) [*Bondur et al.*, 2022].

The total lengths of lineaments (L) were calculated for eight directions using the formula (1):

$$L = \frac{nr}{1000\cos\varphi}, \tag{1}$$

where n is the number of pixels; r is the spatial resolution; and φ is the angle of lineament orientation.

As a result, graphs of relative changes in the total lengths of stripes in different directions were constructed and analyzed.

Studies for the seismic activity period in Türkiye were conducted using such parameters of thermal fields as Surface Skin Temperature (SST), Surface Air Temperature (SAT), Latent Heat Flux (LHF) and Outgoing Longwave Radiation (OLR) as well as a parameter of Relative Humidity at Surface (RHS).

Parameters SST, SAT, RHS, and OLR were registered by the AIRS instrument (Aqua satellite) [*Hearty et al.*, 2013]. LHF data with 6-hour averaging were obtained from the reanalysis dataset available on the Google Earth Engine cloud platform [*Saha et al.*, 2010].

In the study of thermal fields and RHS, a methodology based on the use of the standard deviation interval ($\mu \pm \sigma$) relative to the mean values (μ) was applied. The study area for parameters (SST, SAT, RHS, LHF, OLR) was the zone with coordinates 35°N–40°N, 35°E–40°E including the territory where epicenters of earthquakes were located.

The research of the studied parameters was conducted for the period from January to March 2023, as well as for multi-year data for these months (from 2004 to 2022). A specially developed software module was used for the joint analysis of these parameters [*Bondur et al.*, 2022]. The resulting values were transformed into numerical features within the range of 0 to 1 using formula (2):

$$N_i = \frac{1}{1 + \exp\left(-\left(\frac{(S_d - S^*)}{\sigma}\right)\right)}, \tag{2}$$

where S_d – data for the current day; S^* – arithmetic mean of previous years; σ – standard deviation.

In studying the dynamics of aerosols in the atmosphere during the preparation and occurrence of the analyzed earthquakes, the AOD parameter for the green band of the electromagnetic spectrum (0.55 μm) was used. This parameter was contained in the MCD19A2 Level 2 data product, which combines data from the Terra and Aqua satellites [*Lyapustin and Wang*, 2018]. The data acquisition and processing to detect changes in AOD in the study area were done using the Google Earth Engine platform for scientific analysis and visualization of geospatial data [*Google Earth Engine*, 2023]. Daily average AOD values over land for the study area in Türkiye were obtained based on MCD19A2. Values calculated from satellite image fragments containing less than 1000 pixels were discarded as unreliable data.

For analyzing AOD anomalies, a zone of approximately 140 × 220 km around the earthquake epicenter was used. This size of the study area was chosen to exclude the influence of other aerosol sources such as, for example, UV-absorbing dust particles from the Arabian Peninsula (Syrian Desert).

The variations in ionospheric plasma parameters were studied based on analysis of GPS data using two approaches. The analysis of altitude changes in N_e was conducted using a methodology based on radio occultation of Earth's ionosphere, measuring radio signal parameters obtained from existing satellite navigation systems. This method involves solving inverse problems of radio wave refraction, which are inherently unstable and require special mathematical methods to consider additional information about the active task [*Bondur and Smirnov*, 2005; *Smirnov and Smirnova*, 2008].

The method allows for registering altitude distribution of N_e in quasi-real-time mode based on data from a single ground station, which is particularly important for remote and inaccessible regions of the Earth [*Bondur and Smirnov*, 2005].

As a result of navigation data processing, altitude profiles of N_e were obtained along trajectories of subionospheric points for altitudes ranging from 80 to 1000 km with a 30-second discreetness based on HRMN site data.

To conduct a joint analysis of ionospheric plasma parameter variations with characteristics of other geophysical fields based on long-term data, a normalized index of total electron content of the ionosphere (NTEC) was calculated using formula (3):

$$\text{NTEC} = \frac{(\text{TEC} - \mu)}{\sigma}, \tag{3}$$

where TEC represents the values of total electron content for the current day in 2023 obtained from Global Ionospheric Maps (GIM) [*Noll*, 2010] for the zone with coordinates 35°N–40°N, 35°E–40°E; μ is the arithmetic mean of past years (2001–2022) for the studied day; σ is the standard deviation.

In the final stage of the research, a joint analysis of anomalous variations in lineament systems, thermal fields, RHS, AOD, and ionospheric parameters was conducted to identify correlations between the characteristics of various geophysical fields.

3. Research results and their analysis

3.1. Aspects of seismic activity in the studied region

The strongest earthquakes ($M \geq 6$) in the study area are associated with the deep East Anatolian and North Anatolian faults [*Trifonov*, 2017].

In the first three months of 2023, about 500 earthquakes of $M \geq 3.4$ occurred in the East Anatolian fault zone. Figure 1 shows the locations of earthquake epicenters in Türkiye with $M \geq 4$ (a), as well as a graph of earthquake magnitudes in the East Anatolian fault zone during the first three months of 2023 (b) according to [*Federal Research Center Geophysical Survey of the RAS*, 2023; *United States Geological Survey*, 2023].

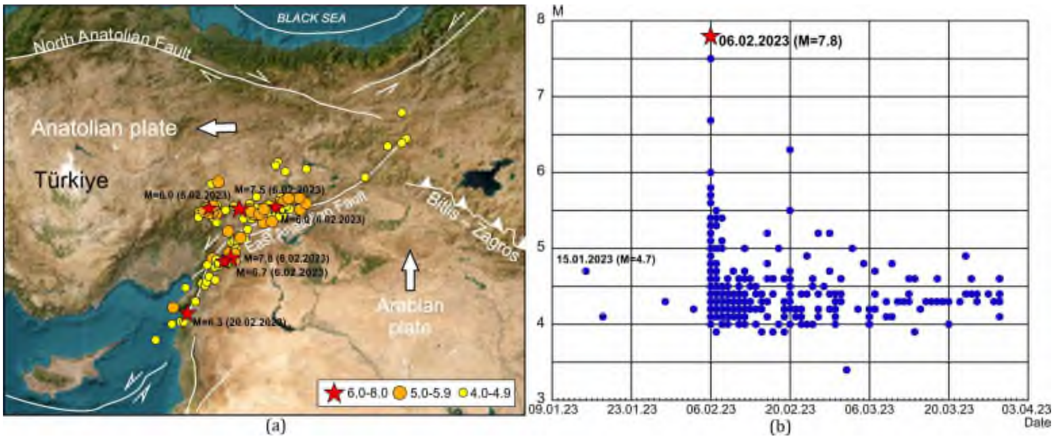

Figure 1. Earthquake epicenter locations in Türkiye (a) and graph of earthquake magnitudes in the East Anatolian fault zone during the first three months of 2023 (b) according to [*United States Geological Survey*, 2023].

Starting from 6 February 2023, five destructive earthquakes of $5 \leq M \leq 7.8$ occurred in Türkiye, along with approximately 200 aftershocks of $4 \leq M \leq 6$. The epicenter of the strongest $M = 7.8$ earthquake was located 27 km from the city of Gaziantep. The focal depth was 17.9 km [*United States Geological Survey*, 2023].

3.2. Results of the analysis of lineament systems

Lineaments were constructed for the epicentral area based on fragments of satellite images in Figure 2. The earthquake epicenter fell within the upper right corners of the satellite image fragments.

Analysis of rose diagrams of regional lineaments in Figure 2 showed that changes in intersecting lineaments (oriented at 315° relative to the main relief structures) occurred before the seismic events under study. This effect is supported by the findings of [*Bondur et al.*, 2022]. The analysis of Figure 2 indicates that from the beginning of observations (20 November 2022) until 10 January 2023, the predominant directions of lineaments of rose diagrams (45°) and their intersecting directions (315°) changed slightly. From 23 to 25 January 2023, there was a decrease in the rays of rose diagrams with directions of 45°, while the rays oriented NW–SE (315°) increased, reaching their maximum length on 3 February 2023 (3 days before the earthquake). They became approximately equal in length to the rays of rose diagrams with directions of 45°.

On the diagrams of elongation lines of local lineaments (stripes) in Figure 2, it can be observed that from 19 December 2022 to 10 January 2023 (5–27 days before the $M = 4.7$ foreshock), there was an increase in elongation lines of stripes in the NE–SW direction (45°). Starting from 23 January 2023 (14 days before the earthquake $M = 7.8$), they gradually changed their orientation towards sub-latitudinal directions (as indicated by red arrows in

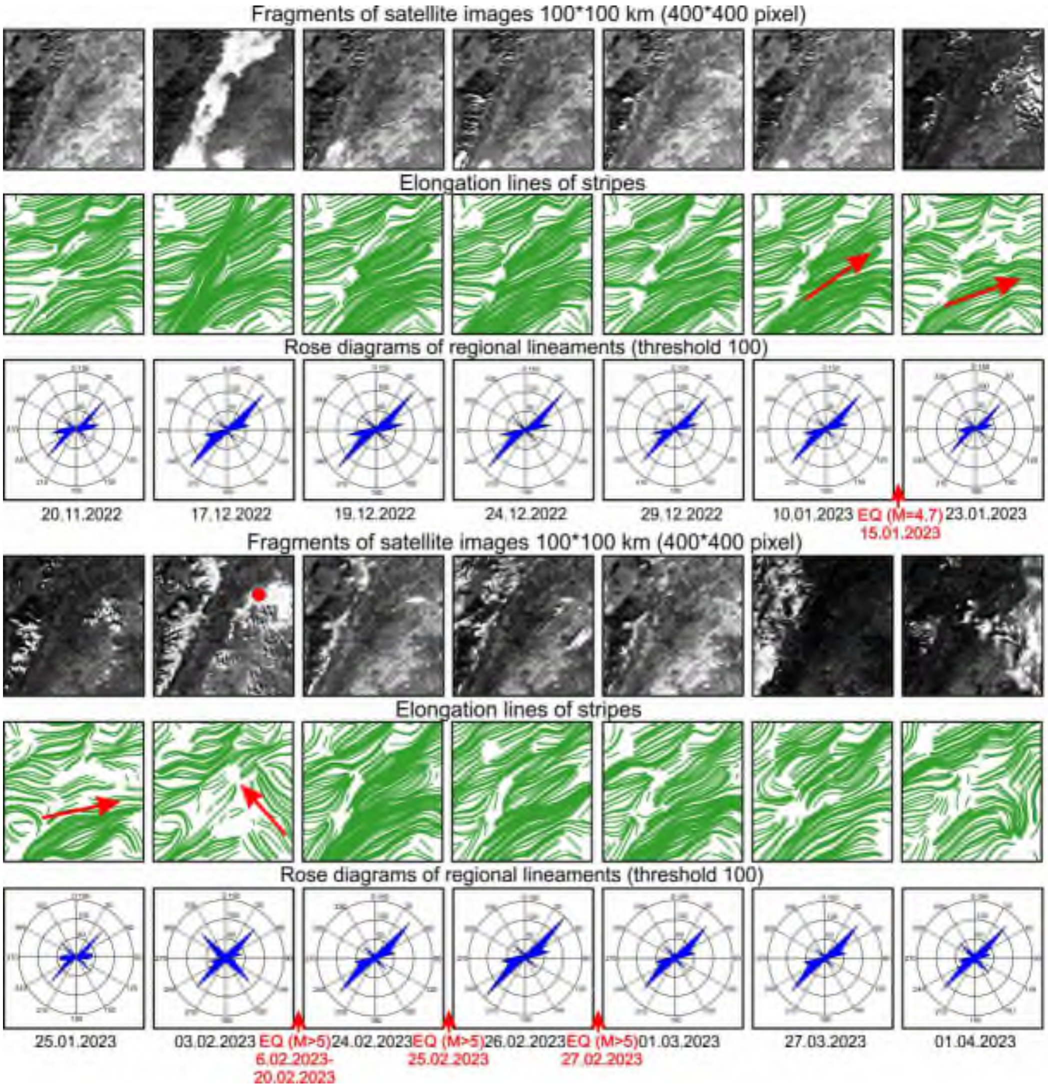

Figure 2. Fragments of satellite images, elongation lines of stripes, and rose diagrams of regional lineaments before the earthquakes on 6 February 2023.

Figure 2). Additionally, on the diagram of elongation lines of stripes obtained on 3 February 2023 (3 days before the earthquake $M = 7.8$), an increase in their quantity was detected for NW–SE directions (315°), intersecting with the main relief structures.

3.3. *Results of the analysis of thermal fields and relative humidity*

Figure 3 presents graphs of changes of SST, SAT, RHS, LHF, and OLR from 1 January to 1 March 2023, compared to the long-term values for these months from previous years (2004–2022). Values of the parameters were considered anomalous if they exceeded the quadratic mean range ($\pm\sigma$).

Analysis of the results presented in Figure 3 showed that the variations of background values (2011 year) of the selected parameters of thermal fields and RHS were moderate and practically did not exceed the intervals of standard deviations.

As a result of the analysis of the changes in the studied parameters (Figure 3), anomalies were identified before the foreshock on 15 January 2023 ($M = 4.7$), as well as before the main earthquake on 6 February 2023 ($M = 7.8$), which are described below.

An anomalous downward trend in SST and SAT changes by 7–8 °C was observed from 2 January 2023, while RHS values rose by 24%. Similar opposite trends in temperature and humidity were studied during several earthquakes in Mexico, for example, in the work of [*Pulinets et al.*, 2006], where the possibility of using these parameters as indicators of impending seismic activity was confirmed.

Since 3 January 2023, anomalous changes in the studied parameters were detected, which manifested in the form of a decrease in temperature and an increase in humidity. After the increase in RHS values, there was a LHF rise starting from 5 January 2023 (by 13 W/m^2).

Anomalous OLR changes were detected during the period from 1 to 12 January 2023, when there was a decrease in values of this parameter by 72 W/m^2.

On 6 February 2023, abnormal changes of the studied parameters were identified (Figure 3). Starting from 14 January 2023, there was an increase in SST and SAT by 5–9 °C above the epicentral area of the impending earthquake. It facilitated intense interaction between land and atmosphere, followed by an LHF increase (by 28 W/m^2). The LHF is strongly influenced by meteorological parameters such as RHS. The increase (up to 86%) in RHS values detected since 12 January 2023 probably caused an increase in the amount of water vapor in the atmosphere (Figure 3). Water vapor carries latent heat, which is released or absorbed during phase changes of water in the process of evaporation or condensation [*Cervone et al.*, 2005]. Therefore, the elevated RHS values from 15 January to 2 February 2023, compared to long-term averages, could have contributed to the LHF increase. The maximum of this parameter (40.5 W/m^2) was revealed on 2 February 2023, four days before the main earthquake (Figure 3). The maximum LHF increase before an earthquake and the strengthening of its interaction between the atmosphere and land are described in the works [*Dey and Singh*, 2003; *Tronin*, 2000].

Analysis of Figure 3 showed that during the preparation period for the main seismic event (6 February 2023), starting from 19 January 2023 abnormally high OLR values were recorded using satellite data. Their maximum value was 252 W/m^2 on 21 January 2023. Next, from 21 January to 4 February 2023, there was a gradual decrease in OLR values by 96 W/m^2.

Besides the decrease in OLR values, a decrease in SST and SAT values by 11–14 °C was observed from 19 January to 2 February 2023 (Figure 3). SST changes prior to destructive earthquakes in Türkiye on 6 February 2023 were also described in the work [*Akhoondzadeh and Marchetti*, 2023], where a decrease by 5–8 °C approximately 18 days before the main seismic event was demonstrated.

3.4. Analysis of aerosol optical depth anomalies

In a number of studies, for example, [*Akhoondzadeh*, 2015; *Bondur et al.*, 2022; *Ganguly*, 2016; *Ghosh et al.*, 2023; *Okada et al.*, 2004] a relation was discovered between AOD anomalies (including those identified using satellite data) and strong earthquakes.

In this work we studied AOD changes based on satellite data during the preparation and occurrence of destructive earthquakes in Türkiye in February 2023.

Figure 4a,b show maps of the study areas with fault lines and epicenters of the main earthquakes that occurred in 2023 (a) and 2020 (b) as well as graphs of AOD changes. Figure 4c shows the average daily AOD values in January–February 2023. The Figure also presents comparison of the daily average AOD values for the previous 10 years and the average daily values for the background year 2011 for the same period.

Analysis of Figure 4c showed that during the period of preparation and occurrence of earthquakes from 15 January to 1 March 2023, low AOD values were observed relative to the average annual value for the previous 2022. The exceptions were AOD values recorded on 15 January, 28 January and 27 February 2023. These days, daily average AOD values exceeded the limit of three standard deviations (3σ) from the annual mean (yellow background). On 15 January 2023, a $M4.7$ earthquake was recorded. It should be noted that some of the data is missing due to cloudiness over the studied region.

Figure 4c shows that from 21 to 28 January 2023 the AOD value continuously increased and reached a maximum value (0.39) on 28 January 2023 (7 days before the earthquake $M = 7.8$), significantly exceeding the 99% confidence interval ($\mu + 3\sigma$). Next, from 29 Jan-

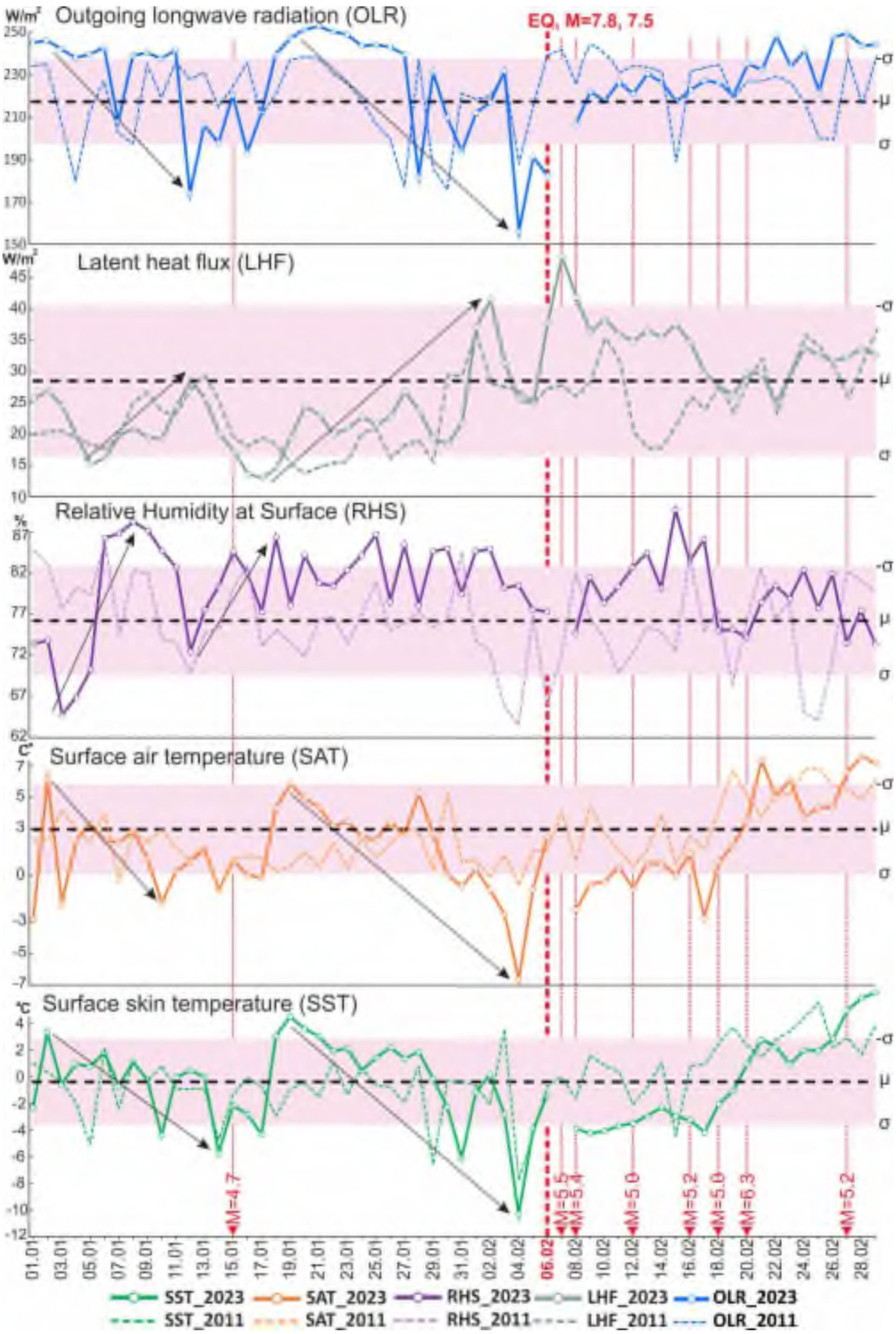

Figure 3. Variations in the values of SST and SAT, RHS, LHF, and OLR during the preparation and occurrence of earthquakes in Türkiye from 1 January to 1 March 2023.

uary to 2 February 2023, there was a decrease of AOD values and a slight increase (up to 0.24) on 4 February 2023 (2 days before the earthquake $M = 7.8$). In the period from 7 to 17 February decreased AOD values were observed. Then, on 20 and 27 February 2023 high

AOD values were identified, reaching 0.24 and 0.309 on the days of aftershocks of $M = 6.3$ and $M = 5.2$, respectively (Figure 4c).

During the study, AOD variations were also researched for other earthquakes that occurred in the zone of the East Anatolian Fault. Similar AOD anomalies detected 4–7 days before the earthquakes were identified in the area where earthquake series occurred in 2020 (Figure 4b): on 4 August four earthquakes with $4 \le M \le 5.6$ were recorded, and on 8 September – three earthquakes with $4.2 \le M \le 4.7$. Analysis of Figure 4d shows a gradual increase in AOD values from 19 to 28 July 2020, reaching a peak value of 0.46 detected 7 days before the earthquakes on 4 August 2020. This was followed by a sharp decrease in AOD values below the average annual value.

The anomaly in AOD values detected on 2 September 2020, before the second series of earthquakes, is weaker and does not exceed the level ($\mu + 3\sigma$), the increase in AOD values was observed for only 4 days reaching a value of 0.34 (Figure 4d).

Thus, based on the results of the analysis of the graphs shown in Figure 4c,d, possible precursor AOD anomalies include a smooth increase in values of this parameter and are going beyond the 99% confidence interval, followed by a decline 6–7 days before significant seismic events. For a more detailed analysis of anomalous AOD changes before seismic events, it is planned to obtain additional data.

3.5. Analysis of ionospheric plasma anomalies

In order to identify anomalous variations of ionospheric parameters during earthquake preparation and occurrence, altitude changes in N_e.

N_e changes in the epicentral region from 24 January to 13 February 2023 were studied based on data Satellites 12 and 24 from the HRMN site (Figure 5a). The satellites' pass times over the study area were as follows: satellite 12: 13:00–20:00 LT; satellite 24: 13:00–18:00 LT.

Figure 5b and 5c show the time series of altitude profile changes in N_e obtained from satellites 12 and 24 in the epicentral zone before the earthquakes in Türkiye in 6 February 2023.

From the analysis of Figure 5b, it follows that from 24 to 28 January 2023, the N_e values remained almost unchanged according to data from satellite 12. Starting from 29 January 2023, there was a gradual decrease. The minimum N_e was recorded on 3 February 2023, three days before the earthquakes of $M = 7.8$ and $M = 7.5$ that occurred on 6 February 2023. The decrease in N_e values amounted to ~ 30% compared to the values registered during the period from 24 to 28 January 2023. A sharp N_e increase was observed on the day of the earthquake on 6 February 2023, which amounted to ~ 42% compared to the previous day.

The analysis of changes in altitude profiles of N_e based on data from satellite 24 (Figure 5c) is identical to the changes registered by satellite 12 (Figure 5b), namely, a N_e drop from 29 January to 3 February 2023 by ~ 20% and a sharp increase by ~ 30% on the day of the earthquakes of $M = 7.8$ and $M = 7.5$ on 6 February 2023 (Figure 5c).

The period from 1 to 10 January 2023 was considered to study background N_e values in the same region (Figure 5d). From the analysis of Figure 5d, it follows that no significant changes in N_e were observed during this period. No earthquakes were recorded during this period, and the geomagnetic conditions were relatively calm, except for 4 January 2023, when a moderate disturbance in the geomagnetic field was observed ($Dst = -61$ nT) [*World Data System*, 2023].

Thus, the analysis of altitude profiles of the N_e revealed anomalous changes, which are expressed in a 20–30% drop in the N_e values on 3 February 2023 (3 days before the earthquake) and in a sharp increase by 30–42% on 6 February 2023 (the first day of the earthquake series) (Figure 5b, c).

The decrease in ionospheric parameter values identified in our study, which occurred 3 days before the start of the earthquake series in Türkiye, coincides with the results

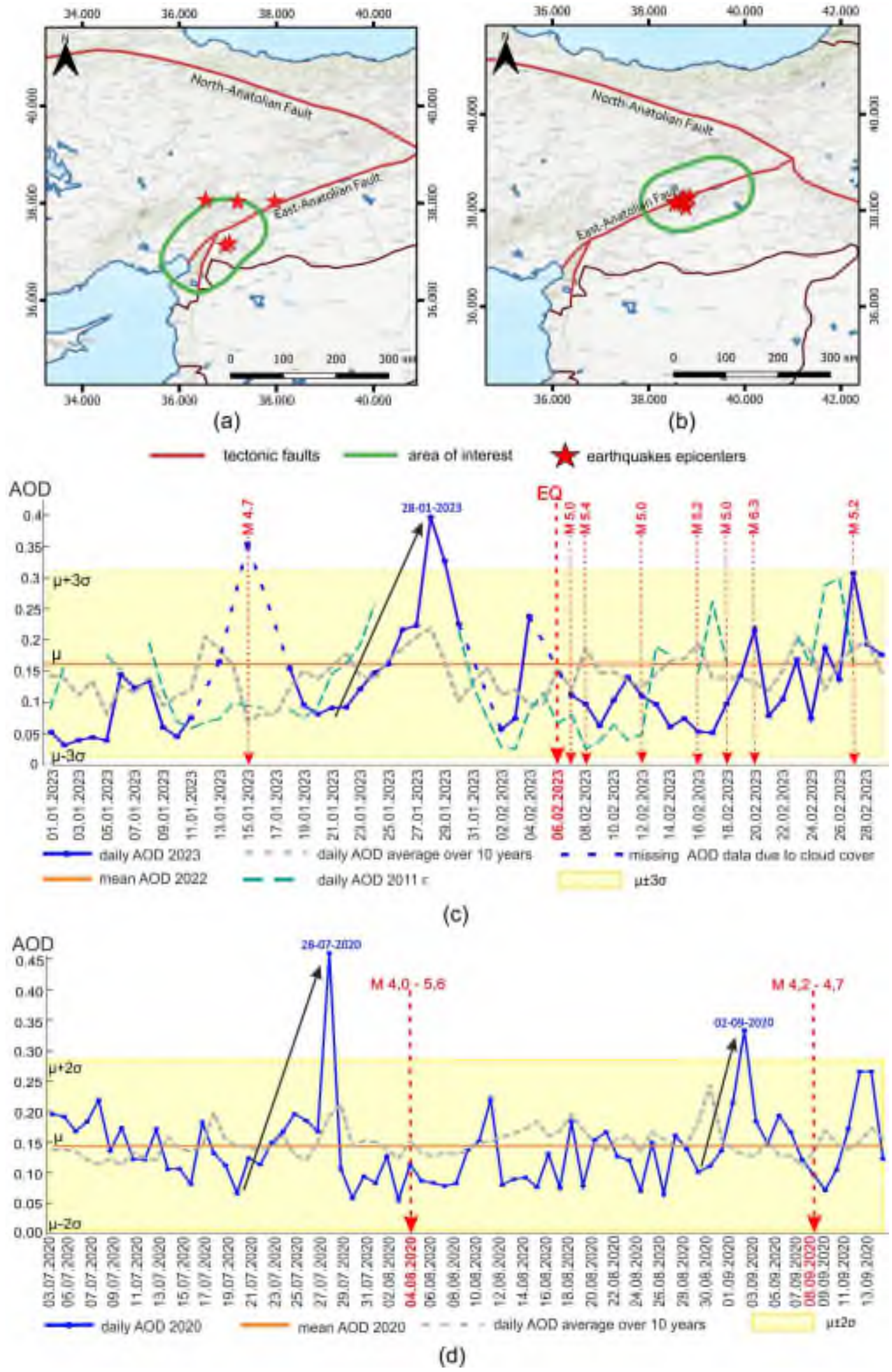

Figure 4. Study areas of AOD for earthquakes that occurred in 2023 (a) and 2020 (b); changes in average daily AOD values during the preparation of earthquakes that occurred in Türkiye on 6 February 2023 (c) and in August-September 2020 (d).

of ionospheric research for this earthquake described in the work by [*Akhoondzadeh and Marchetti*, 2023].

These anomalies can be used as ionospheric precursors of significant seismic events, which can be recorded based on satellite data.

3.6. Joint analysis of anomalies in various geophysical fields

A joint analysis was conducted to identify correlations between the occurrence of anomalous changes in parameters of various geophysical fields during preparation of earthquakes in Türkiye in February 2023.

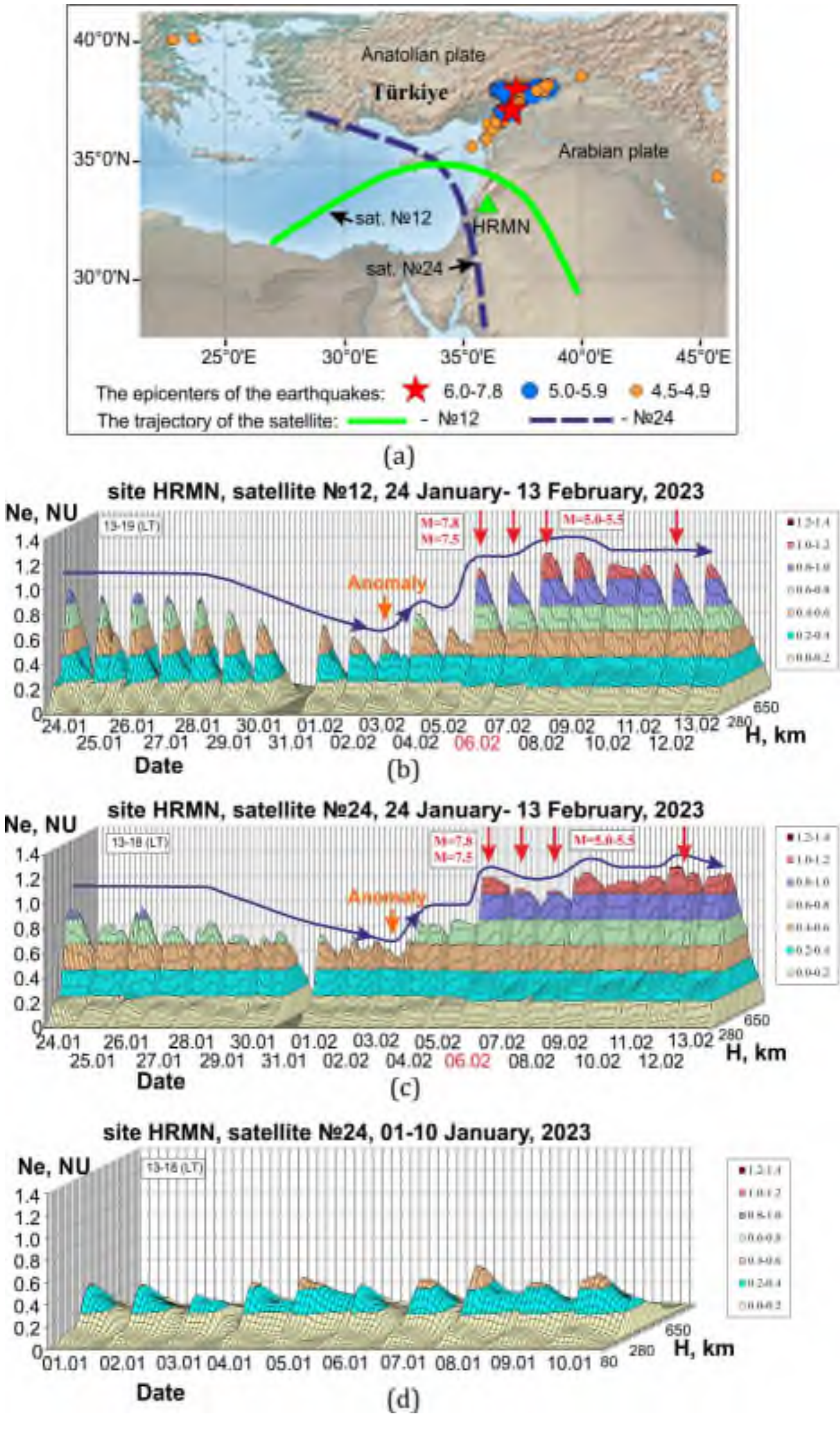

Figure 5. Map of HRMN site location and trajectories of sub-ionospheric points of Satellites 12 and 24 (a); altitude profiles of N_e during the period from 24 January to 13 February 2023, obtained from satellites 12 (b) and 24 (c); from 1 to 10 January 2023, obtained from satellite 24 (d) for HRMN site.

Figure 6 shows graphs of changes in the normalized index of total electron content of the ionosphere (NTEC), calculated using formula (3), normalized index of outgoing longwave radiation (N_{OLR}), normalized index of latent heat flux (N_{LHF}), normalized index of relative humidity (N_{RHS}), normalized index of surface air temperature (N_{SAT}), and normalized index of surface skin temperature (N_{SST}), calculated using formula (2), daily average values of AOD, as well as graphs of changes in total lengths of lineaments of various directions for the period from 1 January to 28 February 2023.

From the analysis of Figure 6, it follows that before the series of destructive earthquakes that occurred in Türkiye in February 2023, anomalies in the atmosphere were registered. These anomalies manifested as a 13% decrease (3 January 2023) and a 55% increase (8 January 2023) in N_{RHS}. The increase in relative humidity contributed to a 22% increase in N_{LHF} occurred from 9 to 12 January 2023. These processes preceded the OLR anomalies, which occurred on 12 January 2023 (25 days prior) and were characterized by a sharp decrease in N_{OLR} values by 54%.

Since a M = 4.7 foreshock occurred on 15 January 2023 on the studied territory, the anomalies manifested in the changes of relative humidity, N_{OLR}, and characteristics of lineament systems registered from 3 to 12 January 2023 may be related to this earthquake.

Starting from 18 January 2023 (19 days before the M = 7.8 earthquake), anomalies in the characteristics of all studied geophysical fields (Figure 6) were registered, which activated a chain of processes preceding the series of strong earthquakes that occurred in Türkiye in February 2023.

Analysis of Figure 6 showed that from 23 January 2023 (14 days before the M = 7.8 earthquake that occurred on 6 February 2023), a restructuring of the relative values of lineament lengths began. An anomalous N_{RHS} increase by 24% was registered on 25 and 27 January 2023, and a sharp N_{OLR} decrease by 61% was recorded on 28 January 2023. Additionally, an AOD anomaly was registered on 28 January 2023, manifesting as a sharp increase in this parameter by 146% (Figure 4c, Figure 6). Subsequently, on 29 January 2023, N_{OLR} increased by 40%, followed by a decrease of 43% until 4 February 2023.

From 31 January to 3 February, the following changes of the parameters were recorded: a decrease of 22% in NTEC, anomalous increase in N_{LHF} by 35% and N_{RHS} by 28%, anomalous decrease in N_{SAT} by 18% and N_{SST} by 8%. On 3 February 2023 (3 days before the earthquakes that occurred on 6 February 2023), the most significant anomalous changes in relative values of lineament lengths of various directions were identified, characterized by their maximum growth or decline (Figure 6).

Thus, the joint analysis of qualitative changes in lineament systems, anomalies in SST, SAT, RHS, LHF, OLR, AOD, and TEC allowed for the identification of a possible sequence of precursor anomalies in the parameters of the studied geophysical fields during the preparation of a series of destructive earthquakes that occurred in Türkiye in February 2023.

4. Conclusion

Variations in significant parameters of various geophysical fields manifested in the lithosphere, atmosphere, and ionosphere during the preparation and occurrence of destructive earthquakes in Türkiye in February 2023 have been studied using satellite data.

Spatial-temporal variations in lineament systems were identified 14 days before the catastrophic earthquake on 6 February 2023. Anomalous changes in regional lineament systems were registered 3 days before the earthquake on 6 February 2023. They manifested in a significant increase in the rays of rose diagrams of intersecting directions in relation to the directions of the main relief structures (lineaments in the direction of 315° almost doubled).

The analysis of changes in SST, SAT, RHS, LHF, and OLR over epicentral areas of seismic events revealed their similar anomalous behavior before the foreshock on 15 January 2023 (M = 4.7) and the catastrophic seismic event on 6 February 2023.

During the preparation of strong earthquakes that occurred in Türkiye in February 2023, a trend towards anomalous decrease of SST and SAT (by 11–14 °C) 18 days before seismic events was identified. Considering the LHF dependence on meteorological parameters such as RHS, the observed RHS increase (up to 86%) 19 days before earthquakes likely contributed to the LHF increase by 26 W/m^2 with its maximum value recorded 4 days

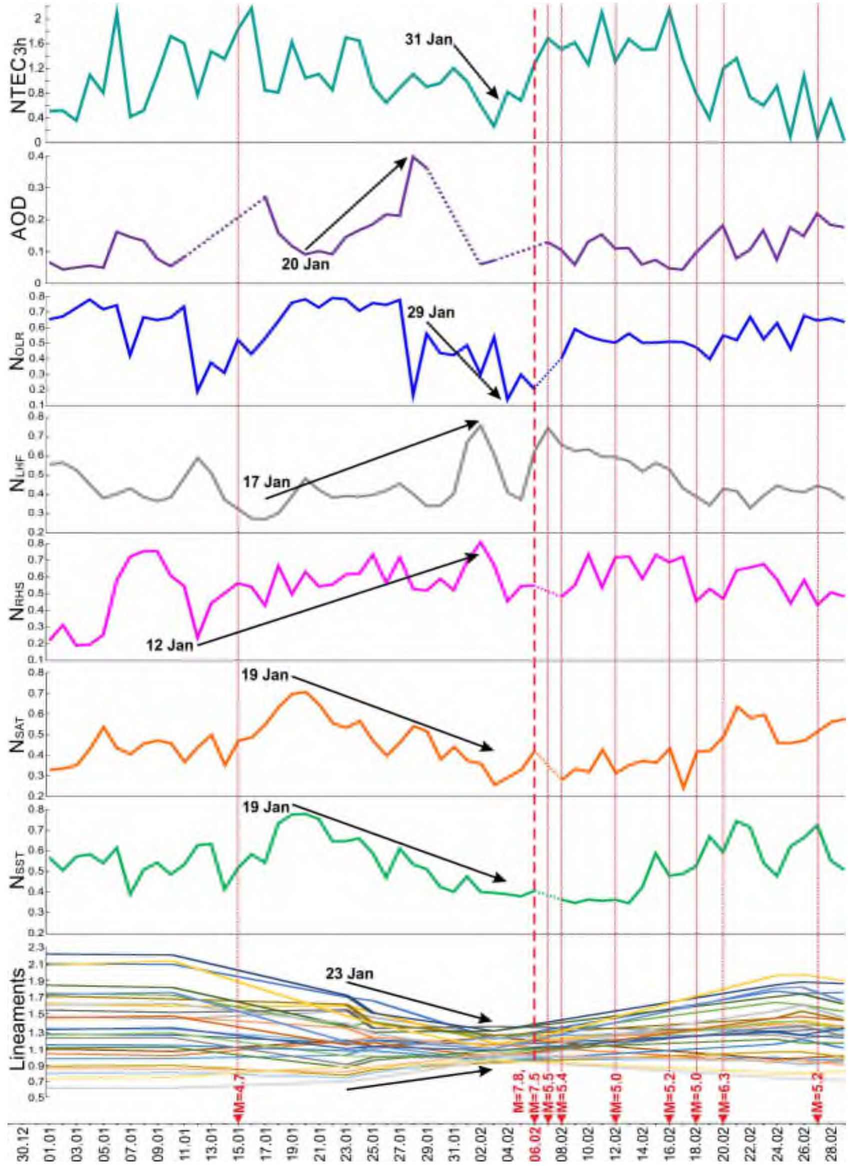

Figure 6. Graphs of changes: NTEC; AOD; N_{OLR}, N_{LHF}, N_{RHS}, N_{SAT} and N_{SST}; relative values of the total lengths of lineaments..

before the strong seismic events on 6 February 2023 of M = 7.5 and M = 7.8. 18 days before the earthquakes, a gradual OLR decrease by 96 W/m^2 was revealed.

5–13 days before the foreshock that occurred on 15 January 2023 (M = 4.7), trends towards a decrease in temperatures and OLR were identified, while the values of LHF and RHS increased. RHS increase (by 24%) probably influenced the increase in LHF values (by 13 W/m^2) detected 10 days before the foreshock. 12 days before the shock, a tendency for OLR decrease (by 72 W/m^2) was discovered.

Analysis of changes in daily average AOD in the earthquake-affected area revealed anomalies characterized by gradual growth of values by 144% relative to the average annual value exceeding the 99% confidence interval 7–8 days before the main M = 7.8 seismic event, followed by a decline by 94% below the annual average value.

Similar anomalies were also observed for other earthquakes with M = 4.0–5.6 that occurred in the studied region in August–September 2020. The excess of the annual average AOD value was 219% and 129% for the earthquakes occurred on 4 August and 8 September 2020, respectively.

Based on the research results of ionospheric plasma parameter variations during the preparation and occurrence of a series of destructive earthquakes in Türkiye in February 2023, seismo-ionospheric anomalies were identified using GPS data. These anomalies manifested in N_e drop at the maximum height of F2 layer (by ~ 20–30%) recorded from vertical profiles on 3 February 2023 (3 days before the earthquake) and a sharp increase by 30–42% on 6 February 2023 (on the day of the devastating earthquakes).

It should be noted that pre-seismic anomalies, expressed as a drop in N_e values at the maximum height of F2 layer, recorded 1–8 days before earthquakes, as well as their sharp increase on the days of earthquakes, were obtained by us earlier, for example [*Bondur and Smirnov*, 2005; *Bondur et al.*, 2022].

Comparison of changes in thermal fields and RHS in 2023 with the background values of these parameters in 2011 verified that the detected anomalous processes were associated with the preparation of the earthquakes that occurred in Türkiye in February 2023.

The joint analysis of the results of the conducted research revealed timed sequences of anomalies in parameters of various geophysical fields (lineament systems, SST, SAT, RHS, LHF, OLR, AOD, and TEC) during the preparation of a series of destructive earthquakes in Türkiye in February 2023.

It was found that before the onset of destructive earthquakes in Türkiye on 6 February 2023 there was a general decrease in values of N_{SST} and N_{SAT} (2–18 days before), N_{OLR} (2–16 days before), NTEC (3 days before), and AOD (2–9 days before). Along with this, increased N_{RHS} values were registered (4–19 days before the destructive earthquakes), which are likely associated with a N_{LHF} increase during the same period. It was also identified that there was a decrease in the number of lineament systems in directions consistent with the extension of the main relief structures of the studied region and an increase in intersecting lineaments 3–14 days before the earthquake on 6 February 2023.

Thus, the analysis of various parameters of geophysical fields registered using satellite data showed that anomalies of all parameters studied in this work most intensely manifested themselves 3–13 days before the start of a series of earthquakes in Türkiye in February 2023.

The conducted research demonstrated that for a better understanding of the processes associated with the preparation of earthquakes, it is promising to carry out a joint analysis of the parameters of various geophysical fields registered from satellite and other data. These parameters can be used as short-term precursors of significant seismic events when monitoring seismically hazardous areas.

Acknowledgments. The work was carried out at ISR “AEROCOSMOS” in the framework of project no. 124102100609-2.

References

Akhoondzadeh, M. (2015), Ant Colony Optimization detects anomalous aerosol variations associated with the Chile earthquake of 27 February 2010, *Advances in Space Research*, *55*(7), 1754–1763, https://doi.org/10.1016/j.asr.2015.01.016.

Akhoondzadeh, M., and D. Marchetti (2023), Study of the Preparation Phase of Turkey's Powerful Earthquake (6 February 2023) by a Geophysical Multi-Parametric Fuzzy Inference System, *Remote Sensing*, *15*(9), 2224, https://doi.org/10.3390/rs15092224.

Bondur, V. G., and V. M. Smirnov (2005), Method for monitoring seismically hazardous territories by ionospheric variations recorded by satellite navigation systems, *Doklady Earth Sciences*, *403*(5), 736–740, EDN: LJHLVP.

Bondur, V. G., I. A. Garagash, M. B. Gokhberg, and M. V. Rodkin (2016), The evolution of the stress state in Southern California based on the geomechanical model and current seismicity, *Izvestiya, Physics of the Solid Earth*, *52*(1), 117–128, https://doi.org/10.1134/S1069351316010043.

Bondur, V. G., M. N. Tsidilina, E. V. Gaponova, and O. S. Voronova (2022), Combined Analysis of Anomalous Variations in Various Geophysical Fields during Preparation of the M5.6 Earthquake near Lake Baikal on September 22, 2020, Based on Satellite Data, *Izvestiya, Atmospheric and Oceanic Physics*, *58*(12), 1532–1545, https://doi.org/10.1134/S0001433822120052.

Bondur, V. G., T. N. Chimitdorzhiev, and A. V. Dmitriev (2023), Anomalous Geodynamics before the 2023 Earthquake in Turkey According to Radar Interferometry 2018-2023, *Issledovanie Zemli iz Kosmosa*, *2023*(3), 3–12, https://doi.org/10.31857/S0205961423030090 (in Russian).

Cervone, G., R. P. Singh, M. Kafatos, and C. Yu (2005), Wavelet maxima curves of surface latent heat flux anomalies associated with Indian earthquakes, *Natural Hazards and Earth System Sciences*, *5*(1), 87–99, https://doi.org/10.5194/nhess-5-87-2005.

Dal Zilio, L., and J.-P. Ampuero (2023), Earthquake doublet in Turkey and Syria, *Communications Earth & Environment*, *4*(1), https://doi.org/10.1038/s43247-023-00747-z.

Dey, S., and R. P. Singh (2003), Surface latent heat flux as an earthquake precursor, *Natural Hazards and Earth System Sciences*, *3*(6), 749–755, https://doi.org/10.5194/nhess-3-749-2003.

Federal Research Center Geophysical Survey of the RAS (2023), Catalog of the last earthquakes from 2000 to 2023, http://www.ceme.gsras.ru (in Russian), (visited on 12/08/2023).

Ganguly, N. D. (2016), Atmospheric changes observed during April 2015 Nepal earthquake, *Journal of Atmospheric and Solar-Terrestrial Physics*, *140*, 16–22, https://doi.org/10.1016/j.jastp.2016.01.017.

Ghosh, S., S. Sasmal, M. Naja, S. Potirakis, and M. Hayakawa (2023), Study of aerosol anomaly associated with large earthquakes (M>6), *Advances in Space Research*, *71*(1), 129–143, https://doi.org/10.1016/j.asr.2022.08.051.

Google Earth Engine (2023), MCD19A2 Level 2 data product 2000-2023, https://earthengine.google.com/, (visited on 12/20/2023).

Gvishiani, A. D., A. A. Soloviev, and B. A. Dzeboev (2020), Problem of Recognition of Strong-Earthquake-Prone Areas: a State-of-the-Art Review, *Izvestiya, Physics of the Solid Earth*, *56*(1), 1–23, https://doi.org/10.1134/s1069351320010048.

Hearty, T., A. Savtchenko, M. Theobald, et al. (2013), *Readme document for AIRS version 006 products*, NASA, GES DISC.

Jiao, Z., J. Zhao, and X. Shan (2018), Pre-seismic anomalies from optical satellite observations: a review, *Natural Hazards and Earth System Sciences*, *18*(4), 1013–1036, https://doi.org/10.5194/nhess-18-1013-2018.

Keilis-Borok, V., A. Gabrielov, and A. Soloviev (2009), Geo-complexity and Earthquake Prediction, in *Encyclopedia of Complexity and Systems Science*, pp. 4178–4194, Springer New York, https://doi.org/10.1007/978-0-387-30440-3_246.

Lyapustin, A., and Y. Wang (2018), MCD19A2 MODIS/Terra+Aqua Land Aerosol Optical Depth Daily L2G Global 1km SIN Grid V006, https://doi.org/10.5067/MODIS/MCD19A2.006.

Mikhailov, V. O., I. P. Babayants, M. S. Volkova, et al. (2023a), Reconstruction of Co-Seismic and Post-Seismic Processes for the February 6, 2023 Earthquake in Turkey from Data of Satellite SAR Interferometry, *Izvestiya, Physics of the Solid Earth*, *59*(6), 888–898, https://doi.org/10.1134/S1069351323060113.

Mikhailov, V. O., I. P. Babayantz, M. S. Volkova, et al. (2023b), The February 6, 2023, Earthquakes in Turkey: A Model of the Rupture Surface Based on Satellite Radar Interferometry, *Doklady Earth Sciences*, *511*(1), 571–577, https://doi.org/10.1134/S1028334X23600627.

Mogi, K. (1985), *Earthquake Prediction*, Academic Press, Tokyo.

Molchan, G., and V. Keilis-Borok (2008), Earthquake prediction: probabilistic aspect, *Geophysical Journal International*, *173*(3), 1012–1017, https://doi.org/10.1111/j.1365-246X.2008.03785.x.

Noll, C. E. (2010), The crustal dynamics data information system: A resource to support scientific analysis using space geodesy, *Advances in Space Research*, *45*(12), 1421–1440, https://doi.org/10.1016/j.asr.2010.01.018.

Okada, Y., S. Mukai, and R. P. Singh (2004), Changes in atmospheric aerosol parameters after Gujarat earthquake of January 26, 2001, *Advances in Space Research*, *33*(3), 254–258, https://doi.org/10.1016/S0273-1177(03)00474-5.

Pulinets, S., and D. Ouzounov (2011), Lithosphere-Atmosphere-Ionosphere Coupling (LAIC) model - An unified concept for earthquake precursors validation, *Journal of Asian Earth Sciences*, *41*(4–5), 371–382, https://doi.org/10.1016/j.jseaes.2010.03.005.

Pulinets, S. A., D. Ouzounov, A. V. Karelin, K. A. Boyarchuk, and L. A. Pokhmelnykh (2006), The physical nature of thermal anomalies observed before strong earthquakes, *Physics and Chemistry of the Earth, Parts A/B/C*, *31*(4–9), 143–153, https://doi.org/10.1016/j.pce.2006.02.042.

Ruzhich, V. V., L. P. Berzhinskaya, E. A. Levina, and E. I. Ponomareva (2023), On the causes and consequences of two devastating earthquakes in the Türkiye on February 6, 2023, *Geology and Environment*, *3*, 22–34, https://doi.org/10.26516/2541-9641.2023.1.22.

Saha, S., S. Moorthi, H.-L. Pan, et al. (2010), The NCEP Climate Forecast System Reanalysis, *Bulletin of the American Meteorological Society*, *91*(8), 1015–1058, https://doi.org/10.1175/2010bams3001.1.

Smirnov, V. M., and E. V. Smirnova (2008), Investigation of the Possibility of Satellite Navigation System Application for Seismic Event Monitoring, *Electromechanics problems*, *105*, 94–104 (in Russian), EDN: KDSVGL.

Sobolev, G. A., and A. V. Ponomarev (2003), *Earthquake physics and precursors*, Nauka, Moscow (in Russian), EDN: RVEBFL.

Soloviev, A. A., and A. I. Gorshkov (2017), Modeling the dynamics of the block structure and seismicity of the Caucasus, *Izvestiya, Physics of the Solid Earth*, *53*(3), 321–331, https://doi.org/10.1134/S1069351317030120.

Trifonov, V. G. (2017), Neotectonics of Mobile Belts, in *Transactions of the Geological Institute*, 614, p. 180, GEOS, Moscow (in Russian), EDN: RTGVPV.

Tronin, A. A. (2000), Thermal IR satellite sensor data application for earthquake research in China, *International Journal of Remote Sensing*, *21*(16), 3169–3177, https://doi.org/10.1080/01431160050145054.

United States Geological Survey (2023), Catalog of the last earthquakes from 2000 to 2023, https://earthquake.usgs.gov, (visited on 12/08/2023).

World Data System (2023), World Data Center for Geomagnetism, Kyoto, http://wdc.kugi.kyoto-u.ac.jp/index.html, (visited on 11/20/2023).

Xiong, P., X. H. Shen, Y. X. Bi, et al. (2010), Study of outgoing longwave radiation anomalies associated with Haiti earthquake, *Natural Hazards and Earth System Sciences*, *10*(10), 2169–2178, https://doi.org/10.5194/nhess-10-2169-2010.

Xu, Y., T. Li, X. Tang, X. Zhang, H. Fan, and Y. Wang (2022), Research on the Applicability of DInSAR, Stacking-InSAR and SBAS-InSAR for Mining Region Subsidence Detection in the Datong Coalfield, *Remote Sensing*, *14*(14), 3314, https://doi.org/10.3390/rs14143314.

Zhang, L., K. Dai, J. Deng, et al. (2021), Identifying potential landslides by stacking-insar in southwestern china and its performance comparison with sbas-insar, *Remote Sensing*, *13*(18), 3662, https://doi.org/10.3390/rs13183662.

RUSSIAN JOURNAL of EARTH SCIENCES

Meridional Oceanic and Atmospheric Heat Fluxes at the Entrance to the Atlantic Sector of the Arctic: Verification of CMIP6 Models and Climate Projections Based on the Selected Sub-Ensembles

M. M. Latonin[1,2,*], I. L. Bashmachnikov[1,2], Iu. V. Radchenko[1], N. V. Gnatiuk[1,2], L. P. Bobylev[1], and L. H. Pettersson[3]

[1]Nansen International Environmental and Remote Sensing Centre, Saint Petersburg, Russia
[2]Saint Petersburg State University, Saint Petersburg, Russia
[3]Nansen Environmental and Remote Sensing Center, Bergen, Norway
* **Correspondence to:** Mikhail M. Latonin, mikhail.latonin@niersc.spb.ru

Abstract: Poleward transports of oceanic and atmospheric heat play an essential role in the Arctic climate system, and their variations in the future will strongly shape the climate of the Arctic. The main aim of this study is to evaluate the performance of the Coupled Model Intercomparison Project phase 6 (CMIP6) models in the historical experiment in simulating the meridional heat fluxes into the Atlantic sector of the Arctic. The secondary objective is to estimate the meridional oceanic and atmospheric heat fluxes up to the end of the 21st century using the best sub-ensembles of the CMIP6 models. According to our results, the CMIP6 models poorly reproduce the interannual variability of the heat fluxes in their historical simulations, and the multi-model ensemble mean values are systematically lower than the mean values derived from the Ocean ReAnalysis System 4 (ORAS4) and European Centre for Medium-Range Weather Forecasts Reanalysis version 5 (ERA5) reanalyses. Climate projections based on the selected CMIP6 models indicate that the future Arctic climate will be characterized by the significantly increased oceanic heat transport at the entrance to the Atlantic sector of the Arctic relative to the period 1958–2014. In contrast, the atmospheric heat and moisture transport will not have dramatic differences in the projected Arctic climate relative to the period 1958–2014. Based on the results obtained, we emphasize that any interpretation of future climate simulations should be done with caution.

Keywords: poleward heat transport, climate of the Arctic, ocean–atmosphere interaction, CMIP6 models, ORAS4 and ERA5 reanalyses, projections, North Atlantic.

Citation: Latonin, M. M., I. L. Bashmachnikov, Iu. V. Radchenko, N. V. Gnatiuk, L. P. Bobylev, and L. H. Pettersson (2024), Meridional Oceanic and Atmospheric Heat Fluxes at the Entrance to the Atlantic Sector of the Arctic: Verification of CMIP6 Models and Climate Projections Based on the Selected Sub-Ensembles, *Russian Journal of Earth Sciences*, 24, ES4007, EDN: CISMVQ, https://doi.org/10.2205/2024es000917

RESEARCH ARTICLE

Received: 26 October 2023
Accepted: 8 July 2024
Published: 31 October 2024

1. Introduction

One of the essential components of the Arctic climate system is the energy (heat) exchange with lower latitudes [*Serreze and Barry*, 2014]. The on-going global warming, amplified in the Arctic, is projected to continue in the 21st century [*Esau et al.*, 2023; *Koenigk et al.*, 2012; *Liang et al.*, 2020]. The annual surface and atmospheric energy budget to the north of the Arctic circle is largely driven by the heat transport in the ocean and atmosphere. The warmer upper ocean gradually releases its heat to the atmosphere, while the thickness of the mixed layer is increasing with winter convection [*Lique et al.*, 2017]. The atmospheric heat transport is largely driven by extratropical cyclones [*Alexeev et al.*, 2017]. The North Atlantic is a region where there is a strong poleward heat transport both in the atmosphere and the ocean [*Graham et al.*, 2017; *Madonna and Sandø*, 2021]. This is also a “hotspot” of ocean–atmosphere interaction, which was originally noted in [*Bjerknes*, 1964] and proved to be the case in many subsequent studies, [e.g., *Outten et al.*, 2018; *van der Swaluw et al.*, 2007]. One of the implications of the horizontally advected oceanic heat into the Arctic is a subsequent change in the vertical heat flux. For instance, numerical ice-ocean models applied in [*Polyakov et al.*, 2010] showed that an increased oceanic heat flux due to the presence of warm Atlantic water makes the sea ice substantially thinner in the Arctic Ocean. In addition, the atmosphere has a strong impact on the Arctic sea ice by wind forcing, which further triggers the local surface albedo feedback [*Zhang et al.*, 2008]. It was also found that warm and moist air intrusions into the Atlantic sector of the Arctic have had a leading role in winter warming events in the Arctic since 1954 [*Graham et al.*, 2017]. Overall, it is difficult to distinguish whether the oceanic or atmospheric warming is dominant in the Atlantic sector of the Arctic. This region is commonly defined up to the North Pole in the western part of the Arctic adjacent to the subpolar North Atlantic, and the eastern border is defined by the Kara Sea.

Although the impacts of poleward oceanic and atmospheric heat transport are widely debated both in the past and future perspectives [*Goosse et al.*, 2018], there is no one standard for the calculation of heat transport in the ocean and atmosphere. The oceanic heat transport is often calculated with the reference temperature and using the temperature scale in degrees Celsius [*Docquier and Koenigk*, 2021; *Årthun et al.*, 2012], whereas the atmospheric sensible heat transport is calculated without the reference temperature in the absolute temperature scale [*Hofsteenge et al.*, 2022; *Latonin et al.*, 2022b; *Overland et al.*, 1996]. Although the mutual variability and trends might not be seriously affected, this makes it difficult to compare the absolute values of heat fluxes in the ocean and atmosphere. However, in this study, we adhere to this classical approach by choosing the reference temperature of -1.8 °C for the calculation of oceanic heat transport. Thus, this study aims at comparing the variability of the oceanic and atmospheric heat fluxes of the latest decades and at evaluating their evolution in a possible future climate derived from the best Coupled Model Intercomparison Project phase 6 (CMIP6) models in the historical simulations.

2. Data and Methods

2.1. Calculation of meridional heat transport in the Atlantic Water column and in the lower troposphere

First, meridional oceanic and atmospheric heat fluxes were calculated using the datasets from the Ocean ReAnalysis System 4 (ORAS4) and European Centre for Medium-Range Weather Forecasts Reanalysis version 5 (ERA5) reanalyses [*Balmaseda et al.*, 2012; *Hersbach et al.*, 2020]. These time series obtained were considered as the benchmarks for comparison with CMIP6 models. The oceanic reanalysis ORAS4 is one of the longest reanalyses for the ocean (along with ORAS5). This allows studying low-frequency climate variability, which is highly relevant for oceanic processes. It is available from 1958 to 2017 on a horizontal $1° \times 1°$ grid at 42 vertical levels. The underlying ocean model is NEMO v3.0. The atmospheric reanalysis ERA5 is a high-resolution dataset including many essential climate variables. It has recently been extended back until 1940, which makes this reanalysis one of the longest for the atmospheric and surface variables. The data is available on a horizontal $0.25° \times 0.25°$ grid at 137 vertical levels. The Integrated Forecasting System Cy41r2 is used as an underlying numerical weather prediction system.

From the website of ORAS4 reanalysis, two variables with monthly temporal resolution were used: seawater potential temperature and meridional current velocity at the different depths within the Atlantic Water layer. The following variables with 6-hourly temporal resolution were analyzed from the archive of the ERA5 reanalysis: air temperature, specific humidity, meridional wind velocity and geopotential at the isobaric surfaces within the lower troposphere (850–1000 hPa). The latter variable was divided by the gravitational acceleration to convert it to the geopotential heights.

Mean annual values of oceanic and atmospheric heat fluxes were calculated according to the methodology described in [*Latonin et al.*, 2022a], but with some minor modifications described below. Figure 1 shows the study area with the sections for the calculation of heat fluxes. An explanation of the choice of these sections is given in [*Latonin et al.*, 2022a].

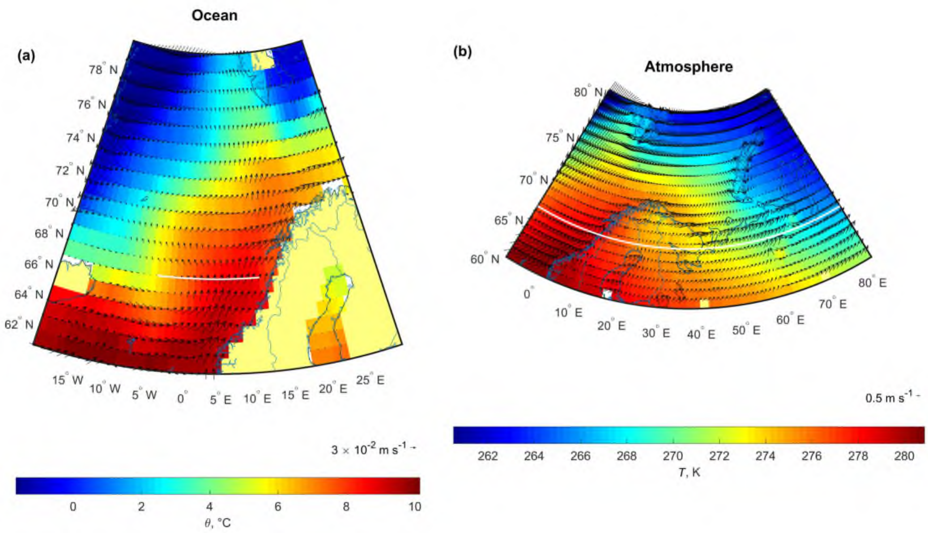

Figure 1. Average temperatures and total velocity vectors based on the ORAS4 and ERA5 reanalyses for the period 1958–2014 with monthly discreteness at a depth of 5 m in the ocean (a) and an isobaric surface of 1000 hPa in the atmosphere (b). The white lines show the sections at 66.5°N across which the heat transports were calculated.

First, the oceanic heat transport was calculated with the temperature scale in degrees Celsius using the reference temperature of -1.8 °C. Second, the horizontal integration for the oceanic heat transport was carried out until 11.5°E instead of 13.5°E because the oceanic variables in the CMIP6 models usually have data until 11.5°E only. The vertical integration in the ocean was carried out down to the lower boundary of the Atlantic Water at the selected section. The boundary is taken at the isothermal of $\theta = 3\,^{\circ}$C. We have empirically found that its position is almost coincident to that of the isopycnal $\sigma = 27.85\,\mathrm{kg\,m^{-3}}$ usually used as the limit of the water masses of Atlantic origin [*Latonin et al.*, 2022a].

The upper boundary of the vertical integration for the atmospheric heat fluxes was changed from 800 hPa to 850 hPa. This is related to the absence of data in the CMIP6 models in the layer 800–850 hPa. In addition, the atmospheric heat fluxes were calculated from daily data, which did not affect the variability characteristics obtained using the monthly discreteness in [*Latonin et al.*, 2022a], but made it possible to obtain more accurate absolute values of heat fluxes.

2.2. CMIP6 models analyzed in the study

Table 1 presents the list of CMIP6 models, which were used for calculations in a historical experiment for both the oceanic and atmospheric heat fluxes.

The CMIP6 models listed in Table 1 have the required parameters at similar levels as in the reanalyses, and the data cover the whole studied period 1958–2014. The number of models used for the calculation of atmospheric heat fluxes is lower than those for the oceanic heat flux. This is because many models lack data on the geopotential heights required to perform a vertical integration in the atmosphere.

The oceanic and atmospheric heat fluxes were calculated based on the CMIP6 models' data using the same specifications as in the reanalyses ORAS4 and ERA5 described in the subsection 2.1. After that, the models have been verified against the reanalyses for the historical period.

2.3. Selection of the scenarios used for the climate projections

For the climate projections in the 21st century, we used all available scenarios from the Shared Socioeconomic Pathways, i.e., from the low-end SSP119 scenario to the high-end SSP585 scenario [*Riahi et al.*, 2017]. The creation of these scenarios, which also take into account the socio-economic development of humanity, is one of the novelties implemented in the latest CMIP6 experimental design [*Eyring et al.*, 2016]. As in the historical simulations, here we also used the first realizations of the projected parameters needed to calculate the poleward transports of oceanic and atmospheric heat.

Table 1. A complete list of the 17 CMIP6 models in the historical experiment for the first ensemble member (`r1i1p1f1`). The bold font highlights the models used for the calculation of **oceanic heat transport**, whereas the bold and italic font indicates the models selected for the ***oceanic and atmospheric heat transports***. Only the models covering consistent data for both flux calculations are used in our study

No.	Name of the CMIP6 Model	Atmospheric Model	Oceanic Model	Reference
1	**ACCESS-ESM1-5**	HadGAM2	ACCESS-OM2	[*Ziehn et al.*, 2019]
2	**BCC-CSM2-MR**	BCC_AGCM3_MR	MOM4	[*Wu et al.*, 2018]
3	**CAMS-CSM1-0**	ECHAM5_CAMS	MOM4	[*Rong*, 2019]
4	**CMCC-CM2-SR5**	CAM5.3	NEMO3.6	[*Lovato and Peano*, 2020]
5	**CMCC-ESM2**	CAM5.3	NEMO3.6	[*Lovato et al.*, 2021]
6	***EC-Earth3***	IFS cy36r4	NEMO3.6	[*EC-Earth Consortium (EC-Earth)*, 2019a]
7	**EC-Earth3-Veg**	IFS cy36r4	NEMO3.6	[*EC-Earth Consortium (EC-Earth)*, 2019b]
8	**EC-Earth3-Veg-LR**	IFS cy36r4	NEMO3.6	[*EC-Earth Consortium (EC-Earth)*, 2020]
9	***FGOALS-f3-L***	FAMIL2.2	LICOM3.0	[*Yu*, 2019]
10	***FGOALS-g3***	GAMIL3	LICOM3.0	[*Li*, 2019]
11	***INM-CM4-8***	INM-AM4-8	INM-OM5	[*Volodin et al.*, 2019a]
12	***INM-CM5-0***	INM-AM5-0	INM-OM5	[*Volodin et al.*, 2019b]
13	**IPSL-CM6A-LR**	LMDZ	NEMO-OPA	[*Boucher et al.*, 2018]
14	**MPI-ESM1-2-HR**	ECHAM6.3	MPIOM1.63	[*Jungclaus et al.*, 2019]
15	***MPI-ESM1-2-LR***	ECHAM6.3	MPIOM1.63	[*Wieners et al.*, 2019]
16	***MRI-ESM2-0***	MRI-AGCM3.5	MRI.COM4.4	[*Yukimoto et al.*, 2019]
17	**NESM3**	ECHAM v6.3	NEMO v3.4	[*Cao and Wang*, 2019]

2.4. Selection of the sub-ensembles of CMIP6 models that most realistically simulate the meridional heat fluxes into the Atlantic sector of the Arctic

The best sub-ensembles of CMIP6 models were selected based on the ranking approach proposed in [*Gnatiuk et al.*, 2020]. This method shows better results compared to other frequently used methods for estimating and selecting a sub-ensemble of climate models.

As the data were analyzed for the study layers (without spatial data), the method for model estimation was applied in a simplified form. Interannual variability of model parameters was compared to reanalyses based on the correlation coefficient (R), root-mean-square error (RMSE), standard deviation (STD), climate prediction index (CPI) [*Agosta et al.*, 2015], trends (Tr) and biases (B_m, B_a). In order to compare the models for all these statistical metrics together, a score from 0 to 3 was assigned for each statistical metric value according to the approach. Specifically, the score was assigned based on falling into a certain percentile threshold from the total range of values for each metric: 0–25% is a score 3, 25–50% is a score 2, 50–75% is a score 1, 75–100% is a score 0. For correlation, it is vice versa. Then, total skill score was calculated for each model by summing the scores for all statistical metrics. The top 25% of considered CMIP6 models were selected as a skillful sub-ensemble based on the obtained total skill score.

The statistical metrics were calculated using the following formulas:

1. Root-mean-square deviation (RMSD):

$$\mathrm{RMSD} = \sqrt{\frac{\sum_{i=1}^{n} \left(P_{\mathrm{m}_i} - P_{o_i}\right)^2}{n}},$$

where P_{m_i} is a parameter value of model data and P_{o_i} is a parameter value of reanalysis data at i time step, n is the number of time steps.

2. Correlation coefficient (R):

$$R = \frac{\frac{1}{n}\sum_{i=1}^{n}\left(P_{o_i} - \overline{P}_o\right)\cdot\left(P_{\mathrm{m}_i} - \overline{P_{\mathrm{m}}}\right)}{\mathrm{STD_o}\cdot\mathrm{STD_m}},$$

where P_{m_i} is a parameter value of model data and P_{o_i} is a parameter value of reanalysis data at i time step, $\overline{P_{\mathrm{m}}}$ is an average parameter value of model data, $\overline{Po}$ is an average parameter value of reanalysis data, n is the number of time steps, $\mathrm{STD_m}$ is a standard deviation of model data and STD_o is a standard deviation of reanalysis.

3. Standard deviation (STD) was calculated as follows:

$$\mathrm{STD} = \sqrt{\frac{\sum_{i=1}^{n}\left(P_i - \overline{P}\right)}{n-1}},$$

where P_i is a parameter value at i time step, $\overline{P}$ is a mean parameter value, and n is the number of time steps.

4. Climate prediction index (CPI):

$$CPI = \frac{\mathrm{RMSD}}{\mathrm{STD_o}},$$

where RMSD is a root-mean-square deviation between model and observational data, $\mathrm{STD_o}$ is a standard deviation of observations.

5. dif_std is the difference between standard deviation of model data and standard deviation of reanalysis:

$$\mathrm{dif\_std} = \left|\mathrm{STD_m} - \mathrm{STD_o}\right|. \tag{1}$$

6. $\mathrm{Tr_m}$ is a difference of trends (model trend minus reanalysis trend). It is calculated as follows:

$$\mathrm{Tr_m} = \left|\mathrm{Tr_{model}} - \mathrm{Tr_{observation}}\right|,$$

where *Tr* is a trend value of model and observational time series.

7. $\mathrm{B_m}$ is a mean bias (model minus reanalysis for all time steps):

$$\mathrm{B_m} = \left|\overline{P_{\mathrm{m}_i} - P_{\mathrm{o}_i}}\right|,$$

where P_{m} and P_{o} are the parameter values of model and observational data accordingly at i time step.

8. $\mathrm{B_a}$ is an amplitude of biases (differences between model and reanalysis data for each time step):

$$\mathrm{B_a} = \left|\max(P_{\mathrm{m}_i} - P_{\mathrm{o}_i}) - \min(P_{\mathrm{m}_i} - P_{\mathrm{o}_i})\right|,$$

where P_{m_i} and P_{o_i} are the parameter values of model and observational data accordingly, max is a maximum value, and min is a minimum value of all time steps.

3. Results

3.1. Oceanic and atmospheric heat transport in the reanalyses and in the historical simulations of the CMIP6 models. Verification of CMIP6 models and selection of the best sub-ensembles

Figure 2 shows the calculated time series of integral oceanic heat fluxes in each CMIP6 model and ORAS4 reanalysis. In addition, Figure A1 shows the oceanic heat transport in the ORAS4 reanalysis calculated using the classical approach with a reference temperature (as in Figure 2 for the red curve) and using the absolute temperature scale without a reference temperature. The correlation coefficient between the blue and orange curves in Figure A1 is 0.95. The ensemble average was calculated from the heat fluxes estimated in the individual models. This is a more accurate way than averaging the data fields in the models before calculating the heat flux [*Smith et al.*, 2019].

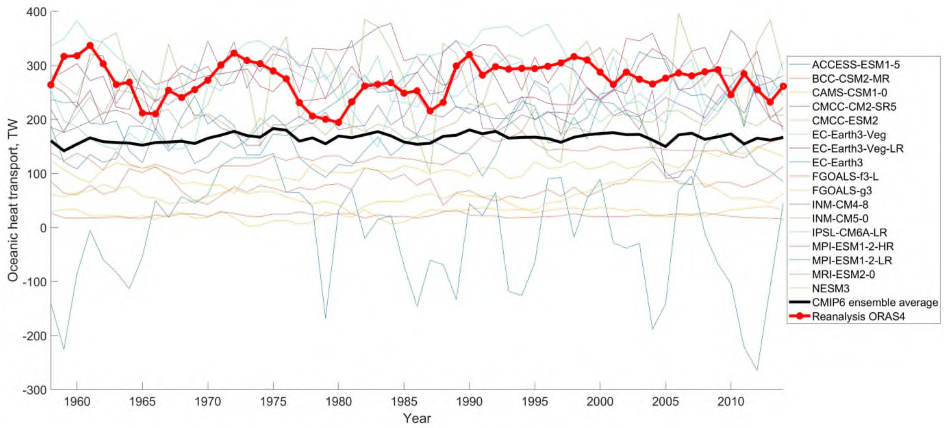

Figure 2. Time series of oceanic heat transport at the entrance to the Atlantic sector of the Arctic (along 66.5°N, between 4.5°W and 11.5°E) based on the ORAS4 reanalysis and CMIP6 models in the historical simulations. 1 TW = 10^{12} W.

The ensemble average curve in Figure 2 indicates that most CMIP6 models underestimate the value of the oceanic heat flux obtained from the ORAS4 reanalysis. Also, the nature of the interannual variability is reproduced by the CMIP6 models very inaccurately (the correlation coefficient between the CMIP6 ensemble average and the reanalysis ORAS4 is 0.26). Moreover, one of the models (MPI-ESM1-2-LR) shows unrealistic negative values of oceanic heat transport of Atlantic water into the Nordic Seas.

Statistical characteristics for assessing the quality of individual models are presented in Table 2. Based on these results, a sub-ensemble of the skillful models was selected according to the methodology described in subsection 2.4.

The results of the calculations indicate the poor quality of the CMIP6 models in simulating the oceanic heat fluxes into the Arctic. Nevertheless, for climate projections based on the SSP scenarios, a sub-ensemble was selected consisting of the four statistically best models: MPI-ESM1-2-HR, EC-Earth3-Veg-LR, CMCC-CM2-SR5, and CMCC-ESM2.

In Figure 3, the calculated time series of integral atmospheric sensible heat fluxes in each CMIP6 model and ERA5 reanalysis are shown. As for the oceanic heat flux, the ensemble average was found from the heat fluxes calculated in the individual models.

Similarly to the results with the oceanic heat flux, most CMIP6 models underestimate the atmospheric sensible heat flux that is derived from the ERA5 reanalysis. This is also reflected in the ensemble average (black curve). In addition, the interannual variability is reproduced very poorly by the CMIP6 historical simulations (the correlation coefficient between the CMIP6 ensemble average and the reanalysis ERA5 is -0.07). Table 3 presents statistical characteristics for assessing the quality of individual models relative to the reanalysis for the past period.

The calculation results confirm the poor quality of the CMIP6 models in reproducing the atmospheric sensible heat fluxes into the Arctic. For climate projections under the SSP scenarios, a sub-ensemble was selected from the two models with the best correlation to the reanalysis: INM-CM4-8 and INM-CM5-0.

Table 2. Statistical characteristics used for the evaluation of the quality of CMIP6 models in reproducing the oceanic heat transport relative to the ORAS4 reanalysis. The bold font highlights the four models selected to be used in the climate projection studies. The dimension of RMSD and dif_std is TW, and the dimension of Tr_m is TW yr^{-1}, of B_m is TW and of B_a is TW, respectively.

No.	Models	RMSD		R		CPI		dif_std		Tr_m		B_m		B_a		Total score
1	ACCESS-ESM1-5	129.10	2	0.19	0	3.90	2	5.70	3	0.11	3	120.50	2	185.10	2	14
2	BCC-CSM2-MR	252.60	0	−0.10	0	7.60	0	29.80	2	0.09	3	250.30	0	151.10	3	8
3	CAMS-CSM1-0	249.40	0	0.15	0	7.50	0	24.10	2	0.15	3	247.10	0	145.20	3	8
4	**CMCC-CM2-SR5**	77.10	2	−0.15	0	2.30	2	8.50	3	0.63	2	62.80	3	184.80	3	**15**
5	**CMCC-ESM2**	83.50	2	0.06	0	2.50	2	11.00	3	0.13	3	73.70	2	170.70	3	**15**
6	EC-Earth3-Veg	63.50	3	0.06	0	1.90	3	14.60	3	1.02	1	28.30	3	255.60	1	14
7	**EC-Earth3-Veg-LR**	58.80	3	−0.05	0	1.80	3	7.90	3	0.00	3	22.10	3	208.10	2	**17**
8	EC-Earth3	78.60	2	−0.21	0	2.30	2	13.20	3	1.37	0	47.30	3	276.90	1	11
9	FGOALS-f3-L	142.80	1	0.23	0	4.30	1	16.10	3	0.61	2	138.70	2	149.80	3	12
10	FGOALS-g3	214.80	0	0.35	1	6.40	0	18.70	2	0.08	3	212.50	1	116.90	3	10
11	INM-CM4-8	72.20	2	0.01	0	2.20	2	27.70	2	1.18	0	19.40	3	306.00	1	10
12	INM-CM5-0	76.80	2	0.07	0	2.30	2	37.80	1	0.15	3	1.20	3	336.40	0	11
13	IPSL-CM6A-LR	57.30	3	0.33	1	1.70	3	21.40	2	1.16	0	18.80	3	234.90	2	14
14	**MPI-ESM1-2-HR**	45.20	3	0.10	0	1.40	3	0.20	3	0.41	2	6.60	3	182.10	3	**17**
15	MPI-ESM1-2-LR	308.60	0	0.14	0	9.20	0	65.80	0	1.08	0	291.90	0	388.60	0	0
16	MRI-ESM2-0	199.20	0	−0.32	0	6.00	0	14.30	3	0.15	3	194.40	1	161.40	3	10
17	NESM3	169.00	1	−0.19	0	5.10	1	15.90	3	0.60	2	164.10	1	171.80	3	11
	max	308.60		1.00		9.20		65.80		1.37		291.90		388.60		
	75%	197.50		0.75		5.90		49.20		1.02		218.00		320.70		
	50%	131.70		0.50		3.90		32.80		0.68		145.30		252.70		
	25%	65.80		0.25		2.00		16.40		0.34		72.70		184.80		
	min	45.20		0.00		1.40		0.20		0.00		1.20		116.90		

very good | satisfactory | unsatisfactory

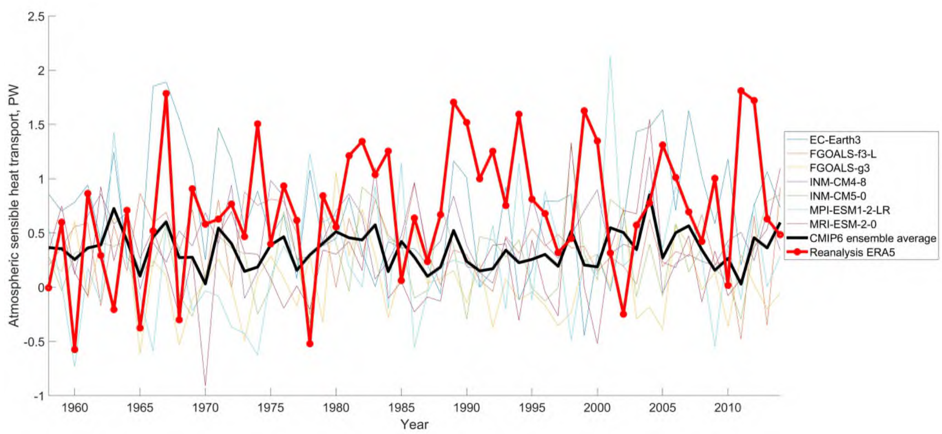

Figure 3. Time series of atmospheric sensible heat transport at the entrance to the Atlantic sector of the Arctic (along 66.5°N, between 5°W and 80°E) using the ERA5 reanalysis and CMIP6 models in the historical experiment. 1 PW = 10^{15} W.

Table 3. Statistical characteristics used for the evaluation of the quality of CMIP6 models in the reproduction of the atmospheric sensible heat transport relative to the ERA5 reanalysis. The bold font highlights the two models selected to be used in the climate projection studies. The dimension of RMSD and dif_std is PW, and the dimension of Tr_m is PW yr^{-1}, of B_m is PW and of B_a is PW, respectively.

No.	Models	RMSD		R		CPI		dif_std		Trm		Bm		Ba		Total score
1	EC-Earth3	0.83	1	−0.11	0	1.4	1	0.06	3	0.012	0	0.01	3	3.9	0	8
2	FGOALS-f3-L	0.75	3	−0.01	0	1.3	3	0.26	0	0.015	0	0.34	1	3.5	1	8
3	FGOALS-g3	0.93	0	−0.02	0	1.6	0	0.24	0	0.014	0	0.64	0	2.9	2	2
4	**INM-CM4-8**	0.69	3	0.09	0	1.2	3	0.29	0	0.011	1	0.27	2	2.4	3	**12**
5	**INM-CM5-0**	0.8	2	0	0	1.4	2	0.24	0	0.008	2	0.43	1	3.1	2	**9**
6	MPI-ESM1-2-LR	0.95	0	−0.07	0	1.6	0	0.04	3	0.004	3	0.46	1	3.9	0	7
7	MRI-ESM2-0	0.86	1	−0.01	0	1.5	1	0.15	1	0.008	2	0.45	1	2.9	2	8
	max	0.95		1		1.6		0.29		0.015		0.64		3.9		
	75%	0.88		0.75		1.5		0.19		0.012		0.47		3.5		
	50%	0.82		0.5		1.4		0.13		0.009		0.31		3.2		
	25%	0.75		0.25		1.3		0.06		0.006		0.16		2.8		
	min	0.69		0		1.2		0.04		0.004		0.01		2.4		

very good | satisfactory | unsatisfactory

In Figure 4, the calculated time series of integral atmospheric latent heat fluxes in each CMIP6 model and ERA5 reanalysis are shown.

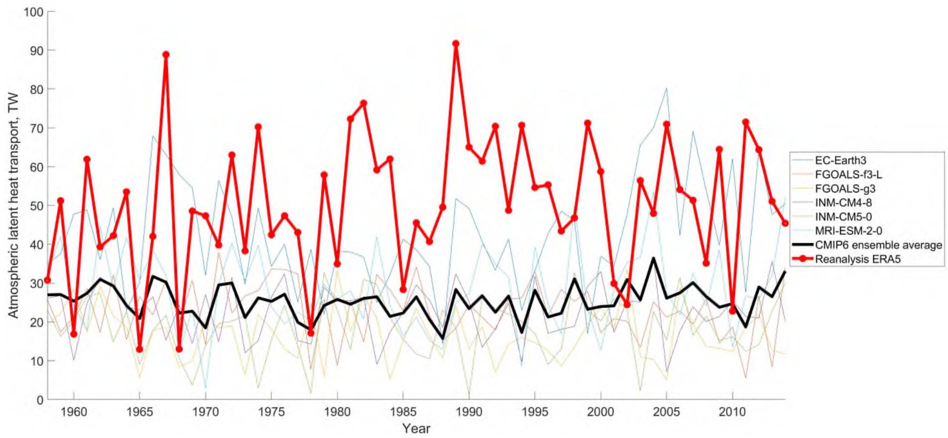

Figure 4. Time series of atmospheric latent heat transport at the entrance to the Atlantic sector of the Arctic (along 66.5°N, between 5°W and 80°E) for the ERA5 reanalysis and CMIP6 models in the historical experiment. 1 TW = 10^{12} W.

The curves in Figure 4 clearly show that CMIP6 models strongly underestimate the magnitude of the atmospheric latent heat transport obtained from the ERA5 reanalysis. The interannual variability is also poorly reproduced by the climate models compared to the reanalysis (the correlation coefficient between the CMIP6 ensemble average and the reanalysis ERA5 is 0.08).

Table 4 presents statistical characteristics for assessing the correlations of individual models with the reanalysis for the past period.

The results in Table 4 confirm the poor quality of the CMIP6 models in reproducing the atmospheric latent heat fluxes into the Arctic. For the assessment of the climate projections, under the SSP scenarios, a sub-ensemble was selected from the two statistically best performing models: EC-Earth3 and MRI-ESM2-0.

Table 4. Statistical characteristics used for the evaluation of the quality of CMIP6 models in the reproduction of the atmospheric latent heat transport relative to the ERA5 reanalysis. The bold font highlights the two models selected to be used in the climate projection studies. The dimension of RMSD and dif_std is TW, and the dimension of Tr_m is TW yr^{-1}, of B_m is TW and of B_a is TW, respectively.

No.	Models	RMSD		R		CPI		dif_std		Trm		Bm		Ba		Total score
1	**EC-Earth3**	23.70	3	−0.01	0	1.40	3	3.50	3	0.05	3	7.40	3	99.20	0	**15**
2	FGOALS-f3-L	33.00	1	0.02	0	1.90	1	10.20	0	0.31	0	27.10	0	86.80	2	4
3	FGOALS-g3	38.40	0	−0.02	0	2.20	0	10.60	0	0.28	0	33.40	0	81.70	3	3
4	INM-CM4-8	33.50	1	0.01	0	1.90	1	10.60	0	0.22	1	27.70	0	84.90	2	5
5	INM-CM5-0	36.70	0	0.11	0	2.10	0	9.70	0	0.19	1	31.70	0	76.80	3	4
6	**MRI-ESM2-0**	29.30	2	0.11	0	1.70	2	6.80	2	0.19	1	21.90	1	84.50	2	**10**
	max	38.40		1.00		2.20		10.60		0.31		33.40		99.20		
	75%	34.70		0.75		2.00		8.80		0.24		26.90		93.60		
	50%	31.00		0.50		1.80		7.10		0.18		20.40		88.00		
	25%	27.40		0.25		1.60		5.30		0.11		13.90		82.40		
	min	23.70		0.00		1.40		3.50		0.05		7.40		76.80		

very good satisfactory unsatisfactory

3.2. Climate projections of oceanic and atmospheric heat transport until 2100

The interannual variability of oceanic heat transport into the Arctic is presented in Figure 5 for the reanalysis ORAS4, CMIP6 historical simulations and five different climate scenarios. The main statistical characteristics for the comparison are given in Table 5.

Figure 5 and Table 5 show that, with the exception of the SSP119 scenario, the future climate of the Arctic is characterized by a significantly increased oceanic heat transport into the Arctic Ocean relative to the past historical period. The interannual variability of the oceanic heat flux in all the future SSP scenarios is also significantly higher than during the historical period. In each of the future scenarios, the linear trends of the oceanic heat flux are positive and statistically significant, with a minimum of 0.6 TW yr^{-1} in the SSP119 scenario and a maximum of 3.3 TW yr^{-1} in the SSP585 scenario, reflecting the climate development in the scenarios studied. The CMIP6 historical simulations also reveal a statistically significant linear increasing trend, but its magnitude is only 0.3 TW yr^{-1}. The oceanic heat transport scenarios are highly coherent and robust: between all pairs of time series, the correlation coefficients are positive and statistically significant, and for the SSP126–SSP585 scenarios, the correlation coefficients are always higher than 0.8.

Figure 6 presents the interannual variability of atmospheric sensible heat transport into the Arctic for the reanalysis ERA5, CMIP6 historical simulations and four different climate scenarios. The corresponding statistical characteristics for the comparison are presented in Table 6.

It is clearly seen from Figure 6 and Table 6 that in the future climate of the Arctic, the order of magnitude and the scale of variability of atmospheric sensible heat transport will remain approximately at the same level as in the historical period, for all future climate development scenarios. However, the mean values steadily increase from the SSP126 scenario to the SSP585 scenario. The pattern of variability from scenario to scenario is unstable: the standard deviations irregularly increase and decrease from one scenario

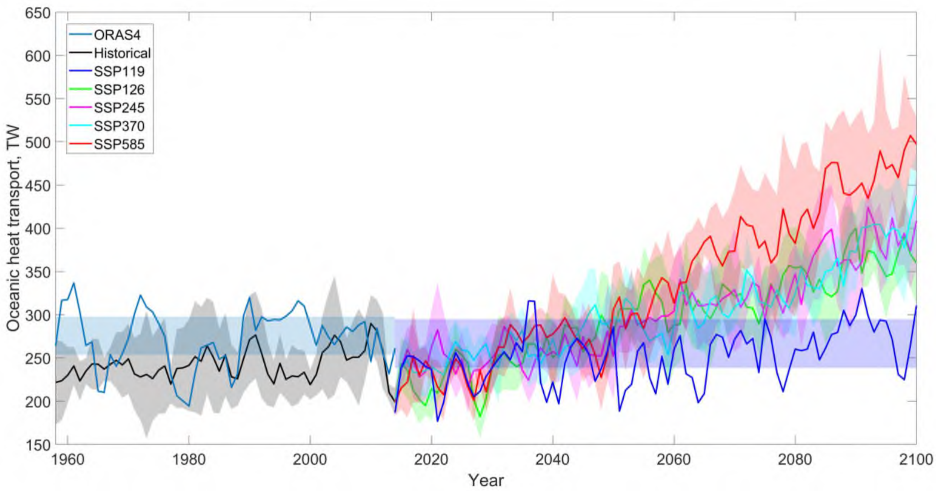

Figure 5. Interannual variability of the oceanic heat transport into the Arctic (TW) according to the ORAS4 reanalysis and the sub-ensemble average of four selected CMIP6 climate models (MPI-ESM1-2-HR, EC-Earth3-Veg-LR, CMCC-CM2-SR5, and CMCC-ESM2) in the historical period (1958–2014) and their climate simulations for five development scenarios (SSP119, SSP126, SSP245, SSP370, and SSP585) for the period 2015–2100. Uncertainty, calculated as the interquartile range (difference between the 75th and 25th percentiles of the data), is highlighted in solid; in the case of one time series (the ORAS4 reanalysis and the SSP119 scenario), such uncertainty is constant. The SSP119 scenario is only available for the EC-Earth3-Veg-LR model. 1 TW = 10^{12} W.

Table 5. Statistical characteristics of the time series of the oceanic heat transport displayed in Figure 5. Std is the standard deviation (TW) and k is the slope of the linear trend (TW yr^{-1}). The values in bold denote statistically significant linear trends at the 5% significance level. The uncertainties of the mean values are based on the standard errors and are calculated for the 5% significance level. 1 TW = 10^{12} W.

	Mean (TW)	Std (TW)	k (TW yr^{-1})
Historical	242 ± 5	18	**0.3**
SSP119	252 ± 7	32	**0.6**
SSP126	297 ± 11	51	**1.9**
SSP245	302 ± 11	53	**1.9**
SSP370	303 ± 11	51	**1.9**
SSP585	336 ± 19	86	**3.3**

Table 6. Statistical characteristics of the time series of the atmospheric sensible heat transport displayed in Figure 6. Std is the standard deviation (TW) and k is the slope of the linear trend (TW yr^{-1}). The values in bold denote statistically significant linear trends at the 5% significance level. The uncertainties of the mean values are based on the standard errors and are calculated for the 5% significance level. 1 TW = 10^{12} W.

	Mean (TW)	Std (TW)	k (TW yr^{-1})
Historical	370 ± 60	230	0.6
SSP126	320 ± 60	260	-2
SSP245	430 ± 60	290	2
SSP370	440 ± 60	270	**3**
SSP585	460 ± 50	250	**3**

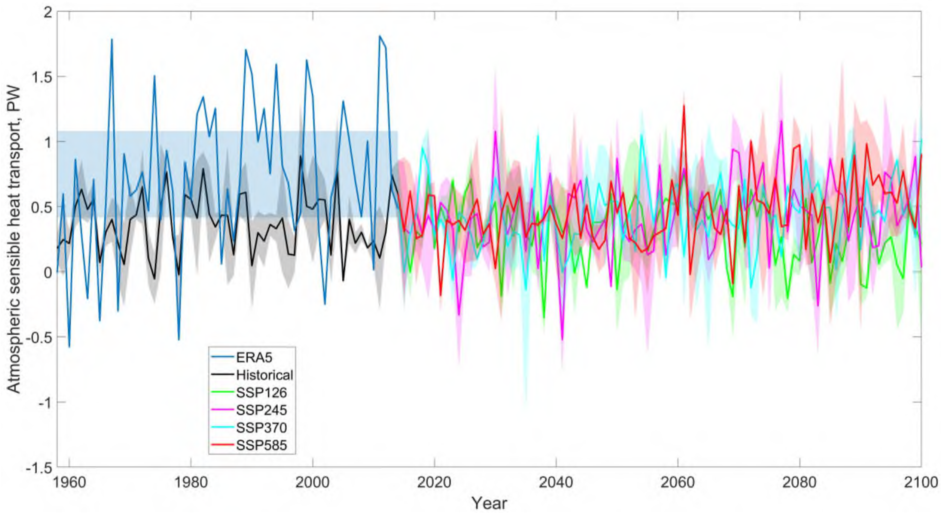

Figure 6. Interannual variability of the atmospheric sensible heat transport into the Arctic (PW) according to the ERA5 reanalysis and the sub-ensemble average of two selected CMIP6 climate models (INM-CM4-8 and INM-CM5-0) in the historical period (1958–2014) and their climate simulations for four development scenarios (SSP126, SSP245, SSP370, and SSP585) for the period 2015–2100. Uncertainty, calculated as the interquartile range (difference between the 75th and 25th percentiles of the data), is highlighted in solid; in the case of one time series (the ERA5 reanalysis), such uncertainty is constant. Positive values correspond to the northward flux direction. 1 PW = 10^{15} W.

to another. In the historical period, there is a very weak positive trend, whereas for the SSP126 future scenario the linear trend is negative. Starting from the SSP245 scenario, the trends are always positive, with the statistically significant maximum values of 3 TW in the SSP370 and SSP585 scenarios. Correlation analysis showed that the scenarios are weakly interconnected because there are no statistically significant correlation coefficients among the scenarios. This stands in contrast to the highly correlated scenarios of oceanic heat transport discussed above and shown in Figure 5.

The interannual variability of atmospheric latent heat transport into the Arctic for the reanalysis ERA5, CMIP6 historical simulations and five different climate scenarios are presented in Figure 7. Table 7 summarizes the respective statistical characteristics.

Table 7. Statistical characteristics of the time series of the atmospheric latent heat transport displayed in Figure 7. Std is the standard deviation (TW) and k is the slope of the linear trend (TW yr^{-1}). The values in bold denote statistically significant linear trends at the 5% significance level. The uncertainties of the mean values are based on the standard errors and are calculated for the 5% significance level. 1 TW = 10^{12} W.

	Mean (TW)	Std (TW)	k (TW yr^{-1})
Historical	36 ± 3	10	0.1
SSP119	30 ± 2	12	−0.1
SSP126	39 ± 2	10	0.03
SSP245	41 ± 3	12	0.1
SSP370	43 ± 3	13	**0.2**
SSP585	47 ± 3	15	**0.3**

The results for the atmospheric latent heat transport in Figure 7 are similar to those shown in Figure 6 for the atmospheric sensible heat transport; however, there are some important differences. The mean annual values in the scenarios SSP119–SSP585 are significantly lower than for the sensible heat transport, but the steady increase from the low-end to the high-end climate scenarios is preserved (Table 7). According to the standard deviations in Table 7, the irregular changes in the variability are present too. The slopes of the linear trends increase from the low-end to the high-end climate scenarios, and two positive trends are statistically significant for the SSP370 and SSP585 scenarios. Thus, for the atmospheric latent heat transport, the trend of increase is stronger than for the atmospheric sensible heat transport from 2015 to 2100. There are few statistically significant correlation coefficients: 0.26 between the SSP370 and SSP585 scenarios and –0.23 between the SSP126 and SSP245 scenarios.

For all climate development scenarios, the components of atmospheric heat transport in the selected models are not correlated with each other. This is expected given different models identified for the sensible and latent heat transport components.

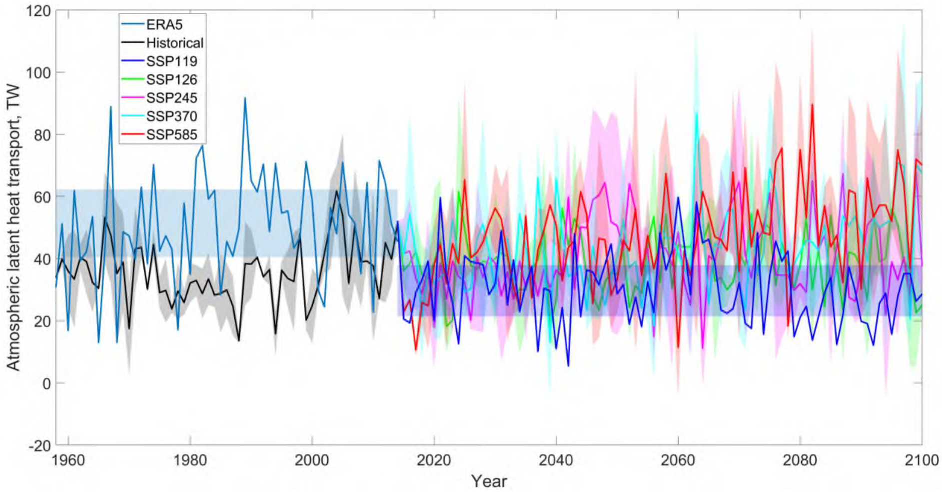

Figure 7. Interannual variability of the atmospheric latent heat transport into the Arctic (TW) according to the ERA5 reanalysis and the sub-ensemble average of two selected climate models CMIP6 (EC-Earth3 and MRI-ESM2-0) in the historical period (1958–2014) and their climate simulations for five development scenarios for the period 2015–2100. Uncertainty, calculated as the interquartile range (difference between the 75th and 25th percentiles of the data), is highlighted in solid; in the case of one time series (the ERA5 reanalysis and the SSP119 scenario), such uncertainty is constant. The SSP119 scenario is only available for the MRI-ESM2-0 model. Positive values correspond to the northward flux direction. 1 TW = 10^{12} W.

4. Discussion and Conclusions

One of the main findings of this study is a poor quality of the state-of-the-art CMIP6 climate models in simulating the meridional oceanic and atmospheric heat fluxes at the entrance to the Atlantic sector of the Arctic. We have shown that for the studied sections, the transports of oceanic and atmospheric heat into the Atlantic sector of the Arctic are not comparable in magnitude. During the period 1958–2014, the mean annual values of oceanic heat transport obtained from the ORAS4 ocean reanalysis and of the atmospheric sensible heat transport from the ERA5 atmospheric reanalysis are 272 ± 9 TW and 720 ± 160 TW, respectively. An additional transport of atmospheric latent heat of 50 ± 5 TW formally indicates that, over the past historical period, the atmosphere transports more heat to the Arctic than the ocean. However, our estimations are obtained along a limited transect at 66.5°N without considering the total heat budget. This means the absolute values of heat fluxes in the ocean and atmosphere cannot be compared due to different temperature scales and reference temperatures in the equations. If the equivalent equations and the same absolute temperature scale are used for the estimation of the advective sensible heat fluxes in the ocean and atmosphere, the ocean transports more heat than the atmosphere [*Latonin et al.*, 2022a]. At the same time, the variability patterns are almost not affected depending on the method used (see also Figure A1).

Validation procedure, using the independent ORAS4 and ERA5 reanalyses, allows choosing the statistically best performing CMIP6 models to project the relative role of the heat transports in respectively the ocean and atmosphere, by the end of the 21st century. We note that the ocean blocks in three of the four selected CMIP6 models (CMCC-CM2-SR5, CMCC-ESM2 and EC-Earth3-Veg-LR models) are based on the NEMO ocean model. It has recently been documented that the projected Arctic climate change will be intensified in the cluster of the NEMO-based models in CMIP6 [*Pan et al.*, 2023]. Based on our analysis, the best performing model for the atmospheric latent heat transport is the EC-Earth3 model. This means that the family of EC-Earth3 models is statistically best in the simulation of both the oceanic heat transport and atmospheric latent heat transport. This could be expected since EC-Earth3 models use the same type of oceanic and atmospheric models as the ORAS4 and ERA5 reanalyses used here for validation of performance of the CMIP6 models. Nevertheless, even the best performing model and the means of the best sub-ensembles of the models, do not reproduce the interannual variability obtained from the reanalyses. This might be related to a common problem of climate models with simulating the internal variability adequately [*Kravtsov et al.*, 2018].

According to our results, independent on the predicted climate scenario, the increase of the meridional oceanic heat transport into the Arctic Ocean in the 21st century will be dominant over the increase of the atmospheric heat transport into the Arctic. In terms of the projected trends, this is consistent with previous studies for the CMIP3 climate models' projections [*Hwang et al.*, 2011].

Acknowledgments. This study was funded by the Russian Science Foundation (RSF), grant number 23-77-01046 (https://rscf.ru/en/project/23-77-01046/).

Appendix A

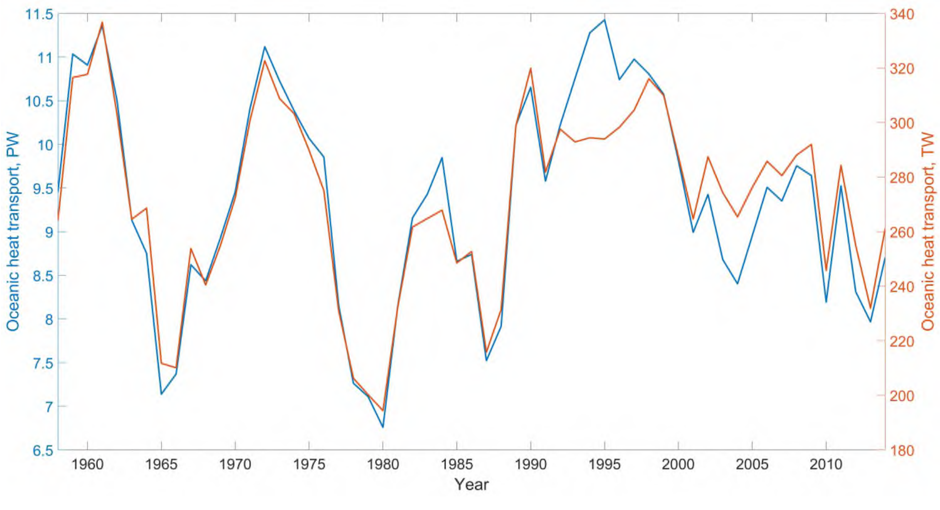

Figure A1. Time series of oceanic heat transport at the entrance to the Atlantic sector of the Arctic (along 66.5°N, between 4.5°W and 11.5°E) based on the ORAS4 reanalysis. The orange curve corresponds to the classical approach of calculation used in the main text of the article (with the subtraction of the reference temperature of −1.8 °C), whereas the blue curve represents an alternative approach of calculation using the absolute temperature scale without a reference temperature. 1 TW = 10^{12} W and 1 PW = 10^{15} W.

References

Agosta, C., X. Fettweis, and R. Datta (2015), Evaluation of the CMIP5 models in the aim of regional modelling of the Antarctic surface mass balance, *The Cryosphere*, *9*(6), 2311–2321, https://doi.org/10.5194/tc-9-2311-2015.

Alexeev, V. A., J. E. Walsh, V. V. Ivanov, V. A. Semenov, and A. V. Smirnov (2017), Warming in the Nordic Seas, North Atlantic storms and thinning Arctic sea ice, *Environmental Research Letters*, *12*(8), 084,011, https://doi.org/10.1088/1748-9326/aa7a1d.

Balmaseda, M. A., K. Mogensen, and A. T. Weaver (2012), Evaluation of the ECMWF ocean reanalysis system ORAS4, *Quarterly Journal of the Royal Meteorological Society*, *139*(674), 1132–1161, https://doi.org/10.1002/qj.2063.

Bjerknes, J. (1964), *Atlantic Air-Sea Interaction*, pp. 1–82, Advances in Geophysics, Elsevier, https://doi.org/10.1016/S0065-2687(08)60005-9.

Boucher, O., S. Denvil, G. Levavasseur, et al. (2018), IPSL IPSL-CM6A-LR model output prepared for CMIP6 CMIP historical, https://doi.org/10.22033/ESGF/CMIP6.5195.

Cao, J., and B. Wang (2019), NUIST NESMv3 model output prepared for CMIP6 CMIP historical, https://doi.org/10.22033/ESGF/CMIP6.8769.

Docquier, D., and T. Koenigk (2021), A review of interactions between ocean heat transport and Arctic sea ice, *Environmental Research Letters*, *16*(12), 123,002, https://doi.org/10.1088/1748-9326/ac30be.

EC-Earth Consortium (EC-Earth) (2019a), EC-Earth-Consortium EC-Earth3 model output prepared for CMIP6 CMIP historical, https://doi.org/10.22033/ESGF/CMIP6.4700.

EC-Earth Consortium (EC-Earth) (2019b), EC-Earth-Consortium EC-Earth3-Veg model output prepared for CMIP6 ScenarioMIP, https://doi.org/10.22033/ESGF/CMIP6.727.

EC-Earth Consortium (EC-Earth) (2020), EC-Earth-Consortium EC-Earth3-Veg-LR model output prepared for CMIP6 CMIP historical, https://doi.org/10.22033/ESGF/CMIP6.4707.

Esau, I., L. H. Pettersson, M. Cancet, et al. (2023), The Arctic Amplification and Its Impact: A Synthesis through Satellite Observations, *Remote Sensing*, *15*(5), 1354, https://doi.org/10.3390/rs15051354.

Eyring, V., S. Bony, G. A. Meehl, et al. (2016), Overview of the Coupled Model Intercomparison Project Phase 6 (CMIP6) experimental design and organization, *Geoscientific Model Development*, *9*(5), 1937–1958, https://doi.org/10.5194/gmd-9-1937-2016.

Gnatiuk, N., I. Radchenko, R. Davy, E. Morozov, and L. Bobylev (2020), Simulation of factors affecting Emiliania huxleyi blooms in Arctic and sub-Arctic seas by CMIP5 climate models: model validation and selection, *Biogeosciences*, *17*(4), 1199–1212, https://doi.org/10.5194/bg-17-1199-2020.

Goosse, H., J. E. Kay, K. C. Armour, et al. (2018), Quantifying climate feedbacks in polar regions, *Nature Communications*, *9*(1), https://doi.org/10.1038/s41467-018-04173-0.

Graham, R. M., L. Cohen, A. A. Petty, et al. (2017), Increasing frequency and duration of Arctic winter warming events, *Geophysical Research Letters*, *44*(13), 6974–6983, https://doi.org/10.1002/2017GL073395.

Hersbach, H., B. Bell, P. Berrisford, et al. (2020), The ERA5 global reanalysis, *Quarterly Journal of the Royal Meteorological Society*, *146*(730), 1999–2049, https://doi.org/10.1002/qj.3803.

Hofsteenge, M. G., R. G. Graversen, J. H. Rydsaa, and Z. Rey (2022), The impact of atmospheric Rossby waves and cyclones on the Arctic sea ice variability, *Climate Dynamics*, *59*(1–2), 579–594, https://doi.org/10.1007/s00382-022-06145-z.

Hwang, Y.-T., D. M. W. Frierson, and J. E. Kay (2011), Coupling between Arctic feedbacks and changes in poleward energy transport, *Geophysical Research Letters*, *38*(17), https://doi.org/10.1029/2011GL048546.

Jungclaus, J., M. Bittner, K.-H. Wieners, et al. (2019), MPI-M MPI-ESM1.2-HR model output prepared for CMIP6 CMIP historical, https://doi.org/10.22033/ESGF/CMIP6.6594.

Koenigk, T., L. Brodeau, R. G. Graversen, et al. (2012), Arctic climate change in 21st century CMIP5 simulations with EC-Earth, *Climate Dynamics*, *40*(11–12), 2719–2743, https://doi.org/10.1007/s00382-012-1505-y.

Kravtsov, S., C. Grimm, and S. Gu (2018), Global-scale multidecadal variability missing in state-of-the-art climate models, *npj Climate and Atmospheric Science*, *1*(1), https://doi.org/10.1038/s41612-018-0044-6.

Latonin, M. M., I. L. Bashmachnikov, and L. P. Bobylev (2022a), Bjerknes compensation mechanism as a possible trigger of the low-frequency variability of Arctic amplification, *Russian Journal of Earth Sciences*, pp. 1–21, https://doi.org/10.2205/2022ES000820.

Latonin, M. M., L. P. Bobylev, I. L. Bashmachnikov, and R. Davy (2022b), Dipole pattern of meridional atmospheric internal energy transport across the Arctic gate, *Scientific Reports*, *12*(1), https://doi.org/10.1038/s41598-022-06371-9.

Li, L. (2019), CAS FGOALS-g3 model output prepared for CMIP6 CMIP historical, https://doi.org/10.22033/ESGF/CMIP6.3356.

Liang, Y., N. P. Gillett, and A. H. Monahan (2020), Climate Model Projections of 21st Century Global Warming Constrained Using the Observed Warming Trend, *Geophysical Research Letters*, *47*(12), https://doi.org/10.1029/2019GL086757.

Lique, C., H. L. Johnson, and Y. Plancherel (2017), Emergence of deep convection in the Arctic Ocean under a warming climate, *Climate Dynamics*, *50*(9–10), 3833–3847, https://doi.org/10.1007/s00382-017-3849-9.

Lovato, T., and D. Peano (2020), CMCC CMCC-CM2-SR5 model output prepared for CMIP6 CMIP historical, https://doi.org/10.22033/ESGF/CMIP6.3825.

Lovato, T., D. Peano, and M. Butenschön (2021), CMCC CMCC-ESM2 model output prepared for CMIP6 CMIP historical, https://doi.org/10.22033/ESGF/CMIP6.13195.

Madonna, E., and A. B. Sandø (2021), Understanding Differences in North Atlantic Poleward Ocean Heat Transport and Its Variability in Global Climate Models, *Geophysical Research Letters*, *49*(1), https://doi.org/10.1029/2021GL096683.

Outten, S., I. Esau, and O. H. Otterå (2018), Bjerknes Compensation in the CMIP5 Climate Models, *Journal of Climate*, *31*(21), 8745–8760, https://doi.org/10.1175/JCLI-D-18-0058.1.

Overland, J. E., P. Turet, and A. H. Oort (1996), Regional Variations of Moist Static Energy Flux into the Arctic, *Journal of Climate*, *9*(1), 54–65, https://doi.org/10.1175/1520-0442(1996)009<0054:RVOMSE>2.0.CO;2.

Pan, R., Q. Shu, Q. Wang, et al. (2023), Future Arctic Climate Change in CMIP6 Strikingly Intensified by NEMO-Family Climate Models, *Geophysical Research Letters*, *50*(4), https://doi.org/10.1029/2022GL102077.

Polyakov, I. V., L. A. Timokhov, V. A. Alexeev, et al. (2010), Arctic Ocean Warming Contributes to Reduced Polar Ice Cap, *Journal of Physical Oceanography*, *40*(12), 2743–2756, https://doi.org/10.1175/2010JPO4339.1.

Riahi, K., D. P. van Vuuren, E. Kriegler, et al. (2017), The Shared Socioeconomic Pathways and their energy, land use, and greenhouse gas emissions implications: An overview, *Global Environmental Change*, *42*, 153–168, https://doi.org/10.1016/j.gloenvcha.2016.05.009.

Rong, X. (2019), CAMS CAMS_CSM1.0 model output prepared for CMIP6 CMIP historical, https://doi.org/10.22033/ESGF/CMIP6.9754.

Serreze, M. C., and R. G. Barry (2014), *The Arctic Climate System*, Cambridge University Press, https://doi.org/10.1017/CBO9781139583817.

Smith, D. M., J. A. Screen, C. Deser, et al. (2019), The Polar Amplification Model Intercomparison Project (PAMIP) contribution to CMIP6: investigating the causes and consequences of polar amplification, *Geoscientific Model Development*, *12*(3), 1139–1164, https://doi.org/10.5194/gmd-12-1139-2019.

van der Swaluw, E., S. S. Drijfhout, and W. Hazeleger (2007), Bjerknes Compensation at High Northern Latitudes: The Ocean Forcing the Atmosphere, *Journal of Climate*, *20*(24), 6023–6032, https://doi.org/10.1175/2007JCLI1562.1.

Volodin, E., E. Mortikov, A. Gritsun, et al. (2019a), INM INM-CM4-8 model output prepared for CMIP6 ScenarioMIP, https://doi.org/10.22033/ESGF/CMIP6.12321.

Volodin, E., E. Mortikov, A. Gritsun, et al. (2019b), INM INM-CM5-0 model output prepared for CMIP6 CMIP historical, https://doi.org/10.22033/ESGF/CMIP6.5070.

Wieners, K.-H., M. Giorgetta, J. Jungclaus, et al. (2019), MPI-M MPI-ESM1.2-LR model output prepared for CMIP6 CMIP historical, https://doi.org/10.22033/ESGF/CMIP6.6595.

Wu, T., M. Chu, M. Dong, et al. (2018), BCC BCC-CSM2MR model output prepared for CMIP6 CMIP historical, https://doi.org/10.22033/ESGF/CMIP6.2948.

Yu, Y. (2019), CAS FGOALS-f3-L model output prepared for CMIP6 CMIP historical, https://doi.org/10.22033/ESGF/CMIP6.3355.

Yukimoto, S., T. Koshiro, H. Kawai, et al. (2019), MRI MRI-ESM2.0 model output prepared for CMIP6 CMIP historical, https://doi.org/10.22033/ESGF/CMIP6.6842.

Zhang, J., R. Lindsay, M. Steele, and A. Schweiger (2008), What drove the dramatic retreat of arctic sea ice during summer 2007?, *Geophysical Research Letters*, *35*(11), https://doi.org/10.1029/2008GL034005.

Ziehn, T., M. Chamberlain, A. Lenton, et al. (2019), CSIRO ACCESS-ESM1.5 model output prepared for CMIP6 CMIP historical, https://doi.org/10.22033/ESGF/CMIP6.4272.

Årthun, M., T. Eldevik, L. H. Smedsrud, Ø. Skagseth, and R. B. Ingvaldsen (2012), Quantifying the Influence of Atlantic Heat on Barents Sea Ice Variability and Retreat, *Journal of Climate*, *25*(13), 4736–4743, https://doi.org/10.1175/JCLI-D-11-00466.1.

Russian Journal of Earth Sciences

Freezing Patterns in Saline Soils: Modeling with Regard to the Osmotic Effect

M. M. Ramazanov[1,2], N. S. Bulgakova[1,*], L. I. Lobkovsky[3,4], E. M. Chuvilin[4,5], S. R. Gadzhimagomedova[1], and N. E. Shakhova[2,4,6]

[1]Institute for Geothermal Research and Renewable Energy, Branch of Joint Institute for High Temperatures, Russian Academy of Sciences, Makhachkala, Russia
[2]Sadovsky Institute of Geosphere Dynamics , Russian Academy of Sciences, Moscow, Russia
[3]P. P. Shirshov Institute of Oceanography, Russian Academy of Sciences, Moscow, Russia
[4] Science Department, Tomsk State University, Tomsk, Russia
[5]Skolkovo Institute of Science and Technology (Skoltech), Innovation Center Skolkovo, Moscow, Russia
[6]V. I. Il'ichev Pacific Oceanological Institute, Far Eastern Branch Russian Academy of Sciences, Vladivostok, Russia
* **Correspondence to:** Natalia S. Bulgakova, ipgnatali@mail.ru

Abstract: Freezing patterns in a porous soil saturated with a saline solution are investigated with regard to osmotic effects, using a model suggested previously by the authors but in a more general formulation. The results include a numerical and an approximate self-similar analytical solution to a nonlinear problem; description of typical freezing behavior in the presence of osmotic pressure. The modeling results agree well with experimental evidence on freezing of saline clay and sand. The model includes three porous domains with ice (I), thermodynamically equilibrated ice+solution (II), and a liquid saline solution (III) in the pores. The modeling is performed for a simplified case of domains II and III that share a mobile phase boundary where the solution freezes up partially, with heat release.

Keywords: freezing, saline rock, osmosis, mathematical model, modeling, physical model.

Citation: Ramazanov, M. M., N. S. Bulgakova, L. I. Lobkovsky, E. M. Chuvilin, S. R. Gadzhimagomedova, and N. E. Shakhova (2024), Freezing Patterns in Saline Soils: Modeling with Regard to the Osmotic Effect, *Russian Journal of Earth Sciences*, 24, ES4008, EDN: HICJYC, https://doi.org/10.2205/2024es000919

Research Article

Received: 17 April 2024
Accepted: 12 July 2024
Published: 13 November 2024

1. Introduction

Freezing of rocks and soils saturated with a solution of salts is a complex process involving different mechanisms for salt and moisture transport, as well as stress and strain dynamics in the mineral skeleton. Since the process of freezing saline soil depends nonlinearly on many factors, the identification of patterns is significantly complicated. It can be investigated on the basis of the mathematical model previously proposed by the authors [*Ramazanov et al.*, 2023], but in a more general formulation, and compare the results with data from physical and field experiments [*Chuvilin*, 1999; *Chuvilin et al.*, 1998; *Ershov et al.*, 1997]. The correlation between the transport of salt and moisture in freezing saline soils was studied in [*Chuvilin et al.*, 1998]. The results of physical experiments reported in [*Chuvilin*, 1999] were used to study the behavior of ions in freezing and thawing soils, and in ice. The available evidence relevant to freezing also includes interactions of frozen soil with saline solutions. In [*Ershov et al.*, 1997], processes associated with different types of interactions between liquid brine and frozen rocks are considered.

According to the present views, the Siberian Arctic shelf underwent repeated freezing and thawing associated with regression and transgression events, which produced permafrost with numerous lenses of brines at negative temperatures called cryopegs [*Dubikov and Ivanova*, 1990; *Streletskaya and Leibman*, 2002]. It is noted in [*Dubikov and Ivanova*, 1990] that frozen saline soils by many of its properties occupy a position between frozen and unfrozen soils. They contain more unfrozen water than the same frozen soils. It determines their peculiarity together with other features of their composition and structure. In [*Streletskaya and Leibman*, 2002], the actual material is considered from the point of view of the formation of cryopegs as residual brines during the formation of ice deposits.

One of possible reason for current climate change in the Arctic is considered to be the formation and release a lot of methane due to subaquatic permafrost degradation, as methane is a potent greenhouse gas. Saline seawater and cryopegs contribute largely to permafrost degradation and the ensuing emission of methane released by dissociating metastable methane hydrates self-preserved in frozen rocks [*Chuvilin et al.*, 2019; *Lobkovskii and Ramazanov*, 2018; *Shakhova et al.*, 2017; *Yakushev*, 2009]. The rate of submarine permafrost degradation and the emergence of gas migration pathways are key factors controlling methane emissions on the East Siberian Arctic shelf [*Shakhova et al.*, 2017].

The process of permafrost degradation and the reverse process of salt rock freezing have the same transport mechanism – osmotic filtration (moisture migration). Osmosis can lead to abnormally high pressures capable of destroying frozen rocks [*Berry and Hanshaw*, 1960; *Marine and Fritz*, 1981]. Thus, developing model can easily describe the degradation of permafrost rocks containing accumulations of gas hydrates and free gas under the influence of solutions and the associated osmotic effect.

There exist various models of freezing and thawing processes in saline rocks and soils [*Maksimov and Tsypkin*, 1987; *Tsypkin*, 2009; *Vasiliev et al.*, 1996], but our model is advantageous by including osmosis. The osmotic motion of water molecules driven by the solute concentration gradient is a powerful mechanism of mass transport in low-permeable porous media [*Ramazanov et al.*, 2019, 2022]. This modeling approach can be used to determine a mathematical criterion for the formation of cryopegs in freezing saline soils, which depends largely on the osmotic filtration [*Ramazanov et al.*, 2023]. Another advantage of our model is in due regarded for deformation of the host rocks, given that osmotic pressure can cause rock failure.

In this paper using the model proposed in [*Ramazanov et al.*, 2023] by numerical and analytical methods, we investigate the processes of freezing of rocks and soils saturated with salt solution, taking into account the osmotic force.

2. Problem Formulation

The model simulates permeable soil saturated with a saline solution of a constant concentration, at a certain temperature. At some moment of time, the temperature of the model top falls below the freezing point at given local pressure and salt concentration values. Thereby two freezing fronts arise and propagate downward (Figure 1): the boundaries between domains I and II (fully and partly frozen domains, with pore ice and ice + saline solution in thermodynamic equilibrium, respectively), and between partly frozen (II) and unfrozen (III) domains. The modeling investigates the patterns of evolution of the multi-phase system with regard to the osmotic effect and deformation of the host rock and compares the results with experimental data.

3. Mathematical Model

A detailed description of the equations in each domain, the boundary conditions, and their transformations are given in the previous paper [*Ramazanov et al.*, 2023] published in this journal. Here, we present these equations immediately in dimensionless and self-similar form [*Ramazanov et al.*, 2023].

The pressure is counted from the hydrostatic level, and the temperature from level T^0. To make them dimensionless, let's introduce the following scales:

$$\begin{aligned}&[z]=h, \quad [\mathrm{v}]=-\frac{k}{\eta h}\frac{dP}{dT}\left(T_0-T^0\right), \quad [t]=\frac{h}{[\mathrm{v}]}, \quad [T]=T_0-T^0,\\&[p]=-\frac{dP}{dT}\left(T_0-T^0\right), \quad [c]=c_0,\end{aligned} \tag{1}$$

where k is the permeability; v is the field of the solution velocity; $T$is the temperature; p is the pressure; c is the concentration; c_0 is the characteristic concentration; η is the solution viscosity; h is the domain thickness; T_0 is the temperature at the lower boundary of domain III, T^0 is the temperature at the boundary $z = z_1$.

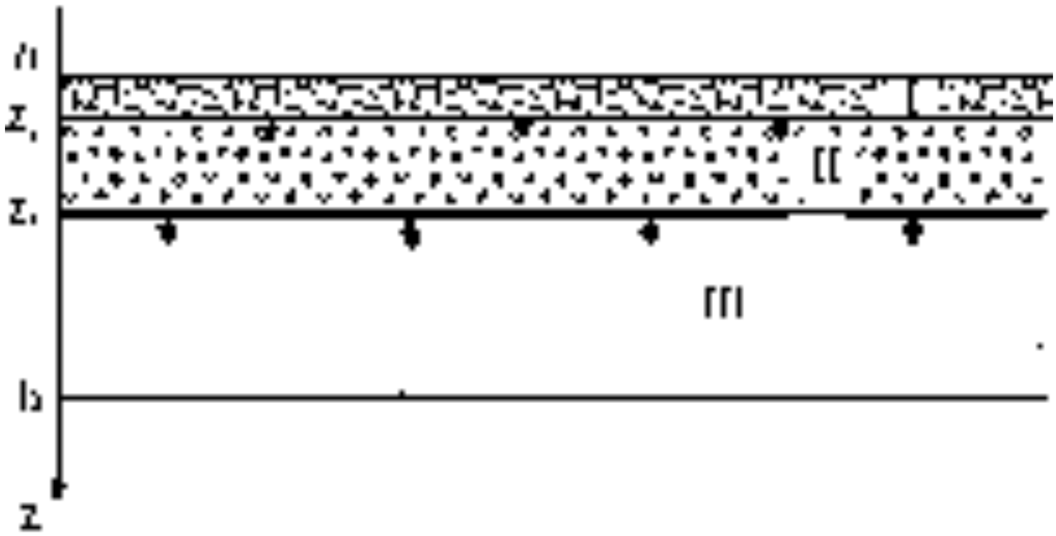

Figure 1. Problem sketch: I – ice-saturated frozen domain; II – partly frozen domain saturated with thermodynamically equilibrated ice and saline solution; III – unfrozen domain saturated with liquid saline solution; $z = z_1(t)$ is the mobile boundary of domain I; $z = z_*(t)$ is the front of partial freezing.

4. Self-Similar Problem Formulation and Solution

The solution is sought in the self-similar form, with the new coordinate ξ

$$\mathrm{v} = \frac{\mathrm{v}(\xi)}{\sqrt{t}}, \quad T = T(\xi), \quad c = c(\xi), \quad p = p(\xi), \quad \xi = \frac{z}{\sqrt{t}}. \tag{2}$$

Then, different domains will be described as follows:

Frozen Domain (I)

$$-\frac{\xi}{2}\frac{dT_i}{d\xi} = \frac{1}{Pe_{T_i}}\frac{d^2T_i}{d\xi^2}. \tag{3}$$

Partly Frozen Domain (II)

$$\begin{aligned}
&\mathrm{v} = s\left[\left(\gamma_f + \psi_0\right)\frac{dc}{d\xi} + \frac{dT}{d\xi}\right];\\
&-\frac{\xi}{2N_s}\frac{ds}{d\xi} + \frac{\xi}{2N_p}\left(\frac{dT}{d\xi} + \psi_0\frac{dc}{d\xi}\right) + \frac{d\mathrm{v}}{d\xi} = 0;\\
&-\left(\frac{\gamma_c\xi}{2} - \mathrm{v}\right)\frac{dc}{d\xi} = \frac{1}{Pe_c}\frac{d^2c}{d\xi^2} + \frac{\gamma_s\xi}{2}\frac{ds}{d\xi};\\
&-\left(\frac{\gamma_T\xi}{2} - \mathrm{v}\right)\frac{dT}{d\xi} = \frac{1}{Pe_T}\frac{d^2T}{d\xi^2} + \frac{\gamma_q\xi}{2}\frac{ds}{d\xi}.
\end{aligned} \tag{4}$$

Unfrozen Domain (III)

$$
\begin{aligned}
&\mathrm{v} = -\frac{dp}{d\xi} + \gamma_f \frac{dc}{d\xi};\\
&-\frac{\xi}{2N_{p0}}\frac{dp}{d\xi} = \frac{d^2p}{d\xi^2} - \gamma_f \frac{d^2c}{d\xi^2};\\
&-\left(\frac{\gamma_c \xi}{2} - \mathrm{v}\right)\frac{dc}{d\xi} = \frac{1}{s_0 Pe_c}\frac{d^2c}{d\xi^2};\\
&-\left(\frac{\gamma_T \xi}{2} - \mathrm{v}\right)\frac{dT}{d\xi} = \frac{1}{Pe_T}\frac{d^2T}{d\xi^2}.
\end{aligned}
\tag{5}
$$

where Pe_T, Pe_c are, respectively, the temperature and concentration Péclet numbers.

$$
\begin{aligned}
&\frac{1}{N_s} = m\left(1 - \frac{\rho_i}{\rho_w}\right), \quad \frac{1}{N_{p_0}} = \frac{1}{m_0}\left[\frac{\partial m}{\partial p} + \frac{m_0}{\rho_w}\frac{\partial \rho_w}{\partial p}\right]\left(T_0 - T^0\right)\left|\frac{dP}{dT}\right|,\\
&\frac{1}{N_p} = \left[\left(s_0 + (1-s_0)\frac{\rho_i}{\rho_w}\right)\frac{\partial m}{\partial p} + \frac{m}{\rho_w}\left(s_0\frac{\partial \rho_w}{\partial p} + (1-s_0)\frac{\partial \rho_i}{\partial p}\right)\right]\left(T_0 - T^0\right)\left|\frac{dP}{dT}\right|,\\
&\gamma_f = \rho_w\left|\frac{\partial \mu_1}{\partial c}\right| c_0\left[\left(T_0 - T^0\right)\left|\frac{dP}{dT}\right|\right]^{-1}, \quad \gamma_T = \frac{C_m + ms\beta_w \overline{T}\left|\frac{dP}{dT}\right|}{\rho_w C_w + \beta_w \overline{T}\left|\frac{dP}{dT}\right|},\\
&\gamma_q = \frac{qm\rho_i}{\left[\rho_w C_w + \beta_w \overline{T}\left|\frac{dP}{dT}\right|\right]\left(T_0 - T^0\right)}, \quad \gamma_c = s_0(m+\Gamma), \quad \gamma_s = m\frac{\rho_i}{\rho_w} + \Gamma,\\
&\Gamma(K,c) = \frac{\partial a(K,c)}{\partial c}, \quad \lim a(K,c)_{Kc\to\infty} = a_\infty,\\
&Pe_T = \frac{[\mathrm{v}]h\left[\rho_w C_w + \beta_w \overline{T}\left|\frac{dP}{dT}\right|\right]}{\lambda_m}, \quad Pe_c = \frac{[\mathrm{v}]h}{ms_0 D}, \quad [\mathrm{v}] = -\frac{k}{\eta h}\frac{dP}{dT}\left(T_0 - T^0\right).
\end{aligned}
$$

where s_0 is the characteristic water saturation in domain II; ρ_w , ρ_i are densities of water and ice, respectively; T_i is the ice temperature; C_m is the effective heat capacity per unit volume of an saturated porous soil; C_w, C_i, C_s are, respectively, the heat capacity of water, ice and soil; λ_m is the effective thermal conductivity of an saturated porous soil; λ_w, λ_i, λ_s are, respectively, the thermal conductivity of water, ice and soil; μ_1 is the chemical potential of solvent; D is the salt diffusion coefficient; q is the specific heat of ice melting; β_w is the thermal expansion coefficient; m is the porosity; a is the concentration of salt in the solid phase of a porous medium; a_∞ the value of the maximum adsorption; K is the constant of the adsorption equilibrium; ψ_0 constant characterizing the degree of decrease in the freezing point of water due to the presence of dissolved salt.

Boundary Conditions

$$
\xi = 0: \quad T_i = \frac{T_i^0 - T^0}{T_0 - T^0}, \tag{6}
$$

$$
\begin{aligned}
&\xi = \xi_1: \quad T_- = T_+ = 0, \quad \frac{1}{Pe_{T_i}}\frac{dT_-}{d\xi} = \frac{\gamma_{qi}s^0}{2}\xi_1 + \frac{1}{Pe_T}\frac{dT_+}{d\xi}, \quad \gamma_{qi} = \frac{qm\rho_i}{\rho_w c_w (T_0 - T^0)},\\
&s^0\left(\frac{1}{s_0 Pe_c}\frac{dc_+}{d\xi} + \frac{\rho_i}{\rho_w}\frac{m\xi_1}{2}c_+\right) = 0, \quad \mathrm{v}_+ = s^0\left(1 - \frac{\rho_i}{\rho_w}\right)\frac{m\xi_1}{2},
\end{aligned}
\tag{7}
$$

$$\xi = \xi_*: \quad \mathrm{v}_- - \frac{m}{2}s_*\xi_* - \frac{\rho_i m}{2\rho_w}(1-s_*)\xi_* = \mathrm{v}_+ - \frac{m}{2}\xi_*,$$
$$T_- = T_+ = T_*, \quad -\gamma_q(1-s_*)\frac{1}{2}\xi_* + \frac{1}{Pe_T}\frac{dT_-}{d\xi} = \frac{1}{Pe_T}\frac{dT_+}{d\xi}$$
$$c_- = c_+ = c_*, \quad -\gamma_s(1-s_*)\frac{c_*}{2}\xi_* + \frac{s_*}{s_0 Pe_c}\frac{dc_-}{d\xi} = \frac{1}{s_0 Pe_c}\frac{dc_+}{d\xi} \tag{8}$$
$$\xi \to \infty: \quad p \to p_0, \quad T \to 1, \quad c \to 1, \tag{9}$$

where s^0 is the water saturation at the boundary $\xi = \xi_1$ between domains I (pore ice) and II (equilibrated pore ice + solution). The subscripts and superscripts have the following meaning: subscripts + and – refer to values approaching the boundaries from below and from above, respectively; subscript $*$ indicates the value at the boundary $\xi = \xi_*$, superscript 0 – at the boundary $\xi = \xi_1$, subscript 0 – at the boundary $\xi \to \infty$ or the characteristic value of the parameter.

With the given parameters T_i^0, T_0, c_0, p_0 and s^0, the sought parameters are: mobile phase boundaries ξ_1, ξ_*, temperature in frozen domain I; temperature, salt concentration, and water saturation in partly frozen domain II and at its boundaries; temperature, salt concentration, and pressure in unfrozen domain III. Note that the boundaries in self-similar coordinates also define the propagation rates of the respective fronts.

Equations (2–9) in the self-similar formulation make up a closed model that simulates freezing of saline soil with regard to osmosis as a driving force. In initial coordinates the model is detailed in [*Ramazanov et al.*, 2023]. In the general case, the model is quite sophisticated, as it contains two moving phase transition boundaries. We consider the particular case when the frozen domain (I) can be neglected. In [*Ramazanov et al.*, 2023], a condition is given under which, as a first approximation, an ice layer can be neglected. It is possible if the front between domains I and II propagates much more slowly than that between II and III, i.e.

$$\xi_1 \ll \xi_*. \tag{10}$$

Then we obtain

$$k \gg m\left(1-\frac{\rho_i}{\rho_w}\right)^2 \frac{\lambda_{m_i}}{\rho_i q}\frac{\eta}{\beta_p(p_*-p_0)^2}\left(T^0 - T_i^0\right) \sim 10^{-18}\left(10 \div 10^{-1}\right) \tag{11}$$

In the conditions considered in this article, inequality (11) holds for permeability $k \sim 10^{-18} \div 10^{-17} m^2$and more. This permeability corresponds to the Péclet numbers $Pe_T \sim 10^{-2} \div 10^{-1}$. On the other hand, osmotic properties are manifested for weakly permeable media (clay, silt, etc.), which are characterized by precisely such permeability and corresponding Péclet numbers. Therefore, the number $Pe_T = 0.1$ is taken as the base number in the calculations below.

Thus, inequality (11) is satisfied under the conditions under consideration, so domain I is excluded from further consideration. Unlike [*Ramazanov et al.*, 2023], in this study, not only the second, but also the third domain is taken into account.

The boundary conditions in domains II and III, given that the origin of coordinates is at the base of domain I, which is immobile in this approximation, are

$$\xi = 0: \quad T = 0, \quad \left(\gamma_f + \psi_0\right)\frac{dc}{d\xi} + \frac{dT}{d\xi} = 0, \tag{12}$$

$$\xi = \xi_*: \quad \mathrm{v}_- - \frac{m}{2}s_*\xi_* - \frac{\rho_i m}{2\rho_w}(1-s_*)\xi_* = \mathrm{v}_+ - \frac{m}{2}\xi_*$$
$$T_- = T_+ = T_*, \quad -\gamma_q(1-s_*)\frac{1}{2}\xi_* + \frac{1}{Pe_T}\frac{dT_-}{d\xi} = \frac{1}{Pe_T}\frac{dT_+}{d\xi}, \tag{13}$$
$$c_- = c_+ = c_*, \quad -\gamma_s(1-s_*)\frac{c_*}{2}\xi_* + \frac{s_*}{s_0 Pe_c}\frac{dc_-}{d\xi} = \frac{1}{s_0 Pe_c}\frac{dc_+}{d\xi},$$

$$\xi \to \infty: \quad p \to p_0 \quad T \to 1, \quad c \to 1. \tag{14}$$

Thus, we have a system of equations (4–5) with boundary conditions (12–14). Since the model is nonlinear and generally has no analytical solution, one can take advantage of the fact that the Péclet number Pe_T of usually small, i.e. the filtration solution rate is much slower than the freezing rate (propagation of the freezing front). Then, the convective components in the transport equations can be neglected. The simplified model is still nonlinear because of generalized Darcy's law (4), since the velocity is proportional to the product of water saturation by concentration and temperature gradients. However, it is possible to find an approximate solution assuming that water saturation s in the first equation of (4) is equal to some unknown average value $\bar{s}$. For the two remaining domains, the solution is as follows.

Partly Frozen Domain I (Pore Ice + Solution)

$$\begin{aligned}
&s - s^0 = -s_T T - s_c\left(c - c^0\right),\\
&c = c^0 + C_1 \mathrm{erf}\left(\frac{\sqrt{\tilde{\alpha}_c}}{2}\xi\right) + \frac{Pe_c \gamma_s s_T}{\alpha_c - \tilde{\alpha}_T} C_3 \mathrm{erf}\left(\frac{\sqrt{\tilde{\alpha}_T}}{2}\xi\right),\\
&T = \frac{Pe_T \gamma_q s_c}{\alpha_T - \tilde{\alpha}_c} C_1 \mathrm{erf}\left(\frac{\sqrt{\tilde{\alpha}_c}}{2}\xi\right) + C_3 \mathrm{erf}\left(\frac{\sqrt{\tilde{\alpha}_T}}{2}\xi\right)
\end{aligned} \tag{15}$$

where C_1, C_3 are determined from the boundary conditions at the moving phase interface $\xi = \xi_*$.

$$\begin{aligned}
&s_T = \frac{\bar{s} Pe_T \gamma_T - \frac{1}{N_p}}{\frac{1}{N_s} + \bar{s}\left[Pe_T \gamma_q + \left(\gamma_f + \psi_0\right) Pe_c \gamma_s\right]},\\
&s_c = \frac{\bar{s}\left(\gamma_f + \psi_0\right) Pe_c \gamma_c - \frac{\psi_0}{N_p}}{\frac{1}{N_s} + \bar{s}\left[Pe_T \gamma_q + \left(\gamma_f + \psi_0\right) Pe_c \gamma_s\right]},\\
&\tilde{\alpha}_c = \frac{\alpha_T + \alpha_c + \sqrt{(\alpha_c - \alpha_T)^2 + 4 Pe_c \gamma_s s_T Pe_T \gamma_q s_c}}{2},\\
&\tilde{\alpha}_T = \frac{\alpha_T + \alpha_c - \sqrt{(\alpha_c - \alpha_T)^2 + 4 Pe_c \gamma_s s_T Pe_T \gamma_q s_c}}{2},\\
&\alpha_T = Pe_T\left(\gamma_T + \frac{N_s}{N_p}\gamma_q\right), \quad \alpha_c = Pe_c \gamma_c.
\end{aligned} \tag{16}$$

We substitute the resulting solution for water saturation into the equation

$$\frac{1}{\xi_*}\int_0^{\xi_*} s(\xi, \bar{s})\, d\xi = \bar{s} \tag{17}$$

and obtain a previously unknown value for the average water saturation $\bar{s}$.

Unfrozen Domain II (Pore Solution)

$$\begin{aligned}
&c = 1 - (1 - c_*)\mathrm{erfc}\left(\frac{\sqrt{s_0 Pe_c \gamma_c}}{2}\xi\right) \Big/ \mathrm{erfc}\left(\frac{\sqrt{s_0 Pe_c \gamma_c}}{2}\xi_*\right),\\
&T = 1 - (1 - T_*)\mathrm{erfc}\left(\frac{\sqrt{Pe_T \gamma_c}}{2}\xi\right) \Big/ \mathrm{erfc}\left(\frac{\sqrt{Pe_T \gamma_c}}{2}\xi_*\right),
\end{aligned} \tag{18}$$

$$\begin{aligned}
&p = p_0 + C_4 \mathrm{erfc}\left(\frac{\sqrt{\beta_{p0}}}{2}\xi\right) + C_2 \mathrm{erfc}\left(\frac{\sqrt{s_0 Pe_c \gamma_c}}{2}\xi\right),\\
&\mathrm{v}_p = \sqrt{\frac{\beta_{p_0}}{\pi}} C_4 e^{-\frac{\beta_{p0}}{4}\xi^2} + \sqrt{\frac{s_0 Pe_c \gamma_c}{\pi}} C_2 e^{-\frac{Pe_c\gamma_c}{4}\xi^2} + \gamma_f \frac{dc}{d\xi}, \quad \beta_{p_0} = \frac{1}{N_{p_0}},
\end{aligned} \tag{19}$$

$$\begin{aligned}
&C_2 = \frac{-\gamma_f(1-c_*)s_0 Pe_c \gamma_c}{\beta_p - s_0 Pe_c \gamma_c} \Big/ \mathrm{erfc}\left(\frac{\sqrt{s_0 Pe_c \gamma_c}}{2}\xi_*\right),\\
&C_4 = p_* - p_0 - C_2 \mathrm{erfc}\left(\frac{\sqrt{s_0 Pe_c \gamma_c}}{2}\xi_*\right) \Big/ \mathrm{erfc}\left(\frac{\sqrt{\beta_{p0}}}{2}\xi_*\right).
\end{aligned} \tag{20}$$

Estimating Moisture Content. If the moisture content density is expressed as the weight ratio of moisture (solid and liquid) to dry soil, then

$$W(\xi) = \begin{cases} m\rho_w \dfrac{1 - \left(1 - \dfrac{\rho_i}{\rho_w}\right)(1-s) + \dfrac{\beta_p}{m}(1 - T - \psi_0 c)}{(1-m)\rho_s}, & \xi \le \xi_* \\ m\rho_w \dfrac{1 + \dfrac{\beta_{p0}}{m}(p - p_0)}{(1-m)\rho_s}, & \xi > \xi_* \end{cases}. \tag{21}$$

5. Results and Discussion

Thus, equations (15–21) provide a complete analytical solution to the nonlinear problem in the self-similar coordinates. The transitions to the initial coordinates and to the dimensional form are possible with equations (2) and (1), respectively.

The solution is valid at small Péclet numbers $Pe_T \ll 1$, which is commonly fulfilled. For the case of greater values, a forward numerical solution of problem (4–5) with boundary conditions (12–14) applied, taking into account convective transfer of heat and solutes. Furthermore, numerical modeling was used to check the analytical solution and proved its good accuracy.

In this problem of freezing saturated soils, two forces act: the force that pushes the solution into the unfrozen domain and the force that retracts the solution in the frozen domain. The pushing force arises due to equilibrium pressure increases with cooling and the water-ice density difference, while retracting force is due to the osmotic force. Depending on the values of the parameters, one or another force prevails.

Some results are illustrated in Figures 2–6.

Figure 2a–c shows patterns of partial freezing front propagation of solution depending on different parameters. With these parameter values, during the first 10 years, the freezing front moves at an average speed of about one meter per year, and then this speed decreases proportionally to $1/\sqrt{t}$. Curves in Figure 2a show that with an increase in the osmotic coefficient, the partial freezing front slows down, which is due to the difficulty of pushing the solution out by the freezing front. Figure 2b shows that as the Péclet number increases, the front moves faster because the rate of convective heat removal from the front increases. According to Figure 2c, as the water capacity of the soils increases, the front also moves faster, which is explained by the easier pushing of the solution into the unfrozen area.

Figure 3a–c shows depth-dependent water saturation distributions for water capacity β_p (a, b) and osmotic coefficient γ_f (a, c), two values each. Curves 1 and 2 correspond to the time $t = 1$ and 4 years, respectively. The curves above refer to the respective filtration solution rates.

Water saturation behind the freezing front decreases monotonically with time (Figure 3) as the soil is freezing up. Figure 3a shows that filtration solution rate is negative in this case, i.e., the solution is drawn from the thawed domain into the partly frozen domain by osmosis.

The pushing force predominates at lower β_p, other parameters being the same (Figure 3b), as well as at lower osmotic coefficients (Figure 3c). In Figure 3c, the osmotic

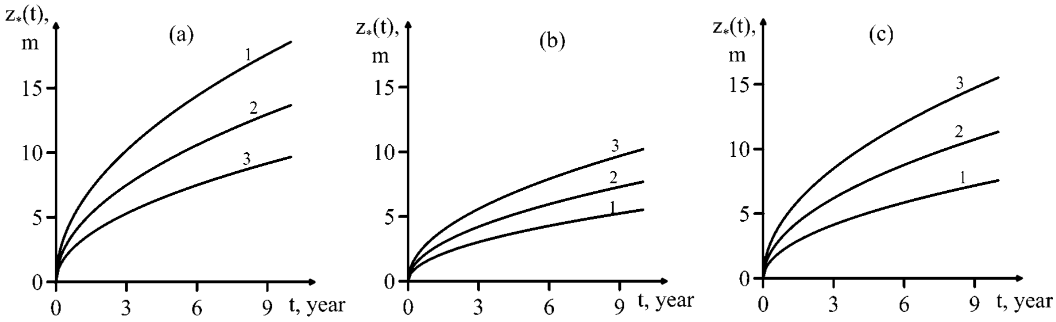

Figure 2. Time-dependent freezing propagation for different values of parameters at $c_0 = 0.8\%$, $T^0 = -2\,°\mathrm{C}$. (a): $Pe_T = 0.1$, $\beta_p = 0.1$, $\gamma_f = 0.27, 0.35, 1(1–3)$; (b): $\beta_p = 0.07$, $\gamma_f = 0.7$, $Pe_T = 0.01, 0.03, 0.3(1–3)$; (c): $Pe_T = 0.1$, $\gamma_f = 0.3$, $\beta_p = 0.01, 0.05, 0.1(1–3)$, where$\beta_p \equiv 1/N_p$ is the compressibility of the saturated porous soil (water capacity).

force coefficient is reduced compared to Figure 3a. As can be seen from the comparison, a decrease in osmotic force also leads to a predominance of the pushing force.

These results are quite consistent with the results of physical experiments [*Chuvilin*, 1999; *Chuvilin et al.*, 1998], showing that clays in the considered freezing conditions draw the solution from the thawed area, and sands, on the contrary, are pushed out. At the same time, it is known that clays have semi-permeable and, consequently, osmotic properties [*Kemper*, 1961].

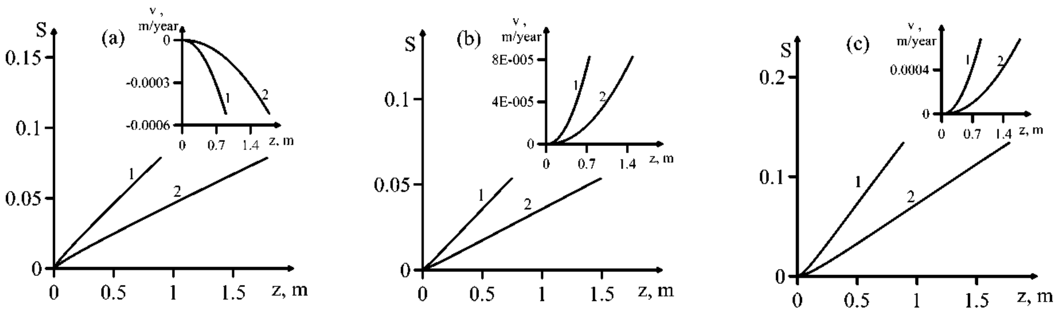

Figure 3. The distribution of water saturation for two time points (the filtration solution rate distributions are shown at the top) at: $Pe_c = 10$, $Pe_T = 0.1$, $c_0 = 1.7\%$, $T^0 = -2\,°\mathrm{C}$, $t = 1$; 4 year (1–2), where: $(\gamma_f, \beta_p) = (1, 0.03)$ (a); $(1, 0.01)$ (b); $(0.1, 0.03)$ (c).

Figure 4a–e shows the distributions of water saturation, velocity field, salt concentration, temperature, and pressure in the partially frozen domain after one year of freezing for two values of pore expansion coefficient β_p (water capacity) and two values of osmotic force coefficient. As you can see, in all cases, the qualitative properties of the distributions coincide, with the exception of the velocity field (Figure 4b). As the temperature increases with depth, water saturation increases at the account of partial melting, which leads to dilution (salt concentration decrease), while the equilibrium pressure decreases (Figure 4a, c–e).

It is pertinent to compare curves that represent different cases, using curves 1 as reference. Figure 4a shows that a decrease in water capacity (compressibility) led to a decrease in water saturation (curve 2), and a decrease in the osmosis coefficient can lead to both a decrease and an increase in water saturation, which explains the intersection of curves 3 and 1. These properties depend on the competition of two factors, the inflow (outflow) of the solution into the two-phase domain and the freezing of water (melting of ice). Curve 2 in Figure 4a is caused by both additional freezing of water (compared to curve 1) and outflow of solution (curve 2 in Figure 4b), and curve 3 is caused to competition between ice melting and moisture outflow (curve 3 in Figure 4b).

The concentration of salt is lower at lower compressibility but higher at lower osmotic coefficients (Figure 4c). To explain this effect, note first of all that the temperature patterns quite close for the three cases (Figure 4d). It follows from the thermodynamic equilibrium condition that lower salinity corresponds to higher pressure and vice versa, the temperature being constant [*Ramazanov et al.*, 2023]. On the other hand, the pressure values are higher at lower compressibility and lower at lower osmotic coefficients (Figure 4e), which accounts for the patterns of Figure 4c.

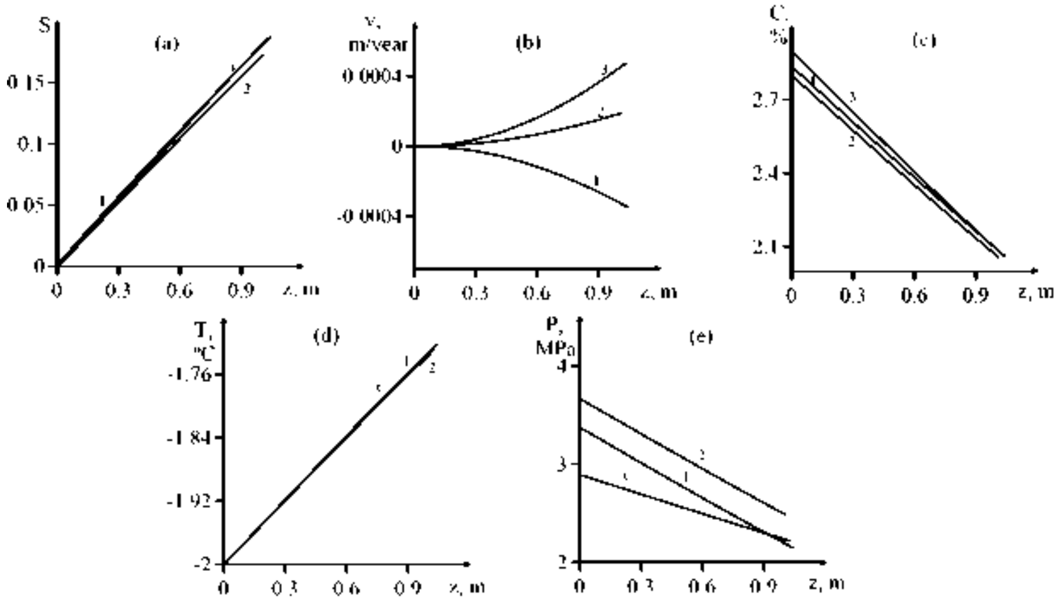

Figure 4. Water saturation (a), filtration solution rate (b), salt concentration (c), temperature (d), and pressure (e) in party frozen domain a year after the onset of freezing, at $Pe_c = 10$, $Pe_T = 0.1$, $c_0 = 1.7\%$, $T^0 = -2\,°\mathrm{C}$, and $\left(\gamma_f, \beta_p = 1/N_p\right) = (0.1, 0.15)$ (1); (0.1, 0.1) (2), (0.05, 0.15) (3).

Figure 4 allows us to estimate the osmotic pressure gradient (osmotic force) under the considered freezing conditions. Consider the curves 1 in Figure 4. It follows from Figure 4b that in this case the solution is drawn from the thawed area into the frozen area. This means that the osmotic pressure gradient is greater than the pressure gradient shown in Figure 4e (curve 1) by the amount causing filtration of the solution. Based on Figure 4b and Darcy's law, it can be shown that the pressure loss for filtration of the solution is small, i.e. the osmotic pressure gradient is approximately equal to the pressure gradient in Figure 4e (curve 1) and is approximately 1 MPa/m. On the other hand, it follows from Figure 4c (curve 1) that this gradient is caused by a salt concentration gradient of the order of $\nabla c_0 \sim 1\%/\mathrm{m} = 10\,\mathrm{g/(L \cdot m)}$. If we take into account the complete dissociation of salt molecules into ions, then this gradient should be doubled. Thus, a salt concentration difference of the order of 10 g/L causes an osmotic pressure of the order of 1 MPa. This is in good agreement with theoretical and experimental estimates for shales [*Neuzil*, 2000].

Note that freezing rocks may have their own characteristics. Namely, near the cooled boundary, as ice forms, areas with a highly concentrated solution (cryopegs) may form. These areas, despite their relatively small size, can make a significant contribution to osmotic pressure. This effect can be taken into account using an effective osmotic coefficient, which can be several times higher than the corresponding coefficient for the thawed domain. In this regard, the values $\gamma_f \sim 1$ are also considered in [*Ramazanov et al.*, 2023] and in this article. It should be noted that a more detailed study of the system of equations (4), with the separation of the boundary layer, allows theoretically calculating the specified effective osmosis coefficient, but goes beyond the scope of this study.

Figure 5 shows of moisture distribution in % of dry weight for different porous materials and different parameters. The upper panels present the results of physical experiments and the lower panels show calculations with the suggested model (4–5; 12–14).

The mathematical and physical modeling differed in temperature conditions on the top of the freezing domain: $-2\,°C$ and $-17\,°C$, respectively. Nevertheless, the theoretical (this study) and laboratory [*Chuvilin*, 1999; *Chuvilin et al.*, 1998] results agree both qualitatively and quantitatively (Figure 5).

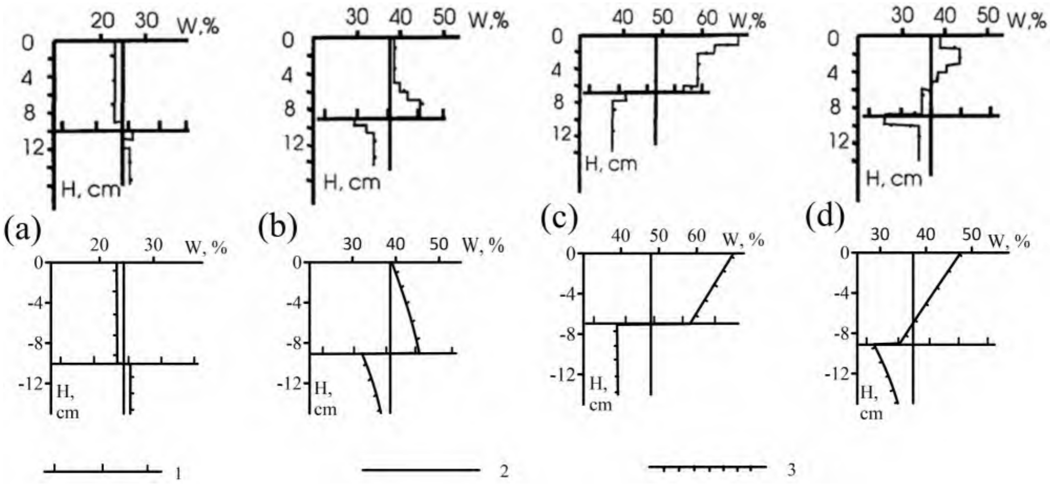

Figure 5. Depth-dependent moisture distribution, in % of dry weight W, according to physical modeling [*Chuvilin*, 1999] (upper panels) and calculations using equations (4–5, 12–14) of the suggested model (lower panels). In the experiment, soil samples: polymineral sand (a); polymineral clay (b); kaolinite clay, at pressures 0.2 MPa (c) and 1 MPa (d). Curve 1 – freezing front; 2 and 3 – initial and final moisture distribution in freezing soil, respectively.

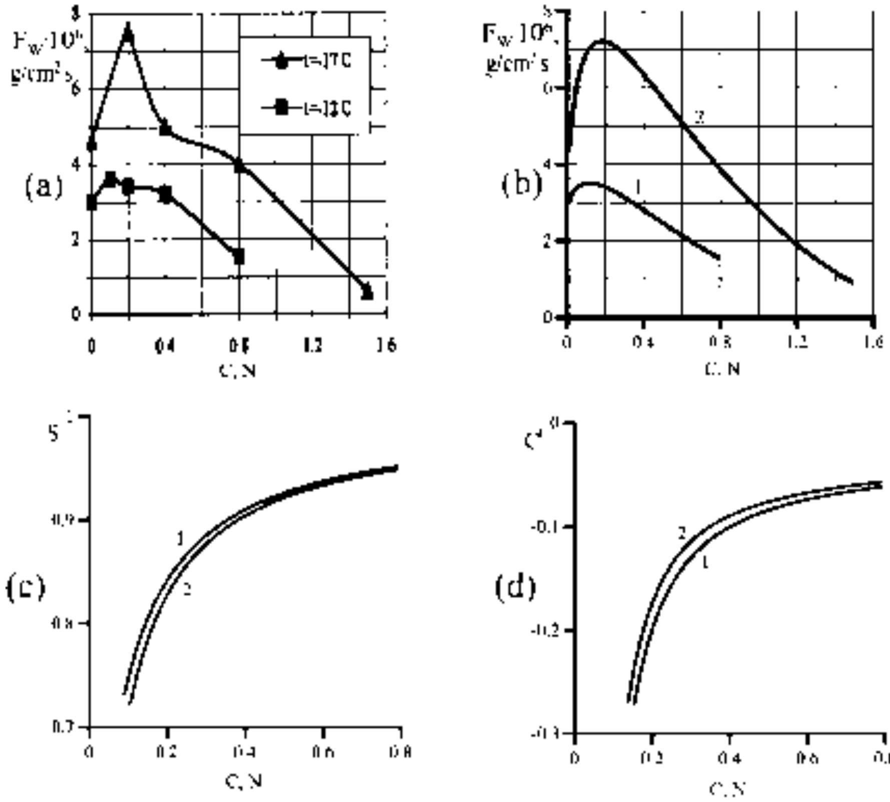

Figure 6. Average moisture expenditure F_w from unfrozen rock to partly frozen domain as a function of initial salinity C solution NaCl in freezing clay according to experiments (a) and modeling with suggested equations (b), and dependence of water saturation S and salinity gradient at the freezing front C' to salinity C calculated with the suggested model (c, d).

Depth-dependent moisture distribution patterns in freezing soils, obtained through mathematical modeling and experiments show the expulsion of pore moisture in wet saline sand, which is respectively observed as higher moisture contents before the freezing front. For clay, on the contrary, before the freezing front the moisture content decreases and in the freezing part it increases. The moisture excess in freezing clay depends on some soil parameters, including contents of moisture and salts, as well as on the conditions of freezing.

Figure 6a shows experimental points for moisture flow from unfrozen to partly frozen domain at different initial NaCl concentrations, from 0 to 1.5 N for two different temperatures [*Chuvilin*, 1999; *Chuvilin et al.*, 1998]. The respective calculated curves (Figure 6b) are in good agreement with the experiment results. Note a peak of moisture flow that can be explained with calculated curves (Figure 6c, d): the moisture flow driven by osmosis is proportional to water saturation and to the magnitude of the concentration gradient. As the initial salinity increases, the former function increases while the latter modulo decreases (Figure 6c, d), and their product has a maximum and allows calculating the optimal salt concentration providing the maximum flow.

Calculations have shown that without the significant role of the osmotic effect, it is impossible to obtain a close description of the experiments. In [*Chuvilin*, 1999; *Chuvilin et al.*, 1998], the important role of advection is noted in physical experiments, partially shown in Figures 5, 6. This study showed that the driving mechanism of this advection in the case of the solution being drawn into the frozen part is precisely the osmotic effect.

At the end of this section, we note that under certain conditions, the process under consideration can lead to the formation of closed "pockets" with brines (cryopegs) in frozen rocks. A mathematical criterion for their formation based on the proposed model was obtained in [*Ramazanov et al.*, 2023].

6. Conclusion

The process of freezing of saline soil has been investigated with regard to the osmosis effect using the previously suggested model [*Ramazanov et al.*, 2023], and an approximate analytical solution was obtained in the self-similarity formulation. In addition, a direct numerical solution has been obtained for large numbers of Péclet. The results demonstrate a good agreement between them.

It has been shown that at high values of the osmotic coefficient in freezing soils, the pore solution is drawn into the freezing domain from the thawed domain, and at low values, it is pushed out, on the contrary. The pushing force is due to the fact that the equilibrium pressure increases with decreasing temperature, as well as the density difference between water and ice. The modeling results are quite consistent with the data of physical experiments that clay with a high osmotic coefficient retract saline solutions, and sand, on the contrary, pushes it out [*Chuvilin*, 1999; *Chuvilin et al.*, 1998]. The results of calculations and physical experiments agree both qualitatively and quantitatively, mainly because the osmotic effect was taken into account: no agreement would be possible otherwise.

The suggested mathematical model, with regard to osmosis, can explain freezing of soils as well as the reverse process of permafrost degradation.

Acknowledgments. This research, in general, was funded by the Russian Science Foundation, grant No. 22-67-00025.

References

Berry, F. A. F., and B. B. Hanshaw (1960), Geologic evidence suggesting membrane properties of shales, in *International Geological Congress: report of the twenty-first session*, p. 209.

Chuvilin, E. M. (1999), Migration of ions of chemical elements in freezing and frozen soils, *Polar Record*, *35*(192), 59–66, https://doi.org/10.1017/S0032247400026346.

Chuvilin, E. M., E. D. Ershov, and N. S. Naletova (1998), Mass transfer and structure formation in freezing saline soils, in *PERMAFROST - Seventh International Conference (Proceedings)*, *Yellowknife (Canada)*, *Collection Nordicana No 55*, Centre d'études nordiques, Université Laval.

Chuvilin, E. M., V. Ekimova, B. Bukhanov, et al. (2019), Role of Salt Migration in Destabilization of Intra Permafrost Hydrates in the Arctic Shelf: Experimental Modeling, *Geosciences*, *9*(4), 188, https://doi.org/10.3390/geosciences9040188.

Dubikov, G. I., and N. V. Ivanova (1990), Saline frozen soils and their distribution in the USSR territory, in *Saline Frozen Soils as Foundations*, pp. 3–9, Nauka, Moscow (in Russian).

Ershov, E. D., I. A. Komarov, and E. M. Chuvilin (1997), Forecast for interaction of liquid technogenous brines buried into permafrost, *Geoekologiya*, (2), 19–29 (in Russian).

Kemper, W. D. (1961), Movement of Water as Effected by Free Energy and Pressure Gradients: II. Experimental Analysis of Porous Systems in Which Free Energy and Pressure Gradients Act in Opposite Directions, *Soil Science Society of America Journal*, *25*(4), 260–265, https://doi.org/10.2136/sssaj1961.03615995002500040010x.

Lobkovskii, L. I., and M. M. Ramazanov (2018), Front Regime of Heat and Mass Transfer in a Gas Hydrate Reservoir under the Negative Temperature Conditions, *Fluid Dynamics*, *53*(4), 517–530, https://doi.org/10.1134/S0015462818040092.

Maksimov, A. M., and G. G. Tsypkin (1987), Overheating and formation of a two-phase zone at phase transitions in permafrost, *DAN USSR*, *294*(5), 1117–1121 (in Russian).

Marine, I. W., and S. J. Fritz (1981), Osmotic model to explain anomalous hydraulic heads, *Water Resources Research*, *17*(1), 73–82, https://doi.org/10.1029/WR017I001P00073.

Neuzil, C. E. (2000), Osmotic generation of 'anomalous' fluid pressures in geological environments, *Nature*, *403*(6766), 182–184, https://doi.org/10.1038/35003174.

Ramazanov, M. M., A. V. Karakin, and L. I. Lobkovskiy (2019), Mathematical Model for the Motion of Solutions Taking into Account the Osmotic Effect, *Doklady Earth Sciences*, *489*(1), 1306–1309, https://doi.org/10.1134/S1028334X19110060.

Ramazanov, M. M., N. S. Bulgakova, and L. I. Lobkovskiy (2022), Osmotic Convection, *Doklady Physics*, *67*(5), 153–158, https://doi.org/10.1134/S1028335822040061.

Ramazanov, M. M., N. Bulgakova, and L. Lobkovsky (2023), Mathematical Model of Freezing of Rocks Saturated With Salt Solution Taking Into Account the Influence of Osmosis, *Russian Journal of Earth Sciences*, *23*(5), 1–15, https://doi.org/10.2205/2023ES000857.

Shakhova, N., I. Semiletov, O. Gustafsson, et al. (2017), Current rates and mechanisms of subsea permafrost degradation in the East Siberian Arctic Shelf, *Nature Communications*, *8*(1), https://doi.org/10.1038/ncomms15872.

Streletskaya, I. D., and M. O. Leibman (2002), Cryogeochemical interrelation of massive ground ice, cryopegs, and enclosing deposits of central Yamal, *Kriosfera Zemli*, *VI*(3), 15–24 (in Russian), EDN: PWYRFB.

Tsypkin, G. G. (2009), *Flows with Phase Transitions in Porous Media*, 232 pp., Fizmatlit (in Russian).

Vasiliev, V. I., A. M. Maksimov, E. E. Petrov, and G. G. Tsypkin (1996), *Heat and Mass Transfer in Freezing and Thawing Soils*, 224 pp., Fizmatlit, Nauka, Moscow (in Russian).

Yakushev, V. S. (2009), *Natural Gas and Gas Hydrate in Permafrost*, 190 pp., VNIIGAZ, Moscow (in Russian), EDN: OTRYFK.

Russian Journal of Earth Sciences

Венд-кембрийские породы Верхне-Каларской грабен-синклинали юга Сибирского кратона: минералогия и особенности геохимии главных петрогенных элементов

С. И. Меренкова[1,*], Т. Г. Кузьмина[2], Е. В. Карпова[3], Р. Р. Габдуллин[2,3], В. Ю. Водовозов[3,4], Т. В. Ромашова[2], и И. В. Хохлова[2]

[1]Институт океанологии им. П. П. Ширшова РАН, Москва, Россия
[2]Институт геохимии и аналитической химии им. В. И. Вернадского РАН, Москва, Россия
[3]Московский государственный университет им. М. В. Ломоносова, Москва, Россия
[4]Геологический институт РАН, Москва, Россия
* **Контакт:** Софья Ивановна Меренкова, koshelevasof@mail.ru

Рассматриваются особенности минерального и химического состава (главные петрогенные элементы) венд-кембрийских пород силимкунской свиты (V-Є$_1$*sl*), обнажающихся на западном борту Верхне-Каларской грабен-синклинали на юго-западе Алданского щита. Изученные породы – песчаники и алевролиты, относятся к аркозам и субаркозам. По хемотипу они отвечают преимущественно нормосилитам и миосилитам. По величине щелочного модуля песчаники и алевролиты являются гиперкалиевыми и служат довольно ярким примером продуктов докембрийского аридного выветривания. Обсуждается нормативный минеральный состав, его вариации, валидность расчетов по данным петрографических исследований, проблемы использования климатических индексов и литохимических диаграмм, направленных на реконструкцию климатических параметров геологического прошлого. Значения индекса химической изменчивости CIA (Chemical Index of Alteration) песчаников и алевролитов варьируют от 49, что соответствует практически неизмененной породе, до 67 ($\text{CIA}_{\text{среднее}} = 58$). Характерные для алевролитов силимкунской свиты с высоким гидролизатным модулем (ГМ) (миосилиты) значения CIA (63–67, $\text{CIA}_{\text{среднее}} = 65$) указывают на доминирование физического выветривания во время формирования исходных для них осадков. Незначительные изменения в величине CIA для данной выборки связаны, в первую очередь, с вариациями содержание иллитного цемента и обломочного мусковита. Значения индекса химического выветривания RW (Robust Weathering) варьируются от 37 до 68 (в среднем около 57).
Ключевые слова: венд, кембрий, Удокан, климат, индикаторы выветривания.

Цитирование: Меренкова, С. И., Т. Г. Кузьмина, Е. В. Карпова, Р. Р. Габдуллин, В. Ю. Водовозов, Т. В. Ромашова, и И. В. Хохлова Венд-кембрийские породы Верхне-Каларской грабен-синклинали юга Сибирского кратона: минералогия и особенности геохимии главных петрогенных элементов // Russian Journal of Earth Sciences. — 2024. — Т. 24. — ES4009. — DOI: 10.2205/2024es000923 — EDN: DNFGSX

https://elibrary.ru/dnfgsx

Получено: 16 февраля 2024 г.
Принято: 15 июля 2024 г.
Опубликовано: 20 ноября 2024 г.

Введение

Несмотря на длительную историю изучения протерозойских-раннепалеозойских осадочных пород Удокана (в первую очередь – как источников рудных полезных ископаемых), остался ряд слабоизученных образований. В частности – силимкунская свита.

Рассматриваемые обнажения венд-кембрийских пород силимкунской свиты (V-Є$_1$*sl*) расположены на западном борту Верхне-Каларской грабен-синклинали на юго-западе Алданского щита, в междуречье рек Чина (верхнее течение Калара) и Кемена. Силимкунская (ранее выделялась как пестроцветная Є$_1$*ps*) свита согласно залегает на бараксанской свите (V*br*), граница с которой проводится по появлению в разрезе красноцветных терригенно-карбонатных пород [*Макарьев и др.*, 2010]. Делится на две пачки – нижнюю красноцветную терригенно-карбонатную, представленную переслаивающимися красноцветными песчаниками, аргиллитами, реже алевролитами с сероцветными доломитами и известняками, и верхнюю сероцветную, преимущественно карбонатную (доломиты). По водорослям, строматолитам, микрофитолитам и следам ползания червеобразных организмов определен венд-нижнекембрийский возраст свиты [*Государственная геологическая карта Российской Федерации масштаба 1 : 1 000 000, новая серия, лист O-(50) 51 и объяснительная записка*, 1998; *Дольник*, 2000; *Макарьев и др.*, 2010]. На поверхностях напластования встречаются хорошо сохранившиеся волновая рябь и глиптоморфозы галита. Породы свиты формировались в мелководных морских условиях [*Пахомов и Барабашева*, 1990].

Целью работы являлось изучение минерального состава и особенностей распределения главных петрогенных элементов в песчаниках и алевролитах силимкунской свиты. На основе имеющихся литологических, петрографических и геохимических данных рассмотрено взаимоотношение лито-, петро- и хемотипов исследуемых пород, а также обсуждаются отдельные аспекты применения индексов выветривания.

Материалы и методы исследования

Песчаники силимкунской свиты из нижней красноцветной подсвиты отобраны В. Ю. Водовозовым с целью палеомагнитного анализа, обрезки этих образцов послужили исходным материалом для настоящих исследований. Отбор проводился из отдельных точек-сайтов. Мощность свиты в разрезе на берегу р. Кемен составляет 283 м, полная мощность превышает 300 м (по литературным данным [*Государственная геологическая карта Российской Федерации*, 2004]). Обнажение 4-1 с видимой мощностью 6 м расположено в пойме ручья Кильчерис (левый приток р. Чина), обнажения 9 и 10, каждое мощностью 15–20 м, расположены в 9 км к СВ от 4-1 в верхнем течении р. Кемен (рис. 1), расстояние между обнажениями 9 и 10–300 м. По расположению точек отбора относительно контакта с нижележащей бараксанской свитой можно определить относительную возрастную последовательность изученных отложений: наиболее древними являются породы обнажения 9, затем 10 и выше залегают породы обнажения 4-1.

Для определения химического состава проб использован рентгенофлуоресцентный волнодисперсионный спектрометр Axios Advanced (PANalytical B. V., Голландия). Рентгенофлуоресцентный анализ (РФА) выполнен в лаборатории методов исследования и анализа веществ и материалов ГЕОХИ РАН (аналитики Т. Г. Кузьмина, Т. В. Ромашова, И. В. Хохлова).

На основе результатов РФА выполнен расчет нормативного минерального состава с применением программы MINLITH [*Розен и др.*, 2000; *Rosen et al.*, 2004]. Ошибка вычислений по программе MINLITH для большинства случаев находится в пределах 5–15 отн.%, и только при содержаниях минерала менее 5 мас.%, она достигает 60–70 отн.% [*Розен и Аббясов*, 2003]. По этой причине в текущем исследовании рассматриваются данные по наиболее значимым в процентном отношении содержаниям минералов, что, даже с поправкой на вышеуказанную ошибку, позволяет судить об определенных изменениях в составе пород.

Методические аспекты, связанные с расчетом индекса химической изменчивости CIA (Chemical Index of Alteration), индекса химического выветривания RW (Robust Weathering) и тетраэдрического пространства A−CN−K−FM подробно представлены в [*Babechuk and Fedo*, 2023; *Fedo and Babechuk*, 2023] и разделе «Обсуждение» настоящей работы.

Результаты

Содержание петрогенных оксидов приведены в табл. 1. Для изучаемых пород (песчаников и алевролитов) силимкунской свиты характерны содержания SiO_2 50–77% (в среднем 62,5%), Al_2O_3 4–10% (в среднем 7%), K_2O 3–5%, $Fe_2O_{3(total)}$ до 6%, MgO до 8%. Содержание CaO варьирует от 2 до 8% (в среднем 5,6%). Содержание Na_2O – 0,17–0,29%. P_2O_5 в среднем составляет 0,11%, MnO – 0,1%, TiO_2 – 0,53%. На основе содержания главных петрогенных оксидов далее выполнен расчет нормативного минерального состава, а также обсуждаемых индексов и модулей.

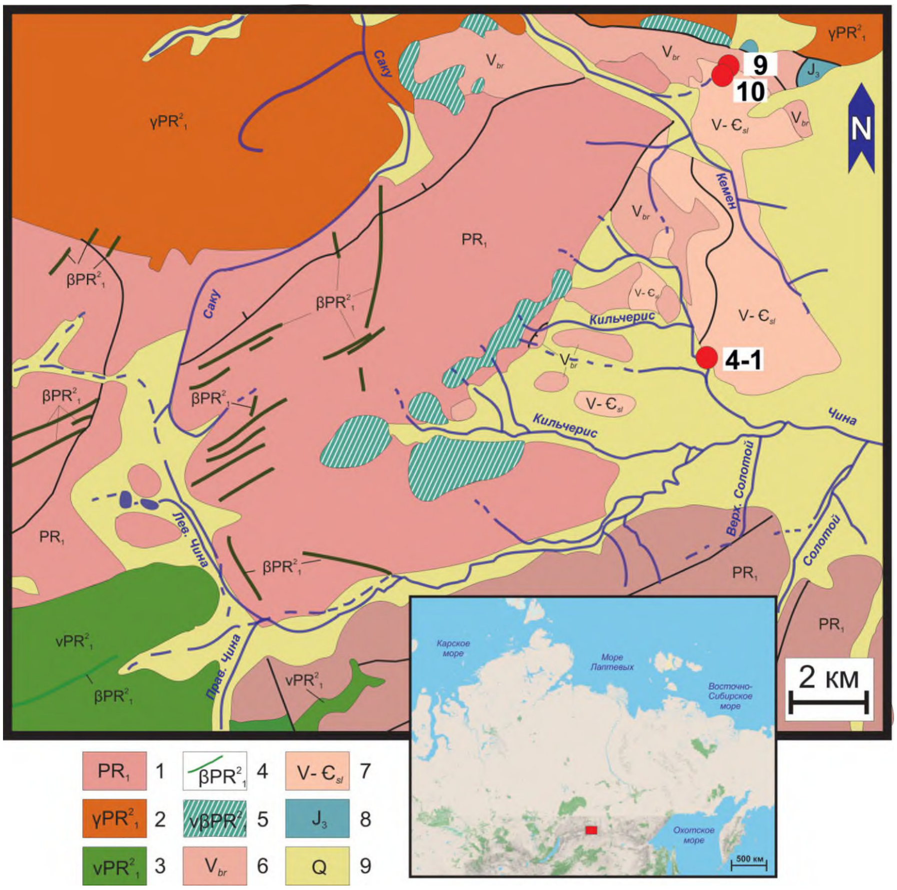

Рис. 1. Положение исследованных авторами выходов пород силимкунской свиты по ([*Государственная геологическая карта Российской Федерации*, 2004], с изменениями). 1 – метаосадочные породы удоканского комплекса нижнего протерозоя; 2 – гранитоиды кодарского комплекса нижнего протерозоя; 3 – габброиды чинейского комплекса нижнего протерозоя; 4, 5 – габбродолериты доросского комплекса нижнего протерозоя (4 – дайки долеритов, 5 – силлы габбродолеритов); 6, 7 – терригенно-карбонатные породы верхнекаларской серии (6 – бараксанская свита венда, 7 – силимкунская свита венда – нижнего кембрия); 8 – верхнеюрские терригенные породы чепинской свиты; 9 – четвертичные отложения.

Петрографические исследования в шлифах

Исследуемые породы силимкунской свиты представлены песчаниками мелко-тонкозернистыми (с примесью среднепесчаного материала и единичными зернами крупнопесчаной размерности) и глинистыми алевролитами. Состав: кварц (70–75%), полевые шпаты (ПШ) (20–27%, представлены калиевыми полевыми шпатами и плагиоклазами). Литокласты (до 5%). Среди них присутствуют обломки вулканитов и метаморфических пород. Магматические породы представлены измененными обломками гранитоидов, а также кислых эффузивов с афировой структурой, в составе которых наблюдается кварц, тонкие кварцево-полевошпатовые сростки и рудные минералы. Осадочные породы присутствуют в образцах 4-1-10, 9-7, 10-6, 10-9 и представлены крупнозернистыми обломками аргиллитов, а в 10-9 – также глинистых известняков (известковых аргиллитов). Среди обломков метаморфических пород наблюдаются полуокатанные кварциты с микрогранобластовой структурой. Слюды (единичные чешуйки) – биотит и, реже, мусковит. Тяжелые акцессории – единичные измененные (серпентинизированные) пироксены, единичные сфены, цирконы. В отдельных образцах присутствует ставролит. Преобладает поровый тонкокристаллический доломитовый цемент (от 7 до 20%); также фиксируются: пленочный иллит-гематитовый цемент (до 7%) и регенерационный кварцевый и полевошпатовый цементы (1–3%).

Таблица 1. Химический состав пород силимкунской свиты (мас.%)

Образец	SiO_2	TiO_2	Al_2O_3	Fe_2O_3	MnO	MgO	CaO	Na_2O	K_2O	P_2O_5	ППП*	Σ
4-1-1	66,49	0,48	8,84	3,16	0,09	5,66	3,61	0,26	4,16	0,10	7,25	100,10
4-1-2	69,11	0,39	6,62	2,03	0,15	5,08	4,70	0,26	3,79	0,08	7,94	100,14
4-1-3	61,71	0,70	9,44	3,52	0,11	6,53	4,32	0,24	4,34	0,14	9,03	100,08
4-1-4	55,50	0,62	9,20	3,96	0,12	7,81	6,19	0,21	4,05	0,13	12,42	100,21
4-1-6 (a)	53,33	0,69	10,10	4,91	0,12	8,18	5,83	0,2	4,03	0,13	12,63	100,15
4-1-7 (a)	71,33	0,36	6,69	2,30	0,10	4,91	3,82	0,24	3,66	0,07	6,7	100,17
4-1-8 (a)	58,84	0,58	8,18	3,61	0,12	7,24	6,03	0,18	3,90	0,12	11,34	100,14
4-1-9 (a)	53,39	0,67	8,91	4,46	0,11	7,71	6,93	0,19	3,89	0,13	13,86	100,24
4-1-10	67,94	0,25	5,43	2,00	0,13	5,22	5,86	0,23	3,33	0,06	9,65	100,10
4-1-11	53,80	0,68	7,91	4,25	0,13	7,62	7,49	0,18	3,67	0,13	14,43	100,27
4-1-13 (a)	51,85	0,69	8,95	4,92	0,11	7,92	7,08	0,17	3,93	0,12	14,49	100,22
4-1-14	71,78	0,35	6,71	2,51	0,09	4,86	3,47	0,23	3,76	0,08	6,35	100,18
4-1-15 (a)	60,88	0,88	10,37	5,84	0,07	6,24	3,12	0,21	4,69	0,17	7,43	99,89
4-1-17	60,49	0,51	6,07	2,56	0,15	6,50	7,23	0,2	3,51	0,12	12,74	100,09
4-1-18	53,02	0,64	7,54	4,17	0,13	7,73	7,79	0,18	3,81	0,13	15	100,15
4-1-19 (a)	56,36	0,79	9,81	5,44	0,10	7,35	5,02	0,19	4,51	0,17	10,56	100,29
4-1-20 (a)	55,17	0,66	9,41	5,47	0,11	7,52	5,66	0,19	4,21	0,12	11,66	100,19
4-1-21 (a)	50,17	0,59	9,20	5,20	0,12	8,41	7,19	0,19	4,08	0,11	14,98	100,23
9-1	62,99	0,39	4,53	1,66	0,10	5,84	8,00	0,22	3,34	0,06	12,82	99,95
9-3	65,83	0,41	4,63	1,48	0,10	5,18	6,94	0,22	3,27	0,09	11,95	100,09
9-7	72,48	0,63	6,10	1,96	0,07	3,26	4,00	0,27	4,42	0,10	6,93	100,22
9-14	71,55	0,15	4,22	1,21	0,09	4,07	5,97	0,29	3,29	0,05	9,23	100,12
9-15	70,92	0,61	6,08	1,75	0,08	3,63	4,52	0,29	4,45	0,08	7,88	100,29
10-4	74,01	0,27	5,01	1,95	0,10	3,06	3,75	0,23	3,90	0,05	7,88	100,21
10-5	68,03	0,38	6,07	1,67	0,08	4,54	5,42	0,24	4,43	0,08	9,23	100,17
10-6	77,13	0,57	6,80	1,86	0,03	2,05	2,20	0,25	5,42	0,09	3,85	100,24
10-9	67,43	0,40	6,27	2,15	0,08	4,71	5,20	0,21	4,57	0,08	9,08	100,17
10-11	54,67	0,33	6,80	2,90	0,11	7,45	8,19	0,17	4,24	0,08	15,15	100,09
10-13	60,01	0,58	7,76	3,83	0,09	6,31	5,79	0,18	4,83	0,15	10,68	100,21
10-15	59,76	0,58	8,18	4,35	0,08	6,60	5,37	0,17	4,64	0,15	10,39	100,27

Примечание. *ППП – потери при прокаливании. Здесь и далее в таблицах (а) обозначает алевролиты, не отмеченные образцы – песчаники.

Нормативный минеральный состав. Минеральный состав пород, рассчитанный по методу О. М. Розена [*Розен и др.*, 2000; *Rosen et al.*, 2004], представлен в табл. 2. Согласно нормативному расчету, породы содержат от 29 до 58% кварца, 13–33% полевых шпатов, глинистые минералы (иллит) в среднем составляют 11% (минимум – менее 1%, максимум 24%). Содержание доломита достигает 27% (в среднем 18%).

При сравнении результатов нормативных расчетов и петрографического изучения в шлифах обнаружены важные моменты, которые необходимо иметь в виду при дальнейшей интерпретации.

При нормативном расчете завышено относительно результатов петрографического изучения содержание ортоклаза, что связано с отсутствием возможности разделить ортоклаз и микроклин. Поэтому расчетные значения ортоклаза в данном случае скорее суммарное содержание полевых шпатов.

Таблица 2. Нормативный минеральный состав пород силимкунской свиты

Образец	Ab	An	Pl	Or	Q	Ill	Ap	Dl	Ank	Srp	Gt	Prl	Pr	Rt
4-1-1	2,22	0,24	2,46	15,48	44,6	16,97	0,23	11,43	0	5,42	2,8	0,11	0,01	0,48
4-1-2	2,04	0,22	2,26	16,19	52,8	9,95	0,17	12,14	0	3,89	2,12	0,12	0,01	0,36
4-1-3	1,54	0,16	1,7	14,54	38,7	16,01	0,3	19,43	0	5,2	3,33	0,14	0,04	0,59
4-1-4	2,21	0,23	2,44	17,54	50,46	8,85	0,19	14,98	0	3,09	1,87	0,18	0,01	0,39
4-1-6 (a)	2,07	0,22	2,29	15,55	38,87	19,1	0,35	13,67	0	6,17	3,14	0,14	0,01	0,71
4-1-7 (a)	1,81	0,19	2	13,52	33,97	19,71	0,31	20,09	0	5,98	3,61	0,15	0,02	0,63
4-1-8 (a)	1,74	0,18	1,92	11,17	31,04	24,09	0,31	19	0	7,07	4,55	0,15	0	0,71
4-1-9 (a)	1,64	0,17	1,81	12,75	33,29	19,41	0,31	22,6	0	4,78	4,22	0,13	0	0,69
4-1-10	1,95	0,21	2,16	16,34	52,18	6,05	0,15	18,91	0	1,83	1,96	0,16	0,01	0,25
4-1-11	1,55	0,17	1,72	13,21	35,38	16,06	0,32	24,41	0	3,95	4,11	0,15	0	0,69
4-1-13 (a)	1,48	0,16	1,64	12,97	31,69	19,63	0,3	23,22	0	4,98	4,75	0,13	0	0,71
4-1-14	1,96	0,21	2,17	17	52,85	9,66	0,19	10,99	0	4,3	2,37	0,11	0,01	0,35
4-1-15 (a)	1,8	0,19	1,99	16,21	36,08	21,86	0,41	9,59	0	7,21	5,66	0,08	0	0,9
4-1-17	1,71	0,18	1,89	16,4	44,05	8,31	0,3	23,38	0	2,44	2,5	0,18	0,03	0,52
4-1-18	1,56	0,17	1,73	15,44	34,47	13,74	0,32	25,48	0	3,87	4,14	0,16	0	0,66
4-1-19 (a)	1,64	0,17	1,81	15,88	32,63	20,38	0,42	15,94	0	6,75	5,27	0,12	0	0,8
4-1-20 (a)	1,64	0,17	1,81	14,3	32,97	20,05	0,3	18,32	0	6,13	5,32	0,13	0	0,68
4-1-21 (a)	1,65	0,18	1,83	13,75	28,92	19,94	0,28	23,68	0	5,78	5,07	0,15	0	0,61
9-1	1,87	0,2	2,07	18,64	48,56	2,1	0,14	25,97	0	0,26	1,76	0,12	0	0,39
9-3	1,88	0,2	2,08	17,94	51,83	2,89	0,21	22,53	0	0,46	1,53	0,12	0,01	0,41
9-7	2,29	0,24	2,53	24,35	53,23	3,44	0,23	12,62	0	0,84	2,04	0,08	0	0,63
9-14	2,45	0,26	2,71	19,2	56,99	0,38	0,11	18,53	0,83	0	0,98	0,11	0,01	0,15
9-15	2,47	0,26	2,73	24,74	51,54	3,06	0,2	14,39	0	0,83	1,82	0,09	0	0,61
10-4	1,98	0,21	2,19	22,66	58,04	1,48	0,13	12,17	0	0,8	2,14	0,12	0	0,27
10-5	2,04	0,22	2,26	24,39	48,74	3,52	0,19	17,45	0	1,27	1,71	0,09	0	0,38
10-6	2,12	0,23	2,35	31,02	54,16	1,94	0,2	6,72	0	1,02	1,99	0,03	0	0,57
10-9	1,79	0,19	1,98	24,98	47,49	4,02	0,2	16,72	0	1,9	2,23	0,09	0	0,4
10-11	1,47	0,16	1,63	20,89	35,63	8,4	0,2	27	0	2,86	2,92	0,13	0	0,34
10-13	1,54	0,16	1,7	23,57	37,59	9,66	0,37	18,48	0	4,04	3,89	0,11	0	0,58
10-15	1,46	0,16	1,62	20,84	37,35	12,58	0,37	17,14	0	5,06	4,36	0,1	0	0,59

Примечание. Ab – альбит, An – анортит, Pl – плагиоклаз, Or – ортоклаз, Q – кварц, минералы кремнезема, Ill – иллит, Ap – апатит, Dl – доломит, Ank – анкерит, Srp – серпентин, Gt – гётит, Prl – пиролюзит., Pr – пирит, Rt – рутил. При содержаниях минерала менее 5 мас.%, ошибка достигает 60–70 отн.% [*Розен и Аббясов*, 2003].

Представляется несколько завышенным количество иллита при нормативном расчете. Это связано, по-видимому, с попаданием в его расчетное количество мусковита. Иллит и мусковит – слоистые силикаты, причем иллит часто является продуктом гидролиза мусковита. Поэтому в данном случае количественные значения по содержанию иллита правильнее будет назвать количеством слоистых силикатов. Проблемой является то, что иллит находится в составе цемента, а мусковит – в обломочной части, и объединение их в общую величину не является информативным.

Стоит отметить, что ранее, при сравнении MINLITH и Mincomp [*Regelink*, 2014], также было обнаружено повышенное количество иллита при расчете в MINLITH. Автор [*Regelink*, 2014] указывает как причины следующее: 1) разница распределении калия между различными минералами (иллит, мусковит, ортоклазом); 2) различие в молекулярной формуле иллита, т.к. разработчики MINLITH [*Rosen et al.*, 2004] включают в него также железо и магний, в результате чего молярная масса минерала значительно увеличивается.

При этом расчётное количество доломита соответствует фактическому.

Обсуждение

Взаимоотношение лито-, петро- и хемотипов

В соответствии с результатами изучения в шлифах и положением точек составов на классификационной диаграмме $\log(Na_2O/K_2O) - \log(SiO_2/Al_2O_3)$ [*Петтиджон и др.*, 1976], песчаники силимкунской свиты относятся к аркозам и субаркозам (рис. 2).

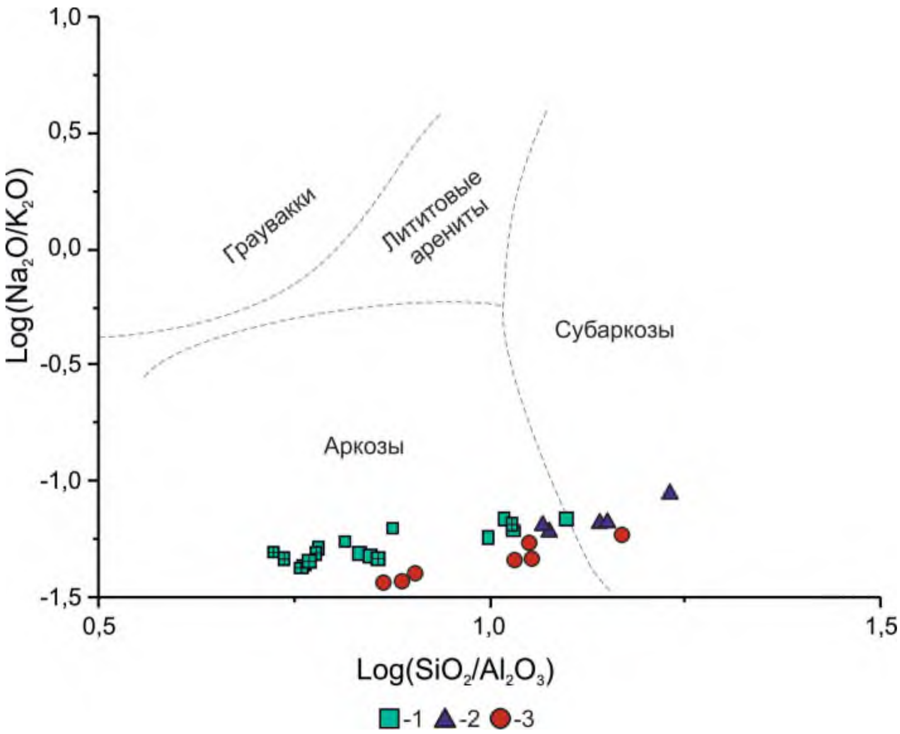

Рис. 2. Классификационная диаграмма [*Петтиджон и др.*, 1976] для песчаников и алевролитов силимкунской свиты. 1 – обнажение 4-1, 2 – обнажение 9, 3 – обнажение 10, крестом отмечены алевролиты.

На основе петрохимических модулей возможно произвести деление пород на хемотипы. Гидролизатный модуль (ГМ) предназначен для количественной оценки выщелачивания и гидролиза. На его основе породы подразделяются на силиты (ГМ $< 0,3$), сиаллиты и сиферлиты (ГМ = 0,31–0,55), гидролизаты (ГМ $> 0,55$) [*Юдович и Кетрис*, 2000]. Изучаемые песчаники и алевролиты силимкунской свиты относятся к хемотипу силиты (рис. 3А, Б). По величине MgO > 3% изучаемые породы, согласно классификации, должны быть отнесены к псевдосилитам. В псевдосилитах и псевдосиаллитах носителем магния является хлорит, монтмориллонит или биотит [*Юдович и Кетрис*, 2000]. В нашем случае достоверно известно, что за высокую магнезиальность отвечает доломит и отнесение к псевдосилитам некорректно.

Собственно силиты подразделяются на классы – гиперсилиты, суперсилиты, нормосилиты и миосилиты [*Юдович и Кетрис*, 2000]. Изучаемые породы силимкунской свиты относятся, в большинстве своем, к нормо- ($n = 15$) и миосилитам ($n = 13$), 2 образца относятся к суперсилитам. Суперсилиты отличают значения ГМ в интервале от 0,06 до 0,10. Для изучаемых пород, аттестованных как суперсилиты, характерна повышенная (относительно других образцов) величина модуля нормированной щёлочности (НКМ) – 0,83–0,85, что обусловлено высоким содержанием полевых шпатов. Также в этих образцах наблюдается наибольшее количество кварца (57–58%), что характерно для суперсилитов.

К нормосилитам относят породы с величиной ГМ 0,11–0,2. В этот класс входят преимущественно песчаники ($n = 14$) и один алевролит с нормативным содержанием полевых шпатов от 16 (в алевролите) до 33%. Количество глинисто-слюдистой части варьируется от 2 до 25%.

Для миосилитов значения ГМ находятся в диапазоне 0,21–0,3. К миосилитам относятся породы с повышенной долей полевошпатового и/или глинисто-слюдистого материала [*Юдович и Кетрис*, 2000]. Среди исследуемых пород силимкунской свиты как миосилиты аттестуются алевролиты ($n = 8$) и некоторые песчаники ($n = 5$), в которых разница между количеством ПШ и глинисто-слюдистых минералов 1–8% (содержание 15–22% и 12–21% соответственно, согласно нормативному расчету).

По величине щелочного модуля (ЩМ) изучаемые силиты являются гиперкалиевыми (ЩМ, 0,04–0,09, $Na_2O + K_2O$ от 3,5 до 5,7%). По мнению Я. Э. Юдовича и М. П. Кетрис [*Юдович и Кетрис*, 2000], такие образования как щелочные силиты, являются характерным продуктом докембрийского аридного выветривания.

Величина титанового модуля (ТМ, TiO_2 / Al_2O_3) находится в пределах 0,035–0,1 (в среднем 0,07), железного (ЖМ, $(Fe_2O_3 + FeO + MnO) / (TiO_2 + Al_2O_3)$) – от 0,26 до 0,55 (в среднем 0,4). Корреляция титанового и железного модулей отсутствует (рис. 3). Величины модулей для исследуемых пород по хемотипам представлены в табл. 3. Фемический модуль (ФМ, $(Fe_2O_3 + FeO + MnO + MgO) / SiO_2$) для пород не рассчитывался из-за высокого содержания доломита.

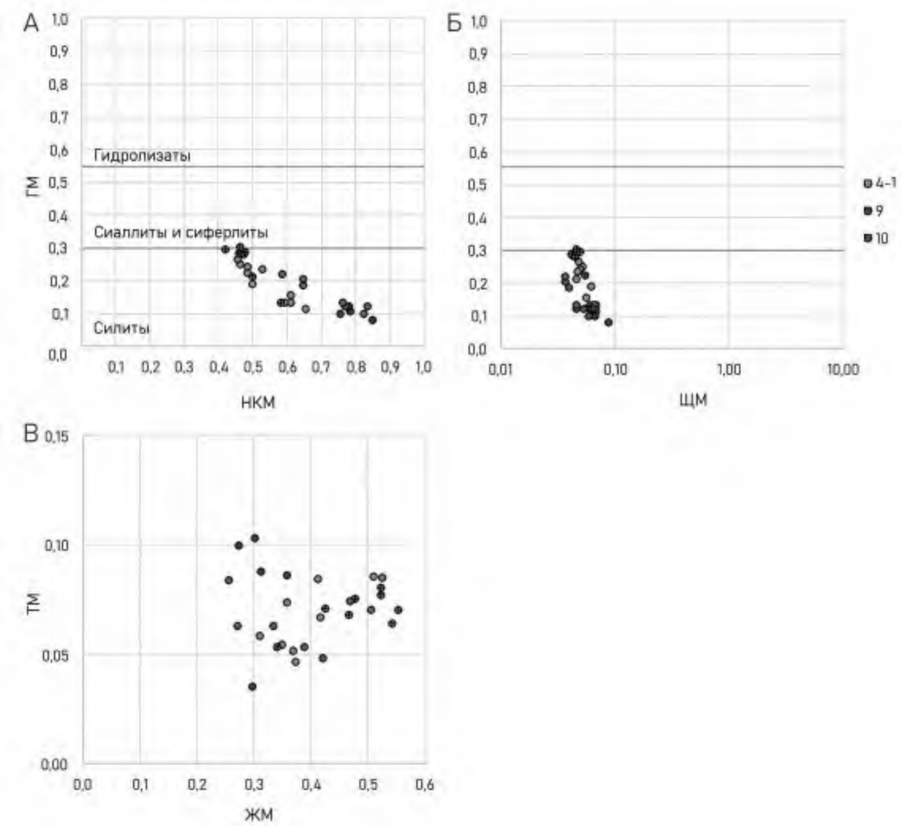

Рис. 3. Модульные диаграммы по [*Юдович и Кетрис*, 2000] для пород силимкунской свиты. Условные обозначения: 4-1 – обнажение в пойме ручья Кильчерис, 9 и 10 – обнажения в верхнем течении р. Кемен, крестом отмечены алевролиты.

Таблица 3. Хемотипы по [*Юдович и Кетрис*, 2000] для песчаников и алевритов силимкунской свиты

Класс	ГМ	ТМ	ЖМ	НКМ	ЩМ
Миосилиты	0,21–0,30	0,06–0,09	0,36–0,55	0,42–0,59	0,04–0,06
Нормосилиты	0,11–0,20	0,05–0,10	0,26–0,47	0,50–0,83	0,04–0,07
Суперсилиты	0,08–0,10	0,04–0,05	0,30–0,39	0,83–0,85	0,06–0,09

Минералогия и диагностика типа выветривания

Изучение выветривания, его типа, характера и динамики, является одним из ключевых инструментов для понимания климатических условий в геологическом прошлом. Химическое выветривание оказывает сильное влияние на углеродный цикл, улавливая атмосферный углерод в виде растворенных продуктов изменения силикатов, переносимых водными потоками в океан. Первичная продукция «запускается» питательными веществами (C, Si, P, N, Ca), которые образуются в результате континентального выветривания [*Lécuyer*, 2016].

До настоящего времени исследователи совершенствуют способы оценки воздействия на породы выветривания, последующего преобразования и вариаций состава пород источника сноса, искажающих палеоклиматические реконструкции. После широкого внедрения в научную практику индекса CIA [*Nesbitt and Young*, 1982], возникла необходимость коррекции этого показателя ввиду влияния на него состава материнских пород (например, [*Lo et al.*, 2017]), эффекта сортировки, диагенеза и метасоматоза [*Fedo et al.*, 1995; *Guo et al.*, 2018]. Также ограничением CIA является то, что он не учитывает роль мафических (оливин, пироксен, амфибол, биотит) и вторичных глинистых минералов (например, смектит, вермикулит, хлорит) в общем составе формируемых терригенных осадочных пород [*Fedo and Babechuk*, 2023].

Логичным следующим шагом стал перевод трендов выветривания в двумерное пространство путем построения тройных диаграмм. Такой тип диаграмм расширил возможности количественного сопоставления данных по терригенным породам, а также позволил сравнивать эмпирические химические тренды с прогнозируемыми для выветривания. С помощью проекции в системе $Al_2O_3 - (CaO^* + Na_2O) - K_2O$ (A – CN – K) по разнице между составом отложений и прогнозируемым трендом выветривания стало возможно выполнить поправку CIA [*Fedo et al.*, 1995].

Важный аспект как CIA, так и тройных диаграмм – влияние наличия кальцита, апатита, биогенного кремнезема и диагенетического кремнёвого цемента в породе. При расчете/построении вышеуказанных индексов необходим некарбонатный CaO*, который нередко можно оценить только косвенно в богатых карбонатами терригенных породах. Предварительная обработка образцов соляной кислотой для устранения карбонатов несет свои риски – например, растворение некоторых глинистых минералов. Можно выполнить поправку на основе измеренных содержаний CO_2 и P_2O_5. Если данных по CO_2 нет, то вносят приблизительные поправки, приняв рациональные соотношения Ca / Na в силикатном материале [*McLennan*, 1993]. Если после корректировки на P_2O_5 оставшееся количество молей меньше, чем у Na_2O, его принимают за значение CaO*. В противном случае CaO* принимается равным Na_2O. Этот подход основан на том, что Ca при выветривании обычно теряется быстрее, чем Na. Наибольшее расхождение с реальным значением CIA (до 3 единиц) будет при его промежуточном значении 60–80, так как при низком CIA этот подход в целом справедлив, а при высоком CIA концентрации Na и Ca низкие, и неопределенности мало влияют на CIA [*McLennan*, 1993]. Это наиболее легко реализуемая поправка, но, тем не менее, несколько влияющая на точность.

Составы пород силимкунской свиты интегрированы в трехмерное тетраэдрическое пространство [*Fedo and Babechuk*, 2023], которое можно разделить на отдельные двумерные грани (рис. 4). Одна из граней позволяет скорректировать CIA в системе A–CN–K. В породах силимкунской свиты не обнаружен кальцит или апатит в значимых количествах, но содержится доломит, поэтому CaO* корректировался как описано выше [*McLennan*, 1993]. Величина CIA для изучаемых пород силимкунской свиты низкая. Минимальные его значения составляют 49–50 что соответствует практически невыветрелой породе. Например, CIA кислых магматических пород около 50 (для основных пород – менее 40) [*Fedo and Babechuk*, 2023]. Максимальные значения CIA достигают 67 (в среднем 58). Граница преобладания химического выветривания над физическим проводится при значении CIA 70–75 [*Fedo and Babechuk*, 2023]. Характерные для алевролитов силимкунской свиты с высоким ГМ (миосилиты) значения CIA (63–67, в среднем 65) указывают на доминирование физического выветривания во время формирования исходных для них осадков. Но на значения CIA в данном случае повлияло содержание иллитного цемента и мусковита, демонстрируя более высокие значения индекса, не связанные с изменением выветривания. В рассматриваемом случае, этим не стоит пренебрегать, т.к. диагенетический иллит и обломочные слюды увеличивают значение индекса CIA в отсутствии других глинистых минералов – продуктов разрушения пород непосредственно во время седиментогенеза, искажая первичную картину.

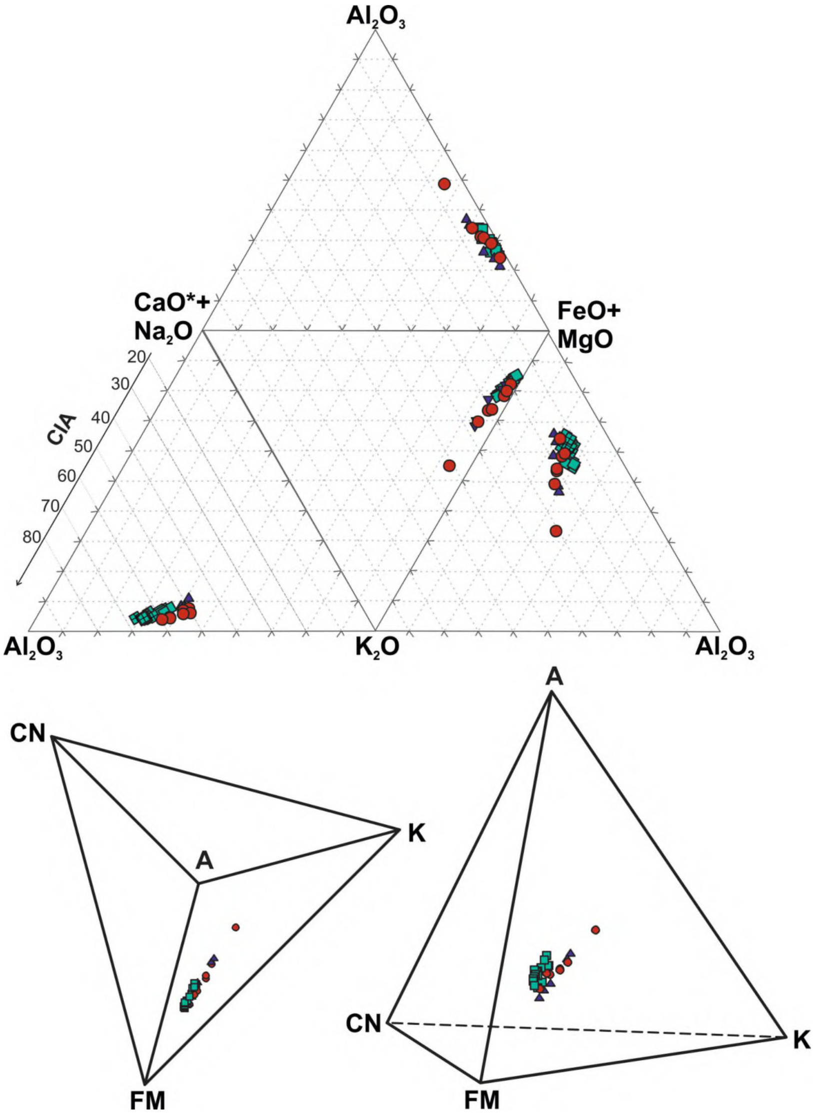

Рис. 4. Положение составов пород силимкунской свиты в композиционном пространстве A–CN–K–FM – развернутом и трехмерном (диаграмма по [*Fedo and Babechuk*, 2023]).

Недавно был предложен [*Cho and Ohta*, 2022] другой вариант для решения проблемы аутигенных и биогенных примесей – индекс RW, который получен с использованием многомерных статистических методов на основе геохимической базы данных магматических пород и профилей их выветривания. По мнению авторов индекса, RW не зависит от содержания SiO_2, CaO и P_2O_5. Визуально индекс RW может быть представлен как в одномерном виде, так и двумерной тройной диаграммой.

Значения RW для пород силимкунской свиты варьируют от 37, что близко к составу невыветрелой породы, до 68 (рис. 5). Для алевролитов, аттестованных как миосилиты, значение RW находятся в диапазоне 62–68. Несмотря на то, что при построении двумерного пространства M–F–RW используется MgO, количество доломита не влияет на значения индекса RW. Также не обнаруживается видимой связи между RW и фактическим содержанием глинисто-гематитового цемента и литокластов.

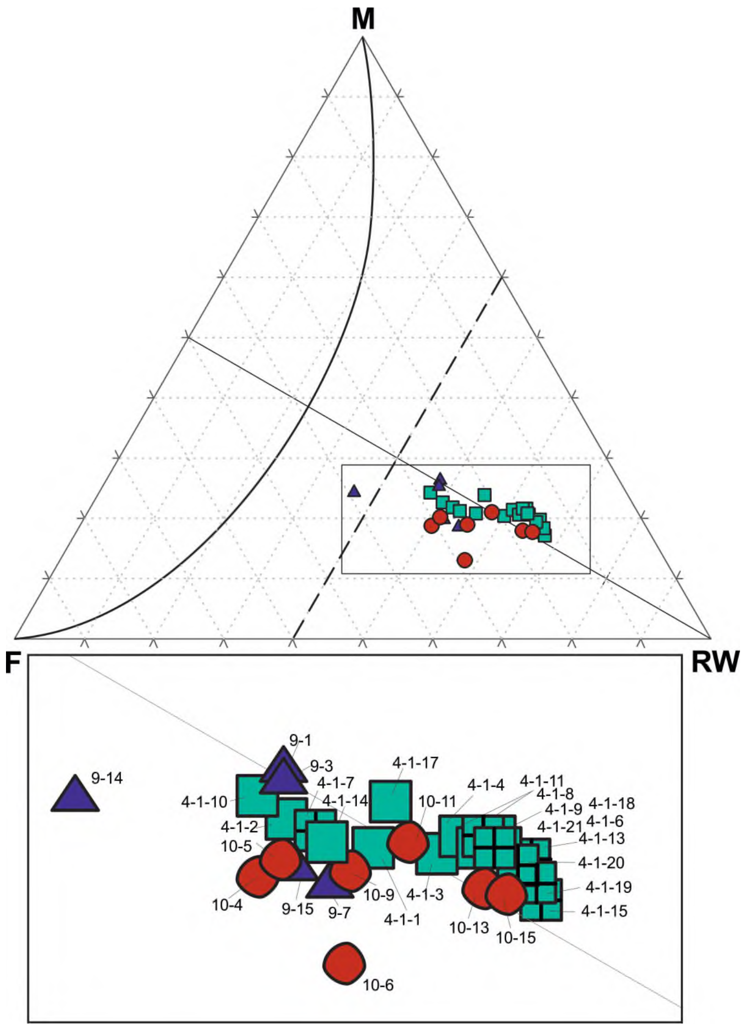

Рис. 5. Тройная диаграмма M-F-RW (Mafic–Felsic–RW, [*Cho and Ohta*, 2022]) и положение на ней точек составов силимкунской свиты.

Авторы публикации [*Cho and Ohta*, 2022] рассчитали RW для почв различных климатических зон. В результате установлено, что в аридных областях и в арктическом климате почвы и коры выветривания имеют низкий RW (в среднем 10–30). В гумидных областях значения RW находятся в диапазоне 70–95. При этом, как и в случае с другими показателями выветривания, нельзя разделить влияние температуры и влажности на выветривание. В случае реконструкций эти значения не стоит принимать как определяющие – RW является относительным параметром.

Выводы

По результатам изучения минерального состава и его вариаций, приняв во внимание вышеописанные нюансы использования нормативного расчета, индексов и литохимических диаграмм, установлены следующие особенности обломочных пород силимкунской свиты (венд-кембрий) Верхне-Каларской грабен-синклинали.

Изученные породы – песчаники и алевролиты, относятся к аркозам и субаркозам. По хемотипу они отвечают преимущественно нормосилитам и миосилитам классификации Я. Э. Юдовича и М. П. Кетрис. По величине щелочного модуля изучаемые силиты являются гиперкалиевыми и служат довольно ярким примером продуктов докембрийского аридного выветривания. Значения индекса CIA для них варьируют от 49, что соответствует практически неизмененной породе, до 67. Незначительные изменения в величине индекса для данной выборки связаны, в первую очередь, с вариациями содержания иллита в цементе и мусковита, демонстрируя более высокие значения индекса, не связанные с изменением выветривания. Значения RW варьируют от 37 до 68 (в среднем около 57).

Полученные результаты для небольшой части разреза силимкунской свиты являются ступенью к диагностике питающих провинций, направления сноса и уточнению истории седиментогенеза в Верхне-Каларской грабен-синклинали юга Сибирского кратона.

Благодарности. Авторы выражают глубокую благодарность анонимным рецензентам за ценные замечания и конструктивные предложения по преобразованию статьи, которые позволили существенно улучшить рукопись. Исследование выполнено в рамках госзадания ИО РАН FMWE-2024-0020. Аналитические работы выполнены при поддержке госзадания ГЕОХИ РАН. Частичное финансирование за счет субсидий на выполнение госзаданий ГИН РАН FMMG-2023-0007 и МГУ АААА-А16-116033010119-4 и АААА-А16-116033010120-0.

Список литературы

Государственная геологическая карта Российской Федерации масштаба 1 : 200 000. Издание второе. Удоканская серия. О-50-XXXV(Наминга) / под ред. Г. Л. Митрофанова. — ВСЕГЕИ, 2004.

Государственная геологическая карта Российской Федерации масштаба 1 : 1 000 000, новая серия, лист О-(50) 51 и объяснительная записка / под ред. Е. П. Миронюка. — СПб : ВСЕГЕИ, 1998. — 428 с.

Дольник Т. А. Строматолиты и микрофитолиты в стратиграфии рифея и венда складчатого обрамления Сибирской платформы. — Новосибирск : Наука, 2000. — 320 с.

Макарьев Л. Б., Митрофанов Г. Л., Митрофанова Н. Н. *и др.* Государственная геологическая карта Российской Федерации масштаба 1 : 1 000 000 (третье поколение). Серия Алдано-Забайкальская. Лист О-50 - Бодайбо. Объяснительная записка. — СПб : Картографическая фабрика ВСЕГЕИ, 2010. — 612 с.

Пахомов Н. Н., Барабашева Е. Е. Новые данные по стратиграфии и фауне венда-нижнего кембрия Верхне-Каларского грабена // Новые данные по биостратиграфии палеозоя и мезозоя юга Дальнего Востока. — Владивосток : ДВО АН СССР, 1990. — С. 24—31.

Петтиджон Ф. Д., Поттер П., Сивер Р. Пески и песчаники. — Москва : Мир, 1976. — 535 с.

Розен О. М., Аббясов А. А. Количественный минеральный состав осадочных пород: расчет по петрохимическим данным, анализ достоверности результатов (компьютерная программа MINLITH) // Литология и полезные ископаемые. — 2003. — № 3. — С. 299—312.

Розен О. М., Аббясов А. А., Мигдисов А. А. *и др.* Программа MINLITH для расчета минерального состава осадочных пород: достоверность результатов в применении к отложениям древних платформ // Геохимия. — 2000. — № 4. — С. 431—444.

Юдович Я. Э., Кетрис М. П. Основы литохимии. — СПб : Наука, 2000. — 479 с.

Babechuk M. G., Fedo C. M. Analysis of chemical weathering trends across three compositional dimensions: applications to modern and ancient mafic-rock weathering profiles // Canadian Journal of Earth Sciences. — 2023. — Vol. 60, no. 7. — P. 839–864. — DOI: 10.1139/cjes-2022-0053.

Cho T., Ohta T. A robust chemical weathering index for sediments containing authigenic and biogenic materials // Palaeogeography, Palaeoclimatology, Palaeoecology. — 2022. — Vol. 608. — P. 111288. — DOI: 10.1016/j.palaeo.2022.111288.

Fedo C. M., Babechuk M. G. Petrogenesis of siliciclastic sediments and sedimentary rocks explored in three-dimensional Al2O3-CaO*+Na2O-K2O-FeO+MgO (A-CN-K-FM) compositional space // Canadian Journal of Earth Sciences. — 2023. — Vol. 60, no. 7. — P. 818–838. — DOI: 10.1139/cjes-2022-0051.

Fedo C. M., Wayne Nesbitt H., Young G. M. Unraveling the effects of potassium metasomatism in sedimentary rocks and paleosols, with implications for paleoweathering conditions and provenance // Geology. — 1995. — Vol. 23, no. 10. — P. 921. — DOI: 10.1130/0091-7613(1995)023<0921:UTEOPM>2.3.CO;2.

Guo Y., Yang S., Su N., *et al.* Revisiting the effects of hydrodynamic sorting and sedimentary recycling on chemical weathering indices // Geochimica et Cosmochimica Acta. — 2018. — Vol. 227. — P. 48–63. — DOI: 10.1016/j.gca.2018.02.015.

Lécuyer C. Seawater residence times of some elements of geochemical interest and the salinity of the oceans // Bulletin de la Société Géologique de France. — 2016. — Vol. 187, no. 6. — P. 245–260. — DOI: 10.2113/gssgfbull.187.6.245.

Lo F.-L., Chen H.-F., Fang J.-N. Discussion of Suitable Chemical Weathering Proxies in Sediments by Comparing the Dissolution Rates of Minerals in Different Rocks // The Journal of Geology. — 2017. — Vol. 125, no. 1. — P. 83–99. — DOI: 10.1086/689184.

McLennan S. M. Weathering and Global Denudation // The Journal of Geology. — 1993. — Vol. 101, no. 2. — P. 295–303. — DOI: 10.1086/648222.

Nesbitt H. W., Young G. M. Early Proterozoic climates and plate motions inferred from major element chemistry of lutites // Nature. — 1982. — Vol. 299, no. 5885. — P. 715–717. — DOI: 10.1038/299715a0.

Regelink J. A. Mincomp-a program to calculate a likely mineralogical bulk composition from XRD and XRF results. Research Minor TA-MI-077. — Delft University of Technology, 2014.

Rosen O. M., Abbyasov A. A., Tipper J. C. MINLITH-an experience-based algorithm for estimating the likely mineralogical compositions of sedimentary rocks from bulk chemical analyses // Computers & Geosciences. — 2004. — Vol. 30, no. 6. — P. 647–661. — DOI: 10.1016/j.cageo.2004.03.011.

Russian Journal of Earth Sciences

Vendian-Cambrian Rocks of the Upper Kalar Graben-Syncline of the Southern Part of Siberian Craton: Mineralogy and Major Elements Geochemistry

S. I. Merenkova[1,*], T. G. Kuzmina[2], E. V. Karpova[3], R. R. Gabdullin[2,3], V. Yu. Vodovozov[3,4], T. V. Romashova[2], and I. V. Khokhlova[2]

[1]Shirshov Institute of Oceanology RAS, Moscow, Russia
[2]Vernadsky Institute of Geochemistry and Analytical Chemistry RAS, Moscow, Russia
[3]Lomonosov Moscow State University, Moscow, Russia
[4]Geological Institute RAS, Moscow, Russia
**Correspondence to: Sofia I. Merenkova, koshelevasof@mail.ru.

The features of the mineral and chemical composition (major elements) of the Vendian-Cambrian rocks of the Silimkun Formation (V-Є$_{1sl}$), exposed on the western side of the Upper Kalar graben syncline in the southwest of the Aldan shield, are considered. The studied rocks – sandstones and siltstones, belong to arkoses and subarkoses. According to their chemotype, they correspond normosilites and myosilites. In terms of the alkaline modulus, the studied silites are hyperpotassium and serve as a fairly striking example of the products of Precambrian arid weathering. The standard mineral composition, its variations, the validity of calculations based on petrographic research data, the problems of using climate indices and lithochemical diagrams aimed at reconstructing climatic changes in the geological past are discussed. Chemical Index of Alteration (CIA) index values range from 49, which corresponds to a virtually unchanged rock, to 67. The average is about 58. Minor changes in the index value for this sample are associated primarily with variations in the content of illite cement and muscovite. Robust Weathering index (RW) values range from 37 to 68 (with an average of about 57).

Keywords: Ediacaran, Cambrian, Udokan region, climate, chemical weathering proxies.

Recieved: 16 February 2024
Accepted: 15 July 2024
Published: 20 November 2024

Citation: Merenkova, S. I., T. G. Kuzmina, E. V. Karpova, R. R. Gabdullin, V. Yu. Vodovozov, T. V. Romashova, and I. V. Khokhlova (2024), Vendian-Cambrian Rocks of the Upper Kalar Graben-Syncline of the Southern Part of Siberian Craton: Mineralogy and Major Elements Geochemistry, *Russian Journal of Earth Sciences*, 24, ES4009, https://doi.org/10.2205/2024ES000923, EDN: DNFGSX

References

Babechuk M. G., Fedo C. M. Analysis of chemical weathering trends across three compositional dimensions: applications to modern and ancient mafic-rock weathering profiles // Canadian Journal of Earth Sciences. — 2023. — Vol. 60, no. 7. — P. 839–864. — DOI: 10.1139/cjes-2022-0053.

Cho T., Ohta T. A robust chemical weathering index for sediments containing authigenic and biogenic materials // Palaeogeography, Palaeoclimatology, Palaeoecology. — 2022. — Vol. 608. — P. 111288. — DOI: 10.1016/j.palaeo.2022.111288.

Dolnik T. A. Stromatolites and microphytolites in the stratigraphy of the Riphean and Vendian folded frame of the Siberian platform. — Novosibirsk : Nauka, 2000. — P. 320.

Fedo C. M., Babechuk M. G. Petrogenesis of siliciclastic sediments and sedimentary rocks explored in three-dimensional Al2O3-CaO*+Na2O-K2O-FeO+MgO (A-CN-K-FM) compositional space // Canadian Journal of Earth Sciences. — 2023. — Vol. 60, no. 7. — P. 818–838. — DOI: 10.1139/cjes-2022-0051.

Fedo C. M., Wayne Nesbitt H., Young G. M. Unraveling the effects of potassium metasomatism in sedimentary rocks and paleosols, with implications for paleoweathering conditions and provenance // Geology. — 1995. — Vol. 23, no. 10. — P. 921. — DOI: 10.1130/0091-7613(1995)023<0921:UTEOPM>2.3.CO;2.

Guo Y., Yang S., Su N., *et al.* Revisiting the effects of hydrodynamic sorting and sedimentary recycling on chemical weathering indices // Geochimica et Cosmochimica Acta. — 2018. — Vol. 227. — P. 48–63. — DOI: 10.1016/j.gca.2018.02.015.

Lécuyer C. Seawater residence times of some elements of geochemical interest and the salinity of the oceans // Bulletin de la Société Géologique de France. — 2016. — Vol. 187, no. 6. — P. 245–260. — DOI: 10.2113/gssgfbull.187.6.245.

Lo F.-L., Chen H.-F., Fang J.-N. Discussion of Suitable Chemical Weathering Proxies in Sediments by Comparing the Dissolution Rates of Minerals in Different Rocks // The Journal of Geology. — 2017. — Vol. 125, no. 1. — P. 83–99. — DOI: 10.1086/689184.

Makaryev L. B., Mitrofanov G. L., Mitrofanova N. N., *et al.* State Geological Map of the Russian Federation, scale 1:1,000,000 (third generation). Aldan-Zabaykalskaya Series. Sheet O-50 - Bodaibo. Explanatory Note. — St. Petersburg : VSEGEI Cartographic Factory, 2010. — P. 612.

McLennan S. M. Weathering and Global Denudation // The Journal of Geology. — 1993. — Vol. 101, no. 2. — P. 295–303. — DOI: 10.1086/648222.

Nesbitt H. W., Young G. M. Early Proterozoic climates and plate motions inferred from major element chemistry of lutites // Nature. — 1982. — Vol. 299, no. 5885. — P. 715–717. — DOI: 10.1038/299715a0.

Pakhomov N. N., Barabasheva E. E. New data on the stratigraphy and fauna of Vend-Lower Cambrian deposits of Upper-Kalar Graben // New data on palaeozoic and mesozoic biostratigraphy of the south Far East. — Vladivostok : Far Eastern Branch of the USSR AS, 1990. — P. 24–31.

Pettyjohn F. J., Potter P., Seaver R. Sands and Sandstones. — Moscow : World, 1976. — P. 535.

Regelink J. A. Mincomp-a program to calculate a likely mineralogical bulk composition from XRD and XRF results. Research Minor TA-MI-077. — Delft University of Technology, 2014.

Rosen O. M., Abbyasov A. A. The Quantitative Mineral Composition of Sedimentary Rocks: Calculation from Chemical Analyses and Assessment of Adequacy (MINLITH Computer Program) // Litologiya i Poleznye Iskopaemye. — 2003. — No. 3. — P. 299–312.

Rosen O. M., Abbyasov A. A., Migdisov A. A., *et al.* MINLITH - a program to calculate the normative mineralogy of sedimentary rocks: the reliability of results obtained for deposits of old platforms // Geochemistry International. — 2000. — Vol. 38, no. 4. — P. 388–400.

Rosen O. M., Abbyasov A. A., Tipper J. C. MINLITH-an experience-based algorithm for estimating the likely mineralogical compositions of sedimentary rocks from bulk chemical analyses // Computers & Geosciences. — 2004. — Vol. 30, no. 6. — P. 647–661. — DOI: 10.1016/j.cageo.2004.03.011.

State Geological map of the Russian Federation scale 1:200000. Second edition. Udokan series. O-50-XXXV(Naminga) / ed. by G. L. Mitrofanova. — VSEGEI, 2004.

State Geological Map of the Russian Federation, scale 1:1,000,000, new series, sheet O-(50) 51 and explanatory note / ed. by E. P. Mironyuk. — St. Petersburg. : VSEGEI, 1998. — P. 428.

Yudovich Y. E., Ketris M. P. Fundamentals of Lithochemistry. — St. Petersburg : Science, 2000. — P. 479.

Russian Journal of Earth Sciences

Assessment of Karst Groundwater Vulnerability to Contamination as a Tool for Delineation of Source Protection Zones: A Case Study in the Crimean Mountains

S. V. Tokarev[1,2,*], **G. N. Amelichev**[1,2], **E. V. Braga**[1], **A. I. Sereda**[1]

[1]V. I. Vernadsky Crimean Federal University, Simferopol, Russia
[2]Water Problems Institute of RAS, Moscow, Russia
* **Correspondence to:** Sergey V. Tokarev, tokcrimea@list.ru

Abstract: The assessment of groundwater vulnerability to contamination provides a hydrogeological basis for the designation of protection zones for drinking water sources. This paper presents a case study from the Crimean Mountains where karst groundwater plays a primary role in water supply. Groundwater vulnerability assessment has been carried out for two large karst springs: the Ayan and Krasnopeshcherny. For this purpose, a method adapted to the conditions of karst water formation in the region, called the Mountain-Crimean method, was used. The resulting source vulnerability maps of selected test sites demonstrate both similarities and differences. The common feature is the area predominance of the moderate vulnerability class, with a minor share of the low vulnerability class. However, the vulnerability classes on the two catchments have different placement patterns, as does the presence or absence of a high vulnerability class. The catchment area of the Krasnopeshcherny spring appeared to be more sensitive to pollution than the Ayan spring. The main reason is the hydrodynamic conditions of the deep parts of the karst aquifers drained by the springs. The karst aquifer of the Krasnopeshcherny spring has a much higher groundwater flow dynamic than that of the Ayan spring. The study closes by proposing a scheme of transition from vulnerability map to sanitary protection zones for karst water intakes in accordance with the regulatory standards of the Russian Federation.

Keywords: karst aquifer, groundwater, vulnerability to contamination, Crimean Mountains, sanitary protection zone, assessment, regional method, water supply source, phreatic zone.

Citation: Tokarev, S. V., G. N. Amelichev, E. V. Braga, and A. I. Sereda (2024), Assessment of Karst Groundwater Vulnerability to Contamination as a Tool for Delineation of Source Protection Zones: A Case Study in the Crimean Mountains, *Russian Journal of Earth Sciences*, 24, ES4010, EDN: JJXUNL, https://doi.org/10.2205/2024es000953

1. Introduction

Karst aquifers are widely distributed across the Earth's land mass. As reported in [*Stevanović*, 2019], karstified rocks crop out over > 14% of ice-free land. In Russia, more than 60% of the territory is underlain by soluble rocks [*Kotlyakov*, 2007]. Karst groundwater serves as a crucial source of drinking water in many parts of the world due to its high natural quality and abundance. Although it accounts for only about 9.2% of global water consumption [*Stevanović*, 2019], it holds significant importance in several countries and regions, including the Balkans, Central and Western Europe, the Middle East, parts of North America's southern regions, North Africa, and the Western Caucasus.

The Crimean Peninsula, where soluble rocks occupy over 84% of its area [*Dublyansky and Dublyanskaya*, 1996], also belongs to such karst water dependent regions. Karst aquifers account for almost all fresh groundwater resources (> 90%) of the peninsula [*Vakhrushev et al.*, 2022]. In Crimea, about 100 karst springs have an average discharge rate exceeding 0.01 m^3/s [*Dublyansky and Dublyanskaya*, 1996]. Of these, about 20 springs have an average discharge rate greater than 0.1 m^3/s and 2 springs (Karasu-Bashi and Skelsky) – greater than 1 m^3/s. Karst springs play a leading role in formation of river flow of the peninsula

Research Article

Received: 5 September 2024
Accepted: 15 November 2024
Published: 22 November 2024

and filling of drinking water reservoirs. Under the conditions of the ongoing rapid socio-economic development of the Crimean region and the continuing water shortage, the issue of preserving the quality and quantity of karst water resources is particularly important.

Karst aquifers, unlike pore and fracture aquifers are characterized by extremely high heterogeneity and anisotropy of capacitance and filtration properties. Most groundwater flow occurs primarily through conduit systems. Accordingly, karst aquifers exhibit peculiar hydrogeological features, among which are high flow concentration, focal nature of recharge and discharge, and high groundwater flow velocities [*Ford and Williams*, 2007; *Klimchouk*, 2008]. As a result, karst waters have a very high overall susceptibility to contamination and a low capacity for self-purification.

Assessing groundwater vulnerability to contamination is a key step in designing effective protection measures for drinking water sources [*Farics et al.*, 2021; *Ravbar et al.*, 2021]. Due to their specific hydrogeological features, assessment of groundwater vulnerability in karst aquifers requires special approaches. Such approaches and methods have been developed primarily in European countries over recent decades [*European Commission: Directorate-General for Research and Innovation*, 2004; *Iván and Mádl-Szőnyi*, 2017; *Ravbar*, 2007].

For the conditions of the Crimean Mountains, a regional modification of the karst groundwater vulnerability assessment methodology has been developed. Previously it was tested on four karst massifs including the Chatyrdag, Dolgorukovsky, Karabi, and Ay-Petri. As a result, maps depicting the vulnerability of groundwater resources to contamination were created [*Tokarev et al.*, 2024].

This study aims to assess the vulnerability of groundwater sources to contamination at the largest karst water outlets on the Chatyrdag and Dolgorukovsky massifs – the Ayan and Krasnopeshcherny springs, which supply water to the city of Simferopol. To achieve this, a regional adaptation of the groundwater vulnerability assessment methodology was applied. The results provide a foundation for designating sanitary protection zones around these sources.

2. Description of the Study Areas

The Ayan (average discharge rate 0.6 m^3/s) and Krasnopeshcherny (0.15 m^3/s) karst springs are located in the central part of the Main Range of the Crimean Mountains (Figure 1a, b). The springs discharge large karst aquifers (KAs). They give rise to the largest tributaries of the Salgir river in the upper part of its basin (average flow rate 1.3 m^3/s). Both springs have highly variable discharge rate dynamic and show rapid response to precipitation events in the recharge area. During continuous low water periods, discharge rate of the springs is reduced to 0.005 m^3/s. On heavy floods, spring discharge may increase rapidly up to 20 m^3/s.

2.1. Ayan Karst Spring, Chatyrdag Massif

2.1.1. Physiography of the Chatyrdag Massif

The Ayan karst spring (44°49’35.6”N, 34°17’30.2”E, altitude 450 m a.s.l.) is located at the northern foothill of the Chatyrdag massif. The area of the massif is about 47 km^2. Approximately half of it represents drainless catchments on the plateau surface and the other half corresponds to the open catchments on the slope of the massif. Two distinct levels are evident on the surface of the Chatyrdag: the Lower Plateau in the north (900–1150 m a.s.l.) and the Upper Plateau in the south (1300–1500 m a.s.l.), with their areas in a ratio of 5:1.

Various surface karst forms are widespread on the Chatyrdag massif, particularly on the plateau, including karst dolines, blind gullies, and karren fields. The total number of dolines exceeds 500. Depths of dolines in most cases (ca. 90%) do not exceed 10 m. The average density of dolines on the Chatyrdag plateau is 22 dolines/km^2. In central part of the lower plateau it reaches 60 dolines/km^2. Such a wide distribution of dolines on the

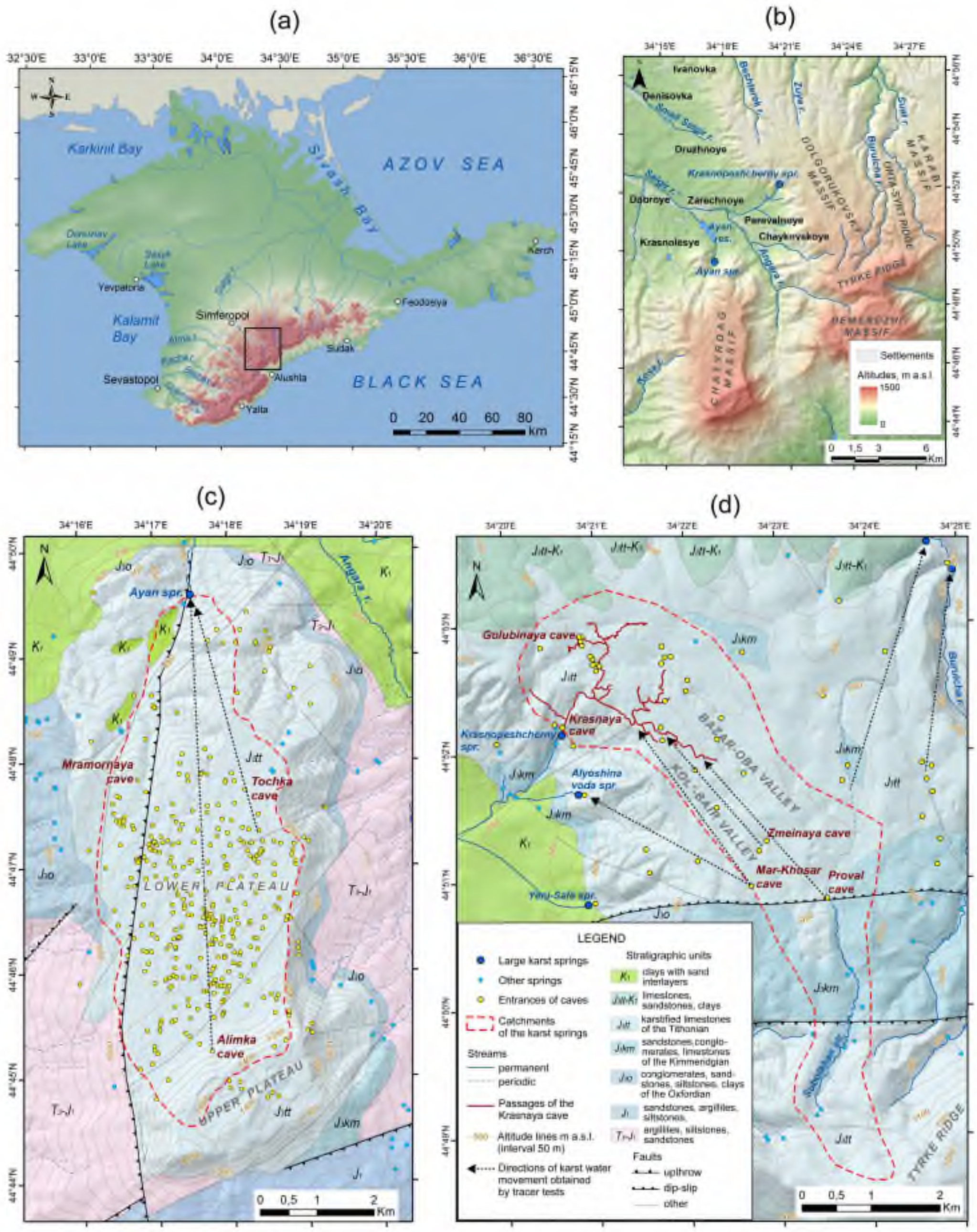

Figure 1. Position of the study area (rectangle) on the map of the Crimean Peninsula (a); physiographic map of the study area (b); and the maps of geological and hydrogeological settings of the Chatyrdag (c) and Dolgorukovsky (d) karst massifs. Geological information (stratigraphic units and faults) is derived from [*State geological survey*, 2008].

plateau indicates, on the one hand, the development of epikarst and, on the other hand, a significant share of focal infiltration of precipitation in recharge of karst waters.

The plateau is dominated by steppe and shrub vegetation with patches of forest restricted to dolines. The slopes of the massif are covered with forests and sparse woodlands. On the plateau and slopes of the massif, low (0–20 cm) and medium-thickness (20–40 cm) soils predominate. In bottoms of dolines soil thickness can reach 80–100 cm. Soils are clayey and loamy with a high proportion of rubble.

2.1.2. Geology and Hydrogeology of the Chatyrdag Massif

The Chatyrdag massif is hydrogeologically isolated from adjacent massifs of the Main range of the Crimean Mountains. It comprises two distinct rock sequences (Figure 2a) with significantly different hydrogeological properties. The lower sequence consists of low-permeability Upper Triassic and Lower Jurassic flysch sediments, including mudstones, siltstones, and sandstones. This sequence acts as an aquitard and is practically devoid of groundwater, except for narrow zones of tectonic fracturing. The upper sequence is composed of Upper Jurassic limestones which are characterised by intense tectonic dislocation, fracturing and karstification. It contains the aquifers with highly developed karst conduit permeability. The KA drained by the Ayan spring is the largest on the massif.

There are two main models of the tectonic structure of the Chatyrdag massif. Most karstologists and hydrogeologists use the fold-block model and consider the Chatyrdag as an autochthonous massif [*Dublyansky and Kiknadze*, 1984]. Some geologists argue for the thrust (overthrust) model of the Chatyrdag tectonic structure [*Kazantsev et al.*, 1989; *Yudin*, 2011]. According to V. V. Yudin, Chatyrdag is an allochthonous massif – olistolite (olistoplaque) – that was thrust onto the underlying terrigenous strata during the Early Cretaceous.

The karst waters are recharged exclusively by atmospheric precipitation. The average annual precipitation in the central part of the Crimean Mountains is 700–900 mm and the evapotranspiration is about 400 mm [*Vyed'*, 2000]. Thus, the annual effective precipitation recharging karst groundwater is 300–500 mm. Quantitatively, precipitation of the cold part of the year (November-March) prevails. Considering the relatively low rates of evapotranspiration during this period, karst waters recharge is provided mainly by winter precipitation. This is confirmed by the isotopic composition of waters of large karst springs, which is significantly shifted to the winter precipitation signal and practically does not change during the year [*Dublyansky et al.*, 2019].

To date, 355 karst caves are known on the Chatyrdag massif, most of them are vertical shafts [*Russian Geographical Society*, 2024]. The deepest shafts reach a depth of 250 m. However, none of the shafts reach the phreatic (saturated) zone of the massif. The density of caves is maximal in central part of the plateau reaching 40 caves/km².

Stratigraphic units (see Legend in Figure 1d): 1 – J_3tt; 2 – J_3km; 3 – J_3o; 4 – T_3-J_1; 5 – K_1. 6 – tectonic faults; 7 – karst caves, 8 – large karst springs, 9 – small springs, 10 – karst water table. Descending flow in vadose zone: 11 – through fractures and small conduits (slow component); 12 – through large conduits (fast component). Lateral flow in phreatic zone: 13 – slow circulation; 14 – fast circulation. 15 – Quaternary calcareous tuffs.

2.1.3. Characteristics of the Ayan Spring

The Ayan spring is associated with a regional tectonic fault bounding the massif from the north-west (Figure 1c). The spring represents a single rising outlet of karst water, equipped with a spring collection system in 1928. The karst water outlet is directly connected with the cave passages explored for a total length of 500 m and mostly located below the karst water table.

In hydrogeological investigations on karst massifs, a key problem is the delineation of KASs catchments, since their boundaries generally do not correspond to topographic watersheds. To solve this problem, the data of structural-geological survey, speleological works, water-balance calculations are involved. Especially valuable information is provided by the results of tracer tests. Using a combination of the above methods, the catchment area of the Ayan karst spring was identified to be approximately 23 km^2. It includes the entire lower plateau and the northern part of the upper plateau of the Chatyrdag massif (Figure 1c).

Tracer tests, besides clarifying the structure of underground catchments, provide information on the direction and velocity of karst water movement. In addition, the density and duration of the tracer output indicates the degree of dilution and attenuation of the possible contaminant. Based on the results of tracing experiments, the average karst water

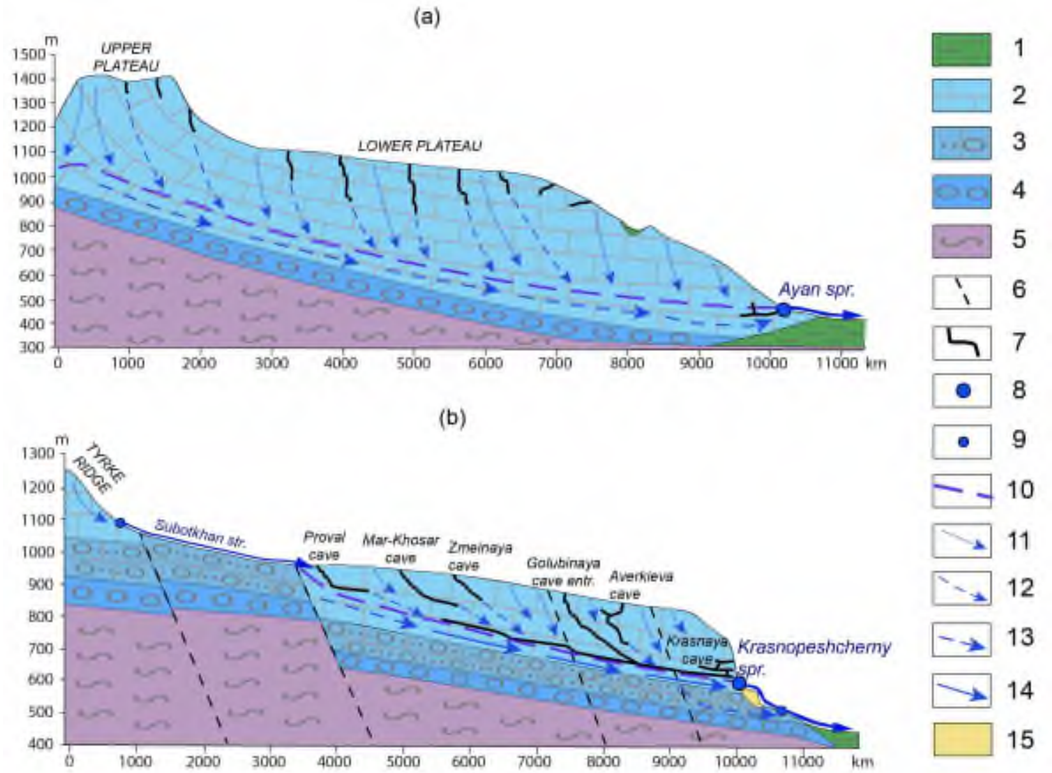

Figure 2. Simplified geological and hydrogeological cross-sections of the Chatyrdag (a) and Dolgorukovsky (b) massifs depicting the catchment areas of the Ayan and Krasnopeshcherny karst springs.

velocity of the Ayan KA in high-water period is 1150 m/day. The concentration of tracers at the spring was very low, indicating a strong dilution along the way of karst water movement. It most likely occurs in the phreatic zone of the massif, which appears to have a high storage capacity and relatively low hydraulic conductivity that retard tracer transit.

2.2. Krasnopeshcherny Spring, Dolgorukovsky Massif

2.2.1. Physiography, Geology and Hydrogeology of the Dolgorukovsky Massif

The Krasnopeshcherny spring (44°52’12.5”N, 34°20’35”E, altitude 570 m a.s.l.) represents a group of compactly located karst water outlets on the western slope of the Dolgorukovsky massif (Figure 1b).

The area of the Dolgorukovsky massif, excluding the Tyrke ridge, is about 52 km^2. The massif has a vast plateau surface called Yayla. Four dry karst-erosion valleys intersect the Yayla from south to north. There are numerous karst dolines at their bottoms. The total number of the dolines is about 130. Their density is relatively low, rarely exceeding 20 dolines/km^2. On the Yayla, soil cover consists of low- to medium-thickness varieties under steppe vegetation, and thicker varieties under meadow and forest vegetation.

Karst waters are recharged mainly by diffuse infiltration, but concentrated infiltration (influation) also common. There is a permanent stream Subotkhan in the southern part of the plateau. It is typically completely swallowed up by sinkholes near the Proval cave, though a significant portion reaches the Burulcha river basin during heavy floods. Also, temporary streams may periodically appear on dry valleys slopes, which are swallowed up by sinkholes in their bottoms. In summer, a significant portion of karst water recharge can be provided by condensation [*Dublyansky and Kiknadze*, 1984].

Several KAs are known within the Dolgorukovsky massif. Some of them discharge on the eastern slope of the massif, feeding the Burulcha river and its tributaries, others discharge on the western slope in the Salgir river basin. Some part of the groundwater of the Dolgorukovsky massif is not discharged on the slopes, but flows to the north and feeds artesian basins of the Crimean Piedmont.

The geological structure and hydrogeological conditions of the Dolgorukovsky massif differ significantly from the Chatyrdag massif. The main karst aquifers of the Dolgorukovsky massif are hosted by Titonian limestones. They are underlain by thick layer of Kimmeridgian conglomerates and sandstones (Figure 2b). It acts as an aquitard for KAs discharging on the western slope of the massif [*Dublyansky et al.*, 2002].

2.2.2. Characteristics of the Krasnopeshcherny Spring

The Krasnopeshcherny spring discharges the KA of the Krasnaya Cave (also known as Kizil-Koba) – the largest cave in the Crimea with the total length exceeding 20 km. The lower levels of the cave are in the phreatic zone. According to results of our dye tracing tests, in high-water periods karst water velocity in the Krasnaya cave system can reach 8 km/day.

Transit of karst water to the discharge points is carried out by well-developed conduit systems, most of which have been investigated and surveyed by speleologists. The Golubinaya cave, which has an entrance on the plateau, was traversed to the junction with the Krasnaya cave. Tracer experiments proved the connection of the Krasnaya cave KA with other large caves on the plateau, e.g., Mar-Khosar (1300 m long), Proval (1250 m), Zmeinaya (850 m) (Figure 1d).

The combined results of speleological exploration and tracer tests allowed delineation of the catchment area of the Krasnaya cave KA with an area of about 15 km^2. The catchment is divided into inner and outer parts. Its inner part comprises the Kol'-Bair and Bazar-Oba dry valleys located in the central and western parts of the Yayla with altitudes 750–950 m a.s.l. The vegetation cover here is mainly steppes on watersheds and slopes and meadows in valley and bottoms of dolines. That area provides an autogenic recharge of the KA, characterised by a rapid signal path from the precipitation events to the Krasnopecherny spring. The outer part corresponds to the Subotkhan stream valley with an area of about 2 km^2 and altitudes 950–1200 m a.s.l., which provides allogenic recharge of the KA. The vegetation of that area is mainly broadleaved forests with patchy meadows.

3. Methodology

The term "vulnerability of groundwater" refers to the susceptibility of a hydrogeological system to contamination, as well as its capacity to neutralize or mitigate such contamination [*Ravbar*, 2007]. To date, many methods have been developed for assessment of karst groundwater vulnerability to contamination (KGV), considering their unique hydrogeological characteristics [*European Commission: Directorate-General for Research and Innovation*, 2004; *Iván and Mádl-Szőnyi*, 2017; *Ravbar*, 2007]. They differ in the estimation procedures, the factors considered, and the resulting outputs.

There is a general methodology that outlines the basic assessment framework and groups of factors to be considered, called the European approach [*Daly et al.*, 2002]. It is based on the "hazard-pathway-target" conceptual model. "Hazard" refers to a potential source of contamination, typically located on the ground surface. "Target" refers to a groundwater object that may be contaminated by a "hazard". The target may be the entire groundwater body or individual groundwater outlet, such as spring, well, or borehole. In the first case the subject of assessment is referred to as "resource vulnerability", while in the second case it is called "source vulnerability". "Pathway" refers to a flow route from the "hazard" to the "target". In the case of resource vulnerability it represents a downward flow through vadose zone of aquifer. If the object of assessment is a specific groundwater outlet (i.e., "source vulnerability"), the pathway of potential pollutant through the phreatic zone of aquifer must also be considered.

The European approach to KGV assessment proposes four groups of factors to be considered: overlying layers above groundwater body (factor O), flow concentration (factor C), precipitation regime (factor P), and development of karst network in phreatic zone (factor K). Factor O characterizes the protective function of the aquifer against contaminant provided by the geological layers in the vadose zone. Factors P and C assess the reduction in this protective function due to heavy rainfall and bypassing of the protective layers by water flows, which can lead to rapid introduction of contaminants into the groundwater. Factor K evaluates the conditions that affect the passage of contaminants through the phreatic zone to groundwater intakes. Thus, the factors O, C and P are used for assessment of resource vulnerability. In the case of source vulnerability assessment, all of four factors have to be evaluated, including factor K.

To date, numerous methods of KGV assessment have been developed; most of them are index methods based on the European approach. Some of them are intended only for resource vulnerability assessment. The most popular ones are the PI method [*Goldscheider et al.*, 2000], COP method [*Vías et al.*, 2006], DRISTPI method [*Jiménez-Madrid et al.*, 2013], and IKAV method [*Moreno-Gómez et al.*, 2022]. A relatively broad variety of methods provide the ability to assess a source vulnerability of karst waters. Among them are the EPIK method [*Doerfliger et al.*, 1999], Slovene approach [*Ravbar and Goldscheider*, 2007], COP+K method [*Andreo et al.*, 2008], PaPRIKa method [*Kavouri et al.*, 2011], and KAVA method [*Biondić et al.*, 2021]. Many of them have been widely tested in different regions of the world, demonstrating their high effectiveness. There are many examples of recent studies using these methods [*Marín et al.*, 2021; *Petrović*, 2020; *Steiakakis et al.*, 2023; *Yogafanny and Legono*, 2021].

It should be noted that in many cases, a comparison of the KGV maps for the same test area derived using different assessment methods revealed significant differences between them [*Marín et al.*, 2011; *Moreno-Gómez et al.*, 2019; *Polemio et al.*, 2009; *Ravbar and Goldscheider*, 2008]. This is manifested even when methods with the same methodological basis, similar input information and estimation procedure are used [*Farics et al.*, 2021; *Marín et al.*, 2014]. It can be concluded that there are no universal methods for KGV assessment. Thus, a careful selection or adaptation of existing methods to regional conditions is necessary to achieve the most adequate assessment results.

The conditions of karst water formation in the Mountain Crimea have their own peculiarities, including a significant share of winter precipitation (snow) in their recharge, predominance of infiltration processes due to the almost complete absence of impermeable cover on the karst massifs, well-developed epikarst zone acting as a protective layer retaining the groundwater contaminant. To account for these features, a regional KGV assessment method designated as the Mountain-Crimean method was developed [*Tokarev et al.*, 2024], based on COP and Slovene methods. The basis for its construction is the methods COP and Slovene. The adjustments included the consideration of epikarst's protective function, the addition of factors characterizing the concentration of underground flow in the vadose zone, and the substitution of mapping individual karst landforms with the use of the spatial density. The Mountain-Crimean method was originally designed for resource vulnerability assessment, but can be extended to assess source vulnerability by adding an additional group of factors. Specifically, for this purpose, the factor K block from the Slovene approach was added to the assessment scheme (Figure 3)

The mapping, calculations, construction of intermediate layers and final vulnerability maps were carried out using ArcGIS 10 software. Initial information on hydrogeological, geomorphological and landscape-topographic conditions was obtained from literature and archive sources. Input analogue data was digitised and converted into geodata formats to perform the assessment procedure in a GIS environment. To estimate the K factor, both archival materials and the results of recent tracer tests were used.

4. Results and discussion

4.1. Assessment of Karst Groundwater Source Vulnerability to Contamination

The resulting maps of karst groundwater source vulnerability for catchment areas of the two selected springs, as well as the maps of the individual factors, are shown in Figure 4 and Figure 5. As observed, the spatial distribution of vulnerability classes

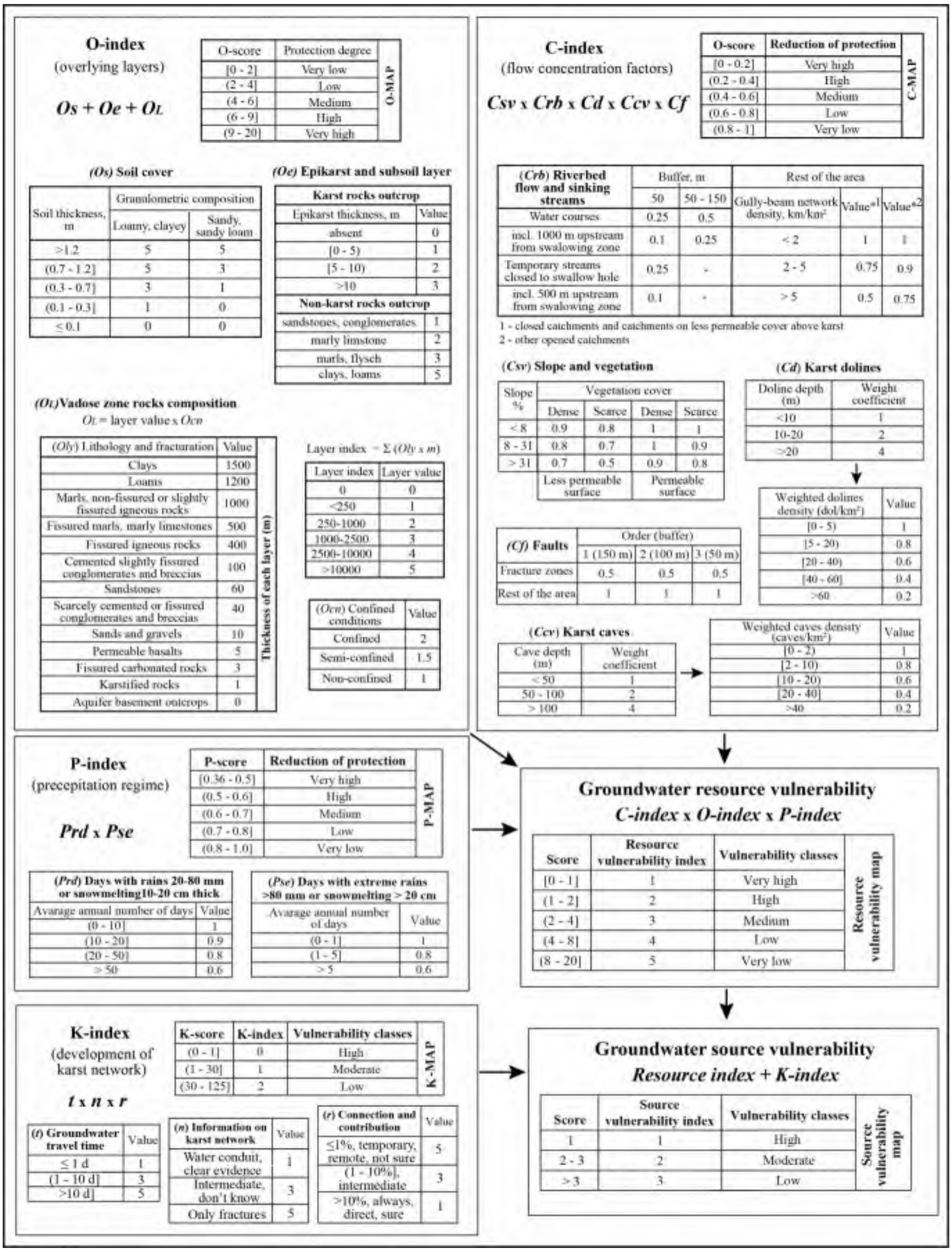

Figure 3. The scheme of the Mountain-Crimean method adapted to groundwater source vulnerability assessment. The block of K-index is taken from the Slovene approach [*Ravbar and Goldscheider*, 2007].

at the two test sites shows both similarities and differences. A common feature is the predominance of the moderate vulnerability class, with a small proportion of the low vulnerability class. However, the placement patterns of the vulnerability classes differ between the two catchments, as does the presence or absence of a high vulnerability class.

Within the catchment area of the Ayan spring, the low vulnerability class occupies about 36% of the area, while the moderate class occupies about 64% of the area. The moderate vulnerability class includes almost the entire the Lower plateau of the Chatyrdag massif and the surroundings of the Ayan spring. The majority of the northern slope of the massif, as well as the slope between the Upper and Lower plateaus, has been assigned a low vulnerability grade. Exceptions to this are gullies enclosed by karst sinkholes and tectonic

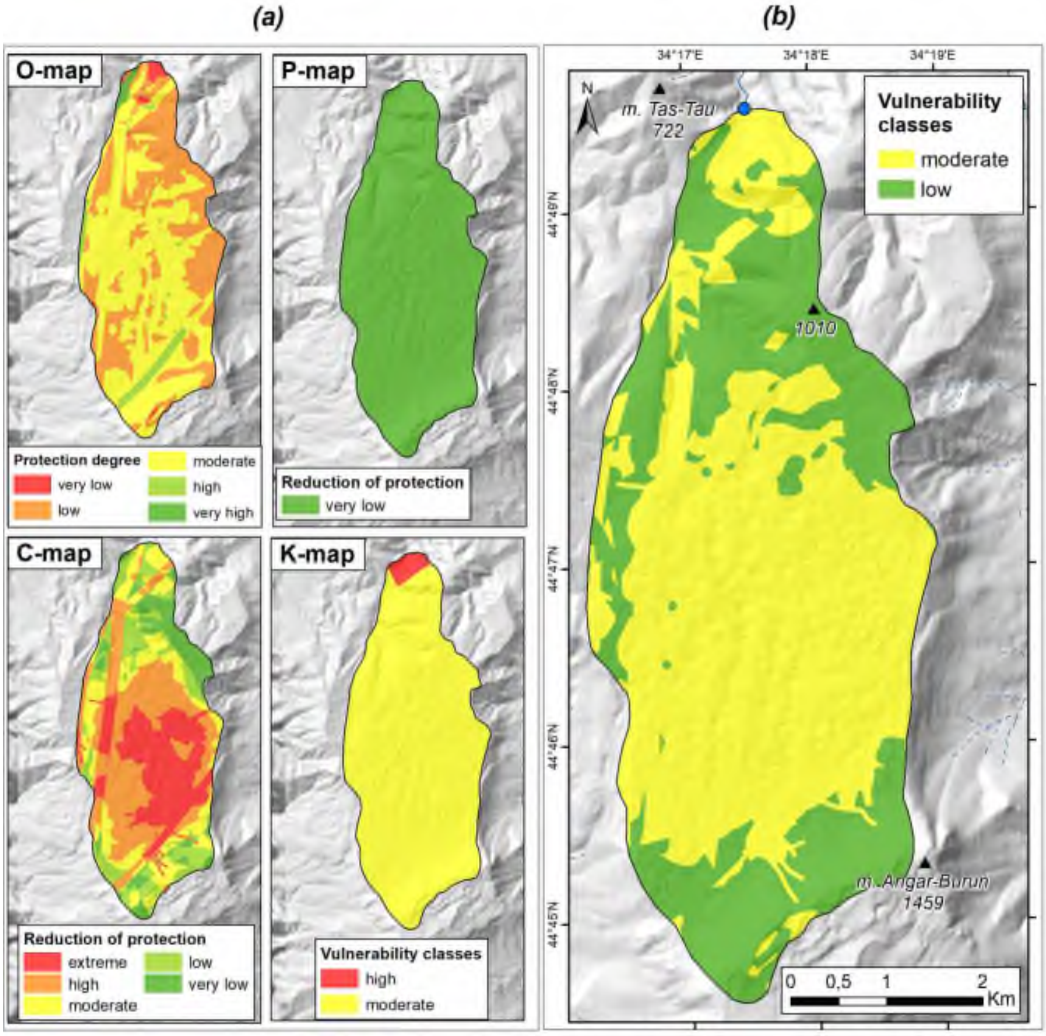

Figure 4. The maps of vulnerability factors (a) and the vulnerability map (b) of the Ayan karst spring.

fracture zones, which have a moderate vulnerability class. On the Upper plateau, areas occupied by karst valleys and dolines also have moderate vulnerability. Notably, the high vulnerability class is completely absent in this catchment.

The assessment results within the Krasnopeshcherny spring catchment revealed a significantly different situation. Approximately 38% of the assessed area was classified as having low vulnerability to contamination. This class is primarily concentrated in the southern part of the catchment, along the slopes of the Subotkhan stream valley, and on the eastern periphery of the basin. The separate areas of low vulnerability are also located as on the western slope of the massif in the vicinity of the Krasnopeshcherny spring. The moderate vulnerability class covers about 58% of the catchment area. It mainly occupies karst-erosion valleys on the plateau, the western slope of the massif and the bottom of the Subotkhan valley with its tributaries in the upper and lower reaches. Just over 4% of the catchment was classified as having high vulnerability class. The most vulnerable areas are the bottoms of gullies with periodic and permanent watercourses, including the part of Subotkhan valley before the sinking zone, and the areas of high density of karst dolines and caves in the northwestern part of the plateau.

Obviously, the absence of high source vulnerability class in the Ayan catchment is due to the hydrodynamic conditions of the deep part of the KA lying in the phreatic zone of the Chatyrdag massif. The relatively low velocity of underground flow in the Ayan KA prevents a potential pollutant from rapidly reaching the spring outlet. In contrast, the Krasnopeshcherny KAS exhibits high groundwater flow dynamics, resulting in the rapid

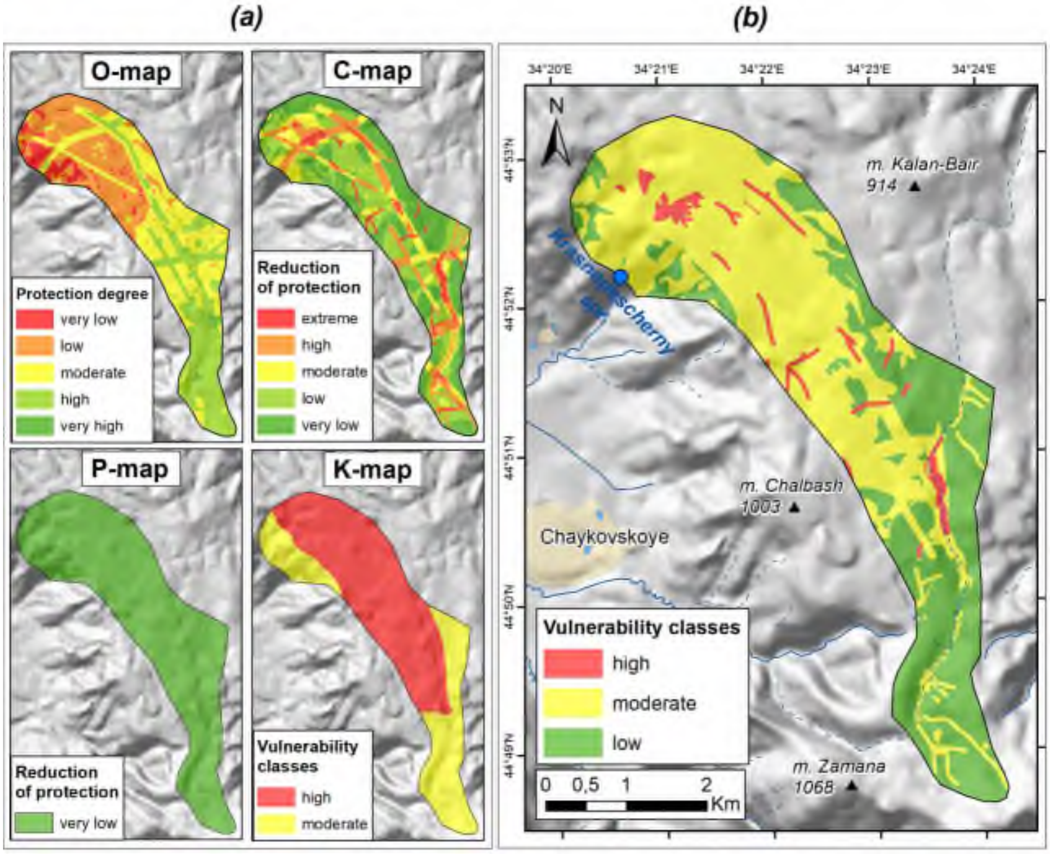

Figure 5. The maps of vulnerability factors (a) and the vulnerability map (b) of the Krasnopeshcherny karst spring.

passage of a pollutant through the phreatic zone of the massif. As a result, the zones of surface runoff sinking on the Dolgorukovskaya Yayla were classified within the high source vulnerability category.

According to the methodology being used, the source vulnerability map is derived by summing the groundwater resource vulnerability index with the K-factor index (Figure 3). The distributions of vulnerability classes for the groundwater resource and source within the assessed areas show significant differences (Figure 6). This is especially pronounced in the Ayan spring catchment, where assessment of groundwater resource vulnerability indicated more than 60% of its area in the classes of high and extreme vulnerability. Notably, the final source vulnerability map of the Ayan spring has no areas of high vulnerability at all. A similar discrepancy is also observed in the catchment of the Krasnopeshcherny spring, although to a much smaller extent.

It may be concluded, that the determining factor of the karst groundwater sources vulnerability is the development of karst conduit network in phreatic zone of the massif. The information on the hydrodynamic conditions of deep KA sections is thus critically important. It can be obtained by means of systematic groundwater tracer tests.

4.2. Application of KGV Maps for Delineation of Source Protection Zones

According to the legislation of the Russian Federation, the primary protective measure for drinking water sources is the establishment of sanitary protection zones (SPZ), which imposes a special usage regime [*Ministry of Health of the Russian Federation*, 2002]. The first (I) SPZ (strict regime) includes the territory of water intakes location and sites of all water supply facilities. The second (II) and third (III) SPZs (restriction regime) include the territory intended for protection from microbial and chemical pollutions of water supply sources, respectively. Considering the hydrogeological features of karst aquifers

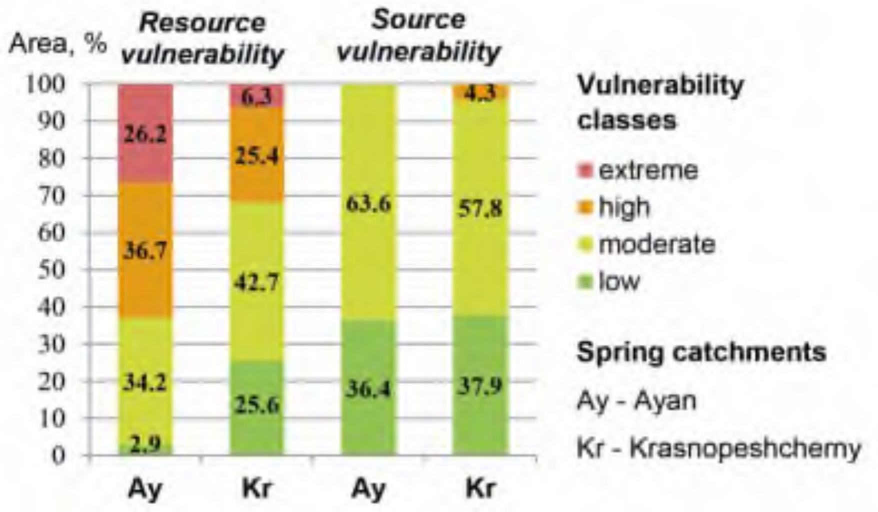

Figure 6. Distribution of source and resource vulnerability classes areas within catchments of the Ayan and Krasnopeshcherny springs.

discussed above, it is essential to differentiate normative approaches to the organization of SPZs for various types of groundwater. For example, the regulatory standards of some countries with a high proportion of karst groundwater in their water supply use specific protocols to determine protection zones for sources derived from karst aquifers [*Ravbar et al.*, 2021]. The results of the groundwater vulnerability assessment should be used as a basis. The following scheme is proposed to proceed from the source vulnerability map to the delineation of SPZs for karst water intakes (Figure 7).

According to the scheme, the I SPZ, besides the immediate vicinity of the water intake, is established within boundaries of high vulnerable areas. The II SPZ corresponds to sites of moderate groundwater vulnerability, and the III SPZ encompasses the rest of the catchment area. The main feature of this scheme is the discrete configuration of the SPZs, in contrast to the belt configuration typically used for other aquifer types. This is due to specific conditions and processes of karst aquifers recharge, including the presence of localized areas of rapid infiltration with direct connection to conduit systems. The consequence of this is the situation observed on the resulting vulnerability maps of the Ayan and Krasnopeshcherny springs, where areas remote from the intake may be more vulnerable than those close to it.

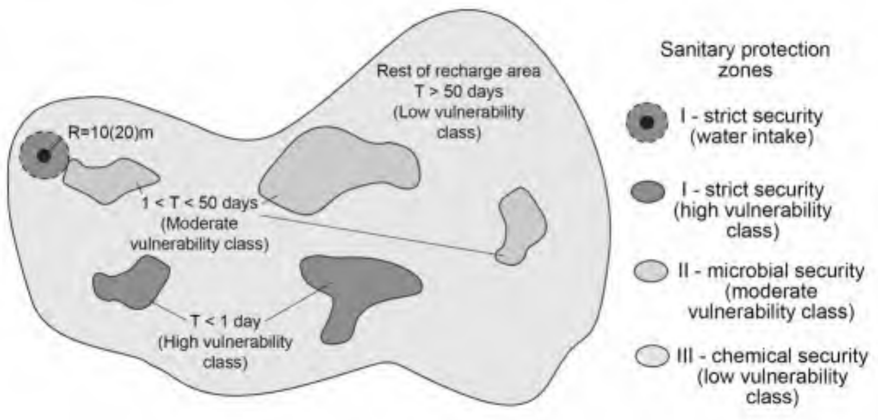

Figure 7. Conceptual scheme of an approach to delineate sanitary protection zones for karst water intakes based on a map of groundwater source vulnerability to contamination (modified after [*Brenčič et al.*, 2009] and [*Klimchouk and Tokarev*, 2014]).

5. Conclusions

The normative indicator for delineation the boundaries of sanitary protection zones for groundwater intakes is the time of its reaching by potential pollutant. Assessment and mapping of groundwater vulnerability to contamination reflects this indicator, as they are based on groundwater travel time as a key physical parameter. Thus, the groundwater vulnerability map serves as an effective tool for organizing the protection of potable water sources.

Due to the hydrogeological characteristics of karst aquifers, specialized methods are used to assess their groundwater vulnerability. To best account for regional karst features, it is often necessary to adapt and modify existing methods to regional conditions. Such modified method was developed for the Crimean Mountains region. In its extended version, it allows to perform a groundwater source vulnerability assessment, the results of which are the basis for the delineation of sanitary protection zones for karst water intakes.

The Ayan and Krasnopeshcherny karst springs, located in the central part of the Crimean Mountains, were selected as test sites for assessment of groundwater source vulnerability. Despite their geographical vicinity, the catchments of these springs are significantly different in terms of their hydrogeological conditions. This refers to both the mechanisms of karst groundwater recharge and the conditions of its transit in saturation zone. The results of vulnerability assessment of the selected springs also show substantial differences. A small portion of the Krasnopeshcherny spring catchment (about 4%) was classified as highly vulnerable, whereas no such areas were identified in the Ayan spring catchment. A common feature of the assessment results for both test sites is the predominance of the moderate vulnerability class, covering approximately 58–64% of the area, with a smaller proportion of the low vulnerability class (36–38%).

The differences identified in vulnerability assessment results are primarily due to the hydrodynamic conditions of the studied karst aquifer within the saturated zone. The KA of the Krasnopeshcherny spring exhibit a much higher groundwater flow dynamic compared to the Ayan KA. As a result, the velocities at which karst water – and consequently potential contaminants – move through the KAs differ by several times. This highlights the crucial importance of factor K in determining the vulnerability of karst groundwater sources.

We propose a scheme for transitioning from vulnerability maps to sanitary protection zones (SPZ) for karst water intakes, in accordance with the regulatory documents of the Russian Federation. According to this scheme, SPZ I is established within areas of high vulnerability, while SPZ II and SPZ III correspond to areas of moderate and low groundwater vulnerability, respectively.

Acknowledgments. The work was supported by Russian Science Foundation project No. 23-27-10045, https://rscf.ru/project/23-27-10045. The authors thank the staff of the Kizil-Koba show cave complex for help in the field works. We are grateful to Yuri Dublyansky and two anonymous reviewers for valuable comments and recommendations that improved the quality of the paper.

References

Andreo, B., N. Ravbar, and J. M. Vías (2008), Source vulnerability mapping in carbonate (karst) aquifers by extension of the COP method: application to pilot sites, *Hydrogeology Journal*, *17*(3), 749–758, https://doi.org/10.1007/s10040-008-0391-1.

Biondić, R., H. Meaški, B. Biondić, and J. Loborec (2021), Karst Aquifer Vulnerability Assessment (KAVA) Method-A Novel GIS-Based Method for Deep Karst Aquifers, *Sustainability*, *13*(6), 3325, https://doi.org/10.3390/su13063325.

Brenčič, M., J. Prestor, B. Kompare, H. Matoz, and S. Kranjc (2009), Integrated approach to delineation of drinking water protection zones, *Geologija*, *52*(2), 175–182, https://doi.org/10.5474/geologija.2009.017.

Daly, D., A. Dassargues, D. Drew, et al. (2002), Main concepts of the "European approach" to karst-groundwater-vulnerability assessment and mapping, *Hydrogeology Journal*, *10*(2), 340–345, https://doi.org/10.1007/s10040-001-0185-1.

Doerfliger, N., P.-Y. Jeannin, and F. Zwahlen (1999), Water vulnerability assessment in karst environments: a new method of defining protection areas using a multi-attribute approach and GIS tools (EPIK method), *Environmental Geology*, *39*(2), 165–176, https://doi.org/10.1007/s002540050446.

Dublyansky, V. N., and G. N. Dublyanskaya (1996), *Karst republic (Karst of the Crimea and its problems)*, Crimean Academy of Sciences, Simferopol (in Russian).

Dublyansky, V. N., and T. Z. Kiknadze (1984), *Karst hydrogeology in the Alpine folded region of the south of the USSR*, 128 pp., Nauka, Moscow (in Russian).

Dublyansky, V. N., B. A. Vakhrushev, G. N. Amelichev, and Y. I. Shutov (2002), *Krasnaya cave: experience of complex karstological studies*, 190 pp., RUDN, Moscow (in Russian).

Dublyansky, Y. V., A. B. Klimchouk, S. V. Tokarev, G. N. Amelichev, and C. Spötl (2019), Groundwater of the Crimean peninsula: a first systematic study using stable isotopes, *Isotopes in Environmental and Health Studies*, *55*(5), 419–437, https://doi.org/10.1080/10256016.2019.1650743.

European Commission: Directorate-General for Research and Innovation (2004), *COST Action 620: vulnerability and risk mapping for the protection of carbonate (karst) aquifers : final report*, Publications Office.

Farics, E., A. Halász, S. Czigány, and E. Pirkhoffer (2021), Vulnerability mapping of karst springs and its application for the delineation of protection zones (Mecsek Karst, Hungary), *Acta Carsologica*, *50*(2–3), https://doi.org/10.3986/ac.v50i2-3.8583.

Ford, D., and P. Williams (2007), *Karst Hydrogeology and Geomorphology*, Wiley, https://doi.org/10.1002/9781118684986.

Goldscheider, N., M. Klute, S. Sturm, and H. Hötzl (2000), The PI method - a GIS-based approach to mapping groundwater vulnerability with special consideration of karst aquifers, *Zeitschrift für angewandte Geologie*, *46*(3), 157–166.

Iván, V., and J. Mádl-Szőnyi (2017), State of the art of karst vulnerability assessment: overview, evaluation and outlook, *Environmental Earth Sciences*, *76*(3), https://doi.org/10.1007/s12665-017-6422-2.

Jiménez-Madrid, A., F. Carrasco, C. Martínez, and R. C. Gogu (2013), DRISTPI, a new groundwater vulnerability mapping method for use in karstic and non-karstic aquifers, *Quarterly Journal of Engineering Geology and Hydrogeology*, *46*(2), 245–255, https://doi.org/10.1144/qjegh2012-038.

Kavouri, K., V. Plagnes, J. Tremoulet, et al. (2011), PaPRIKa: a method for estimating karst resource and source vulnerability-application to the Ouysse karst system (southwest France), *Hydrogeology Journal*, *19*(2), 339–353, https://doi.org/10.1007/s10040-010-0688-8.

Kazantsev, Y. V., T. T. Kazantseva, M. Y. Arzhavitina, et al. (1989), *Structural geology of the Crimea*, 152 pp., UrB AS USSR, Ufa (in Russian).

Klimchouk, A. B. (2008), Principal features and problems of karst hydrogeology: Speleogenetic approach, *Speleology and Karstology*, *1*, 23–46 (in Russian).

Klimchouk, A. B., and S. V. Tokarev (2014), Recommendations on groundwater source protection for drinking water supply in karst regions, *Speleology and Karstology*, (12), 5–16 (in Russian).

Kotlyakov, V. M. (Ed.) (2007), *National Atlas of Russia: in 4 volumes. Vol. 2: Environment (Nature). Ecology*, Yantarny Skaz, Kaliningrad (in Russian).

Marín, A. I., N. Dörfliger, and B. Andreo (2011), Comparative application of two methods (COP and PaPRIKa) for groundwater vulnerability mapping in Mediterranean karst aquifers (France and Spain), *Environmental Earth Sciences*, *65*(8), 2407–2421, https://doi.org/10.1007/s12665-011-1056-2.

Marín, A. I., N. Ravbar, G. Kovačič, B. Andreo, and M. Petrič (2014), Application of Methods for Resource and Source Vulnerability Mapping in the Orehek Karst Aquifer, SW Slovenia, in *H2Karst Research in Limestone Hydrogeology*, pp. 139–150, Springer International Publishing, https://doi.org/10.1007/978-3-319-06139-9_10.

Marín, A. I., J. F. Martín Rodríguez, J. A. Barberá, et al. (2021), Groundwater vulnerability to pollution in karst aquifers, considering key challenges and considerations: application to the Ubrique springs in southern Spain, *Hydrogeology Journal*, *29*(1), 379–396, https://doi.org/10.1007/s10040-020-02279-8.

Ministry of Health of the Russian Federation (2002), *Sanitary Regulations 2.1.4.1110-02. Zones of sanitary protection of water supply sources and drinking water pipelines*, Ministry of Health of the Russian Federation (in Russian).

Moreno-Gómez, M., C. Martínez-Salvador, A.-W. Moulahoum, et al. (2019), First Steps into an Integrated Karst Aquifer Vulnerability Approach (IKAV). Intrinsic Groundwater Vulnerability Analysis of the Yucatan Karst, Mexico, *Water*, *11*(8), 1610, https://doi.org/10.3390/w11081610.

Moreno-Gómez, M., C. Martínez-Salvador, R. Liedl, C. Stefan, and J. Pacheco (2022), First application of the Integrated Karst Aquifer Vulnerability (IKAV) method - potential and actual vulnerability in Yucatan, Mexico, *Natural Hazards and Earth System Sciences*, *22*(5), 1591–1608, https://doi.org/10.5194/nhess-22-1591-2022.

Petrović, B. (2020), Intrinsic groundwater vulnerability assessment by multiparameter methods, a case study of Suva Planina Mountain (SE Serbia), *Environmental Earth Sciences*, *79*(4), https://doi.org/10.1007/s12665-020-8825-8.

Polemio, M., D. Casarano, and P. P. Limoni (2009), Karstic aquifer vulnerability assessment methods and results at a test site (Apulia, southern Italy), *Natural Hazards and Earth System Sciences*, *9*(4), 1461–1470, https://doi.org/10.5194/nhess-9-1461-2009.

Ravbar, N. (2007), *The protection of karst waters*, 254 pp., Inštitut za raziskovanje krasa ZRC SAZU.

Ravbar, N., and N. Goldscheider (2007), Proposed Methodology of Vulnerability and Contamination Risk Mapping for the Protection of Karst Aquifers in Slovenia, *Acta Carsologica*, *36*(3), https://doi.org/10.3986/ac.v36i3.174.

Ravbar, N., and N. Goldscheider (2008), Comparative application of four methods of groundwater vulnerability mapping in a Slovene karst catchment, *Hydrogeology Journal*, *17*(3), 725–733, https://doi.org/10.1007/s10040-008-0368-0.

Ravbar, N., M. Petrič, M. Blatnik, and A. Švara (2021), A multi-methodological approach to create improved indicators for the adequate karst water source protection, *Ecological Indicators*, *126*, 107,693, https://doi.org/10.1016/j.ecolind.2021.107693.

Russian Geographical Society (2024), Information retrieval system "Caves". Catalogue of caves, https://speleoatlas.ru/caves/ (in Russian), (visited on 21/08/2024).

State geological survey (2008), *State geologic maps of Ukraine. Scale 1:200 000. Sheets L-36-XXIX (Simferopol), L-36-XXXV (Yalta)*, 143 pp., Yuzhakogeocentre, Kiev (in Ukrainian).

Steiakakis, E., D. Vavadakis, and O. Mourkakou (2023), Groundwater Vulnerability and Delineation of Protection Zones in the Discharge Area of a Karstic Aquifer-Application in Agyia's Karst System (Crete, Greece), *Water*, *15*(2), 231, https://doi.org/10.3390/w15020231.

Stevanović, Z. (2019), Karst waters in potable water supply: a global scale overview, *Environmental Earth Sciences*, *78*(23), https://doi.org/10.1007/s12665-019-8670-9.

Tokarev, S., G. Amelichev, and Y. Amelichev (2024), Assessment of karst ground water vulnerability to contamination on the main massifs of the Mountain Crimea using regional methods, *Sustainable Development of Mountain Territories*, *16*(1), 397–409, https://doi.org/10.21177/1998-4502-2024-16-1-397-409 (in Russian).

Vakhrushev, B. A., G. N. Amelichev, S. V. Tokarev, and G. V. Samokhin (2022), The Main Problems of Karst Hydrogeology in the Crimean Peninsula, *Water Resources*, *49*(4), 595–604, https://doi.org/10.1134/S0097807822040182.

Vías, J. M., B. Andreo, M. J. Perles, et al. (2006), Proposed method for groundwater vulnerability mapping in carbonate (karstic) aquifers: the COP method: Application in two pilot sites in Southern Spain, *Hydrogeology Journal*, *14*(6), 912–925, https://doi.org/10.1007/s10040-006-0023-6.

Vyed', I. P. (2000), *Climatic atlas of Crimea. Supplement to "Questions of development of Crimea"*, 120 pp., Tavriya-Plus, Simferopol (in Russian).

Yogafanny, E., and D. Legono (2021), Assessment of Groundwater Vulnerability using COP Method to Support the Groundwater Protection in Karst Area, *IOP Conference Series: Earth and Environmental Science*, *930*(1), 012,036, https://doi.org/10.1088/1755-1315/930/1/012036.

Yudin, V. V. (2011), Tectonics of karst massif Chatyrdag in Crimea, *Speleology and Karstology*, (8), 5–17 (in Russian).

Russian Journal of Earth Sciences

Low-Magnitude Seismicity of the Continent-Ocean Transition Zone in the Eurasian Arctic

A. N. Morozov[1,2,3], N. V. Vaganova[2], Ya. V. Konechnaya[2,4], Ya. A. Mikhailova[2], and N. V. Petrova[4]

[1]Schmidt Institute of Physics of the Earth of the Russian Academy of Sciences, Moscow, Russia
[2]N. Laverov Federal Center for Integrated Arctic Research of the Ural Branch of the Russian Academy of Sciences, Arkhangelsk, Russia
[3]Geophysical Center of the Russian Academy of Sciences, Moscow, Russia
[4]Geophysical Survey of the Russian Academy of Sciences; Obninsk, Russia
* **Correspondence to:** Alexey Morozov, morozovalexey@yandex.ru

Abstract: A significant increase in the number of seismic stations occurred in the Eurasian Arctic during the late 20th to early 21st century, which led to a decrease in the minimum magnitude of earthquake registration for some Arctic regions. One of the areas that have been until recently poorly studied in terms of low-magnitude seismicity includes the continent-ocean transition zone in the northern Eurasian shelf. An analysis of the monitoring performed using the seismic stations in operation in the Franz Josef Land and Severnaya Zemlya archipelagos complemented with data from the seismic stations on the Svalbard archipelago for the period from December 2011 to November 2020 made it possible to study the space-time patterns in the low magnitude seismicity at the continent-ocean transition zone. The most active features are the Franz Victoria and St. Anna grabens, and the Bely and Victoria High.

Keywords: continent-ocean transition zone, continental slope, Eurasian Arctic, seismicity.

Citation: Morozov, A. N., N. V. Vaganova, Ya. V. Konechnaya, Ya. A. Mikhailova, and N. V. Petrova (2024), Low-Magnitude Seismicity of the Continent-Ocean Transition Zone in the Eurasian Arctic, *Russian Journal of Earth Sciences*, 24, ES4011, EDN: PRLQWW, https://doi.org/10.2205/2024es000927

Research Article

Received: 5 March 2024
Accepted: 30 July 2024
Published: 10 December 2024

Introduction

The start of seismological observations in the Arctic dates back to 1906 when seismological observations began in Vassijaure, northern Sweden. The Vassijaure seismic station was the first to be operated north of the Arctic Circle. The station was equipped with a horizontal Wiechert instrument which was subsequently, in 1915, transferred to the Abisko Research Station [*Avetisov*, 1996; *Kulhánek*, 1988]. However, the first important data on the seismicity of the Arctic territories in the early twentieth century was given by the Disko (Godhavn) seismic station, which operated from October 1907 to 1912 on Disko Island off the west coast of Greenland [*Harboe*, 1911], as well as studies of regional seismicity in the area of the Svalbard archipelago, which were carried out under the direction of G. Rempp from November 1911 to 1912 [*Rempp*, 1914].

The total number of seismic stations north of the Arctic Circle has been gradually, and at variable rates, increasing. However, until the beginning of the 21st century, the extensive Arctic territory was extremely unevenly covered by stations because of a severe climate and unfavorable geographic conditions (Figure 1a). As a result, the minimum magnitude of completeness varied widely over the Arctic region, from 2.0–2.5 for northern Scandinavia to as high as 4.0 in some areas, such as eastern part of the mid-oceanic Gakkel Ridge [*Avetisov*, 1996; *Engen et al.*, 2003].

However, this was sufficient to get a good general notion of the seismicity in the main seismic zones of the Arctic, viz., the spreading boundary between the North American and Eurasian plates. The boundary runs from Iceland through the Eurasian Basin, and the Laptev Sea shelf as far as Northeast Eurasia. However, the total number of stations and

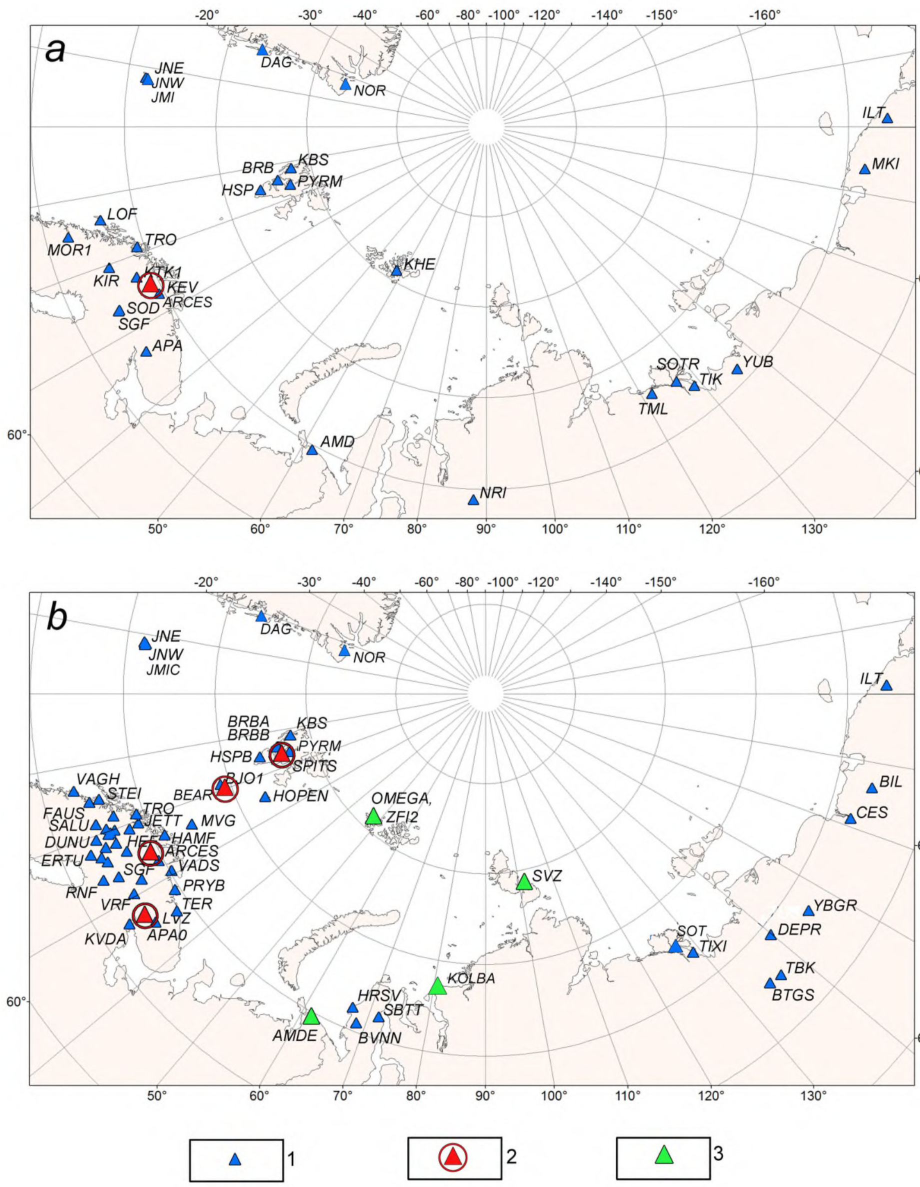

Figure 1. Map of seismic stations in the Eurasian Arctic, operating in the 80s of the XX century (a) and at the time of 2019 (b): 1 – seismic stations of the GE network (GEOFON Global Seismic Network), NO network (NORSAR Station Network), NS network (University of Bergen Seismic Network), and PL network (Polish Seismic Network) by [*FDSN*, 2024]; 2 – seismic arrays of the NO network; 3 – seismic stations of the AH network (Arkhangelsk Seismic Network) by [*FDSN*, 2024].

their density was quite insufficient for detailed studies of seismicity in some Arctic areas [*Avetisov*, 1996]. As a result, it was not possible to register low-magnitude earthquakes for some areas of the Arctic. The study of low-magnitude earthquakes provides much evidence from which to infer space-time variations of seismicity and to the geodynamic processes in that area [*Panasenko*, 1986].

The number of seismic stations in the Eurasian Arctic considerably increased in the late 20th to early 21st century. The stations were equipped with advanced sensitive instruments, reducing the lower magnitude of complete reporting for some Arctic areas (Figure 1b). The use of new seismic stations and improved algorithms for seismic signal processing and earthquake location gave more knowledge of seismicity both for the Arctic as a whole and for individual areas [*Antonovskaya et al.*, 2020; *Gibbons et al.*, 2017; *Morozov et al.*, 2016; *Rogozhin et al.*, 2016; *Schweitzer et al.*, 2021].

The areas that until recently were poorly studied in terms of low-magnitude seismicity include the continent-ocean transition zone in the northern Eurasian shelf. The research of the spatial distribution of seismicity in this area is important and topical. In the first place, in virtue of its geographic and climate conditions, the region remains poorly studied so far. Secondly, the incoming seismic data in combination with available geophysical information shed new light on the geodynamics of the region.

Previously [*Morozov et al.*, 2014] we did a preliminary analysis of seismicity occurring in the continent-ocean transition zone of the Barents-Kara region in the Arctic. However, that analysis was based on the data of a single station ZFI2 (AH network by [*FDSN*, 2024]) with additional data from stations in the Svalbard archipelago. The study covers period from December 2011 to January 2014. Subsequently, new seismic stations were installed on Franz Josef Land and in Severnaya Zemlya (AH network by [*FDSN*, 2024]) (Figure 1b), considerably expanding the area of study and providing seismic data for the period from December 2011 to November 2020 (Figure 2). This article presents the results of registration, location and analysis of the spatial-temporal distribution of low-magnitude earthquakes within the continent-ocean transition zone in the Eurasian Arctic.

Description of Data Set and Methods

The area of study is the northern part of the Arctic Eurasian shelf (Figure 2). The seismic monitoring of the study area was based on data coming from the AH network [*FDSN*, 2024] stations operated on Franz Josef Land (ZFI and OMEGA) and Severnaya Zemlya (SVZ) for the period from October 2011 to November 2020. Their frequency characteristics are shown in Figure 3. Seismic stations are located on Arctic islands, so their frequency characteristics can vary greatly depending on the season. For example, in the winter months, the sea area is under ice cover and economic activity on the islands sharply decreases, which is reflected in the frequency characteristics of seismic stations.

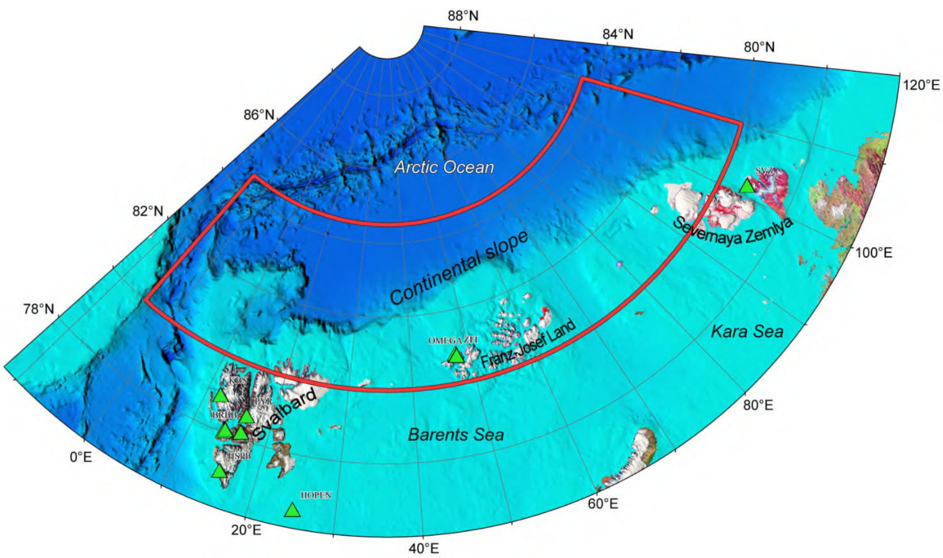

Figure 2. Map showing the boundaries of the area of study (red line) and location of seismic stations (green triangles).

We minimized the epicenter location uncertainty by also using waveform data recorded by the stations operated on Svalbard and in northern Scandinavia. These are KBS of the GE network (GEOFON, Global Seismic Network), HSPB of the PL network (Polish Seismic Network), HOPEN and BJO1 of the NS network (Norwegian National Seismic Network University of Bergen Norway), as well as the SPA0 stations in the SPITS seismic array (NORSAR Station Network) [*FDSN*, 2024]. Data access was via the electronic resource GEOFON [*GFZ German Research Center for Geosciences*, 2021]. If the earthquakes were also

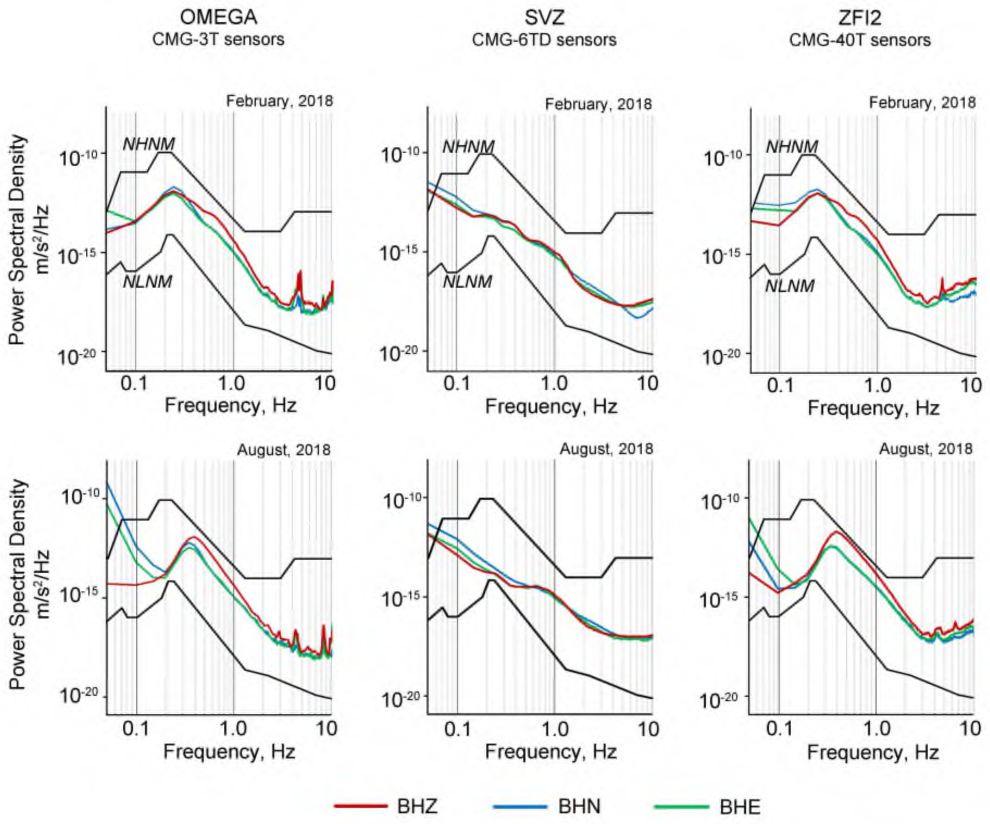

Figure 3. Power spectral density for seismic stations calculated from BHZ, BHN, and BHE components of the seismic stations. The New High and New Low Noise Models (NHNM and NLNM) are marked by black lines [*Peterson*, 1993].

recorded by remote seismic stations, then we took the arrival times of these stations from the International Seismological Centre [*International Seismological Centre*, 2024].

As mentioned above, at the present time, the number of permanent seismic stations in the Eurasian Arctic is the greatest for the entire period of instrumental observation. However, the conditions are still unfavorable for reliable epicenter location, especially as concerns low-magnitude earthquakes. The reasons for this are low number of stations, the great interstation distances, and their location in space relative to the epicenter of the arctic earthquakes. For the continental slope between the archipelagos of Svalbard and Franz Josef Land, earthquakes were located under conditions when seismic stations were located to the west and east of the earthquake epicenters (Figure 2, see also Figure 5). On the contrary, within the continental slope between the archipelagos of Franz Josef Land and Severnaya Zemlya until 2016, the location of earthquakes occurred in a narrow azimuthal coverage. After the start of operation of the SVZ seismic station (AH network by [*FDSN*, 2024] in 2016 it became possible to locate earthquakes according to stations located in the west and east relative to the epicenters.

Earthquakes that occurred in the study area during the period from October 2011 to November 2020 were recorded by a different number of seismic stations. One part of the earthquakes was recorded by three or more stations, and the other part by only two stations. Some earthquakes were recorded by only one single seismic station.

To locate earthquakes that were recorded by three or more stations, we used the algorithm of the NAS program (New Association System) [*Asming et al.*, 2016; *Fedorov et al.*, 2019], which implements the Generalized beamforming method [*Kværna and Ringdal*, 1996]. The algorithm calculates error ellipses based on the assumption that the velocity model error estimate is $\Delta v = 0.15$ km/s, and the seismic phase arrival time measurement error estimate is $\Delta t = 0.3$ s (level of confidence is 0.95). Because the stations were remote and few, it has not been possible to find the depths of focus, so the calculation was based on a fixed depth of 5 km.

To locate earthquakes that were recorded by only two stations, we used the "circle and chord" method [*Havskov et al.*, 2002] implemented in WSG (Windows Seismic Grafer) program developed by the Geophysical Survey of the Russian Academy of Sciences (GS RAS) [*Akimov and Krasilov*, 2020]. This method draws circles with the center at the station locations and the radii equal to the epicentral distances calculated from the S-P times. The calculation of epicenter parameters was also based on a fixed depth of 5 km. The WSG program does not implement error ellipse calculation. We estimate a formal location error of at least 30 km for the study area.

For earthquakes that were recorded by only one single seismic station, we used the algorithm of the EL (Event Location) program [*Kremenetskaya and Asming*, 2002]. To locate a seismic event by a single station EL algorithm uses the distance defined by S-P time difference and the backazimuth computed by P wave polarization. The depth is assumed to be 5 km. To minimize the possible uncertainty in the location of such earthquakes, we analyzed only earthquakes with clear arrivals of P and S, i.e., with a high signal/noise ratio. The EL program does not implement error ellipse calculation. We estimate the formal location error ±35 km for an epicentral distance of 200 km ($h = 5$ km). This surely is a less reliable location method, but it still provides an idea of the epicenter distribution.

Of course, we get very inaccurate location results based on data from only two or one seismic stations and the methods implemented in the WSG and EL programs. But, they allowed us to get a rough idea of the distribution of the epicenters for low-magnitude earthquakes, which were recorded by only one or two stations. And as will be shown below, this distribution in general terms corresponds to the distribution of epicenters calculated on the basis of data from three or more seismic stations.

The earthquake coordinates and origin times were calculated using the NOES velocity model [*Morozov and Vaganova*, 2017]. The model is based on the crustal velocity structure for the area of the Franz Josef Land Archipelago by receiver functions (Table 1). We calculated the M_L magnitude using the average calibration function for North Eurasia [*Gabsatarova*, 2006] and implemented in the WSG program [*Akimov and Krasilov*, 2020].

Table 1. NOES velocity model by [*Morozov and Vaganova*, 2017]

Depth, km	V_p, km/s	V_s, km/s	Note
0	4.3	2.36	
4	6.1	3.6	
17	6.8	3.94	
30	8.15	4.52	
43	8.25	4.75	
71	8.35	4.81	
> 210	8.37	4.56	from IASP 91

Results

A total of 192 earthquakes have been recorded in the continent-ocean transition zone from October 2011 to November 2020. Only 87 earthquakes were recorded by three or more seismic stations, 36 earthquakes were recorded by two stations. And 69 earthquakes were recorded by only one seismic station.

The M_L magnitudes of the earthquakes vary between 0.7 and 3.9 (Figure 4a). Nearly half of all recorded earthquakes have magnitudes $M_L \leq 2.1$. Those with magnitudes $M_L \geq 3.0$ make up a mere 20% of the total number. It can thus be said that the area of study mostly produces low-magnitude earthquakes.

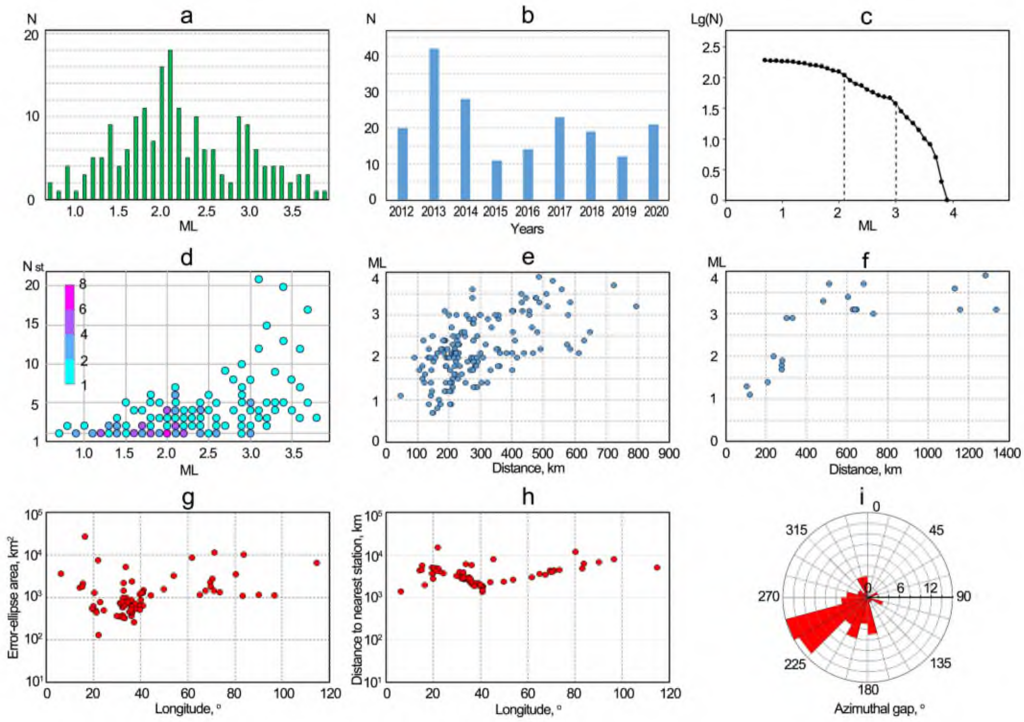

Figure 4. Data analysis of the final catalog of earthquakes: (a) the distribution of the number of recorded earthquakes by their magnitude; (b) the distribution of the number of recorded earthquakes by year; (c) the cumulative frequency-magnitude curve; (d) the number of stations that recorded earthquakes depending on the magnitude (color scale shows the number of earthquakes); (e,f) the distribution of earthquake magnitudes depending on the distance to the seismic station ZFI2 (e) and SVZ (f); (g) the distribution of the area of the earthquake error ellipse depending on latitude; (h) the distribution of distances from earthquake epicenters to the nearest seismic station depending on latitude; (i) the distribution of azimuthal gap values.

However, the functioning of seismic stations on the Franz Josef Land and Severnaya Zemlya archipelagos in different years was affected by technical problems and anthropogenic factors. Technical problems frequently arose at the stations because of extreme conditions in which the instruments were operated. The areas are hardly accessible, so it was impossible to resolve technical problems quickly and take preventive maintenance measures for seismic instrumentation. In addition, increased human activities caused considerable increases in the level of man-induced noise on Alexandra Land (Franz Josef Land archipelago) where seismic instrumentation is installed at the ZFI2 and OMEGA stations (Figure 1b). Therefore, the number of recorded earthquakes and the minimum magnitudes of recorded earthquakes varied greatly depending on the years (Figure 4b). On the diagram of the distribution of the number of recorded earthquakes by their magnitude, we observe several maxima (Figure 4a). In particular, for magnitudes with values of 2.1 and 2.9. For these magnitudes, we also observe inflection points in the cumulative frequency-magnitude curve (Figure 4c).

Figure 4d shows the number of stations that recorded earthquakes depending on the magnitude. Only earthquakes with magnitudes greater than 1.4 could be recorded by three stations. At the same time, some earthquakes with magnitudes up to 3.0 were recorded by only one single station. This is also due to technical problems at the seismic stations closest to such earthquakes.

Figure 4e,f show the distribution of earthquake magnitudes depending on the distance to the seismic station ZFI2 (Figure 4e) and SVZ (Figure 4f). From distances up to 430 km, the ZFI2 station recorded earthquakes with magnitudes M_L below 2.0, and from distances up to 650 km, earthquakes with magnitudes below 3.0. Within distances up to 340 km, the continental slope falls within the range from 22° E to 70° E. And within distances up to 650 km, practically most of the study area falls in this.

There is not much data for the SVZ seismic station, because the station began to function only in 2016. From distances up to 230 km, the SVZ station recorded earthquakes with magnitudes M_L below 2.0, and from distances up to 330 km, earthquakes with magnitudes below 3.0. Only a small part of the continental slope within our study area falls within these distances. Thus, the capabilities of seismic stations to register low-magnitude earthquakes within the continent-ocean transition zone to the west and east of the Franz Josef Land archipelago were different.

Figure 4g shows the dependence of the area of the error-ellipse on longitude for earthquakes recorded by three or more seismic stations. Overall solution accuracy depends on longitude. The smallest error-ellipses are typical for earthquakes from the region ranging from 20° E to 40° E. This effect is explained by network geometry for this region, reflecting the distance of the located epicenters from the nearest seismic stations (Figure 4h). However, the coverage of the network is unsatisfactory, with most location estimates achieving primary azimuthal gaps between 165° and 270° (Figure 4i).

Discussion of Results

Figure 5 shows the earthquake epicenters recorded within the study area. The epicenters are depicted in different colors. Red epicenters with error ellipses are earthquake recorded by three or more seismic stations. The size and orientation of the error ellipse depends on the number of stations and epicenter geometry. Green epicenters are earthquakes recorded by only two stations. And yellow epicenters are earthquakes recorded by only one station. The spatial distribution of green epicenters corresponds to the distribution of red ones. The distribution of yellow epicenters is more chaotic. But most of these epicenters are also confined to seismically active regions.

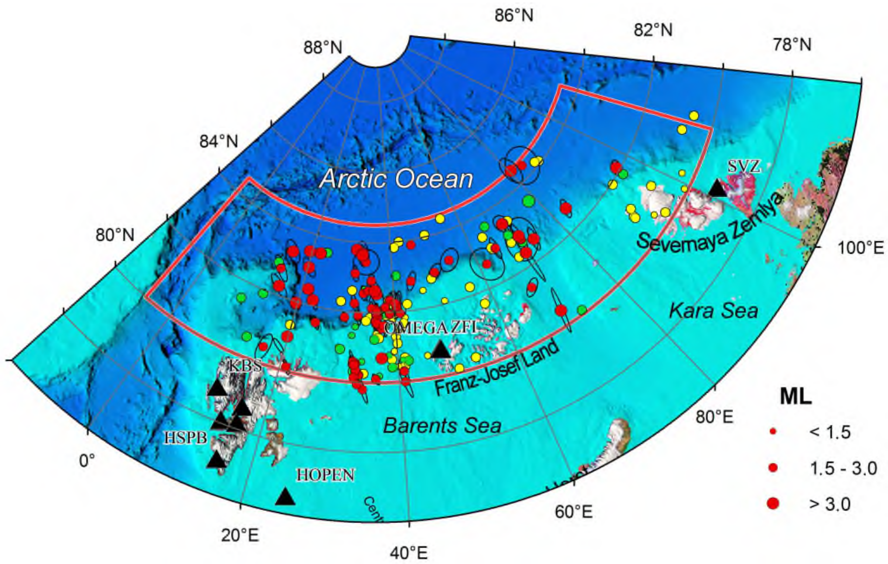

Figure 5. Bathymetric map (https://www.ngdc.noaa.gov) of the distribution of earthquakes (red circles) in the continent-ocean transition zone of the Eurasia Arctic region during the period from October 2011 to November 2020. The red line indicates the study area, and the black triangles indicate seismic stations.

The distribution of epicenters of the recorded earthquakes is not uniform over the area of study (Figure 5). The pronounced occurrence of the epicenters at negative morphostructures of the continental slope, namely, grabens and positive morphostructures –

highs should be noted. Most of the recorded earthquakes occurred at the Franz Victoria and St. Anna grabens, also at Kvitøya (Bely) island (Figure 6).

The earthquake epicenters recorded in the Franz Victoria graben area tend to occur in several parts of the graben area. Most epicenters are in the immediate vicinity of the continental slope, and at the boundary between the graben and the Bely and Victoria High, in its northern and southern parts (Figure 6).

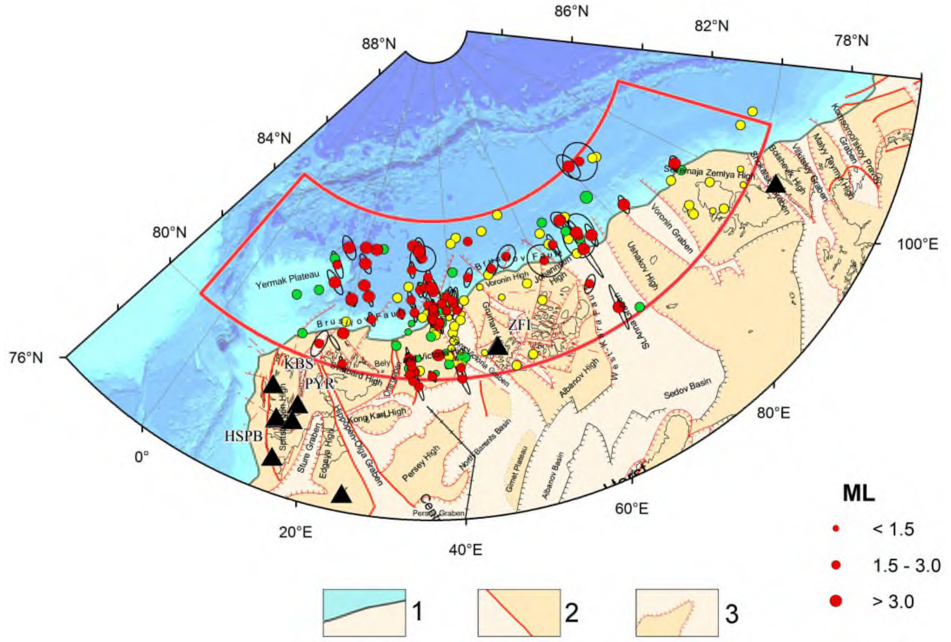

Figure 6. Map of the neotectonic structures and active faults [*Alekseev*, 2004] and distribution of earthquakes of the continent-ocean transition zone of the Eurasia Arctic region during the period from October 2011 to November 2020: 1-shelf edge, steep of flexure-fault zone; 2-main neotectonic faults; 3-dislocation with a break of continuity.

We relocated in [*Morozov et al.*, 2018] the earthquakes occurring in the western sector of the Russian Arctic for the period from the early 20th century to 1989. It was shown that the Franz Victoria graben is one of the main seismically active areas of the Barents-Kara region. Seven earthquakes with $m_b(ISC) \geq 4.3$ had been recorded within the graben during the instrumental period (until 1989), while two events (1908 and 1948) had magnitudes 6.5 at the lowest; in particular, the 1908 earthquake had M_w(ISC-GEM) = 6.6 (Table 2). Earthquakes of smaller magnitude were not recorded in the Franz-Victoria Graben region due to the remoteness of seismic stations and their small number (Figure 1a). Thus, our results supplement the information about the seismicity features of this region.

The epicenters of the earthquakes recorded in the St. Anna graben area also tend to occur in several parts of the graben. Most epicenters are in the immediate vicinity of the continental slope. A few earthquakes are confined to the middle of the graben (Figure 5, 6).

West of the Franz Victoria graben is the Orle graben. Surveys conducted in the area showed an abnormally high heat flow at the graben, 300 to 520 $\mathrm{mW/m^2}$ which is nearly 10 times the background value [*Khutorskoi et al.*, 2009]. This anomalous heat flow is characteristic for the entire Orle graben and its extension in the continental slope up to a depth of 1200 m. [*Khutorskoi et al.*, 2009] hypothesized crustal destruction in the graben area throughout its entire depth accompanied by the emplacement of hot mantle material, which provides evidence of an active phase in the graben evolution. High temperatures in the lithosphere can be invoked to explain a virtually complete absence of recorded earthquakes in the Orle graben area. Just two earthquakes can be supposed to have originated in the graben area. Further west, in the area of the Yermak Plateau, we have seismicity confined to the plateau slopes (Figure 6).

Table 2. Catalog of relocated seismic events in an area of the Franz Victoria Trench for the period from the beginning of the 20th century to 1989

Date dd.mm.yyyy	Time hh:mm:ss.0	Hypocenter			Error ellipse			Magnitude	Source of the hypocenter
		ϕ, °	λ,°	h*, km	Az_{major}, °	S_{minor}, km	S_{major}, km		
14.10.1908	14.56:17.5	82.13	36.19	12f	100	87.0	193.0	M_w(ISC) = 6.61	by [*Morozov et al.*, 2019]
18.02.1948	20:29:52.8	82.53	41.42	(0) 0–16	80	18.0	24.4	M = 6.5	by [*Morozov et al.*, 2014]
26.09.1948	05:51:18.4	82.30	40.22	(4) 0–99	70	40.5	104.7	–	by [*Morozov et al.*, 2014]
22.11.1948	23:32:48.0	82.42	41.90	(1) 0–65	90	25.8	38.1	–	by [*Morozov et al.*, 2014]
13.03.1967	21:44:07.8	82.30	40.71	(0) 0–32	100	12.3	21.7	m_b(ISC)=4.3	by [*Morozov et al.*, 2014]
14.03.1967	07:50:18.1	82.33	40.12	(4) 0–36	100	10.2	20.3	m_b(ISC)=4.3 M(MOS)=5.5	by [*Morozov et al.*, 2014]
25.06.1975	10:14:57.9	82.42	39.54	(0) 0–43	100	14.1	35.5	m_b(ISC)=4.6 m_b(NEIS)=4.6 M(LAO) = 4.8	by [*Morozov et al.*, 2014]

* – (h) means a fixed depth value when calculating the parameters of the epicenter; the number in brackets means the most probable depth value in the depth range.

From 2006 to 2009, researchers of the Geological Institute of the Russian Academy of Sciences, in collaboration with the Norwegian Petroleum Directorate, undertook three expeditions aimed at clarifying the structure of individual sections of the continent-ocean transition zone of the Barents Sea's northwestern margins [*Zaionchek et al.*, 2010]. These expeditions revealed a system of large landsides on the continental slope of the Arctic Ocean. Landslides had previously been found on the Norwegian continental slope, in the Litke graben and at the extension of the Hinlopen Strait [*Hjelstuen et al.*, 2007; *Vanneste et al.*, 2006; *Winkelmann and Stein*, 2007].

During one of the expeditions, signs of the intensive offset of large rock fragments of turbidite fracture and alluvial cone formation were detected inside the Orle graben formation. Similar phenomena were also observed on the western side, mainly occurring due to the isostatic compensation of avalanche sedimentation. It is therefore possible to assume that the eastern grabens, starting from the Franz Victoria, also act as channels for sedimentary material transport.

Researchers at the Kola Branch, GS RAS [*Vinogradov and Baranov*, 2013] studied the nature of seismic events in the western part of the Barents Sea shelf, within the continental slope area. Regarding minor seismicity ($M_L \leq 2.2$), seasonality was observed for the earthquakes registered in the area from the Strait of Storfjorden (Svalbard archipelago) to Bjornoya Island. In accordance with the suggested hypothesis, most of the low-magnitude earthquakes are the result of the landslide processes taking place in steep shelf areas, with their seasonality reflecting rapid changes in alluvial material mass flow during the warm season. In particular, by analyzing the records of the SPITS seismic group, the authors were able to identify waveforms caused by landslide events in the north of Spitsbergen.

Therefore, based on an overall analysis of the available geophysical, geotectonic and new seismic data, it can be assumed that the prevailing geodynamic factor responsible for the occurrence of low-magnitude earthquakes is the isostatic compensation of sedimentation in the continent-ocean transition zone.

Seismic activity is also observed within the easternmost island, Bely (Kvitøya) in the Svalbard archipelago, which also belongs to the Bely and Victoria High. On January 30, 2013, an earthquake with a magnitude of $M_L = 3.4$ occurred near Bely Island. After this earthquake, six earthquakes were recorded within five hours, which are aftershocks.

Disperse seismicity occurs in the area of Franz Josef Land and Severnaya Zemlya within the region of study. Since the time that a seismic station began operation on Severnaya Zemlya in 2016, some earthquakes have been recorded in the continental slope; however, the first thing to be noted consists in the fact that these were too few to infer definite occurrence at certain tectonic features. Secondly, nearly all events were located using records of a single station.

Conclusions

On the basis of the performed seismic monitoring of the continent-ocean transition zone of the Barents-Kara region during the period from October 2011 to November 2020, the following can be deduced:

1. A total of 192 earthquakes have been recorded during the period of observation with magnitudes in the range between 0.7 and 3.9. The pronounced occurrence of the epicenters at negative morphostructures of the continental slope, namely, grabens and positive morphostructures – highs should be noted.
2. The areas of highest seismicity are the Franz Victoria and St. Anna grabens and Bely and Victoria High. The prevailing geodynamic factor in the seismicity of the Franz Victoria and St. Anna grabens is most likely isostatic compensation of sedimentation in the continent-ocean transition zone.
3. The Orle graben is nearly free of earthquake occurrence. Surveys conducted in the Orle graben area showed an abnormally high heat flow at the graben, 300 to 520 mW/m^2, which is nearly 10 times the background value [*Khutorskoi et al.*, 2009]. High temperatures in the lithosphere can be invoked to explain a virtually complete absence of recorded earthquakes in the Orle graben area.

Data and Resources

Access to the data from broadband stations operating in the Svalbard Archipelago was through the GEOFON program (HYPERLINK, https://geofon.gfz-potsdam.de/waveform/, visited on July, 2024). The bathymetry is from the National Geophysical Data Center and is available at https://www.ngdc.noaa.gov/mgg/bathymetry/maps/nos_intro.html (visited on July, 2024). Description of the AH network is available at DOI: https://doi.org/10.7914/SN/AH, the GE network – DOI: https://doi.org/10.14470/TR560404, the PL network – https://www.fdsn.org/networks/detail/PL/ (visited on July, 2024), the NS network – DOI: https://doi.org/10.7914/SN/NS, the NO network – https://www.fdsn.org/networks/detail/NO/ (visited on July, 2024), the II network – DOI: https://doi.org/10.7914/SN/II, the CN network – DOI: https://doi.org/10.7914/SN/CN, and the DK network – https://www.fdsn.org/networks/detail/DK/ (visited on July, 2024).

Acknowledgments. The study was carried out under state contracts with N. Laverov Federal Center for Integrated Arctic Research of the Ural Branch of the Russian Academy of Sciences (project no. 122011300389-8), Schmidt Institute of Physics of the Earth of the Russian Academy of Sciences (project no. 075-00693-22-00), Geophysical Center of the Russian Academy of Sciences (project no. 075-00443-24-01), and Geophysical Survey of the Russian Academy of Sciences (state contract no. 075-00682-24, project no.122040800176-9).

References

Akimov, A. P., and S. A. Krasilov (2020), Software complex WSG "Seismic Data Processing System". Certificate of state registration of the computer program No 2020664678 dated November 16, 2020 (in Russian), EDN: IJOVUE.

Alekseev, M. N. (Ed.) (2004), *Atlas: geology and mineral resources of the shelf of Russia*, Geological Institute RAS (in Russian).

Antonovskaya, G. N., N. K. Kapustian, Y. V. Konechnaya, and A. V. Danilov (2020), Registration Capabilities of Russian Island-Based Seismic Stations: Case Study of the Gakkel Ridge Monitoring, *Seismic Instruments*, *56*(1), 33–45, https://doi.org/10.3103/S0747923920010028.

Asming, V. E., A. V. Fedorov, A. N. Vinogradov, et al. (2016), The System of Automatic Seismological Monitoring of the Nort-West Russia and tth Western Arctica, in *Moderm Methods of Processing and Interpretation of Seismological Data. Proc. XI International Seismological Workshop. Kyrgyzstan, September 12-16*, pp. 34–36, GS RAS, Obninsk (in Russian).

Avetisov, G. P. (1996), *Seismically active zones of the Arctic*, VNIIOkeangeologiya, St. Petersburg (in Russian).

Engen, Ø., O. Eldholm, and H. Bungum (2003), The Arctic plate boundary, *Journal of Geophysical Research: Solid Earth*, *108*(B2), https://doi.org/10.1029/2002JB001809.

FDSN (2024), Arkhangelsk Seismic Network, https://www.fdsn.org/networks/, https://doi.org/10.7914/SN/AH, (visited on 07/31/2024).

Fedorov, A. V., V. E. Asming, Z. A. Jevtjugina, and A. V. Prokudina (2019), Automated Seismic Monitoring System for the European Arctic, *Seismic Instruments*, *55*(1), 17–23, https://doi.org/10.3103/S0747923919010067.

Gabsatarova, I. P. (2006), Introduction into routine practice divisions of the Geophysical Survey of RAS calculation procedure of the local magnitude, in *MODERN METHODS OF PROCESSINGAND INTERPRETATION OF SEISMOLOGICAL DATA. Materials from International seismological schooldedicated to 100-annivesary foundationof seismic stations "Pulkovo" and "Ekaterinburg"*, pp. 49–53, GS RAS, Obninsk (in Russian).

GFZ German Research Center for Geosciences (2021), GEOFON, http://geofon.gfz-potsdam.de/geofon, (visited on 07/31/2024).

Gibbons, S. J., D. B. Harris, T. Dahl-Jensen, et al. (2017), Locating seismicity on the Arctic plate boundary using multiple-event techniques and empirical signal processing, *Geophysical Journal International*, *211*(3), 1613–1627, https://doi.org/10.1093/gji/ggx398.

Harboe, E. G. (1911), *Das Erdbebenobservatorium auf der Disko-Insel*, Gerlands Beiträge zur Geophysik.

Havskov, J., P. Bormann, and J. Schweitzer (2002), Earthquake location, in *New Manual of Seismological Observatory Practice (NMSOP)*, Deutsches GeoForschungsZentrum GFZ.

Hjelstuen, B. O., O. Eldholm, and J. I. Faleide (2007), Recurrent Pleistocene mega-failures on the SW Barents Sea margin, *Earth and Planetary Science Letters*, *258*(3–4), 605–618, https://doi.org/10.1016/j.epsl.2007.04.025.

International Seismological Centre (2024), Searching the ISC Bulletin, https://doi.org/10.31905/D808B830, (visited on 07/31/2024).

Khutorskoi, M. D., Y. G. Leonov, A. V. Ermakov, and V. R. Akhmedzyanov (2009), Abnormal heat flow and the trough's nature in the Northern Svalbard plate, *Doklady Earth Sciences*, *424*(1), 29–35, https://doi.org/10.1134/S1028334X09010073.

Kremenetskaya, E., and V. Asming (2002), Problems of regional seismic event location and depth estimation in the European Arctic, *Workshop on IMS Location Calibration and Screening*, *4* (in Russian).

Kulhánek, O. (1988), The status, importance, and use of historical seismograms in Sweden, in *Symposium on historical seismograms and earthquakes*, pp. 64–69, Academic Press.

Kværna, T., and F. Ringdal (1996), Generalized Beamforming, Phase Association and Threshold Monitoring using a Global Seismic Network, in *Monitoring a Comprehensive Test Ban Treaty*, pp. 447–466, Springer Netherlands, https://doi.org/10.1007/978-94-011-0419-7_24.

Morozov, A. N., and N. V. Vaganova (2017), The travel times of regional P and S for spreading ridges in the European Arctic, *Journal of Volcanology and Seismology*, *11*(2), 156–163, https://doi.org/10.1134/S0742046317020051.

Morozov, A. N., N. V. Vaganova, Y. V. Konechnaya, and V. E. Asming (2014), New data about seismicity and crustal velocity structure of the "continent-ocean" transition zone of the Barents-Kara region in the Arctic, *Journal of Seismology*, *19*(1), 219–230, https://doi.org/10.1007/s10950-014-9462-z.

Morozov, A. N., N. V. Vaganova, E. V. Ivanova, et al. (2016), New data about small-magnitude earthquakes of the ultraslow-spreading Gakkel Ridge, Arctic Ocean, *Journal of Geodynamics*, *93*, 31–41, https://doi.org/10.1016/j.jog.2015.11.002.

Morozov, A. N., N. V. Vaganova, V. E. Asming, Y. V. Konechnaya, and Z. A. Evtyugina (2018), The instrumental seismicity of the Barents and Kara sea region: relocated event catalog from early twentieth century to 1989, *Journal of Seismology*, *22*(5), 1171–1209, https://doi.org/10.1007/s10950-018-9760-y.

Morozov, A. N., N. V. Vaganova, and Y. V. Konechnaya (2019), The October 14, 1908 MW 6.6 earthquake in the Barents and Kara sea region of the Arctic: Relocation based on instrumental data, *Polar Science*, *20*, 160–166, https://doi.org/10.1016/j.polar.2019.05.001.

Panasenko, G. D. (1986), Problems of seismic zoning of the Western sector of the Soviet Arctic, in *Nature and economy of the North*, vol. 14, pp. 4–6, AS USSR, Geographical Society of the USSR, Northern Branch (in Russian).

Peterson, J. R. (1993), *Observations and modeling of seismic background noise*, US Geological Survey, https://doi.org/10.3133/ofr93322.

Rempp, G. (1914), *Aufstellung und Betrieb eines Seismographen auf der Deutschen Geophysikalischen Station Adventbai (Spitzbergen) 1911/12*, Gerlands Beiträge zur Geophysik.

Rogozhin, E. A., G. N. Antonovskaya, N. K. Kapustian, and I. V. Fedorenko (2016), Features of seismicity of the Euro-Arctic region, *Doklady Earth Sciences*, *467*(2), 389–392, https://doi.org/10.1134/S1028334X16040140.

Schweitzer, J., B. Paulsen, G. N. Antonovskaya, et al. (2021), A 24-Yr-Long Seismic Bulletin for the European Arctic, *Seismological Research Letters*, *92*(5), 2758–2767, https://doi.org/10.1785/0220210018.

Vanneste, M., J. Mienert, and S. Bunz (2006), The Hinlopen Slide: A giant, submarine slope failure on the northern Svalbard margin, Arctic Ocean, *Earth and Planetary Science Letters*, *245*(1–2), 373–388, https://doi.org/10.1016/j.epsl.2006.02.045.

Vinogradov, A., and S. Baranov (2013), The possible impact of landslide processes on the seismicity of the North-Western part of the Barents sea, in *Modern methods of processing and interpretation of seismological data. Materials of theEighth International Seismological Workshop*, pp. 99–103, GS RAS, Obninsk.

Winkelmann, D., and R. Stein (2007), Triggering of the Hinlopen/Yermak Megaslide in relation to paleoceanography and climate history of the continental margin north of Spitsbergen, *Geochemistry, Geophysics, Geosystems*, *8*(6), https://doi.org/10.1029/2006GC001485.

Zaionchek, A., H. Brekke, S. Y. Sokolov, et al. (2010), The structure of the transition zone continent-ocean north-western periphery of the Barents Sea (according to 24, 25 and 26 flights vessel "Akademik Nikolai Strakhov" 2006-2009), in *The structure and evolution of the lithosphere*, pp. 111–157, Paulsen (in Russian).

Russian Journal of Earth Sciences

Monitoring Land Cover Dynamics and Forest Degradation in South Sumatra Peatlands from 2015 to 2023 by Remote Sensing Application

M. Y. N. Khakim[*,1], **A. A. Bama**[1], **and T. Tsuji**[2]

[1] Physics Department, Faculty of Mathematics and Natural Sciences, Universitas Sriwijaya, Indonesia
[2] School of Engineering, University of Tokyo, Japan
* **Correspondence to:** Mokhamad Yusup Nur Khakim, myusup_nkh@mipa.unsri.ac.id

Abstract: Most Peat Hydrological Units (PHU) in South Sumatra, Indonesia, have been threatened by degradation from climate changes, human activities, and environmental factors. This study mapped land cover using Random Forest Classification and identified forest degradation using NDFI (Normalized Difference Forest Index) change analysis in several PHUs of the South Sumatra peatland from 2015 to 2023. We combined Sentinel-1, Sentinel-2, and Landsat-8 data for the land cover classification. Meanwhile, we utilized Landsat-8 to identify forest degradation. Our findings indicate that tree cover significantly decreased in 2015, 2019, and 2023, coinciding with severe drought conditions driven by El Niño events. A significant decrease in forest cover in 2019 was suggested by low tree cover, up to 47.1% of the total area of 1.054 million ha. Therefore, grassland and bare/sparse vegetation had more significant coverage percentages, reaching 22.89% and 11.40%, respectively, in 2019. Deforestation varied but generally decreased from 2015 to 2023, according to the analysis of NDFI changes. Vegetation regrowth increased notably from 2016 to 2020 and remained relatively stable afterward. In addition, forest disturbance decreased from 2015 to 2020 but slightly increased in the last few years. Although two PHUs have encountered more severe degradation, their peatland ecosystems included inside them have distinct characteristics. Specifically, the PHU of Sungai Saleh – Sungai Sugihan encompasses cultivated areas, whereas the PHU of Sungai Sugihan – Sungai Lumpur comprises protected areas. These findings highlight the need for restoration and sustainable land management to prevent further degradation.

Keywords: Peatland, Land cover, Degradation, Random Forest, NDFI, South Sumatra, Remote Sensing.

Citation: Khakim, M. Y. N., A. A. Bama, and T. Tsuji (2024), Monitoring Land Cover Dynamics and Forest Degradation in South Sumatra Peatlands from 2015 to 2023 by Remote Sensing Application, *Russian Journal of Earth Sciences*, 24, ES4012, EDN: YGBEBU, https://doi.org/10.2205/2024es000914

Research Article

Received: 3 February 2024
Accepted: 28 May 2024
Published: 16 December 2024

1. Introduction

Hydrologically and ecologically different peat forest habitats regulate the global carbon cycle, biodiversity, and climate [*Page et al.*, 2011]. Peat forest degradation and land cover changes due to drainage, deforestation, and land conversion pose unprecedented risks to these vital ecosystems [*Hooijer et al.*, 2010; *Vijay et al.*, 2016]. Peatlands are carbon sinks that help mitigate climate change [*Page et al.*, 2011]. Due to soil oxidation and degradation, peat forests emit greenhouse gases when drained and deforested [*Hooijer et al.*, 2010; *Khakim et al.*, 2020].

There are direct and indirect drivers of peatland deforestation and degradation in the study area. Logging, industrial plantations, artificial drainage canals, recurrent fires, and fire-based traditional farming practices are direct contributors. Indirect factors include climate change, land use policy inconsistency, and inadequate management [*Dohong et al.*, 2017]. The logging and industrial plantations driving the degradation by agricultural conversion are mainly for palm oil and acacia plantations [*Astuti*, 2021; *Cooper et al.*, 2020;

Miettinen et al., 2012; Nurhayati et al., 2021]. Industrial plantations and small holder areas occupy a minimum of 21% of the peatland in South Sumatra [Putra et al., 2019]. In addition, the usage of uncontrolled fire has progressively increased over time in relation to the traditional cultivation of sonor or swamp rice [Chokkalingam et al., 2006]. Land clearance removes woody and non-woody plants for agricultural or industrial use. Logging roads make interior forests simpler to access and move, worsening deforestation. Artificial drainage systems lower the groundwater table for crop cultivation and timber transport. However, drainage systems disrupt the hydrological equilibrium, increasing surface runoff and decreasing water storage capacity. Consequently, the draining of peatlands can alter hydrology and ecosystem processes.

Furthermore, drainage for agricultural and plantation development increases peat soil subsidence and fire risk [Khakim et al., 2020]. The subsidence rate of peatlands in South Sumatra increased by 6.4 times after the 2015 El Niño event [Khakim et al., 2020]. In addition, the rate ranged from -567 to 347 mm/year between 2019 and 2022 [Zheng et al., 2023]. Higher temperatures, less precipitation, and more peat evaporation in droughts reduce peatland groundwater tables. Drawdown accelerates peat oxidation and breakdown, causing subsidence and carbon emissions. Peat fires are a significant issue in Indonesia, notably in South Sumatra. Dry drainage makes peatlands more combustible [Khakim et al., 2022]. Air pollution and climate change can result from peat fires releasing substantial volumes of carbon dioxide and other pollutants [Cobb et al., 2017; Dommain et al., 2014; Page et al., 2011].

Sustainable management and peatland degradation have been addressed. Strategies include avoiding peatland conversion, encouraging rewetting and regenerating degraded peatlands, and restricting burning [Dohong, 2017; Harrison et al., 2019; Uda et al., 2020; Yuwati et al., 2021]. Due to their environmental and climate implications, peatland conservation and management in Indonesia, including South Sumatra, have garnered international attention. Initiatives like the Indonesian Peatland Restoration Agency (BRG) have been established to coordinate restoration efforts [Humas, 2016]. Information on peatland degradation is essential for designing effective policies and regulations that promote sustainable land use practices, prevent further degradation, and support restoration efforts. Understanding and addressing peatland degradation in South Sumatra is crucial for mitigating climate change, preserving biodiversity, regulating water resources, preventing fires, promoting sustainable agriculture, supporting local communities, meeting international commitments, and maintaining the ecosystem's overall health. The urgent need to understand the drivers and consequences of such changes underscores the importance of advanced remote sensing technologies, which offer invaluable insights for effective conservation strategies [Miettinen et al., 2017].

Ecological, hydrological, and environmental indices are used to estimate peatland deterioration. Peatland degradation is quantified and monitored in several ways. Satellite imaging (Landsat, Sentinel) can track land cover, vegetation health, and water levels. Using Landsat-8, Sentinel-1, and Sentinel-2 satellite data to analyze peat forest degradation and land cover changes is challenging. Landsat-8's multispectral capabilities allow it to identify deforested areas, agricultural growth, and vegetation health changes [Pettorelli et al., 2014]. Sentinel-1 SAR technology provides all-weather imaging and reliable water table monitoring, which is crucial for peatland health assessment [Asmußet al., 2019; Khakim et al., 2022; Toca et al., 2023]. The spectral richness and high geographical resolution of Sentinel-2 data improve peat forest ecosystem study. Its regular return intervals allow monitoring of land cover changes, revealing subtle changes in vegetation composition and structure [Carrasco et al., 2019; Poortinga et al., 2019; Urban et al., 2018]. Advanced analytical methods are needed to obtain comprehensive information from these databases.

Unsupervised and supervised classification analyze land cover. Automatic, data-driven unsupervised classification is ideal for land cover pattern research, especially in areas with little prior knowledge. However, unsupervised classification has lower accuracy and subjectivity in interpretation. In addition, unsupervised methods can produce numerous classes that might not have precise ecological or practical meanings, making interpretation difficult. On the contrary, supervised classification allows us to differentiate between them accurately based on your training samples. On the other hand, random forest classification enables the automated identification and classification of land cover types based on the spectral signatures of different land features, contributing to precise mapping and monitoring [*Gómez et al.*, 2016; *Malinowski et al.*, 2020; *Shih et al.*, 2021; *Tian et al.*, 2016]. It allows for identifying and monitoring degradation-related changes in land cover proportions. Landsat endmembers were successfully applied to derive a Normalized Difference Fraction Index (NDFI) for monitoring forest degradation in several environmental, such as Amazon forest [*Souza Jr. et al.*, 2013], non-Amazonian tropical forest [*Schultz et al.*, 2016], and tropical peatland [*Numata et al.*, 2022]

Spectral analysis examines peatland surface reflectance in different bands. Spectral signatures can reveal vegetation, water, and soil changes. Changes in vegetation composition, density, and health indicate peatland degradation. Monitoring monoculture plantations vs. diversified native vegetation can indicate a decline. Land cover changes caused by peatland forest degradation can have serious ecological, environmental, and socioeconomic consequences. Spectral Mixture Analysis (SMA) is a typical remote sensing approach for assessing land cover component proportions in mixed pixels. Assessing peatland deterioration is another use for it. SMA and machine learning algorithms like random forest classification are used for classifying complicated ecosystems like peat forests. SMA uses remote sensing data to assess the fractional cover of vegetation, soil, and water [*Adams*, 1995; *Sakti and Tsuyuki*, 2015].

This study employed a supervised random forest (RF) classification method to gain insight into the various types and spatial distribution of land cover. Furthermore, the SMA and NDFI were utilized to identify peatland vegetation degradation in the South Sumatra peatland. The relationship between peatland forest degradation and land cover refers to how changes in the condition and quality of peatland ecosystems affect the types and distribution of vegetation and other land cover components within those ecosystems.

2. Materials and Methods

2.1. Study area

The study area is peatland, situated on the eastern coast of the island of Sumatra, adjacent to the Musi River delta (Figure 1). The study area is in two Bayuasin and Ogan Ilir Regencies and consists of nine peat hydrological units (PHUs). In 2015, the South Sumatra region experienced a catastrophic event when the El Niño phenomenon triggered devastating fires in its vulnerable peatlands. These fires ravaged a substantial area, estimated to be between 117,367 and 144,410 hectares (ha) of peatland within the province [*KLHK*, 2020]. The impact of these fires was particularly severe in specific areas, with approximately 6580 ha of burned peatlands located in villages situated within or adjacent to former restoration and conservation project areas in the Banyuasin, Muba, and Ogan Komering Ilir Regencies. Furthermore, an additional 13,061 ha of peatland succumbed to the flames within oil palm plantations, while a staggering 67,846 ha were engulfed in fires within logging concessions [*Budiman et al.*, 2021].

Within the PHU Sugihan-Lumpur area, four villages have implemented livelihood revitalization initiatives and participated in the Peat Care Village programs. These efforts included providing essential livelihood support to the local community. However, it's noteworthy that these villages did not undertake additional restoration activities, such as peat rewetting. Unfortunately, the reliance solely on livelihood revitalization and the programs proved insufficient to mitigate peatland fire risk. From September to October 2019, these villages experienced fires that ravaged 14,113 ha of peatland. A notable fire vulnerability persists despite groundwater monitoring stations in 8 out of 10 restoration areas [*Budiman et al.*, 2021].

While notable progress has been made in peatland protection, significant threats still loom. Before recent conservation endeavors, numerous companies obtained concession

Figure 1. Study area consisting of nine peat hydrological units.

permits encompassing vast protected peatland expanses. Alarmingly, over 25 percent of the total 12.2 million hectares (30 million acres) of protected peatland has already been allocated for concession areas, primarily geared toward pulpwood and palm oil plantations, or possesses the potential for conversion into plantation or agricultural usage [*Hidayah et al.*, 2018]. It highlights the persistent challenge of safeguarding these critical ecosystems against existing and potential land use pressures.

2.2. Land Cover Classification

We classified land cover over the study area by combining 544 radar images from Sentinel-1 and 2923 optical imageries, comprising 2318 Sentinel-2, and 605 Landsat-8 from January 2015 to August 2023. We preprocessed the image using Google Earth Engine (GEE). The radar data analysis involved using dual-polarized C-band data acquired by the Synthetic Aperture Radar (SAR) instrument aboard the S1A satellite.

The Level-1 Ground Range Detected product (GRD), as provided by GEE, was employed in this analysis. These GRD images underwent radiometric calibration and orthorectification. Two distinct polarization modes were used: single and dual-band co-polarization with vertical transmit/receive (VV) and horizontal receive (VH). An additional preprocessing step was implemented, which involved spatial filtering through a 7×7 Refined Lee speckle filter to mitigate the inherent speckle noise found in radar images. This preprocessing step was crucial for enhancing the suitability of the images for land cover detection at the spatial resolution employed in this research.

Furthermore, additional bands, such as the VH/VV ratio, the normalized ratio procedure between bands (NRPB) [*Filgueiras et al.*, 2019], and the radar vegetation index (RVI) [*Yamada*, 2015] were generated. For each observation date, a composite image comprising five bands (VV, VH, VH/VV ratio, NRPB, and RVI) was created, as this combination has been identified as optimal for characterizing land cover. Images were temporally combined by calculating median values for each band, resulting in the generation of composites spanning a one-year timeframe.

Sentinel-2 data, processed at level 1C as sourced from GEE, were employed. These data have undergone orthorectification and radiometric correction, resulting in top-of-atmosphere reflectance values. Bands 2 to 8 were selected and four indexes, namely Normalized Difference Vegetation Index (NDVI), Normalized Difference Built-up Index

Table 1. Bands and indices of each satellite for classification

Satellite	Bands/Indices
Sentinel-1	VV, VH, VH/VV, NRPB, and RVI
Sentinel-2	B2-8, 11, 12, NDVI, NDBI, S2REP, and IRECI,
Landsat-8	B2-7, soil, GV, NPV, GVs, shade, and NDFI

(NDBI), Sentinel-2 Red-Edge Position (S2REP), and Inverted Red-Edge Chlorophyll Index (IRECI), were derived for use, with their initial spatial resolutions at 10 meters. An automated cloud masking procedure was implemented to ensure data quality, utilizing band QA60 from the S2 1C product, effectively masking both opaque and cirrus clouds. Moreover, parameters derived from Landsat-8 are described in the following sub-section.

Table 1 shows the bands of each satellite for the classification input dataset. Several indices were also derived from each dataset to be included as the input. These bands and indices from Sentinel-1, Sentinel-2, and Landsat-8 images were merged into a single fused image using the 'addBands( ) function' in Google Earth Engine. Parameters were derived from unmixed fractions of the Landsat-8, such as Soil, Green Vegetation (GV), Non-Photosynthetic Vegetation (NPV), Shade-normalized Green Vegetation (GVs), Shade, and NDFI. More relevant feature variables boost classification accuracy [*Amoakoh et al.*, 2021].

Following the standardization of band values through band normalization, band stacking was carried out by aggregating all the processed radar and optical images for input each year. In this study, the Random Forest algorithm has been selected as the classifier. This algorithm assigns equal weight to each of the band layer stack images. Equal weighting in Random Forest (RF) classification ensures all features contribute equally to the model's decision-making process. This approach simplifies the modeling process, prevents bias, makes the model more robust to changes in the dataset, promotes balanced decision-making, and assumes equal importance. The RF approach employs a collection of decision trees to enhance prediction accuracy [*Breiman*, 2001]. We applied the Random Forest classification algorithm due to its robustness and ability to handle complex land cover patterns.

Based on field observation and image identification, we created point features for different land cover classes. Each point was assigned a class label representing the land cover class. To avoid overfitting, the labeled data was split into training and validation sets, 60% and 40%, respectively. The RF classifier with 120 trees was trained using the training dataset, and the classifier learned the underlying patterns and relationships between the features and class labels in the training data. The classifier performance was evaluated using the validation set. The trained model was then deployed to predict land cover across the study area.

2.3. Mapping Peatland Degradation

Peatland degradation is a critical environmental issue; remote sensing techniques are used on satellites. This study mapped peatland degradation using USGS Landsat 8 Level 2, Collection 2, Tier 1 from 2015 to 2023. We removed clouds and shadows from Landsat 8 imagery in GEE using the Quality Assessment ("QA_PIXEL") band to mask out pixels with clouds and shadows. To create a cloud-free composite image, we used the median to combine multiple cloud-masked images into one representative image for a year.

We Applied an SMA algorithm to find the linear combination of endmember spectra that best matches the observed mixed pixel spectrum. The output of SMA is a set of fractional maps representing the spatial distribution of different land cover components within each pixel. These maps indicate the proportion of each endmember (e.g., vegetation, soil, water) present in each pixel. By comparing fractional maps from different periods, we

Table 2. Reflectance values of the Landsat-8 endmembers

Endmember	Reflectance Values of Landsat-8					
	Band 2 (Blue)	Band 3 (Green)	Band 4 (Red)	Band 5 (NIR)	Band 6 (SWIR 1)	Band 7 (SWIR 2)
NPV	0.1514	0.1597	0.1421	0.3053	0.7707	0.1975
GV	0.0119	0.0475	0.0169	0.6250	0.2399	0.0675
Soil	0.1799	0.2479	0.3158	0.5437	0.7707	0.6646
Cloud	0.4031	0.8714	0.7900	0.8989	0.7002	0.6607

identified changes in the distribution of land cover components. It is beneficial for tracking the progression of peatland degradation, such as changes in vegetation and soil exposure.

We defined the Landsat-8 endmembers based on a previous study [*Souza Jr. et al.*, 2005]. The pure reflectance values for the blue, green, red, NIR, SWIR1, and SWIR2 bands of the Landsat-8 for different endmember materials like NPV, GV, Soil, and Cloud are presented in Table 1.

Unmixing the Landsat-8 image using the built-in '`unmix()`' function in Google Earth Engine involves estimating the fractional abundances of endmembers in each image pixel. The unmixed fractions were then converted to the image of the SMA model of the study area. The Shade and GVs fractions are used in the spectral mixture analysis to estimate the proportion of shaded and sunlit vegetation within a pixel. These fractions provide information about the vegetation canopy structure and can be calculated from the SMA results. The Shade fraction represents the pixel proportion covered by shadows or shaded areas. It is calculated by subtracting the sum of the GV and NPV fractions from 1:

$$\mathrm{Shade} = 1 - (\mathrm{GV} - \mathrm{NPV}).$$

The GVs was accounted for the shading effect by dividing the Green Vegetation (GV) fraction by the complement of the Shade fraction:

$$\mathrm{GV}_S = \frac{GV}{100 - \mathrm{Shade}}.$$

The NDFI enhancing the degradation signal caused by selective logging and burning was computed using the derived fraction images by:

$$\mathrm{NDFI} = \frac{\mathrm{GV}_S - (\mathrm{NPV} + \mathrm{Soil})}{\mathrm{GV}_S + \mathrm{NPV} + \mathrm{Soil}}.$$

Water and clouds affecting how we monitor forest degradation and loss were masked using a thresholding method based on the values of the fraction images. A water mask was created using threshold values for the Shade, GV, and Soil bands, where Shade is greater than or equal to 0.65, GV is less than or equal to 0.15, and Soil is less than or equal to 0.05. Meanwhile, a cloud mask was created by applying a threshold of 0.1 or more significant to the Cloud band.

Changes in NDFI that indicate forest change were obtained by calculating the difference between the two images. A temporal color composite was generated using two yearly NDFI images to enhance changes between them. The NDFI changes were then classified by defining a threshold based on inspecting the histogram and the NDFI temporal color composite.

3. Results and Discussion

3.1. Land cover analysis

Figure 2 shows the classified land cover over the study area. This land cover was classified into seven major land cover classes, i.e., tree cover, shrubland, grassland, cropland, built-up, bare/sparse vegetation, and water bodies. The tree cover class includes peat forests, oil palm plantations, rubber plantations, and mangroves. We defined shrub class as woody perennial plants characterized by persistent, woody stems and no single, well-defined main stem, typically standing at a height of less than 5 meters. Any geographic area dominated by natural herbaceous plants (without persistent stems or shoots above ground and lacking defined hard structure) is classified as grass. Grasslands, prairies, steppes, savannahs, and pastures are examples of grasslands. Cropland refers to cultivated land that can be harvested at least once within a 12-month following the first sowing or planting. Built-up refers to areas occupied by buildings, roads, and various other human-made constructions, including railroads. Built-up refers to areas occupied by buildings, roads, and different other human-made constructions, including railroads. Furthermore, the term "water class" is employed to categorize various aquatic environments such as fish ponds, rivers, and other bodies of water.

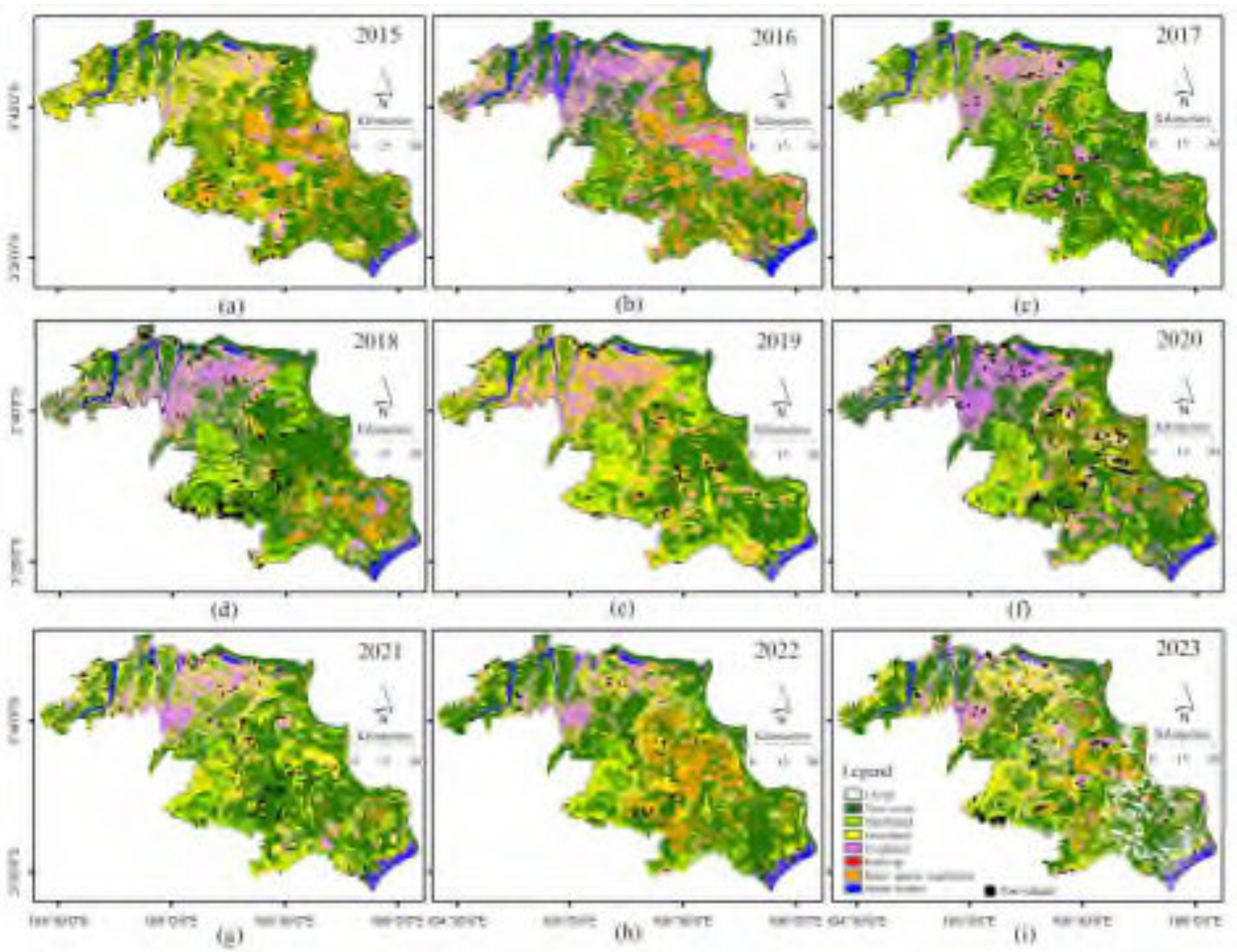

Figure 2. Classified land cover overlaid with hotspots from 2015–2023.

The overall accuracy (OA) of our land cover classification for 2015–2023 ranges from 90–94%, with a Kappa coefficient of 0.87–0.92, indicating a high level of accuracy and agreement between predicted and observed land cover classes, as shown in Table 3. The accuracy of the producers' (PA) and users' (UA) is also presented in this table. We randomly selected validation points to validate the classification and compared the predicted classes with observed land cover types in the field. The accuracy assessment showed that the model performed well across different land cover classes, with minimal misclassifications.

Table 3. Accuracy measurements of land cover

Year	Kappa	OA	Tree Cover		Shrubland		Grassland		Cropland		Built-up		Bare/sparse vegetation		Water bodies	
			PA	UA	PA	UA	PA	UA	PA	UA	PA	UA	PA	UA	PA	UA
2015	0.92	0.94	0.96	1.00	1.00	0.90	0.85	0.86	0.80	0.80	0.67	1.00	1.00	0.94	1.00	1.00
2016	0.90	0.92	1.00	0.88	1.00	0.93	0.80	0.92	0.80	1.00	1.00	1.00	0.70	1.00	1.00	1.00
2017	0.87	0.90	0.94	0.91	0.82	0.90	0.90	0.90	0.80	1.00	1.00	1.00	1.00	0.80	0.71	1.00
2018	0.90	0.92	0.92	0.95	0.85	1.00	1.00	0.82	1.00	0.86	0.67	1.00	0.90	0.90	1.00	1.00
2019	0.88	0.91	1.00	0.97	0.86	0.86	0.94	0.76	0.57	1.00	0.00	0.00	0.81	1.00	1.00	1.00
2020	0.89	0.91	0.91	0.94	1.00	0.93	0.95	1.00	1.00	0.50	1.00	0.75	0.67	0.80	1.00	1.00
2021	0.90	0.93	1.00	0.89	1.00	0.90	1.00	1.00	1.00	1.00	1.00	1.00	0.62	1.00	1.00	1.00
2022	0.89	0.92	0.94	0.96	0.77	0.90	1.00	0.82	0.83	0.83	1.00	1.00	0.92	0.86	1.00	1.00
2023	0.87	0.90	0.96	1.00	0.67	1.00	0.91	0.83	0.80	0.67	0.67	1.00	1.00	0.75	1.00	1.00

Detailed information on the extent percentage of each class's area is presented in Figure 3. The tree cover shows some fluctuations over the years. Land cover changes in a region like South Sumatra can be complex and influenced by multiple factors spatially and temporally. The extreme climate, El Niño events, are generally associated with drier conditions and increased fire risk, leading to potential negative impacts on vegetation. Tree cover increased in 2017 and 2020 but was lower in 2015, 2019, and 2023, directly correlated with El Niño which had lower precipitation and drier over the study area. In such situations, vegetation may already be stressed and more susceptible to degradation.

By comparing our classification results with historical data, we observed a significant decrease in forest cover in 2019, indicated by low tree cover (47.1% of the total area of 1.054 million ha), primarily attributed to fires and logging. Therefore, grassland and bare/sparse vegetation had more significant coverage percentages, reaching 22.89% and 11.40%, respectively. It suggests that the severity of the peat fires in South Sumatra in 2019 might surpass those observed in 2015. However, both El Niño in 2015 and 2019 likely contributed to reduced precipitation in those years, which could have led to drier conditions and increased fire risk.

The increase in 2017 and 2020 could be related to recovery after the El Niño events. However, tree cover had a slightly larger percentage in 2015 than in 2016. The impact of an El Niño event on any specific vegetation type may not be immediate. It can take some time for the full effects of decreased precipitation and increased fire activity to manifest. In some ecosystems, fire is a natural and essential ecological process. Certain plant species have adaptations that allow them to thrive after a fire. However, intense fires can still lead to degradation if ecosystems cannot regenerate properly between fire events. In the case of the study area, the reduced precipitation and increased fire risk during the 2015 El Niño event might have directly affected shrubland in that year and tree cover in subsequent years, including 2016.

On the other hand, human activities play a significant role in shaping land cover changes. Human activities, such as agricultural burning, land clearing, or accidental ignition, start many fires. Most fires occurred over the cultivation area in the PHU of Sungai Saleh – Sungai Sugihan in 2015, 2018, and 2023. In these areas, drained peatlands were used for agriculture and cultivation. In areas where human-induced fires are common, vegetation degradation can occur due to the cumulative impact of these fires. On the other hand, many hotspots can also be identified in the protected area, especially in the PHU of Sugai Sugihan – Sungai Lumpur, in 2017, 2018, 2020, and 2021. Spatial correlations between land cover changes and fire hotspots often result from natural ecological processes, human activities, and environmental factors.

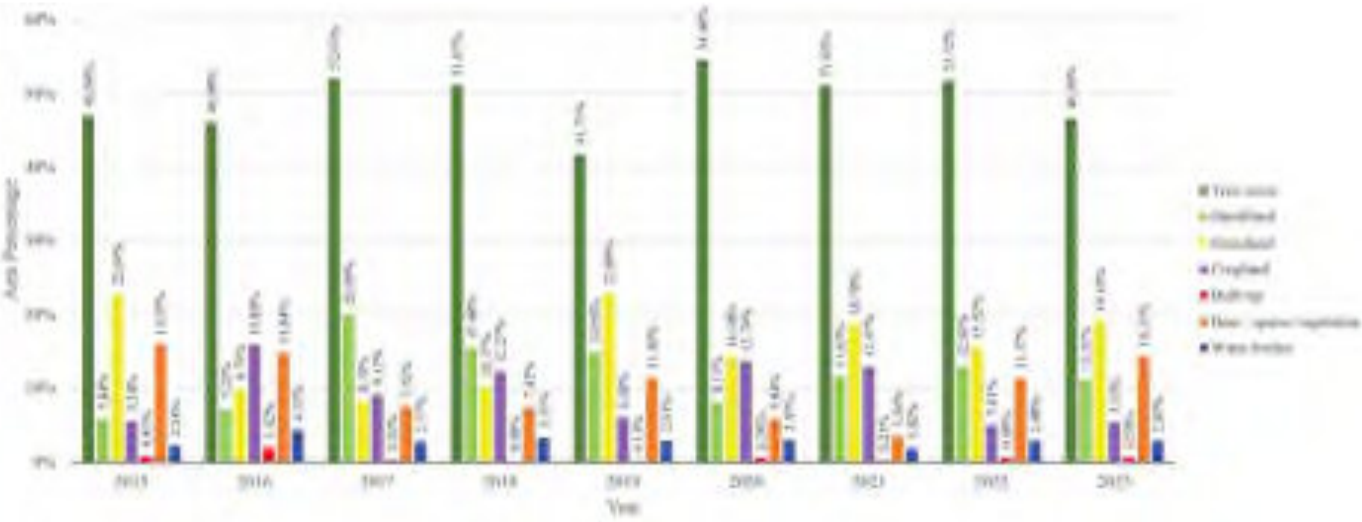

Figure 3. Percentages of classified land cover classes from 2015–2023.

3.2. Degradation analysis

This study also mapped peatland degradation to identify the factors causing changes in land cover. The data used for the degradation analysis consisted of Landsat-8 images from 2015 to 2023, covering the study area. The pure reflectance values for the blue, green, red, SWIR1, and SWIR2 spectral bands from the Landsat images were utilized for identifying endmembers such as NPV, GV, and Soil, as illustrated in Figure 4b–d. Unmixing the Landsat-8 images using the Singular Value Decomposition (SVD) method involved estimating the abundance fractions of endmembers in each image pixel.

The fractions obtained from the singular value docomposition were then transformed into a SMA model image for the study area. The Shade and GVs fractions, as shown in Figure 4e,f, were used in spectral mixture analysis to estimate the proportions of vegetation in a pixel that was shaded and exposed to sunlight. These fractions provide information about the canopy structure of vegetation and can be computed from the SMA results. The Shade fraction represents the proportion of pixels covered by shadows or areas shaded by vegetation. Then, from the GVs, NPV, and Soil fractions, the NDFI is calculated. For example, NDFI maps for 2019 and 2020 were used to map land degradation in 2020 by mapping the NDFI changes between these two consecutive years. The NDFI for those years and their changes can be displayed in Figure 4g–i.

Water and cloud, which can affect the mapping of forest degradation and damage, must be excluded from the calculations, often referred to as masking, using a threshold-based method based on the values of the fraction images. The water mask is created using threshold values for the Shade, GV, and Soil fractions, where Shade is greater than or equal to 0.65; GV is less than or equal to 0.15; and Soil is less than or equal to 0.05. Meanwhile, the cloud mask is created by applying a threshold of 0.1 or greater to the Cloud fraction.

Changes in NDFI indicating land changes are obtained by calculating the difference between these two images. A temporal color composite is generated using two annual NDFI images to highlight the changes between them. The changes in NDFI are then classified by defining thresholds and the temporal color composite of NDFI. In the Landsat 8 composite map (Figure 4a), green indicates vegetation, and brown represents bare land. Bare land without vegetation corresponds to what the Soil fraction map shows, which appears whiter. The whiter the color in the GV and GVs fraction maps, the more vegetated the area. Similarly, for other fraction maps, such as NPV and Shade, the whiter color indicates higher fraction values, reflecting the condition of the depicted objects.

Peatland degradation in South Sumatra, Indonesia, is primarily caused by human activity and environmental factors. Draining peatlands for agricultural purposes, particularly the creation of oil palm plantations and rice fields, upsets the natural hydrological

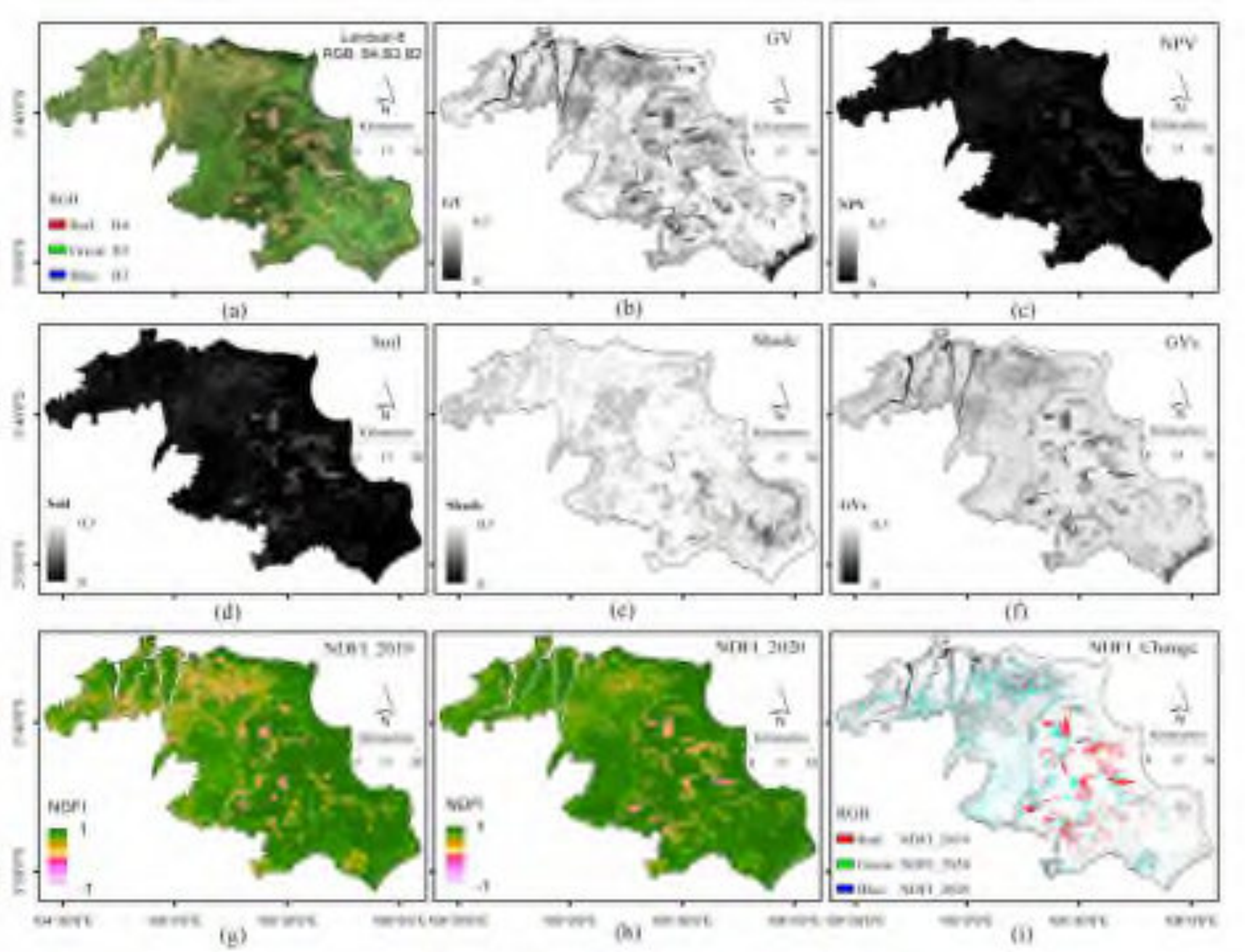

Figure 4. Maps of (a) Landsat-8 RGB composite, (b-f) Landsat-8 fractions, (g) NDFI 2019, (h) NDFI 2020, and (i) NDFI change from 2019–2020.

equilibrium, causing the water table to decrease and the peat to dry out. This accelerates the breakdown process and releases stored carbon into the environment. Large-scale land conversion exacerbates the problem, as enormous sections of peatland are removed and transformed into plantations. The loss of natural vegetation exposes the peat to oxidation, accelerating decomposition. Furthermore, the region is prone to peat fires, particularly during the dry season. Climate change exacerbates these difficulties by changing precipitation patterns and increasing the frequency of extreme weather events like droughts and wildfires, putting additional strain on already degraded peatlands. The orange on the NDFI maps (Figure 4g,h) indicates forest disturbance related to fires and selective logging. Meanwhile, the pink and white colors represent dry vegetation and bare land in previously logged forests. In grassland areas, the orange color indicates dry vegetation. The NDFI change map in Figure 4i used red to depict new deforestation, and pink represents selective logging. The cyan color indicates vegetation regrowth in areas logged or burned a year or more ago.

NDFI changes were classified to identify vegetation disturbances, deforestation, and vegetation regrowth spatially and temporally from 2015 to 2023, as presented in Figure 5. These maps are overlaid with the distribution of fire hotspots to analyze the relationship between the NDFI change classification and the locations of fire occurrences. Generally, these changes relatively corresponded to the identified hotspot distribution, indicating

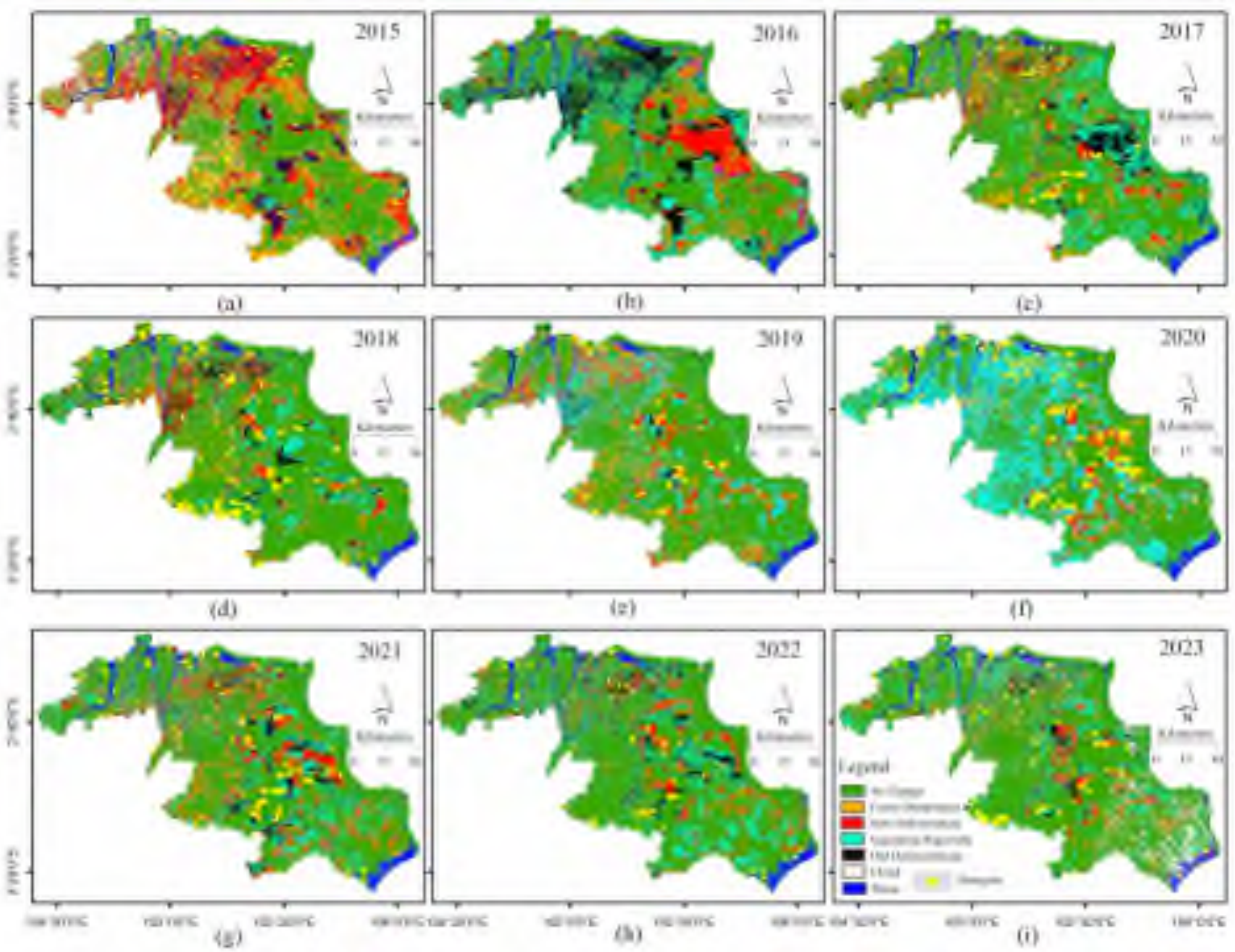

Figure 5. NDFI changes classes overlaid the hotspot from 2015–2023.

that the degradation caused by land fires obtained from the NDFI change classification aligns with the observed fire events. According to the NDFI change categorization map, the PHU of Sungai Sugihan – Sungai Lumpur, situated in the eastern region of the research area, had the highest degree of degradation. Subsequently, the adjacent PHU located to the west, specifically Sungai Saleh – Sungai Sugihan, exhibits a similarly significant level of degradation. Although these PHUs have encountered more severe degradation, it is essential to note that the peatland ecosystems within them exhibit distinct characteristics. Specifically, the PHU Sungai Saleh – Sungai Sugihan encompasses cultivated areas, whereas the PHU Sungai Sugihan – Sungai Lumpur comprises protected areas.

In addition, the extent of the percentage of degraded areas can be calculated based on the NDFI change classification, as presented in Figure 6. According to these calculations, the most severe degradation occurred in 2015, followed by 2019. The percentage of no forest change has gradually increased from 2015 to 2018, showing that these areas have comparatively recovered from the effects of the El Niño in 2015. On the other hand, it declined between 2019 and 2020 before climbing back up to 2023. Forest disturbance includes activities that negatively impact the forest but may not necessarily result in deforestation. This category covers disturbances such as logging, selective harvesting, or fires. Forest disturbance decreased from 2015 to 2018 but slightly increased in the last few years. New deforestation refers to converting forested areas into non-forest land cover types. It indicates the loss of forested land. New deforestation varied over the years but showed a declining trend from 2015 to 2023, suggesting that efforts might have been made to reduce deforestation. Vegetation regrowth represents areas where new vegetation has grown, naturally or through reforestation, following previous disturbances. Vegetation regrowth increased notably from 2016 to 2020 and remained relatively stable afterward. It may indicate successful reforestation or natural regeneration.

Figure 6. Variation of area percentages for four NDFI change classes from 2015–2023.

Key observations from the results are the data suggests that there has been a reduction in new deforestation over the years, which is a positive sign for forest conservation efforts; the increase in vegetation regrowth from 2016 to 2020 is noteworthy and indicates restoration efforts or natural recovery in previously disturbed areas; forest disturbance decreased from 2015 to 2020 but showed a slight increase in the last few years, which should be monitored to ensure sustainable forest management practices.

4. Conclusion

Our study analyzed land cover dynamics and forest degradation in South Sumatra's peatlands from 2015 to 2023 using Random Forest classification and NDFI change analysis with a multi-temporal dataset from Sentinel-1, Sentinel-2, and Landsat-8. The classification results showed seven land cover classes consisting of tree cover, shrubland, grassland, farmland, built-up regions, bare/sparse vegetation, and water bodies, offering a comprehensive picture of land cover changes in the study area. Accuracy of 90% to 94% and a Kappa coefficient of 0.87 to 0.92 shows significant agreement between predicted and actual land cover classifications across categories. Our classification model's low misclassification rate proves its usefulness for monitoring peatland land cover changes.

The comprehensive examination of land cover alterations throughout the study unveiled variations in the extent of tree cover, which were impacted by intricate spatial and temporal factors. It is worth mentioning that the effects of El Niño occurrences, which are linked to arid conditions and heightened susceptibility to fires, were noted during periods of diminished tree coverage. The year 2019 experienced a notable decline in forest area, predominantly because of fires and logging operations. Consequently, there was an expansion in grassland coverage and an increase in areas with limited or no vegetation. Forest disturbance increased slightly in recent years after decreasing from 2015 to 2020. Anthropogenic activities, such as the deliberate burning of agricultural fields and the clearance of land, have significantly influenced alterations in land cover. The areas in the two PHUs have more severe degradation, and the gradation occurred in regions with distinct peatland ecosystem functions. The PHU of Sungai Saleh – Sungai Sugihan degraded mainly in the cultivation area, while the PHU of Sungai Sugihan – Sungai Lumpur in the protected areas.

The areas with the highest levels of fire activity were primarily located in regions where fires caused by human activities were prevalent, namely on drained peatlands utilized for agricultural purposes. Furthermore, the presence of fire hotspots was seen within designated protected areas, indicating the intricate relationship between natural biological processes, human actions, and environmental elements in influencing alterations in land cover and degradation of forests.

Our study suggests that South Sumatra peatlands are ecologically important and vulnerable to natural and human-induced processes, making monitoring and conservation essential. Advanced remote sensing and historical data help policymakers and land managers establish proactive policies to conserve these vital ecosystems in the face of changing environmental challenges.

Acknowledgments. We would like to acknowledge Direktorat Riset, Teknologi, dan Pengabdian kepada Masyarakat (DRTPM) for financial support through "Penelitian Fundamental Reguler", Contract Number: 164/E5/PG.02.00.PL/2023, dated 5 July 2023. We also thank the European Space Agency (ESA) for providing Sentinel-1 data, anonymous reviewers, and the academic editor for their valuable comments and suggestions.

References

Adams, J. (1995), Classification of multispectral images based on fractions of endmembers: Application to land-cover change in the Brazilian Amazon, *Remote Sensing of Environment*, *52*(2), 137–154, https://doi.org/10.1016/0034-4257(94)00098-8.

Amoakoh, A. O., P. Aplin, K. T. Awuah, et al. (2021), Testing the Contribution of Multi-Source Remote Sensing Features for Random Forest Classification of the Greater Amanzule Tropical Peatland, *Sensors*, *21*(10), 3399, https://doi.org/10.3390/s21103399.

Asmuß, T., M. Bechtold, and B. Tiemeyer (2019), On the Potential of Sentinel-1 for High Resolution Monitoring of Water Table Dynamics in Grasslands on Organic Soils, *Remote Sensing*, *11*(14), 1659, https://doi.org/10.3390/rs11141659.

Astuti, R. (2021), Governing the ungovernable: The politics of disciplining pulpwood and palm oil plantations in Indonesia's tropical peatland, *Geoforum*, *124*, 381–391, https://doi.org/10.1016/j.geoforum.2021.03.004.

Breiman, L. (2001), Random Forests, *Machine Learning*, *45*(1), 5–32, https://doi.org/10.1023/A:1010933404324.

Budiman, I., R. D. Hapsari, C. I. Wijaya, and E. N. N. Sari (2021), The Governance of Risk Management on Peatland: A Case Study of Restoration in South Sumatra, Indonesia, *World Resources Institute*, https://doi.org/10.46830/wriwp.20.00008.

Carrasco, L., A. W. O'Neil, R. D. Morton, and C. S. Rowland (2019), Evaluating Combinations of Temporally Aggregated Sentinel-1, Sentinel-2 and Landsat 8 for Land Cover Mapping with Google Earth Engine, *Remote Sensing*, *11*(3), 288, https://doi.org/10.3390/rs11030288.

Chokkalingam, U., Suyanto, R. P. Permana, et al. (2006), Community fire use, resource change, and livelihood impacts: The downward spiral in the wetlands of southern Sumatra, *Mitigation and Adaptation Strategies for Global Change*, *12*(1), 75–100, https://doi.org/10.1007/s11027-006-9038-5.

Cobb, A. R., A. M. Hoyt, L. Gandois, et al. (2017), How temporal patterns in rainfall determine the geomorphology and carbon fluxes of tropical peatlands, *Proceedings of the National Academy of Sciences*, *114*(26), https://doi.org/10.1073/pnas.1701090114.

Cooper, H. V., S. Evers, P. Aplin, N. Crout, M. P. B. Dahalan, and S. Sjogersten (2020), Greenhouse gas emissions resulting from conversion of peat swamp forest to oil palm plantation, *Nature Communications*, *11*(1), https://doi.org/10.1038/s41467-020-14298-w.

Dohong, A. (2017), Bolstering Peatlands Restoration in Indonesia through 3Rs Approach, in *Developing International Collaborations to Address Fire and Other Conservation Issues in Central Kalimantan, Indonesia*, https://doi.org/10.13140/RG.2.2.33080.19200.

Dohong, A., A. A. Aziz, and P. Dargusch (2017), A review of the drivers of tropical peatland degradation in South-East Asia, *Land Use Policy*, *69*, 349–360, https://doi.org/10.1016/j.landusepol.2017.09.035.

Dommain, R., J. Couwenberg, P. H. Glaser, et al. (2014), Carbon storage and release in Indonesian peatlands since the last deglaciation, *Quaternary Science Reviews*, *97*, 1–32, https://doi.org/10.1016/j.quascirev.2014.05.002.

Filgueiras, R., E. C. Mantovani, D. Althoff, E. I. Fernandes Filho, and F. F. da Cunha (2019), Crop NDVI Monitoring Based on Sentinel 1, *Remote Sensing*, *11*(12), 1441, https://doi.org/10.3390/rs11121441.

Gómez, C., J. C. White, and M. A. Wulder (2016), Optical remotely sensed time series data for land cover classification: A review, *ISPRS Journal of Photogrammetry and Remote Sensing*, *116*, 55–72, https://doi.org/10.1016/j.isprsjprs.2016.03.008.

Harrison, M. E., J. B. Ottay, L. J. D'Arcy, et al. (2019), Tropical forest and peatland conservation in Indonesia: Challenges and directions, *People and Nature*, *2*(1), 4–28, https://doi.org/10.1002/pan3.10060.

Hidayah, H., J. Reidinar, N. S. Tjokorda, and W. Arief (2018), Indonesia's Deforestation Dropped 60 Percent in 2017, but There's More to Do, https://www.wri.org/insights/indonesias-deforestation-dropped-60-percent-2017-theres-more-do.

Hooijer, A., S. Page, J. G. Canadell, M. Silvius, J. Kwadijk, H. Wösten, and J. Jauhiainen (2010), Current and future CO2 emissions from drained peatlands in Southeast Asia, *Biogeosciences*, *7*(5), 1505–1514, https://doi.org/10.5194/bg-7-1505-2010.

Humas (2016), President Jokowi Establishes Peat Land Restoration Agency (BRG), https://setkab.go.id/en/president-jokowi-establishes-peat-land-restoration-agency-brg/.

Khakim, M. Y. N., A. A. Bama, I. Yustian, P. Poerwono, T. Tsuji, and T. Matsuoka (2020), Peatland subsidence and vegetation cover degradation as impacts of the 2015 El niño event revealed by Sentinel-1A SAR data, *International Journal of Applied Earth Observation and Geoinformation*, *84*, 101,953, https://doi.org/10.1016/j.jag.2019.101953.

Khakim, M. Y. N., A. A. Bama, and T. Tsuji (2022), Spatiotemporal Variations of Soil Moisture and Groundwater Level in a South Sumatra Peatland, Indonesia During 2015-2018, *GEOGRAPHY, ENVIRONMENT, SUSTAINABILITY*, *15*(2), 58–70, https://doi.org/10.24057/2071-9388-2021-137.

KLHK (2020), Karhutla Monitoring System, https://sipongi.menlhk.go.id/.

Malinowski, R., S. Lewiński, M. Rybicki, et al. (2020), Automated Production of a Land Cover/Use Map of Europe Based on Sentinel-2 Imagery, *Remote Sensing*, *12*(21), 3523, https://doi.org/10.3390/rs12213523.

Miettinen, J., A. Hooijer, C. Shi, et al. (2012), Extent of industrial plantations on Southeast Asian peatlands in 2010 with analysis of historical expansion and future projections, *GCB Bioenergy*, *4*(6), 908–918, https://doi.org/10.1111/j.1757-1707.2012.01172.x.

Miettinen, J., A. Hooijer, R. Vernimmen, S. C. Liew, and S. E. Page (2017), From carbon sink to carbon source: extensive peat oxidation in insular Southeast Asia since 1990, *Environmental Research Letters*, *12*(2), 024,014, https://doi.org/10.1088/1748-9326/aa5b6f.

Numata, I., A. J. Elmore, M. A. Cochrane, C. Wang, J. Zhao, and X. Zhang (2022), Deforestation, plantation-related land cover dynamics and oil palm age-structure change during 1990-2020 in Riau Province, Indonesia, *Environmental Research Letters*, *17*(9), 094,024, https://doi.org/10.1088/1748-9326/ac8a61.

Nurhayati, A. D., B. Hero Saharjo, L. Sundawati, S. Syartinilia, and M. A. Cochrane (2021), Forest and Peatland Fire Dynamics in South Sumatra Province, *Forest and Society*, pp. 591–603, https://doi.org/10.24259/fs.v5i2.14435.

Page, S. E., J. O. Rieley, and C. J. Banks (2011), Global and regional importance of the tropical peatland carbon pool, *Global Change Biology*, *17*(2), 798–818, https://doi.org/10.1111/j.1365-2486.2010.02279.x.

Pettorelli, N., K. Safi, and W. Turner (2014), Satellite remote sensing, biodiversity research and conservation of the future, *Philosophical Transactions of the Royal Society B: Biological Sciences*, *369*(1643), 20130,190, https://doi.org/10.1098/rstb.2013.0190.

Poortinga, A., K. Tenneson, A. Shapiro, et al. (2019), Mapping Plantations in Myanmar by Fusing Landsat-8, Sentinel-2 and Sentinel-1 Data along with Systematic Error Quantification, *Remote Sensing*, *11*(7), 831, https://doi.org/10.3390/rs11070831.

Putra, R., E. Sutriyo, S. Kadir, and I. Iskandar (2019), Understanding of Fire Distribution in the South Sumatra Peat Area During the Last Two Decades, *International Journal of GEOMATE*, *16*(54), https://doi.org/10.21660/2019.54.8243.

Sakti, A. D., and S. Tsuyuki (2015), Spectral Mixture Analysis (SMA) of Landsat Imagery for Land Cover Change Study of Highly Degraded Peatland in Indonesia, *The International Archives of the Photogrammetry, Remote Sensing and Spatial Information Sciences*, *XL-7/W3*, 495–501, https://doi.org/10.5194/isprsarchives-XL-7-W3-495-2015.

Schultz, M., J. G. P. W. Clevers, S. Carter, et al. (2016), Performance of vegetation indices from Landsat time series in deforestation monitoring, *International Journal of Applied Earth Observation and Geoinformation*, *52*, 318–327, https://doi.org/10.1016/j.jag.2016.06.020.

Shih, H., D. A. Stow, K. Chang, D. A. Roberts, and K. G. Goulias (2021), From land cover to land use: applying random forest classifier to Landsat imagery for urban land-use change mapping, *Geocarto International*, *37*(19), 5523–5546, https://doi.org/10.1080/10106049.2021.1923827.

Souza Jr., C. M., D. A. Roberts, and M. A. Cochrane (2005), Combining spectral and spatial information to map canopy damage from selective logging and forest fires, *Remote Sensing of Environment*, *98*(2-3), 329–343, https://doi.org/10.1016/j.rse.2005.07.013.

Souza Jr., C. M., J. V. Siqueira, M. H. Sales, et al. (2013), Ten-Year Landsat Classification of Deforestation and ForestDegradation in the Brazilian Amazon, *Remote Sensing*, (5), 5493–5513, https://doi.org/10.3390/rs5115493.

Tian, S., X. Zhang, J. Tian, and Q. Sun (2016), Random Forest Classification of Wetland Landcovers from Multi-Sensor Data in the Arid Region of Xinjiang, China, *Remote Sensing*, *8*(11), 954, https://doi.org/10.3390/rs8110954.

Toca, L., R. R. E. Artz, C. Smart, et al. (2023), Potential for Peatland Water Table Depth Monitoring Using Sentinel-1 SAR Backscatter: Case Study of Forsinard Flows, Scotland, UK, *Remote Sensing*, *15*(7), 1900, https://doi.org/10.3390/rs15071900.

Uda, S. K., G. Schouten, and L. Hein (2020), The institutional fit of peatland governance in Indonesia, *Land Use Policy*, *99*, 103,300, https://doi.org/10.1016/j.landusepol.2018.03.031.

Urban, M., C. Berger, T. E. Mudau, et al. (2018), Surface Moisture and Vegetation Cover Analysis for Drought Monitoring in the Southern Kruger National Park Using Sentinel-1, Sentinel-2, and Landsat-8, *Remote Sensing*, *10*(9), 1482, https://doi.org/10.3390/rs10091482.

Vijay, V., S. L. Pimm, C. N. Jenkins, and S. J. Smith (2016), The Impacts of Oil Palm on Recent Deforestation and Biodiversity Loss, *PLOS ONE*, *11*(7), e0159,668, https://doi.org/10.1371/journal.pone.0159668.

Yamada, Y. (2015), Preliminary Study on the Radar Vegetation Index (RVI) Application to Actual Paddy Fields by ALOS/PALSAR Full-polarimetry SAR Data, *The International Archives of the Photogrammetry, Remote Sensing and Spatial Information Sciences*, *XL-7/W3*, 129–131, https://doi.org/10.5194/isprsarchives-XL-7-W3-129-2015.

Yuwati, T. W., D. Rachmanadi, Pratiwi, M. Turjaman, et al. (2021), Restoration of Degraded Tropical Peatland in Indonesia: A Review, *Land*, *10*(11), 1170, https://doi.org/10.3390/land10111170.

Zheng, X., C. Wang, Y. Tang, et al. (2023), Adaptive High Coherence Temporal Subsets SBAS-InSAR in Tropical Peatlands Degradation Monitoring, *Remote Sensing*, *15*(18), 4461, https://doi.org/10.3390/rs15184461.

Сравнительное влияние гидрометеорологических процессов на межгодовую изменчивость сезонных колебаний уровня Балтийского моря

Е. А. Захарчук[1], **М. В. Виноградов**[1,2], **В. Н. Сухачев**[*,1,2] и **Н. А. Тихонова**[1,2]

[1]Санкт-Петербургский Государственный университет, г. Санкт-Петербург, Россия
[2]Государственный океанографический институт имени Н. Н. Зубова, г. Москва, Россия
* **Контакт:** Владимир Николаевич Сухачев, Syhachev@mail.ru

С помощью продолжительных среднесуточных мареографных наблюдений за уровнем моря, спутниковых альтиметрических измерений и данных реанализов метеорологических и гидрофизических полей исследуются особенности и физические механизмы межгодовой изменчивости сезонных колебаний уровня Балтийского моря. Показано, что за период 1889–2022 гг. в Стокгольме в межгодовых изменениях амплитуд гармоник Sa, Ssa, Sta, Sqa не отмечаются статистически значимые линейные тренды, но наблюдаются долгопериодные циклы с временными масштабами от 20–35 до 55 лет и очень значительными изменениями амплитуд от 0,5–1,0 до 25–27 сантиметров. В последние десятилетия у гармоник Sa, Ssa, Sta наблюдается заметное уменьшение амплитуд и дисперсии колебаний. Результаты взаимного корреляционного и множественного регрессионного анализов аномалий сезонных колебаний уровня моря и различных гидрометеорологических процессов свидетельствуют, что самый большой вклад в межгодовую изменчивость сезонных колебаний уровня моря оказывают изменения касательного трения ветра. Вторыми по значимости процессами являются изменения атмосферного давления над морем и водообмена между Балтийским и Северным морями. Самое незначительное воздействие на межгодовую изменчивость характеристик сезонных колебаний уровня моря оказывают изменения составляющих пресного баланса и плотности воды.

Ключевые слова: уровень моря, спутниковые альтиметрические измерения, данные реанализа, сезонные колебания, скользящий гармонический анализ, межгодовая изменчивость, тренды, касательное напряжение трения ветра, атмосферное давление, стерические колебания, пресноводный баланс, водообмен, множественный регрессионный анализ.

Цитирование: Захарчук, Е. А., М. В. Виноградов, В. Н. Сухачев и Н. А. Тихонова Сравнительное влияние гидрометеорологических процессов на межгодовую изменчивость сезонных колебаний уровня Балтийского моря // Russian Journal of Earth Sciences. — 2024. — Т. 24. — ES4013. — DOI: 10.2205/2024es000922 — EDN: RNZFKL

https://elibrary.ru/rnzfkl

Получено: 17 января 2024 г.
Принято: 12 июля 2024 г.
Опубликовано: 17 декабря 2024 г.

1. Введение

Сезонные колебания уровня играют важную роль в динамике вод почти полностью замкнутого, мелководного Балтийского моря. Они являются индикаторами изменений метеорологических процессов, наблюдающегося потепления климата [*Гордеева и Малинин*, 2014; *Männikus et al.*, 2020], водообмена с Северным морем [*Ekman*, 2009; *Gustafsson and Andersson*, 2001; *Samuelsson and Stigebrandt*, 1996] и оказывают заметное воздействие на берега и прибрежную инфраструктуру Балтики [*Labuz and Kowalewska-Kalkowska*, 2011; *Weisse et al.*, 2021]. В отдельные годы отмечается заметный вклад сезонных колебаний Балтийского моря в опасные подъёмы уровня на востоке Финского залива [*Захарчук и Тихонова*, 2011]. Исследования на востоке Финского залива показывают, что в 95% случаев, опасные подъёмы уровня в Кронштадте происходили в годы с положительной аномалией сезонных колебаний уровня моря. Результаты численного гидродинамического моделирования свободных колебаний Балтийского моря свидетельствуют, что в стратифицированном море генерируются бароклинные моды собственных колебаний с периодами около одного года, величина которых сравнима со средними многолетними оценками годовых колебаний уровня, полученными на основе анализа мареографных и спутниковых альтиметрических данных [*Zakharchuk et al.*, 2021].

Обладая выраженной ритмикой сезонные колебания имеют наибольшие амплитудные максимумы в спектрах среднемесячных значений уровня Балтики [*Медведев*, 2014; *Ekman and Stigebrandt*, 1990].

Теоретические исследования свидетельствуют, что сезонные вариации уровня моря вызываются сезонными изменениями касательного трения ветра, атмосферного давления, морских течений, плотности морской воды, количества атмосферных осадков, испарения с поверхности моря, материкового стока и водообмена с прилегающими морскими бассейнами [*Фукс*, 2003; *Gill and Niller*, 1973; *Leppäranta and Myrberg*, 2009].

Выраженными характерными особенностями среднего многолетнего сезонного хода уровня Балтийского моря являются весенний минимум, осенне-зимний максимум и асимметрия сезонных изменений уровня, проявляющаяся в сравнительно быстром понижении уровня моря зимой-весной, в течение 4–5 месяцев, до минимального значения в апреле-мае, и более продолжительном подъёме уровня летом и осенью, в течение 7–8 месяцев, до максимума в ноябре-январе [*Гидрометеорология и гидрохимия морей СССР: Проект «Моря СССР». Том III Балтийское море. Выпуск I Гидрометеорологические условия*, 1992; *Захарчук и др.*, 2022; *Cheng et al.*, 2018; *Männikus et al.*, 2020; *Zakharchuk et al.*, 2022].

По мнению исследователей, сезонное понижение уровня Балтийского моря зимой и весной происходит из-за наблюдающегося в этот период роста атмосферного давления, уменьшения количества атмосферных осадков, низких значений материкового стока, увеличения плотности морских вод, снижения скорости юго-западных ветров и смене их направления на северо-восточные румбы, что способствует усилению оттока вод из Балтийского моря в Северное [*Гидрометеорология и гидрохимия морей СССР: Проект «Моря СССР». Том III Балтийское море. Выпуск I Гидрометеорологические условия*, 1992; *Lisitzin*, 1974; *Zakharchuk et al.*, 2022].

Среднее многолетнее сезонное повышение уровня Балтики от весны к зиме является следствием весеннего увеличения речного стока, летнего роста количества атмосферных осадков, осенне-зимнего понижения атмосферного давления и плотности морских вод, а также осеннего усиления юго-западных ветров, способствующих притоку вод из Северного моря в Балтийское [*Гидрометеорология и гидрохимия морей СССР: Проект «Моря СССР». Том III Балтийское море. Выпуск I Гидрометеорологические условия*, 1992; *Zakharchuk et al.*, 2022].

Асимметрия среднего сезонного хода уровня Балтики связана с тем, что метеорологические и океанологические процессы, вызывающие понижение уровня моря имеют весенние экстремумы, в то время, как у процессов, которые приводят к росту уровня моря, экстремальные значения разнесены во времени: максимумы речного стока наблюдаются весной, а у количества атмосферных осадков – летом, минимальные значения атмосферного давления и максимумы юго-западных ветров отмечаются осенью и зимой [*Гидрометеорология и гидрохимия морей СССР: Проект «Моря СССР». Том III Балтийское море. Выпуск I Гидрометеорологические условия*, 1992; *Zakharchuk et al.*, 2022].

В ряде работ изучались причины сезонного хода уровня Балтийского моря. В начале 1970-х годов Е. Лисицына предположила, что такие компоненты водного баланса, как водообмен через Датские проливы и речной сток, могут быть основными факторами, ответственными за стационарные сезонные изменения уровня Балтийского моря [*Lisitzin*, 1974]. Позднее была подтверждена важность водообмена с Северным морем для сезонных колебаний уровня моря [*Ekman*, 2009; *Gustafsson and Andersson*, 2001; *Samuelsson and Stigebrandt*, 1996], в то время как корреляции сезонных колебаний уровня Балтики с речным стоком выявлено не было [*Stramska et al.*, 2013]. *Johansson* *and Kahma* [2016] обнаружили хорошую связь между рядами среднемесячных значений зонального компонента геострофического ветра и мареографных измерений уровня Балтийского моря, за исключением юго-западной части. Они показали, что с изменчивостью зональной составляющей геострофического ветра может быть связано примерно 75% изменчивости объема воды Балтийского моря.

Значительное увеличение к концу XX века количества станций мареографных измерений уровня способствовало появлению работ, в которых исследовались региональные различия в изменении характеристик сезонных колебаний уровня в прибрежных районах Балтийского моря. В работах [*Захарчук и др.*, 2022; *Медведев*, 2014; *Ekman*, 1996] с помощью гармонического анализа многолетних рядов мареографных измерений уровня моря изучалась пространственная изменчивость амплитуд сезонных колебаний в береговой зоне Балтийского моря. Результаты свидетельствовали об увеличении амплитуды годовой гармоники Sa от 4–6 см в Датских проливах до 12–14,5 см в вершинах Финского и Ботнического заливов [*Захарчук и др.*, 2022; *Медведев*, 2014; *Ekman*, 1996]. Амплитуды полугодовой гармоники Ssa оказались в несколько раз меньше и менялись от 1–3 см в пр. Каттегат и Датских проливах, до 5–6 см в Финском заливе, в районе Аландских островов, а также у восточного побережья Швеции в Ботническом море [*Захарчук и др.*, 2022; *Медведев*, 2014; *Ekman*, 1996]. Средние амплитуды треть годовых (Sta) и четверть годовых (Sqa) гармоник оказались значительно меньше амплитуд гармоник Sa и Ssa и варьировали от 0.1–0.8 см на юго-западе моря до максимальных значений 1,4–2,6 см в Финском заливе [*Захарчук и др.*, 2022; *Медведев*, 2014].

Большая продолжительность рядов измерений уровня моря (153–200 лет) на некоторых мареографных станциях Балтики позволила оценить межгодовую изменчивость сезонных колебаний в XIX – начале XXI века [*Захарчук и др.*, 2022; *Медведев*, 2014; *Ekman and Stigebrandt*, 1990; *Hünicke and Zorita*, 2008; *Plag and Tsimplis*, 1999]. Результаты *Ekman and Stigebrandt* [1990] показали наличие значимого положительного тренда в изменениях годовой компоненты уровня моря за период 1825–1984 гг, который они связывали с вековыми изменениями океанографических условий в северо-восточной части Северной Атлантики за счет движения океанического полярного фронта [*Ekman and Stigebrandt*, 1990]. Однако, исследование межгодовой изменчивости гармоники Sa в Стокгольме за более поздний период 1889–2020 гг. показало уже наличие незначимого положительного линейного тренда, на фоне которого наблюдались цикличности в изменениях амплитуды гармоники Sa с периодами около 20–30 и 60 лет, причем самое значительное уменьшение амплитуд годовых колебаний уровня моря в различных районах Балтики отмечалось с начала 1980-х по настоящее время, когда в изменениях амплитуд гармоники Sa в этот период в разных районах моря отмечались значимые отрицательные тренды, в то время как в изменениях гармоник Ssa, Sta, Sqa трендов не наблюдалось [*Захарчук и др.*, 2022]. Межгодовые изменения гармоники Sa авторы связывали с Североатлантическим колебанием и общей тенденцией потепления климата [*Медведев*, 2014; *Plag and Tsimplis*, 1999], с вековыми изменениями атмосферных осадков в регионе Балтийского моря [*Hünicke and Zorita*, 2008], а также с межгодовыми изменениями ветра и атмосферного давления [*Захарчук и др.*, 2022].

С. Барбоса и Р. Доннер исследовали годовые изменения уровня Балтийского моря за период 1900–2012 гг. по данным его среднемесячных значений на 9 береговых станциях с помощью дискретного вейвлет-анализа [*Barbosa and Donner*, 2016]. Они не оценивали линейный тренд в изменении амплитуды годовой компоненты сезонных колебаний уровня, который выделялся другими авторами [*Захарчук и др.*, 2022; *Ekman and Stigebrandt*, 1990; *Hünicke and Zorita*, 2008; *Plag and Tsimplis*, 1999], но обнаружили чередующиеся периоды высоких и низких амплитуд в изменениях годового цикла сезонных колебаний уровня [*Barbosa and Donner*, 2016]. В работе [*Zakharchuk et al.*, 2022] эти особенности межгодовых изменений годовых колебаний связывались с их амплитудной модуляцией, однако причины этой модуляции не исследовались.

В работе [*Захарчук и др.*, 2022] с помощью взаимного корреляционного анализа рядов межгодовых изменений амплитуды годового компонента сезонных колебаний уровня в 20 береговых пунктах Балтики было показано, что изменения амплитуды годовых колебаний на ст. Стокгольм очень хорошо связаны с ее межгодовыми изменениями в других прибрежных районах Балтийского моря.

По сравнению с мареографными данными спутниковые альтиметрические измерения открыли возможность изучения колебаний уровня в открытых районах океанов и морей. Сравнение характеристик сезонных изменений уровня моря, полученных на основе альтиметрических и мареографных измерений, показало, что спутниковая альтиметрия способна достаточно точно описывать пространственную и временную изменчивость сезонных колебаний уровня Балтийского моря [*Cheng et al.*, 2018; *Kowalczyk et al.*, 2021; *Pajak and Kowalczyk*, 2019; *Stramska and Chudziak*, 2013; *Zakharchuk et al.*, 2022].

На основе результатов гармонического анализа спутниковых альтиметрических данных было показано, что годовые возмущения в поле уровня Балтийского моря распространяются с юго-запада на северо-восток в виде низкочастотных волн со скоростями 15–36 см/с, которые хорошо согласуются с теоретическими фазовыми скоростями бароклинных волн Кельвина [*Zakharchuk et al.*, 2022].

Cheng et al. [2018] использовали метод циклостационарных эмпирических ортогональных функций для исследования закономерностей пространственной структуры и временных изменений годового цикла уровня в Балтийском море на основе среднемесячных данных спутниковой альтиметрии за период 1993–2014 гг. [*Cheng et al.*, 2018]. Для исследования причин межгодовых изменений оценок годового хода уровня Балтики проводился взаимный корреляционный анализ между главными компонентами годового хода уровня моря, рассчитанными по спутниковым альтиметрическим данным, и главными компонентами различных метеорологических параметров (зональным ветром, значениями индекса Северо-Атлантического колебания, атмосферным давлением и температурой воздуха). Результаты показали во всех случаях высокие оценки коэффициентов корреляции, достигающие значений 0,60–0,80 [*Cheng et al.*, 2018].

В работе *Zakharchuk et al.* [2022] для более представительной оценки корреляционных связей между межгодовыми изменениями сезонных колебаний уровня моря и различных гидрометеорологических процессов, было предложено исключать перед взаимным корреляционным анализом стационарную компоненту из рядов гармоник Sa, Ssa, Sta, Sqa, полученных с помощью скользящего гармонического анализа, у всех гидрометеорологических процессов. По сравнению с другими работами в статье *Zakharchuk et al.* [2022] оценивались корреляции не только с компонентами скорости ветра, температурой воздуха и атмосферным давлением, но также и со всеми составляющими водного баланса (осадками, испарением, речным стоком и водообменом с Северным морем). Результаты взаимного корреляционного анализа показали, что для всех 4-х гармоник отмечается высокая корреляция с межгодовыми изменениями ветра и атмосферного давления; для 3-х гармоник (Ssa, Sta, Sqa) была выявлена высокая связь с изменениями водообмена. С температурой воздуха высокие значения коэффициентов корреляции были отмечены только для гармоники Sa. Для всех четырёх гармоник не было обнаружено связи с изменениями осадков, испарения, материкового стока [*Zakharchuk et al.*, 2022].

В перечисленных работах не исследовалось влияние на изменения сезонных колебаний уровня моря межгодовых изменений плотности водных масс Балтийского моря, хотя высокие коэффициенты корреляции между изменениями гармоники Sa и годовыми колебаниями температуры воздуха, выявленные в работах [*Cheng et al.*, 2018; *Zakharchuk et al.*, 2022], могут свидетельствовать о наличие связи с термостерической составляющей уровня моря.

В ряде работ исследовалась связь между сезонными колебаниями уровня моря и изменениями ветра [*Barbosa and Donner*, 2016; *Cheng et al.*, 2018; *Johansson and Kahma*, 2016; *Zakharchuk et al.*, 2022]. Однако колебания уровня вызываются не самим ветром, а касательным напряжением трения ветра, которое имеет квадратичную зависимость от ветра. Поэтому, физически, более правильно будет оценивать корреляцию между колебаниями уровня и касательным напряжением трения ветра.

Плохо изученным остаётся вопрос о долях влияния различных метеорологических и гидрологических процессов на межгодовую изменчивость сезонных колебаний уровня моря. Взаимный корреляционный анализ позволяет получить представление лишь о качественной характеристике связи между процессами. Для сравнительных количественных оценок таких связей следует использовать другие методические подходы.

В данной статье мы постарались учесть перечисленные недостатки и методические ограничения при исследовании сезонных колебаний уровня Балтийского моря.

Цель работы – исследовать с помощью длительных мареографных измерений уровня моря в Стокгольме особенности межгодовых изменений сезонных колебаний за период 1889–2022 гг. и оценить на основе спутниковых альтиметрических измерений уровня моря, а также данных реанализов метеорологических и гидрофизических полей, сравнительные количественные вклады влияния изменений касательного напряжения трения ветра, атмосферного давления, плотности воды и компонент водного баланса на межгодовую изменчивость составляющих сезонных колебаний уровня Балтийского моря в период 1993–2022 гг.

2. Данные и методы

Для исследования причин межгодовых изменений характеристик сезонных колебаний уровня Балтийского моря привлекались следующие данные:

1. Мареографные измерения уровня моря с временным шагом одни сутки на станциях Стокгольм за период с 1889 по 2022 г., Гедсер (1993–2021 гг.), Хорнбаек (1993–2021 гг.), полученные с ресурса E.U. Copernicus Marine Service Information (https://doi.org/10.48670/moi-00032), и Кронштадт за период с 1971 по 2015 гг. (см. рис. 1а), предоставленные Северо-Западным Управлением Росгидромета (http://www.meteo.nw.ru).

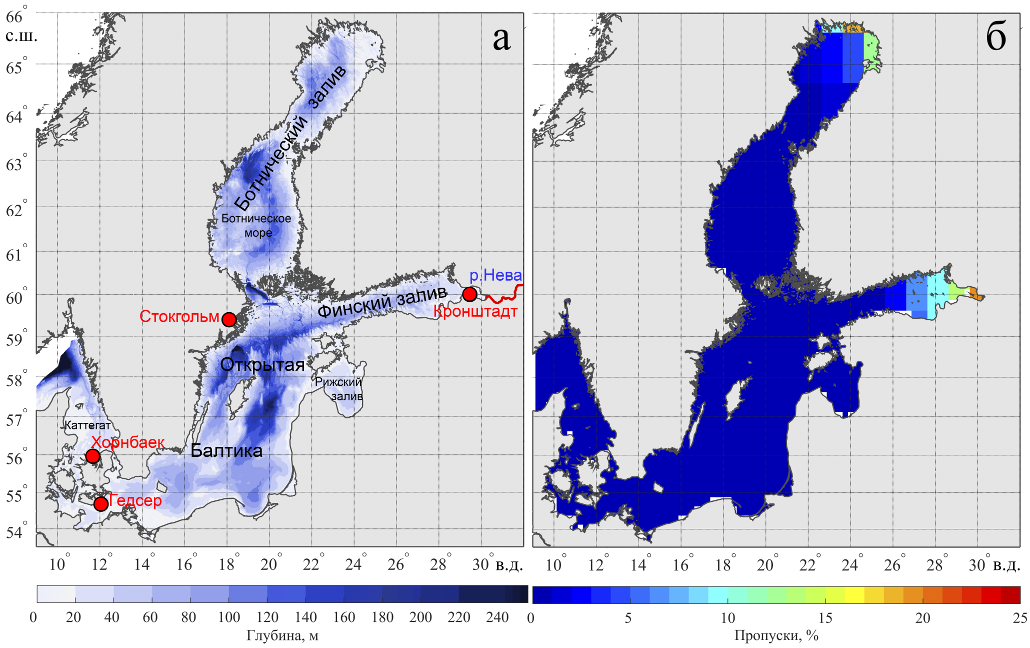

Рис. 1. Батиметрия Балтийского моря и местоположение мареографных станций (красные кружки (а). Количество пропусков (в процентах от общего количества членов ряда) в узлах сеточной области альтиметрических данных (б).

2. Среднесуточные данные о стоке Невы за период 1971–2015 гг. предоставленные Северо-Западным Управлением Росгидромета (http://www.meteo.nw.ru).

3. Массив комбинированных альтиметрических данных нескольких спутников: Jason-3, Sentinel-3A, HY-2A, Saral/AltiKa, Cryosat-2, Jason-2, Jason-1, T/P, ENVISAT, GFO, ERS1/2, включающий поля аномалий уровня моря (SLA) с пространственным разрешением $0{,}25° \times 0{,}25°$ и дискретностью 1 сутки (E.U. Copernicus Marine Service Information (https://doi.org/10.48670/moi-00145), полученный методом оптимальной интерполяции за период 1993–2021 гг. [*Bretherton et al.*, 1976; *Pujol et al.*, 2016]. При создании массива в исходные альтиметрические данные была введена поправка на орбитальную ошибку, коррекции на инструментальные ошибки, поправка на влияние тропосферы и ионосферы на запаздывание зондирующего и отраженного импульса альтиметра [*Le Traon et al.*, 1998]. Кроме этого, из альтиметрических данных были исключены колебания, связанные со статическим эффектом атмосферного давления, воздействие ветровых волн, океанских и земных приливов.
   В большинстве работ, посвящённых исследованиям сезонного хода уровня Балтийского моря, использовались данные среднемесячных значений уровня [*Медведев*, 2014; *Ekman*, 1996; *Ekman and Stigebrandt*, 1990; *Hünicke and Zorita*, 2008; *Plag and Tsimplis*, 1999]. Однако в работе [*Захарчук и др.*, 2022] было показано, что для более точной оценки характеристик сезонных колебаний уровня моря следует использовать ряды не среднемесячных, а среднесуточных значений уровня моря. Поэтому в данной работе используются данные среднесуточных значений спутниковых альтиметрических и мареографных наблюдений за уровнем Балтийского моря.
   Альтиметрические данные проверялись на наличие пропусков. Наибольшее количество пропусков, варьирующее от 2 до 25%, связано с наличием припайного и дрейфующего льда в зимний период и приходится на северную часть Ботнического залива, а также на центральную и восточную части Финского залива (рис. 1б).
4. Данные реанализа метеорологических полей ERA5 о скорости и направлении ветра на высоте 10 м и атмосферного давления на уровне моря с пространственным разрешением $0{,}25 \times 0{,}25$ градусов за период 1993–2022 гг. (https://doi.org/10.24381/cds.adbb2d47).
5. Данные регионального реанализа гидрофизических полей Baltic Sea Physics Reanalysis (`BALTICSEA_MULTIYEAR_PHY_003_011`) о температуре, солёности Балтики на разных горизонтах с пространственным разрешение 2×2 км и 56 слоями по вертикали (толщина слоев меняется в зависимости от глубины от 3 до 22 м) за период 1993–2022 гг. (https://doi.org/10.48670/moi-00013). Эти данные получены с помощью численной реализации гидродинамической модели NEMO v3.6 (Nucleus for European Modeling of the Ocean) [*Hordoir et al.*, 2015; *Pemberton et al.*, 2017], для условий Балтийского моря, в которой используется процедура ассимиляции контактной и спутниковой информации на основе алгоритма одной из разновидностей фильтра Кальмана (Local singular evolutive interpolated Kalman (LSEIK) filter) [*Nerger et al.*, 2005]. В качестве ассимилируемых переменных в модели NEMO v3.6 использовались спутниковые данные поверхностной температуры воды, полученные Шведской ледовой службой в SMHI (Swedish Meteorological and Hydrological Institute), а также in-situ измерения T и S из базы данных ICES (http://www.ices.dk/).

Выделение сезонных колебаний в исходных рядах уровня моря и других гидрометеорологических процессов производилось с помощью гармонического анализа. Амплитуды (A) и фазы (G) сезонных колебаний уровня в стационарном приближении $\overline{\zeta(t)}$ рассчитывались с помощью гармонического анализа, выполненного по методу наименьших квадратов, с учетом рекомендаций, представленных в работе Г. Н. Войнова

[*Voinov*, 2002]. Оценивались 4 гармоники: годовая (Sa) – 365,2 сут, полугодовая (Ssa) – 182,6 сут, третьгодовая (Sta) – 121,8 сут и четвертьгодовая (Sqa) – 91,3 сут.

$$\overline{\zeta(t)} = A_{\mathrm{sa}}\cos(\omega_{\mathrm{sa}}t - G_{\mathrm{sa}}) + A_{\mathrm{ssa}}\cos(\omega_{\mathrm{ssa}}t - G_{\mathrm{ssa}}) + \\ + A_{\mathrm{sta}}\cos(\omega_{\mathrm{sta}}t - G_{\mathrm{sta}}) + A_{\mathrm{sqa}}\cos\left(\omega_{\mathrm{sqa}}t - G_{\mathrm{sqa}}\right), \quad (1)$$

где A_{sa}, A_{ssa}, A_{sta}, A_{sqa} – амплитуды годовой, полугодовой, треть годовой и четверть годовой гармоник; G_{sa}, G_{ssa}, G_{sta}, G_{sqa} – фазы этих гармоник; ω_{sa}, ω_{ssa}, ω_{sta}, ω_{sqa} – частоты гармоник, t – время.

Чтобы исследовать особенности межгодовой изменчивости сезонных колебаний, ряд уровня моря в Стокгольме подвергался скользящему гармоническому анализу [*Plag and Tsimplis*, 1999; *Zakharchuk et al.*, 2022]. Для годовой гармоники Sa период квазистационарности (отрезок ряда для расчетов) принимался равным 1 год, и скользящий гармонический анализа проводился без перекрытия (т.е. за каждый последующий год). Для других гармоник эта процедура проводилась с перекрытием. Для полугодовой компоненты Ssa период квазистационарности принимался равным 1 год, и скольжение проводилось с перекрытием через каждые полгода; для треть-годовой гармоники Sta период квазистационарности принимался равным 8 месяцев, и скольжение проводилось через каждые 4 месяца; для четверть-годовой гармоники Sqa период квазистационарности принимался равным 6 месяцев, и скольжение проводилось через каждые 3 месяца. По оцененным амплитудам и фазам для каждого периода квазистационарности предвычислялись ряды компонент сезонных колебаний, которые затем склеивались в ряд $\zeta(t)$, описывающий межгодовые изменения каждой компоненты сезонных колебаний. В местах соединений предвычисленных рядов иногда отмечались резкие скачки уровня по высоте, которые сглаживались методом кубического сплайна [*de Boor*, 1978] с окном сглаживания 60 суток (последние 30 суток предыдущего периода квазистацонарности и первые 30 суток следующего периода квазистационарности).

Среднеквадратические ошибки расчета амплитуд гармоник, оцененных с помощью скользящего гармонического анализа вычислялись следующим образом. По остаточным рядам, полученным для каждого периода квазистационарности, оценивались амплитуды на частотах гармоник Sa, Ssa, Sta, Sqa. По рядам этих амплитуд оценивалось их среднеквадратическое отклонение, которое принималось за среднеквадратическую ошибку расчета амплитуд исследуемых гармоник [*Захарчук и др.*, 2022]

В полученных по результатам скользящего гармонического анализа рядах амплитуд гармоник Sa, Ssa, Sta, Sqa выделялись линейные тренды. Значимость линейных трендов в межгодовых изменениях амплитуд гармоник Sa, Ssa, Sta, Sqa оценивалась с помощью критерия Стьюдента [*Малинин*, 2008].

Для исследования причин и механизмов современных изменений характеристик сезонных колебаний уровня Балтийского моря проводился взаимный корреляционный и множественный регрессионный анализы межгодовых вариаций уровня моря на частоте гармоник Sa, Ssa, Sta, Sqa, рассчитанных с помощью спутниковых альтиметрических данных, с такими же колебаниями различных гидрометеорологических процессов, оцененных на основе, описанных выше, данных реанализов метеорологических и гидрофизическх полей: касательного напряжения трения ветра ($\vec{\tau}_w$), атмосферного давления (P_a), стерических колебаний уровня моря (ζ_ρ), атмосферных осадков (Pr), речного стока (R), испарения (E), водообмена между Балтийским и Северным морями через Датские проливы (Q).

Вектор касательного напряжения трения ветра ($\vec{\tau}_w$) рассчитывался по известной формуле:

$$\vec{\tau}_w = c\rho_0\vec{W}\left|\vec{W}\right|$$

где c – безразмерный коэффициент, ρ_0 – плотность воздуха, $\vec{W}$ – вектор скорости ветра.

Стерические колебания уровня моря (ζ_ρ) рассчитывались по данным о температуре (T) и солёности (S) воды из регионального реанализа

BALTICSEA_MULTIYEAR_PHY_003_011 (https://doi.org/10.48670/moi-00013). Несмотря на то, что для этого реанализа используется численная гидродинамическая модель NEMO v3.6, основанная на приближении Буссинеска, которое не позволяет описывать изменение объёма столба морской воды без изменения его массы [*Greatbatch*, 1994], применяемые в рамках данного реанализа алгоритмы усвоения спутниковой и контактной информации об изменении T и S, дают возможность подстраивать рассчитанные по модели поля океанологических характеристик к их наблюдаемым значениям. В работе [*Захарчук и др.*, 2023] было проведено сравнение стерических колебаний уровня в нескольких районах Балтики, оцененных по данным контактных измерений T и S, и по данным регионального реанализа. Результаты сравнения свидетельствовали, что данные регионального реанализа по T и S позволяют достаточно точно воспроизводить колебания уровня моря, вызванные изменениями плотности вод Балтийского моря [*Захарчук и др.*, 2023].

Стерические колебания уровня моря оценивались по следующей формуле [*Белоненко и Колдунов*, 2006]:

$$\frac{\Delta\zeta_\rho}{\Delta t} = -\sum_{i=1}^{n} \frac{1}{\rho_0} \frac{\Delta\rho_i}{\Delta t} \Delta z_i,$$

где $\frac{\Delta\zeta_\rho}{\Delta t}$ – стерические изменения уровня моря за отрезок времени Δt, ρ_0 – средняя плотность воды, $\frac{\Delta\rho_i}{\Delta t}$ – изменение во времени плотности воды в каждом i-м слое ($i = 1, 2, 3, \ldots,\ n$), Δz_i – толщина каждого слоя. Плотность воды (ρ) рассчитывалась по уравнению состояния, описанному в работе [*Jackett and Mcdougall*, 1995].

Расчет водообмена (Q) через Датские проливы выполнялся по методике, описанной в работах *Jakobsen et al.* [2010] и *Mohrholz* [2018], по формуле:

$$Q = \sqrt{\frac{\Delta\zeta_s - B}{K_f}},$$

где K_f – эмпирический коэффициент трения. Согласно [*Jakobsen et al.*, 2010] для проливов он равен от $1{,}6\times10^{-10}$ с^{2}м$^{-5}$ до 2×10^{-11} с^{2}м$^{-5}$; B – коррекционная добавка на разницу уровней моря за счт градиента плотности вдоль пролива (бароклинная добавка). Обычно величина этой добавки составляет несколько сантиметров; $\Delta\zeta_s$ – разница уровня моря между Каттегатом и Западной Балтикой. Для оценки разности уровня моря ($\Delta\zeta_s$) использовались ряды синхронных ежечасных мареографных наблюдений за уровнем моря на станциях Гедсер и Хорнбаек за период 1993–2021 гг. Данные по уровню моря были получены с ресурса Copernicus Marine Service (http://marine.copernicus.eu). Исходные ряды уровня усреднялись до суток и затем из данных уровня моря на станции Хорнбаек вычитались синхронные значения уровня моря на станции Гедсер.

Следуя методическим рекомендациям, изложенным в работе [*Zakharchuk et al.*, 2022], перед взаимным корреляционным и множественным регрессионным анализами из рядов составляющих сезонных колебаний уровня моря, полученных с помощью скользящего гармонического анализа $\zeta(t)$, вычитались ряды составляющих $\overline{\zeta(t)}$, рассчитанные на основе стационарного гармонического анализа (1):

$$\zeta(t)' = \zeta(t) - \overline{\zeta(t)},$$

где $\zeta(t)'$ – аномалии составляющих сезонных колебаний уровня моря.

Такая же процедура была произведена для рядов нестационарных составляющих других гидрометеорологических процессов, в результате чего были получены ряды аномалий касательного напряжения трения ветра $\vec{\tau}_w(t)'$, атмосферного давления $P_a(t)'$, стерических колебаний уровня моря $\zeta\rho(t)'$, атмосферных осадков $Pr(t)'$, речного стока $R(t)'$, испарения $E(t)'$, водообмена между Балтийским и Северным морями через Датские проливы $Q(t)'$.

Взаимный корреляционный анализ между аномалиями составляющих сезонных колебаний уровня моря $\zeta(t)'$ и различными скалярными гидрометеорологическими процессами $P(t)'$, $\zeta\rho(t)'$, $Pr(t)'$, $R(t)'$, $E(t)'$, $Q(t)'$ производился путем оценивания нормированной взаимной корреляционной функции:

$$r_{\zeta,\eta}(\tau)=\frac{K_{\zeta,\eta}(\tau)}{\sqrt{K_{\zeta}(0)K_{\eta}(0)}} \tag{2}$$

где $K_{\zeta}(0)$, $K_{\eta}(0)$ – дисперсии двух скалярных процессов $\zeta(t)$ и $\eta(t)$, а $K_{\zeta,\eta}(\tau)=\frac{1}{T-\tau}\int_0^{T-\tau}\zeta(t)\eta(t+\tau)dt$ – их взаимная ковариационная функция, τ – временной сдвиг.

Оценка взаимосвязи между аномалиями составляющих сезонных колебаний уровня моря $\zeta(t)'$, и касательного напряжения трения ветра $\vec{\tau}_w(t)'$производилась путём расчета множественных коэффициентов корреляции по методике взаимного корреляционного анализа между скалярными и векторными процессами, изложенной в работе В. А. Рожкова [*Рожков*, 2002]. Следуя этой методике, в начале, оценивались матрицы коэффициентов взаимных корреляций следующего вида:

$$D_{\eta\mathbf{V}}=\begin{vmatrix} r_{\eta\eta} & r_{\eta u} & r_{\eta v}\\ r_{u\eta} & r_{uu} & r_{uv}\\ r_{v\eta} & r_{vu} & r_{vv}\end{vmatrix},\qquad D_{uv}=\begin{vmatrix} r_{uu} & r_{uv}\\ r_{vu} & r_{vv}\end{vmatrix}$$

где $D_{\eta\mathbf{V}}$ и D_{uv} – определители матриц, η – скалярный процесс, $\mathbf{V}$ – векторный процесс, u,v – составляющие векторного процесса на параллель и меридиан, соответственно, $r_{\eta\eta},\ r_{\eta v},\ r_{uv},\ldots,\ r_{vv}$ – коэффициенты взаимной корреляции.

Затем, рассчитывался множественный коэффициент корреляции (M) между скалярным (η) и векторным процессами ($\mathbf{V}$):

$$M_{\eta\mathbf{V}}=\sqrt{1-\frac{D_{\eta V}}{D_{uv}}} \tag{3}$$

Коэффициенты корреляции, рассчитанные по формулам (2) и (3), оценивались на разных временных сдвигах и, затем, выбирались их максимальные значения (см. рис. 3).

Для того, чтобы количественно оценить относительные вклады различных гидрометеорологических процессов в межгодовую изменчивость составляющих сезонных колебаний уровня Балтийского моря проводился множественный регрессионный анализ. С этой целью уравнения множественной регрессии записывались в следующем виде:

$$\begin{aligned}\zeta_{\mathrm{sa}}(t)' = {}& a_0+a_1[\tau u_{\mathrm{sa}}(t)']+a_2[\tau v_{\mathrm{sa}}(t)']+a_3[P_{\mathrm{sa}}(t)']+\\ &+\ a_4[\zeta\rho_{\mathrm{sa}}(t)']+a_5[Pr_{\mathrm{sa}}(t)']\ +a_6[R_{\mathrm{sa}}(t)']+a_7[Q_{\mathrm{sa}}(t)']+a_8[E_{\mathrm{sa}}(t)'],\end{aligned} \tag{4}$$

$$\begin{aligned}\zeta_{\mathrm{ssa}}(t)' = {}& a_0+a_1[\tau u_{\mathrm{ssa}}(t)']+a_2[\tau v_{\mathrm{ssa}}(t)']+a_3[P_{\mathrm{ssa}}(t)']+\\ &+\ a_4[\zeta\rho_{\mathrm{ssa}}(t)']+a_5[Pr_{\mathrm{ssa}}(t)']+a_6[R_{\mathrm{ssa}}(t)']+a_7[Q_{\mathrm{ssa}}(t)']+a_8[E_{\mathrm{ssa}}(t)'],\end{aligned} \tag{5}$$

$$\begin{aligned}\zeta_{\mathrm{sta}}(t)' = {}& a_0+a_1[\tau u_{\mathrm{sta}}(t)']+a_2[\tau v_{\mathrm{sta}}(t)']+a_3[P_{\mathrm{sta}}(t)']+\\ &+\ a_4[\zeta\rho_{\mathrm{sta}}(t)']+a_5[Pr_{\mathrm{sta}}(t)']+a_6[R_{\mathrm{sta}}(t)']+a_7[Q_{\mathrm{sta}}(t)']+a_8[E_{\mathrm{sta}}(t)'],\end{aligned} \tag{6}$$

$$\begin{aligned}\zeta_{\mathrm{sqa}}(t)' = {}& a_0+a_1[\tau u_{\mathrm{sqa}}(t)']+a_2[\tau v_{\mathrm{sqa}}(t)']+a_3\left[P_{\mathrm{sqa}}(t)'\right]+\\ &+\ a_4\left[\zeta\rho_{\mathrm{sqa}}(t)'\right]+a_5\left[Pr_{\mathrm{sqa}}(t)'\right]+a_6\left[R_{\mathrm{sqa}}(t)'\right]+a_7\left[Q_{\mathrm{sqa}}(t)'\right]+a_8\left[E_{\mathrm{sqa}}(t)'\right],\end{aligned} \tag{7}$$

где a_0 – свободный член уравнения множественной регрессии, а $a_1,\ a_2,\ldots,\ a_8$ – коэффициенты этого уравнения, $\tau u(t)',\tau v(t)'$ – зональная и меридиональная компоненты аномалий сезонных колебаний касательного напряжения трения ветра $\vec{\tau}_w(t)'$, остальные члены уравнений описаны в тексте выше. Перед проведением регрессионного анализа все переменные, входящие в уравнение (4)–(7) приводились к безразмерному виду, путём нормирования рядов на их ср. кв. отклонения.

Количественные оценки относительных вкладов каждого гидрометеорологического предиктора из уравнений (4)–(7) рассчитывались следующим образом:

$$B_i = \frac{|a_i|}{\sum_{i=1}^{n}|a_i|}\cdot 100\%,$$

где B_i – процентный вклад i-ого гидрометеорологического фактора в межгодовую изменчивость аномалий сезонных гармоник Sa, Ssa, Sta, Sqa, a_i– коэффициенты математического разложения уравнения множественной регрессии ($i = 1, 2, \dots,\ n$), где $n = 8$.

3. Результаты и их интерпретация

3.1. Изменчивость амплитуд составляющих сезонных колебаний уровня моря в Стокгольме за период с 1889–2022 гг.

На рис. 2 представлены результаты скользящего гармонического анализа 133-летнего ряда среднесуточных значений уровня моря в Стокгольме, которые демонстрируют очень значительную межгодовую изменчивость амплитуд у всех 4-х гармоник сезонных колебаний. В зависимости от года они меняются от 0,5–1,0 до 25–27 сантиметров. У всех 4-х гармоник выделяются положительные линейные тренды, которые не являются статистически значимыми. Сглаживание рядов полиномом 15 степени демонстрирует, что в межгодовой изменчивости составляющих сезонных колебаний наблюдаются долгопериодные циклы с временными масштабами от 20–35 до 55 лет. Наибольшая величина амплитуд этих цикличностей отмечается для годовой гармоники Sa, с увеличением частоты её обертонов размах колебаний долгопериодных циклов уменьшается (рис. 2). Для гармоники Sa с конца 1890-х до начала 1980-х годов отмечается квазициклическое увеличение её амплитуд после чего, до настоящего времени, наблюдается резкое волнообразное их уменьшение (рис. 2). Максимальные значения дисперсии годовых колебаний наблюдались в 1920-е, 1940-е – 1950-е и в конце 1970-х начале 1980-х годов. После этого периода дисперсия годовых колебаний резко уменьшалась, достигнув в самом начале 2000-х годов второго, после 1910-х годов, минимума (рис. 2). В работе *Захарчук и др.* [2022] было показано, что резкое уменьшение амплитуд гармоники Sa в последние десятилетия обусловлено снижением интенсивности годовых колебаний ветра, и, в меньшей степени, атмосферного давления [*Захарчук и др.*, 2022].

Межгодовая изменчивость полугодовой гармоники Ssa демонстрирует выраженный период увеличения её амплитуд и дисперсии в 1890-е – 1920-е годы, после чего они уменьшались до 1930-х – 1940-х годов, затем отмечался продолжительный рост амплитуд и дисперсии до 1990-х годов. В последние двадцать лет наблюдается снижение амплитуд и дисперсии полугодовых колебаний (рис. 2).

Дисперсия третьгодовых колебаний (Sta) циклически уменьшалась с 1880-х годов, достигнув своего основного минимума в 1930-х годах, после чего она росла до начала 2000-х годов. В последние 20 лет дисперсия третьгодовых колебаний уровня в Стокгольме слабо уменьшается (рис. 2).

Самые низкие значения дисперсии четвертьгодовых колебаний (Sqa) отмечались в 1940-е годы, а самые большие – в 1970-е и в начале 1980-х годов. В последние 20 лет наблюдается слабый рост их дисперсии (рис. 2).

3.2. Взаимный корреляционный анализ изменчивости сезонных колебаний уровня моря, рассчитанных по алтиметрическим данным, и гидрометеорологических процессов

Результаты взаимного корреляционного анализа между аномалиями составляющих сезонных колебаний уровня моря, рассчитанными по альтиметрическим данным, и различных гидрометеорологических процессов, представленные на рис. 3, свидетельствуют, что самые большие коэффициенты корреляции, достигающие 0,8–1,0, отмечаются между аномалиями сезонных колебаний уровня моря $\zeta(t)'$ и касательного

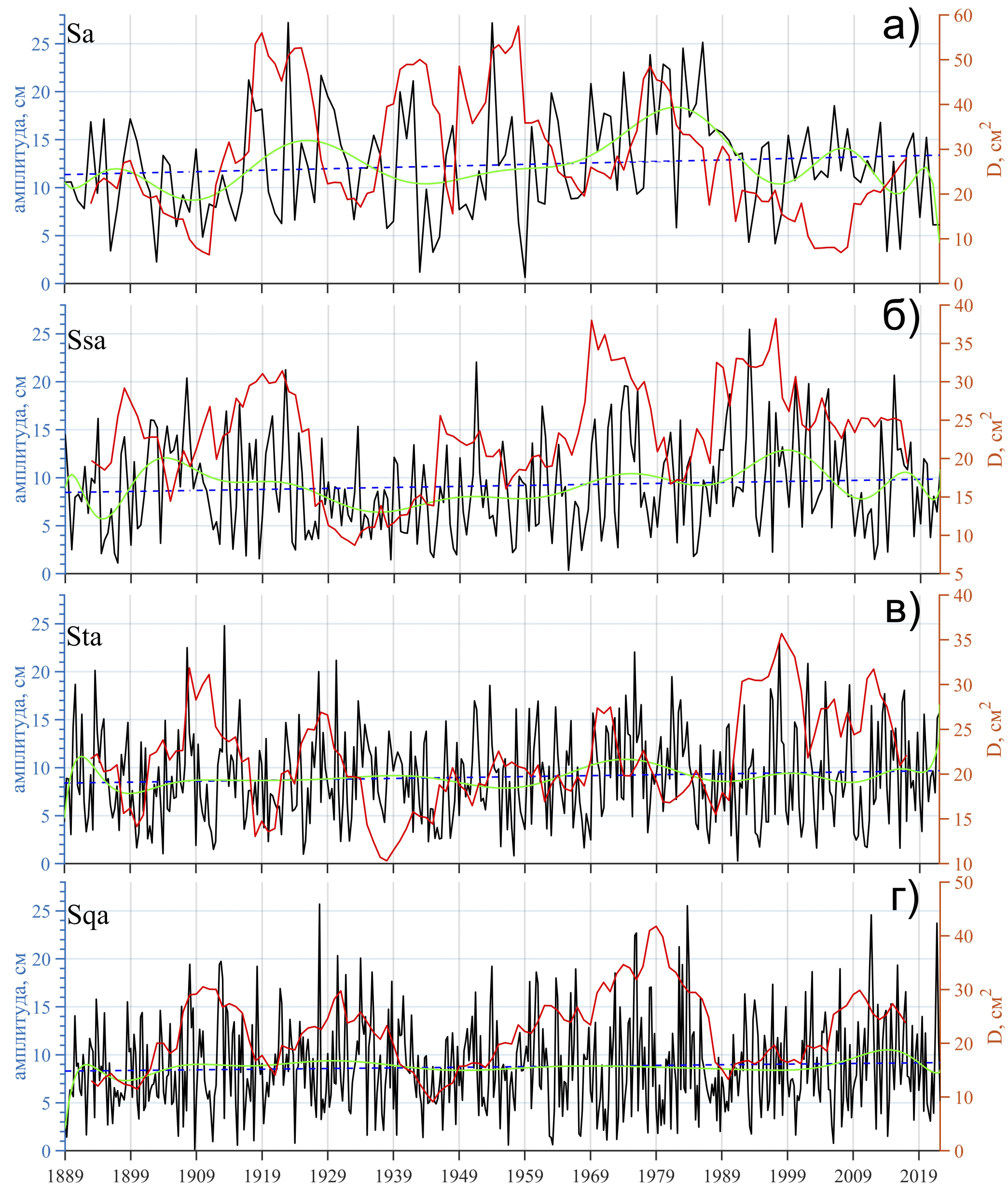

Рис. 2. Межгодовые изменения амплитуд годовой (Sa), полугодовой (Ssa), третьгодовой (Sta), и четвертьгодовой (Sqa) компонент сезонных колебаний уровня моря в Стокгольме, рассчитанных по мареографным измерениям за период с 1889–2022 гг. (черная линия). Линейный тренд обозначен прямой синей пунктирной линией; зелёная линия – полином 15 степени, красная линия – изменение дисперсии амплитуд гармоник (правая шкала), рассчитанной с периодом скольжения 10 лет и перекрытием 1 год.

напряжения трения ветра $\vec{\tau}_w(t)'$. Однако при движении с юга на север моря связь между этими процессами снижается, и для аномалий гармоник Ssa, Sta, Sqa на севере Ботнического залива коэффициенты корреляции между $\zeta(t)'$) и $\vec{\tau}_w(t)'$уменьшаются до значений 0,3–0,4 (рис. 3). Эти оценки, в основном, хорошо согласуются с результатами работы [*Zakharchuk et al.*, 2022], в которой на основе альтиметрических данных меньшей продолжительности (1993–2018 гг.) проводился взаимный корреляционный анализ между $\zeta(t)'$ и сезонными аномалиями не $\vec{\tau}_w(t)'$, а ветра. Хотя, при сравнении с работой [*Zakharchuk et al.*, 2022], выявляются и некоторые региональные различия, например, в нашем случае для всех гармоник увеличивается корреляция в проливе Каттегат, а для гармоники Sqa и на юге открытой Балтики.

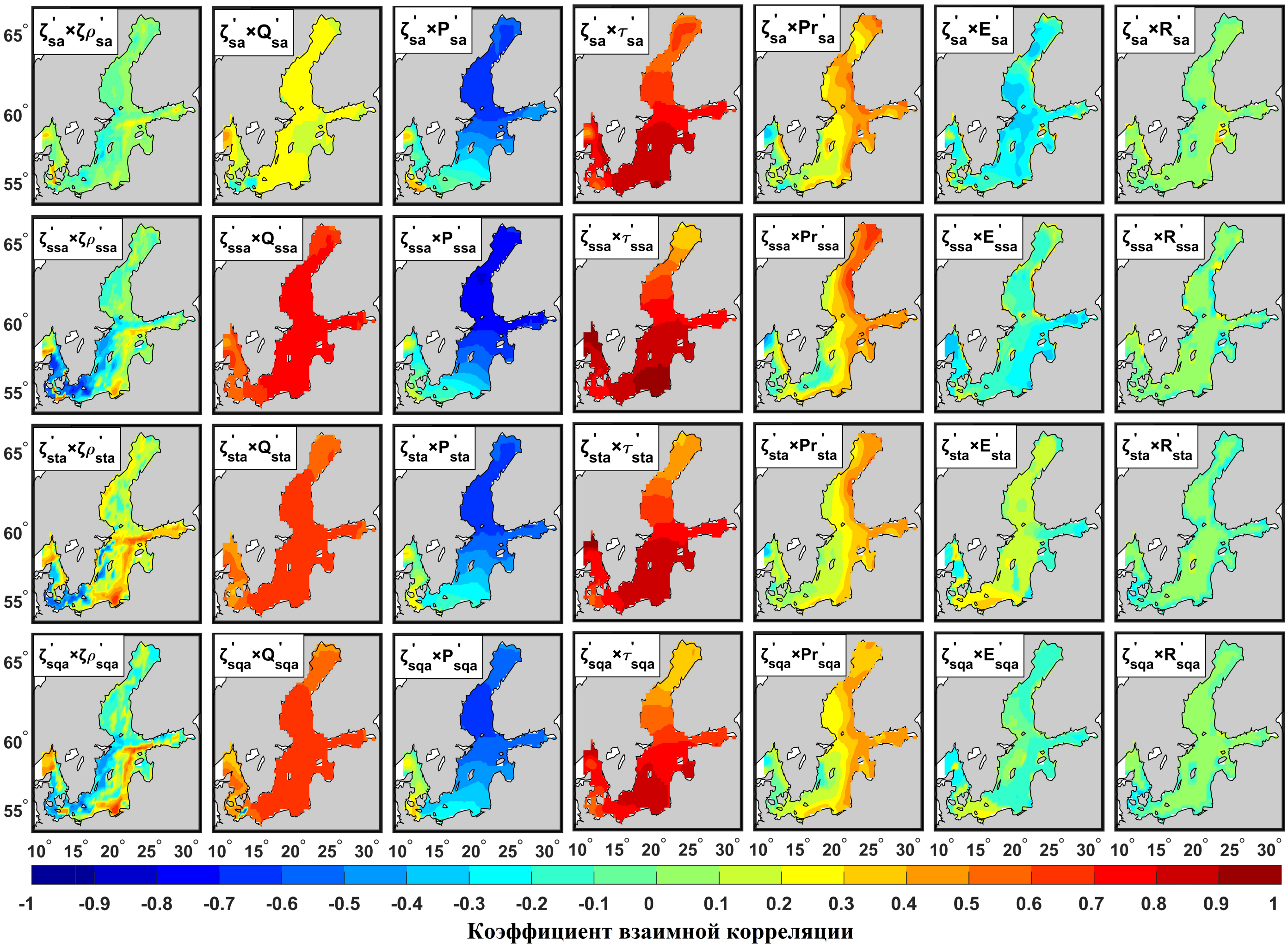

Рис. 3. Коэффициенты максимальной корреляции между аномалиями составляющих сезонных колебаний уровня моря, рассчитанными по альтиметрическим данным, и различных гидрометеорологических процессов (обозначения смотрите в тексте).

В Ботническом и Финском заливах, а также на севере открытой Балтики, высокая обратная связь, достигающая $-0{,}6\ldots-0{,}8$ отмечается между $\zeta(t)'$ и аномалиями составляющих сезонных колебаний атмосферного давления $P(t)'$, в то время как на юге открытой Балтики связь между $\zeta(t)'$ и $P(t)'$ отсутствует (рис. 3). Похожие результаты были получены в работе [*Johansson and Kahma*, 2016], в которой оценивалась корреляция между среднемесячными значениями уровня моря на различных мареографных станциях Балтики и изменениями атмосферного давления.

Для аномалий гармоник Ssa, Sta, Sqa на большей части акватории Балтийского моря наблюдаются высокие значения коэффициентов корреляции (0,6–0,7) между $\zeta(t)'$ и аномалиями водообмена между Северным морем и Балтикой $Q(t)'$, однако связь между этими процессами отсутствует для аномалий гармоники Sa (рис. 3).

С межгодовыми изменениями атмосферных осадков $Pr(t)'$, высокая связь отмечается только для полугодовой гармоники Ssa на востоке и севере Ботнического залива, в то время как для других районов моря коэффициенты корреляции между $\zeta(t)'$ и $Pr(t)'$ низкие (рис. 3).

Для всех четырёх гармоник на большей части акватории моря отсутствует взаимосвязь между $\zeta(t)'$ и аномалиями стерических колебаний уровня моря $\zeta\rho(t)'$. Исключение составляет район Гданьского залива, где для гармоник Sta и Sqa отмечаются коэффициенты корреляции со значениями до 0,6 между $\zeta(t)'$ и $\zeta\rho(t)'$, а также юго-западная часть моря, где для гармоники Ssa наблюдаются значения обратной корреляции, достигающие 0,6.

рис. 3 свидетельствует также об отсутствии связи для всех гармоник между сезонными аномалиями уровня моря $\zeta(t)'$ и испарением $E(t)'$, а также речным стоком $R(t)'$ (рис. 3). Хорошо известно, что р. Нева имеет самый большой объём речного стока, по сравнению с другими реками, впадающими в Балтийское море [*Гидрометеорология и гидрохимия морей СССР: Проект «Моря СССР». Том III Балтийское море. Выпуск I Гидрометеорологические условия*, 1992; *Leppäranta and Myrberg*, 2009]. Поэтому, для проверки результатов, представленных на рис. 3, был также произведён взаимный корреляционный анализ между аномалиями сезонных составляющих уровня моря $\zeta(t)'$, полученными на основе мареографных измерений в Кронштадте и сезонными аномалиями стока Невы, полученными по инструментальным измерениям. Результаты такого анализа представлены в табл. 1. Они подтверждают результаты, показанные на рис. 3, свидетельствующие, что и анализ инструментальных измерений в Невской губе Финского залива для всех 4-х гармоник показывает отсутствие корреляции между $\zeta(t)'$ и $R(t)'$.

Таблица 1. Максимальные значения коэффициентов корреляции (τ) между изменениями аномалий составляющих сезонных колебаний уровня моря в Кронштадте $\zeta(t)'$ и аномалиями стока Невы $R(t)'$

Коррелируемые процессы	$K(\tau)$
$\zeta'_{\mathrm{sa}}(t) \times R'_{\mathrm{Sa}}(t)$	0,19
$\zeta'_{\mathrm{ssa}}(t) \times R'_{\mathrm{Ssa}}(t)$	0,04
$\zeta'_{\mathrm{sta}}(t) \times R'_{\mathrm{Sta}}(t)$	−0,09
$\zeta'_{\mathrm{sqa}}(t) \times R'_{\mathrm{Sqa}}(t)$	0,19

При проведении взаимного корреляционного анализа статистически достоверные оценки временных сдвигов могут быть получены только для случаев, когда наблюдались высокие значения коэффициентов взаимной корреляции (>0,6). Если коэффициенты корреляции меньше 0,6, то линейная связь между процессами отсутствует и не имеет смысла оценивать временные сдвиги. В нашем случае большие значения корреляции отмечается только с изменениями касательного напряжения трения ветра (до 0,8–1,0), атмосферного давления (до −0,6...−0,8), а для гармоник Ssa, Sta, Sqa – с изменениями водообмена через Датские проливы (до 0,6–0,7). Не отмечалось связи аномалий сезонных колебаний уровня моря с составляющими пресного баланса и стерическими колебаниями уровня моря (см. рис. 3).

Анализ временных сдвигов для случаев высокой корреляции (>0,6) показал, что они отрицательные (сезонные колебания уровня запаздывают относительно сезонных колебаний гидрометеорологических процессов) и варьируют от −5 до −15 суток для касательного напряжения трения ветра, а также атмосферного давления, и от −20 до −35 суток для колебаний водообмена через Датские проливы.

3.3. Множественный регрессионный анализ сезонных колебаний уровня моря

Перед проведением множественного регрессионного анализа все гидрометеорологические предикторы, которые являются переменными в уравнениях (4)–(7), были проверены на степень их взаимосвязанности. В табл. 2 представлены средние по акватории Балтийского моря значения максимальных коэффициентов корреляции между гидрометеорологическими процессами. Как следует из таблицы 2, коэффициенты корреляции во всех случаях низкие. Этот результат демонстрирует, что гидрометеорологические предикторы не являются связанными, что делает их выбор репрезентативным для проведения множественного регрессионного анализа.

На рис. 4 представлены результаты множественного регрессионного анализа, демонстрирующие выраженные количественно вклады сезонных аномалий различных

Таблица 2. Средние по акватории Балтийского моря значения максимальных коэффициентов корреляции между гидрометеорологическими процессами

Гармоника 1,0 год								
Предиктор	$\zeta\rho_{sa}(t)'$	$Q_{sa}(t)'$	$P_{sa}(t)'$	$\tau u_{sa}(t)'$	$\tau v_{sa}(t)'$	$Pr_{sa}(t)'$	$E_{sa}(t)'$	$R_{sa}(t)'$
$\zeta\rho_{sa}(t)'$	1,00							
$Q_{sa}(t)'$	0,01	1,00						
$P_{sa}(t)'$	−0,02	−0,05	1,00					
$\tau u_{sa}(t)'$	0,00	−0,26	−0,35	1,00				
$\tau v_{sa}(t)'$	−0,01	0,06	−0,21	0,33	1,00			
$Pr_{sa}(t)'$	0,00	0,22	−0,46	0,05	0,22	1,00		
$E_{sa}(t)'$	0,03	−0,08	−0,13	0,10	0,15	−0,02	1,00	
$R_{sa}(t)'$	0,24	0,01	−0,07	0,00	0,03	0,06	0,02	1,00
Гармоника 0,5 года								
Предиктор	$\zeta\rho_{ssa}(t)'$	$Q_{ssa}(t)'$	$P_{ssa}(t)'$	$\tau u_{ssa}(t)'$	$\tau v_{ssa}(t)'$	$Pr_{ssa}(t)'$	$E_{ssa}(t)'$	$R_{ssa}(t)'$
$\zeta\rho_{ssa}(t)'$	1,00							
$Q_{ssa}(t)'$	0,00	1,00						
$P_{ssa}(t)'$	0,04	0,09	1,00					
$\tau u_{ssa}(t)'$	−0,12	−0,35	−0,42	1,00				
$\tau v_{ssa}(t)'$	−0,02	−0,23	−0,20	0,34	1,00			
$Pr_{ssa}(t)'$	−0,05	−0,04	−0,43	0,11	0,06	1,00		
$E_{ssa}(t)'$	0,01	−0,06	−0,02	−0,01	0,18	−0,11	1,00	
$R_{ssa}(t)'$	0,09	0,04	−0,04	0,01	0,02	0,02	−0,03	1,00
Гармоника 0,33 года								
Предиктор	$\zeta\rho_{sta}(t)'$	$Q_{sta}(t)'$	$P_{sta}(t)'$	$\tau u_{sta}(t)'$	$\tau v_{sta}(t)'$	$Pr_{sta}(t)'$	$E_{sta}(t)'$	$R_{sta}(t)'$
$\zeta\rho_{sta}(t)'$	1,00							
$Q_{sta}(t)'$	0,04	1,00						
$P_{sta}(t)'$	0,08	0,24	1,00					
$\tau u_{sta}(t)'$	−0,11	−0,46	−0,35	1,00				
$\tau v_{sta}(t)'$	−0,05	−0,08	−0,14	0,26	1,00			
$Pr_{sta}(t)'$	0,06	−0,04	−0,45	0,02	0,15	1,00		
$E_{sta}(t)'$	−0,38	0,03	0,01	0,01	0,20	−0,18	1,00	
$R_{sta}(t)'$	−0,09	0,02	0,03	−0,02	−0,03	−0,05	0,08	1,00
Гармоника 0,25 года								
Предиктор	$\zeta\rho_{sqa}(t)'$	$Q_{sqa}(t)'$	$P_{sqa}(t)'$	$\tau u_{sqa}(t)'$	$\tau v_{sqa}(t)'$	$Pr_{sqa}(t)'$	$E_{sqa}(t)'$	$R_{sqa}(t)'$
$\zeta\rho_{sqa}(t)'$	1,00							
$Q_{sqa}(t)'$	−0,03	1,00						
$P_{sqa}(t)'$	0,08	0,35	1,00					
$\tau u_{sqa}(t)'$	−0,04	−0,44	−0,33	1,00				
$\tau v_{sqa}(t)'$	0,00	−0,09	−0,06	0,24	1,00			
$Pr_{sqa}(t)'$	0,07	−0,16	−0,53	0,08	0,11	1,00		
$E_{sqa}(t)'$	−0,25	0,04	−0,03	0,05	0,17	−0,22	1,00	
$R_{sqa}(t)'$	−0,05	0,04	−0,01	−0,02	−0,02	−0,05	0,10	1,00

гидрометеорологических процессов в межгодовую изменчивость составляющих сезонных колебаний уровня Балтийского моря. Значения коэффициентов множественной корреляции для всех 4-х гармоник являются высокими и варьируют от 0,7 до 1,0 (см. рис. 4). Этот результат свидетельствует, что предложенная нами модель множественной регрессии достаточно адекватно описывает межгодовую изменчивость составляющих сезонных колебаний уровня Балтийского моря. Наибольшее воздействие на их изменения в течение последних 30 лет оказывают сезонные аномалии касательного напряжения трения ветра, вклады которых в открытой Балтике, пр. Каттегат и Рижском заливе достигают 40–70%, уменьшаясь, в зависимости от гармоники, до 30–60% в Финском заливе, и до 15–35% в Ботническом заливе (рис. 4).

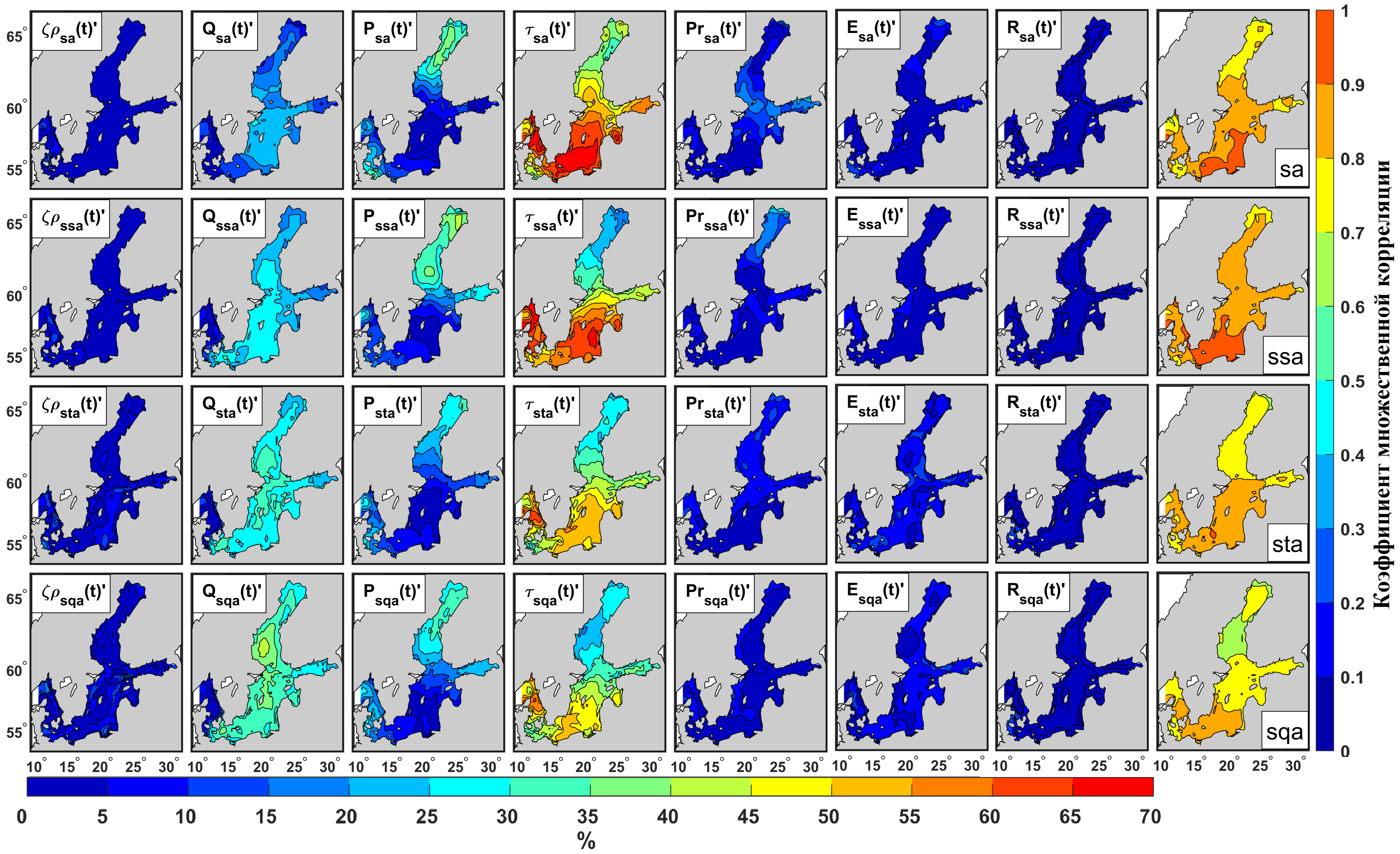

Рис. 4. Доли влияния (в %) различных гидрометеорологических процессов в межгодовую изменчивость аномалий составляющих сезонных колебаний уровня Балтийского моря (первые 7 столбцов). В последнем столбце представлены коэффициенты множественной корреляции.

Вторыми по значимости процессами, влияющими на межгодовую изменчивость сезонных колебаний уровня моря, являются сезонные аномалии атмосферного давления $P(t)'$ и водообмена Балтийского и Северного морей $Q(t)'$. Вклады $P(t)'$ в Ботническом заливе достигают 25–45%. Однако при движении на юг влияние $P(t)'$ заметно ослабевает, и в открытой Балтике, а также в Рижском заливе оно составляет всего 5–15%. В Финском заливе заметное влияние $P(t)'$, достигающее 20–30%, отмечается только для полугодовой гармоники Ssa (рис. 4).

Рис. 4 свидетельствует, что влияние сезонных аномалий водообмена $Q(t)'$ на межгодовую изменчивость сезонных колебаний уровня моря $\zeta(t)'$ увеличивается при уменьшении периодов обертонов годовой волны. Если для годовой гармоники вклады $Q(t)'$ меняются от 5 до 25%, то для четвертьгодовой гармоники Sqa они увеличиваются до 30–45% (рис. 4).

По сравнению с вкладами сезонных аномалий касательного напряжения трения ветра, атмосферного давления и водообмена через Датские проливы на $\zeta(t)'$, влияние других гидрометеорологических процессов на межгодовую изменчивость сезонных колебаний уровня моря заметно меньше. Вклады сезонных аномалий атмосферных осадков $Pr(t)'$, в основном, не превышает 5–15% и только для годовой гармоники на юге Ботнического залива и востоке Финского залива, а также для полугодовой гармоники на севере Ботнического залива, вклады $Pr(t)'$ в изменения $\zeta(t)'$ достигают 20–25%.

Воздействие сезонных аномалий испарения $E(t)'$ на изменения $\zeta(t)'$ для всех гармоник везде не превышает 5–15%.

Самые незначительные вклады в изменения $\zeta(t)'$, не превышающие 5–10%, оказывают сезонные аномалии стерических колебаний уровня моря $\zeta\rho(t)'$и речного стока $R(t)'$.

Наши результаты множественного регрессионного анализа заметно отличаются от оценок вклада ветра и атмосферного давления в изменения сезонных колебаний уровня Балтийского моря, полученных в работах *Johansson and Kahma* [2016] и *Barbosa and Donner* [2016] с помощью парной регрессии с использованием мареографных измерений уровня моря. В работе *Johansson and Kahma* [2016] влияние зонального ветра в межгодовую изменчивость среднемесячных значений уровня для всех прибрежных районов моря равно около 75%, в то время как наши результаты показывают снижение влияния ветра до 30–60% в Финском заливе и до 15–35% в Ботническом заливе (рис. 4). Из результатов работы [*Johansson and Kahma*, 2016] следует также, что воздействие атмосферного давления на сезонные изменения уровня моря является незначительным. Однако наши результаты показывают, что в Ботническом заливе влияние атмосферного давления достигает 45% (рис. 4). Эти различия могут быть связаны с тем, что *Johansson and Kahma* [2016] использовали для анализа среднемесячные ряды уровня, геострофического ветра и атмосферного давления, из которых, предварительно, были исключены тренды. В отличие от использованных нами среднесуточных данных, среднемесячные данные не являются эквидистантными, что приводит к ошибкам при расчете амплитуд и фаз сезонных колебаний уровня моря [*Захарчук и др.*, 2022; *Cartwright*, 1983]. Среднемесячное осреднение рядов также не исключает сигналы колебаний из низкочастотного диапазона синоптической изменчивости с периодами около 40 суток, которые хорошо выражены в нестационарных (частотно-временных) спектрах среднесуточных рядов уровня Балтики [*Захарчук*, 2008]. Кроме того, колебания уровня моря вызываются не геосторофическим ветром, а касательным напряжением трения приводного ветра. Из-за трения о подстилающую поверхность приводный ветер имеет отличные от геострофического ветра направление и скорость.

Сравнение наших оценок количественного влияния касательного напряжения трения ветра на изменения годовых колебаний уровня моря с результатами работы *Barbosa and Donner* [2016], показывает хорошее согласие для Финского залива, северо-западного, а также юго-западного районов открытой Балтики, и заниженные в 1,5–2 раза, по сравнению с нашими, оценки для центральной Балтики и Каттегата. Для оценок влияния атмосферного давления, хорошее согласие с результатами работы *Barbosa and Donner* [2016] отмечается только для северной части Ботнического залива, в то время как для Финского залива и открытой Балтики у *Barbosa and Donner* [2016] отмечается существенное завышение воздействия атмосферного давления, по сравнению с нашими оценками: у нас вклады атмосферного давления в изменчивость годовых колебаний уровня моря здесь составляют 5–10%, а у них 35–52% [*Barbosa and Donner*, 2016]. Столь значительное влияние атмосферного давления на изменчивость годовых колебаний уровня моря в Финском заливе и открытой Балтике в работе *Barbosa and Donner* [2016] на наш взгляд сомнительно, так как статистический анализ изменений атмосферного давления над Балтикой показывает существенное уменьшение размаха его колебаний при движении с севера на юг моря [*Захарчук и др.*, 2017]. Несоответствие результатов *Barbosa and Donner* [2016] нашим, может быть связано с рядом причин. Во-первых, С. Барбоса и Р. Доннер анализировали, в отличие от нас, ряды среднемесячных значений уровня моря, полученные по мареографным измерениям за другой временной период (1979–2012 гг.). Во-вторых, они применили для выделения годовых колебаний уровня моря иной метод – непрерывное вейвлет-преобразование, и, в третьих, они использовали метеорологические данные других реанализов (20th century reanalysis, ERA-interim reanalysis).

4. Заключение

1. Результаты скользящего гармонического анализа 133-летнего ряда (1889–2022 гг.) среднесуточных значений мареографных измерений уровня моря в Стокгольме

показывают очень значительную межгодовую изменчивость амплитуд гармоник Sa, Ssa, Sta, Sqa. В зависимости от года они меняются от 0,5–1,0 до 25–27 сантиметров. У всех четырёх составляющих сезонных колебаний уровня моря отсутствуют статистически значимые линейные тренды, но наблюдаются долгопериодные цикличности с временными масштабами от 20–35 до 55 лет. Наибольшая величина этих цикличностей отмечается для годовой гармоники Sa, но с увеличением частоты её обертонов размах колебаний долгопериодных циклов уменьшается. В последние три десятилетия у гармоник Sa, Ssa, Sta наблюдается заметное уменьшение амплитуд и дисперсии колебаний. Учитывая, что в работе [*Захарчук и др.*, 2022] была выявлена высокая корреляция (0,8–1,0) между изменчивостью сезонных колебаний уровня в Стокгольме и в других прибрежных районах Балтийского моря, можно предположить, что описанные нами особенности межгодовой изменчивости характеристик сезонных колебаний в Стокгольме свойственны и другим регионам Балтики.

2. Взаимный корреляционный анализ между аномалиями составляющих сезонных колебаний уровня моря, рассчитанных с помощью спутниковых альтиметрических данных, и такими же аномалиями различных гидрометеорологических процессов показал, что самая большая корреляция отмечается с изменениями касательного напряжения трения ветра (до 0,8–1,0), атмосферного давления (до −0,6...−0,8), а для гармоник Ssa, Sta, Sqa и с изменениями водообмена через Датские проливы (до 0,6–0,7). Корреляция с касательным напряжением трения ветра уменьшается при движении с юга на север до 0,3–0,4, в то время как с атмосферным давлением она, наоборот, уменьшается до −0,1...−0,2 при движении с севера на юг моря. Не отмечалось связи аномалий сезонных колебаний уровня моря с составляющими пресного баланса и стерическими колебаниями уровня моря.
3. Результаты множественного регрессионного анализа свидетельствуют, что наибольшее воздействие на межгодовые изменения сезонных колебаний уровня моря в течение последних 30 лет оказывают сезонные аномалии касательного напряжения трения ветра, вклады которых в открытой Балтике, пр. Каттегат и Рижском заливе достигают 40–70%, уменьшаясь, в зависимости от гармоники, до 30–60% в Финском заливе, и до 15–35% в Ботническом заливе. Вторыми по значимости процессами, влияющими на межгодовую изменчивость сезонных колебаний уровня моря, являются сезонные аномалии атмосферного давления и водообмена Балтийского и Северного морей, вклады которых, в зависимости от районов моря, варьируют от 5–15% до 25–45%. Вклады составляющих пресного баланса и изменений плотности воды в межгодовую изменчивость сезонных колебаний уровня моря незначительны, и не превышают 5–15%.

Благодарности. Исследование выполнено за счет гранта Российского научного фонда № 22-27-00209, https://rscf.ru/project/22-27-00209/.

Список литературы

Белоненко Т. В. *и* Колдунов А. В. Стерические колебания уровня в северо-западной части Тихого океана // Вестник СПбГУ. — 2006. — Т. 7, № 3. — С. 81—88. — EDN: RTTKQN.

Гидрометеорология и гидрохимия морей СССР: Проект «Моря СССР». Том III Балтийское море. Выпуск I Гидрометеорологические условия / под ред. Ф. С. Терзиева, В. А. Рожкова *и* А. И. Смирнова. — Санкт-Петербург : Гидрометеоиздат, 1992. — 451 с. — EDN: QKFOVS.

Гордеева С. М. *и* Малинин В. Н. Изменчивость морского уровня Финского залива. — Санкт-Петербург : РГГМУ, 2014. — 180 с. — EDN: VWABFU.

Захарчук Е. А. Синоптическая изменчивость уровня и течений в морях, омывающих северо-западное и арктическое побережья России. — Санкт-Петербург : Гидрометеоиздат, 2008. — 359 с. — EDN: QKIBRH.

Захарчук Е. А., Литина Е. Н., Клеванцов Ю. П. *и др.* Нестационарность гидрометеорологических процессов Балтийского моря в условиях меняющегося климата // Труды ГОИН. — 2017. — Т. 218. — С. 6—62. — EDN: YLMAZW.

Захарчук Е. А., Сухачев В. Н., Тихонова Н. А. *и др.* Стационарное и нестационарное описание сезонной изменчивости уровня Балтийского моря по данным мареографических измерений // Морской гидрофизический журнал. — 2022. — Т. 38, № 6. — С. 655—678. — DOI: 10.22449/0233-7584-2022-6-655-678.

Захарчук Е. А., Сухачев В. Н., Тихонова Н. А. *и др.* Стерические колебания уровня Балтийского моря // Russian Journal of Earth Sciences. — 2023. — Т. 23. — ES4014. — DOI: 10.2205/2023ES000846.

Захарчук Е. А. *и* Тихонова Н. А. О пространственно-временной структуре и механизмах формирования невских наводнений // Метеорология и гидрология. — 2011. — Т. 8. — С. 54—64. — EDN: NXUMIN.

Малинин В. Н. Статистические методы анализа гидрометеорологической информации. — Санкт-Петербург : РГГМУ, 2008. — 408 с. — EDN: QKIFPF.

Медведев И. П. Сезонные колебания уровня Балтийского моря // Метеорология и гидрология. — 2014. — Т. 12. — С. 42—54. — EDN: TACMRT.

Рожков В. А. Теория и методы статистического оценивания вероятностных характеристикам случайных величин и функций с гидрометеорологическими примерами. Книга II. — Санкт-Петербург : Гидрометеоиздат, 2002. — 780 с.

Фукс В. Р. Гидродинамические основы интерпретации альтиметрических съемок морской поверхности // Колебания уровня в морях. — СПб : РГГМУ, 2003. — С. 79—91.

Barbosa Susana M. *and* Donner Reik V. Long-term changes in the seasonality of Baltic sea level // Tellus A: Dynamic Meteorology and Oceanography. — 2016. — Vol. 68, no. 1. — P. 30540. — DOI: 10.3402/tellusa.v68.30540.

Bretherton F. P., Davis R. E. *and* Fandry C. B. A technique for objective analysis and design of oceanographic experiments applied to MODE-73 // Deep Sea Research and Oceanographic Abstracts. — 1976. — Vol. 23, no. 7. — P. 559–582. — DOI: 10.1016/0011-7471(76)90001-2.

Cartwright D. E. On the smoothing of climatological time series, with application to sea-level at Newlyn // Geophysical Journal International. — 1983. — Vol. 75, no. 3. — P. 639–658. — DOI: 10.1111/j.1365-246X.1983.tb05003.x.

Cheng Y., Xu Q. *and* Li X. Spatio-Temporal Variability of Annual Sea Level Cycle in the Baltic Sea // Remote Sensing. — 2018. — Vol. 10, no. 4. — P. 528–552. — DOI: 10.3390/rs10040528.

de Boor C. A Practical Guide to Splines. — Springer-Verlag, 1978. — 325 p.

Ekman M. A common pattern for interannual and periodical sea level variations in the Baltic Sea and adjacent waters // Geophysica. — 1996. — Vol. 32, no. 3. — P. 261–272.

Ekman M. The Changing Level of the Baltic Sea during 300 Years: A Clue to Understanding the Earth. — Summer Institute for Historical Geophysics, 2009.

Ekman M. *and* Stigebrandt A. Secular change of the seasonal variation in sea level and of the pole tide in the Baltic Sea // Journal of Geophysical Research: Oceans. — 1990. — Vol. 95, no. C4. — P. 5379–5383. — DOI: 10.1029/JC095iC04p05379.

Gill A. E. *and* Niller P. P. The theory of the seasonal variability in the ocean // Deep Sea Research and Oceanographic Abstracts. — 1973. — Vol. 20, no. 2. — P. 141–177. — DOI: 10.1016/0011-7471(73)90049-1.

Greatbatch R. J. A note on the representation of steric sea level in models that conserve volume rather than mass // Journal of Geophysical Research: Oceans. — 1994. — Vol. 99, no. C6. — P. 12767–12771. — DOI: 10.1029/94jc00847.

Gustafsson B. G. *and* Andersson H. C. Modeling the exchange of the Baltic Sea from the meridional atmospheric pressure difference across the North Sea // Journal of Geophysical Research: Oceans. — 2001. — Vol. 106, no. C9. — P. 19731–19744. — DOI: 10.1029/2000JC000593.

Hordoir R., Axell L., Löptien U., *et al.* Influence of sea level rise on the dynamics of salt inflows in the Baltic Sea // Journal of Geophysical Research: Oceans. — 2015. — Vol. 120, no. 10. — P. 6653–6668. — DOI: 10.1002/2014jc010642.

Hünicke B. *and* Zorita E. Trends in the amplitude of Baltic Sea level annual cycle // Tellus A: Dynamic Meteorology and Oceanography. — 2008. — Vol. 60, no. 1. — P. 154–164. — DOI: 10.1111/j.1600-0870.2007.00277.x.

Jackett D. R. *and* Mcdougall T. J. Minimal Adjustment of Hydrographic Profiles to Achieve Static Stability // Journal of Atmospheric and Oceanic Technology. — 1995. — Vol. 12, no. 2. — P. 381–389. — DOI: 10.1175/1520-0426(1995)012<0381:MAOHPT>2.0.CO;2.

Jakobsen F., Hansen I. S., Ottesen Hansen N.-E., *et al.* Flow resistance in the Great Belt, the biggest strait between the North Sea and the Baltic Sea // Estuarine, Coastal and Shelf Science. — 2010. — Vol. 87, no. 2. — P. 325–332. — DOI: 10.1016/j.ecss.2010.01.014.

Johansson M. M. *and* Kahma K. K. On the statistical relationship between the geostrophic wind and sea level variations in the Baltic Sea // Boreal Environment Research. — 2016. — Vol. 21. — P. 25–43.

Kowalczyk K., Pajak K., Wieczorek B., *et al.* An Analysis of Vertical Crustal Movements along the European Coast from Satellite Altimetry, Tide Gauge, GNSS and Radar Interferometry // Remote Sensing. — 2021. — Vol. 13, no. 11. — P. 2173. — DOI: 10.3390/rs13112173.

Labuz T. A. *and* Kowalewska-Kalkowska H. Coastal erosion caused by the heavy storm surge of November 2004 in the southern Baltic Sea // Climate Research. — 2011. — Vol. 48, no. 1. — P. 93–101. — DOI: 10.3354/cr00927.

Le Traon P. Y., Nadal F. *and* Ducet N. An Improved Mapping Method of Multisatellite Altimeter Data // Journal of Atmospheric and Oceanic Technology. — 1998. — Vol. 15, no. 2. — P. 522–534. — DOI: 10.1175/1520-0426(1998)015<0522:AIMMOM>2.0.CO;2.

Leppäranta M. *and* Myrberg K. Physical Oceanography of the Baltic Sea. — Springer Berlin Heidelberg, 2009. — DOI: 10.1007/978-3-540-79703-6.

Lisitzin E. Sea-Level Changes. — Elsevier Science & Technology Books, 1974.

Männikus R., Soomere T. *and* Viška M. Variations in the mean, seasonal and extreme water level on the Latvian coast, the eastern Baltic Sea, during 1961-2018 // Estuarine, Coastal and Shelf Science. — 2020. — Vol. 245. — P. 106827. — DOI: 10.1016/j.ecss.2020.106827.

Mohrholz V. Major Baltic Inflow Statistics - Revised // Frontiers in Marine Science. — 2018. — Vol. 5. — DOI: 10.3389/fmars.2018.00384.

Nerger L., Hiller W. *and* Schröter J. A comparison of error subspace Kalman filters // Tellus A: Dynamic Meteorology and Oceanography. — 2005. — Vol. 57, no. 5. — P. 715–735. — DOI: 10.3402/tellusa.v57i5.14732.

Pajak K. *and* Kowalczyk K. A comparison of seasonal variations of sea level in the southern Baltic Sea from altimetry and tide gauge data // Advances in Space Research. — 2019. — Vol. 63, no. 5. — P. 1768–1780. — DOI: 10.1016/j.asr.2018.11.022.

Pemberton P., Löptien U., Hordoir R., *et al.* Sea-ice evaluation of NEMO-Nordic 1.0: a NEMO-LIM3.6-based ocean-sea-ice model setup for the North Sea and Baltic Sea // Geoscientific Model Development. — 2017. — Vol. 10, no. 8. — P. 3105–3123. — DOI: 10.5194/gmd-10-3105-2017.

Plag H.-P. *and* Tsimplis M. N. Temporal variability of the seasonal sea-level cycle in the North Sea and Baltic Sea in relation to climate variability // Global and Planetary Change. — 1999. — Vol. 20, no. 2/3. — P. 173–203. — DOI: 10.1016/S0921-8181(98)00069-1.

Pujol M.-I., Faugère Y., Taburet G., *et al.* DUACS DT2014: the new multi-mission altimeter data set reprocessed over 20 years // Ocean Science. — 2016. — Vol. 12, no. 5. — P. 1067–1090. — DOI: 10.5194/os-12-1067-2016.

Samuelsson M. *and* Stigebrandt A. Main characteristics of the long-term sea level variability in the Baltic sea // Tellus A: Dynamic Meteorology and Oceanography. — 1996. — Vol. 48, no. 5. — DOI: 10.3402/TELLUSA.V48I5.12165.

Stramska M. *and* Chudziak N. Recent multiyear trends in the Baltic Sea level // Oceanologia. — 2013. — Vol. 55, no. 2. — P. 319–337. — DOI: 10.5697/oc.55-2.319.

Stramska M., Kowalewska-Kalkowska H. *and* Świrgoń M. Seasonal variability in the Baltic Sea level // Oceanologia. — 2013. — Vol. 55, no. 4. — P. 787–807. — DOI: 10.5697/oc.55-4.787.

Voinov G. N. Tides and Tidal streams // Polar Seas Oceanography. An integrated case study of the Kara Sea. — Springer, 2002. — P. 61–77.

Weisse R., Dailidienė I., Hünicke B., *et al.* Sea level dynamics and coastal erosion in the Baltic Sea region // Earth System Dynamics. — 2021. — Vol. 12, no. 3. — P. 871–898. — DOI: 10.5194/esd-12-871-2021.

Zakharchuk E. A., Sukhachev V. N., Tikhonova N. A., *et al.* Seasonal fluctuations in Baltic sea level determined from satellite altimetry // Continental Shelf Research. — 2022. — Vol. 249. — P. 104863. — DOI: 10.1016/j.csr.2022.104863.

Zakharchuk E. A., Tikhonova N., Zakharova E., *et al.* Spatiotemporal structure of Baltic free sea level oscillations in barotropic and baroclinic conditions from hydrodynamic modelling // Ocean Science. — 2021. — Vol. 17, no. 2. — P. 543–559. — DOI: 10.5194/os-17-543-2021.

Comparative Influence of Hydrometeorological Processes on the Interannual Variability of Seasonal Fluctuations of the Baltic Sea Level

E. A. Zakharchuk[1], M. V. Vinogradov[1,2], V. N. Sukhachev[*,1,2], and N. A. Tikhonova[1,2]

[1]St. Petersburg State University, Saint-Petersburg, Russia
[2]N. N. Zubov's State Oceanographic Institute, Roshydromet., Moscow, Russia
**Correspondence to: Vladimir Sukhachev, Syhachev@mail.ru .

With the help of long-term average daily tide gauge observations of sea level, satellite altimetry measurements and data from reanalyses of meteorological and hydrophysical fields, the features and physical mechanisms of interannual variability of seasonal fluctuations in the level of the Baltic Sea are investigated. It is shown that for the period 1889-2022 in Stockholm, in interannual changes in the amplitudes of harmonics Sa, Ssa, Sta, Sqa, there are statistically insignificant positive linear trends, against the background of which long-term cycles with time scales approximately from 20–35 to 55 years and very significant changes in amplitudes from 0.5–1.0 to 25–27 centimeters are observed. In recent decades, the harmonics Sa, Ssa, and Sta have seen a noticeable decrease in the amplitudes and dispersion of oscillations. The results of mutual correlation and multiple regression analyses of anomalies of seasonal fluctuations in sea level and various hydrometeorological processes indicate that the largest contribution to the interannual variability of seasonal fluctuations in sea level is made by changes in the tangential friction of the wind. The second most important processes are changes in atmospheric pressure over the sea and water exchange between the Baltic and North Seas. Changes in freshwater balance and density have the smallest impact on interannual variability in seasonal sea-level patterns.

Keywords: sea level, satellite altimeter measurements, reanalysis data, seasonal fluctuations, moving harmonic analysis, interannual variability, trends, wind stress, atmospheric pressure, steric sea level oscillations, fresh balance, water exchange, multiple regression analysis.

Recieved: 17 January 2024
Accepted: 12 July 2024
Published: 17 December 2024

Citation: Zakharchuk, E. A., M. V. Vinogradov, V. N. Sukhachev, and N. A. Tikhonova (2024), Comparative Influence of Hydrometeorological Processes on the Interannual Variability of Seasonal Fluctuations of the Baltic Sea Level, *Russian Journal of Earth Sciences*, 24, ES4013, https://doi.org/10.2205/2024ES000922, EDN: RNZFKL

References

Barbosa Susana M. *and* Donner Reik V. Long-term changes in the seasonality of Baltic sea level // Tellus A: Dynamic Meteorology and Oceanography. — 2016. — Vol. 68, no. 1. — P. 30540. — DOI: 10.3402/tellusa.v68.30540.

Belonenko T. V. *and* Koldunov A. V. Steric oscillations of the sea level in the north-western Pacific // Vestnik of St. Petersburg State University. — 2006. — Vol. 7, no. 3. — P. 81–88. — EDN: RTTKQN.

Boor C. de. A Practical Guide to Splines. — Springer-Verlag, 1978. — P. 325.

Bretherton F. P., Davis R. E. *and* Fandry C. B. A technique for objective analysis and design of oceanographic experiments applied to MODE-73 // Deep Sea Research and Oceanographic Abstracts. — 1976. — Vol. 23, no. 7. — P. 559–582. — DOI: 10.1016/0011-7471(76)90001-2.

Cartwright D. E. On the smoothing of climatological time series, with application to sea-level at Newlyn // Geophysical Journal International. — 1983. — Vol. 75, no. 3. — P. 639–658. — DOI: 10.1111/j.1365-246X.1983.tb05003.x.

Cheng Y., Xu Q. *and* Li X. Spatio-Temporal Variability of Annual Sea Level Cycle in the Baltic Sea // Remote Sensing. — 2018. — Vol. 10, no. 4. — P. 528–552. — DOI: 10.3390/rs10040528.

Ekman M. A common pattern for interannual and periodical sea level variations in the Baltic Sea and adjacent waters // Geophysica. — 1996. — Vol. 32, no. 3. — P. 261–272.

Ekman M. The Changing Level of the Baltic Sea during 300 Years: A Clue to Understanding the Earth. — Summer Institute for Historical Geophysics, 2009.

Ekman M. *and* Stigebrandt A. Secular change of the seasonal variation in sea level and of the pole tide in the Baltic Sea // Journal of Geophysical Research: Oceans. — 1990. — Vol. 95, no. C4. — P. 5379–5383. — DOI: 10.1029/JC095iC04p05379.

Fuchs V. R. Hydrodynamic principles of interpretation of altimetry surveys of the sea surface // Sea level variations. — Saint Petersburg : RSHU, 2003. — P. 79–91.

Gill A. E. *and* Niller P. P. The theory of the seasonal variability in the ocean // Deep Sea Research and Oceanographic Abstracts. — 1973. — Vol. 20, no. 2. — P. 141–177. — DOI: 10.1016/0011-7471(73)90049-1.

Gordeeva S. M. *and* Malinin V. N. Gulf of Finland sea level Variability. — Saint Petersburg : RSHU, 2014. — P. 180. — EDN: VWABFU.

Greatbatch R. J. A note on the representation of steric sea level in models that conserve volume rather than mass // Journal of Geophysical Research: Oceans. — 1994. — Vol. 99, no. C6. — P. 12767–12771. — DOI: 10.1029/94jc00847.

Gustafsson B. G. *and* Andersson H. C. Modeling the exchange of the Baltic Sea from the meridional atmospheric pressure difference across the North Sea // Journal of Geophysical Research: Oceans. — 2001. — Vol. 106, no. C9. — P. 19731–19744. — DOI: 10.1029/2000JC000593.

Hordoir R., Axell L., Löptien U., *et al.* Influence of sea level rise on the dynamics of salt inflows in the Baltic Sea // Journal of Geophysical Research: Oceans. — 2015. — Vol. 120, no. 10. — P. 6653–6668. — DOI: 10.1002/2014jc010642.

Hünicke B. *and* Zorita E. Trends in the amplitude of Baltic Sea level annual cycle // Tellus A: Dynamic Meteorology and Oceanography. — 2008. — Vol. 60, no. 1. — P. 154–164. — DOI: 10.1111/j.1600-0870.2007.00277.x.

Hydrometeorology and hydrochemistry of the seas of the USSR: Project "Seas of the USSR". Volume III Baltic Sea. Issue I Hydrometeorological conditions / ed. by F. S. Terzieva, V. A. Rozhkova *and* A. I. Smirnova. — Saint Petersburg : Gidrometeoizdat, 1992. — P. 451. — EDN: QKFOVS.

Jackett D. R. *and* Mcdougall T. J. Minimal Adjustment of Hydrographic Profiles to Achieve Static Stability // Journal of Atmospheric and Oceanic Technology. — 1995. — Vol. 12, no. 2. — P. 381–389. — DOI: 10.1175/1520-0426(1995)012<0381:MAOHPT>2.0.CO;2.

Jakobsen F., Hansen I. S., Ottesen Hansen N.-E., *et al.* Flow resistance in the Great Belt, the biggest strait between the North Sea and the Baltic Sea // Estuarine, Coastal and Shelf Science. — 2010. — Vol. 87, no. 2. — P. 325–332. — DOI: 10.1016/j.ecss.2010.01.014.

Johansson M. M. *and* Kahma K. K. On the statistical relationship between the geostrophic wind and sea level variations in the Baltic Sea // Boreal Environment Research. — 2016. — Vol. 21. — P. 25–43.

Kowalczyk K., Pajak K., Wieczorek B., *et al.* An Analysis of Vertical Crustal Movements along the European Coast from Satellite Altimetry, Tide Gauge, GNSS and Radar Interferometry // Remote Sensing. — 2021. — Vol. 13, no. 11. — P. 2173. — DOI: 10.3390/rs13112173.

Labuz T. A. *and* Kowalewska-Kalkowska H. Coastal erosion caused by the heavy storm surge of November 2004 in the southern Baltic Sea // Climate Research. — 2011. — Vol. 48, no. 1. — P. 93–101. — DOI: 10.3354/cr00927.

Le Traon P. Y., Nadal F. *and* Ducet N. An Improved Mapping Method of Multisatellite Altimeter Data // Journal of Atmospheric and Oceanic Technology. — 1998. — Vol. 15, no. 2. — P. 522–534. — DOI: 10.1175/1520-0426(1998)015<0522:AIMMOM>2.0.CO;2.

Leppäranta M. *and* Myrberg K. Physical Oceanography of the Baltic Sea. — Springer Berlin Heidelberg, 2009. — DOI: 10.1007/978-3-540-79703-6.

Lisitzin E. Sea-Level Changes. — Elsevier Science & Technology Books, 1974.

Malinin V. N. Statistical methods of hydrometeorological information analysis. — Saint Petersburg : RSHU, 2008. — P. 408. — EDN: QKIFPF.

Männikus R., Soomere T. *and* Viška M. Variations in the mean, seasonal and extreme water level on the Latvian coast, the eastern Baltic Sea, during 1961-2018 // Estuarine, Coastal and Shelf Science. — 2020. — Vol. 245. — P. 106827. — DOI: 10.1016/j.ecss.2020.106827.

Medvedev I. P. Seasonal fluctuations of the Baltic Sea level // Russian Meteorology and Hydrology. — 2014. — Vol. 39, no. 12. — P. 814–822. — DOI: 10.3103/S106837391412005X.

Mohrholz V. Major Baltic Inflow Statistics - Revised // Frontiers in Marine Science. — 2018. — Vol. 5. — DOI: 10.3389/fmars.2018.00384.

Nerger L., Hiller W. *and* Schröter J. A comparison of error subspace Kalman filters // Tellus A: Dynamic Meteorology and Oceanography. — 2005. — Vol. 57, no. 5. — P. 715–735. — DOI: 10.3402/tellusa.v57i5.14732.

Pajak K. *and* Kowalczyk K. A comparison of seasonal variations of sea level in the southern Baltic Sea from altimetry and tide gauge data // Advances in Space Research. — 2019. — Vol. 63, no. 5. — P. 1768–1780. — DOI: 10.1016/j.asr.2018.11.022.

Pemberton P., Löptien U., Hordoir R., *et al.* Sea-ice evaluation of NEMO-Nordic 1.0: a NEMO-LIM3.6-based ocean-sea-ice model setup for the North Sea and Baltic Sea // Geoscientific Model Development. — 2017. — Vol. 10, no. 8. — P. 3105–3123. — DOI: 10.5194/gmd-10-3105-2017.

Plag H.-P. *and* Tsimplis M. N. Temporal variability of the seasonal sea-level cycle in the North Sea and Baltic Sea in relation to climate variability // Global and Planetary Change. — 1999. — Vol. 20, no. 2/3. — P. 173–203. — DOI: 10.1016/S0921-8181(98)00069-1.

Pujol M.-I., Faugère Y., Taburet G., *et al.* DUACS DT2014: the new multi-mission altimeter data set reprocessed over 20 years // Ocean Science. — 2016. — Vol. 12, no. 5. — P. 1067–1090. — DOI: 10.5194/os-12-1067-2016.

Rozhkov V. A. Theory and methods of statistical estimation of probability characteristics of random variables and functions with hydrometeorological examples. Book II. — Saint Petersburg : Gidrometeoizdat, 2002. — P. 780.

Samuelsson M. *and* Stigebrandt A. Main characteristics of the long-term sea level variability in the Baltic sea // Tellus A: Dynamic Meteorology and Oceanography. — 1996. — Vol. 48, no. 5. — P. 672. — DOI: 10.3402/TELLUSA.V48I5.12165.

Stramska M. *and* Chudziak N. Recent multiyear trends in the Baltic Sea level // Oceanologia. — 2013. — Vol. 55, no. 2. — P. 319–337. — DOI: 10.5697/oc.55-2.319.

Stramska M., Kowalewska-Kalkowska H. *and* Świrgoń M. Seasonal variability in the Baltic Sea level // Oceanologia. — 2013. — Vol. 55, no. 4. — P. 787–807. — DOI: 10.5697/oc.55-4.787.

Voinov G. N. Tides and Tidal streams // Polar Seas Oceanography. An integrated case study of the Kara Sea. — Springer, 2002. — P. 61–77.

Weisse R., Dailidienė I., Hünicke B., *et al.* Sea level dynamics and coastal erosion in the Baltic Sea region // Earth System Dynamics. — 2021. — Vol. 12, no. 3. — P. 871–898. — DOI: 10.5194/esd-12-871-2021.

Zakharchuk E. A. Synoptic variability of sea level and currents in the seas washing the northwestern and arctic coasts of Russia. — Saint Petersburg : Gidrometeoizdat, 2008. — P. 359. — EDN: QKIBRH.

Zakharchuk E. A., Litina E. N., Klevantsov Yu. P., *et al.* Nonstationarity of the hydrometeorological processes in the Baltic sea at climate changing conditions // Proceedings of SOI. — 2017. — Vol. 218. — P. 6–62. — EDN: YLMAZW.

Zakharchuk E. A., Sukhachev V. N., Tikhonova N. A., *et al.* Seasonal fluctuations in Baltic sea level determined from satellite altimetry // Continental Shelf Research. — 2022a. — Vol. 249. — P. 104863. — DOI: 10.1016/j.csr.2022.104863.

Zakharchuk E. A., Sukhachev V. N., Tikhonova N. A., *et al.* Stationary and Non-Stationary Description of the Seasonal Sea Level Oscillations in the Baltic Sea Based on the Tide Gauge Data // Physical Oceanography. — 2022b. — Vol. 29, no. 6. — P. 636–658. — DOI: 10.22449/1573-160X-2022-6-636-658.

Zakharchuk E. A., Sukhachev V. N., Tikhonova N. A., *et al.* Steric Oscillations of the Baltic Sea Level // Russian Journal of Earth Sciences. — 2023. — Vol. 23. — ES4014. — DOI: 10.2205/2023ES000846.

Zakharchuk E. A., Tikhonova N., Zakharova E., *et al.* Spatiotemporal structure of Baltic free sea level oscillations in barotropic and baroclinic conditions from hydrodynamic modelling // Ocean Science. — 2021. — Vol. 17, no. 2. — P. 543–559. — DOI: 10.5194/os-17-543-2021.

Zakharchuk E. A. *and* Tikhonova N. A. On the spatiotemporal structure and mechanisms of the Neva River flood formation // Russian Meteorology and Hydrology. — 2011. — Vol. 36, no. 8. — P. 534–541. — DOI: 10.3103/S106837391108005X.

Моделирование переноса и накопления взвешенных веществ в условиях маловодья и нагонных явлений в устьевой области р. Дон

С. В. Бердников[1], **И. В. Шевердяев**[1], **А. В. Клещенков**[1], **В. В. Кулыгин**[1], **Н. В. Лихтанская**[*,1]

[1]Южный научный центр Российской академии наук, Ростов-на-Дону, Россия

* **Контакт:** Наталия Викторовна Лихтанская, natalikht@gmail.com

Предложен подход к совместному применению модели, реализованной в программном комплексе HEC-RAS, и балансовой модели для описания переноса и трансформации взвешенных веществ в речной дельте. В устьевой области реки выделяются гидрологические районы: русловые районы, пойменные районы, затапливаемые при высоких паводках и штормовых нагонах со стороны моря, и районы авандельты. Для гидрологических районов строится динамическая модель баланса воды и веществ, переносимых водным потоком. Вводится параметризация процессов осаждения взвешенных веществ и их взмучивания в зависимости от скорости движения воды и размера частиц. Рассматривается три градации взвеси по размерам: пелитовая фракция (глина), алевритовая фракция (ил) и мелкий песок. Акцент делается на оценке влияния морских штормовых нагонов на перенос взвешенных веществ в речную дельту и их осаждение. Для описания потоков воды между районами, скоростей ее движения, динамики ее уровня и процессов затопления поймы применяется детальная модель на базе программного комплекса HEC-RAS, адаптированная к условиям устьевой области р. Дон. Выполнены расчеты переноса и накопления взвешенных веществ в устьевой области Дона для двух вариантов гидрологических условий – с нагоном воды со стороны моря и без него. Рассмотрена пространственно-временная изменчивость концентрации и гранулометрического состава взвешенных наносов в зависимости от гидрологических условий. Показано, что в отсутствие нагонных явлений при небольших расходах воды взвешенные вещества в основном осаждаются в авандельте за пределами морского края дельты, а в период нагона насыщают воду и на этапе подъема ее уровня поступают в дельту, частично осаждаясь в рукавах и в пойменных районах. При этом на этапе спада уровня воды из русловых районов они выносятся за морской край дельты, а в пойменных в основном остаются. Для условий маловодья при наблюдаемой частоте нагонных явлений и при отсутствии паводков устьевая область Дона задерживает в среднем 20% взвешенных веществ, поступающих со стоком р. Дон.

Ключевые слова: балансовая модель, взвешенное вещество, программный комплекс HEC-RAS, штормовой нагон, дельта Дона.

Цитирование: Бердников, С. В., И. В. Шевердяев, А. В. Клещенков, В. В. Кулыгин и Н. В. Лихтанская Моделирование переноса и накопления взвешенных веществ в условиях маловодья и нагонных явлений в устьевой области р. Дон // Russian Journal of Earth Sciences. — 2024. — Т. 24. — ES4013. — DOI: 10.2205/2024es000926 — EDN: NYRZMC

https://elibrary.ru/nyrzmc

Получено: 12 марта 2024 г.
Принято: 30 июля 2024 г.
Опубликовано: 25 Декабря 2024 г.

1. Введение

Дельты рек мира являются важными географическими районами, включающими в себя всего около 0,5% площади суши, но населенными почти 5% населения мира [*Dunn et al.*, 2019]. Еще 140 миллионов человек проживают в пределах 25 км от дельт, а 3,5 миллиарда – в дельтовых водосборных бассейнах [*Tessler et al.*, 2015]. Таким образом, почти половина населения земного шара проживает в дельтах или вблизи них и в их водосборных бассейнах.

Дельты включают в себя разнообразные ландшафты, такие как водно-болотные угодья, прибрежную растительность, реки, приливные каналы и эстуарные водоемы, которые обеспечивают важные экосистемные услуги. Вместе с тем дельты сталкиваются с различными угрозами [*Day et al.*, 2016; *Day and Rybczyk*, 2019; *Giosan et al.*, 2014; *Syvitski and Milliman*, 2007], которые снижают ценность этих услуг. Глобальное эвстатическое повышение уровня моря, превышающее 3–4 мм/год [*Dieng et al.*, 2017], рассматривается как реальная угроза для дельт мира [*Day and Rybczyk*, 2019; *Giosan et al.*, 2014]. Плотины и водохранилища, как в самих дельтах, так и вверх по течению, также представляют серьезную угрозу для дельт из-за сокращения поступления взвешенных наносов, а также из-за использования пресной воды населением, промышленностью и сельским хозяйством [*Wolters and Kuenzer*, 2015].

За последние 60 лет морской край дельты Дона перестал выдвигаться в море после введения в эксплуатацию Цимлянского водохранилища в 1952 г. и низконапорных плотин ниже по течению [*Venevsky et al.*, 2023; 2022]. На отдельных участках фронт дельты даже стал двигаться в сторону суши. Причиной, с одной стороны, стало уменьшение поступления речных наносов (более чем в 10 раз). С другой стороны, в тот же период времени произошли изменения в региональной атмосферной циркуляции. Преобладающими стали западные и юго-западные ветры, формирующие значительные штормовые нагоны морской воды в дельту и способные приносить большое количество взвеси. В последние годы положение фронта дельты стабилизировалось.

Кроме стабилизации морского края дельты с середины 1980-х годов начала уменьшаться ширина речных каналов. Максимальное изменение проявляется на расстоянии 15–20 км от морского края. Здесь к 2020 г. суммарная ширина каналов уменьшилась на 80–100 м или 10%. Возможное объяснение этому – зарастание и заиление каналов из-за поступления взвешенных веществ при нагонах воды с моря.

Экосистема Азовского моря, куда впадает р. Дон, в настоящее время испытывает влияние беспрецедентного сочетания негативных факторов, включающих в себя повышение солености и температуры вод [*Бердников и др.*, 2022], трансформацию водного сообщества, вызванную вытеснением аборигенных видов инвазионными таксонами, предположительно в связи с изменением климата в регионе [*Berdnikov et al.*, 2023].

Большие нагоны приносят соленую воду, что должно неизбежно сказаться как на развитии водно-болотных сообществ дельты, так и на процессах биогеохимической трансформации веществ, поступающих с рекой и из моря, в зоне их взаимодействия [*Герасюк и Бердников*, 2021]. Последняя все чаще смещается вглубь дельты.

Целью настоящей работы является описание подхода к моделированию влияния штормовых нагонов на перенос и накопление взвешенных веществ в дельте Дона в условиях недостаточной водности речного стока (период маловодья).

2. Материалы и методы исследования

2.1. Регион исследования

Регионом исследования является часть устьевой области р. Дон, которая начинается от станицы Раздорской (здесь находится гидрологический стоковый пост) и включает в себя участок реки до г. Ростова-на-Дону (здесь имеется ряд боковых притоков – реки Аксай, Тузлов, Маныч и Темерник), донскую дельту и авандельту – прилегающий участок Таганрогского залива за пределами морского края дельты (рис. 1А). Вся устьевая область Дона простирается от ст. Раздорской на востоке до Должанской косы на западе [*Михайлов*, 1997], но в данной статье под устьевой областью будет подразумеваться регион исследования.

Дельта Дона имеет классическую треугольную форму с вершиной на востоке в г. Ростове-на-Дону, где рукав Мертвого Донца ответвляется от реки Дон, фронтом дельты на западе (39°11′–39°43′ в. д. и 47°05′–47°16′ с. ш.) и занимает площадь около 540 км^2.

В ландшафте дельты Дона, близком к уровню моря, преобладают водно-болотные угодья и множество водотоков (от первичных и вторичных до небольших каналов, соединяющих внутренние водоемы дельты). Основными рукавами в дельте являются Старый Дон, Большая Каланча, Мокрая Каланча, Большая и Средняя Кутерьма, Мертвый Донец. Ниже г. Азова Старый Дон превращен в Азово-Донской судоходный канал (более подробно см. [*Матишов и др.*, 2019]).

2.2. Подход к моделированию водного и вещественного баланса устьевой области Дона

Для моделирования динамики воды и вещества предлагается подход, учитывающий разный пространственно-временной масштаб наблюдаемых здесь явлений. События, связанные с нагоном воды со стороны моря, как правило, не превышают трех-четырех суток. В остальные периоды времени, более длительные, территория дельты не затапливается. Таким образом, годовой временной интервал можно разбить на подинтервалы с разными гидрологическими условиями: относительно короткие по времени, когда дельта подвержена затоплению в результате поступления воды со стороны моря при штормовом нагоне, и более длительные, когда пойменные и русловые районы гидрологически не связаны. Вода и находящиеся в ней взвешенные вещества перемещаются по русловым районам в сторону моря, а в районах суши, расположенных в пойме дельты, протекают независимые от гидрологии реки процессы.

В пространственном аспекте выделены следующие типы районов устьевой области. Во-первых, это русловые районы, которые постоянно находятся под водой и по которым вода и содержащиеся в ней взвешенные вещества перемещаются в сторону моря, а при нагонах воды с моря могут перемещаться и в обратном направлении. Во-вторых, это районы поймы дельты, которые в основном в течение года представляют собой сушу, но иногда, в период нагонов или речных паводков затапливаются. В-третьих, это район Таганрогского залива – авандельта (подводная наклонная часть дельты).

Разделив русловые сегменты на отдельные районы с учетом ветвления основного русла на рукава и протяженности каждого сегмента, получаем гидрологическое районирование устьевой области Дона (рис. 1Б).

Для моделирования переноса и осаждения взвешенных веществ в устьевой области используются две модели: модель устьевой области Дона на базе программного комплекса HEC-RAS – DeltaDonHECRAS и балансовая модель DeltaRiverBalanceModel.

Информационной основой для исследования служат: база данных автоматизированных наблюдений за уровнем воды на гидрологических постах Южного научного центра Российской академии наук (ЮНЦ РАН) в дельте Дона и база данных гидрохимических показателей, полученных в ходе экспедиционных работ ЮНЦ РАН в устьевой области Дона в 2007–2021 гг. [*Клещенков и др.*, 2023].

2.3. Модель устьевой области Дона на базе программного комплекса HEC-RAS – DeltaDonHECRAS

Программный комплекс HEC-RAS, предназначенный для моделирования течения воды по системам открытых каналов, применяется, в частности, в исследованиях по управлению поймами для оценки последствий затопления [*Hicks and Peacock*, 2005; *Kleinschmidt Associates*, 2020]. Исследование с его помощью течения воды в дельтах в условиях сгонно-нагонных и приливных колебаний уровня моря в последнее время также получает распространение [*Pandey et al.*, 2021; *Wang et al.*, 2021]. Здесь мы опираемся на опыт оценки затопления дельты Дона в период экстремального нагона в сентябре 2014 г. [*Шевердяев и др.*, 2017].

Расчетная область делится на 101 095 ячеек средним размером 100 на 100 м (рис. 1 В). Приток речной воды по основному руслу в районе станицы Раздорской и динамика уровня воды в Таганрогском заливе при ветровом нагоне задаются в качестве граничных условий. Затем рассчитываются потоки воды между ячейками и объем воды в них. Расчетный шаг модели – 10 минут. Эти значения записываются в базу данных и используются моделью DeltaRiverBalanceModel.

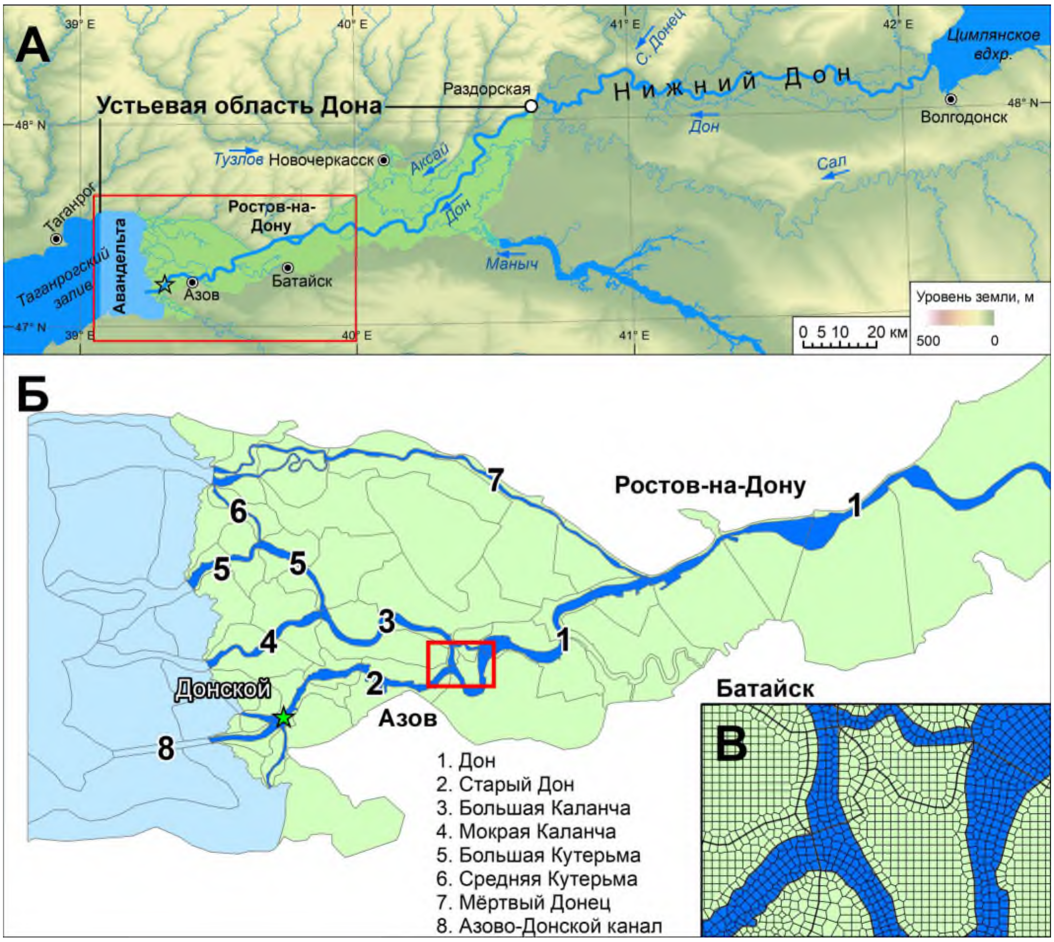

Рис. 1. Регион исследования: гидрографическая сеть (А) (звездочкой отмечен пункт наблюдения за уровнем воды), гидрологическое районирование устьевой области Дона (Б) и пример сеточного разбиения для моделирования гидрологических условий с применением программного комплекса HEC-RAS (В).

2.4. Балансовая модель переноса растворенных и взвешенных веществ

Модель DeltaRiverBalanceModel включает в себя следующие блоки (модули): водного баланса и переноса и осаждения взвешенного вещества.

Для каждого из выделенных гидрологических районов справедливо следующее уравнение водного баланса (1):

$$V_i(t+dt) = V_i(t) + \sum_j Q_{i,j}(t,t+dt) - Q_{i,i}(t,t+dt) + Q_{in,i}(t,t+dt), \tag{1}$$

где $V_i(t+dt)$, $V_i(t)$ – объем воды в i-м районе в моменты времени $t+dt$ и t соответственно, тыс. м^3; $Q_{i,j}(t,t+dt)$ – объем воды, поступивший в i-й район из j-того района в период времени $(t,t+dt)$, тыс. м^3 (суммирование идет по всем j-м районам, которые имеют с i-м районом общую границу и для которых поток воды направлен в i-й район); $Q_{i,i}(t,t+dt)$ – объем воды, который вытек из i-го района в период времени $(t,t+dt)$, тыс. м^3; $Q_{in,i}(t,t+dt)$ – объем воды, поступивший в i-й район из внешних источников в период времени $(t,t+dt)$, тыс. м^3.

В рассматриваемом случае внешние источники – это приток речной воды по основному руслу и поступление морской воды из Таганрогского залива при ветровом нагоне. Другие внешние источники (сбросы сточных вод, приток подземных вод и осадки) не рассматриваются. Также не принимаются во внимание испарение и потери на инфильтрацию воды в почву.

Величины $Q_{in,i}(t,t+dt)$ задаются в качестве внешних факторов в модели DeltaDonHEC-RAS, а величины $Q_{i,j}(t,t+dt)$, $Q_{i,i}(t,t+dt)$ рассчитываются в этой модели как потоки воды через границы между районами.

Модуль водного обмена необходим для согласования модели DeltaDonHEC-RAS с гидрологическим районированием, где объединяются все ячейки, входящие в тот или иной район, обобщается информация по уровню воды, объему воды, площади затопления, потокам и скоростям движения воды через границы между ячейками и районами.

Для расчета динамики взвешенных веществ рассматривается следующее балансовое уравнение (2):

$$\begin{aligned} &V_i(t+dt)\cdot b_i(t+dt) = \\ &\qquad = V_i(t)\cdot b_i(t) + \sum_j Q_{i,j}(t,t+dt)\cdot b_j(t) - \\ &\qquad - Q_{i,i}(t,t+dt)\cdot b_i(t+dt) + Q_{in,i}(t,t+dt)\cdot b_{in,i}(t) + \\ &\qquad + \omega\cdot S_i(t,t+dt)\cdot[\alpha^0\cdot b_i^*(t,t+dt) - b_i(t+dt)]\cdot dt, \end{aligned} \tag{2}$$

где $b_i(t+dt)$, $b_i(t)$ – средняя по объему концентрация взвешенного вещества в i-м районе в моменты времени $t+dt$ и t соответственно, мг/дм^3; $b_{in,i}(t)$ – концентрация взвешенного вещества в водных потоках, поступающих извне, мг/дм^3; ω – скорость осаждения (гидравлическая крупность) взвешенного вещества, м/с; $S_i(t,t+dt)$ – площадь района под водой, средняя в интервале времени $(t,t+dt)$, тыс. м^2; α^0 – параметр, отвечающий за интенсивность взмучивания; $b_i^*(t,t+dt)$ – концентрация взвешенного вещества, обусловленная транспортирующей способностью потока, средняя в интервале $(t,t+dt)$, мг/дм^3.

Величина b^*, следуя [*Zhang et al.*, 2014], оценивается по следующей формуле (3):

$$b^* = K\left[\frac{u^3}{gR\omega}\right]^m, \tag{3}$$

где K, m – эмпирические параметры, $K = 5{,}0$ г/м^3, $m = 0{,}92$; u – средняя (по вертикали) скорость течения, м/с; g – ускорение свободного падения, $g = 9{,}81$ м/с^2; R – гидравлический радиус, м. Нижние индексы принадлежности к определенному району опущены.

Гидравлический радиус для р. Дон в нижнем течении и рукавов дельты можно считать пропорциональным средней глубине.

Таким образом, изменение концентрации взвешенного вещества в гидрологических районах кроме процессов его поступления и выноса через боковые границы определяется процессами его осаждения и взмучивания из донных отложений. Интенсивность взмучивания корректируется параметром α^0.

Скорость осаждения частиц зависит от их размера k (м) и рассчитывается, следуя [*Барышников и Попов*, 1988], по формуле (4):

$$\omega = \frac{\left(\dfrac{2g(\rho_1-\rho)k}{1{,}75\rho}\right)^{1/2}}{\varphi}, \tag{4}$$

где ρ_1 – плотность частиц, $\rho_1 = 2650$ кг/м^3; ρ – плотность воды, $\rho = 1000$ кг/м^3; φ – параметр турбулентного поведения наносов в потоке, который отражает особенности осаждения частиц в реальных условиях водоема.

Взвесь делится на три группы по размерам: пелитовая фракция (глина, clay), частицы размером меньше 0,01 мм; алевритовая фракция (ил, silt), частицы размером 0,1–0,01 мм и песчаная фракция (песок, sand), частицы размером более 0,1 мм.

3. Результаты исследования и их обсуждение

3.1. Калибровка параметров и верификация модели DonDeltaHECRAS

Проверка гидрологического блока модели проводилась путем сравнения результатов расчетов с измерениями расходов воды на поперечных профилях в судоходном русле Дона, в рукавах Каланча и Кутерьма и в гирлах юго-западной части дельты, выполненными 13–15 сентября 2016 г. для калибровки параметров модели и 22–23 сентября 2014 г. для контрольной проверки (распределение точек измерений в дельте Дона представлено на рис. 2А).

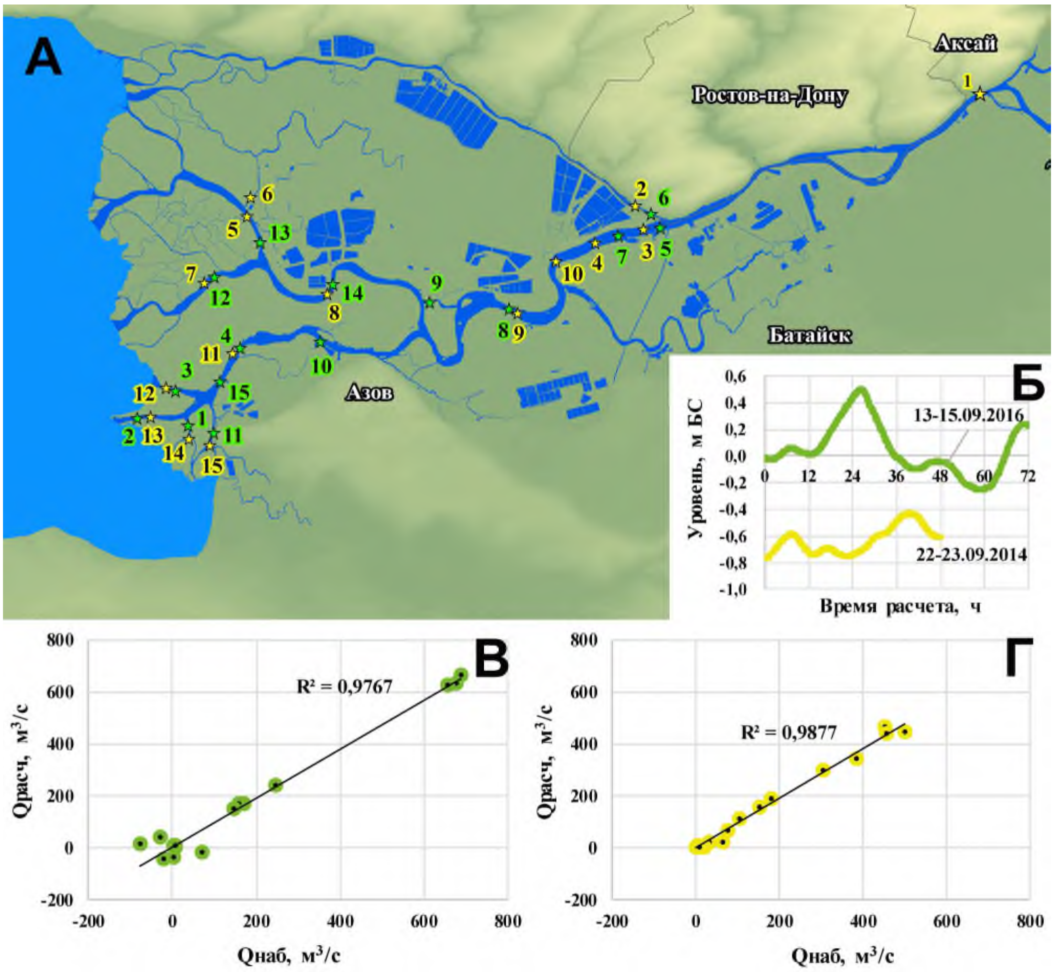

Рис. 2. Результаты верификации модели устьевой области Дона по данным 13–15 сентября 2016 г. (зеленый цвет) и 22–23 сентября 2014 г. (желтый цвет): распределение точек измерений в дельте Дона (А); ход уровня воды на уровнемере на причале «Донской» (Б); сопоставление результатов расчета расходов воды с данными наблюдений при калибровке параметров модели (В); сопоставление результатов расчета расходов воды с данными наблюдений при верификации модели (Г) (отрицательные значения расходов воды соответствуют условиям, когда вода движется от морского края в направлении вершины дельты).

В период 13–15 сентября 2016 г. расход воды в ст. Раздорской в среднем был равен 390 м^3/с, в период 22–23 сентября 2014 г. – 430 м^3/с. На участке от ст. Раздорской до вершины дельты имеется боковая приточность из рек Маныч, Тузлов, Аксай и Темерник. Так как систематические наблюдения здесь отсутствуют, то рассматривались разные сценарии поступления воды с малыми реками в интервале от 50 до 150 м^3/с, что вносило неопределенность в получаемые результаты. Уровень воды на морской границе устьевой области задавался по данным уровнемера, установленного на причале «Донской» Южного научного центра РАН, который расположен примерно в 20 км от границы расчетной области в Таганрогском заливе со сдвигом по времени 20 минут назад и отмечен звездочкой на рис. 1А (ход уровня воды на уровнемере представлен на рис. 2Б).

В качестве калибровочных параметров рассматривались цифровая модель местности (ЦММ) и коэффициенты шероховатости русел. Из-за практически равнинного ландшафта дельты и отсутствия детальных промеров профиля русел, особенно на несудоходных участках, ЦММ имеет много неопределенностей и требует уточнения. В результате серии вычислительных экспериментов, направленных на приближение расчетных расходов воды данными наблюдений в точках измерений, для коэффициентов шероховатости русел везде были приняты одинаковые значения – 0,0125. Сопоставление результатов расчета расходов воды с данными наблюдений представлено на рис. 2В. Для авандельты было использовано то же значение коэффициента шероховатости, что и для русел, а для поймы – 0,08 (рекомендованное значение для заросших пойм по М. Ф. Срибному).

Проверочные расчеты проводились без изменения значений ЦММ и коэффициента шероховатости. Расчетные расходы воды сравнивались с данными измерений, выполненными 22–23 сентября 2014 г. (рис. 2Г).

Результаты проверки [см. табл. ДМ3 и ДМ4, *Бердников и др.*, 2023] показывают, что модель дельты Дона воспроизводит особенности распределения воды по основным рукавам, несмотря на некоторые различия, как в судоходном канале, так и в несудоходных гирлах Мериново и Каменное (главным образом, вблизи морского края дельты). Отмечается повышенное распределение стока в судоходную часть Дона по сравнению с рукавами Каланча и Большая Кутерьма.

3.2. Математическое моделирование гидрологических условий устьевой области Дона при различных расходах воды и нагонных колебаниях ее уровня в Таганрогском заливе

В период 2015–2020 гг. в дельте Дона наблюдалось 50 нагонов с максимальным подъемом уровня воды от 1,0 до 1,77 м относительно среднемноголетнего положения [*Лихтанская и др.*, 2023]. Из этого перечня выбрано 5 нагонов, имеющих разную обеспеченность и разный расход воды в ст. Раздорская (табл. 1), и один экстремальный нагон 23–25 сентября 2014 г. с максимальным превышением уровня воды 3,7 м. Кроме этого рассмотрены: характерные для устьевой области гидрологические условия, когда явный нагон отсутствует, но на морском крае дельты наблюдается периодическое изменение уровня воды до минус 0,5 м относительно среднемноголетнего значения с периодом 12 часов (сценарий БН-2), а также гидрологические условия постоянного расхода воды при полном отсутствии изменения уровня воды на левой границе расчетной области – в Таганрогском заливе (сценарий БН-1). Для каждого нагона выбраны дата и время максимального подъема уровня воды. Расчеты по модели DeltaDonHEC-RAS проводились для четырех суток (двух суток до наступления максимального уровня воды и двух – после). Краткие характеристики рассмотренных нагонов воды со стороны Таганрогского залива приведены ниже.

Сценарий Н-1. Расчёт проводился для периода между 16:40 19 марта и 16:40 23 марта 2018 г. с максимальным подъемом уровня воды на 1,77 м в 16:30 21 марта (рис. А2). Расход воды в Дону в эти даты сначала снижался с 514 м^3/с (19 марта) до 432 м^3/с (21 марта), а затем возрастал до 631 м^3/с 23 марта. Рост уровня воды начался с отметки минус 0,7 м относительно его среднемноголетнего положения. Наблюдаются 3 волны роста уровня воды, сменяющиеся падениями: первая – в ночь на 20 марта примерно на 1 м, вторая – в течение 21 марта до максимального нагонного уровня воды (1,77 м), третья – во второй половине 22 марта примерно на 0,5 м.

Сценарий Н-2. Расчёт проводился для периода между 10:00 15 апреля и 10:00 19 апреля 2020 г. с максимальным подъемом уровня воды на 1,75 м в 9:50 17 апреля (рис. А3). Расход воды в Дону в эти даты был стабильно очень низким – около 300 м^3/с. Рост

Таблица 1. Характеристики расчетных сценариев нагонов в дельте Дона

№ пп	Условное обозначение сценария	Максимальный подъем уровня воды от среднемноголетнего значения, м	Дата начала нагона	Дата окончания нагона	Средний расход воды в ст. Раздорской за период нагона, м^3/с	Обеспеченность нагона, %	Концентрация взвешенного вещества в воде, поступающей в устьевую область из Таганрогского залива, мг/л
1	Н-1	1,77	18/03/2018	22/03/2018	507	27	120
2	Н-2	1,75	14/04/2020	18/04/2020	300	29	120
3	Н-13	1,4	30/03/2016	03/04/2016	407	54	70
4	Н-16	1,36	19/04/2018	23/04/2018	1462	59	70
5	Н-40	1,06	22/02/2019	26/02/2019	525	85	50
6	НЭ-3,7	3,7	23/09/2014	25/09/2014	541	0,8	160

Примечание: Концентрация взвешенного вещества в воде, поступающей в устьевую область из Таганрогского залива, оценивалась по материалам исследований в дельте Дона и Таганрогском заливе для нагонов-аналогов, а также по описанным в [*Ганичева*, 1985] зависимостям взмучивания донных отложений в Таганрогском заливе от силы ветра и волнения моря. В нумерации сценариев нагонов используется их порядковый номер в таблице нагонов, зафиксированных в период с января 2015 г по май 2020 г. на гидрометеопосту ЮНЦ РАН в хуторе Донском [*Лихтанская и др.*, 2023].

уровня воды начался с отметки 0,43 м относительно его среднемноголетнего положения. Выделяется сначала небольшое падение уровня воды на 0,5 м, затем примерно 1,5 суток плавного нагонного роста до максимума и небольшой всплеск уровня воды в конце 18 апреля на 0,3 м. В сравнении со сценарием Н-1 этот сценарий интересен тем, что при том же максимальном нагонном уровне воды ее расход в Дону примерно в 2 раза меньше, хотя продолжительность нагона примерно в 2 раза больше.

Сценарий Н-13. Расчёт проводился для периода между 10:30 31 марта и 10:30 5 апреля 2016 г. с максимальным подъемом уровня воды на 1,4 м в 10:30 2 апреля (рис. А4). Расход воды в ст. Раздорской в целом пониженный (около 400 м^3/с), но с устойчивым ростом от 383 до 440 м^3/с. На протяжении всего сценария уровень воды был выше его среднемноголетнего положения, максимальный нагонный уровень воды 1,4 м был достигнут примерно за 10 часов ростом на 0,7 м, затем примерно за то же время уровень воды упал до 0,7 м и постепенно падал до 0,2 м, сменившись в конце сценария скачком уровня воды на 0,4 м. В целом можно отметить, что в этом сценарии имитируется ветровой всплеск уровня воды на 0,7 м на фоне повышенного уровня воды и меженного расхода воды в Дону.

Сценарий Н-16. Расчёт проводился для периода между 10:00 20 апреля и 10:00 25 апреля 2018 г. с максимальным подъемом уровня воды на 1,36 м в 10:00 22 апреля (рис. А5). Это сценарий небольшого ветрового нагона на фоне половодного расхода воды в Дону – рост от 1330 до 1550 м^3/с. Подъем уровня воды начался с отметки 0,4 м относительно его среднемноголетнего положения. После небольшого снижения на 0,2 м в течение суток наблюдался нагонный рост уровня воды примерно на 1,2 м.

Сценарий Н-40. Расчёт проводился для периода между 0:00 24 февраля и 0:00 1 марта 2019 г. с максимальным подъемом уровня воды на 1,06 м в 0:00 26 февраля (рис. А6). Это самый слабый нагон из рассмотренных, развивавшийся на фоне среднего расхода воды в Дону – от 491 до 565 м^3/с. По форме нагон близок к сценарию Н-13. Такие нагоны на фоне среднего расхода воды в Дону наиболее часты.

Сценарий НЭ-3,7. Это наиболее экстремальный нагон за последние 100 лет наблюдений. Расчёт проводился для периода между 17:20 22 сентября и 17:20 27 сентября

2014 г. с максимальным подъемом уровня воды на 3,70 м в 17:20 24 сентября (рис. A7). Рост уровня воды составил порядка 3,5 м за 12 часов на фоне стабильного меженного расхода воды в Дону – 430 м^3/с. За пиком подъема уровня воды наблюдалось его падение в течение полутора дней.

Для оценки полученных результатов моделирования гидрологических условий при нагонах разной обеспеченности выделено три русловых гидрологических района (16, 23 и 42), расположенных на разном расстоянии от фронта дельты, и один (4), являющийся продолжением Азово-Донского судоходного канала в авандельте.

Для русловых районов в период действия нагонов с превышением уровня воды в диапазоне от 1,0 до 3,7 м (рисунки A2–A7) наблюдается сначала замедление скоростей потоков, направленных в сторону залива, а затем потоки разворачиваются в обратную сторону и их скорость растет вплоть до достижения пика уровня воды, который наступает раньше пика скорости потока. Затем скорости потоков быстро падают до нуля, потоки разворачиваются в направлении от реки к морю, и восстанавливаются обычные значения их скоростей. Амплитуды скоростей обратных потоков при удалении от морского края дельты уменьшаются. Потоки в русловых районах вдали от моря под воздействием нагонов только замедляются (без изменения направления). Чем интенсивней нагон (выше максимальный уровень) и ниже речной расход, тем дальше от морского края дельты формируются обратные течения [*Клещенков и Шевердяев*, 2023].

Важно отметить, что при падении уровня воды после достижения максимума нагона в русловых районах дельты, скорости потоков, направленных в сторону залива, превышают значения, которые были в период роста уровня воды. Для районов, расположенных в авандельте, это не так. В период падения уровня воды скорости потоков ниже, чем в период его роста. Особенно это заметно для экстремального нагона (рис. A7). Однако, при расходе воды в Дону близком к значениям, характерным для половодья (рис. A5), и не очень высоком уровне нагона, эта особенность нарушается – практически всегда скорость потока при уменьшении уровня воды выше (сравните рисунки A5–A6 для района 4).

Для пойменных районов дельты по мере их затопления скорости потоков уменьшаются при удалении от граничных русловых районов к периферии, при падении уровня воды на отдельных участках рельефа (ерики, каналы стока) скорости потоков могут возрастать из-за более быстрого уменьшения площади района, подверженного затоплению, чем в период подъема уровня воды.

Таким образом в периоды нагонов скорости потоков в авандельте и русловых районах могут достигать достаточно высоких значений (до 0,4–0,5 м/с и более), что создает сначала условия для взмучивания донных отложений в районах авандельты, а затем на этапе падения уровня воды и в русловых районах.

При осреднении скоростей потоков по выделенным гидрологическим районам (за период расчета) получаем их распределение вдоль основных русел (рис. 3). При этом рассмотрим отдельно:

1) основное судоходное русло «Дон – Старый Дон – АДСК», представлено последовательностью гидрологических районов 78→64→57→42→30→23→22→16→9 от вершины дельты к морскому краю (рис. 3А);

2) рукав «Дон – Большая Каланча – Мокрая Каланча», представлен последовательностью районов 78→64→57→42→30→33→50→52→51→41 (рис. 3Б);

3) рукав «Дон – Большая Каланча – Большая Кутерьма – Кутерьма», представлен районами 78→64→57→42→30→33→50→52→68→76→75→70 (рис. 3В);

4) рукав «Дон – Большая Каланча – Большая Кутерьма – Средняя Кутерьма», представлен районами 78→64→57→42→30→33→50→52→68→76→89→96→100 (рис. 3Г);

5) рукав «Дон – Мертвый Донец», представлен районами 78→83→107→111→115→114 (рис. 3Д).

Для сценария БН-1 при отсутствии изменения уровня воды в заливе в вершине дельты средняя скорость потока составляет примерно 15 см/с и падает до 10–5 см/с в гирлах Мокрая Каланча, Большая Кутерьма на морской границе дельты. В рукаве Мертвый Донец скорость потока еще меньше – до 3 см/с. Это связано с последовательным ветвлением русла Дона на протоки и расширением суммарной ширины русел по мере приближения к морскому краю. На отдельных участках рукавов средние скорости потоков из-за особенностей морфометрии русел локально возрастают (см., например, рис. 3 районы 68, 57, 50 и 52).

Для сценария БН-2 в районах, близких к морскому краю дельты, из-за колебаний уровня воды с амплитудой 0,5 м в течение суток, скорости потоков опять возрастают до 15–20 см/с.

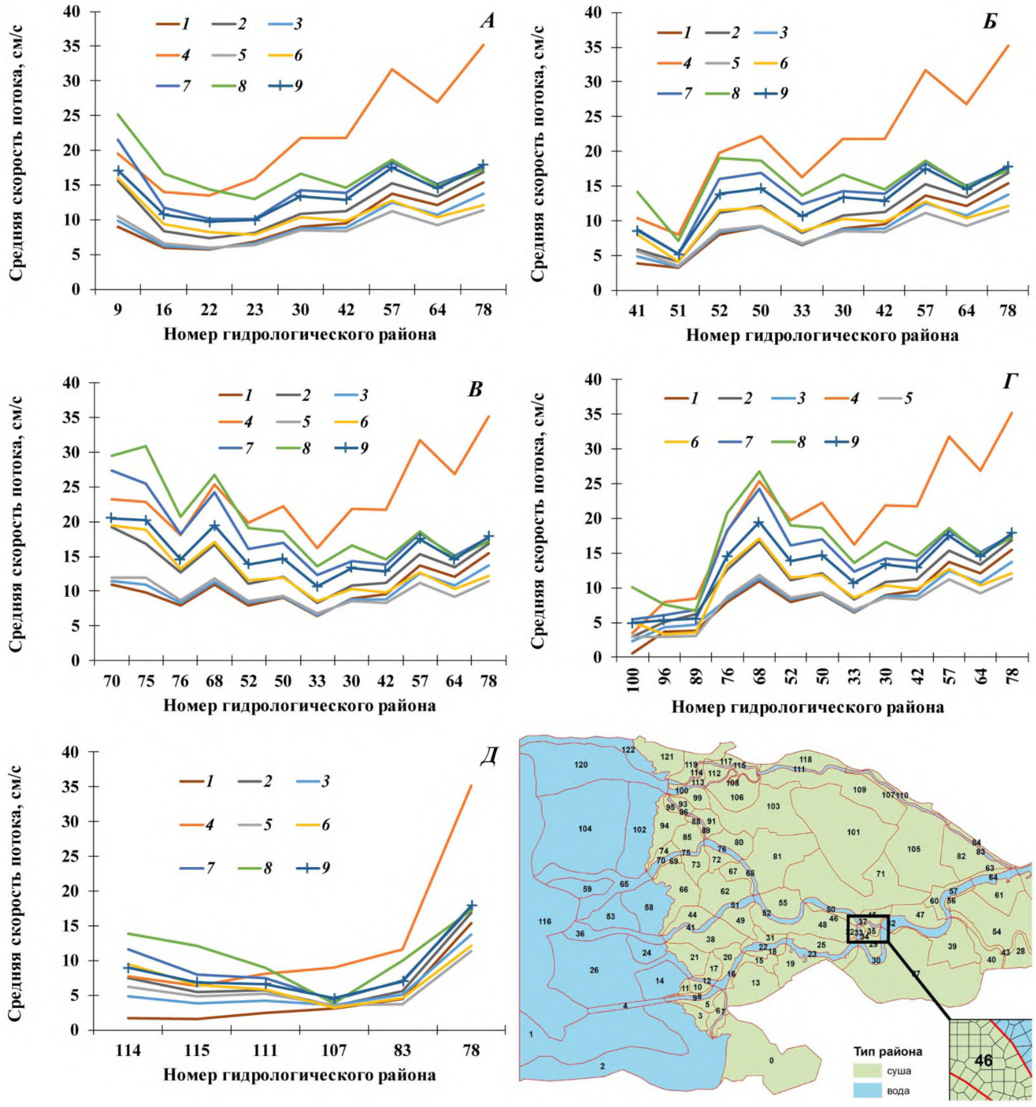

Рис. 3. Распределение средних скоростей потоков по рукавам дельты: «Дон – Старый Дон – АДСК» (А), «Дон – Большая Каланча – Мокрая Каланча» (Б), «Дон – Большая Каланча – Большая Кутерьма – Кутерьма» (В), «Дон – Большая Каланча – Большая Кутерьма – Средняя Кутерьма» (Г), «Дон – Мертвый Донец» (Д). 1 – сценарий БН-1, 2 – сценарий БН-2, 3 – сценарий Н-40, 4 – сценарий Н-16, 5 – сценарий Н-13, 6 – сценарий Н-2, 7 – сценарий Н-1, 8 – сценарий НЭ-3,7, 9 – среднее по всем сценариям нагонов.

Нагонные явления приводят к существенному (в 2–3 раза) увеличению средней скорости потоков в гидрологических районах практически до середины дельты со стороны моря. При этом амплитуда колебаний существенно выше (рисунки A2–A7). Гидрологические условия сценария Н-16 отличаются большими расходами воды (до 1550 м^3/с), поэтому здесь скорости потоков в вершине дельты существенно выше по сравнению с тем, когда расходы воды находятся на уровне 300–500 м^3/с.

Все это в совокупности влияет на процессы переноса взвешенных частиц.

3.3. Моделирование динамики взвешенного вещества

Для расчета динамики взвешенного вещества приняты следующие граничные условия.

Суммарная концентрация взвешенного вещества в речном стоке в ст. Раздорской принята равной 17 мг/л [*Клещенков и др.*, 2023] при следующем распределении по фракциям: пелит (44,5%), алеврит (51,3%), песок (4,2%). Это средний гранулометрический состав взвеси по данным наблюдений сети Росгидромета РФ в ст. Раздорской за период 2005–2020 гг.

Суммарная концентрация взвешенного вещества в период нагона в Таганрогском заливе принималась равной значению из табл. 1 при следующем распределении по фракциям: пелит (64,5%), алеврит (35,5%). Частиц песчаной фракции – менее 0,1%.

Структура донных отложений задавалась следующим образом. Для русловых районов предполагалось, что соотношение частиц такое: пелит (10%), алеврит (25%), песок (65%), а для авандельты – пелит (20%), алеврит (50%), песок (30%). Для пойменных районов был принят гранулометрический состав, характерный для луговых аллювиальных почв [*Исаев и др.*, 2022]: пелит (50,5%), алеврит (45,5%), песок (4%).

В качестве начальных значений для всех районов задавалась концентрация частиц соответствующего размера, определяемая транспортирующей способностью потока, рассчитанной по средней скорости, характерной для района в случае отсутствия нагона (сценарий БН-1).

Динамика взвешенного вещества при отсутствии нагона (сценарий БН-1). В данном вычислительном эксперименте рассматривалась ситуация, когда на границе расчетной области в Таганрогском заливе уровень моря не изменяется относительно его среднемноголетнего значения, осаждение взвешенного вещества происходит везде, а взмучивание – только в заливе и в русловых районах. В районах, расположенных на пойме дельты, взмучивание донных отложений не задается.

При выполнении расчетов проводились эксперименты с параметром α^0 для корректировки скорости взмучивания частиц соответствующего размера. Задача заключалась в том, чтобы «уравновесить» процессы осаждения и взмучивания для русловых районов. Подобранные значения α^0 для частиц пелитовой, алевритовой и песчаной размерности: 0,35; 3,0 и 5,0 соответственно. Уменьшение параметра α^0 от песчаной к пелитовой фракции может быть объяснено тем, что мелкие частицы слипаются и их труднее оторвать от дна.

В данных гидрологических условиях в конце расчетного периода устанавливается стационарное по пространству распределение концентрации взвешенных веществ, определяемое их поступлением с донской водой и процессами осаждения и взмучивания.

Для остальных сценариев значение параметра α^0 не изменялось.

Результаты вычислительных экспериментов представлены на рис. 4 как распределение концентрации взвешенных частиц вдоль основных русел дельты (по аналогии с рис. 3).

По мере продвижения воды от ст. Раздорской к вершине дельты концентрация взвешенного вещества увеличивается примерно до 20 мг/л (рис. 4). В дельте из-за снижения скоростей потоков их транспортирующая способность ослабевает, и общая концентрация взвешенного вещества уменьшается до 15-10 мг/л.

Похожая ситуация характерна и для второго сценария без явно выраженного нагона (сценарий БН-2), но в отдельных районах дельты, примыкающих к морскому краю, концентрация взвешенного вещества возрастает до 30 мг/л (рис. 4). Это связано

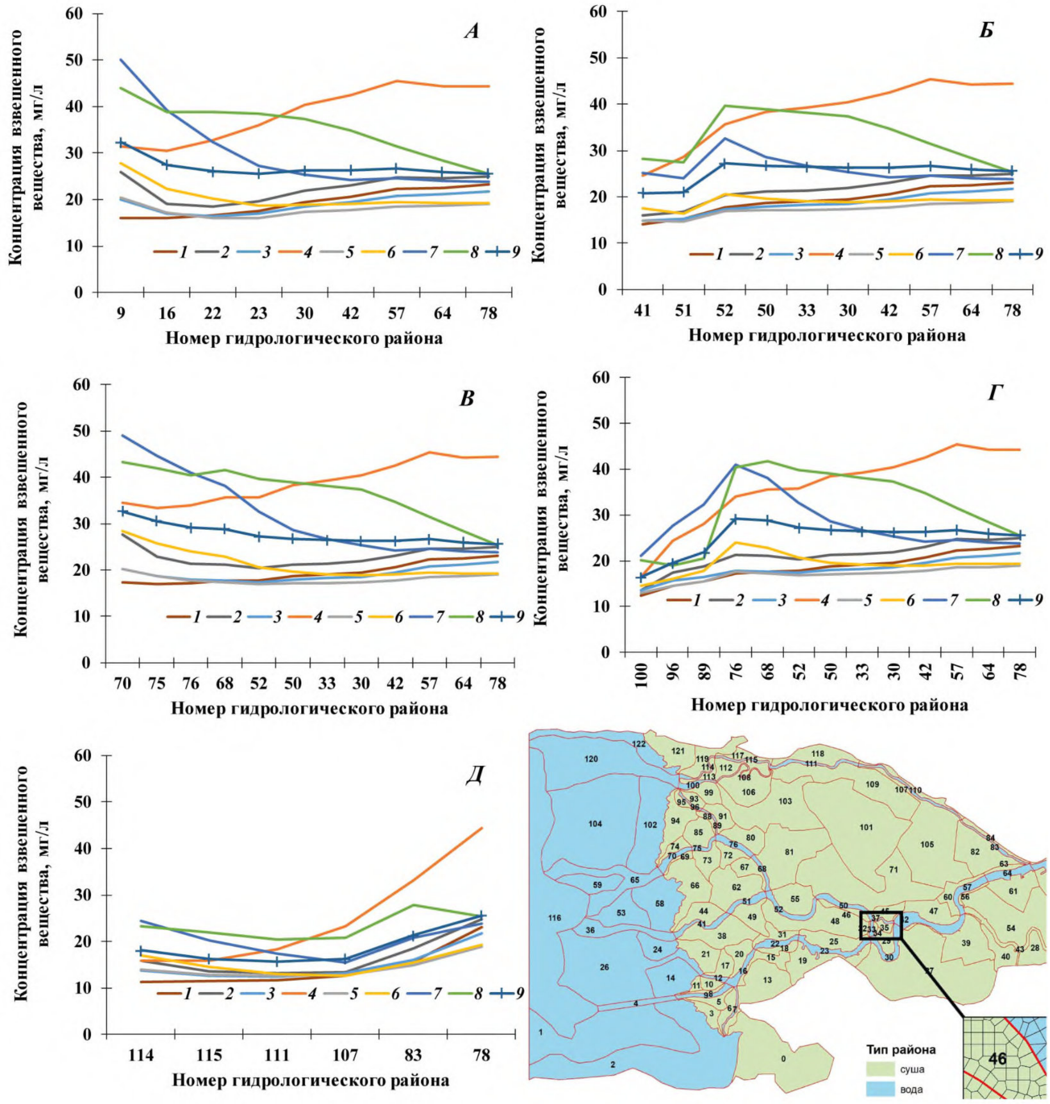

Рис. 4. Распределение средней концентрации взвешенного вещества по рукавам дельты: «Дон – Старый Дон – АДСК» (А), «Дон – Большая Каланча – Мокрая Каланча» (Б), «Дон – Большая Каланча – Большая Кутерьма – Кутерьма» (В), «Дон – Большая Каланча – Большая Кутерьма – Средняя Кутерьма» (Г), «Дон – Мертвый Донец» (Д). 1 – сценарий БН-1, 2 – по сценарий БН-2, 3 – сценарий Н-40, 4 – сценарий Н-16, 5 – сценарий Н-13, 6 – сценарий Н-2, 7 – сценарий Н-1, 8 – сценарий НЭ-3,7, 9 – среднее по всем сценариям нагонов.

с суточными колебательными движениями уровня воды и увеличением скоростей потоков.

По мере продвижения воды от вершины дельты к морскому краю существенно меняется гранулометрический состав взвешенного вещества (рис. 5А) – доля частиц пелитовой размерности увеличивается до 80%.

Динамика взвешенного вещества при нагонах. В данных расчетах для сравнения с гидрологическими условиями при отсутствии нагона концентрация взвешенного вещества в каждом районе усреднялась за весь период нагона.

В авандельте в условиях штормового нагона происходит волновое взмучивание донных отложений, и в дельту поступают водные потоки, насыщенные взвешенным материалом (табл. 1). Концентрация взвешенного вещества в воде существенно меня-

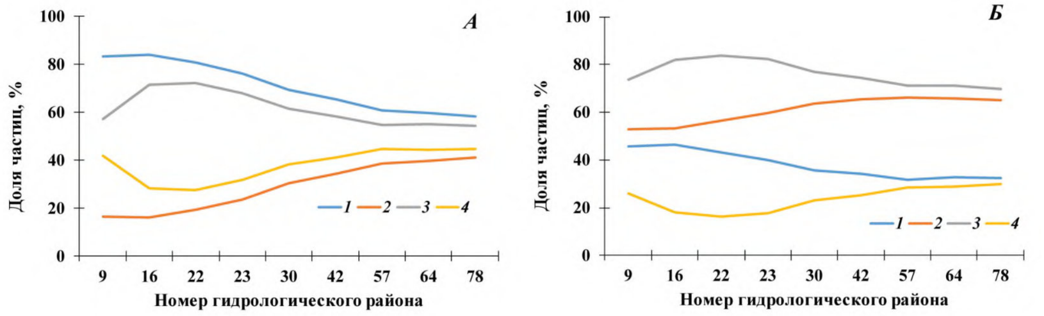

Рис. 5. Гранулометрический состав взвешенного вещества в основном русле «Дон – Старый Дон – АДСК»: А – сценарий БН-1 (1 – глина, 2 – ил) и сценарий БН-2 (3 – глина, 4— ил), Б – сценарий Н-16 (1 – глина, 2 – ил) и сценарий Н-1 (3 – глина, 4 – ил).

ется во времени из-за изменения средних скоростей потоков в широком диапазоне от практически нулевых значений до 40–50 см/с (рисунки A2–A7).

В период нагона (рис. 5Б) из-за процессов осаждения и взмучивания происходит как увеличение концентрации взвешенного вещества, так и изменение его гранулометрического состава (увеличение доли алевритовой фракции). Концентрация взвешенного вещества в пойменных районах дельты увеличивается, как только они затапливаются нагонными водами, при этом взвесь в основном представлена частицами пелитовой размерности, т.к. в этих районах отсутствует (в модели) взмучивание почвенных частиц, а алевритовая фракция осаждается на почву.

3.4. Осаждение взвешенного вещества в дельте

В сентябре 2021 г. во время нагона, который по гидрологическим условиям соответствует сценарию Н-40, были установлены седиментационные ловушки, конструктивно схожие с МСЛ-110 [*Лукашин и др.*, 2011], в приурезовой пойменной части рукавов Старый Дон, в гирле Свиное и в протоке острова Бирючий, кроме того, анализировались данные долговременных экспозиций русловых седиментационных ловушек в рукавах Старый Дон и Каланча (рис. 6В). После обработки взвеси, накопленной в седиментационных ловушках, получены оценки скоростей осаждения и сопоставлены с результатами расчета скоростей осаждения взвешенного материала для сценария Н-40 (рис. 6А, Б).

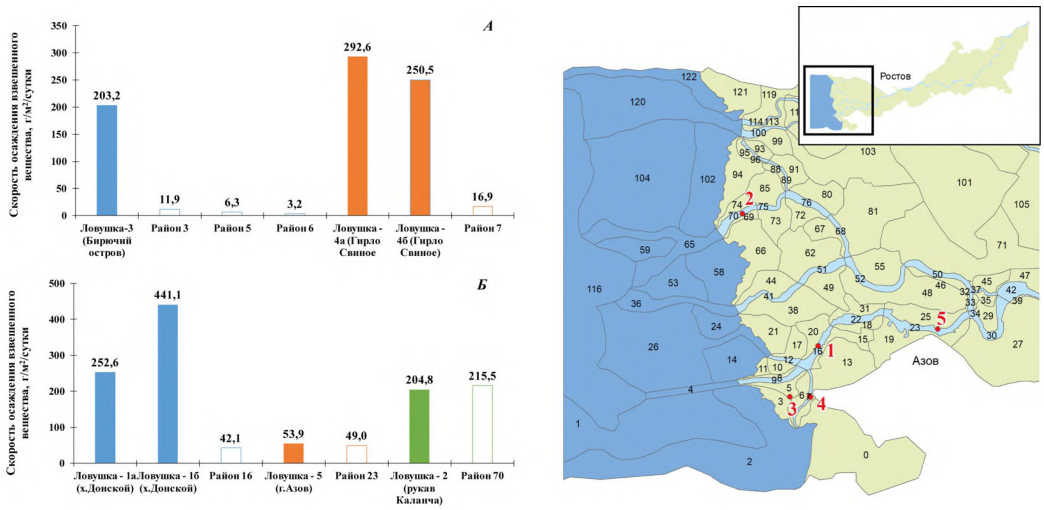

Рис. 6. Скорость осаждения взвешенного вещества в пойменных (А) и русловых (Б) районах дельты по результатам расчетов в сопоставлении с материалом, накопленным в седиментационных ловушках. В – места установки ловушек.

Можно отметить, что для русловых гидрологических районов суточные величины осаждения взвешенного вещества близки к модельным оценкам в большей степени, чем для пойменных районов. Для ловушек, установленных в районе причала в хуторе Донском (район 16), значительные отличия (в 5–10 раз) возможно связаны с усреднением модельных оценок в пределах всего района и особенностями расположения ловушек. Для пойменных районов дельты (ловушка 3, остров Бирючий и ловушки 4а и 4б, гирло Свиное) возможен недоучет в модели интенсивного взмучивания донных отложений, что потребует в дальнейшем корректировки параметров модели.

При выполнении вычислительных экспериментов рассчитывались значения разницы между взвешенным веществом, которое оседает на дно, и взвешенным веществом, которое переходит из донных отложений в воду в результате их взмучивания – результирующие величины баланса «оседание – взмучивание» в г/м^2/сут. Для сценария БН-1 они представлены на рис. 7 для основных рукавов дельты в зависимости от расстояния от ее вершины (графики с индексом «1»). Чтобы сравнить их с величинами, характерными для сценариев с нагонами, значения баланса «оседание – взмучивание» были усреднены по сценариям Н-40, Н-13, Н-2 и Н-1, а затем из них были вычтены значения баланса «оседание – взмучивание» для сценария БН-1 (показаны на рис. 7 с индексом «2»). Сценарий НЭ-3,7 не рассматривался, т.к. он является экстремальным. Сценарий Н-16 также не рассматривался, т.к. здесь нагон происходит при высоком расходе воды.

При отсутствии нагона баланс «оседание – взмучивание» положителен, и по всем руслам происходит накопление взвешенного материала. Вклад нагонов приводит к взмучиванию донных отложений на участках от вершины дельты примерно до 25 км (за исключением Мертвого Донца), затем наблюдается переключение: процессы накопления материала начинают превалировать над размывом, но потом возле морского края дельты взмучивание опять начинает доминировать. Это подтверждает вывод о том, что речная вода на этапе падения ее уровня начинает выносить накопленный в русловых районах осадочный материал за пределы морского края дельты, где скорости потоков резко падают и взвешенное вещество начинает накапливаться на дне.

Количественные оценки взвешенного вещества, оседающего в устьевой области Дона (в пойменных районах, в русловых районах и районах авандельты) при нагонах разной обеспеченности, представлены в табл. A1.

Данная версия модели, предусматривающая процессы осаждения взвешенного вещества и взмучивания донных отложений, демонстрирует следующий механизм, определяющий разную динамику взвешенных наносов в различных районах устьевой области. Скорость потока при спаде уровня воды после прохождения пика нагона в русловых районах становится существенно выше, чем при подъеме ее уровня. В результате взвешенное вещество, поступающее в дельту при подъеме уровня воды и оседающее в районах с околонулевыми скоростями потоков, затем опять выносится за пределы морского края дельты.

При нагонах с небольшими расходами воды (300–600 м^3/с) в русловых ячейках взвешенное вещество накапливается, но с ростом расходов воды до 1400–1550 м^3/с баланс смещается в сторону взмучивания донных отложений (табл. A1). Тот же эффект характерен и для экстремального нагона 3,7 м при средних расходах воды (450 м^3/с).

Ранее нами в работе [*Лихтанская и др.*, 2023] были представлены оценки накопления взвешенных веществ в дельте Дона, которые опирались на расчеты, выполненные в работе [*Шевердяев и Клещенков*, 2020]. Здесь, с применением нового подхода к моделированию переноса и осаждения взвешенных веществ устьевой области Дона эти оценки уточнены (табл. 2).

Наибольшее накопление взвешенного вещества отмечается для районов, расположенных в авандельте. Фактически взвешенные вещества, поднятые волнением со дна в период развития нагона, возвращаются обратно, за исключение той части, которая оседает в пойменных районах и в отдельных рукавах дельты.

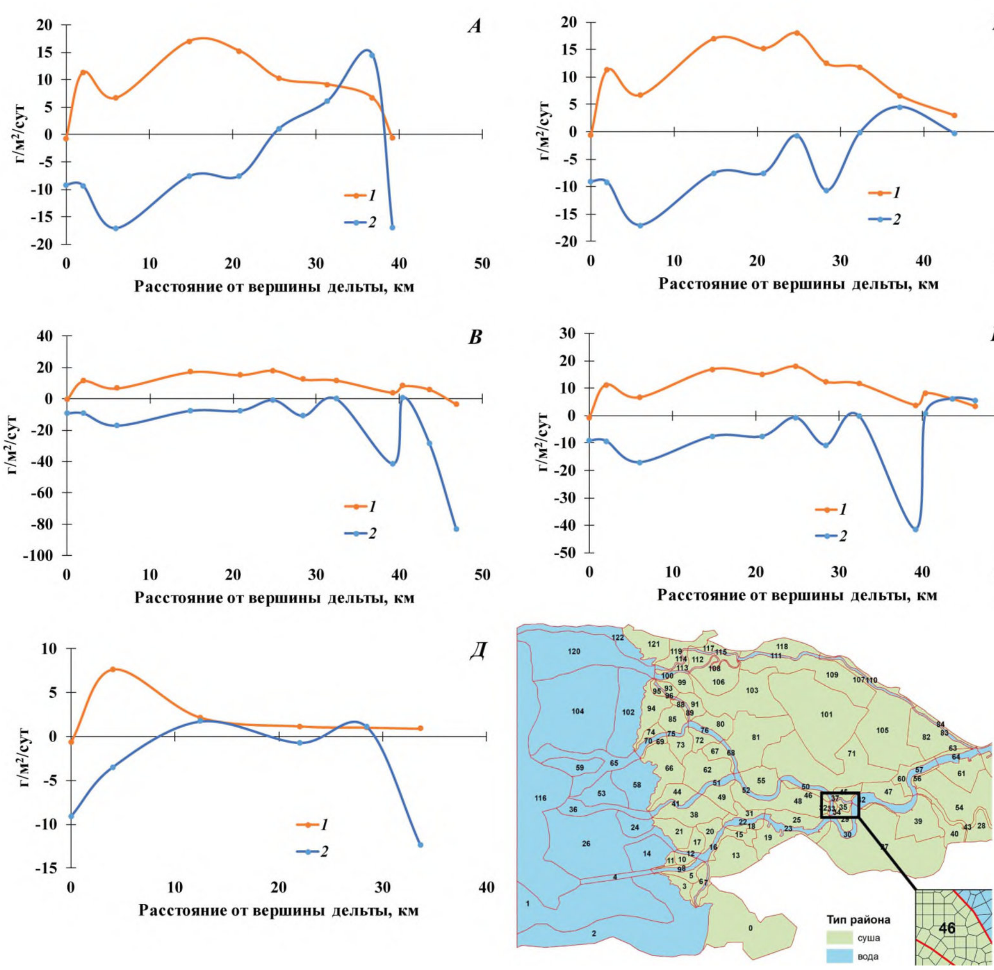

Рис. 7. Потоки взвешенного материала при обмене с дном по рукавам дельты: «Дон – Старый Дон – АДСК» (А), «Дон – Большая Каланча – Мокрая Каланча» (Б), «Дон – Большая Каланча – Большая Кутерьма – Кутерьма» (В), «Дон – Большая Каланча – Большая Кутерьма – Средняя Кутерьма» (Г), «Дон – Мертвый Донец» (Д). 1 – баланс «оседание – взмучивание» для сценария БН-1, 2 – разница в значениях баланса «оседание – взмучивание» между сценариями с нагонами и сценарием БН-1.

Таблица 2. Твердый сток р. Дон (ст. Раздорская) и осаждение взвешенных веществ в дельте Дона при штормовых нагонах

Год	Число дней с нагоном	По [*Лихтанская и др.*, 2023]		Осаждение взвешенных веществ в дельте Дона, тыс. т
		Сток взвешенных веществ, тыс. т	Осаждение взвешенных веществ в дельте Дона, тыс. т	
2015	37	65,2	129,6	15,04
2016	51	72,9	176,5	22,72
2017	36	356,8	143,5	18,54
2018	12	331,6	52,0	7,46
2019	35	496,6	99,5	10,61
2020	19	318,3	77,1	10,13

Число дней с нагонами в 2015–2020 гг. изменялось от 12 до 51 дня. В остальное время взвешенные вещества, переносимые речной водой, могли накапливаться в русловых районах дельты (в условиях маловодья при расходах воды 300–600 м^3/с вода на пойму не выходит). Но периодические нагоны могут способствовать в дальнейшем выносу этого материала за пределы морского края дельты.

4. Выводы

1. В отсутствие нагонных явлений при расходах воды ниже среднемноголетних за современный маловодный период 2007–2020 гг. взвешенные вещества практически транзитом проходят через дельту, незначительно осаждаясь в рукавах с небольшими скоростями потоков, но в основном осаждаются в авандельте за пределами морского края дельты.

2. При нагоне любой обеспеченности взвешенные вещества, накопленные в авандельте, под воздействием волнения насыщают воду и на этапе подъема ее уровня поступают в дельту, частично осаждаясь в рукавах и в залитых водой пойменных районах. При снижении уровня нагона вещества, осевшие в пойменных районах дельты, в основном там и остаются, а вещества, накопленные в русловых районах, выносятся за морской край дельты. При этом из рукавов дельты могут быть вынесены и вещества, накопленные там между нагонами.

3. Для условий маловодья при наблюдаемой в период 2015–2020 гг. частоте нагонных явлений и при отсутствии паводков устьевая область Дона задерживает в среднем 20% взвешенных веществ, поступающих со стоком р. Дон.

Благодарности. Работа выполнена в рамках ГЗ ЮНЦ РАН: № госрегистрации 122013100131-9, № госрегистрации 122011900153-9, № госрегистрации 122103100027-3 и научного проекта РНФ №22-27-00818 «Влияние длительного маловодья и изменений климата (на рубеже XX–XXI веков) на динамику взвешенного вещества в устьевой области Дона».

Приложение А

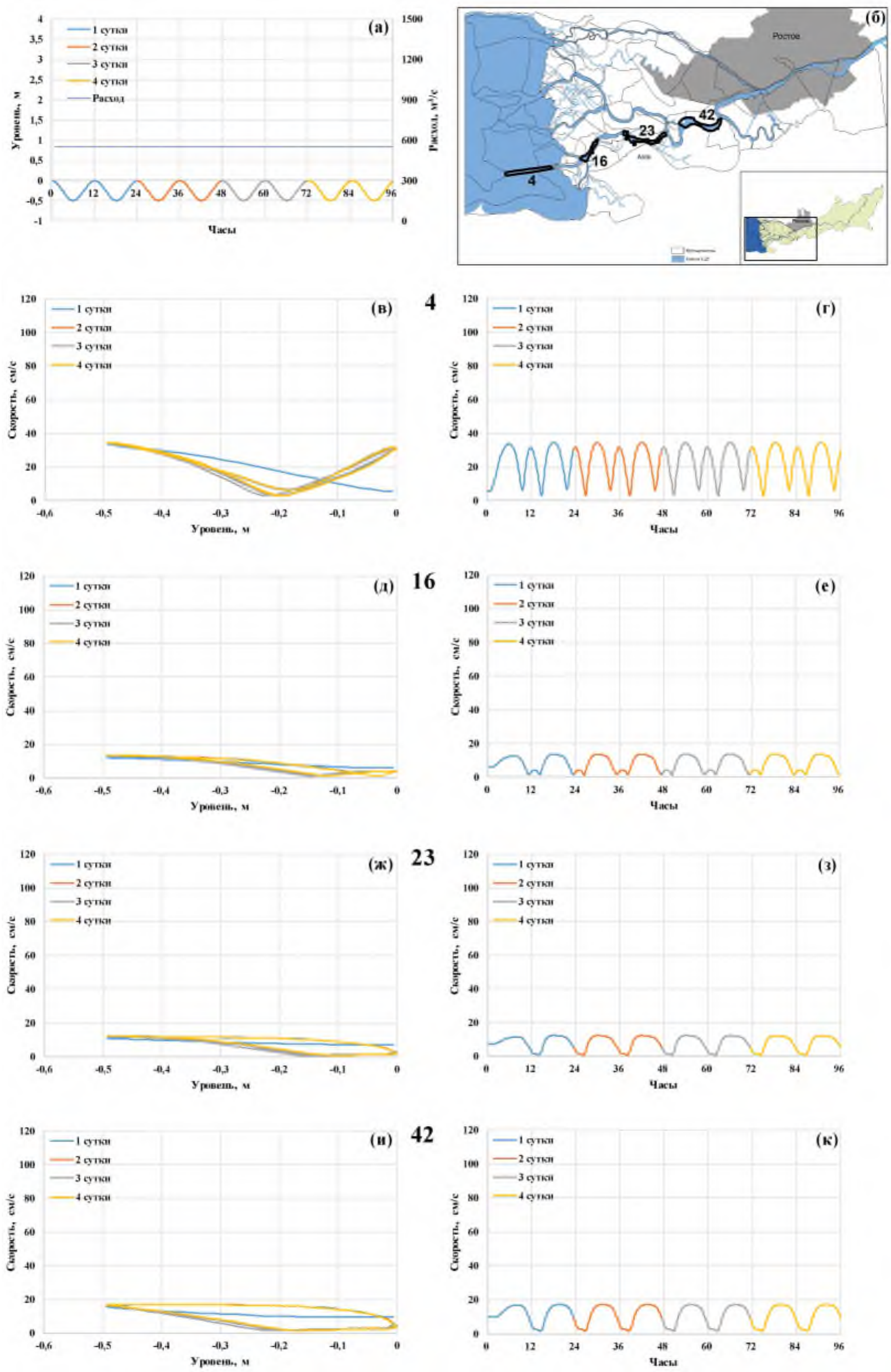

Рис. А1. Сценарий «без нагона» – БН-2. Колебание уровня воды на морском крае дельты с амплитудой 0,5 м и расход воды в станице Раздорской (а), расчётная зона затопления (б), связь средней скорости потоков и уровня воды в 4 (в), 16 (д), 23 (ж) и 42 (ж) гидрологических районах. Динамика средней скорости потоков в 4 (г), 16 (е), 23 (з) и 42 (л) гидрологических районах.

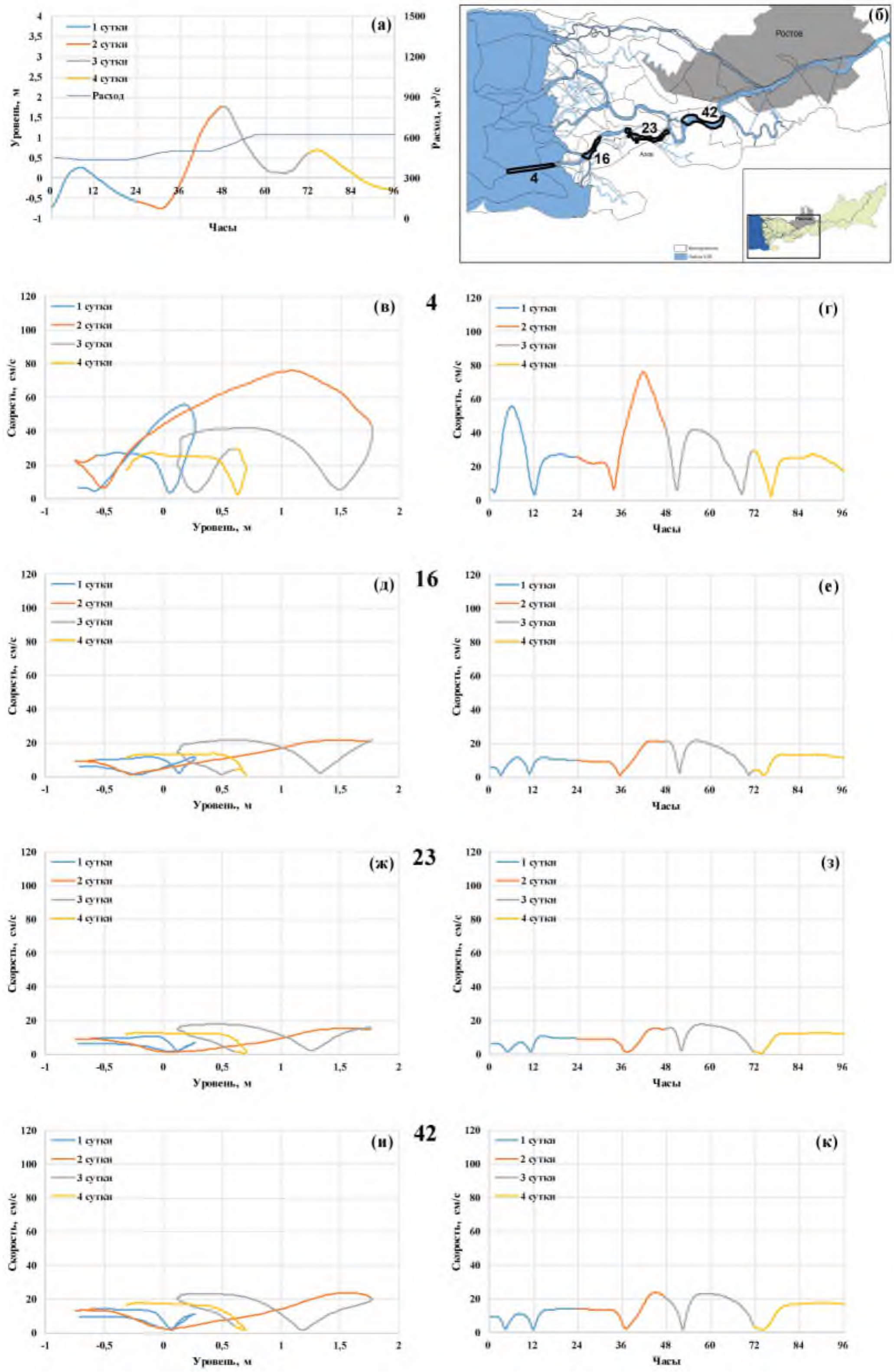

Рис. А2. Сценарий Н-1. Динамика уровня воды по данным уровнемера в х. Донском и расход воды в ст. Раздорской (а), расчётная зона затопления (б), связь средней скорости потоков и уровня воды в 4 (в), 16 (д), 23 (ж) и 42 (ж) гидрологических районах. Динамика средней скорости потоков в 4 (г), 16 (е), 23 (з) и 42 (л) гидрологических районах.

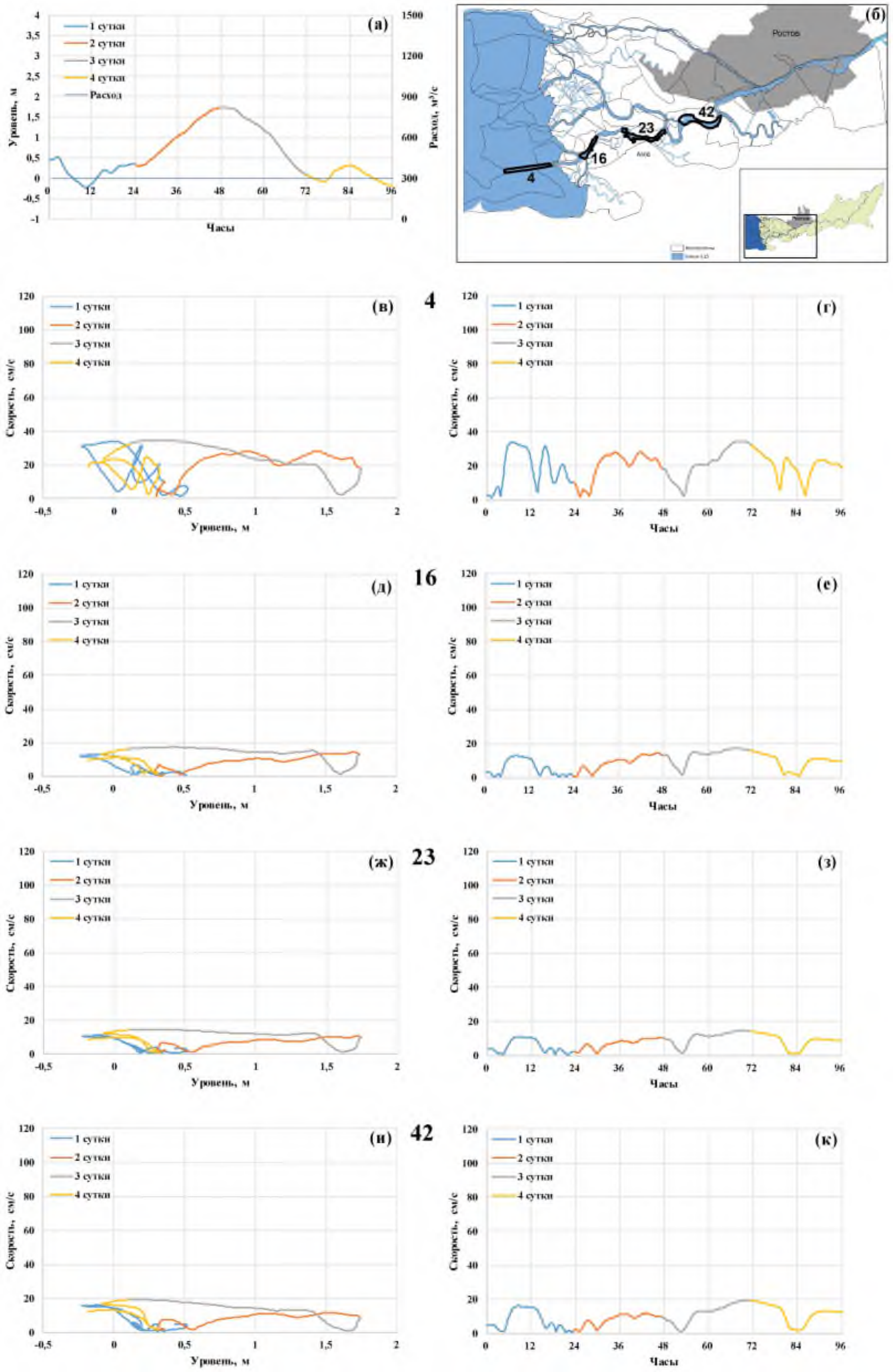

Рис. А3. Сценарий Н-2. Динамика уровня воды по данным уровнемера в х. Донском и расход воды в станице Раздорской (а), расчётная зона затопления (б), связь средней скорости потоков и уровня воды в 4 (в), 16 (д), 23 (ж) и 42 (ж) гидрологических районах. Динамика средней скорости потоков в 4 (г), 16 (е), 23 (з) и 42 (л) гидрологических районах.

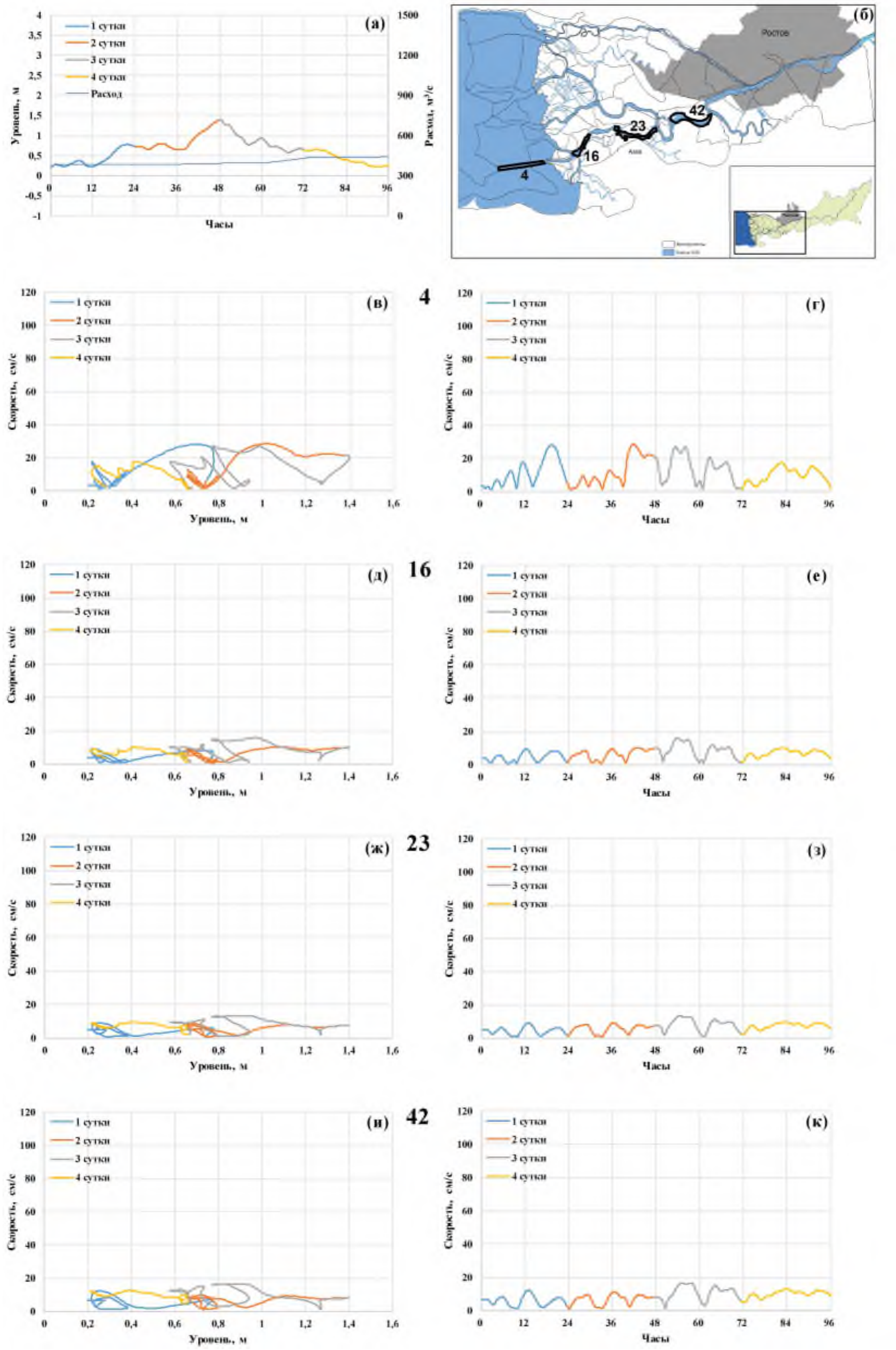

Рис. A4. Сценарий Н-13. Динамика уровня воды по данным уровнемера в х. Донском и расход воды в станице Раздорской (а), расчётная зона затопления (б), связь средней скорости потоков и уровня воды в 4 (в), 16 (д), 23 (ж) и 42 (ж) гидрологических районах. Динамика средней скорости потоков в 4 (г), 16 (е), 23 (з) и 42 (л) гидрологических районах.

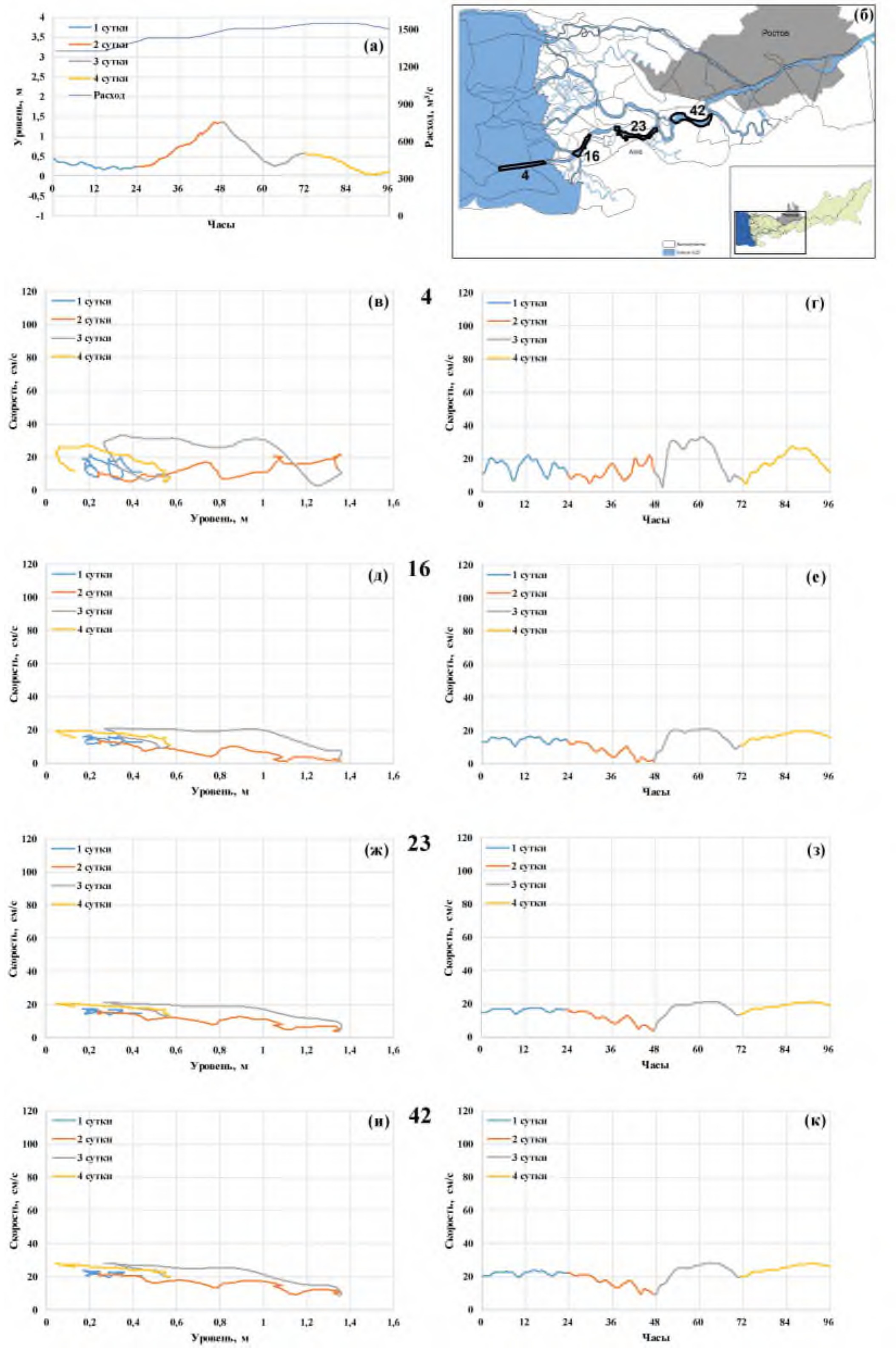

Рис. А5. Сценарий Н-16. Динамика уровня воды по данным уровнемера в х. Донском и расход воды в станице Раздорской (а), расчётная зона затопления (б), связь средней скорости потоков и уровня воды в 4 (в), 16 (д), 23 (ж) и 42 (ж) гидрологических районах. Динамика средней скорости потоков в 4 (г), 16 (е), 23 (з) и 42 (л) гидрологических районах.

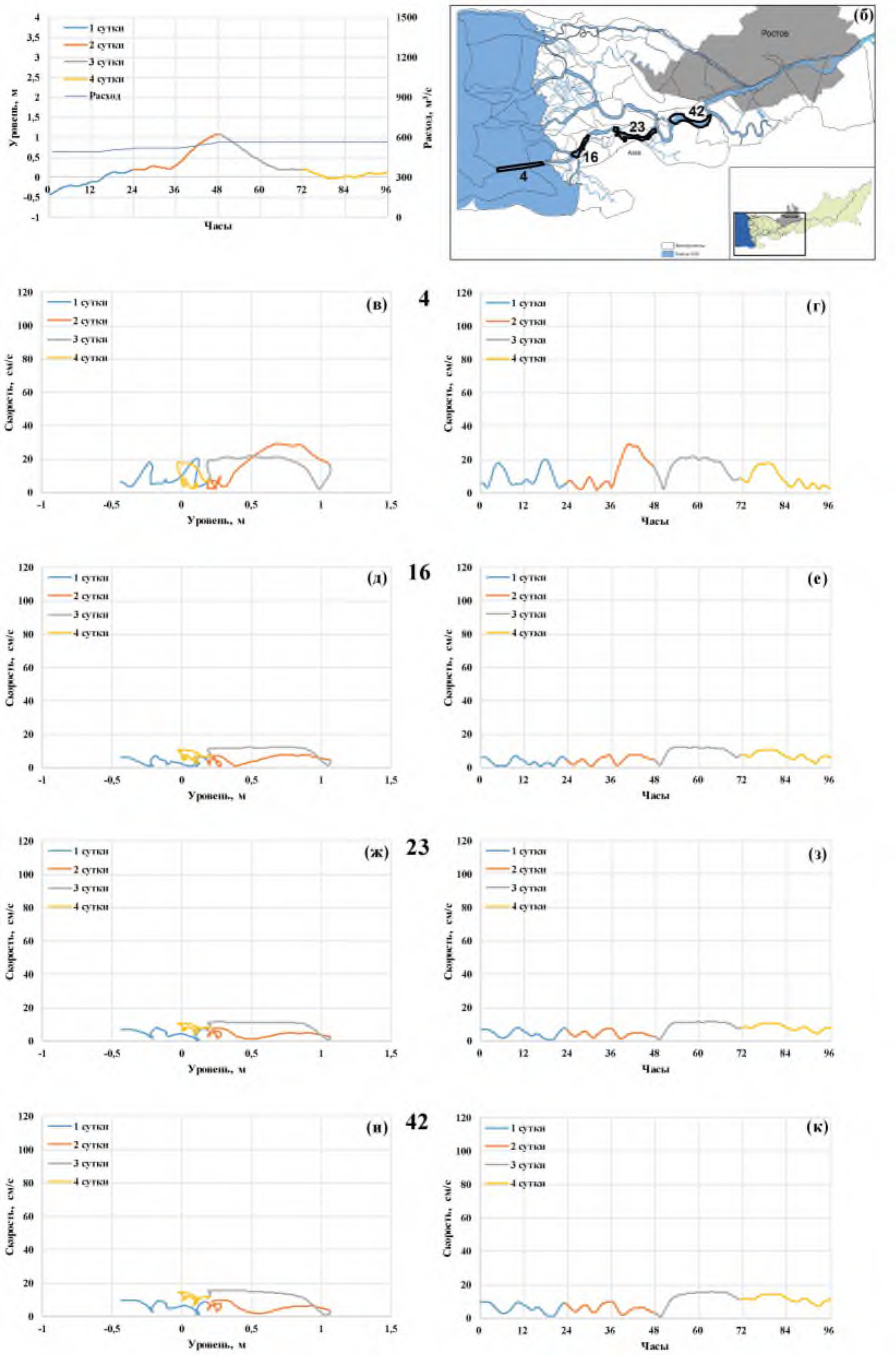

Рис. А6. Сценарий Н-40. Динамика уровня воды по данным уровнемера в х. Донском и расход воды в станице Раздорской (а), расчётная зона затопления (б), связь средней скорости потоков и уровня воды в 4 (в), 16 (д), 23 (ж) и 42 (ж) гидрологических районах. Динамика средней скорости потоков в 4 (г), 16 (е), 23 (з) и 42 (л) гидрологических районах.

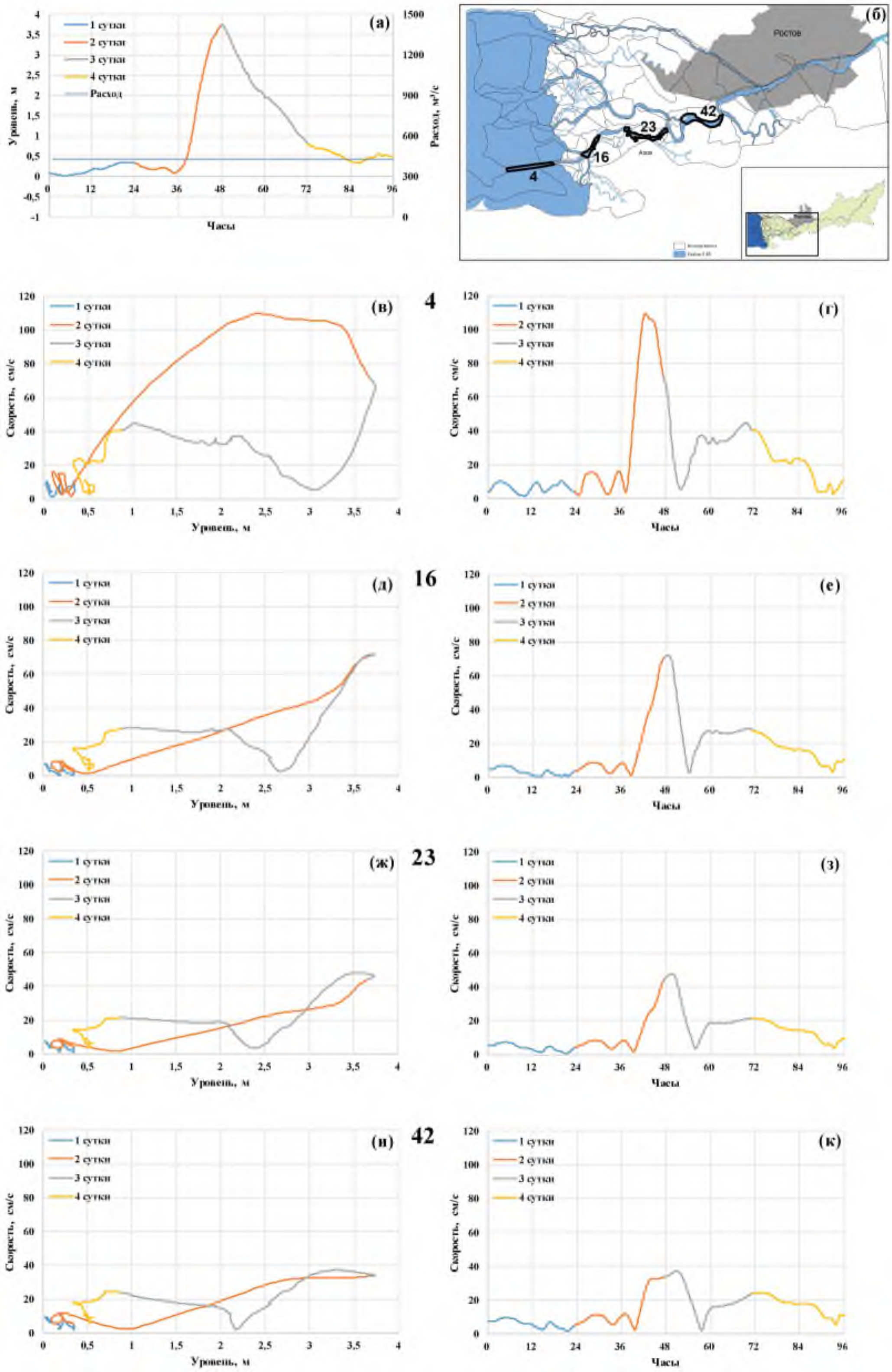

Рис. А7. Сценарий НЭ-3,7. Динамика уровня воды по данным уровнемера в х. Донском и расход воды в станице Раздорской (а), расчётная зона затопления (б), связь средней скорости потоков и уровня воды в 4 (в), 16 (д), 23 (ж) и 42 (ж) гидрологических районах. Динамика средней скорости потоков в 4 (г), 16 (е), 23 (з) и 42 (л) гидрологических районах.

Таблица A1. Динамика взвешенного вещества в устьевой области Дона за период нагона, тыс. т

Статья (приход, расход) расхода воды	Без нагона, колебание уровня воды от −50 см до 0 см	Параметры нагонов					
Номер сценария	БН-2	Н-40	Н-16	Н-13	Н-2	Н-1	НЭ-3,7
Максимальное изменение уровня воды при нагоне, см	50	106	136	140	175	177	370
Средний расход воды, м^3/с	550	525	1462	407	300	507	541
Изменения в осаждении взвешенного вещества, тыс. т							
Осело всего, в том числе:	1,23	0,25	3,37	0,32	1,00	1,40	3,79
В пойменных районах дельты	0,00	0,02	0,02	0,05	0,19	0,07	1,77
В русловых районах дельты	0,11	0,12	0,02	0,24	0,60	1,82	2,93
В районах авандельты	1,12	0,11	3,33	0,03	0,21	−0,49	−0,91

Список литературы

Барышников Н. Б. *и* Попов И. В. Динамика русловых процессов. — Ленинград : Гидрометеоиздат, 1988. — 455 с. — EDN: YOETUN.

Бердников С. В., Дашкевич Л. В. *и* Кулыгин В. В. Новое состояние гидрологического режима Азовского моря в XXI веке // Доклады Российской академии наук. Науки о Земле. — 2022. — Т. 503, № 1. — С. 65—70. — DOI: 10.31857/S2686739722030057.

Бердников С. В., Шевердяев И. В., Клещенков А. В. *и др.* Совместное применение гидрологической модели HEC RAS и мультикомпартментальной балансовой модели для описания переноса и трансформации взвешенных веществ в речной дельте: случай устьевой области р. Дон // Elpub.Preprints. — 2023. — DOI: 10.24108/preprints-3112769.

Ганичева Л. З. Закономерности седиментогенеза в Азовском море (взвеси и условия их образования) : дис. . . . канд. / Ганичева Л. З. — Ростов-на-Дону, 1985.

Герасюк В. С. *и* Бердников С. В. Экспериментальная оценка скорости осаждения взвешенного вещества вод в устье Дона и Таганрогском заливе // Океанология. — 2021. — Т. 61, № 5. — С. 780—790. — DOI: 10.31857/S0030157421040055.

Исаев А. В., Демаков Ю. П. *и* Шарафутдинов Р. Н. Закономерности изменения гранулометрического состава аллювиальных почв в процессе развития пойм рек // Вестник Поволжского государственного технологического университета. Серия: Лес. Экология. Природопользование. — 2022. — Т. 2, № 54. — С. 80—93. — DOI: 10.25686/2306-2827.2022.2.80.

Клещенков А. В., Герасюк В. С., Кулыгин В. В. *и др.* Взвешенное вещество вод от Цимлянского водохранилища до Таганрогского залива в период длительного маловодья 2006-2020 гг. // Наука Юга России. — 2023. — № 1. — С. 29—39. — DOI: 10.7868/25000640230104.

Клещенков А. В. *и* Шевердяев И. В. Численное исследование условий осаждения взвеси в дельте Дона при нагонах // Пятые Виноградовские чтения. Гидрология в эпоху перемен: Сборник докладов международной научной конференции памяти выдающегося русского ученого Юрия Борисовича Виноградова, Санкт-Петербург, 05-14 октября 2023 года. — СПб : ВВМ, 2023. — С. 257—262. — EDN: JIBVDI.

Лихтанская Н. В., Бердников С. В. *и* Клещенков А. В. Твердый сток реки Дон и поступление взвеси в дельту при нагонах: статистическое моделирование и сопоставление в период маловодья // Russian Journal of Earth Sciences. — 2023. — Т. 23, № 4. — С. 1—15. — DOI: 10.2205/2023es000856.

Лукашин В. Н., Клювиткин А. А., Лисицын А. П. *и др.* Малая седиментационная ловушка МСЛ-110 // Океанология. — 2011. — Т. 51, № 4. — С. 746—750. — EDN: NXXEWJ.

Матишов Г. Г., Московец А. Ю., Инжебейкин Ю. И. *и др.* Этапы сооружения плотин, пересыпей, каналов и трансформация речного стока в авандельте Дона (XVIII-XXI века) // Наука Юга России. — 2019. — № 4. — С. 46—54. — DOI: 10.7868/S25001640190406.

Михайлов В. Н. Устья рек России и сопредельных стран: прошлое, настоящее и будущее. — Москва : ГЕОС, 1997. — 413 с.

Шевердяев И. В., Бердников С. В. *и* Клещенков А. В. Применение программного комплекса HEC-RAS для моделирования гидрологического режима дельты Дона // Экология. Экономика. Информатика. Серия: Системный анализ и моделирование экономических и экологических систем. — 2017. — Т. 1, № 2. — С. 113—122. — EDN: ZNARIL.

Шевердяев И. В. *и* Клещенков А. В. Выявление вклада нагонных явлений в поступление тяжелых металлов в дельту Дона // Морской гидрофизический журнал. — 2020. — Т. 36, № 5. — С. 582—594. — DOI: 10.22449/0233-7584-2020-5-582-594.

Berdnikov S. V., Sorokina V. V., Kleshchenkov A. V., *et al.* Marine indicators of climate change in the Azov Sea ecosystem // Journal of Sea Research. — 2023. — Vol. 193. — P. 102373. — DOI: 10.1016/j.seares.2023.102373.

Day J. W., Agboola J., Chen Zh., *et al.* Approaches to defining deltaic sustainability in the 21st century // Estuarine, Coastal and Shelf Science. — 2016. — Vol. 183. — P. 275–291. — DOI: 10.1016/j.ecss.2016.06.018.

Day J. W. *and* Rybczyk J. M. Global Change Impacts on the Future of Coastal Systems: Perverse Interactions Among Climate Change, Ecosystem Degradation, Energy Scarcity, and Population // Coasts and Estuaries. — Elsevier, 2019. — P. 621–639. — DOI: 10.1016/B978-0-12-814003-1.00036-8.

Dieng H. B., Cazenave A., Meyssignac B., *et al.* New estimate of the current rate of sea level rise from a sea level budget approach // Geophysical Research Letters. — 2017. — Vol. 44, no. 8. — P. 3744–3751. — DOI: 10.1002/2017GL073308.

Dunn F. E., Darby S. E., Nicholls R. J., *et al.* Projections of declining fluvial sediment delivery to major deltas worldwide in response to climate change and anthropogenic stress // Environmental Research Letters. — 2019. — Vol. 14, no. 8. — P. 084034. — DOI: 10.1088/1748-9326/ab304e.

Giosan L., Syvitski J., Constantinescu S., *et al.* Climate change: Protect the world's deltas // Nature. — 2014. — Vol. 516, no. 7529. — P. 31–33. — DOI: 10.1038/516031a.

Hicks F. E. *and* Peacock T. Suitability of HEC-RAS for Flood Forecasting // Canadian Water Resources Journal. — 2005. — Vol. 30, no. 2. — P. 159–174. — DOI: 10.4296/cwrj3002159.

Kleinschmidt Associates. The Place for HEC-RAS Modelers. — 2020. — URL: https://www.kleinschmidtgroup.com/raspost/hec-ras-6-0-beta-is-now-available/ (visited on 11/17/2023).

Pandey S., Rao A. D. *and* Haldar R. Modeling of Coastal Inundation in Response to a Tropical Cyclone Using a Coupled Hydraulic HEC-RAS and ADCIRC Model // Journal of Geophysical Research: Oceans. — 2021. — Vol. 126, no. 7. — DOI: 10.1029/2020JC016810.

Syvitski J. P. M. *and* Milliman J. D. Geology, Geography, and Humans Battle for Dominance over the Delivery of Fluvial Sediment to the Coastal Ocean // The Journal of Geology. — 2007. — Vol. 115, no. 1. — P. 1–19. — DOI: 10.1086/509246.

Tessler Z. D., Vörösmarty C. J., Grossberg M., *et al.* Profiling risk and sustainability in coastal deltas of the world // Science. — 2015. — Vol. 349, no. 6248. — P. 638–643. — DOI: 10.1126/science.aab3574.

Venevsky S., Berdnikov S., Day J. W., *et al.* Don River Delta Hydrological and Geomorphological Transformation Under Anthropogenic and Natural Factors: Century and Decadal Perspectives // Elsevier BV. Preprint. — 2023. — DOI: 10.2139/ssrn.4474057.

Venevsky S., Berdnikov S., Sorokina V., *et al.* Coastal Deltas of Big Rivers as Synergetic Transformation Elements of the Earth System-(An Example of the Don River Delta) // New Prospects in Environmental Geosciences and Hydrogeosciences. — Springer International Publishing, 2022. — P. 79–81. — DOI: 10.1007/978-3-030-72543-3_18.

Wang X., Guo Y. *and* Ren J. The Coupling Effect of Flood Discharge and Storm Surge on Extreme Flood Stages: A Case Study in the Pearl River Delta, South China // International Journal of Disaster Risk Science. — 2021. — Vol. 12, no. 4. — P. 1–15. — DOI: 10.1007/s13753-021-00355-5.

Wolters M. L. *and* Kuenzer C. Vulnerability assessments of coastal river deltas - categorization and review // Journal of Coastal Conservation. — 2015. — Vol. 19, no. 3. — P. 345–368. — DOI: 10.1007/s11852-015-0396-6.

Zhang W., Jia Q. *and* Chen X. Numerical Simulation of Flow and Suspended Sediment Transport in the Distributary Channel Networks // Journal of Applied Mathematics. — 2014. — Vol. 2014. — P. 1–9. — DOI: 10.1155/2014/948731.

Russian Journal *of* Earth Sciences

Modeling the Transport and Deposition of Suspended Solids Under Conditions of Low Water and Surge Phenomena in the Don River Estuary Area

S. V. Berdnikov[1], I. V. Sheverdyaev[1], A. V. Kleshchenkov[1], V. V. Kulygin[1], and N. V. Likhtanskaya[*,1]

[1]Southern Scientific Center RAS, Rostov-on-Don, Russia
****Correspondence to:** Nataliya V. Likhtanskaya, natalikht@gmail.com .

An approach is proposed for the joint use of the model implemented in the HEC-RAS software and a balance model to describe the transport and transformation of suspended solids in a river delta. In the river estuary region, hydrological areas are distinguished: channel areas, floodplain areas, flooded during high floods and storm surges from the sea, and the delta front areas. For the hydrological areas, a dynamic model of the balance of water and substances transported by water flow is built. Parameterization of the suspended solids sedimentation processes and their resuspension is introduced depending on the speed of water movement and particle size. Three gradations of suspended solids in size are considered: pelitic fraction (clay), alevrit fraction (silt) and fine sand. The emphasis is on assessing the impact of marine storm surges on the transport of suspended solids into the river delta and their deposition. To describe water flows between areas, movement speeds, level dynamics and floodplain flooding processes, a detailed model based on the HEC-RAS software adapted to the conditions of the Don River estuary area is used. Calculations of the transport and accumulation of suspended solids in the Don River estuary area were carried out for two variants of hydrological conditions – with the water surge from the sea and without it. The spatiotemporal variability of the concentration and granulometric composition of suspended sediment depending on hydrological conditions is considered. It is shown that in the absence of surge phenomena and low water flow rates, suspended solids are mainly deposited in the avandelta outside the sea edge of the delta, and during the surge period they saturate the water and, at the stage of rising its level, enter the delta, partially settling in the branches and in the floodplain areas. At the same time, at the stage of the water level decline, they are carried out of the channel segments beyond the sea edge of the delta, and mostly remain in the floodplain areas. For low-water conditions with the observed frequency of surge events and in the absence of floods, the Don estuary area retains on average 20% of suspended solids entering with the Don River runoff.

Keywords: balance model, suspended matter, modeling system HEC-RAS, storm surge, the Don River delta.

Recieved: 12 March 2024
Accepted: 30 July 2024
Published: 25 December 2024

Citation: Berdnikov, S. V., I. V. Sheverdyaev, A. V. Kleshchenkov, V. V. Kulygin, and N. V. Likhtanskaya (2024), Modeling the Transport and Deposition of Suspended Solids Under Conditions of Low Water and Surge Phenomena in the Don River Estuary Area, *Russian Journal of Earth Sciences*, 24, ES4013, https://doi.org/10.2205/2024ES000926, EDN: NYRZMC

References

Baryshnikov N. B. *and* Popov I. V. Dynamics of channel processes. — Leningrad : Gidrometeoizdat, 1988. — P. 455. — EDN: YOETUN.

Berdnikov S. V., Dashkevich L. V. *and* Kulygin V. V. A New State in the Hydrological Regime of the Sea of Azov in the 21th Century // Doklady Earth Sciences. — 2022. — Vol. 503, no. 1. — P. 123–128. — DOI: 10.1134/S1028334X22030059.

Berdnikov S. V., Sheverdyaev I. V., Kleshchenkov A. V., *et al.* Combined Application of the Hydrological Model HEC RAS and a Multicompartmental Balance Model to Describe the Transport and Transformation of Suspended Solids in a River Delta: A Case Study of the Don River Estuary Area // Elpub.Preprints. — 2023a. — DOI: 10.24108/preprints-3112769.

Berdnikov S. V., Sorokina V. V., Kleshchenkov A. V., *et al.* Marine indicators of climate change in the Azov Sea ecosystem // Journal of Sea Research. — 2023b. — Vol. 193. — P. 102373. — DOI: 10.1016/j.seares.2023.102373.

Day J. W., Agboola J., Chen Zh., *et al.* Approaches to defining deltaic sustainability in the 21st century // Estuarine, Coastal and Shelf Science. — 2016. — Vol. 183. — P. 275–291. — DOI: 10.1016/j.ecss.2016.06.018.

Day J. W. *and* Rybczyk J. M. Global Change Impacts on the Future of Coastal Systems: Perverse Interactions Among Climate Change, Ecosystem Degradation, Energy Scarcity, and Population // Coasts and Estuaries. — Elsevier, 2019. — P. 621–639. — DOI: 10.1016/B978-0-12-814003-1.00036-8.

Dieng H. B., Cazenave A., Meyssignac B., *et al.* New estimate of the current rate of sea level rise from a sea level budget approach // Geophysical Research Letters. — 2017. — Vol. 44, no. 8. — P. 3744–3751. — DOI: 10.1002/2017GL073308.

Dunn F. E., Darby S. E., Nicholls R. J., *et al.* Projections of declining fluvial sediment delivery to major deltas worldwide in response to climate change and anthropogenic stress // Environmental Research Letters. — 2019. — Vol. 14, no. 8. — P. 084034. — DOI: 10.1088/1748-9326/ab304e.

Ganicheva L. Z. Patterns of Sedimentogenesis in the Sea of Azov (Suspensions and Conditions of their Formation) : PhD thesis / Ganicheva L. Z. — Rostov-on-Don, 1985.

Gerasyuk V. S. *and* Berdnikov S. V. Experimental Estimation of the Deposition Rate of Water Suspended Particulate Matter in the Mouth of the Don River and in Taganrog Bay // Oceanology. — 2021. — Vol. 61, no. 5. — P. 687–696. — DOI: 10.1134/S0001437021040056.

Giosan L., Syvitski J., Constantinescu S., *et al.* Climate change: Protect the world's deltas // Nature. — 2014. — Vol. 516, no. 7529. — P. 31–33. — DOI: 10.1038/516031a.

Hicks F. E. *and* Peacock T. Suitability of HEC-RAS for Flood Forecasting // Canadian Water Resources Journal. — 2005. — Vol. 30, no. 2. — P. 159–174. — DOI: 10.4296/cwrj3002159.

Isaev A. V., Demakov Yu. P. *and* Sharafutdinov R. N. Patterns of Changes in the Granulometric Composition of Alluvial Soils During the Development of River Floodplains // Bulletin of the Volga State Technological University. Series: Forest. Ecology. Nature Management. — 2022. — Vol. 2, no. 54. — P. 80–93. — DOI: 10.25686/2306-2827.2022.2.80.

Kleinschmidt Associates. The Place for HEC-RAS Modelers. — 2020. — (visited on 2023/11/17). https://www.kleinschmidtgroup.com/raspost/hec-ras-6-0-beta-is-now-available/.

Kleshchenkov A. V., Gerasyuk V. S., Kulygin V. V., *et al.* Suspended Matter of the Water from the Tsimlyansk Reservoir to the Taganrog Bay in the Period of Long Low Water in 2006-2020 // Science of the South of Russia. — 2023. — No. 1. — P. 29–39. — DOI: 10.7868/25000640230104.

Kleshchenkov A. V. *and* Sheverdyaev I. V. Numerical Study of the Conditions for Sedimentation of Suspended Matter in the Don Delta during Surges // Fifth Vinogradov Readings. Hydrology in an Era of Change: Collection of Reports of the International Scientific Conference in Memory of the Outstanding Russian Scientist Yuri Borisovich Vinogradov, Saint Petersburg, October 5-14, 2023. — St. Petersburg : VVM, 2023. — P. 257–262. — EDN: JIBVDI.

Likhtanskaya N., Berdnikov S. *and* Kleshchenkov A. Solid runoff of the Don River and suspended matter flow into the delta during surges: statistical modeling and comparison in the low water period // Russian Journal of Earth Sciences. — 2023. — Vol. 23, no. 4. — P. 1–15. — DOI: 10.2205/2023es000856.

Lukashin V. N., Klyuvitkin A. A., Lisitzin A. P., *et al.* The MSL-110 small sediment trap // Oceanology. — 2011. — Vol. 51, no. 4. — P. 699–703. — DOI: 10.1134/s0001437011040126.

Matishov G. G., Moskovets A. Yu., Inzhebeikin1 Yu. I., *et al.* Stages of Construction of Dams, Embankments, and Canals and the Transformation of River Runoff in the Front-Delta of the Don (the 18th-21st Centuries) // Science in the South of Russia. — 2019. — No. 4. — P. 46–54. — DOI: 10.7868/S25001640190406.

Mikhailov V. N. River mouths of Russia and adjacent countries: past, present and future. — Moscow : GEOS, 1997. — P. 413.

Pandey S., Rao A. D. *and* Haldar R. Modeling of Coastal Inundation in Response to a Tropical Cyclone Using a Coupled Hydraulic HEC-RAS and ADCIRC Model // Journal of Geophysical Research: Oceans. — 2021. — Vol. 126, no. 7. — DOI: 10.1029/2020JC016810.

Sheverdyaev I. V., Berdnikov S. V. *and* Kleshchenkov A. V. HEC-RAS Using for Hydrologic Regime Modeling on the Don's Delta // Ecology. Economy. Series: Informatics. System analysis and mathematical modeling of ecological and economic systems. — 2017. — Vol. 1, no. 2. — P. 113–122. — EDN: ZNARIL.

Sheverdyaev I. V. *and* Kleschenkov A. V. Revealing the Surge Phenomena Contribution of the Heavy Metals Inflow to the River Don Delta // Physical Oceanography. — 2020. — Vol. 27, no. 5. — DOI: 10.22449/1573-160X-2020-5-535-546.

Syvitski J. P. M. *and* Milliman J. D. Geology, Geography, and Humans Battle for Dominance over the Delivery of Fluvial Sediment to the Coastal Ocean // The Journal of Geology. — 2007. — Vol. 115, no. 1. — P. 1–19. — DOI: 10.1086/509246.

Tessler Z. D., Vörösmarty C. J., Grossberg M., *et al.* Profiling risk and sustainability in coastal deltas of the world // Science. — 2015. — Vol. 349, no. 6248. — P. 638–643. — DOI: 10.1126/science.aab3574.

Venevsky S., Berdnikov S., Day J. W., *et al.* Don River Delta Hydrological and Geomorphological Transformation Under Anthropogenic and Natural Factors: Century and Decadal Perspectives // Elsevier BV. Preprint. — 2023. — DOI: 10.2139/ssrn.4474057.

Venevsky S., Berdnikov S., Sorokina V., *et al.* Coastal Deltas of Big Rivers as Synergetic Transformation Elements of the Earth System-(An Example of the Don River Delta) // New Prospects in Environmental Geosciences and Hydrogeosciences. — Springer International Publishing, 2022. — P. 79–81. — DOI: 10.1007/978-3-030-72543-3_18.

Wang X., Guo Y. *and* Ren J. The Coupling Effect of Flood Discharge and Storm Surge on Extreme Flood Stages: A Case Study in the Pearl River Delta, South China // International Journal of Disaster Risk Science. — 2021. — Vol. 12, no. 4. — P. 1–15. — DOI: 10.1007/s13753-021-00355-5.

Wolters M. L. *and* Kuenzer C. Vulnerability assessments of coastal river deltas - categorization and review // Journal of Coastal Conservation. — 2015. — Vol. 19, no. 3. — P. 345–368. — DOI: 10.1007/s11852-015-0396-6.

Zhang W., Jia Q. *and* Chen X. Numerical Simulation of Flow and Suspended Sediment Transport in the Distributary Channel Networks // Journal of Applied Mathematics. — 2014. — Vol. 2014. — P. 1–9. — DOI: 10.1155/2014/948731.